université PARIS-SACLAY

Advancement of Laser-Induced Incandescence for simultaneous estimation of soot volume fraction, maturity, primary particle size, and gas temperature

Développement de l'incandescence induite par laser pour l'estimation simultanée de la fraction volumique de suie, de la maturité des suies, de la taille des particules primaires des suies et de la température du gaz

Thèse de doctorat de l'université Paris-Saclay

École doctorale n°579, Sciences Mécaniques et Energétiques, Matériaux et Géosciences (SMEMaG)
Spécialité de doctorat: Energétique
Graduate School : Sciences de l'ingénierie et des systèmes. Référent : CentraleSupélec

Thèse préparée au **Laboratoire EM2C** (Université Paris-Saclay, CNRS, CentraleSupélec), sous la direction de **Benedetta FRANZELLI**, Chargée de recherche, et du co-encadrement de **Christopher BETRANCOURT**, Maître de conférence

Thèse soutenue à Paris-Saclay, le 31 janvier 2025, par

Geoffrey GUY

Composition du jury

Membres du jury avec voix délibérative

Thomas PINO Directeur de recherche, Institut des Sciences Moléculaires d'Orsay, CNRS, France	Président
Francesca MIGLIORINI Chargée de recherche, CNR-ICMATE, Milan, Italie	Rapporteur & Examinatrice
Xavier MERCIER Directeur de recherche, Laboratoire PC2A, Université de Lille, CNRS, France	Rapporteur & Examinateur
Cornelia IRIMIEA Ingénieure de recherche, ONERA, France	Examinatrice
Jérôme YON Professeur, Laboratoire CORIA, Université de Normandie, CNRS, INSA Rouen, France	Examinateur

THESE DE DOCTORAT

NNT : 2025UPAST007

université PARIS-SACLAY

ÉCOLE DOCTORALE
Sciences mécaniques et énergétiques, matériaux et géosciences (SMEMAG)

Titre: Développement de l'incandescence induite par laser pour l'estimation simultanée de la fraction volumique de suie, de la maturité des suies, de la taille des particules primaires des suies et de la température du gaz

Mots clés: diagnostics optiques, incandescence induite par laser, fonction d'absorption, fraction volumique des suies, temperature de suies, taille des particules primaires de suies

Résumé: Les particules de suie sont des particules carbonées formées par la combustion incomplète de combustibles contenant du carbone. Elles sont une agrégation de particules plus petites - les particules primaires de suie - d'une taille typique de 3 à 50 nm. Les particules de suie sont des polluants atmosphériques nocifs qui ont un impact significatif sur la santé humaine. En raison de leurs effets néfastes, les réglementations en matière d'émissions deviennent de plus en plus strictes. Pour réduire efficacement les émissions de suie, la recherche fondamentale est essentielle pour mieux comprendre les processus de formation de la suie et améliorer notre connaissance de leurs propriétés. Les travaux expérimentaux jouent un rôle essentiel dans l'amélioration de notre compréhension des processus de formation de la suie et dans la validation des modèles de formation de la suie.
La technique d'incandescence induite par laser (LII), qui est au cœur de cette thèse, est un diagnostic optique permettant de mesurer *in situ* les particules de suie dans les flammes. La LII permet de mesurer la température des suies, la fraction volumique de suie f_v, le diamètre des particules primaires de suie d_p, et la fonction d'absorption des suies $E(m_\lambda)$, qui caractérise l'émission des particules et est liée à leur maturité.
Reconnaissant que les flammes brûlent principalement dans le régime turbulent, une technique basée sur la LII a été développée pour mesurer $E(m_\lambda)$ et la température du gaz T_0 dans des conditions de flammes turbulentes : la technique de la LII à pulses séparés (SP-LII). Une analyse numérique de la technique a été réalisée pour évaluer ses performances et ses incertitudes. Dans un premier temps, la faisabilité de la technique SP-LII a été démontrée en considérant des flammes de diffusion laminaire et des mesures ponctuelles. Pour ce faire, un banc d'essai expérimental a été conçu et mis en œuvre. Des mesures quantitatives de $E(m_\lambda)$ et T_0 ont été effectuées, complétées par des mesures de f_v et d_p via la LII auto-compensée et la LII résolue en temps, respectivement. Ces quatre quantités ont été dérivées uniquement à partir des mesures LII, ce qui a permis de minimiser le besoin de diagnostics supplémentaires et de réduire la complexité et le coût de la campagne expérimentale.
Dans un deuxième temps, le banc expérimental a été modifié pour effectuer des mesures 2D de $E(m_\lambda)$, T_0, f_v, et d_p. Ces mesures ont été effectuées dans une flamme de diffusion laminaire de référence afin de valider la stratégie proposée par rapport aux données de la littérature existante. Un effort particulier a été fait pour améliorer la précision de la caractérisation des suies, notamment en réduisant la dépendance des estimations de f_v par rapport à la fluence laser.
Enfin, ce travail a exploré les effets de l'hydrogène sur la formation de suie en comparant une flamme d'éthylène de référence à une flamme d'hydrogène-éthylène, en se concentrant sur les différences de f_v, d_p, et $E(m_\lambda)$. Les résultats expérimentaux ont ensuite été utilisés pour valider un modèle de suie détaillé en comparant les résultats numériques à la nouvelle base de données expérimentale.
Cette thèse démontre que quatre quantités clé pour l'étude des suies peuvent être mesurées dans des flammes laminaires à l'aide d'un seul dispositif expérimental, qui pourrait être étendu à des applications dans des conditions de flammes turbulentes.

Title: Advancement of Laser-Induced Incandescence for simultaneous estimation of soot volume fraction, maturity, primary particle size, and gas temperature

Keywords: optical diagnostics, laser-induced incandescence, absorption function, soot volume fraction, soot temperature, primary particle size

Abstract: Soot particles are carbonaceous particles formed from the incomplete combustion of carbon-containing fuel species. They are an aggregation of smaller particles -the soot primary particles- having a typical size of$\sim$3-50 nm. Soot particles are a harmful atmospheric pollutant with significant impacts on human health. Due to their adverse effects, emissions regulations are becoming increasingly strict. To effectively reduce soot emissions, fundamental research is essential to understand the soot formation processes better and to improve our knowledge of their properties. Experimental works play a critical role in enhancing our understanding of soot formation processes and validating soot formation models. The Laser-Induced Incandescence (LII) technique -the technique at the core of this thesis- is an optical diagnostic allowing for *in-situ* measurements of soot particles in flame. LII allows for the measurement of soot temperature, soot volume fraction f_v, soot primary particle diameter d_p, and soot absorption function $E(m_\lambda)$, which characterises the emission property of the particles and is linked to the particle maturity.
Recognising that flames mainly operate in turbulent regimes, an LII-based technique was developed to measure $E(m_\lambda)$ and the gas temperature T_0 in turbulent flame conditions: the separated-pulses LII (SP-LII) technique. A numerical analysis of the technique was conducted to evaluate its performance and uncertainties.
As a first step, the feasibility of the SP-LII technique has been proven by considering laminar diffusion flames and pointwise measurements. To achieve this, an experimental test bench was designed and implemented. Quantitative measurements of $E(m_\lambda)$ and T_0 were carried out, complemented by f_v and d_p measurements via auto-compensated LII and time-resolved LII, respectively. All four quantities were derived only from LII measurements, minimising the need for additional diagnostics and reducing the complexity and cost of the experimental campaign.
In a second step, the experimental system was extended to perform 2D measurements of $E(m_\lambda)$, T_0, f_v, and d_p. These measurements were conducted in a reference laminar diffusion flame to validate the proposed strategy against existing literature data. Particular effort was made to improve the accuracy of soot characterisation, especially in reducing the dependence on the laser fluence of f_v estimations.
Finally, this work explored the effects of hydrogen on soot formation by comparing the reference ethylene flame to a hydrogen-ethylene flame, focusing on differences in f_v, d_p, and $E(m_\lambda)$. The experimental results were then used to validate a detailed state-of-the-art soot model by comparing the numerical results to the newly produced experimental database.
This thesis demonstrates that four key soot parameters can be measured in laminar flames using a single experimental setup that has the potential to be extended for applications in turbulent flame conditions.

Remerciements

Je voudrais remercier toutes les personnes ayant participé directement ou indirectement à l'accomplissement de cette thèse.

Tout d'abord, je tiens à remercier les membres de mon jury pour avoir accepté de prendre part à l'évaluation de mes travaux, pour avoir lu mon manuscrit et pour avoir participé à ma soutenance. Merci aux rapporteurs Francesca Migliorini et Xavier Mercier qui ont pris le temps de rédiger un rapport sur mon manuscrit, en donnant des commentaires pertinents sur le travail réalisé. Je remercie également les examinateurs Jérôme Yon et Cornelia Irimiea ainsi que Thomas Pino pour avoir accepté de présider le jury.

Ensuite, je voudrais remercier l'équipe encadrante avec Benedetta Franzelli (directrice de thèse) et Christopher Betrancourt (encadrant) pour m'avoir donné l'opportunité de participer à des recherches dans un laboratoire de classe internationale sur un sujet difficile mais intéressant. J'ai particulièrement apprécié la confiance qui m'a été accordée au travers de l'autonomie qui m'a été laissée, ce qui m'a permis de suivre les pistes qui me semblaient intéressantes. J'ai apprécié l'aide apportée, notamment dans la préparation des communications écrites et orales pour les conférences. Les corrections apportées en ont grandement amélioré la qualité. Je tiens particulièrement à remercier Jérôme Bonnety qui, même s'il n'a pas fait partie de l'encadrement de cette thèse, a joué un rôle important dans son déroulement via sa grande expertise technique et sa bienveillance. J'ai vraiment apprécié les échanges que nous avons pu avoir au cours de ma thèse.

Merci également à tout le personnel de l'EM2C sans qui il ne serait pas possible de mener à bien une thèse : Erika, Yannick, Koro, Hubert, Jérôme, Jean Michel, Valérie, Brigitte, Nathalie et Sébastien.

Au laboratoire l'EM2C, nous avons la chance d'avoir un grand nombre de doctorants avec qui il est possible de passer de bons moments. Je tiens donc à remercier les doctorants, je ne vais pas nommer tout le monde car il serait difficile de n'oublier personne. Mais je voudrais remercier en particulier mes co-bureaux, les membres du fameux Bureau Des Légendes pour l'excellente ambiance : Luc, Valentin, Roxane, Julien, Frédéric, Jules, RENO, Quentin, PA, Touf-Touf et bien sûr Yu-Yu, mais aussi les nouveaux membres Natacha, Audrey et Tobias, qui assureront la relève du BDL. On gardera je pense tous de (très) bons souvenirs du temps passé au BDL. Je voudrais aussi remercier un autre groupe de doctorants avec qui j'ai passé les meilleurs moments de ces 3 dernières années : les grimpeurs de l'EM2C avec Victorien, Cyrine, RENO, JBTP et les nouveaux grimpeurs Sara, PA et Audrey. Merci aussi aux amis et coloc avec qui j'ai passé de bons moments en dehors du labo : Ludo, François, Julien, Aïoli, Ben, Mathieu, Andry, Gaël, Vincent et Wietze.

Finalement, je voudrais remercier mes deux frères et mes parents notamment pour le soutien apporté. Merci à mes parents pour nous avoir toujours fait confiance et nous avoir laissé choisir notre propre voie.

Contents

I Introduction 12

1 Context and content of the thesis 13

2 Soot particles 18
- **2.1 Definition of a soot** . . . 20
- **2.2 The concept of soot maturity** . . . 20
- **2.3 Soot structure** . . . 21
  - *2.3.1 Soot size* . . . 21
  - *2.3.2 Soot morphology* . . . 22
  - *2.3.3 Soot internal structure* . . . 22
- **2.4 Environmental and health risks** . . . 23
  - *2.4.1 Health concerns* . . . 23
  - *2.4.2 Environmental effects* . . . 25
- **2.5 Soot formation and evolution** . . . 26
  - *2.5.1 Gaseous phase: soot precursors formation* . . . 27
  - *2.5.2 Condensate phase: soot formation and evolution* . . . 29
  - *2.5.3 Which conditions favour soot production?* . . . 32
- **2.6 Important soot properties for this thesis** . . . 33
  - *2.6.1 Carbon-to-hydrogen ratio* $\frac{C}{H}$ . . . 33
  - *2.6.2 Soot absorption function* $E(m_\lambda)$ . . . 34
  - *2.6.3 Volumetric heat capacity* V_c . . . 37

II The laser-induced incandescence technique 38

3 The laser-induced incandescence principle 39
- **3.1 Laser-induced incandescence (LII)** . . . 41
  - *3.1.1 Principle of LII* . . . 41
  - *3.1.2 A typical LII setup* . . . 41
  - *3.1.3 Expression of the soot incandescence signal* . . . 43
- **3.2 Modelling the LII process** . . . 45
  - *3.2.1 Physical processes affecting the soot particles during LII* . . . 45
  - *3.2.2 The energy balance equation* . . . 46
- **3.3 LII codes** . . . 49
  - *3.3.1 The LII code used in this work* . . . 49
  - *3.3.2 What are LII codes used for?* . . . 50
- **3.4 Computation of soot temperature, concentration and size from the incandescence signal** . . . 50
  - *3.4.1 Expression of the incandescence signal collected by optical sensors* . . . 50
  - *3.4.2 Soot temperature* T *measurements* . . . 51
  - *3.4.3 Soot volume fraction* f_v *measurements* . . . 53
  - *3.4.4 Soot primary particle diameter* d_p *measurements* . . . 55
- **3.5 Advantages of the LII experimental technique** . . . 59

4 The Separated Pulses Laser-Induced Incandescence technique (SP-LII) 61

4.1 Literature review: how to obtain the soot absorption function $E(m_\lambda)$? . . . 63
4.1.1 Ex-situ techniques . . . 63
4.1.2 In-situ techniques . . . 63
4.1.3 Why a new technique? . . . 65
4.2 The Separated Pulses Laser-Induced Incandescence technique (SP-LII) . . . 65
4.2.1 Reference input parameters for the LII code . . . 66
4.2.2 Principle of the SP-LII technique . . . 66
4.2.3 The SP-LII technique for single-shot measurements . . . 67
4.2.4 Advantages and drawbacks of the SP-LII . . . 71
4.3 Post-processing of the data: computation of $E(m_\lambda)$ and T_0 . . . 71
4.3.1 The absorption model (AM) . . . 72
4.3.2 The look-up table (LUT) . . . 73
4.4 Theoretical evaluation of the SP-LII technique . . . 75
4.4.1 Procedure for the theoretical evaluation of the SP-LII technique . . . 75
4.4.2 Performance of the technique . . . 76
4.4.3 Uncertainty analysis . . . 77
4.4.4 Effect of an error on the estimation of the peak soot temperature . . . 80
4.5 Conclusion . . . 82

III Experimental application: validation and limits of the SP-LII technique 84

5 Pointwise measurements in a CH_4/air laminar diffusion flame 85
5.1 Experimental setup . . . 87
5.2 Improving the quality of low LII signals . . . 89
5.3 First application of the SP-LII in a laminar diffusion CH_4/air flame . . . 90
5.3.1 Selection of the laser fluence . . . 90
5.3.2 Axial evolution of the soot absorption function $E(m_\lambda)$ and gas temperature T_0 . . . 93
5.4 Cartography of $E(m_\lambda)$, T_0, f_v, and d_p . . . 100
5.4.1 Soot absorption function $E(m_\lambda)$ and gas temperature T_0 . . . 100
5.4.2 Soot volume fraction f_v . . . 102
5.4.3 Soot primary particle diameter d_p . . . 107
5.5 Summary on the dependence to T_M of d_p and f_v . . . 113
5.6 Conclusion . . . 113

6 2D measurements in a C_2H_4+N_2/air reference flame 115
6.1 Experimental setup . . . 117
6.1.1 Setup . . . 117
6.1.2 Data acquisition . . . 118
6.2 From pointwise measurements (0D) to 2D spatially resolved measurements . . . 119
6.2.1 Image pre-processing . . . 119
6.2.2 Temporal resolution: selection of the gate delay . . . 122
6.2.3 Comparison with photomultiplier tubes . . . 124
6.3 Guidelines and data correction methodology . . . 126
6.3.1 Selection of the laser fluence . . . 126
6.3.2 Background subtraction: impact, correction procedure and application . . . 135
6.4 Benchmark with the literature data . . . 144
6.4.1 Soot absorption function $E(m_\lambda)$ . . . 145
6.4.2 Gas temperature T_0 . . . 147
6.4.3 Soot primary particle diameter d_p . . . 149
6.4.4 Soot fraction volume f_v . . . 151
6.5 Conclusion . . . 154

IV Insight on soot formation in $C_2H_4 - H_2$ flames 156

7 Effect on soot production of blending H_2 to C_2H_4 157
7.1 Dilution of carbonaceous fuels . . . 159
7.1.1 Why hydrogen blending? . . . 159
7.1.2 Effects of blending hydrocarbons fuels . . . 159
7.1.3 Hydrogen blends in literature . . . 160
7.1.4 Objectives of the present work . . . 161
7.2 Experimental and numerical setup . . . 162
7.2.1 Flame conditions . . . 162
7.2.2 Experimental setup . . . 162
7.2.3 Numerical setup . . . 162
7.3 Experimental comparison of the reference and H_2-blended flames . . . 163
7.3.1 Flame natural emission . . . 164
7.3.2 LII signal . . . 165
7.3.3 Soot absorption function $E(m_\lambda)$ . . . 166
7.3.4 Gas temperature T_0 . . . 168
7.3.5 Soot volume fraction f_v . . . 170
7.3.6 Soot primary particle diameter d_p . . . 172
7.4 Comparison of the numerical results with the experimental profiles of f_v, T_0, and $E(m_\lambda)$ . . . 174
7.4.1 Comparison of the gas temperature T_0 . . . 175
7.4.2 Comparison of f_v . . . 176
7.4.3 Comparison of $E(m_\lambda)$ . . . 178
7.5 Conclusion . . . 180

8 Conclusions and perspectives 182
8.1 Conclusions . . . 182
8.2 Perspectives . . . 183

A Prerequisites for radiative heat transfer 185
A.1 Monochromatic directional flux . . . 185
A.2 Monochromatic surface flux . . . 186
A.3 Radiative fluxes of simple surfaces . . . 186

B Expression of the collected incandescence signal 188

C Calibration of the optical system 190
C.1 Calibration source . . . 190
C.2 Calibration procedure . . . 191
C.2.1 Expression of the signal collected during calibration . . . 191
C.2.2 Computation of the calibration constant $C_{calib,\lambda}$ . . . 191

D Spectroscopic measurements 193
D.1 Experimental setup . . . 193
D.2 Apparition of Swan bands . . . 194
D.3 Temperature measurements from spectral fit . . . 196

E Gas temperature by emission pyrometry 198

F RANSAC algorithm for the automatic computation of $E(m_\lambda)$, and T_0 201

G Polydispersion of the temperature of laser-heated soot in the probe volume 203
G.1 Numerical setup . . . 203

G.2 Polydispersion of laser fluence: top-hat non-uniformity . . . 204
G.3 Polydispersion of the soot absorption function in the probe volume . . . 207
G.4 Discussion on the possibility of attributing the f_v anomaly to temperature inhomogeneities . . . 208

H Computation of the carbon-to-hydrogen ratio **210**

List of Figures

1.1 Evolution of global energy supply by source (1990-2021). The red line indicates the total energy supply in exajoules (10^{18} J). Data from the International Energy Agency [1]. . . . 13
1.2 Historical fossil fuel consumption since the year 2000 and projected future consumption up to 2050 under the Stated Policies Scenario (STEPS). Data from the 2023 World Energy Outlook report of the International Energy Agency [2]. . . . 14

2.1 Scheme illustrating the evolution of some soot properties with the soot maturation along the flame height above the burner and residence time t_{res}. . . . 20
2.2 Comparison of the size of soot particles with microscopic objects. Images are taken from the public domain and from references [57–62]. . . . 21
2.3 Image of a soot particle taken with a Transmission Electron Microscope (TEM). Yellow arrows point to the building blocks of the soot aggregate: the soot primary particles. Adapted from [61]. . . . 22
2.4 TEM images of soot particles with different fractal dimensions: 1.8 and 2.5 from left to right, respectively. Images are taken from [66]. . . . 22
2.5 Schematic of the internal structure of a diesel soot particle. Image taken from [69]. . . . 23
2.6 High-resolution TEM images of soot particles from methane (a-d) and ethylene (e-h) flames. Figures (a, c, e, g) represent young soot, and figures (b, d, f, h) represent mature soot. Adapted from [70]. . . . 23
2.7 Scheme illustrating the penetration of particles in the body according to their size: particles above 10 μm deposit in the nasopharynx, PM_{10} in the upper respiratory region, $PM_{2.5}$ reach the bronchia, and $PM_{0.1}$ penetrate the alveoli, potentially reaching other organs via the bloodstream. Adapted from [8]. . . . 24
2.8 Illustration of the steps of the soot formation process. Adapted from [52]. . . . 27
2.9 PAHs viewed with an Atomic Force Microscope. Image taken from [58]. . . . 29
2.10 Schematic illustrating various soot inception mechanisms from [87]. Acetylene, polyyne, and polyaromatic pathways fall under the chemical inception category. Image taken from [87]. . . . 30
2.11 TEM images of soot primary particles. The first image represents a primary particle that has grown from a single core, and the second image represents a primary particle resulting from the merging of two incipient particles (pointed by red arrows). Images are taken from [60, 104]. . . . 31
2.12 TEM images of soot particles at varying burn-off stages: 0%, 40%, and 75% (left to right). Images taken from [107]. . . . 32
2.13 Distributions of soot particle mobility diameters measured using a scanning mobility particle sizer (SMPS) in a premixed C_2H_4+O_2+Ar flame. Different colours indicate various HABs. Adapted from [108]. . . . 32
2.14 Carbon-to-hydrogen ratio versus the HAB in premixed methane flames. Blue and red circles correspond to different injection velocity of the mixture. Data taken from [122]. . . . 34
2.15 (a): Soot absorption function at 1064 nm versus the HAB in laminar premixed flames. Results 1 and 2 correspond to C_2H_4+air flames [54, 131], and 3 to a CH_4+air flame [141]. The solid line is the best fit for the data. Figure taken from [54]. (b): Soot absorption function at 810 nm in a C_2H_4/air laminar diffusion flame. Figure taken from [51]. . . . 35
2.16 (a) and (b): Wavelength dependence of the soot absorption function. In figure (b), OC and TC stand for organic carbon and total carbon, respectively. Figures are taken from [50, 148]. . . . 36

3.1 Schematic of a typical LII setup. It includes a burner that generates a flame containing soot particles, a pulsed laser for heating the soot particles, and an optical sensor for collecting the LII signal. . . . 42

3.2 Directional spectral radiance for a black body (solid line, left axis) and for a soot particle (dashed line, right axis) as a function of wavelength. Spectral radiances are shown for temperatures between 2000 and 4000 K. The directional spectral radiance of a soot particle $q_{\lambda_{em}}\pi I_{BB}$ is computed considering a wavelength-independent soot absorption function $E(m_\lambda)$ = 0.4, and a particle diameter of d_p = 20 nm. Figure (b) presents the same data as figure (a) but on a logarithmic scale. 44
3.3 Scheme of a soot particle and the interactions it can have with its environment during an LII experiment. Image taken from [190]. 46
3.4 Emission spectra obtained 5 ns after irradiating soot particles with a 1064 nm laser beam with a laser fluence of (a): 300 to 800 mJ/^{2}, and (b): 3500 mJ/cm^2. Images taken from [212]. 52
3.5 Example of LII signal collected at 578 nm tube as a function of laser fluence. Soot particles are generated from a C_2H_4+N_2/air laminar diffusion flame using a 1064 nm laser. Data were obtained with the setup described in Section 5.1. 54
3.6 $ln\left(\frac{T-T_0}{T_M-T_0}\right)$ determined experimentally at different instants after laser heating (solid lines), and fit of the experimental data (dashed lines). Colours correspond to different flame positions. The soot particles are generated by a C_2H_4+N_2/air laminar diffusion flame. Data were obtained using the setup described in Section 6.1 and will be presented in Chapter 6. 57
3.7 Temporal evolution of LII signals collected at 578 nm with a photomultiplier tube (solid lines). Dashed lines give the fit to the experimental data, and the corresponding soot primary particle diameters are given in the legend. Colours correspond to different flame positions. The soot particles are generated by a CH_4/air laminar diffusion flame. Data were obtained using the setup described in Section 6.1 and will be presented in Chapter 6. 58
3.8 (a) Normalised numerically synthesised LII signal decay (blue), and function fitted with Eq. (3.29) to this LII signal (red). (b): Sensitivity of d_p estimation to a $\pm$ 10% uncertainty in the parameters: T_0, T_M, λ, α, ρc, M_{gas}, and γ_{gas}. 59

4.1 Experimentally determined T_M for different laser fluences (circles symbols linked by solid lines) and fit of the experimental data in the linear regime (dashed lines). Colours correspond to different flame positions. The soot particles are generated by a C_2H_4+N_2/air laminar diffusion flame. 65
4.2 (a) Peak soot temperature as a function of laser fluence for three different values of the absorption function: $E(m_\lambda)$ = 0.2 (green), 0.3 (blue) and 0.4 (red). The dashed lines represent the initial slope of the curves. The horizontal black line represents the separation between the linear and sublimation regimes. (b): Peak temperature of the soot particles as a function of laser fluence for four different values of soot primary particle diameter: d_p = 1 (green), 10 (blue), 20 (red) and 50 nm (black). 67
4.3 Scheme of the experimental setup for the SP-LII technique for measurements in turbulent flames. 68
4.4 Temporal evolution of the soot particle temperature (left axis, solid blue line) and the power absorbed by the soot particle (right axis, dashed red line) after being heated by two laser pulses separated by 3 μs. 68
4.5 Cooling time as a function of d_p for a thermal accommodation coefficient α of 0.1 ($\star$), 0.3 ($\times$), 0.5 (dotted line), 0.7 (dashed line) and 0.9 (solid line). The cooling time is defined as the time elapsed between $T = T_{M_1}$ and $T = T_{0_{ref}} + 10$ K = 1870 K. 69
4.6 Estimations with the AM method of deviations of $E(m_\lambda)$ (left axis, in blue) and T_0 (right axis, in pink) as a function of F_2. The symbols represent the results obtained when different loss mechanisms are included in the energy balance equation: no losses ($\diamond$), radiation losses only ($\times$), radiation and conduction losses ($\bullet$), and the combination of radiation, conduction, and sublimation losses (solid lines). 72
4.7 Inverse of Ξ (define by Eq.(4.8)) versus $E(m_\lambda)$ and T_0. The white dashed lines help to visualise the low error regions for the two pulses considered alone. 74
4.8 Scheme describing the SP-LII performance and uncertainty analysis procedure. The Ω sets contain: $\Omega = \{F_1, F_2, \rho, d_p, \alpha, \beta\}$. . 75
4.9 Deviations in $E(m_\lambda)$ (a), and T_0 (b) obtained with the AM (solid lines) and the LUT methods (dotted line) as a function of F_2. The symbols and colours correspond to different F_1: 50 (green $\times$), 100 (blue $\star$) and 150 mJ/cm^2 (red +). 76
4.10 Deviations of $E(m_\lambda)$ (left axis, in blue) and T_0 (right axis, in pink) obtained with the AM (solid lines) and the LUT methods (dotted line) as a function of d_p. 77
4.11 Deviations of $E(m_\lambda)$ (left axis, in blue) and T_0 (right axis, in pink) as a function of the density used for the post-processing. Results obtained with the AM and LUT methods are plotted with solid and dotted lines, respectively. The vertical black dashed lines represent the reference density. 78
4.12 Deviations of $E(m_\lambda)$ (left axis, in blue) and T_0 (right axis, in pink) as a function of the primary particle diameter used for the post-processing. Results obtained with the AM and LUT methods are plotted with solid and dotted lines, respectively. The vertical black dashed lines represent the reference primary particle diameter. 78
4.13 Deviations of $E(m_\lambda)$ (left axis, in blue) and T_0 (right axis, in pink). The X-axis represents α^{PP}, the thermal accommodation coefficient used for the post-processing of the LUT method. The symbols differentiate the value of the soot primary particle diameter used for the data generation: d_p^{SIM}: 1 ($\diamond$), 26 ($\star$) and 41 nm ($\times$). The vertical black dashed line represents the reference thermal accommodation coefficient $\alpha_{ref} = 0.3$. 79
4.14 Deviations of $E(m_\lambda)$ (a) and T_0 (b) as a function of β^{SIM}: the mass accommodation coefficient used for the data generation. The deviations are represented for the AM and LUT methods in solid and dotted lines, respectively. The symbols differentiate the results of the LUT method obtained with the different assumptions on the value of β^{PP}: 0 (black), 0.25 (red $\times$), 0.5 (green $\star$) and 1 (blue $\diamond$). 80

4.15 Scheme describing the procedure for the analysis of the impact of peak temperature errors on the estimation of $E(m_\lambda)$ and T_0 with the SP-LII method. The sets Ω contains: $\Omega = \{F_1, F_2, \rho, d_p, \alpha, \beta\}$. 81
4.16 Deviations of $E(m_\lambda)$ (left axis, in blue) and T_0 (right axis, in pink) obtained using the AM method (solid lines) and the LUT method (dotted line) as a function of F_2 when (a): only T_{M_1} is overestimated by 10%, and (b): both T_{M_1} and T_{M_2} are overestimated by 10%. 82

5.1 (a): Scheme of the LII experimental bench. (b): Image of the CH_4/air flame stabilised on the Yale diffusion burner. 87
5.2 Bottom left: normalised profile of the top-hat averaged over 50 laser shots obtained with the beam profiler. Bottom right: horizontal summation of the top-hat profile. Top left: vertical summation of the top-hat profile. Top right: histogram of occurrences of the normalised intensities in the top hat. 88
5.3 Noise from the laser recorded without the flame. The blue and red curves are the noise signals recorded on the oscilloscope channel of the PM1 and PM2, respectively. 89
5.4 (a): LII signals recorded with the PM2 for different flame positions along the flame centreline. (b): LII signals recorded with the PM2 for different flame positions along the flame centreline after the correction procedure for the laser-generated noise. These signals were recorded in the CH_4/air flame with a laser fluence of 105 mJ/cm^2. 90
5.5 (a): Maximum of the LII signal as a function of the laser fluence for five different HAB on the flame's centreline: 29 mm (blue o), 30 mm (red $\times$), 32 mm (black $*$), 34 mm (cyan $\square$) and 36 mm (magenta $\diamondsuit$). (b): Normalised version of figure (a). These curves were obtained at 578 nm, and the curves are similar for the wavelength 716 nm. 91
5.6 Soot peak temperature as a function of the laser fluence for five different HAB along the flame centreline: 29 mm (blue o), 30 mm (red $\times$), 32 mm (black $*$), 34 mm (cyan $\square$) and 36 mm (magenta $\diamondsuit$). The horizontal dashed lines represent the temperature limits of 2600 K and 4000 K. The oblique dashed lines represent linear regressions of the temperature curves in the linear regime. The blue zone represents the fluences compatible with the SP-LII technique for the five HABs. 92
5.7 Maximum of (a): the LII signal and (b): the soot temperature along the flame axis for three different laser fluences: 62 mJ/cm^2 (blue), 106 mJ/cm^2 (red), and 146 mJ/cm^2(black). Figure (a) was obtained using the PMT equipped with a bandpass filter centred on 578 nm, and the curves are similar for the wavelength of 716 nm. 93
5.8 Evolution of (a): $E(m_\lambda)$ and (b): T_0 along the flame centreline for three couple of laser fluences: 64/106 mJ/cm^2 (blue $\circ$), 64/149 mJ/cm^2 (red $\times$) and 106/149 mJ/cm^2 (black $*$). The solid lines represent the estimations obtained using the AM method, while the dotted lines are for the LUT method for β = 0. 95
5.9 Evolution of (a): $E(m_\lambda)$ and (b): T_0 along the flame centreline for three couple of laser fluences: 64/106 mJ/cm^2 (blue $\circ$), 64/149 mJ/cm^2 (red $\times$) and 106/149 mJ/cm^2 (black $*$). The solid lines represent the estimations obtained using the AM method, while the dotted lines are for the LUT method for β = 0.2. 96
5.10 Evolution of (a): $E(m_\lambda)$ and (b): T_0 along the flame centreline for three couple of laser fluences: 64/106 mJ/cm^2 (blue $\circ$), 64/149 mJ/cm^2 (red $\times$) and 106/149 mJ/cm^2 (black $*$). The solid lines represent the estimations obtained using the AM method, while the dotted lines are for the LUT method for β = 0.13. 97
5.11 (a): $E(m_\lambda)$, and (b): T_0 along the flame centreline estimated with the AM method for three couple of laser fluences: couple 1 (blue $\circ$), couple 2 (red $\times$) and couple 3 (black $*$). Estimated with the linear regression method are given by the black dashed line. 98
5.12 $E(m_\lambda)$ (a), and T_0 (b) along the flame centreline (red $\circ$). The red-shaded region represents the +15% and -1% uncertainties on $E(m_\lambda)$ and T_0, respectively, due to the effect of d_p on the conduction losses. 99
5.13 (a): $E(m_\lambda)$ and (b): T_0 along the flame centreline considering three different values of R_{12}: 0.94 (blue dotted line), 1 (red $\circ$) and 1.3 (black dashed line). The blue-shaded region between the dotted and dashed lines represents the uncertainty regions due to the uncertainty on R_{12}. 100
5.14 Cartography of (a): $E(m_\lambda)$ at λ = 1064 nm and (b): T_0. The size of the coloured disks is representative of the collection surface of 375 μm diameter of the collection system. 101
5.15 Evolution of f_v along the flame axis. The blue and red curves represent the estimations based on the LII signal at 578 and 716 nm, respectively. Both use the $E(m_\lambda)$ estimation given by the SP-LII. The black curve is obtained using the LII signal at 578 nm and assuming a uniform $E(m_\lambda)$ of 0.39. Results are obtained for a fluence of 106 mJ/cm^2. 103
5.16 Evolution of f_v for five HABs along the flame axis, versus (a): the laser fluence, and (b): the peak soot temperature. 104
5.17 (a): Normalised estimation of f_v at HAB = 32 mm (in blue) used to create the function to correct the temperature dependence of f_v (red). (b): Estimations of normalised f_v versus peak soot temperature after correction for temperature dependence for five HABs along the flame axis. 105
5.18 Evolution of f_v along the flame axis for the three selected laser fluences: F_1 = $\sim$65 mJ/cm^2 (blue), F_2 = $\sim$105 mJ/cm^2 (red), and F_3 = $\sim$150 mJ/cm^2 (black). Solid and dashed lines correspond to data corrected and uncorrected for T_M, respectively. The absorption function used to compute f_v is the distribution obtained with the SP-LII. 105
5.19 Cartography of f_v computed assuming (a): the varying distribution of $E(m_\lambda)$ of Fig. 5.14a, and (b): a uniform $E(m_\lambda)$ = 0.39. Figure (c) corresponds to the relative difference between (b) and (a): $\frac{f_v(E(m_\lambda)=0.39)-f_v}{f_v}$. f_v is computed from the LII signal collected at 578 nm. The data are obtained for a fluence of 106 mJ/cm^2 and are corrected for the peak temperature dependence. 106

5.20 (a): Normalised LII signal decay at various HAB along the flame axis. (b): Normalised LII signal decay at HAB = 28, 32, and 36 mm, with corresponding fits using Eq. (3.29), and assuming T_0 as determined by SP-LII. The laser fluence is 105 mJ/cm^2, and the detection wavelength is 578 nm. 108
5.21 Evolution of d_p along the flame axis. The blue and red curves represent the estimations based on the LII signal at 578 and 716 nm, respectively. Both use the T_0 estimation given by the SP-LII. The varying grey curves represent the LII decay at 578 nm, assuming uniform T_0 values of 1600 K, 1800 K, and 2000 K, with the shade darkening as the temperature increases. Results are obtained for a fluence of 106 mJ/cm^2. 109
5.22 Evolution of d_p, for five HABs along the flame axis, versus (a): the laser fluence, and (b): the peak soot temperature. 110
5.23 (a): Normalised estimation of d_p at HAB = 30 mm (in blue) used to create the function to correct the temperature dependence of d_p (red). (b): Normalised d_p versus peak temperature after correction for temperature dependence for five HABs along the flame axis. 111
5.24 Evolution of d_p along the flame axis for the three selected laser fluences: F_1 = ∼65 mJ/cm^2 (blue), F_2 = ∼105 mJ/cm^2 (red), and F_3 = ∼150 mJ/cm^2 (black). Solid and dashed lines correspond to data corrected and uncorrected for T_M, respectively. A uniform value of T_0 = 1800 K was assumed to compute d_p. 111
5.25 Cartography of d_p computed assuming (a): the varying distribution of T_0 of Fig. 5.14b obtained with the SP-LII, and (b): a uniform T_0 = 1800 K. d_p is computed from the LII signal decay obtained at 578 nm. The data are obtained for a fluence of 106 mJ/cm^2 and are corrected for the peak temperature dependence. 112

6.1 (a): Image of the C_2H_4+N_2/air flame stabilised on the Yale diffusion burner. (b): Scheme of the 2C-LII experimental bench. . . 117
6.2 LII signal recorded at (a): 578 nm and at (b): 716 nm for a laser fluence of ∼55 mJ/cm^2. The background was subtracted from the LII signal. Red arrays in figure (a) show the reference positions selected in this chapter. 118
6.3 Calibration images for both cameras. The top image is for the camera 1 (578 nm), and the bottom one is for the camera 2 (716 nm). The intensity is given in W/sr/m^2. 120
6.4 (a): LII signal recorded with at 578 nm, for a laser fluence of ∼100 mJ/cm^2 at HAB = 30 mm. The top image represents the raw signal (background subtracted), while the bottom image is after the flatfield correction. (b): Radial evolution of the raw and flatfield corrected LII signals (normalised) for a single row of pixels of image (a). 121
6.5 Ratio of LII signals at wavelengths 578 and 716 nm before (top image) and after the application of the alignment procedure (bottom image), for a laser fluence of ∼100 mJ/cm^2 at HAB = 30 mm. 122
6.6 (a): Raw image of the LII signal recorded at 578 nm at a HAB of 28 mm (top image), and corresponding temperature (bottom image). The white squares represent the three positions considered for the gate delay study. Positions 1, 2, and 3 are defined from the left to the right of the image. (b): Normalised LII signals versus time for both camera and for the three positions of figure (a): Position 1 (solid line and ○), 2 (dashed line with ×) and 3 (dotted line with △). 123
6.7 (a): Soot temperature versus gate delay. Temperatures are given for three laser fluences: 40 mJ/cm^2 (blue), 100 mJ/cm^2 (red), 150 mJ/cm^2 (black), and for the three positions of Fig. 6.6a: Position 1 (solid line and ○), 2 (dashed line with ×) and 3 (dotted line with △). (b): Normalised version of (a). The choice of the instant corresponding to GD = 0 is arbitrary and does not impact the results. 123
6.8 (a): Soot temperature versus radial position for multiple laser fluences. Temperatures computed using PMTs and cameras are given by the solid lines with ○ symbols and by the dashed lines, respectively. (b): Soot temperature versus laser fluence for multiple radial positions. Temperatures computed using PMTs and cameras are given by the solid lines with ○ symbols and by the dashed lines with × symbols, respectively. As the collection surface for the PMT is 225 μm, almost 5 times the size of a camera pixel, the estimations of temperature using the data from the cameras have been averaged over 5x5 pixels. 125
6.9 Radial distribution of absorption function (top) and gas temperature (bottom) computed using PMTs (solid line with ○ symbols) and cameras (dashed line). Measurements are done at HAB = 30 mm. 125
6.10 Temperatures for different laser fluences: (a): 25, (b): 55, (c): 100, and (d): 160 mJ/cm^2. For 160 mJ/cm^2, temperatures are not reported in the wings and in some positions in the middle of the flame due to camera saturation: the cameras were set and calibrated for low fluence measurements. 127
6.11 (a): Soot peak temperature versus laser fluence for different pixel locations (solid line with ○). Each colour corresponds to a different pixel location (Fig. 6.2). The dashed lines represent the linear regression obtained considering the temperatures below 3500 K. The horizontal black dashed line represents the temperature limit of 3500 K. Figure (b) is identical to figure (a), but only the three laser fluences 25, 55, and 100 mJ/cm^2 are considered. 128
6.12 Soot absorption function determined with: (a): all measurements, and (b): measurements at 25, 55, and 100 mJ/cm^2. In both cases, only measurements with a temperature below 3500 K are considered. (c): Relative difference between the two maps (b) and (a). Subscripts "SP-LII" and "fit" refer to the data obtained considering three laser fluences and all the fluences, respectively. 130
6.13 Gas temperature determined with: (a): all measurements having a temperature below 3500 K, and (b): measurements at 25, 55, and 100 mJ/cm^2 having a temperature below 3500 K. (c): Relative deviation between the two maps (b) and (a). Subscripts "SP-LII" and "fit" refers to the data obtained considering three laser fluences, and all the fluences, respectively. 131

6.14 $ln\left(\frac{T-T_0}{T_M-T_0}\right)$ versus time after the laser pulse (solid line with ○). Each colour corresponds to a different pixel location (Fig. 6.2). The dashed lines represent the linear regression obtained considering the temperatures below 3500 K. The x symbols represents measurements below 3500 K. 132
6.15 Soot primary particle diameter determined from: (a): all temperature measurements, and (b): measurements having a temperature below 3500 K. (c) and (d): Difference, and relative deviation between the two maps (b) and (a), respectively. Subscripts "T_M < 3500 K" and "all T_M" refers to the d_p obtained considering only T_M below 3500 K, and considering all T_M, respectively. 133
6.16 Soot volume fraction for different laser fluences: (a): 25, (b): 55, (c): 100, and (d): 160 mJ/cm^2. The spatial variation of $E(m_\lambda)$ is accounted for, and is the one computed considering three laser fluence (Fig. 6.12b). In figure (d), estimations are not available on the flame wings due to camera saturation. 134
6.17 Soot volume fraction versus the laser fluence. Each colour corresponds to a different pixel location (Fig. 6.2). 134
6.18 Schemes illustrating the origin of the signal measured in a flame with an optical sensor in the presence of a laser beam (top scheme) and without a laser beam (bottom scheme). 135
6.19 Ratio of the background subtracted (purely LII) signal $S_\lambda^{LII^*}$ to the total incandescence signal S_λ^{LII} as a function of laser-heated soot temperature. Results are given for two wavelengths, 578 nm (blue) and 716 nm (red), and for three local gas temperatures: 1800 K (dotted lines), 2000 K (dashed lines), and 2200 K (solid lines). 137
6.20 (a): Difference between soot temperature T^* estimated by 2C-LII from the background-subtracted signals and true laser-heated soot temperature T. (b): Ratio of the soot volume fraction $f_v{}^*$ estimated considering T^* and the background subtracted signals $S_\lambda^{LII^*}$ to the true soot volume fraction f_v. Results are given versus the true soot temperature and for three local gas temperatures: 1800 K (dotted lines), 2000 K (dashed lines), and 2200 K (solid lines). 138
6.21 Scheme of the correction procedure adopted to account for the background subtraction. 139
6.22 (a): LII signal recorded at 578 nm versus flame radius at HAB = 28 mm. (b): Soot peak temperature computed by 2C-LII versus flame radius at HAB = 28 mm. Colours from cyan to magenta represent the different laser fluences from 25 to 160 mJ/cm^2. The continuous line represents uncorrected data, while the dashed line indicates data that has been corrected for background subtraction. To smooth the visualisation, the pixels have been averaged in super-pixels of 3x3. 140
6.23 Relative difference between corrected and uncorrected (a): absorption function, (b): gas temperature. 141
6.24 Radial evolution of (a): absorption function, and (b): gas temperature for four HAB, from bottom to top: 20, 28, 42, and 48 mm. The continuous and dashed lines are for corrected and uncorrected data, respectively. 141
6.25 (a): Relative difference between corrected and uncorrected soot primary particle diameter. (b): Radial evolution of the soot primary particle diameter for four HABs: 20 mm (cyan), 28 mm (blue), 42 mm (magenta), and 48 mm (red). The continuous and dashed lines are for corrected and uncorrected data, respectively. 142
6.26 (a): Soot volume fraction versus laser fluence for the reference pixel locations. Data corrected for the background subtraction are given in solid lines, while uncorrected ones are in dashed lines. (b): $\frac{f_v}{f_v(\sim 3100K)}$. Each colour corresponds to a different pixel location (Fig. 6.2). 143
6.27 Soot volume fraction estimated by AC-LII for different laser fluences: (a): 25, (b): 55, (c): 100, and (d): 160 mJ/cm^2. The actual $E(m_\lambda)$ spatial distribution was considered. In figure (d), estimations are not available on the flame wings due to camera saturation. Data are corrected for background subtraction. 144
6.28 Axial evolution of the soot absorption function at 1064 nm. 145
6.29 (a): Soot absorption function at 1064 nm. (b): Dispersion exponent α_{disp}. Adapted from [146]. 146
6.30 (a): Axial, and (b): radial evolution of the gas temperature in the 60% reference Yale flame, obtained from LII with the method of [33, 134] in this work (red), and by ratio pyrometry [216] (dashed black lines), and [233] (solid black lines). The radial profiles in figure (b) correspond to HAB = 20, 28, 34, and 48 mm from bottom to top. The axial profile for the data of [233] is not plotted as it is too noisy on the axis. 148
6.31 Gas temperature in the 60% reference Yale flame, obtained (a) with the method of [33, 134] (this work), (b): by ratio pyrometry (from [216]), and (c): by ratio pyrometry (from [233]). 148
6.32 LII Signal at 578 nm for a laser fluence of ∼100 mJ/cm^2 in the reference 60% Yale flame, obtained at (a): 0 ns, (b): 60 ns, and (c): 240 ns after the laser pulse. 149
6.33 Soot primary particle size obtained by TIRE-LII. Figures (a), this work (considering only temperatures below 3500 K), and (b) [233] are obtained assuming a monodispersed soot population, while for the figure (c) [233], a polydisperse soot population was assumed. 150
6.34 Soot primary particle size versus HAB obtained with TIRE-LII in red and blue (this work) and with TEM in black (from [228]). LII measurements of d_p are given along the flame axis in blue and averaged over the flame radius in red. 151
6.35 Soot volume fraction for the reference 60% Yale flame obtained with (a): pyrometry [216], and (b): LII at λ_{laser} = 532 nm with a laser fluence of 300 mJ/cm^2 [194]. (c): LII at λ_{laser} = 1064 nm with a laser fluence of 450 mJ/cm^2 [233]. (d): relative difference of f_v between the AC-LII profile obtained at F = 160 mJ/cm^2 and the pyrometry profile of (a). 152

6.36 (a): Axial, and (b): radial evolution of the soot volume fraction in the 60% reference Yale flame obtained by AC-LII for four laser fluences: 25, 55, 100, and 160 mJ/cm^2 in cyan, blue, magenta, and red, respectively. The radial profiles in figure (b) correspond to HAB = 20, 28, 34, and 48 mm from bottom to top. Results obtained by pyrometry presented in [216] are given by the black dashed lines, LII results obtained at λ_{laser} = 532 nm with a laser fluence of 300 mJ/cm^2 [194] are given by the black dotted lines, and LII at λ_{laser} = 1064 nm with a laser fluence of 450 mJ/cm^2 [233] 153
6.37 (a): Axial, and (b): radial evolution of $f_v E(m_\lambda)$ in the 60% reference Yale flame obtained by AC-LII for four laser fluences: 25, 65, 100, and 160 mJ/cm^2 in cyan, blue, magenta, and red, respectively. The ratio of absorption function was taken equal to 1.085 and corresponds to the assumption that $E(m_\lambda)$ vary as $\lambda^{-0.38}$. The radial profiles in figure (b) correspond to HAB = 20, 28, 34, and 48 mm from bottom to top. Results obtained by pyrometry presented in [216] are given by the black dashed lines. 154

7.1 Mesh of the numerical domain and image of the C_2H_4+N_2/air flame. 163
7.2 Pictures of the reference flame (left) and of the H_2 flame (right). Pictures were obtained using a commercial camera without a filter. 164
7.3 LII signal at 578 nm for a laser fluence of 55 mJ/cm^2 in (a): the reference flame, and (b): the H_2 flame. 165
7.4 Soot absorption function for (a): the reference flame, and (b): the H_2 flame. 166
7.5 (a): Soot absorption function versus the HAB for the reference flame (blue) and the H_2 flame (red). (b): Soot absorption function versus the radius at different HABs (from bottom to top: 20, 22, 28, 40 mm) for the reference flame (blue) and the H_2 flame (red).167
7.6 Histogram of the soot absorption function for the reference flame (blue) and the H_2 flame (red). 167
7.7 (a) and (b): Gas temperature obtained from LII measurements (linear fit method) for the reference flame and the H_2 flame, respectively. (c) and (d): Gas temperature obtained by pyrometry for the reference flame and the H_2 flame, respectively. . . . 168
7.8 (a): Gas temperature versus the HAB for the reference flame (blue) and the H_2 flame (red). Estimations by LII are in dashed lines with circles, while estimations from pyrometry are in solid lines. For the pyrometry data, as the data on the centreline are of poor quality, it is the data for R = -150μm is plotted instead of R = 0 mm. (b): Gas temperature versus the radius at different HABs (from bottom to top: 20, 22, 28, 40 mm), for the reference flame (blue) and for the H_2 flame (red). In order to reduce fluctuation, the axial plot is smothered with a rectangular window of 5 pixels. 169
7.9 Experimental soot volume fraction for (a): the reference flame, and (b): the H_2 flame. The laser fluence is 55 mJ/cm^2. 170
7.10 (a): Soot volume fraction versus the HAB for the reference flame (blue) and the H_2 flame (red). (b): Soot volume fraction versus the radius at different HABs (from bottom to top: 20, 22, 28, 40 mm), for the reference flame (blue) and for the H_2 flame (red). 171
7.11 Radially integrated soot volume fraction versus the HAB. Blue and red curves correspond to the reference and H_2 flames, respectively. 172
7.12 Experimental soot primary particle diameter for (a): the reference flame, and (b): the H_2 flame. 173
7.13 (a): Soot primary particle size versus the HAB for the reference flame (blue) and the H_2 flame (red). (b): Soot primary particle diameter versus the radius at different HABs (from bottom to top: 20, 22, 28, 40 mm), for the reference flame (blue) and for the H_2 flame (red). 173
7.14 Histogram of soot primary particle size for the reference flame (blue) and the H_2 flame (red). 174
7.15 Numerical estimation of the gas temperature for the reference flame (left part), and the H_2 flame (right part). 175
7.16 (a): Gas temperature versus the HAB for the reference flame (blue) and the H_2 flame (red). (b): Gas temperature versus the radius at different HABs (from bottom to top: 20, 22, 28, 40 mm), for the reference flame (blue) and for the H_2 flame (red). Estimations from the experimental results are in dashed lines (LII) and solid lines (pyrometry), and the dotted lines correspond to the numerical results. For the pyrometry data, as the data on the centreline are of poor quality, it is the data for R = -150μm is plotted instead of R = 0 mm. In order to reduce fluctuation, the axial plot is smothered with a rectangular window of 5 pixels. 176
7.17 (a): Numerical soot volume fraction for the reference flame (left) and the H_2 flame (right). (b): Soot volume fraction versus the radius at different HABs (from bottom to top: 20, 22, 28, 40 mm) for the reference flame (blue) and for the H_2 flame (red). Estimations from the experimental results are in dashed lines, and the solid lines correspond to the numerical results. 177
7.18 (a): Axial evolution of the soot volume fraction for the reference flame (blue) and the H_2 flame (red). (b): Radially integrated soot volume fraction versus the HAB. Blue and red curves correspond to the reference and H_2 flames, respectively. Experimental results are in dashed lines and were obtained with a laser fluence of 55 mJ/cm^2, while experimental ones are in solid lines. . . 178
7.19 (a): Numerical estimation of the carbon-to-hydrogen ratio for the reference flame (left part) and the H_2 flame (right part). $\frac{C}{H}$ is given only in zones where f_v > 1 ppb. (b): Soot absorption function versus the radius at different HABs (from bottom to top: 20, 22, 28, 40 mm) for the reference flame (blue) and for the H_2 flame (red). Experimental estimations are in dashed lines, and the solid lines correspond to the numerical estimation of $\frac{C}{H}$. 179
7.20 (a): Soot absorption function obtained from the LII measurements versus the HAB for the reference flame (blue dashed) and the H_2 flame (red dashed), and carbon-to-hydrogen ratio obtained from the numerical simulations for the reference flame (blue solid) and the H_2 flame (red solid). (b): Soot absorption function (experimental) versus carbon-to-hydrogen ratio (numerical) for the reference flame (blue) and for the H_2 flame (red). 180

A.1 Scheme of two surfaces exchanging by radiation. Image taken from [310]. 185
A.2 Element of surface emitting in a solid angle delimited by a cone centred on O_1, and of normal n_1. 186

B.1 Scheme representing the probe volume corresponding to the crossing of the laser beam and the sensor's line of sight. 189

C.1 (a): Scheme of the calibration source. (b): Spectral radiance of the calibration source furnished by the lamp manufacturer at a brightness temperature 3000 K and for the reference luminance: Γ_{ref} = 32877 fL. 190
C.2 (a) and (b): Transmission of the bandpass filters centred on 578 nm (Edmund Optics 87766) in blue and on 716 nm (Edmund Optics 67053) in red. Figure (b) is identical to figure (a) on a reduced wavelength range. The data are those of the manufacturer. 192

D.1 Scheme of the experimental bench for spectroscopic measurements. 193
D.2 Incandescence spectra for radial positions varying from 0 to 3 mm at HAB = 28 mm in the C_2H_4+N_2/air flame diffusion flame Measurements are given in Figs. (a) to (e) for multiple laser fluence: 0, 35, 75, 150, and 300 mJ/cm^2, respectively. 195
D.3 Incandescence spectra and their corresponding fit for a radial position of 2 mm at HAB = 28 mm in the C_2H_4+N_2/air flame diffusion flame. Temperatures obtained are given in the legend. Figure (a) gives $ln\left(\frac{S_\lambda^{LII}}{S_{\lambda_{ref}}^{LII}}\left(\frac{\lambda}{\lambda_{ref}}\right)^6\frac{E(m_{\lambda_{ref}})}{E(m_\lambda)}\right)$ while figure (b) gives the normalised incandescence spectra. For a better visualisation, signals are averaged using a rectangular window of 10 points. 196
D.4 Comparison of the soot peak temperature obtained by 2C-LII (dashed line with x symbols) and by spectral fit (solid line with o symbols), versus the laser fluence, and for (a): different positions along the flame centreline, and (b): different radial positions at HAB = 28 mm. 197

E.1 (a): Signal recorded at 578 nm in the $C_2H_4 + N_2$/air flame. (b): Signal recorded with camera 1 after Abel inversion. (c): Soot temperature without laser heating obtained by emission pyrometry in the reference $C_2H_4 + N_2$/air flame, assuming a dispersion exponent of 1.38. 199
E.2 (a): Difference between the soot temperature obtained in this work and obtained by Kuhn et al. [216]. Both are obtained assuming a dispersion exponent of 1.38. (b): Difference between the soot temperature obtained assuming a dispersion exponent of 1 (wavelength independent) and 1.38, respectively. (c): Difference between the soot temperature obtained with the SP-LII and by emission pyrometry. A dispersion exponent of 1 (wavelength independent) is assumed in both cases. 200

F.1 (a): Dataset with many outliers for which a line has to be fitted. (b): Inliers found by the RANSAC algorithm are in blue, while outliers are in red. Figures from [312]. 202
F.2 Peak soot temperature versus laser fluence for different pixel locations. The black cross represents the data points retained by the RANSAC algorithm for computing $E(m_\lambda)$ and T_0 with a linear regression. Each colour corresponds to a different pixel location. The dashed black horizontal line represents the 3500 K limit imposed in Chapter 6 for the data processing. 202

G.1 (a): Normalised maximum of the LII signal at 578 nm versus the average laser fluence for the cold soot heated at F_1 (blue) and the hot soot heated at F_2 (red). The total incandescence signal resulting from the two soot particles is given in black. The signals are normalised by their maximum. The green line represents the ratio of the blue and red curves. (b): Peak soot temperatures versus the average laser fluence for the soot heated at F_1 (blue), the soot heated at F_2 (red), and the effective soot temperature (black) computed from the total incandescence signal. The black dashed line is the linear regression of the effective temperature curve. This linear regression, corresponds to $E(m_\lambda)$ = 0.46, and T_0 = 1858 K. (c): Normalised soot volume fraction versus the average laser fluence. The soot volume fraction is computed by AC-LII assuming: $E(m_\lambda)$ = 0.4 (dashed black), and $E(m_\lambda)$ = 0.46, (solid black). The actual soot volume fraction, including soot sublimation, is given in green. The profiles are normalised by the initial value of the soot volume fraction. (d): Normalised soot primary particle diameter versus the average laser fluence. The actual values of d_p for the cold and hot soot are given by the solid blue and red lines, respectively. The estimated values of d_p with the methodology presented in Sec. 3.4.4 are given for the cold and hot soot by the dashed blue and red lines. The values of d_p estimated from the effective soot temperature are given in black. The average laser fluence is the mean between F_1 and F_2. 206

G.2 (a): Normalised maximum of the LII signal at 578 nm versus the laser fluence for the cold soot having $E(m_\lambda)$ = 0.2 (blue), and the hot soot having $E(m_\lambda)$ = 0.4 (red). The total incandescence signal resulting from the two soot particles is given in black. The signals are normalised by their maximum. The green line represents the ratio of the blue and red curves. (b): Peak soot temperatures versus the average laser fluence for the cold soot (blue), the hot soot (red), and the effective soot temperature (black) computed from the total incandescence signal. The black dashed line is the linear regression of the effective temperature curve. This linear regression, corresponds to $E(m_\lambda)$ = 0.36, and T_0 = 1862 K. (c): Normalised soot volume fraction versus the laser fluence. The soot volume fraction is computed by AC-LII assuming: $E(m_\lambda)$ = 0.3 (dashed black), and $E(m_\lambda)$ = 0.36, (solid black). The actual soot volume fraction, including soot sublimation, is given in green. The profiles are normalised by the initial value of the soot volume fraction. (d): Normalised soot primary particle diameter versus the average laser fluence. The actual values of d_p for the cold and hot soot are given by the solid blue and red lines, respectively. The estimated values of d_p with the methodology presented in Sec. 3.4.4 are given for the cold and hot soot by the dashed blue and red lines. The values of d_p estimated from the effective soot temperature are given in black. 208

List of Tables

2.1 WHO air quality guidelines for airborne particles for 2005 and 2021, alongside EU standards. Limit values are shown for both annual and 24-hour exposure periods. Sources are the WHO and "Airparif" websites. 25

3.1 Reference input parameters of the LII code. 50

4.1 Reference input parameters for the LII code and reference peak temperatures that are extracted from the simulations done with the reference input parameters. 66
4.2 Values of the input parameters of the LII code used to create the look-up table. 73

6.1 Coordinates of the reference positions of Fig. 6.2a. 119
6.2 $E(m_\lambda)$ and T_0, obtained considering three laser fluences and all fluences. The d_p values obtained by considering only temperatures below 3500 K, as well as those calculated using all temperature values, are reported. Results are given for the six positions represented in Fig. 6.2. 129

7.1 Summary of several studies in the literature that have investigated the mixing of H_2 in laminar diffusion flames. "Exp" and "Num" refer to experimental and numerical studies, respectively. "CFR", "MFR", and "VFR" represent carbon, mass, and volumetric flow rate, respectively. "A" and "S" indicate addition and substitution of the diluent, respectively, and are followed by the species considered for the dilution. 160
7.2 Summary of several studies in the literature that have investigated the mixing of H_2 in laminar premixed flames. "Exp" and "Num" refer to experimental and numerical studies, respectively. "CFR", "MFR", and "VFR" represent carbon, mass, and volumetric flow rate, respectively. "A" and "S" indicate addition and substitution of the diluent, respectively, and are followed by the species considered for the dilution. 161
7.3 Flame conditions for the reference flame and the H_2-blended flame. 162

G.1 Reference input parameters for the LII code. 204

H.1 Hydrogen-to-carbon ratio for each class of BIN representing either heavy PAHs (BIN1 to 4) or soot particles (BIN5 to 25). Values from [314]. 212

Part I

Introduction

Chapter 1

Context and content of the thesis

Worldwide energy demand

Nowadays, in the early 2020s, the global energy demand stands at around 600 exajoules, as shown in Fig. 1.1. Over the past 30 years, this demand has been increasing at an average rate of approximately 1.5% per year. The only exceptions to this trend were in 2008, due to the global economic crisis, and in 2020, due to the COVID-19 pandemic. However, these declines were followed by stronger growths that compensated for the previous decreases. According to the 2021 forecast by the International Energy Agency (IEA), the global energy demand is projected to grow by nearly 50% by 2050 compared to 2020 level. Currently, fossil fuels (coal, oil, and gas) account for approximately 80% of total energy consumption, indicating a heavy reliance on these sources.

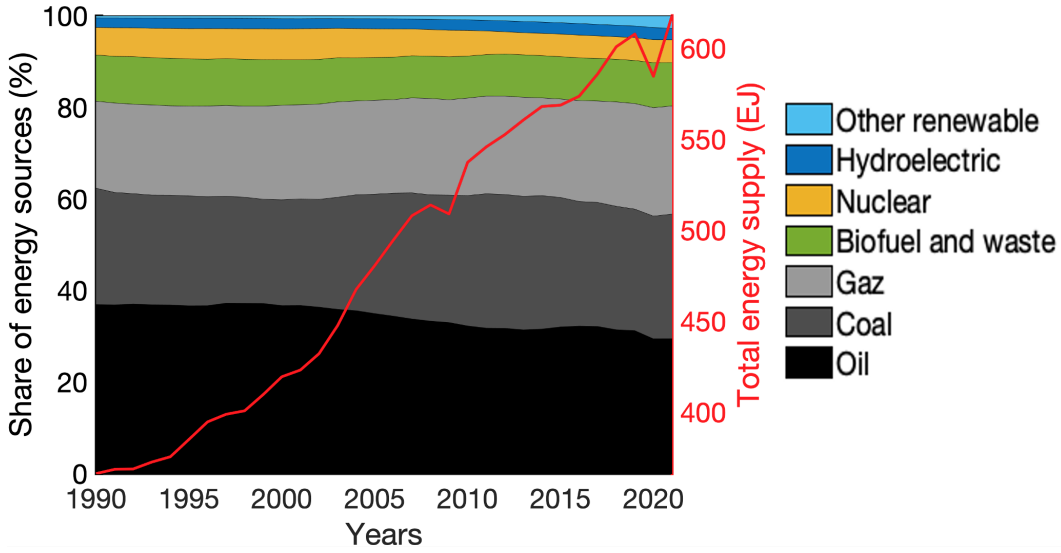

Figure 1.1: Evolution of global energy supply by source (1990-2021). The red line indicates the total energy supply in exajoules (10^{18} J). Data from the International Energy Agency [1].

Despite growing concern about reducing CO_2 emissions, the share of fossil fuel in the total energy consumption has stayed equal to 80% in the last 30 years. As the global energy demand has increased by about 65% over this period, the demand for fossil fuels increased by the same amount. For the future, the IEA forecasts in its Stated Policies Scenario (STEPS) a peak in demand for all three types of fossil fuel (oil, coal and gas) by 2030, followed by almost

constant demand for oil and gas until 2050, and a slight decrease for coal, bringing it back to the level of year 2000 (Fig. 1.2). Therefore, the reliance on fossil fuels to satisfy the global energy demand is overwhelmingly dominant and is expected to persist for some time.

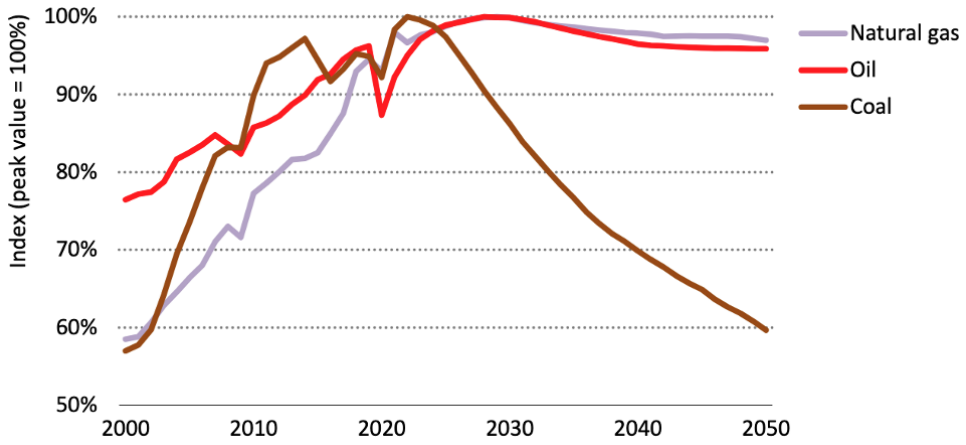

Figure 1.2: Historical fossil fuel consumption since the year 2000 and projected future consumption up to 2050 under the Stated Policies Scenario (STEPS). Data from the 2023 World Energy Outlook report of the International Energy Agency [2].

According to the IEA (Fig. 1.1), approximately 10% of the energy sources are biofuels and waste, meaning that the combustion process accounts for roughly 90% of the world's energy production. The combustion of fossil fuels is a well-known driver of global warming, primarily due to the release of greenhouse gases such as CO_2 and, to a lesser extent, NO_x. Additionally, the extraction and use of fossil fuels contribute to the release of unburned CH_4, a powerful greenhouse gas. However, the combustion of carbonaceous species, whether from fossil fuels, biofuels, or waste, also generates another significant air pollutant: **soot particles**.

The problems with soot particles

Soot are small carbonaceous particles originating from the incomplete combustion of carbon-containing species. The typical size of soot particles ranges from a few nanometers to hundreds of micrometres. They are composed of an aggregation of multiple spherical-like particles, called soot primary particles. Soot particles are of interest to several scientific communities as their production and emission come with consequences:

- **Health hazard:** Soot particles, which fall into the category of fine particulate matter, are significant air pollutants and pose a serious health hazard. They are linked to various health issues, including cardiovascular and respiratory diseases, cancer, and other pathologies [3–10]. In 2020 alone, exposure to fine particles, including soot, was estimated to have resulted in 253,000 deaths across Europe [11].
- **Environmental effects:** Soot has diverse environmental impacts, particularly on the climate, through mechanisms that can either warm or cool the atmosphere. Soot particles, especially the highly absorbent soot particles usually referred to as black carbon, play a significant role in climate warming [12–16]. Estimating the total radiative forcing of soot is challenging and has significant uncertainties [13]. Some estimations suggest that the overall radiative forcing of soot and co-emitted aerosols could be neutral or even negative (global cooling effect), with a 90% uncertainty range from -1.45 to +1.29 W/m^2 [13, 17]. However, black carbon alone is estimated to have a significant positive radiative forcing of +1.1 W/m^2 [13]. If these estimates are accurate, black carbon would be the second-largest contributor to climate warming after CO_2 (1.82 W/m^2 [18]) and before

CH_4 (0.48 W/m^2 [18]) [13, 16, 18], highlighting the importance of reducing black carbon emissions to mitigate global warming.

- **Effect on combustion devices:** In combustion devices, soot particles may settle on the walls of the combustion system or the downstream devices. This can lead to obstructions or blockages, inducing efficiency loss or malfunction [19–21]. In addition, soot particles significantly radiate when heated. This is desirable for furnace and boiler applications as it enhances the heat transfer and the efficiency of such devices [22, 23]. However, this is highly undesirable for engines as soot radiation increases the total wall heat flux [24, 25], which decreases the efficiency of the system.

The pathway to a cleaner combustion

Controlling soot production and reducing their emissions would be beneficial in many ways. Unfortunately, this is not an easy task, and the development of cleaner combustion technologies would benefit from:

1. The ability to precisely measure the soot produced and emitted by a combustion device.
2. The ability to predict reliably soot emissions for a given operating condition.

This requires, at the same time, the development of more precise experimental techniques for the detection and characterisation of soot particles and the development of high-fidelity soot prediction models. Such objectives require a better knowledge of the soot properties and a better understanding of the mechanisms by which soot particles are formed and destroyed. Such understanding can be gained from fundamental studies on laboratory flames.

Over time, several experimental techniques have been developed for soot characterisation. In particular, the Laser-Induced Incandescence (LII) experimental technique [26] -the core technique used in this thesis- is a widely used *in-situ* technique in soot science that allows studying spatially and temporally soot directly inside flames. It was initially developed to measure the soot volume fraction f_v and to give information on the soot primary particle diameter d_p [27–29]. The soot volume fraction is a measure of the proportion of soot particles in a given volume. This parameter allows for the quantification of soot production and emission. It is a dimensionless quantity usually expressed in parts per million (ppm) or parts per billion (ppb). The soot primary particle diameter represents the diameter of the so-called soot primary particles, which are the building blocks of the larger soot aggregates. In addition to the measurements of f_v and d_p, the LII principle was also used to retrieve information on the soot absorption function $E(m_\lambda)$ [30]. $E(m_\lambda)$ is a soot optical property characterising the ability of the soot to absorb and emit radiations. It is a key property as its value is required for the computation of f_v with optical techniques such as LII or extinction. Accurately measuring $E(m_\lambda)$ improves the precision of f_v estimates. Moreover, $E(m_\lambda)$ is linked to the so-called soot maturity [31], the process that characterises the soot development from incipient particles towards a fully graphitic state [32]. As such, it provides valuable insights into the maturity stage of soot particles. LII measurements were later processed to obtain at the same time $E(m_\lambda)$, along with the gas temperature T_0 [33].

The complementary information that can be extracted from LII measurements makes it a valuable tool to characterise soot particles without multiplying the experimental diagnostics that go with an increased time and cost for the measurement campaign.

The LII technique has been used to exhibit the effects of several experimental factors on soot production, including, but not limited to: reactant injection temperature [34–36], pressure [37–42], fuel composition [43, 44], or oxygen content [28, 41, 45–47]. However, LII experimental results are not just confined to observational studies. They play a crucial role in tuning and validating numerical models developed to represent soot formation and destruction

processes. By incorporating LII data, the predictive capabilities of Computational Fluid Dynamics (CFD) simulations can be evaluated and refined. Once validated, these simulations complement the experimental data and provide access to quantities that LII alone cannot measure, such as the concentration of gaseous species. This additional data is vital for identifying key species and reactions involved in soot chemistry, enhancing our understanding of the underlying processes. Alternatively, CFD simulations, once carefully validated with experimental data, could be used to predict soot emission in combustion devices where experimental measurements are either challenging to perform or prohibitively expensive. Such an accurate predictive ability of the simulations would be extremely valuable for assessing soot emission of complex combustion devices. Currently, CFD simulations offer a useful but not yet fully reliable means of predicting soot emissions in combustion devices. Therefore, the synergy between LII experiments and numerical simulations provides a powerful tool for understanding and controlling soot production. By continually refining these numerical models with experimental data, these models become more reliable, ultimately contributing to the development of cleaner combustion systems while improving our understanding of the underlying chemical and physical processes involved in the soot formation.

Content of this thesis

This thesis aims to advance the current knowledge of soot properties and formation mechanisms. To that end, the LII experimental technique is at the centre of this work. A dedicated experimental setup has been designed and implemented to directly measure key soot parameters in flames using only LII measurements. This includes soot volume fraction, primary particle diameter, and soot absorption function, while gas temperature is also retrieved. The experimental setup developed here is of great utility as it provides complementary information directly in flames while being simple to utilise.

The soot absorption function and the gas temperature are determined using an innovative LII-based technique: the Separated Pulses Laser-Induced Incandescence (SP-LII). This novel approach was developed with the objective to be applicable to instantaneous measurements in view of turbulent flame measurements. Although designed for potential use in turbulent flames -which are more representative of industrial conditions- this thesis focuses on its development, validation, and application in laminar flames. Therefore, this work establishes a foundation for future studies in more complex flame environments.

Three different laminar diffusion flames with varying fuels are investigated. Initial measurements focused on two hydrocarbon flames (methane and ethylene), which were crucial for setting up the apparatus, processing data, identifying problems, and developing solutions. Then, in light of the current trend toward decarbonising energy production, the impact of blending hydrogen with hydrocarbon fuels was experimentally investigated by comparing a hydrogen-ethylene blend to a reference flame. The analysis focused on changes in soot volume fraction, primary particle size, and absorption properties induced by hydrogen.

The experimental work conducted in this thesis provides a comprehensive database for the different flames studied, which is critical for validating and refining CFD models. To this end, the experimental results were compared to numerical results to validate the qualitative and/or quantitative behaviour of the numerical model.

Structure of the document.

This document is structured as follows:

- **Chapter 2** is dedicated to define and present soot particles. Notably, the geometry of soot particles is pre-

sented before introducing the important concept of soot maturity. The adverse effects of soot particles on health and the environment are discussed. Then, current knowledge of the soot formation and development processes is reviewed. Finally, the soot properties (volumetric heat capacity, absorption function and carbon-to-hydrogen ratio) that are of prime importance in this thesis are addressed through a literature review.

- **Chapter 3** focuses on the experimental technique at the core of this thesis: the Laser-Induced Incandescence technique (LII). It begins with an overview of the fundamental operating principles of LII, followed by a description of the numerical code used in subsequent chapters to simulate the LII process. Finally, it details the computational methods employed to derive soot temperature, volume fraction, and primary particle diameter from LII measurements.
- **Chapter 4** is dedicated to a new LII-based technique called the Separated Pulses LII (SP-LII) technique, which was developed with the aim to be applicable in turbulent flames. The SP-LII furnishes the soot absorption function and the gas temperature from two measurements of the soot temperature at two different laser fluences. After a literature review on the way to access the soot absorption function, the theoretical background of the SP-LII is given. Its theoretical application to turbulent flames is considered by providing an adequate experimental setup and considering some major issues this would raise. Two methods for the data post-processing are discussed: a simplified one called the absorption model (AM) and a more complex but more precise one called the look-up table (LUT). The performance of the SP-LII is then theoretically evaluated under varying conditions using numerically generated LII signals from the code introduced in Chapter 3.
- **Chapter 5** gives the first experimental application of the SP-LII in a steady flame. It begins with a description of the two-colour LII setup used to conduct point-wise (0D) LII measurements in a CH_4/air laminar diffusion flame. Following this, the application of the SP-LII is thoroughly detailed, with particular emphasis on the fluence selection step, which is crucial for the technique to work well. The soot absorption function and gas temperature are computed with both the AM and LUT post-processing methods, and several sources of uncertainties are characterised. Then, the spatial evolution in the flame of the soot absorption function and gas temperature are discussed and are completed by estimations of soot volume fraction and soot primary particle diameter.
- In **Chapter 6**, the collection system of the experimental setup has been modified to enable 2D measurements, enhancing spatial resolution. The flame considered in this chapter is a reference laminar diffusion $C_2H_4 + N_2$/air flame, allowing for comparison with the literature data. This chapter also includes an analysis aimed at improving the data processing of LII signals to refine estimates of soot quantities. Notably, a correction method for background subtraction to LII measurements is proposed. The chapter concludes with a comparative analysis of the results against the literature data.
- As hydrogen is often regarded as a fuel for the future, **Chapter 7** focuses on analysing the effects of hydrogen substitution on soot formation in the reference flame discussed in Chapter 6. The chapter begins with a literature review that highlights existing findings on the impact of hydrogen blending on soot production. Following this, the flame conditions investigated in this study are presented. Next, the soot absorption function, volume fraction, primary particle diameter, and gas temperature of the hydrocarbon reference flame are compared with the corresponding estimates from the H_2-blended flame to emphasise the effects of hydrogen. The chapter concludes with a comparison of numerical results against experimental data from the same flame, validating the qualitative behaviour of the soot model used in the CFD simulations.

Chapter 2

Soot particles

This chapter is dedicated to the presentation of soot particles. It begins with a general definition of "soot" and introduces the concept of soot maturity. An overview of soot particle geometry follows, detailing their size, morphology, and internal structure. The chapter then addresses the significant health and environmental concerns associated with soot, emphasising its harmful effects on human health and its detrimental impact on the environment. A review of the current understanding of soot formation and evolution processes provides insights into the species and mechanisms involved. Finally, the chapter discusses key soot properties relevant to this thesis, presenting their orders of magnitude and their dependence on various parameters.

Contents

2.1 Definition of a soot **20**
2.2 The concept of soot maturity **20**
2.3 Soot structure **21**
2.3.1 Soot size 21
2.3.2 Soot morphology 22
2.3.3 Soot internal structure 22
2.4 Environmental and health risks **23**
2.4.1 Health concerns 23
Size classification 24
Effect on health 24
Regulations and exposition to fine particles 25
2.4.2 Environmental effects 25
2.5 Soot formation and evolution **26**
2.5.1 Gaseous phase: soot precursors formation 27
2.5.2 Condensate phase: soot formation and evolution 29
2.5.3 Which conditions favour soot production? 32
2.6 Important soot properties for this thesis **33**
2.6.1 Carbon-to-hydrogen ratio $\frac{C}{H}$ 33
2.6.2 Soot absorption function $\boldsymbol{E}(\boldsymbol{m}_{\lambda})$ 34
Maturity dependence 35
Wavelength dependence 36
Summary on $\boldsymbol{E}(\boldsymbol{m}_{\lambda})$ 36

2.6.3 Volumetric heat capacity $\boldsymbol{V_c}$ 37

2.1 Definition of a soot

The term soot is challenging to define precisely as it encompasses a large variety of particles in terms of size, morphology, chemical composition, and properties. Thus, a definition inspired from [32] is given: soot particles are small particles formed during the incomplete combustion or pyrolysis of carbon-containing fuels (gasoline, methane, diesel, biofuels, biomass...). It includes all stages of the evolution of a soot particle, from its inception to its development into a mature soot particle (the concept of maturity is defined in section 2.2). Soot particles are mainly composed of carbon and hydrogen atoms, but they can also contain other species in small quantities (O, S, N, metals) [48, 49]. Soot particles consist of organic content (OC) and elemental carbon (EC) [13, 50]. The organic content encompasses a diverse range of compounds, including saturated and unsaturated hydrocarbons, aliphatics, aromatics, polycyclic aromatic hydrocarbons (PAHs), and oxidised organics that have condensed onto the particles. In contrast to the volatile organic content, elemental carbon remains stable even in high-temperature flame environments [51].

An important feature of soot is that they interact with light by absorption and scattering. These interactions with light make it possible to gather information on soot by using optical techniques: this is what is done in this thesis.

2.2 The concept of soot maturity

Once formed, the soot particles evolve within the flame due to the chemical and physical reactions they undergo. This results in a change in their morphology, composition, and properties [51–55]. These changes are characterised by the maturity level of the soot particle, which tends to increase with the residence time. Michelsen et al. [32] define the maturity level as a way to describe the progress of soot from inception to fully mature soot, where mature soot is a graphite-like particle that has fully evolved at high temperature. The incipient (just formed) and fully mature soot particles would be the lower and higher maturity states. Young particles refer to an intermediate state between incipient and fully mature, while mature particles generally refer to particles approaching the fully mature state.

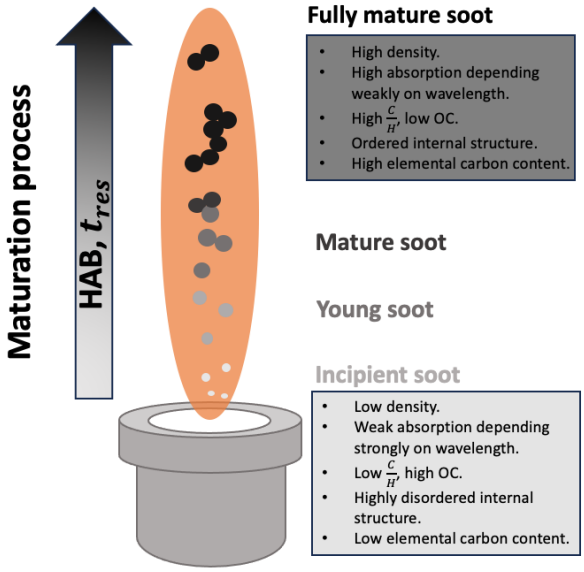

Figure 2.1: Scheme illustrating the evolution of some soot properties with the soot maturation along the flame height above the burner and residence time t_{res}.

As soot particles mature, their internal structure and properties undergo significant changes. The proportion of OC reduces while the EC increases significantly [51]. Both the carbon-to-hydrogen ratio $\frac{C}{H}$ and bulk density increase [56], reflecting a more graphitic structure. Additionally, the optical properties evolve: mature soot particles exhibit enhanced light absorption in the visible and infrared ranges, with a reduced spectral dependence [31]. This maturation process, along with the corresponding changes in soot properties, is illustrated in Figure 2.1. The impact of soot maturation on density, absorption characteristics, and the ratio $\frac{C}{H}$ will be discussed in detail later in this chapter.

2.3 Soot structure

2.3.1 Soot size

Soot particles can have sizes which differ by several orders of magnitude. Their size can vary from a few nanometers for the smallest one up to several hundreds of micrometres for largely aggregated particles [32]. The important size variation of soot particles is illustrated in Fig. 2.2 where the different sizes of soot particles are compared to other classical microscopic objects: the smallest soot particles are smaller than a virus, but the largest soot particles are thicker than a human hair!

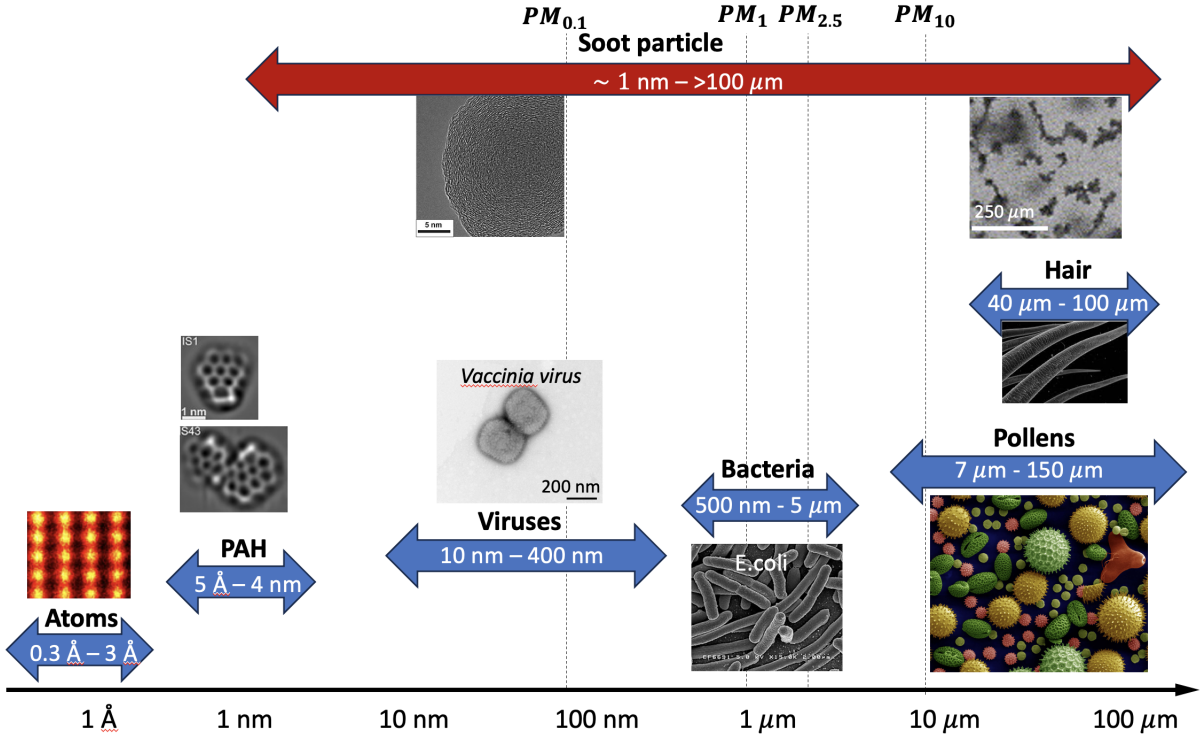

Figure 2.2: Comparison of the size of soot particles with microscopic objects. Images are taken from the public domain and from references [57–62].

Soot particles can be composed of one or more small spherical-like particles that are called soot primary particles. These primary particles typically have a size from a few nanometres up to ∼50nm [52]. They can stick together to form large soot particles called soot aggregates. Soot aggregates can exceed 1 μm and are called super-aggregates when their size is in the range ∼2 to 100 μm [32]. Figure 2.3 represents a soot aggregate that is composed of several tens of soot primary particles issued from the combustion of propane [61].

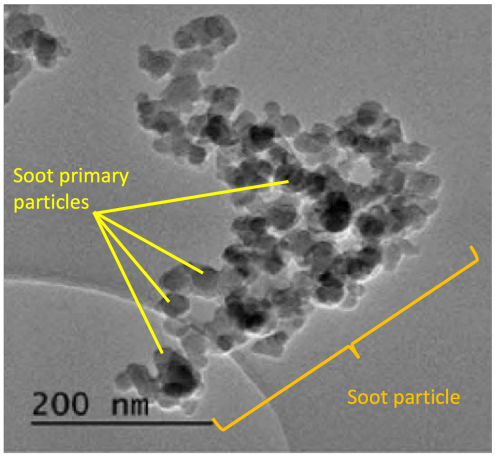

Figure 2.3: Image of a soot particle taken with a Transmission Electron Microscope (TEM). Yellow arrows point to the building blocks of the soot aggregate: the soot primary particles. Adapted from [61].

2.3.2 Soot morphology

Soot aggregates can be described as fractal [63, 64]: their morphology is scale invariant. Because of this fractal morphology, the number of primary particles of a soot aggregate follows:

$$N_p = k_f \left(\frac{2R_g}{d_p} \right)^{D_f}, \tag{2.1}$$

where k_f is the scaling pre-factor, R_g is the radius of gyration, d_p is the primary particle diameter, and D_f is the fractal dimension. The fractal dimension varies between 1 for a linear shape and 3 for a spherical shape. For flame-generated soot aggregates, D_f is typically 1.7-1.9 [32, 65–67]. Figure 2.4 gives Transmission Electron Microscopy (TEM) images of two soot aggregates having a D_f of 1.8 and 2.47 [66].

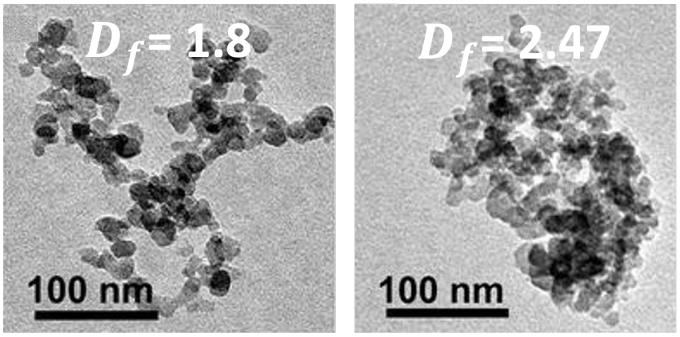

Figure 2.4: TEM images of soot particles with different fractal dimensions: 1.8 and 2.5 from left to right, respectively. Images are taken from [66].

2.3.3 Soot internal structure

Soot particles are composed of graphitic layer plane segments that can have different lengths and orientations and can be stacked to form crystallites [68]. Ishiguro et al. [69] describes soot primary particles as depicted in Fig. 2.5: they are composed of an inner core and an outer shell. The inner core is the centre of the primary particle, which has a size of $\sim$10 nm. It is composed of one or more incipient particles covered by randomly oriented graphitic layers (called turbostratic structures). The outer shell is composed of crystallites that are tangentially oriented (with

respect to the surface of the particle) and form an onion-like structure.

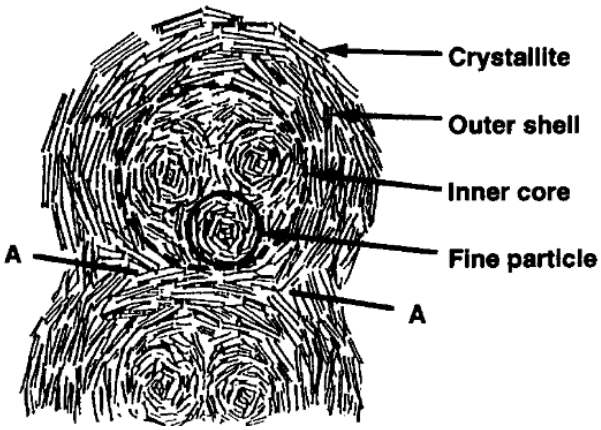

Figure 2.5: Schematic of the internal structure of a diesel soot particle. Image taken from [69].

The internal structure of soot is different according to the maturity level. Figure 2.5 is representative of a mature particle, while a young particle would correspond to the inner core of the particle of Fig. 2.5. Figure 2.6 shows HRTEM images of young and mature soot particles formed from methane and ethylene. The mature particles (images d and h) show a more ordered external structure than the young ones (images c and g).

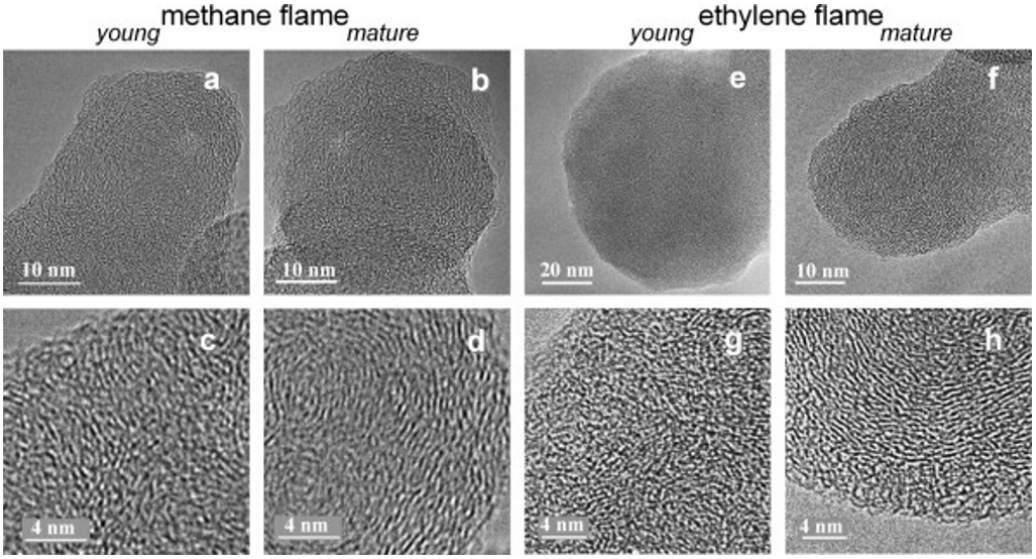

Figure 2.6: High-resolution TEM images of soot particles from methane (a-d) and ethylene (e-h) flames. Figures (a, c, e, g) represent young soot, and figures (b, d, f, h) represent mature soot. Adapted from [70].

2.4 Environmental and health risks

2.4.1 Health concerns

The World Health Organisation (WHO) defines air pollution as the "contamination of the indoor or outdoor environment by any chemical, physical or biological agent that modifies the natural characteristics of the atmosphere". Therefore, airborne particles such as pollen, dust, sand, tyre and brake abrasion, but also soot particles are a source

of air pollution. As such, these particles have adverse effects on human health, and are classified according to their size.

Size classification

Not all particles pose the same level of risk to human health: their size is a crucial determinant of their potential harm. The finest particles are particularly hazardous as they penetrate deeper into the body, potentially impacting multiple organs. As illustrated in Figure 2.7, coarse particles are typically trapped in the upper respiratory system, while ultrafine particles can disperse throughout the body, reaching and affecting various organs. That is why particles are generally classified considering their size:

- Supercoarse particles are particles with an aerodynamical diameter above 10 μm.
- Coarse particles or PM_{10} are particles smaller than 10 μm.
- Fine particles or $PM_{2.5}$ are particles smaller than 2.5 μm.
- Very fine particles or PM_1 are particles smaller than 1 μm.
- Ultra-fine particles or $PM_{0.1}$ are particles smaller than 100 nm.

It has to be noted that smaller particles are subsets of larger categories (PM_{10} includes $PM_{2.5}$, PM_1, and $PM_{0.1}$).

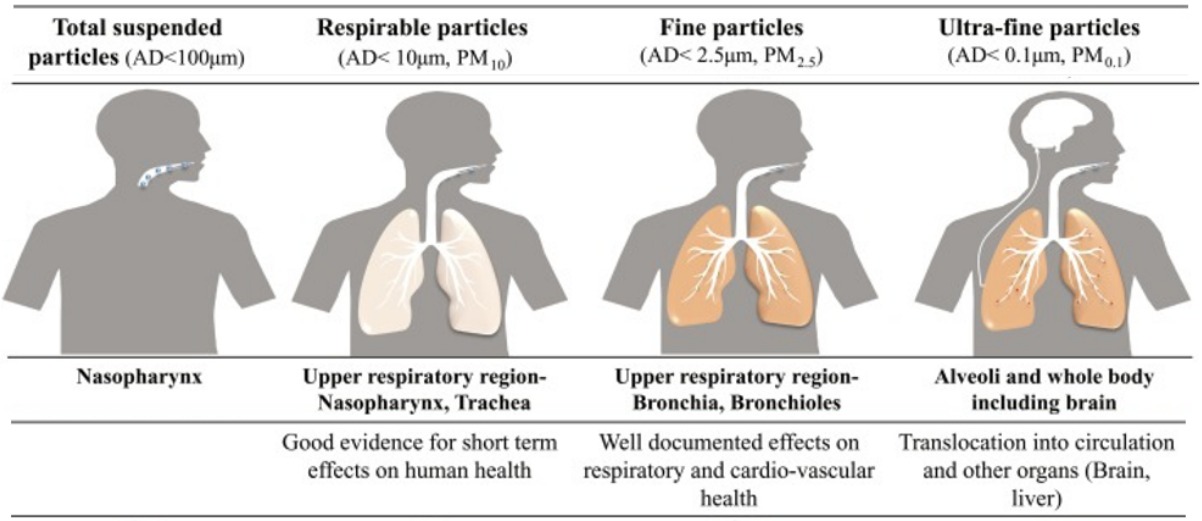

Figure 2.7: Scheme illustrating the penetration of particles in the body according to their size: particles above 10 μm deposit in the nasopharynx, PM_{10} in the upper respiratory region, $PM_{2.5}$ reach the bronchia, and $PM_{0.1}$ penetrate the alveoli, potentially reaching other organs via the bloodstream. Adapted from [8].

Effect on health

As shown in Fig. 2.2, soot particles vary widely in size, encompassing all size categories, including the smallest: $PM_{0.1}$. This size range allows the finest soot particles to penetrate deeply into the body and potentially affect various organs. However, the toxicity of soot particles is not determined solely by their size but also by their composition [4]. In particular, soot particles contain adsorbed polycyclic aromatic hydrocarbons (PAHs), which are known to be hazardous [3, 4]. Thus, soot particles combine their ability to reach deep into the body with surface toxicity.

Numerous studies have investigated the health effects of airborne particles, specifically of soot particles [3–10].

Among other adverse effects, soot particles are linked to respiratory and cardiovascular diseases [3, 10], DNA damage [9], and cancer [9].

It is not easy to put a precise figure on the impact of particulate matter on health. However, exposure to $PM_{2.5}$, including soot, above the 2021 WHO guidelines (Table 2.1) was estimated to cause 253,000 deaths in Europe in 2020 [11]. Worldwide, the WHO estimates that about 3.2 million deaths annually are linked to household air pollution from cooking stoves due to incomplete fuel combustion. Beyond premature mortality, fine particulate pollution also leads to a significant loss of healthy life years, contributing to chronic illnesses that cause daily suffering and incur substantial healthcare costs.

Regulations and exposition to fine particles

To address the adverse health effects of fine particles, including soot, air quality standards have been established. The standards adopted in Europe and the WHO guidelines for $PM_{2.5}$ and PM_{10} are detailed in Table 2.1. The values are categorised into annual and daily limits, with the daily limits set higher than the annual ones. The updated 2021 guidelines reflect a tightening of the 2005 to protect public health better. It is interesting to note that the European standards are below the WHO recommendations.

	2005 WHO Guidelines		**2021 WHO Guidelines**		**EU standards**	
Averaging time	**Annual**	**24-hours**	**Annual**	**24-hours**	**Annual**	**24-hours**
$\boldsymbol{PM_{10}}$ **(**μ**g.m**$^{-3}$**)**	20	50	15	45	40	50
$\boldsymbol{PM_{2.5}}$ **(**μ**g.m**$^{-3}$**)**	10	25	5	15	30	-

Table 2.1: WHO air quality guidelines for airborne particles for 2005 and 2021, alongside EU standards. Limit values are shown for both annual and 24-hour exposure periods. Sources are the WHO and "Airparif" websites.

Air quality is closely monitored to allow local authorities to implement temporary restrictions on pollutant emissions when thresholds are exceeded. This monitoring also helps estimate population exposure to particulate matter. According to the WHO's 2020 air quality report, 70% of the European urban population was exposed to PM_{10} levels above the 2021 WHO guidelines, and this figure rises to 96% for $PM_{2.5}$. In comparison, EU standards indicate that only 11% of the population exceeds PM_{10} limits, and less than 1% exceeds $PM_{2.5}$ limits. These numbers underscore the public health risks associated with air pollution, highlighting the benefits of reducing soot emissions.

To address air quality concerns, regulations on emissions have been established. In Europe, the automotive sector is governed by the Euro standards, which impose limits on particle emissions for both diesel and gasoline engines. These standards have become progressively stricter with each new tier. Particle emissions are regulated in terms of mass emitted per kilometre, and from Euro 5a (2009) for diesel vehicles and Euro 6b for gasoline vehicles, the number of emitted particles has also been regulated, highlighting the toxicity of the smallest particles.

2.4.2 Environmental effects

Soot particles have multiple detrimental effects on the environment. They harm vegetation by reducing solar radiation, which impairs photosynthesis [5], and by altering precipitation patterns through interactions with clouds [5]. Additionally, soot can increase soil and water contamination, contribute to acid rain, and adversely affect animal life [5]. Above all, soot emissions affect the climate.

Globally, aerosols (airborne particles including soot particles) contribute to a reduction in global radiative forcing [14], primarily through light scattering and interactions with clouds. However, the impact of soot particles on the

radiative forcing is more uncertain. While soot particles do scatter light, producing a cooling effect similar to other aerosols, they are also highly absorbent. This leads to both warming and cooling effects on the climate, driven by mechanisms such as light absorption, albedo modification, accelerated snow and ice melting, and cloud interactions [12, 13, 15].

Estimating the radiative forcing due to soot is particularly challenging. Often, the literature focuses only on black carbon, which are particles composed of aggregated spheres formed during combustion or pyrolysis which are characterised by a strong absorption in the visible spectrum, high sublimation temperature, and resistance to solubility in water and organic solvents [13]. While mature soot particles make up the majority of atmospheric black carbon [32], not all soot particles are classified as black carbon due to their varying stages of maturity. The estimated radiative forcing of black carbon varies widely in the literature [12, 16, 17, 71]. The reviewing work of Bond et al. [13] provides a value of +1.1 W/m^2 with a 90% uncertainty range from +0.17 to +2.1 W/m^2 highlighting the warming effect on the climate of back carbon. The accuracy of these estimates is hindered by several challenges [13], including the inconsistent definition of black carbon, the potential underestimation of emissions, particularly in Asia and Africa, and the limitations of current Earth system models for which the uncertainties due to model biases have not been assessed. Altitude and removal rates, which are crucial in determining black carbon's impact, are also poorly represented in models, adding to the uncertainty surrounding black carbon's effects on cloud formation. When accounting for all co-emitted species alongside black carbon, including sulphur dioxide and organic matter, as well as emissions from open burning (forests, grasslands, and agricultural residues), the overall net radiative forcing is slightly negative, with a best estimate of -0.06 W/m^2 with a 90% uncertainty bounds of-1.45 to +1.29 W/m^2. Excluding open burning emissions, the net climate forcing becomes +0.22 W/m^2 with a 90% uncertainty bounds of -0.50 to +1.08 W/m^2. Therefore, reducing emissions from these sources (engines, industry, and residential solid fuels), even beyond just black carbon, would likely help to reduce radiative forcing.

2.5 Soot formation and evolution

Understanding soot formation is essential for controlling its production and emission. The soot formation process is highly complex, involving a range of species and intricate physical and chemical reactions. The formation of soot is sensitive to multiple factors, including temperature [34, 72–80], pressure [23, 42, 74, 81–83], mixture ratio and fuel composition [73, 76, 84–92], which adds further complexity.

This section explores the current understanding of soot formation, emphasising key stages and the challenges that continue to obstruct a comprehensive understanding of this complex phenomenon. The soot formation process is illustrated in Fig. 2.8 and is divided into two major phases: the formation of the soot precursors in the gas phase and the subsequent formation and development of soot particles in the condensate phase.

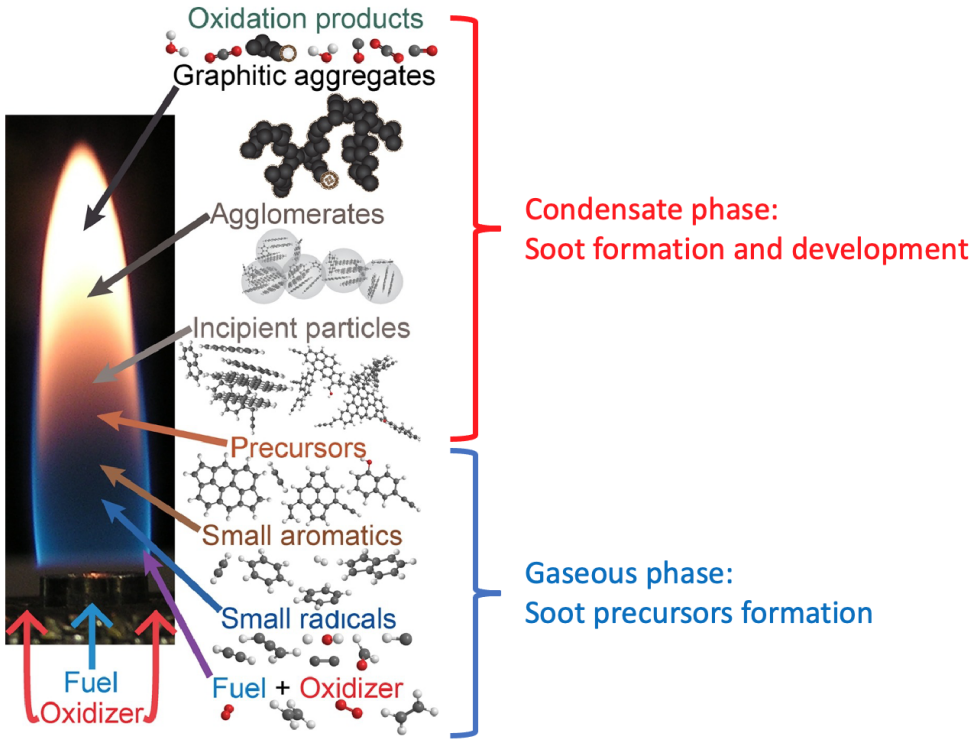

Figure 2.8: Illustration of the steps of the soot formation process. Adapted from [52].

Soot formation begins with the pyrolysis of fuel molecules, which generates radicals that react to form increasingly complex molecules, including small aromatic species [93]. These molecules then further react to produce polycyclic aromatic hydrocarbons (PAHs), identified as soot precursors. The transition from the gaseous phase to the formation of solid soot particles occurs during the inception phase. Following this, particles grow either through chemical and physical mass addition from the gaseous phase and/or by colliding with other particles, forming larger particles and/or aggregates. Eventually, soot particles may experience mass loss through oxidation. Despite extensive research, the precise mechanisms underlying these stages -especially the transition from gaseous molecules to solid particles- are not fully understood [52, 94].

2.5.1 Gaseous phase: soot precursors formation

PAHs have been identified to be soot precursors [87, 95]. PAHs are gaseous molecules containing more than one aromatic cycle. The steps leading to the formation of the pyrogenic PAH (as opposed to the petrogenic PAHs which are initially present in the fuel) are the following [20, 52, 93, 96–98]:

1. **Fuel decomposition:** The hot and oxidising environment of the flame decomposes the fuel. Radical species are created, and hydrocarbon species such as acetylene are formed.
2. **Formation of small cyclic compounds:** Benzene (C_6H_6), which is the simplest aromatic molecule and is the basic brick of PAH, can be formed through combinations of smaller hydrocarbons molecules or radicals with

a carbon number from 1 to 5 [95]:

$$C_5H_5 + CH_3 \rightleftharpoons C_6H_6,$$

$$C_4H_3 + C_2H_2 \rightleftharpoons C_6H_5,$$

$$C_6H_5 + H \rightleftharpoons C_6H_6, \tag{2.2}$$

$$C_4H_5 + C_2H_2 \rightleftharpoons C_6H_6 + H,$$

$$C_3H_3 + C_3H_3 \rightleftharpoons C_6H_6,$$

The primary pathways for forming the initial aromatic ring are highly dependent on the fuel composition [97]. McEnally et al. [97] offer an extensive review of research on the mechanisms involved in the formation of the first aromatic rings in flames.

3. **Growth of PAH:** Aromatic molecules (such as benzene) can grow into PAHs, which are larger and more complex hydrocarbons containing more than one aromatic ring. The HACA (H-abstraction-C_2H_2-addition) mechanism [99] is thought to play an essential role in the growth of PAH. HACA is a simple but realistic way to represent PAH growth from acetylene proposed by Frenklach [95, 100, 101]:

$$A_i + H \rightleftharpoons {A_i}^* + H_2,$$

$${A_i}^* + C_2H_2 \rightleftharpoons A_i{C_2H_2}^*, \tag{2.3}$$

$$A_i{C_2H_2}^* + C_2H_2 \rightarrow A_{i+1} + H.$$

where A_i corresponds to an aromatic molecule containing i fused aromatic rings, and A_i^* is an aromatic radical. Of course, C_2H_2 is not the only species involved in the growth of PAH; other species, including aromatics molecules, participate in the growth of PAHs [95]. Figure 2.9 shows images taken with an atomic force microscope (AFM) of several PAHs produced in a flame [58], illustrating the variety of the PAHs class of molecules, which contains countless different molecules.

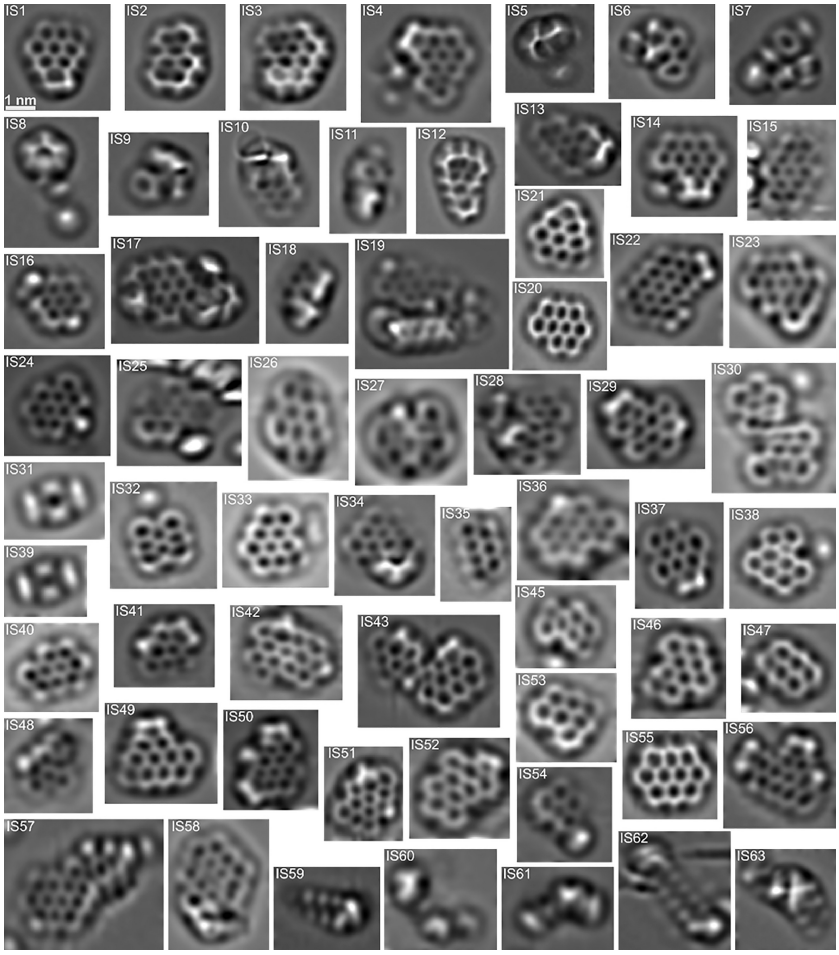

Figure 2.9: PAHs viewed with an Atomic Force Microscope. Image taken from [58].

2.5.2 Condensate phase: soot formation and evolution

1. **Inception:** Soot inception corresponds to the transition from the gaseous phase to a condensate phase [32], marking the formation of solid soot particles. This process increases the number of soot particles in the flame, thereby raising the soot volume fraction. Proposed precursors of soot particles include PAHs, ionic species, and polyacetylene, with PAHs being widely accepted as the primary contributors to soot formation [95]. Incipient particles can be formed from a wide variety of PAHs [58] or from ionic species [102]. Despite its significance, the mechanisms of soot inception remain poorly understood [32], and the exact transition from PAHs to solid soot particles is still unclear. Typically, it is assumed that a PAH transitions into a soot particle when its mass exceeds a specific, albeit somewhat arbitrary, threshold [87, 95, 103]. The review by Martin et al. [87] examines the transformation of gas-phase molecules into condensed phase, comparing different inception mechanisms, which can be grouped into three main categories.

    - **Chemical inception:** Soot particles are formed through the chemical growth of PAHs interacting with other species, such as acetylene, polyynes, or additional PAHs. In this process, the PAH and the other molecules chemically bond to create the incipient soot particle.
    - **Physical inception:** Soot particles are formed through the stacking of PAHs with other PAHs or species. In this process, the PAHs and additional species are not chemically bonded but are physically associated.

- **Chemical + physical inception:** Combination of the two previous inception mechanisms. An issue with soot formation is that the physical condensation of precursors is rapid but weak, while chemical bonds are strong but slow. Thus, a mechanism that integrates both physical stabilisation and chemical bonding -known as physically stabilised soot inception- can be introduced to explain the observed rapid soot growth.

Figure 2.10 gives the schematic representation of some chemical, physical, and chemical+physical mechanisms. A more detailed list of the mechanisms that can be encountered in the literature are gathered and discussed in [87]. The plausibility of each proposed mechanism is also discussed.

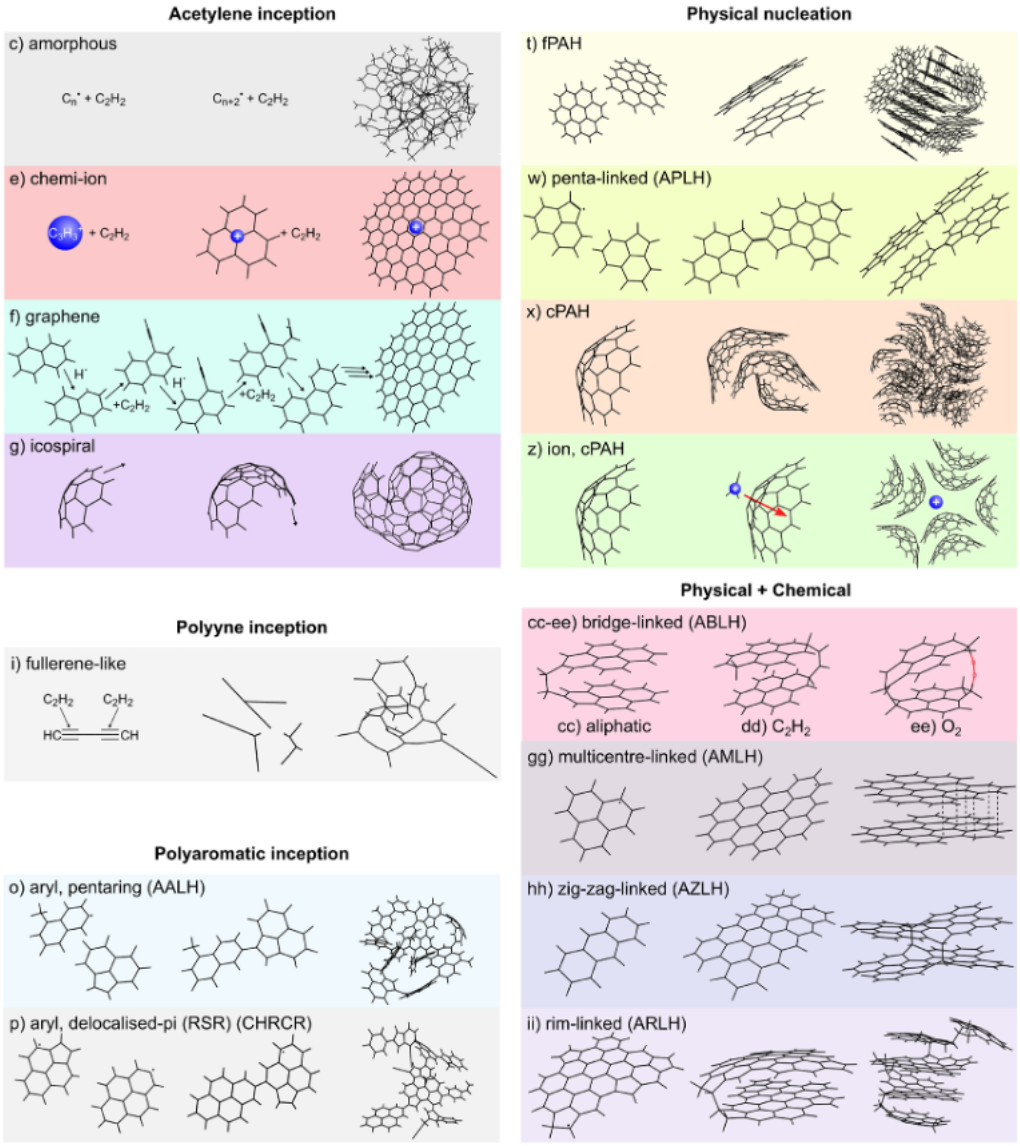

Figure 2.10: Schematic illustrating various soot inception mechanisms from [87]. Acetylene, polyyne, and polyaromatic pathways fall under the chemical inception category. Image taken from [87].

2. **Surface growth:** Surface growth is the process according to which gaseous species are added to the particle's surface by adsorption (condensation, deposition, physisorption, and chemisorption) [32], thereby increasing the soot volume fraction and the soot particles size. Surface growth can occur at any stage of the soot evolution

(from incipient soot to large soot aggregates). Surface growth is mainly represented by two mechanisms: the HACA and PAH condensation, with the contribution of the two mechanisms depending on the flame conditions [96, 99]. Figure 2.11 represents soot primary particles that have grown from one or more incipient particles.

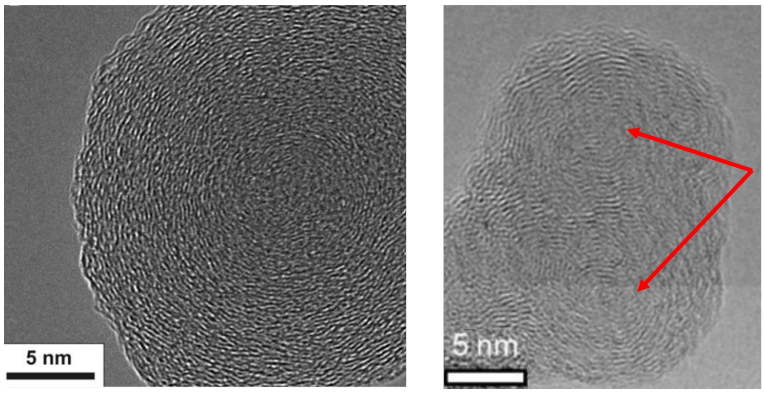

Figure 2.11: TEM images of soot primary particles. The first image represents a primary particle that has grown from a single core, and the second image represents a primary particle resulting from the merging of two incipient particles (pointed by red arrows). Images are taken from [60, 104].

3. **Coagulation:** Coagulation refers to the different processes that join particles together, including coalescence, aggregation, and agglomeration [32].
    - **Coalescence:** Coalescence describes the process by which incipient soot particles merge, forming a larger particle by eliminating the boundaries between the initial particles [32]. Coalescence leads to a reduction in the number of particles and an increase in primary particle size while maintaining a constant soot volume fraction.
    - **Agglomeration:** Agglomeration refers to the loose attachment of primary particles, likely through mechanisms such as Van der Waals forces, though these are not fully understood. Because of this weak bonding, agglomerates can easily break apart. Agglomeration occurs before aggregation [32]. It leads to a decrease in the number of particles and an increase in the size of the soot agglomerates while the soot volume fraction and primary particle size remain unchanged.
    - **Aggregation:** Aggregation refers to soot primary particles that strongly stick together (as opposed to agglomeration) to form a soot aggregate. According to the definition of Michelsen et al. [32]: "Mature soot particles are formed as aggregates of primary particles by the growth of layers of graphene on the surface of agglomerates of primary particles."
4. **Oxidation:** Oxidation reduces the mass of soot particles by converting them into CO or CO_2, and can cause fragmentation of soot aggregates. The primary oxidising agents are OH, O, and O_2. OH is the dominant reactant under fuel-rich conditions, while O_2 plays a larger role under fuel-lean conditions [96]. As a result of oxidation, both soot volume fraction and particle size decrease, leading to a reduction in the mass of soot emitted compared to the mass generated in the flame. Oxidation happens on the particle surface [105], but also on the core of the particle [106, 107]. Core oxidation is evidenced by the hollow, oxidised soot in Fig. 2.12.

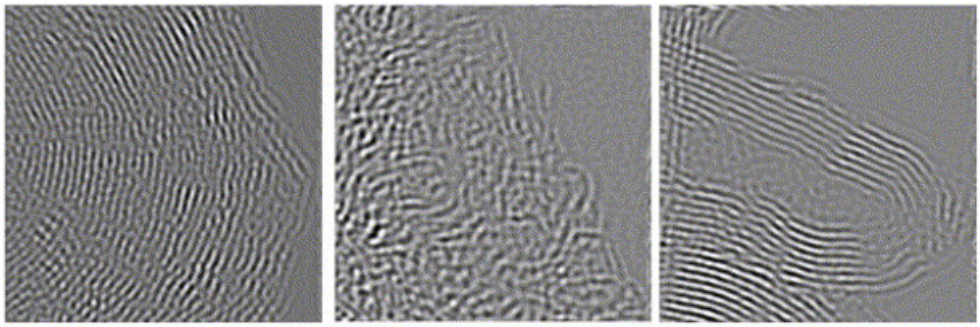

Figure 2.12: TEM images of soot particles at varying burn-off stages: 0%, 40%, and 75% (left to right). Images taken from [107].

In practice, at a given flame position, soot particles of diverse sizes co-exist, and multiple processes (for instance, inception and surface growth) can occur simultaneously. For instance, Fig. 2.13 shows the distribution of soot particles by mobility diameter at different axial positions in a laminar premixed flame. Each height above the burner (HAB) exhibits a polydisperse distribution, with two distinct modes appearing at heights above 60 mm. The figure illustrates that the number of larger particles increases with HAB, indicating particle growth through coagulation and/or surface growth. Additionally, at lower HAB, the total particle count rises with height, suggesting ongoing particle inception. This demonstrates that particle inception and particle growth (by surface reactions or coagulation) can occur simultaneously.

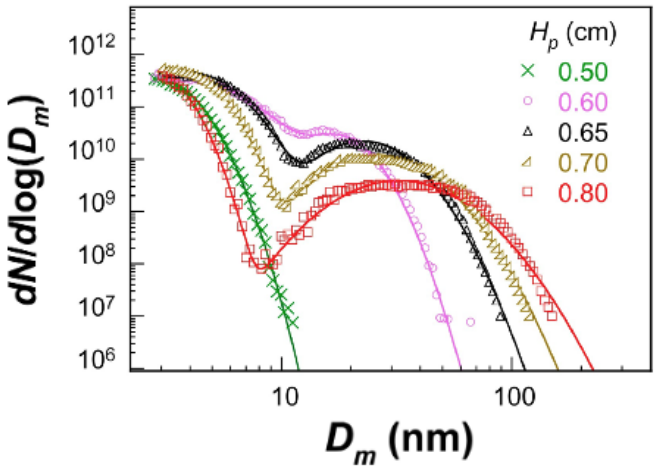

Figure 2.13: Distributions of soot particle mobility diameters measured using a scanning mobility particle sizer (SMPS) in a premixed C_2H_4+O_2+Ar flame. Different colours indicate various HABs. Adapted from [108].

2.5.3 Which conditions favour soot production?

To effectively control soot production and emissions, it is crucial to understand the conditions that favour soot formation. Several key factors play a significant role in this process:

- **Temperature:** Temperature plays a crucial role in both the production and destruction of soot. Research indicates that soot inception requires a minimum temperature of around 1400 K, regardless of the fuel used [72–75]. Numerous experimental [34, 76–80] and numerical [82, 109, 110] studies have demonstrated that higher flame temperatures lead to increased soot production in laminar flames. Specifically, in diffusion flames, peak soot volume fraction tends to rise linearly with temperature [34, 82, 110], and soot particle size also increases

as temperature rises, due to enhanced surface growth [80]. However, elevated temperatures also accelerate soot oxidation in the presence of oxidative species [82, 109, 110]. Consequently, depending on the local gas composition, higher temperatures simultaneously promote both soot formation and its destruction.

- **Pressure:** Pressure effect on soot production has also been extensively addressed in the literature [23, 42, 74, 81–83]. It was found that f_v scales with the pressure according to the relationship: $f_v \propto P^N$ where N varies from 1 to 3 depending on the flame conditions [23, 83].
- **Equivalence ratio:** Soot formation in premixed flames is strongly influenced by the local equivalence ratio, with fuel-rich conditions favouring the production of soot. In premixed flames, the number, size, and volume fraction of soot was found to increase with the equivalence ratio [111–114]. In diffusion flames, the presence of inherently fuel-rich regions creates favourable conditions for soot precursor generation and soot formation.
- **Type of fuel:** Although the fundamental mechanisms of soot formation are similar across various fuels [72, 73], the composition of the fuel is crucial in determining its sooting tendency. The fuel components can be classified into classes, each with varying potential to promote soot production. Fuels containing key soot-forming species, such as PAHs, are generally more prone to producing soot. Among hydrocarbons, the tendency to form soot generally decreases in the following order: PAHs, aromatics, alkynes, alkenes, and alkanes [73, 76, 84–88]. On the other hand, oxygenated fuels typically generate less soot compared to pure hydrocarbon fuels [89–92].

These factors highlight the inherent challenges in effectively reducing soot production, making it a complex and difficult task. High temperatures and pressures, which are known to favour soot formation, are typically desirable for achieving better thermodynamic efficiency in engines. Moreover, many combustion systems, such as diesel engines, direct injection gasoline engines, rocket engines, solid fuel combustion systems, gas turbines, and industrial burners, operate totally or partially in diffusion-burning mode. This mode of operation tends to create regions with high local mixture ratios, further promoting soot formation. Additionally, aromatic hydrocarbons, which is the fuel class that favours the most soot formation, constitute a significant portion of traditional fuel compositions [115–119]. Reducing the aromatic content in fuels would not only increase costs but also negatively impact gasoline engines. Indeed, aromatics play a crucial role in raising the octane number [88, 120], an important characteristic for gasoline fuels that prevents knocking which is harmful to the engine. Furthermore, aromatics are essential for preventing leaks in the seals of jet combustion systems [118]. Producing aromatic-free fuels would, therefore, be more expensive and may not necessarily be compatible with existing engines for retrofitting.

2.6 Important soot properties for this thesis

This section presents a brief discussion on three essential quantities for the analyses and calculations performed later in this thesis: the carbon-to-hydrogen ratio $\frac{C}{H}$, the soot absorption function $E(m_\lambda)$, and the soot volumetric heat capacity V_c.

2.6.1 Carbon-to-hydrogen ratio $\frac{C}{H}$

Soot particles are mainly composed of carbon and hydrogen atoms [48, 49]. During the soot maturation process, particles undergo dehydrogenation, or graphitisation, resulting in an increase in the carbon-to-hydrogen ratio, which is defined as $\frac{C}{H} = \frac{\text{number of C atoms}}{\text{number of H atoms}}$.

Harris and Weiner [121] observed that in ethylene premixed flames, the $\frac{C}{H}$ ratio rises with residence time and reaches similar values across flames with different mixture ratios. This trend leads to an increase in the $\frac{C}{H}$ ratio with increas-

ing HAB [122, 123]. The increase in the $\frac{C}{H}$ with the HAB is illustrated in Fig. 2.14 for two methane-premixed flames with different injection velocities. Both flames show an upward trend in the C/H ratio with HAB, highlighting the ongoing dehydrogenation of soot particles as they progress along the flame centreline.

Incipient soot particles typically have a $\frac{C}{H}$ ratio of around 1-2, while mature soot can reach ratios between 8 and 20 [52, 70, 124–128]. This progression in $\frac{C}{H}$ with soot maturation makes it a good tracer for soot maturity [56, 129].

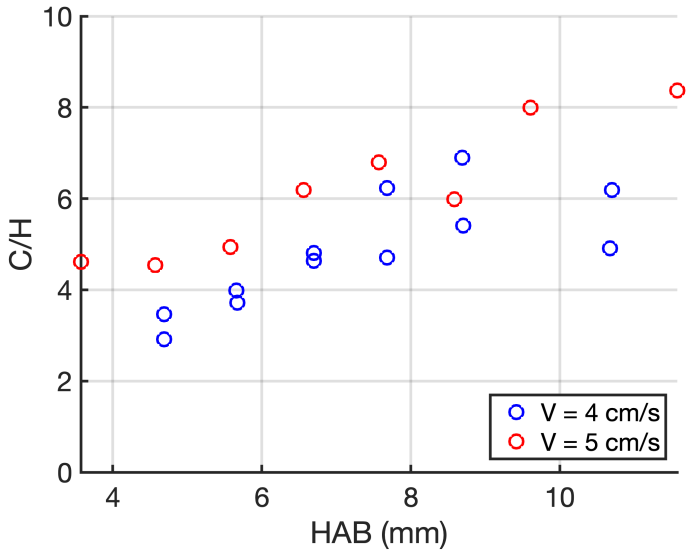

Figure 2.14: Carbon-to-hydrogen ratio versus the HAB in premixed methane flames. Blue and red circles correspond to different injection velocity of the mixture. Data taken from [122].

2.6.2 Soot absorption function $E(m_\lambda)$

Soot optical properties characterise the interactions of the soot particles with light: absorption and scattering. The soot refractive index m_λ -a wavelength-dependent quantity- characterises the soot absorption and scattering. Specifically, the absorption function $E(m_\lambda)$ represents the soot absorption and emission coefficient. It is defined from the refractive index m_λ as: $E(m_\lambda) = -\text{Im}\left(\frac{m_\lambda^2-1}{m_\lambda^2+2}\right)$. The absorption function is a key property for soot optical diagnostics to compute the soot temperature and the volume fraction f_v (by LII, light extinction or flame emission measurements [31]). In addition, $E(m_\lambda)$ is linked to the level of maturity of the soot particles [31]. As such, it is a good tracer for soot maturity along particles trajectory: young soot have low $E(m_\lambda)$ values, and mature ones (particles that have experienced important composition and structural changes) have higher values. So, accessing the value of $E(m_\lambda)$ gives information about the ageing of the soot.

Because of its importance for optical diagnostics and/or its link to the soot maturity, $E(m_\lambda)$ has been a major topic in the soot community over the years. Numerous studies [30, 31, 33, 50, 51, 54, 130–138] have been devoted to the measure of its absolute value or its wavelength dependence. Due to the double dependence of $E(m_\lambda)$ to the wavelength and soot maturity, but also because of the variety of experimental conditions and assumptions done in the different studies, there is a large spreading in the absolute values retrieved (even at a given wavelength). Values range from 0.05 [139] up to 0.52 [31] with a majority of values in the range 0.3-0.45 (see the reviews: [31, 136, 140]).

The dependence of $E(m_\lambda)$ on soot maturity and wavelength is discussed below, while the experimental methods for determining it are covered in Chapter 4.

Maturity dependence

The dependence of $E(m_\lambda)$ on soot maturity is well-known and reflects the changes in optical properties as soot particles maturate. Eremin [139] studied $E(m_\lambda)$ (at 1064 nm) during the pyrolysis of C_2H_2 behind a reflected shock wave, observing that $E(m_\lambda)$ initially ranged from 0.05 to 0.07 shortly after the shock wave arrival but increased to 0.2-0.25 with increasing time. This illustrates the maturation process of soot occurring over time, which increases the $E(m_\lambda)$ values. In laminar diffusion and premixed flames, where residence time along the centreline correlates with the HAB, a similar trend can be observed. Younger particles at lower HAB show lower $E(m_\lambda)$ values compared to older particles at higher HAB. Multiple studies on laminar premixed flames have demonstrated this axial behaviour of $E(m_\lambda)$ (at 1064 nm) [54, 131, 141]. As shown in Fig. 2.15a, $E(m_\lambda)$ increases from approximately 0.2 at the lowest HAB to around 0.45 at the highest HAB in several laminar premixed flames. In laminar diffusion flames, recent studies [51, 138, 142, 143] have provided 2D maps of $E(m_\lambda)$, revealing a more complex spatial evolution. Figure 2.15b shows the 2D spatial variations of $E(m_\lambda)$ at 810 nm in a laminar diffusion C_2H_4/air flame [51]. Here, $E(m_\lambda)$ still increases with the HAB but also varies radially, with higher values near the flame wings.

In a review, Liu et al. [31] set the range of $E(m_\lambda)$ for mature soot between 0.32 and 0.4 in the visible and infrared range.

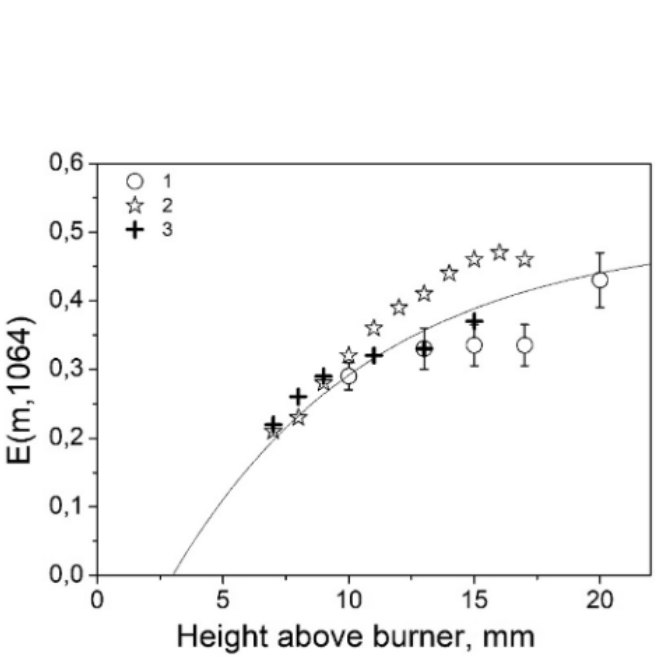

(a)

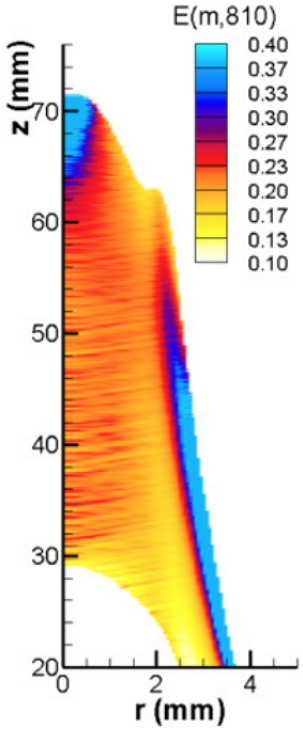

(b)

Figure 2.15: (a): Soot absorption function at 1064 nm versus the HAB in laminar premixed flames. Results 1 and 2 correspond to C_2H_4+air flames [54, 131], and 3 to a CH_4+air flame [141]. The solid line is the best fit for the data. Figure taken from [54]. (b): Soot absorption function at 810 nm in a C_2H_4/air laminar diffusion flame. Figure taken from [51].

Wavelength dependence

The knowledge of the wavelength dependence of $E(m_\lambda)$ is crucial for the computation of the soot particle temperature (Sec. 3.4.2). This has led to extensive research focused on understanding the spectral behaviour of $E(m_\lambda)$[54, 132, 137, 144–150]. Figures 2.16a and 2.16b present $E(m_\lambda)$ versus λ for several studies. The figures highlight the variability in spectral dependence, which is partly due to the variety of soot particles considered. From these studies, it is observed that the spectral dependence of soot is more pronounced in the UV and short visible wavelength ranges compared to the visible and infrared regions. Specifically, $E(m_\lambda)$ decreases rapidly with λ at wavelengths between $\sim$300-400 nm, with a slower decrease at longer wavelengths, eventually becoming nearly wavelength-independent in the upper visible and infrared ranges. Additionally, as illustrated in Fig. 2.16b, the spectral dependence of $E(m_\lambda)$ is influenced by soot maturity: younger particles, characterized by a higher organic content (OC) relative to total carbon content (TC), display a stronger wavelength dependence, compared to more mature particles, especially in the UV range [50, 132, 149]. In contrast, mature soot particles typically exhibit $E(m_\lambda)$ values that are nearly wavelength-independent, at least within the visible to infrared range (approximately 500 to 1064 nm) [31, 136, 145, 148].

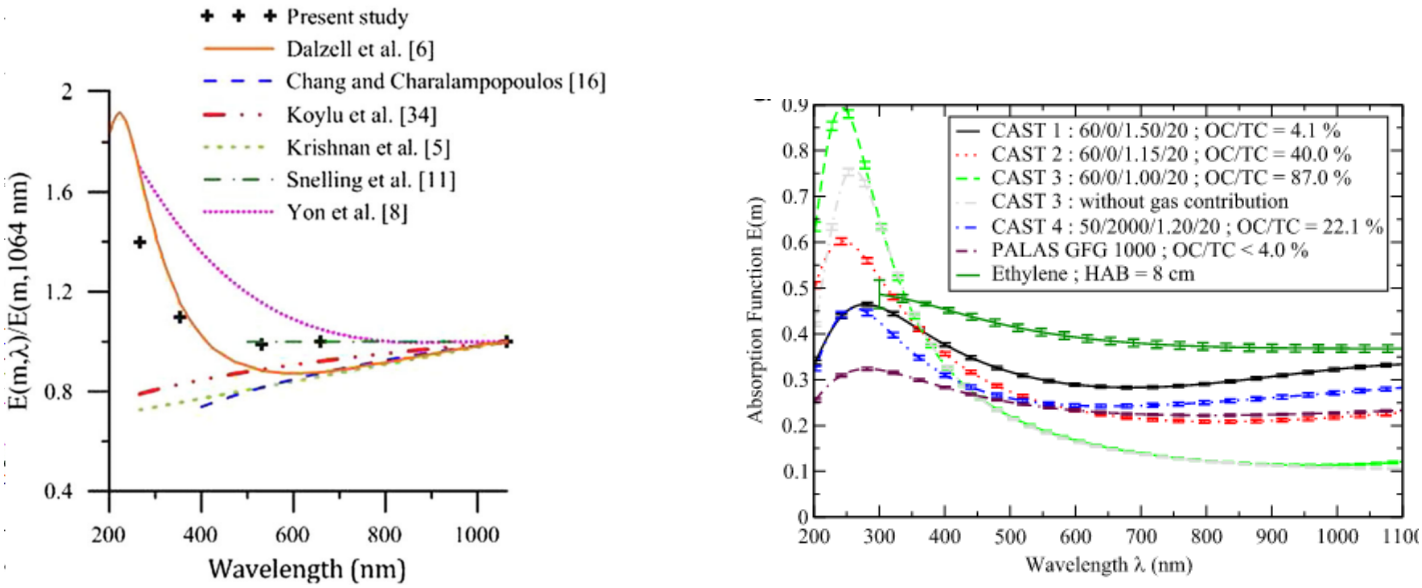

(a) (b)

Figure 2.16: (a) and (b): Wavelength dependence of the soot absorption function. In figure (b), OC and TC stand for organic carbon and total carbon, respectively. Figures are taken from [50, 148].

Summary on $E(m_\lambda)$

From the multiple studies done on $E(m_\lambda)$, it can be concluded that:

- The absolute value of $E(m_\lambda)$ increases with maturity.
- $E(m_\lambda)$ at 1064 nm for mature soot is most likely in the range 0.3-0.45.
- The spectral dependence of $E(m_\lambda)$ is often found to decrease with increasing wavelength so that the absorption function becomes weakly dependent on the wavelength in the visible and infrared range.
- The spectral dependence of $E(m_\lambda)$ decreases with maturity: youngest soot particles show a stronger spectral dependence than more mature ones.

2.6.3 Volumetric heat capacity V_c

The volumetric heat capacity is the product of the soot bulk density ρ and specific heat c: $V_c = \rho c$. It corresponds to the energy required to increase the temperature of a given volume of soot. As such, its value is required to describe the temperature evolution of soot during and after soot heating by a laser pulse (see chapter 3). The literature provides limited data on soot bulk density and specific heat, both of which are expected to vary with temperature and soot maturity.

Concerning bulk density, values ranging from $\sim$1100 to $\sim$2200 kg/m^3 can be found in the literature [31, 56, 151–154]. Similarly to $E(m_\lambda)$, and $\frac{C}{H}$, its value increases with the soot maturity. Values near 1800-1900 kg/m^3, i.e. value for mature soot are often encountered [30, 31, 130, 154]. However, very few values for the specific heat are available, and values for graphite are generally used [154, 155]. As a consequence, the volumetric heat capacity of soot particles is not well known.

The work of Michelsen [56] focuses on the temperature and maturity dependence of the soot volumetric heat capacity by considering PAHs (with $\frac{C}{H}$ between 1 and 2.4) and graphite data. Michelsen observed that the density increases with $\frac{C}{H}$ while the specific heat decreases, leading to a volumetric heat capacity independent of $\frac{C}{H}$. As the $\frac{C}{H}$ ratio reflects the maturity, Michelsen suggests that V_c may not vary much with the soot particle maturity. Similarly, with increasing temperature, density decreases while specific heat increases, and for high temperatures (above $\sim$1800 K), V_c is nearly temperature independent and equal to 4.6·10^6 J/K/m^3 [56, 105].

Part II

The laser-induced incandescence technique

Chapter 3

The laser-induced incandescence principle

As Laser-Induced Incandescence (LII) is the primary tool used in this thesis, this chapter is dedicated to its presentation. LII is an experimental technique particularly adapted to study soot particles in flames as multiple pieces of information can be extracted from the collected LII signal (soot temperature, soot volume fraction, soot primary particle diameter, soot absorption function). The chapter begins by introducing the fundamental concept behind the LII technique, along with a description of the typical experimental setup used for LII measurements. Then, the physical processes governing the LII phenomenon are presented, including the models used in this work to represent these processes. The LII principle can also be reproduced numerically using LII codes, which provide a numerical representation of the LII process. These codes are based on calculating the soot particle temperature by solving the energy balance equation, allowing synthetic LII signals to be generated. Such simulations can serve two purposes: they can be combined with experimental data to extract information about soot properties, or they can be used to theoretically investigate complex scenarios, quantifying the impact of influential factors on LII measurements. Accordingly, the third section of this chapter is dedicated to presenting the numerical LII code utilised in this thesis. Finally, the data processing of the LII measurements to obtain soot information is given. Equations for the computation of the temperature, soot volume fraction, and primary particle diameter are derived, while the computation of the absorption function from LII measurements is the object of the next chapter.

Contents

3.1 Laser-induced incandescence (LII) **41**
3.1.1 Principle of LII 41
3.1.2 A typical LII setup 41
3.1.3 Expression of the soot incandescence signal 43
3.2 Modelling the LII process **45**
3.2.1 Physical processes affecting the soot particles during LII 45
3.2.2 The energy balance equation 46
3.3 LII codes **49**
3.3.1 The LII code used in this work 49
3.3.2 What are LII codes used for? 50
3.4 Computation of soot temperature, concentration and size from the incandescence signal **50**
3.4.1 Expression of the incandescence signal collected by optical sensors 50

3.4.2 Soot temperature T measurements . . . 51
Two-Colour LII pyrometry (2C-LII) . . . 51
Spectrally resolved technique . . . 53
3.4.3 Soot volume fraction f_v measurements . . . 53
Traditional LII . . . 54
Auto-Compensated LII (AC-LII) . . . 55
3.4.4 Soot primary particle diameter d_p measurements . . . 55
Time resolved LII (TIRE-LII) . . . 56
Sensitivity analysis . . . 58
3.5 Advantages of the LII experimental technique . . . **59**

3.1 Laser-induced incandescence (LII)

The laser-induced incandescence (LII) technique was developed in the 70s-80s [26, 27] and is still one of the most used experimental techniques for the study of soot particles. It is mainly utilised to measure the soot volume fraction f_v [28, 43, 156–162], and the size of the soot primary particles d_p [37, 161, 163–169]. However, it can also provide information on the soot absorption function $E(m_\lambda)$ [30, 42, 54, 114, 130, 131, 134, 136, 141, 145, 147, 162, 170].

3.1.1 Principle of LII

LII involves heating soot particles to extremely high temperatures by irradiating them with a laser beam. Depending on the laser fluence (energy per unit area per pulse), the particles can reach temperatures exceeding 4000 K [52]. At such high temperatures, soot emit by incandescence as grey bodies, radiating across the ultraviolet, visible, and infrared spectra. The emitted radiation is collected by optical sensors and analysed to extract detailed information about the soot particles within the probe volume.

3.1.2 A typical LII setup

Figure 3.1 shows a typical LII experimental setup. The setup can be separated into three parts: the soot generation device, the excitation system, and the collection system.

Soot generation device
The soot particles are typically generated by dedicated burners [76, 171–175], soot generators [147, 170, 176, 177], or real-scale engines [37, 155, 174, 178]. A wide range of fuels and fuel blends can be employed for soot generation. Hydrocarbons like methane (CH_4) [34, 42, 79, 122, 125, 127, 134, 179–181] and ethylene (C_2H_4) [30, 51, 80, 108, 110, 159, 161, 182, 183] are among the most commonly used. However, other carbonaceous fuels, including alcohols, esters, and ethers, are also utilised for soot production in various experimental setups [89, 92, 135, 138, 184].

The use of standardised burners, such as the Yale [171] or the McKenna burner [185], enable reproducible experiments across different laboratories and provide optical access to the flame. Burners are typically operated at atmospheric pressure, though some experiments are conducted under reduced [132, 180] or elevated [40, 42, 186] pressures. Both diffusion and rich premixed flames can be operated in laminar or turbulent regimes, with laminar flames offering a stable and reproducible source of soot particles, while turbulent flames better mimic realistic conditions of applications. Aerosol generators are another method used to produce soot in a controlled environment, either through combustion or spark discharges. They are particularly useful for generating soot with specific characteristics. The use of engines to produce soot particles allows accessing real-world combustion scenarios and provides realistic soot samples. These engines can be equipped with optical access [37, 155, 174], allowing LII measurements directly inside the engine. Soot particles can be studied either directly within the flame or post-flame. In some cases, soot is collected from the flame or the exhaust of the generation device before being introduced into the probe region, where the LII technique is applied to study their properties.

Excitation system
The excitation system is composed of a laser source and optics to shape and relay the laser beam. The laser beam can be continuous [67, 187], but more commonly, it is pulsed with a typical duration of 10 ns. Such short pulses allow the soot to heat rapidly, minimising thermal losses during the laser heating. In this thesis, pulsed laser sources are utilised, so the focus is on these types of lasers.

The laser wavelength is classically the harmonic generated by a Nd-YAG laser: 1064 nm [28, 30, 131, 134, 140]. This

infrared wavelength is selected because it permits heating the soot particles without interacting with the gaseous species present in the flame with the soot [28, 140]. Indeed, shorter wavelengths, from ultraviolet to visible, up to 680 nm [188, 189] can be absorbed by the gas phase. Absorption by the gas phase is problematic as excited gaseous species emit fluorescence signals that interfere with the soot incandescence signal [140, 190], acting as a noise source. Nevertheless, laser wavelengths shorter than 680 nm, especially the second harmonic of Nd-YAG lasers (532 nm) are often encountered [42, 140, 162, 190–194]. In these cases, additional precautions should be taken for the signal collection to reject non LII signals (spectral window excluding fluorescence of the excited gaseous species, detection of the signal with temporal delay long enough to allow the fluorescence phenomenon to decay [28, 42, 140, 148, 195]).

At the laser output, the beam's fluence is typically non-uniform, with some areas being more intense than others (often, though not always, following a Gaussian distribution). This uneven laser fluence results in inhomogeneous heating of the soot particles in the probe volume, which can lead to inaccuracies in estimating soot properties [196]. In order to mitigate this issue, the laser beam's uniformity can be enhanced by employing specific optics designed to even out the distribution [196]. Alternatively, the most uniform portion of the laser beam can be isolated using a rectangular or round aperture, while the less uniform areas are removed. This produces a "top-hat" laser beam [113, 134, 192, 197], characterised by a more uniform fluence distribution. The diameter of the laser beam at the output is typically less than 1 cm, making it impractical for 2D imaging of flames several centimetres high. In order to address this, the laser beam can be expanded in one direction and narrowed in the other using lenses to create a laser sheet [28, 159, 164, 191, 198], which can illuminate the entire flame or at least a significant portion of it.

Collection system

The incandescence signal can be captured using photomultiplier tubes or cameras. Photomultiplier tubes offer high temporal resolution (typically around 1 ns), making them ideal for tracking the decay of the incandescence signal, which lasts for tens to hundreds of nanoseconds. However, as 0D sensors, they can only provide point-wise measurements. In contrast, cameras are 2D sensors that offer high spatial resolution, though they sacrifice temporal precision. Alternatively, combining a spectrometer with a camera enables access to the full spectrum of the incandescence signal, providing spectral information.

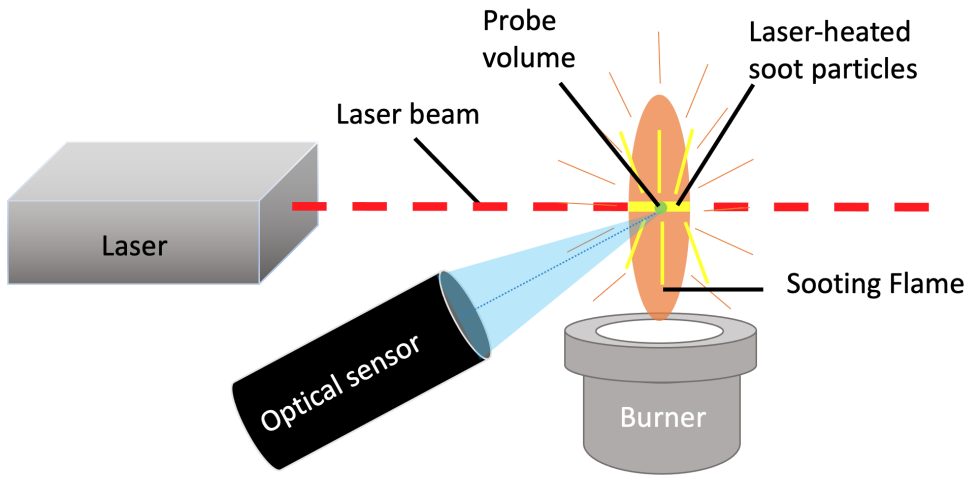

Figure 3.1: Schematic of a typical LII setup. It includes a burner that generates a flame containing soot particles, a pulsed laser for heating the soot particles, and an optical sensor for collecting the LII signal.

3.1.3 Expression of the soot incandescence signal

This subsection derives the theoretical expression for the incandescence signal emitted by soot particles. Additional details on radiation fundamentals relevant to the derivation are provided in Annex A. This expression is essential for both the LII computational models (Section 3.3) and the extraction of soot parameters from experimentally collected LII data (Section 3.4).

Incandescence signal from a spherical soot particle

Soot particles radiate over a broad spectrum. They follow Planck's law with a wavelength-dependent emission efficiency. The intensity radiated at a wavelength λ of a single spherical soot particle of diameter d_p heated at a temperature T over 4π steradians is given by [154]:

$$I_{one\ soot}(\lambda, T) = A_p q_{\lambda em} \pi I_{BB}(\lambda, T) \qquad [W.nm^{-1}] \tag{3.1}$$

where $I_{one\ soot}(\lambda, T)$ is the soot monochromatic spectral radiance, $A_p = \pi d_p^2$ is the soot surface, $q_{\lambda em}$ is the soot emission efficiency, and $I_{BB}(\lambda, T)$ is the monochromatic directional spectral radiance of a black body which is given by the Planck's law:

$$I_{BB}(\lambda, T) = \frac{2hc_{light}^2}{\lambda^5} \frac{1}{e^{\frac{hc_{light}}{\lambda k_B T}} - 1} \qquad [W.m^{-2}.sr^{-1}.nm^{-1}] \tag{3.2}$$

where h, k_B, and c_{light} are the constants of Planck, Boltzmann, and the light velocity, respectively.

For a spherical particle, the Rayleigh approximation gives a wavelength-dependent emission efficiency:

$$q_{\lambda em} = \frac{4\pi d_p E(m_\lambda)}{\lambda}. \tag{3.3}$$

The Rayleigh approximation (a particular case of the Mie scattering theory) [199] is valid when the size parameter defined as $x = \frac{\pi d_p}{\lambda}$ is small compared to 1: $x << 1$. For wavelengths of 400 and 1064 nm and for a typical primary particle diameter of 20 nm, the size parameter is 0.16 and 0.06, respectively. Therefore, the Rayleigh approximation is valid, but for shorter wavelengths and larger particles, the criterion $x << 1$ might not be respected anymore, preventing the use of this approximation.

Combining Eq. (3.1), Eq. (3.2), and Eq. (3.3) results in:

$$I_{one\ soot}(\lambda, T) = 8\pi^3 h c_{light}^2 d_p^3 \frac{E(m_\lambda)}{\lambda^6} \frac{1}{e^{\frac{hc_{light}}{\lambda k_B T}} - 1} \quad [W.nm^{-1}]. \tag{3.4}$$

Figure 3.2 gives the directional spectral radiance of a black body (i.e. the Planck's law given in Eq. 3.2) over the range 400-1000 nm and for temperatures representative of LII: from 2000 to 4500 K. The figure also gives the directional spectral radiance for a soot particle ($q_{\lambda em}\pi I_{BB}$) assuming a wavelength-independent soot absorption function of $E(m_\lambda)$ = 0.4, and a soot diameter of d_p = 20 nm. The figure shows that the higher the temperature, the higher the emission for all wavelengths and the shorter the wavelength of maximum emission. Due to the wavelength dependence of $q_{\lambda em}$, at a given temperature, the maximum of emission is shifted to a lower temperature for soot particles compared to a black body. The figures also demonstrate that at 600 nm, a soot particle heated to 3500 K emits 170 times more radiation than one at 2000 K. This highlights how significantly the incandescence signal is amplified when soot is heated by a laser, becoming dominant compared to the natural incandescence (or thermal emission) emitted by unheated soot at typical flame temperatures (around 1500-2000 K).

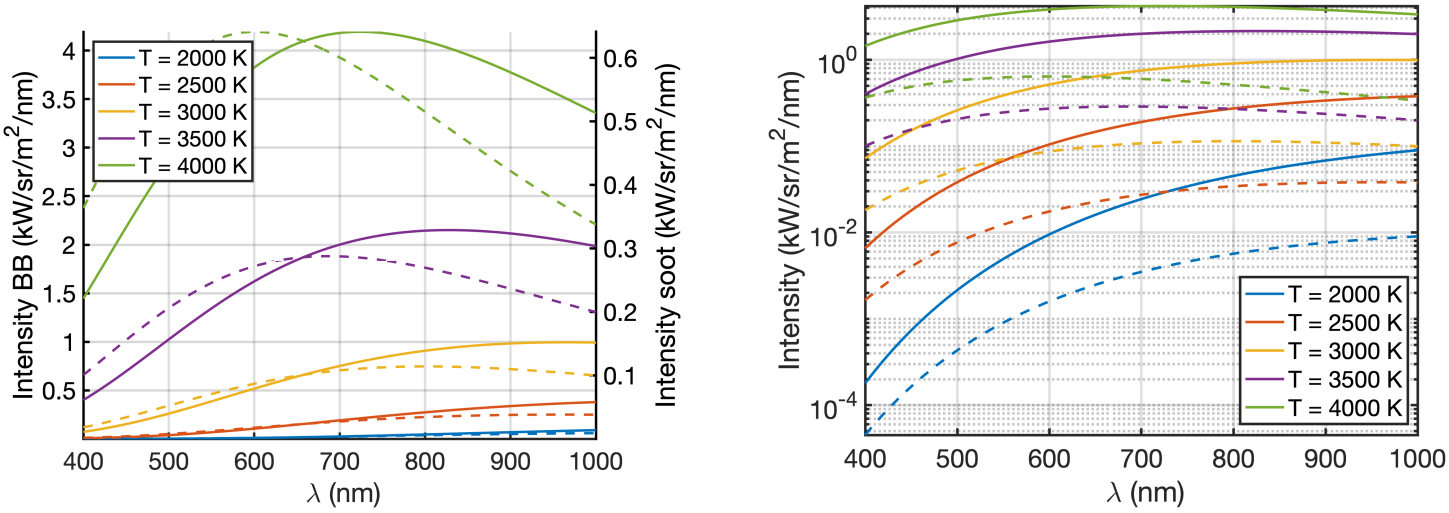

Figure 3.2: Directional spectral radiance for a black body (solid line, left axis) and for a soot particle (dashed line, right axis) as a function of wavelength. Spectral radiances are shown for temperatures between 2000 and 4000 K. The directional spectral radiance of a soot particle $q_{\lambda_{em}}\pi I_{BB}$ is computed considering a wavelength-independent soot absorption function $E(m_\lambda)$ = 0.4, and a particle diameter of d_p = 20 nm. Figure (b) presents the same data as figure (a) but on a logarithmic scale.

Incandescence signal from a collection of soot aggregates

In practice, the soot particles can be aggregates of spherical-like primary particles of different sizes d_p. The Rayleigh-Debye-Gans theory for fractal aggregates (RDG-FA) [64, 199] is used to describe the interaction with light of soot aggregates [50, 200–203]. Within the RDG-FA, the incandescence signal of an aggregate is the summation of the incandescence signal of each particle constituting the aggregate: the primary particles constituting the aggregate are treated independently. Also, the signal emitted by multiples aggregates is the summation of individual signal of each aggregates: interactions between aggregates are neglected. Thus, assuming that all primary particles are spherical, the incandescence signal of a collection of soot aggregates is the summation of the signal of each primary particle constituting these aggregates. If the distribution of these primary particles of different diameters is given by $\Psi(d_p)$, the total incandescence signal is:

$$I_{soot}(\lambda,T) = 8\pi^3 hc_{light}^2 \int_0^\infty \Psi(d_p) d_p^3 \frac{E(m_\lambda)}{\lambda^6} \frac{1}{e^{\frac{hc_{light}}{\lambda k_B T}} - 1} dd_p \quad [W.nm^{-1}]. \tag{3.5}$$

The soot volume fraction f_v is defined as the portion of the volume V occupied by the soot particles:

$$f_v = \frac{V_{soot}}{V}, \tag{3.6}$$

where V_{soot} is the volume occupied by the soot. For a single particle $V_{soot} = \pi \frac{d_p^3}{6}$, and for a distribution of spherical soot particles: $V_{soot} = \int_0^\infty \Psi(d_p) \frac{\pi d_p^3}{6} dd_p$. Therefore, the signal coming from all the soot particles present in the volume V is:

$$I_{soot}(\lambda,T) = 48\pi^2 hc_{light}^2 f_v V \frac{E(m_\lambda)}{\lambda^6} \frac{1}{e^{\frac{hc_{light}}{\lambda k_B T}} - 1} \quad [W.nm^{-1}]. \tag{3.7}$$

Equation 3.7 shows that the incandescence signal emitted by soot particles in a probe volume V at a given wavelength depends:

- On the soot temperature T through Planck's law.

- Linearly on the soot volume f_v.
- Linearly on the soot absorption function $E(m_\lambda)$.

It has to be noticed that Eq. (3.5) was obtained, assuming that all the particles have the same temperature and absorption function.

3.2 Modelling the LII process

The initial efforts to model the LII process were pioneered by Eckbreth [26] and Melton [27]. Their work laid the foundation for understanding the LII process by focusing on solving the energy balance equation for soot particles during LII experiments, laying the groundwork for the development of the first numerical LII models capable of reproducing experimental results.

This section begins by introducing the key physical processes affecting soot particles during LII experiments, followed by a presentation of the models retained in this thesis to represent these phenomena. These models serve two essential purposes here. First, they are integral to the LII code considered in this thesis (Sec. 3.3). Second, under specific conditions, these models can be simplified to yield analytical solutions of the energy balance equation. These simplified expressions offer a practical framework for extracting soot properties from experimental data (Sec. 3.4), providing an efficient approach for estimating soot characteristics.

3.2.1 Physical processes affecting the soot particles during LII

When heated by a high-energy laser pulse, a soot particle strongly interacts with its environment by exchanging thermal energy and mass [154, 190]. Figure 3.1 represents the different interactions happening during LII between a soot particle and its environment. The different interactions are:

- **Absorption:** The soot particle absorbs the photons of the laser beam. This results in an elevation of the soot particle temperature.
- **Conduction:** The soot particle cools by exchanging energy with the colder surrounding gas.
- **Sublimation:** When heated to a temperature above the sublimation temperature ($\sim$ 4000-4500 K), the soot particle undergoes a phase change: a portion of the soot is lost to the gas phase. The mass of the particles decreases, and so is its thermal energy as sublimation is endothermic.
- **Radiation:** The soot particle radiates energy to cool down. It is these radiations that form the incandescence signal collected during LII experiments. In general (with the exception of low-pressure flames), radiation cooling is negligible compared to the other cooling mechanisms (especially conduction and sublimation if the sublimation temperature is reached) [154].
- **Oxidation:** Oxygenated species (mainly O_2, OH, O) oxidise the soot particle, resulting in a reduction of the particle's mass and size and an increase in the thermal energy of the particle. It has little contribution to the thermal and mass balance of the soot but can impact the particle size [154, 190].
- **Annealing:** Annealing is a thermally induced process that results in a modification of the physical and/or chemical properties of soot particles through a displacement of carbon atoms [32].
- **Thermionic emission:** Thermionic emission represents the thermal ejection of the electrons from the particle. It has a negligible effect at low laser fluences but gains in importance at higher fluences [154]. According to

[190], the utility of thermionic emission is to estimate the charging of the soot particle caused by the laser heating.

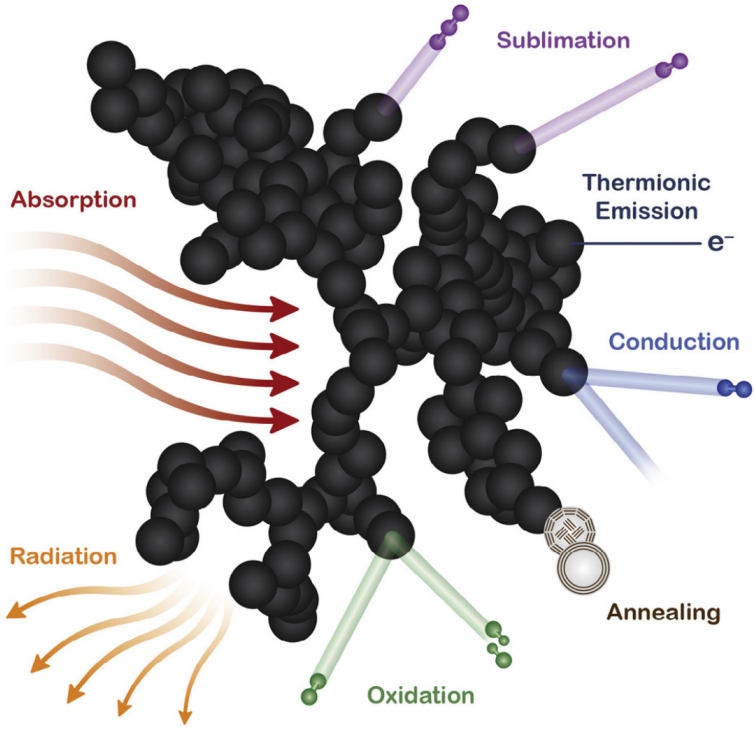

Figure 3.3: Scheme of a soot particle and the interactions it can have with its environment during an LII experiment. Image taken from [190].

3.2.2 The energy balance equation

The LII process can be modelled by applying the energy balance equation to a soot particle. The terms of the energy equation are the one of Fig. 3.3, except for oxidation, thermionic emission and annealing, which are generally neglected in the literature [154]. Thus, only the absorption, conduction, radiation and sublimation are retained here:

$$\frac{dU}{dt} = \dot{Q}_{abs} - \dot{Q}_{cond} - \dot{Q}_{rad} - \dot{Q}_{sub}. \tag{3.8}$$

U is the internal energy, $\dot{Q}_{abs}$ is the thermal power absorbed by the soot particles, $\dot{Q}_{cond}$, $\dot{Q}_{sub}$ and $\dot{Q}_{rad}$ are the power lost by the soot particles by conduction, sublimation and radiation, respectively. The models retained in this thesis for these terms are presented hereafter.

Internal energy

The internal energy U for a spherical particle of diameter d_p, density ρ, specific heat c and at temperature T is expressed as:

$$U = \frac{\pi d_p^3}{6} \rho c T. \tag{3.9}$$

Absorption term

The absorbed power is given by:

$$\dot{Q}_{abs} = \sigma_{abs} \dot{Q}_{laser}(t), \tag{3.10}$$

where σ_{abs} is the absorption cross-section of a soot particle and $\dot{Q}_{laser}(t)$ is the instantaneous surface power of the laser pulse verifying: $\int_{t_0}^{t_0+\Delta t_{pulse}} \dot{Q}_{laser}(t)dt = F$, F being the laser fluence, t_0 is the beginning of the laser pulse and

Δt_{pulse} is the pulse's duration.

The RDG-FA approximation [64, 199] is used to describe the interaction with light of soot aggregates [50, 200–203]. Therefore, the soot aggregate absorption cross-section is the summation of the cross-sections of each particle constituting the aggregate: the primary particles constituting the aggregate are treated independently. In addition, for a laser wavelength λ_{laser} = 1064 nm and a typical primary particle diameter of 20 nm, the size parameter of the primary particle is 0.06 $<<$ 1. Thus, the absorption behaviour can be described by the Rayleigh regime. Therefore, the absorption cross-section of primary particles is given by:

$$\sigma_{abs} = q_{\lambda abs} A_p = \frac{\pi^2 d_p^3 E(m_\lambda)}{\lambda_{laser}}. \tag{3.11}$$

Under the Kirchhoff law stating that for an arbitrary body emitting and absorbing thermal radiation in thermodynamic equilibrium, the emission is equal to the absorption $q_{\lambda abs} = q_{\lambda em}$. Therefore, the power absorbed by a primary particle is given by:

$$\dot{Q}_{abs} = \frac{\pi^2 d_p^3 E(m_{\lambda_{laser}})}{\lambda_{laser}} \dot{Q}_{laser}(t). \tag{3.12}$$

It should be noted that within the Rayleigh regime, the emission efficiency of the particle depends on its size, implying that the absorption (and emission) of a particle is volumetric and not proportional to its surface.

Conduction term

Conduction cooling is generally the most important cooling mechanism in LII. An accurate conduction model is required to retrieve information on the soot primary particle diameter from experimental data. Three conduction regime can be encountered [204] depending on the Knudsen number K_n:

- K_n < 0.01: continuum regime.
- 0.01 < K_n < 10: transition regime.
- K_n > 10: free molecular regime.

The Knudsen number is given by $K_n = \frac{2\lambda_{MFP}}{d_p}$ where λ_{MFP} is the mean free path of gas molecules constituting the gas around the particle. The following definition for the mean free path is considered [204]:

$$\lambda_{MFP} = \frac{k_B T_0}{\sqrt{2}\sigma_{gas} P_{gas}}, \tag{3.13}$$

where k_B is the Boltzmann constant, P_{gas} is the ambient gas pressure, and σ_{gas} is the mean collision sectional area of gas molecules. Assuming a gas temperature of 1700 K, and with σ_{gas} = 4.21$\cdot$ 10^{-19} m^2 [205], one obtains a mean free path of $\sim$400 nm. For a soot particle with a typical sot primary particle diameter of d_p = 20 nm, the Knudsen number is 40. Thus, the heat conduction can be described by the free molecular regime. The model retained in this work to describe conduction in the free molecular regime is given by Eq. (3.14). Models describing other conduction regimes and other models for the free molecular regime can be found in [154, 204].

$$\dot{Q}_{cond} = \alpha \pi d_p^2 P_{gas} \sqrt{\frac{R}{8\pi W_{gas} T_0}} \frac{\gamma_{gas}+1}{\gamma_{gas}-1} \left(T - T_0\right), \tag{3.14}$$

where R is the universal gas constant, W_{gas} is the average gas molar mass, and γ_{gas} represents the mean value of the gas specific heat ratio γ between the temperature of the gas T_0 and of the particle T. The gas is usually assumed to have the properties of N_2. The thermal accommodation coefficient α characterises the efficiency of the energy

exchange between a soot particle and the bath gas. Its expression is given by [206]:

$$\alpha = \frac{T_{gas,final} - T_{gas,initial}}{T_{particle} - T_{gas,initial}}, \tag{3.15}$$

where $T_{gas,initial}$, $T_{gas,final}$ are the temperature of a gas molecule before and after colliding with a particle at a temperature $T_{particle}$. α = 1 means thermal equilibrium between the particle and the gas molecule colliding with it, while α = 0 if no energy is exchanged.

Multiple values are encountered in the literature for the thermal accommodation coefficient. Experimentally determined ones for graphite or soot originating from different sources and for different bath gases are gathered in [136, 190]. Values range from 0.05 to 1, with most values in the range 0.25-0.45. These differences partly come from the dependence of α with the bath gas composition (molar mass, monoatomic/polyatomic molecules), but α may also depend on the soot maturity and temperature [136, 190].

In large, non-linear aggregates with a high fractal dimension, some primary particles are partially masked by others. This reduces the effective surface area for heat conduction, thereby decreasing thermal losses through conduction. This phenomenon, known as the shielding effect [207], causes the aggregates to cool more slowly, increasing their cooling time and making the primary particles appear bigger than they are. In the current formulation of conduction cooling, the shielding effect is not considered.

Radiative term

For the radiation loss term, the expression of [207] is considered:

$$\dot{Q}_{rad} = 8\pi^3 d_p^3 E(m_\lambda) \frac{(k_B T)^5}{h^4 c_{light}^3} \int_0^\infty \frac{t^4}{e^t - 1} dt, \tag{3.16}$$

where $\int_0^\infty \frac{t^4}{e^t-1} dt = 24.886$. It has to be noted that for atmospheric (or pressurised) flames, the energy lost by radiation is, in general, negligible compared to the conduction term [154].

Sublimation term

The sublimation term is given by:

$$\begin{aligned} \dot{Q}_{sub} &= \frac{\Delta H_{vs}}{W_{vs}} J_{sub}, \\ J_{sub} &= \frac{\pi d_p^2 W_{vs}}{N_{Av}} \frac{1}{\frac{1}{N_C} + \frac{1}{N_{FM}}}, \end{aligned} \tag{3.17}$$

where J_{sub} is the particle mass lost by sublimation. The continuum flux term is $N_C = \frac{2 P_{vs} a_{diff}}{k_B T d_p}$, with $a_{diff} = \frac{f k_B T}{4\sigma(W_{vs}) P_{gas}} \sqrt{\frac{RT}{\pi W_{vs}}}$, $f = \frac{9\gamma - 5}{4}$, and the free molecular flux term is: $N_{FM} = \frac{\beta P_{vs}}{k_B T} \sqrt{\frac{RT}{2\pi M_{vs}}}$. ΔH_{vs}, W_{vs}, P_{vs}, are respectively the average enthalpy of formation, the molar mass and the partial pressure of sublimed carbon clusters. σ is an average molecular cross-section for subliming species that depends on W_{vs}. β is the mass accommodation coefficient.

Values encountered in literature for β are very dispersed (from 0 when sublimation is neglected to 1 when it is maximised) [154]. There is currently no consensus on the value one should use. In most cases, the sublimation models fail to reproduce experimental LII signals, and temperatures decay accurately in the first tens of nanoseconds after the laser pulse when high temperatures are reached [190]. This indicates that the sublimation model does not represent well the actual physical processes happening at high fluences and that the high-temperature mechanisms -including sublimation- are currently poorly understood [136, 190].

Other models

Models for the annealing, oxidation or thermionic emission terms can be found in [154, 190]. It has to be pointed

out that the models retained here for the conduction, radiation, and sublimation terms are not universal; different formulations exist and can be found in [154, 190].

3.3 LII codes

LII codes provide a numerical representation of the LII process. They give the temporal evolution of the soot temperature and incandescence signal. Such codes are based on obtaining the particle temperature by solving the energy balance equation of soot particles (Eq. (3.8)). Once the temporal evolution of the temperature is known, the incandescence signal is obtained with Eq. (3.5). This section aims to describe the LII code used in this work and its usage.

3.3.1 The LII code used in this work

Numerous LII codes have been developed in the literature, each employing distinct models or tuning parameters to represent the physical processes presented in section 3.2.1. A description of the different models can be found in the following reviews [140, 154].

The present work uses a modified version of the LII code developed by A. Cuoci in the framework of the thesis of A. Bodor [208] as a collaboration between the EM2C laboratory and the CRECK modelling team [209]. The modifications include a change in the model for the radiation losses in the energy equation and the capability to simulate soot particle heating with two consecutive laser pulses. This LII code considers only the most commonly used terms: absorption, conduction, sublimation and radiation, while oxidation, annealing and thermionic emission are neglected. The models retained for these terms have been described in Sec. 3.2. In this work, a monodisperse population of non-aggregated spherical soot particles will be considered, and the shielding effect [207] is neglected.

Reference input parameters of the LII code

Several parameters are required as input of this code: $E(m_\lambda)$, T_0, P_{gas}, F, λ_{laser}, the duration of the laser pulse: $FWHM_{laser}$ (full width at half maximum), ρ, d_p, α, and β. These parameters represent either laser pulse parameters (F, λ_{laser}, $FWHM_{laser}$), flame conditions (P_{gas}, T_0), soot properties (ρ, d_p, $E(m_\lambda)$) or modelling parameters (α, β). It has to be noted that with this code, the density is one of the inputs of the LII code and is constant, while the specific heat is hard-coded with a temperature-dependent expression for carbon coming from [155].

The selected reference values for all the input parameters of the LII code are gathered in Table 3.1. The values of $E(m_\lambda)$, T_0, ρ and d_p are chosen to be representative of soot particles and flame conditions. For the thermal accommodation coefficient, a value of 0.3 is selected since the values commonly used in the literature (collected in [154]) are generally close to 0.3. For the mass accommodation coefficient, given the spread of its value in literature [140, 154], and with the purpose of testing the technique proposed in the next chapter (Chapter 4) in unfavourable conditions (high sublimation), a value of 1 is retained, corresponding to the maximum possible value, i.e. strong sublimation is assumed. The laser pulse is represented by a Gaussian function having a full width at half maximum of 12 ns and a wavelength of 1064 nm. Finally, the gas pressure is equal to 1 atmosphere. These three last parameters are kept constant throughout the thesis.

LII code inputs		
Parameter	**Unit**	**Value**
$E(m_\lambda)_{ref}$	–	0.37
$T_{0_{ref}}$	K	1860
$d_{p_{ref}}$	nm	26
ρ_{ref}	kg/m^3	1950
α_{ref}	–	0.3
β_{ref}	–	1
P_{gas}	Pa	101300
λ_{laser}	nm	1064
$FWHM_{laser}$	ns	12

Table 3.1: Reference input parameters of the LII code.

3.3.2 What are LII codes used for?

LII codes have two major uses:

- Soot property estimation: By fitting experimental data to numerical simulations, LII codes can estimate soot properties like the absorption function [30], primary particle size [37, 40, 167], and thermal accommodation coefficient [30]. The values that best match the experimental data are considered the most probable.
- Theoretical analysis: LII codes allow for the theoretical study of the LII technique, helping to quantify the impact of complex factors. For instance, Liu et al. [196, 210] used an LII code to demonstrate that inhomogeneities in the laser beam impact the f_v measurement. They have been able to quantify its impact and have identified conditions for reducing it.

In this thesis, the LII code described previously is principally used for theoretical analysis: it is used to theoretically assess the performances of the new LII-based experimental technique presented in chapter 4, and will be used in multiple other occasions when a theoretical analysis is required.

3.4 Computation of soot temperature, concentration and size from the incandescence signal

This section outlines the methods used in this thesis to compute soot temperature, volume fraction, and primary particle diameter. Since these quantities are derived from the measured incandescence signal, the section begins by presenting the expression for the collected LII signal. It then reviews experimental techniques for determining these key soot properties, with a focus on the LII-based methods that are employed in this work. The following chapter (Chapter 4) will detail the procedures for deriving the soot absorption function and the gas temperature from the LII signal.

3.4.1 Expression of the incandescence signal collected by optical sensors

The LII signal S_λ^{LII} collected by an optical sensor over the rectangular spectral window [λ_{inf}, λ_{sup}], for an exposure time $\tau_{exposure}$, over a solid angle Ω, and for a probe volume V can be expressed from the theoretical expression of

the incandescence signal of Eq. (3.7) as:

$$S_\lambda^{LII} = 12\pi h c_{light}^2 f_v V \Omega \tau_{exposure} \Sigma_\lambda E(m_\lambda) \frac{\Delta\lambda}{\lambda^6} \frac{1}{e^{\frac{hc}{\lambda k_B T}} - 1}, \tag{3.18}$$

where $\Delta\lambda = \lambda_{sup} - \lambda_{inf}$, and Σ_λ accounts for the quantum efficiency of the sensor and the transmitivity of the different optics of the collection system.

This expression can be simplified using Wien's approximation: $e^{\frac{hc_{light}}{k_B \lambda T}} >> 1$. Indeed, for a wavelength of 800 nm and a temperature of 4000 K, Wien's approximation results in an underestimation of 1.1% of the black body emission computed with the Planck's law (Eq. (3.2)). This percentage goes down for lower temperatures or wavelengths. As both lower wavelength and temperatures are considered for most of this work, Wien's approximation can be used with a negligible impact on the results.

For a rectangular laser beam propagating perpendicularly to the collection system, the collection volume is $V = L_{laser} S_{coll}$ where L_{laser} is the laser beam width, and S_{coll} is the collection surface. Then, Eq. (3.18) can be rewritten as:

$$S_\lambda^{LII} = 12\pi h c_{light}^2 f_v L_{laser} C_{calib,\lambda} E(m_\lambda) \frac{\Delta\lambda}{\lambda^6} e^{-\frac{hc}{\lambda k_B T}}, \tag{3.19}$$

where $C_{calib,\lambda}$ is a calibration constant (for a given wavelength) equals to $C_{calib,\lambda} = S_{coll} \cdot \Omega \cdot \tau_{exposure} \cdot \Sigma_\lambda$. The detailed procedure for calculating the equation (3.19) is described in the annex B. It has to be pointed out that this equation does not consider auto-absorption of the signal by the soot, scattering, nor any inhomogeneities in the probe volume (soot temperature or soot properties such as $E(m_\lambda)$, or d_p). Additionally, it is important to note that the quantities computed from LII signals do represent averaged values in the probe volume.

3.4.2 Soot temperature T measurements

The two main techniques used to compute the soot temperature after laser heating are the Two-Colour LII pyrometry (2C-LII), and the spectrally resolved LII.

Two-Colour LII pyrometry (2C-LII)

The 2C-LII [130, 131, 160] is the main technique used in this thesis, the soot temperature T is obtained from the ratio of the incandescence signal S_λ^{LII} (Eq. (3.19)) at two different wavelengths λ_1 and λ_2:

$$T = \frac{h c_{light}}{k_B} \left(\frac{1}{\lambda_2} - \frac{1}{\lambda_1} \right) \frac{1}{\ln \left(\frac{S_{\lambda_1}^{LII}}{S_{\lambda_2}^{LII}} \frac{E(m_{\lambda_2})}{E(m_{\lambda_1})} \left(\frac{\lambda_1}{\lambda_2} \right)^6 \frac{\Delta\lambda_2}{\Delta\lambda_1} \frac{C_{calib,\lambda_2}}{C_{calib,\lambda_1}} \right)}. \tag{3.20}$$

It is important to note that not all soot particles within the collection volume reach the same temperature due to variations in energy absorption and emission, which can arise from differences in soot properties or local laser fluence. Consequently, the temperature calculated using Eq. (3.20) represents an "effective" temperature: a weighted average temperature that is biased in favour of the hottest particles.

Equation (3.20) requires the knowledge of the ratio $\frac{E(m_{\lambda_1})}{E(m_{\lambda_2})}$. That is to say, it requires knowing the wavelength dependence of $E(m_\lambda)$ between the two collection wavelengths. This quantity is a priori unknown. Thus, a spectral behaviour for $E(m_\lambda)$ has to be assumed or measured.

Selection of the collection wavelengths λ_1, and λ_2

The selection of the two spectral windows is essential for an accurate temperature estimation. The criteria consid-

ered in this thesis for the selection of the two collection wavelengths are presented here. Several limitations, both physical and material-related, must be considered when selecting the collection wavelengths:

- Liu et al. [211] conducted a theoretical and numerical analysis on the accuracy of measuring soot temperature and volume fraction using 2C-LII with various pairs of detection wavelengths in the visible range. Their findings indicate that the lower detection wavelength should be as short as possible, while the upper detection wavelength should be as long as possible. In other words, maximising the separation between the two detection wavelengths enhances the precision in determining soot temperature and volume fraction.
- Longer wavelengths in the visible range are advised [210] to help reduce the effect of inhomogeneities in the laser beam. Indeed, laser inhomogeneities bias the temperature computations toward the hottest soot in the probe volume and lead to an underestimation of the soot volume fraction. The shorter the detection wavelengths, the more biased the temperature estimations.
- The wavelength dependency of the absorption function is more important in the ultraviolet and near visible range (Fig. 2.16) than in the upper visible and infrared range. This is especially true for younger soot particles. Thus, it is preferable to avoid detection wavelengths in the ultraviolet and near visible ranges.
- Fluorescence signals from excited species can occur during experiments. In this study, a laser wavelength of 1064 nm was chosen to avoid inducing fluorescence from the gaseous phase [133, 188, 189]. However, even at this wavelength, C_2 Swan and C_3 Swing band fluorescence emissions can appear due to partial soot vaporisation when high laser fluences are used (around 500 mJ/cm^2) [212]. The most intense Swan bands are spread across the visible range, particularly at 467, 516, and 544 nm, while Swings bands primarily emit between 360 and 440 nm [212, 213]. Only minor fluorescence can be observed between 580 and 620 nm (Fig. 3.4).

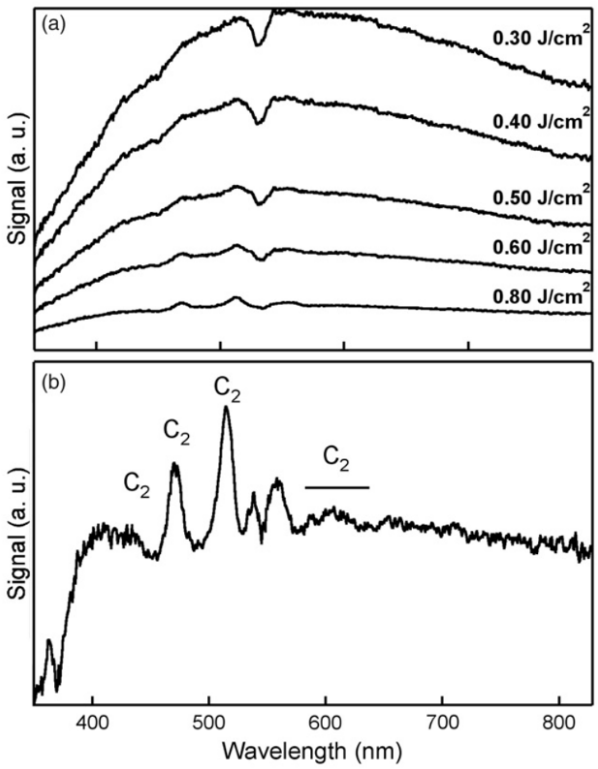

Figure 3.4: Emission spectra obtained 5 ns after irradiating soot particles with a 1064 nm laser beam with a laser fluence of (a): 300 to 800 mJ/^{2}, and (b): 3500 mJ/cm^2. Images taken from [212].

- The quantum efficiencies of the optical sensors available peak near the middle of the visible range. The sensors available for this thesis are usable between ∼300 nm and ∼720 nm.

As these recommendations are sometimes in conflict, a trade-off has to be made. Here, the selected collection wavelengths are 578 and 716 nm. Both windows are outside of the strongest fluorescence bands of C_2 and C_3. It was verified in annex D that no strong fluorescence appear for these wavelengths. The longer wavelength was selected to be at the limit of the quantum efficiency of the sensors available. The shortest wavelength was chosen to be far from the longer while not being in the ultraviolet or near visible range to limit the wavelength dependency of $E(m_\lambda)$ between these two wavelengths. That way, the variation of the absorption function between 578 and 716 nm should be reduced.

As the spectral dependence of soot particles can vary with soot maturity [50, 51, 133, 149] (which is a priori unknown), and because the wavelength independent assumption is quite good for wavelengths in the upper visible range [31], the assumption $\frac{E(m_{\lambda_1})}{E(m_{\lambda_2})} = 1$ is retained in this work. The impact of a deviation from this assumption is discussed later.

As a final remark, the 2C-LII pyrometry is identical to traditional 2C pyrometry [214–216] (that is considered in annex E), the only difference being that in 2C-LII pyrometry, the soot particles are laser-heated to higher temperatures than the local temperature, while with traditional 2C pyrometry, no laser is used. Therefore, with 2C-LII, the measured signal comes mainly from the heated soot, while only a small part of the signal comes from the soot present in the sensor's line of sight. This makes it possible to compute the temperature of the laser-heated region directly. With 2C pyrometry, additional post-processing (e.g. Abel's inversion algorithm in the case of an axisymmetric flame) would be required. For a turbulent flame, a "line-of-sight" averaged temperature would be obtained.

Spectrally resolved technique

2C-LII pyrometry is the main technique used to compute the soot temperature in this thesis. However, the spectrally resolved technique [144] for temperature determination is also considered in annex D. Soot emission spectrum can be recorded on a large spectral range with a spectrometer. Then, the soot temperature can be computed by fitting the normalised emission spectrum to the theoretical soot emission:

$$ln\left(\frac{S_\lambda^{LII}}{S_{\lambda_{ref}}^{LII}}\left(\frac{\lambda}{\lambda_{ref}}\right)^6\frac{E(m_{\lambda_{ref}})}{E(m_\lambda)}\right) = -\frac{hc}{k_BT}\frac{1}{\lambda}. \tag{3.21}$$

As this method considers the soot emission at more than two wavelengths, it should be more precise than the 2C-LII. However, the results still depend on the assumption made for the wavelength dependence of the soot absorption function.

3.4.3 Soot volume fraction f_v measurements

This thesis only uses the Auto-Compensated LII (AC-LII) technique to compute the soot volume fraction, but other techniques exist and are listed here. These techniques can be divided into *ex-situ* techniques (techniques that require soot sampling and are therefore intrusive) and *in-situ* techniques (techniques that allow working directly in the flame and are therefore little or non-intrusive).

Among the *ex-situ*, one can cite: thermophoretic sampling [217], gravimetric sampling [157, 178, 218, 219], particle densitometry [220]. These techniques present the advantage of not depending on the soot optical properties (which are not known with precision, see section 2.6.2 of Chapter 2) and are sensitive to the weakly absorbing particles.

However, the spatial resolution is limited and more importantly, as *ex-situ* techniques, they are intrusive: they disturb the flame and possibly alter the soot particles.

Several *in-situ* techniques allow overcoming these drawbacks. They are less intrusive, but most of these techniques require the knowledge of soot optical properties. Among these techniques, one can cite the emission pyrometry [216, 221], modulated absorption-emission (MAE) [222, 223], extinction (either single-pass [28, 173, 181, 224] or multi-pass [114, 156]), and of course LII which is widely used to retrieve f_v. Three LII-based techniques can be listed: modulated LII [225], which is rarely used, LII (which will be referred as "traditional LII" to distinguish it from other LII applications that can measure other parameters than f_v like d_p, and $E(m_\lambda)$) and Auto-Compensated LII (AC-LII).

Traditional LII

The laser-induced incandescence technique traditionally refers to the determination of f_v. This is the technique most commonly used to recover f_v. The soot volume fraction can be retrieved, taking advantage of the proportionality between the soot volume fraction and the incandescence signal (Eq. (3.19)). f_v can be expressed as:

$$f_v = D_{calib} S_\lambda^{LII}, \tag{3.22}$$

where D_{calib} is a calibration constant, which is obtained from the knowledge of f_v in a reference measurement point. This reference measurement can be obtained using another technique such as gravimetric sampling [157, 178, 218], single-pass extinction [28, 173, 181] or multi-pass extinction [114, 156]), for example.

To effectively use Eq. (3.22), it is crucial to operate within the so-called "plateau regime" in which the LII signal remains relatively independent of the laser fluence [28, 52]. As shown in Eq. (3.19), the LII signal is directly influenced by the soot temperature.

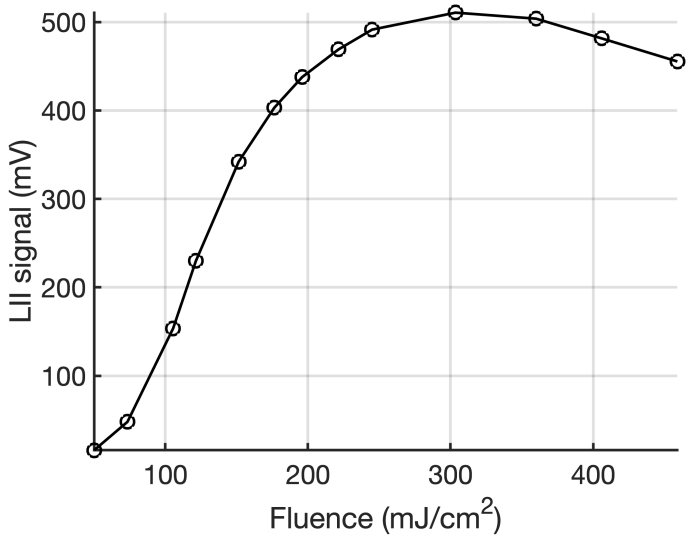

Figure 3.5: Example of LII signal collected at 578 nm tube as a function of laser fluence. Soot particles are generated from a C_2H_4+N_2/air laminar diffusion flame using a 1064 nm laser. Data were obtained with the setup described in Section 5.1.

At lower fluences, the soot temperature increases with the laser fluence. However, as the fluence approaches higher levels, the soot temperature reaches the sublimation temperature ($\sim$4000-4500 K) and ceases to rise further. Consequently, while the LII signal initially increases with fluence, it becomes less fluence-dependent once the sublimation

temperature is reached. This behaviour is depicted in Fig. 3.5, which shows the LII signal as a function of the laser fluence. The figure illustrates that, under the experimental conditions considered, the LII signal varies by only 10% within the fluence range of 220 to 450 mJ/cm^2, suggesting that a fluence in this range should be used to have reliable measurements for f_v.

The advantage of this technique is that it is quite simple to implement and requires only a single measurement of the LII signal at one wavelength. However, the calibration relies on another experimental technique (gravimetric sampling, extinction,...) or a stable source producing a known f_v quantity, adding additional sources of uncertainties and increasing complexity due to additional experimental apparatus. In addition, the calibration conditions and the LII measurements should produce similar particles in terms of emission properties for this technique to be accurate. Also, the high laser fluences used sublimate a fraction of the soot particles and may alter the soot properties. Finally, obtaining a homogeneous temperature over the flame is, in practice, difficult due to the diversity of particles in terms of absorption. This last disadvantage can be removed if the soot temperature is known, for example, by collecting the LII signal at two wavelengths and using 2C-LII pyrometry [114, 162]. In this case, it is similar to AC-LII, only the calibration procedure differs.

Auto-Compensated LII (AC-LII)

With AC-LII, f_v can be expressed by inverting the incandescence signal of Eq. (3.19):

$$f_v = \frac{1}{12\pi hc^2 E(m_\lambda) L_{laser} C_{calib,\lambda}} \frac{S_\lambda^{LII}}{\frac{\Delta\lambda}{\lambda^6} e^{-\frac{hc}{\lambda k_B T}}}. \tag{3.23}$$

f_v can be computed once all other quantities of Eq. (3.23) are known: temperature, absorption function, and calibration constant. This technique was first presented by Snelling et al. [160]. AC-LII has the advantage of accounting for the soot temperature, making it possible to measure f_v at low fluences for which soot alteration is limited. In addition, it does not rely on other techniques for calibration except for the absolute calibration of the collection system, which requires a light source of known spectral radiance. It is also established that f_v estimations via AC-LII exhibit an anomalous dependence on the laser fluence, a phenomenon known as the f_v anomaly [226]. This issue will be explored in details in Chapters 5 and 6, where further analysis and potential solutions are discussed.

3.4.4 Soot primary particle diameter d_p measurements

The soot primary particle diameter, d_p, can be determined through various *ex-situ* and *in-situ* methods. *Ex-situ* techniques include scanning electron microscopy (SEM) [227] and transmission electron microscopy (TEM) [67, 70, 104, 146, 228, 229]. These methods provide high-resolution images of soot particles (see Fig. 2.3 for illustration), allowing for the measurement of d_p, along with other parameters such as the number of particles per aggregate, the fractal exponent, fringe length, and inter-fringe distance. However, all *ex-situ* techniques require soot sampling and extraction, which can disturb the flame flow and potentially alter the soot properties. Additionally, the extracted soot often represents an average over extended flame regions (i.e., integrated across the radius), complicating efforts to achieve high spatial resolution.

In-situ techniques overcome the disadvantages associated with *ex-situ* methods. *In-situ* techniques like Small Angle X-ray Scattering (SAXS) [230, 231] and Time-Resolved Laser-Induced Incandescence (TIRE-LII) [163] allow estimating the soot primary particle diameter, averaged within the probe volume directly within the flame without disturbing the flow. TIRE-LII is of particular interest in this work as an LII-based experimental technique.

Time resolved LII (TIRE-LII)

The soot primary particle diameter can be inferred from the temporal decay of the LII signal: the smaller the particles, the faster the decay of the LII signal. This forms the basis of Time-Resolved Laser-Induced Incandescence (TIRE-LII) [163, 168], where the rate of signal decay is used to estimate d_p.

d_p is typically obtained by comparing experimentally measured time-resolved LII signal decays to those generated using LII numerical codes [139, 168, 186, 232–234]. This approach allows the incorporation of all physical processes affecting the particles during cooling (Fig. 3.3). Notably, the shielding effect affecting the conduction losses can be accounted for [207].

While LII codes can consider particle size distributions (typically assuming a shape such as Gaussian or log-normal), the mathematical process of extracting the primary particle size distribution from experimental LII signals is considered ill-posed [140, 235, 236], meaning that there is no guarantee of retrieving the true distribution. Therefore, in this work, d_p is determined under the assumption of a monodisperse soot population. This is achieved using analytical expressions derived from either the soot temperature or the temporal decay of the LII signal, avoiding the use of an LII code for simplicity.

***d_p* from the temporal decay of the soot temperature**

The evolution of the soot temperature after the laser pulse can be expressed using the energy balance equation (Eq. (3.8)). The absorption term is null as the laser pulse is terminated, and radiation losses are considered negligible in atmospheric flames [154]. Once the laser fluence is low enough to limit the alteration of the soot particles, sublimation (and any other high-temperature phenomenon) can be neglected. Then, the dominant cooling mechanism is conduction, and the energy balance equation reduces to:

$$\frac{dU}{dt} = -\dot{Q}_{cond}. \tag{3.24}$$

Replacing the internal energy and conduction loss term by the expression given by Eq. (3.10) and Eq. (3.14):

$$\frac{dT}{dt} = \frac{\alpha}{d_p}\frac{P}{\rho c}\sqrt{\frac{9R}{2\pi W_{gas}T_0}}\frac{\gamma_{gas}+1}{\gamma_{gas}-1}(T_0 - T). \tag{3.25}$$

If γ_{gas} is taken as temperature independent, the analytical solution of Eq. (3.25) allows expressing the temporal evolution of the soot temperature as [234, 237]:

$$T = (T_M - T_0)e^{-\frac{t}{\tau}} + T_0, \tag{3.26}$$

where:

$$\tau = \frac{d_p}{\alpha}\frac{\rho c}{P_{gas}}\frac{\gamma_{gas}-1}{\gamma_{gas}+1}\sqrt{\frac{2\pi W_{gas}T_0}{9R}}, \tag{3.27}$$

Taking the logarithm of Eq. (3.26) gives:

$$ln\left(\frac{T-T_0}{T_M-T_0}\right) = -\frac{t}{\tau}, \tag{3.28}$$

Then, experimental data can be fitted to Eq. (3.28) to obtain τ. Once τ is known, d_p is computing with Eq. (3.27). It has to be noticed that the gas temperature T_0 is required to obtain τ. Figure 3.6 illustrates the post-processing method. It gives the experimentally determined quantity: $ln\left(\frac{T-T_0}{T_M-T_0}\right)$ at different instants after the laser pulse. The fit of the data is also represented in dashed lines, and the corresponding d_p values are given in the legend.

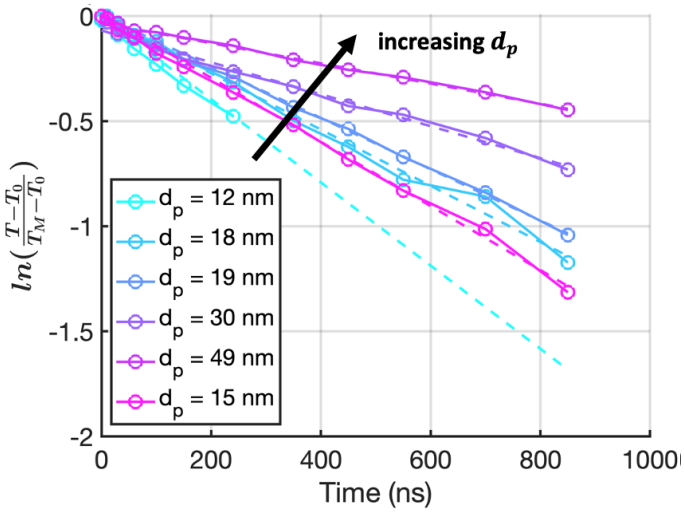

Figure 3.6: $ln\left(\frac{T-T_0}{T_M-T_0}\right)$ determined experimentally at different instants after laser heating (solid lines), and fit of the experimental data (dashed lines). Colours correspond to different flame positions. The soot particles are generated by a C_2H_4+N_2/air laminar diffusion flame. Data were obtained using the setup described in Section 6.1 and will be presented in Chapter 6.

d_p from the temporal decay of the soot incandescence signal

Alternatively, the primary particle diameter can be estimated from the temporal decay of the LII signal, S_λ^{LII}, from which the background (signal recorded without laser heating) has been subtracted. Using the expression of the incandescence signal of Eq. (3.19), the expression of the soot temperature of Eq. (3.28), and normalising the equation by the instant $t = 0$ (immediately after the end of the laser pulse, when the soot temperature is maximum: $T = T_M$), one obtains:

$$\frac{S_\lambda^{LII}(t) - S_\lambda^{FE}}{S_\lambda^{LII}(t=0) - S_\lambda^{FE}} = \frac{e^{\frac{-\beta_\lambda}{(T_M-T_0)e^{-\frac{t}{\tau}}+T_0}} - e^{-\frac{\beta_\lambda}{T_0}}}{e^{-\frac{\beta_\lambda}{T_M}} - e^{-\frac{\beta_\lambda}{T_0}}}, \tag{3.29}$$

where $\beta_\lambda = \frac{hc}{\lambda}$. S_λ^{FE} represents the incandescence signal of the soot particles in the absence of laser heating (flame natural incandescence). Effects of background subtraction are discussed in greater detail in section 6.3.2.

From that, τ can be obtained by fitting the expression of Eq. (3.29) to the experimentally obtained decay of the normalised LII signal. Then, d_p is computed by inverting Eq. (3.27). It has to be noted that similarly to the temperature decay fit, the expression requires an estimation of T_0. Figure 3.7 shows an example of the experimental decay of LII signals and the fit to the experimental data. The corresponding d_p values are provided in the legend.

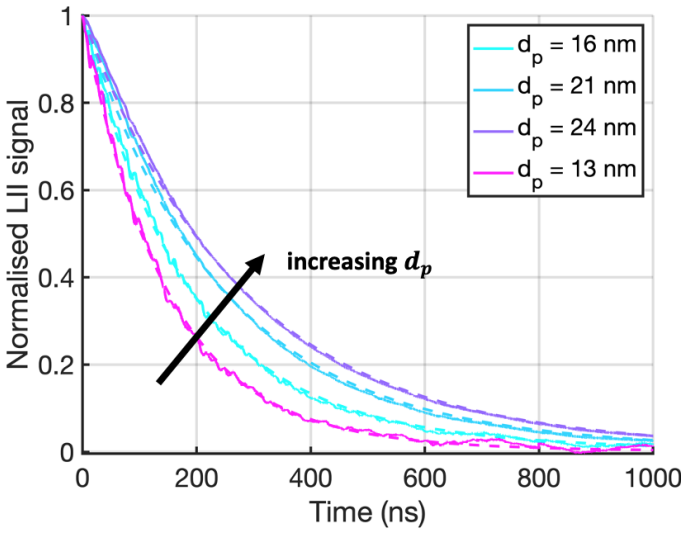

Figure 3.7: Temporal evolution of LII signals collected at 578 nm with a photomultiplier tube (solid lines). Dashed lines give the fit to the experimental data, and the corresponding soot primary particle diameters are given in the legend. Colours correspond to different flame positions. The soot particles are generated by a CH_4/air laminar diffusion flame. Data were obtained using the setup described in Section 6.1 and will be presented in Chapter 6.

Sensitivity analysis

Since calculating d_p from the decay of the LII signal requires several parameters (T_0, T_M, α, λ, ρc, M_{gas}, and γ_{gas}), which are either measured with inherent uncertainties, or assumed from literature data or unknown, and because to the knowledge of the author, the fit of Eq. (3.29) has never been done, the method's sensitivity to these parameters is analysed using a numerically synthesised LII signal (generated by the LII code).

The LII code is fed with the reference parameters of Table 3.1, the fluence is 90 mJ/cm^2, and the wavelength window is: [559, 588] nm. The resulting signal is fitted to Eq. (3.29), and d_p is computed from τ with Eq. (3.27). For that, λ was taken equal to the central wavelength of the code reference window: 573.5 nm. As the LII code has a temperature-dependent c, it was decided to take its average value between T_0 and T_M (c = 2155 J/K/kg). For the gas properties, properties of N_2 at flame temperature are considered: γ_{gas}=1.29 and M_{gas}= 28 g/mol.

To demonstrate the good behaviour and the fitting process, d_p is computed from the numerical LII signal, assuming that all parameters are known. Figure 3.8a represents the normalised numerical LII signal (blue) and the best-fitted function (red). Although not superimposed, the curves are very close to each other. The value for d_p retrieved is 24 nm to be compared to the 26 nm given as input of the LII code. This -7% error can be explained by the fact that unlike with the LII code, the method proposed here does not account for the temperature dependence of c, and γ_{gas}, and it also does not account for the other loss terms (radiation and sublimation).

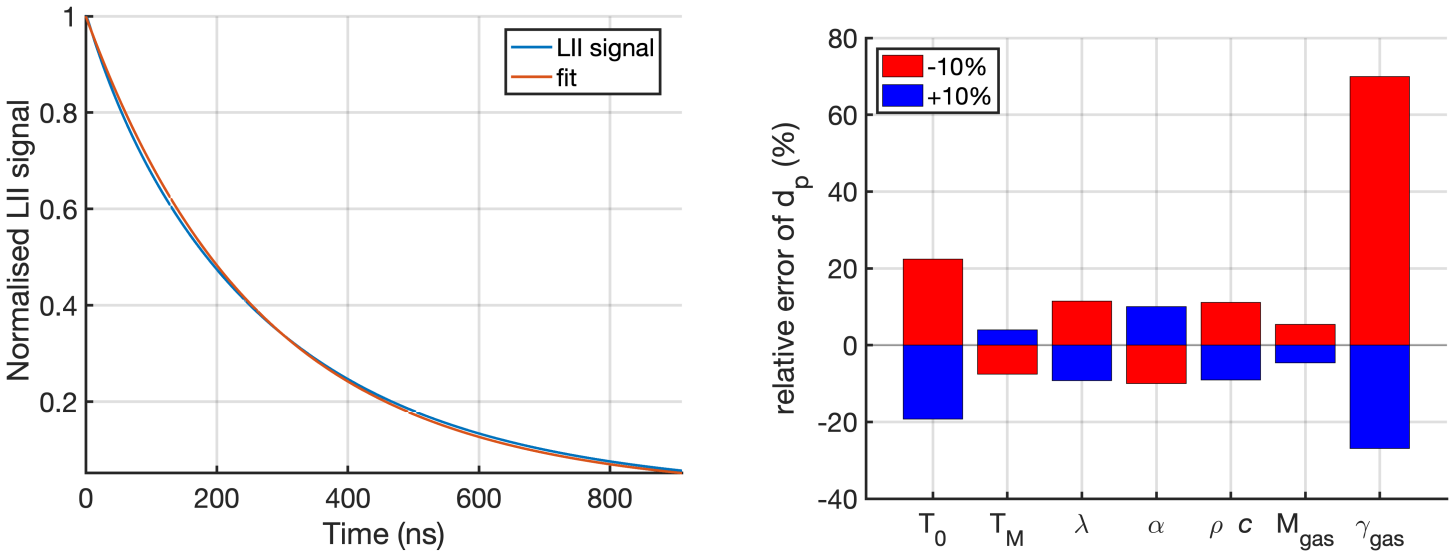

(a) (b)

Figure 3.8: (a) Normalised numerically synthesised LII signal decay (blue), and function fitted with Eq. (3.29) to this LII signal (red). (b): Sensitivity of d_p estimation to a $\pm$ 10% uncertainty in the parameters: T_0, T_M, λ, α, ρc, M_{gas}, and γ_{gas}.

To study the impact on d_p of an uncertainty on: T_0, T_M, λ, α, ρc, M_{gas}, and γ_{gas}, a one parameter at a time procedure is retained where d_p is computed considering a $\pm$ 10% on each parameter separately. The retrieved values of d_p are compared to the one obtained when considering no error on the parameters (24 nm).

Figure 3.8b represents the sensitivity of d_p to uncertainties on T_0, T_M, λ, α, ρc, M_{gas}, and γ_{gas}. The most influential parameter appears to be γ_{gas}, which highly impacts d_p: a 10% overestimate in γ_{gas} results in approximately a 25% underestimate of d_p, while a 10% underestimate of γ_{gas} leads to an overestimate of d_p by around 70%. The next most significant factor is T_0, which affects d_p by about 20%. Following that, λ, α, and ρc each contribute roughly 10% to the variation in d_p, while M_{gas} and T_M have an influence of around 5%.

In practice, predicting the gas properties γ_{gas} (the heat capacity ratio) and M_{gas} (the molar mass) is challenging due to the unknown and varying gas composition in the flame. While M_{gas} has a relatively minor effect on d_p, and precise knowledge of it is not critical, γ_{gas} significantly influences d_p, particularly if overestimated. Molecules with more than two atoms tend to have γ_{gas} values of 1.3 or lower. This value tends to decrease as the temperature rises, suggesting that the value of 1.29 used here might be an overestimation at flame temperatures. However, due to the fluctuating gas composition and temperature within the flame, accurately assessing the impact of this potential overestimation on d_p remains challenging. Therefore, the sensitivity of d_p to variations in γ_{gas} should be kept in mind.

3.5 Advantages of the LII experimental technique

The laser-induced incandescence experimental technique is a very used tool for soot study as it presents several advantages:

- It is an *in-situ* method. As such, it does not require extraction and manipulation of soot particles. Thus, alteration of the particles is limited, and LII can be considered non-intrusive. However, the use of high laser fluences should be avoided as it might alter the soot, making LII an intrusive technique.
- A careful selection of the laser wavelength makes LII selective for soot particles only (no interferences from

other sources).

- LII allows particles to be probed in the core of the flame (non-path integrated measurements).
- It offers a fine spatial resolution.
- Multiples quantities can be extracted from LII measurements only:
  - soot temperature T after laser heating,
  - soot volume fraction f_v,
  - soot primary particle size d_p,
  - absolute value of the soot absorption function $E(m_\lambda)$,
  - unheated soot temperature T_0. If thermal equilibrium between the gas and the soot is assumed, T_0 is equivalent to the local gas temperature,
  - ratio of soot absorption function at two wavelengths λ_1, and λ_2, $\frac{E(m_{\lambda_1})}{E(m_{\lambda_2})}$ [145].

Chapter 4

The Separated Pulses Laser-Induced Incandescence technique (SP-LII)

The ability to estimate $E(m_\lambda)$ enables the differentiation between young and mature soot. This distinction is otherwise challenging, particularly in turbulent flames where soot particles are transported due to mixing. This differentiation, combined with data on soot volume fraction and particle size, may help to enhance our understanding of soot formation, development, and oxidation in flames. Therefore, this chapter introduces a new experimental technique developed in this thesis to obtain the absorption function and gas temperature solely from LII measurements. This technique, named the separated pulse LII (SP-LII) method, was designed for single-shot measurements in view of application in turbulent flames. However, it was tested in this thesis only on averaged measurements in laminar flames. The chapter begins by reviewing existing techniques used to access $E(m_\lambda)$, followed by an explanation of the SP-LII principle. Its application to single-shot measurements is then presented, the difficulties arising from single-shot measurements are underlined and discussed, and a proposition for an adequate experimental setup is given. Two methods for post-processing data to compute $E(m_\lambda)$ and T_0 are introduced. The first, the "absorption model" (AM), calculates these values using an analytical equation derived by neglecting all loss terms in the energy balance equation (3.8)). The second method uses a look-up table (LUT) generated from solving the entire energy equation with the LII code under various input parameters. The chapter concludes with a theoretical evaluation of the SP-LII technique, assessing its performance under different conditions and conducting an uncertainty analysis on several soot properties. The impact of errors in determining the laser-heated soot temperature on $E(m_\lambda)$ and T_0 is also explored. This chapter is focused on the theoretical aspects of the technique, while the experimental application in a laminar flame will be discussed in the following chapter. It has to be noted that the work in this chapter has been published in an article: ***G. Guy et al. "Estimation of soot absorption function via the two separated pulses laser-induced incandescence technique", Applied Physics B, 129.8 (2023), p. 127*** *[134].*

Contents

4.1 Literature review: how to obtain the soot absorption function $E(m_\lambda)$? 63

4.1.1 Ex-situ techniques . . . 63

4.1.2 In-situ techniques . . . 63

4.1.3 Why a new technique? . . . 65

4.2 The Separated Pulses Laser-Induced Incandescence technique (SP-LII) . 65

4.2.1 Reference input parameters for the LII code . . . 66

4.2.2 Principle of the SP-LII technique . . . 66

4.2.3 The SP-LII technique for single-shot measurements . . . 67

LII pulse delay . . . 69
Gas heating by the laser-heated soot particles . . . 70
Alteration of the soot properties after the first laser pulse . . . 70
4.2.4 Advantages and drawbacks of the SP-LII . . . 71
4.3 Post-processing of the data: computation of $E(m_\lambda)$ and T_0 . . . **71**
4.3.1 The absorption model (AM) . . . 72
4.3.2 The look-up table (LUT) . . . 73
4.4 Theoretical evaluation of the SP-LII technique . . . **75**
4.4.1 Procedure for the theoretical evaluation of the SP-LII technique . . . 75
4.4.2 Performance of the technique . . . 76
4.4.3 Uncertainty analysis . . . 77
4.4.4 Effect of an error on the estimation of the peak soot temperature . . . 80
4.5 Conclusion . . . **82**

4.1 Literature review: how to obtain the soot absorption function $E(m_\lambda)$?

Several techniques have been developed to estimate soot particles' optical properties. Here, the most common approaches to determine the absolute value of $E(m_\lambda)$ are quickly presented and are separated into two categories: *ex-situ* and *in-situ* techniques (although some methods are halfway between *ex-situ* and *in-situ*). The listing has no intention of being exhaustive and clearly focuses on the *in-situ* LII-based methods. Other methods can be found in one of the following reviews: [31, 136, 140].

4.1.1 *Ex-situ* techniques

Ex-situ techniques require extracting the soot particles from the flame. The sampling and processing are intrusive and may alter the soot properties, including $E(m_\lambda)$, in a way difficult to quantify. Among them, the reflectometry [238, 239] allows access to the soot refractive index from measurements of plane-polarised reflected intensities from a polished compressed soot sample. To this end, soot particles are collected in a flame and compressed at very high pressure (≈ 400 bars) to form a ~ 1 gramme pellet before being polished. This intrusive technique may significantly change soot properties during the extraction, compression or polishing phase.

4.1.2 *In-situ* techniques

Unlike *ex-situ* techniques, *in-situ* ones allow the estimation of soot properties directly in the flame and do not require soot extraction, so they are generally less intrusive.

Non-LII based techniques

$E(m_\lambda)$ can be obtained using the relation existing between the extinction coefficient K_{ext}, the volume fraction f_v, the ratio of the scattering to the absorption coefficient ρ_{sa}:

$$K_{ext} = \frac{6\pi(1+\rho_{sa})f_v E(m_\lambda)}{\lambda}. \tag{4.1}$$

The extinction coefficient is obtained from extinction measurements, ρ_{sa} can be computed with the RDG theory, while f_v has to be determined with a technique that does not rely on assumptions on the absorption function such as MLII [225] or gravimetric analysis [179]. Once all these quantities are known, $E(m_\lambda)$ is computed by inverting Eq. 4.1.

Yon et al. [51] have recently presented a new technique to characterise soot maturity. It relies on linking the spectral dependence of the absorption function to its absolute value. The technique uses line-of-sight-attenuation (LOSA) and flame emission measurements at multiple wavelengths to access the ratios $\frac{E(m_\lambda)}{E(m_{\lambda_{ref}})}$ for multiple wavelengths. Then, the spectral dependence of $E(m_\lambda)$ is characterised by the maturity coefficient β_m which is obtain from the fit of the ratios $\frac{E(m_\lambda)}{E(m_{\lambda_{ref}})}$ to:

$$\frac{E(m_\lambda)}{E(m_{\lambda_{ref}})} = \left(\frac{\lambda_{ref}}{\lambda}\right)^{-\beta_m}. \tag{4.2}$$

Then, the results of a previous work [50] are used to directly link the determined value of β_m to the organic content of the soot and to the absolute value of $E(m_\lambda)$. $\beta_m = 0$ corresponds to totally mature soot, i.e. no spectral dependence of $E(m_\lambda)$, while higher values correspond to the less mature soot particles that show a spectral dependency for $E(m_\lambda)$.

LII based techniques

Several LII-based methods exist for computing $E(m_\lambda)$ in flames, and they all share the same principle. One of the most used techniques is the one developed by Snelling et al. [30]. It relies on the comparison of the experimental and numerical maximum effective temperatures reached by the heated soot particles T_M. It requires the knowledge of the product of the soot-specific heat with density ρc, the peak soot temperature, the initial soot temperature (supposed to be equal to the local gas temperature) and the primary particle diameter (although they show that d_p has in fact little influence on the results). The absorption function is retrieved by adjusting its value as input of an LII code, minimising the difference between the numerical effective soot temperature and the experimental one. This technique requires that the laser fluence is chosen in the low fluence regime to avoid triggering high-temperature phenomena that alter the soot particles and are hard to model.

More simply, one can neglect all the loss terms in the energy balance equation (Eq. (3.8)) during the laser absorption phase (radiation is negligible, sublimation is negligible due to the usage of low laser fluences, and conduction has a small impact during the laser absorption phase). As a result, the energy balance equation has only two terms (absorption and internal energy) and can be integrated over the laser pulse duration and solved analytically:

$$\int_{T_0}^{T_M} \frac{\pi d_p^3}{6} \rho c dT = \int_{t_0}^{t_0+\Delta t_{pulse}} \pi^2 d_p^3 \frac{E(m_\lambda)}{\lambda_{laser}} \dot{Q}_{laser}(t) dt, \tag{4.3}$$

which reduces to:

$$E(m_\lambda) = \overline{\rho c} \frac{\lambda_{laser}}{6\pi} \frac{T_M - T_0}{F}, \tag{4.4}$$

where $\overline{\rho c} = \frac{1}{T_M - T_0} \int_{T_0}^{T_M} \rho c \, dT$ when ρc is assumed to be temperature dependent, and $\overline{\rho c} = \rho c$ if it is not.
In this way, $E(m_\lambda)$ can be estimated once T_0 is known, without the need to estimate the diameters of the primary particles or to use an LII code. This was applied in several works [30, 114, 147, 170].

Alternatively, one can use the fluence dependence of the LII signal with [42] or without [162] the help of an LII code to determine $E(m_\lambda)$. The low fluence part of the experimental curves of the LII signal (before the inflexion point) versus the laser signal are compared to numerical [42] or theoretical [162] ones. The numerical/theoretical curve the closest to the experimental one gives $E(m_\lambda)$.

All these methods have the disadvantage of requiring an additional approach for the gas temperature estimation (coherent anti-Stokes Raman spectroscopy [30], NO-LIF [141], thermocouples [54, 130], or numerical simulations [42, 162]).

However, it is possible to calculate $E(m_\lambda)$ without having to estimate the gas temperature but by determining the laser-heated soot temperature at multiple laser fluences. It is based on a linear fit of T_M versus F curves. Indeed, Eq (4.4) can be rearranged in:

$$T_M = \frac{6\pi}{\rho c \lambda_{laser}} E(m_{\lambda_{laser}}) F + T_0, \tag{4.5}$$

A linear fit of Eq. (4.5) to the measurements of the evolution of T_M with F gives the slope of the curve: $\Gamma = \frac{6\pi}{\lambda_{laser}} \frac{E(m_{\lambda_{laser}})}{\rho c}$, and the ordinate at the origin T_0. Then, $E(m_{\lambda_{laser}})$ is computed from Γ once the product ρc is known. Figure 4.1 gives an illustration of the technique. Values of absorption function and gas temperature computed from the linear fit of the data are displayed in the legend.

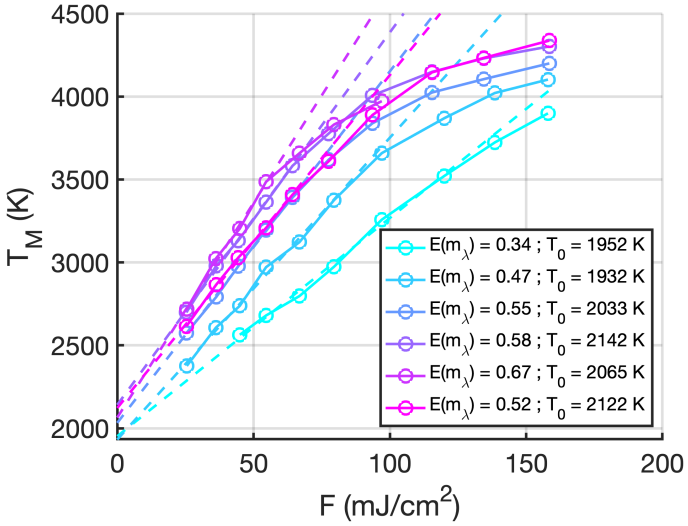

Figure 4.1: Experimentally determined T_M for different laser fluences (circles symbols linked by solid lines) and fit of the experimental data in the linear regime (dashed lines). Colours correspond to different flame positions. The soot particles are generated by a C_2H_4+N_2/air laminar diffusion flame.

This technique was first seen in [33]. It is a convenient technique as, in addition to requiring only an LII experimental device, the technique does not need to measure the gas temperature and even gives an estimate of it.

4.1.3 Why a new technique?

It was shown that several ways to estimate $E(m_\lambda)$ directly in flames already exist. However, the presented methods are hardly applicable to turbulent flames, and most of them require multiple experimental diagnostics. Indeed, several of these methods require knowledge of the gas temperature to estimate $E(m_\lambda)$. Accessing T_0 in turbulent flames is more challenging than in laminar flames. In addition, turbulent flames T_0 might show significant spatial and temporal variations due to strong mixing. Concerning the *ex-situ* techniques, alteration of the particles is hardly controllable and obtaining temporally and spatially resolved information is almost not possible. The SP-LII has been developed with the intent of being usable in turbulent flames with little experimental equipment and without altering the probed soot particles.

4.2 The Separated Pulses Laser-Induced Incandescence technique (SP-LII)

The SP-LII technique aims to determine the ratio $\frac{E(m_\lambda)}{\rho c}$ and the gas temperature T_0 by analysing consecutive single-shot measurements. This involves measuring the peak temperatures of soot particles heated by at least two laser pulses with different fluences. By assuming a value for ρc, it becomes possible to extract the absolute value of $E(m_\lambda)$. While similar to the technique used in [33] (the SP-LII approach was developed before noticing this technique), which involves fitting T_M and F, the SP-LII technique is specifically designed for application in turbulent flames and determines $E(m_\lambda)$ and T_0 using only two laser fluences.

It has to be noted that, similarly to all other LII-based methods, the SP-LII face certain limitations. It relies on low laser fluences, which can result in lower signal-to-noise ratios. Additionally, the measurement gives the ratio $\frac{E(m_\lambda)}{\rho c}$, meaning that uncertainties in ρc directly affect $E(m_\lambda)$. The problem is that there is limited information on the precise value of ρc and its potential dependence on temperature and soot maturity. Furthermore, calculating soot

temperatures requires assumptions about the wavelength dependency of $E(m_\lambda)$, which is known to vary with soot maturity.

This section is dedicated to presenting the SP-LII. As the theoretical development and analysis of SP-LII (section 4.4) were conducted using the LII code introduced in Chapter 3, this section first presents the reference parameters of the LII code used for these analyses, then, it explains the principles of the SP-LII and provides a theoretical discussion on the requirements for effectively applying the technique to single-shot measurements (in view of an application in a turbulent environment).

4.2.1 Reference input parameters for the LII code

The LII code presented in section 3.3 is used in this chapter to:

1. Introduce theoretical behaviours to illustrate the principle of the SP-LII technique (Sec. 4.2.2).
2. Construct a look-up table used to determine $E(m_\lambda)$ and T_0 from two peak soot temperature values at different laser fluences (Sec. 4.3.2).
3. Evaluate a priori the performance and robustness of the SP-LII technique (Sec. 4.4).

The reference parameters for the LII code used in these analyses are presented in Table 4.1. This table reminds the reference parameters from Table 3.1, but also includes the two reference fluences, $F_{1_{ref}}$ and $F_{2_{ref}}$. Additionally, the resulting reference peak temperatures $T_{M_{1_{ref}}}$ and $T_{M_{2_{ref}}}$, are also provided, corresponding to the peak temperatures obtained using the LII code with the specified reference inputs.

LII code inputs		
Parameter	**Unit**	**Value**
$E(m_\lambda)_{ref}$	–	0.37
$T_{0_{ref}}$	K	1860
$F_{1_{ref}}$	mJ/cm^2	50
$F_{2_{ref}}$	mJ/cm^2	100
$d_{p_{ref}}$	nm	26
ρ_{ref}	kg/m^3	1950
α_{ref}	–	0.3
β_{ref}	–	1
LII code outputs		
$T_{M_{1_{ref}}}$	K	2955
$T_{M_{2_{ref}}}$	K	3818

Table 4.1: Reference input parameters for the LII code and reference peak temperatures that are extracted from the simulations done with the reference input parameters.

In the following to simplify notation, the mathematical set Ω_{ref} will refer to $\Omega_{ref} = \left\{F_{1_{ref}}, F_{2_{ref}}, \rho_{ref}, d_{p_{ref}}, \alpha_{ref}, \beta_{ref}\right\}$.

4.2.2 Principle of the SP-LII technique

The peak temperature T_M (Eq. (4.5)) reached by the soot particles after a laser pulse depends on the laser pulse, the initial temperature of the particle, and its absorption function. This is illustrated by Fig. 4.2a in which the peak soot temperature is calculated with the LII code with the reference parameters $\left\{ T_{0ref},\ d_{p_{ref}},\ \rho_{ref},\ \alpha_{ref},\ \beta_{ref} \right\}$ for

various laser fluences and three values of $E(m_\lambda)$. T_M is linearly proportional to F for low fluences values. This linear behaviour is lost for fluences high enough to activate the sublimation. In the specific conditions of these simulations, the temperature for which sublimation starts to play a non-negligible role is $\sim$ 3500 K. Looking at Fig. 4.2a, it is clear that the slope of the linear part of the peak temperature curves depends on $E(m_\lambda)$.

Figure 4.2b represents the laser fluence dependence of T_M for four soot primary particle diameters. Results are obtained for the reference input parameters: $\{E(m_\lambda)_{ref},\ T_{0ref},\ \rho_{ref},\ \alpha_{ref},\ \beta_{ref}\}$, and with various values of laser fluences. Below $\sim$3500 K, the curves are almost superimposed for diameters larger than 10 nm, meaning that the peak temperature is mostly independent of the soot primary particle diameter for this range of values (confirming the results of Snelling et al. [30]). However, this is not true anymore for the smallest particles as the curve for d_p = 1 nm is clearly detached from the others. This is due to the fact that small particles are characterised by a larger surface-to-volume ratio compared to big particles, inducing more significant conduction losses during laser heating. As the initial slope of the d_p = 1 nm curve is lower than for bigger particles, it is to be expected that the value of $E(m_\lambda)$ computed from it would be underestimated. This will be addressed later.

Therefore, taking advantage of the linear evolution of T_M with F at a fixed $E(m_\lambda)$, the SP-LII technique proposes to retrieve both $E(m_\lambda)$ and T_0 from two measurements of the peak temperature (T_{M1}, T_{M2}), corresponding to two different laser fluences F_1 and F_2. Two methods to compute $E(m_\lambda)$ and T_0 from T_{M1} and T_{M2} will be considered in section 4.3, and will be compared in section 4.4. The first approach, called the "absorption model" (AM), neglects the thermal losses happening during the laser pulse and provides an analytical expression for $E(m_\lambda)$ and T_0. The second strategy uses a look-up table (LUT) built with the LII code and accounts for the thermal losses.

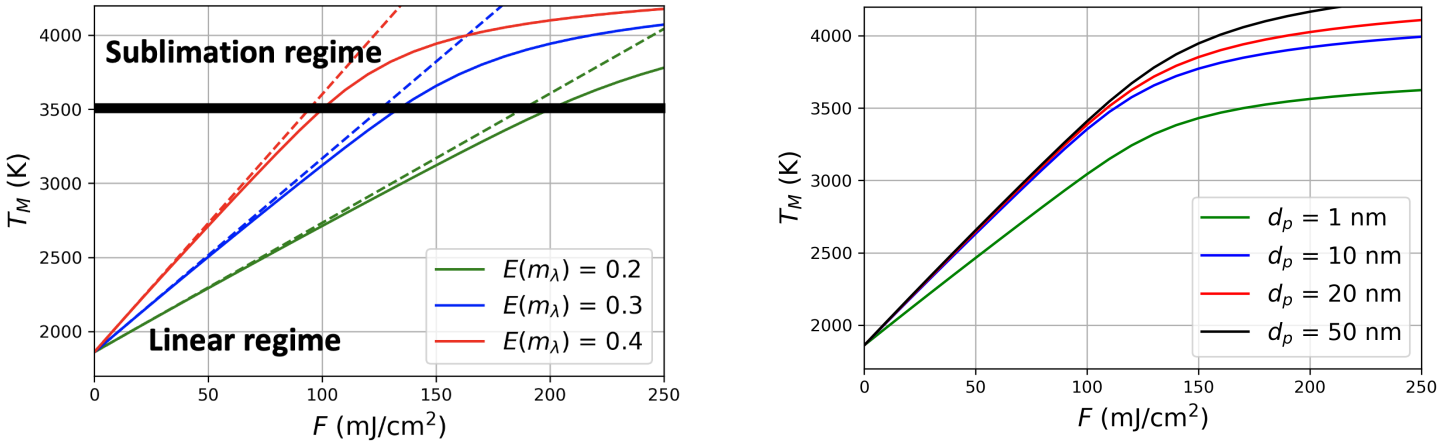

(a) (b)

Figure 4.2: (a) Peak soot temperature as a function of laser fluence for three different values of the absorption function: $E(m_\lambda)$ = 0.2 (green), 0.3 (blue) and 0.4 (red). The dashed lines represent the initial slope of the curves. The horizontal black line represents the separation between the linear and sublimation regimes. (b): Peak temperature of the soot particles as a function of laser fluence for four different values of soot primary particle diameter: d_p = 1 (green), 10 (blue), 20 (red) and 50 nm (black).

4.2.3 The SP-LII technique for single-shot measurements

The SP-LII technique is readily applicable to stationary flames, in which the soot distribution is supposed to be stationary, meaning that the characteristics of the particles in the probe volume are expected not to vary with time. Thus, various acquisitions at different laser fluences can be performed in sequence. The SP-LII is then only a different way to process the LII data that are recorded with a traditional 2C-LII setup, and, strictly speaking, it is not a new experimental technique. However, for turbulent flames in which the soot distribution constantly varies, the time decorrelation of the pulse is not possible, and single shots measurements must be exploited. To measure the

temperature of the same soot particles at two different laser fluences, two consecutive laser pulses from separate laser heads are required. The experimental setup that would be required is illustrated in Fig. 4.3. The output beams of two laser heads that would operate in different polarising modes are superposed using a polarising beamsplitter cube. The delay between the laser pulse would be of 1-10 μs and is discussed hereafter.

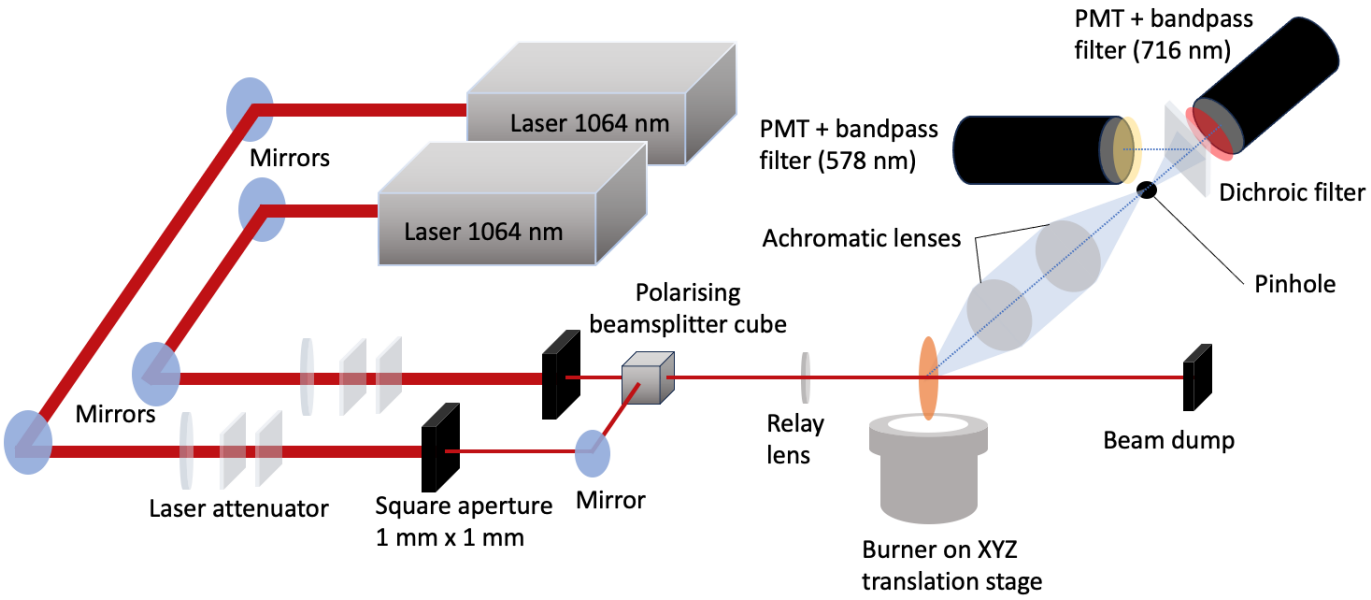

Figure 4.3: Scheme of the experimental setup for the SP-LII technique for measurements in turbulent flames.

Using this setup, a first laser pulse with fluence F_1 heats the soot particles, initially at temperature T_0 (assumed to be the same as the gas temperature), to a peak temperature T_{M_1}. The particles then cool back down to T_0. After a short delay, a second laser pulse with fluence F_2 heats the same group of soot particles to a temperature T_{M_2}. Figure 4.4 illustrates the theoretical power absorbed by the soot during two laser pulses, separated by 3 μs, along with the corresponding evolution of the soot particle temperature over time. For the specific conditions in this simulation, the 3 μs delay allows the soot particles to fully cool back to the gas temperature.

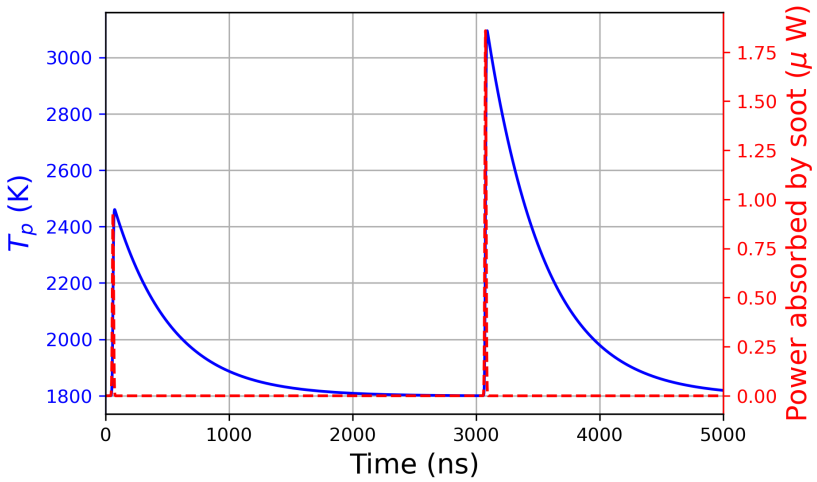

Figure 4.4: Temporal evolution of the soot particle temperature (left axis, solid blue line) and the power absorbed by the soot particle (right axis, dashed red line) after being heated by two laser pulses separated by 3 μs.

The need to heat the same group of soot particles with two laser pulses while ensuring sufficient time between the pulses for the soot to cool back to the gas temperature introduces certain challenges that are presented hereafter.

LII pulse delay

The delay between the pulses is fundamental for the application of the SP-LII technique in turbulent flames. If the delay is too short, the temperatures of the soot particles before the first and second laser pulses would not be equal, introducing a bias in the estimation of both $E(m_\lambda)$ and T_0. In contrast, a delay that is too long makes the soot particles probed by the first laser pulse leave the probe volume. In that case, the pulses may probe different populations of soot particles (with possibly different properties), leading to erroneous results. Thus, it is necessary to correctly set the delay between the pulses by accounting for the soot particles' cooling time and the displacement of the group of soot probed by the first laser pulse.

Soot cooling time: For atmospheric flames, the cooling time is dominated by the conductive exchange term, which mainly depends on d_p and α. In order to quantify the cooling time, simulations are run with $\Omega_{ref}/\left\{d_{p_{ref}}, \alpha_{ref}\right\}$ for d_p ranging from 1 to 50 nm, and for different values of α. Here, the cooling time is defined as the time elapsed between $T = T_{M_1}$ and $T = T_{0_{ref}} + 10$ K = 1870 K. It is represented in Fig. 4.5 as a function of d_p for five values of α. It is reminded that the retained LII code assumes monodispersed, non-aggregated soot particles, and it does not account for the shielding effect. Thus, the cooling time would probably be more important for large soot aggregates. Figure 4.5 shows the same conclusion as one can find by analytically solving the energy balance equation considering only conduction: the cooling time is proportional to d_p and inversely proportional to α. The figure shows that setting the cooling time to $\Delta t = 10$ μs would be enough to cool the soot to T_0 for all soot primary particle sizes (below 50 nm) if the thermal accommodation coefficient α -which is not perfectly known- is $\alpha \geq\sim 0.3$, while only the particles bigger than 24 nm would not be in thermal equilibrium with the gas if α = 0.1. Thus, with $\Delta t = 10$ μs, and considering that α is indeed near 0.3, all soot particles would have cooled back to the gas temperature (except maybe for large aggregates having a large fractal dimension).

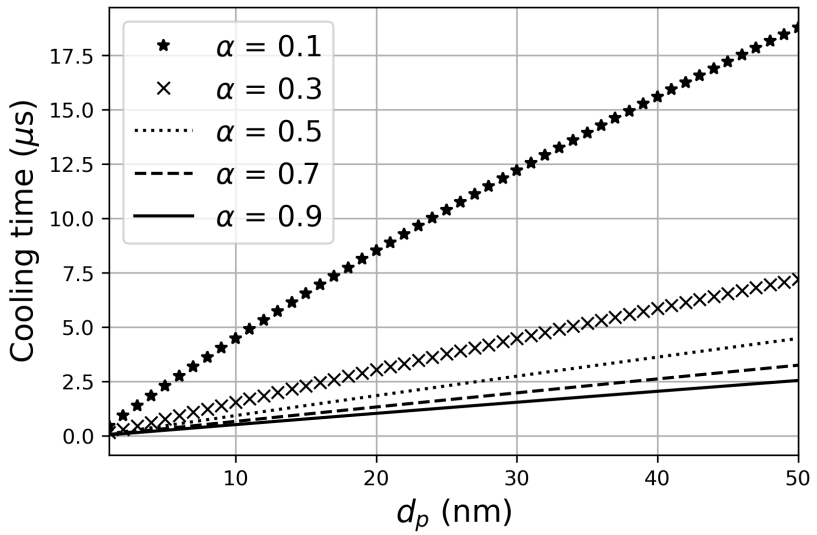

Figure 4.5: Cooling time as a function of d_p for a thermal accommodation coefficient α of 0.1 ($\star$), 0.3 ($\times$), 0.5 (dotted line), 0.7 (dashed line) and 0.9 (solid line). The cooling time is defined as the time elapsed between $T = T_{M_1}$ and $T = T_{0_{ref}} + 10$ K = 1870 K.

Soot displacement: Concerning the soot displacement, here, it is assumed that the second pulse should also heat at

least 75% of the soot particles heated by the first pulse to have results representative of the probed soot population. Assuming a uniform soot displacement in a probe volume having a characteristic size of $L^* = 1$ mm and a pulses' delay of 10 μs, the maximum allowable velocity could be estimated by: $\frac{L^*}{4\Delta t} = 25$ m/s. This limit may still be exceeded in case of highly turbulent flames and would be lower for smaller sizes of the probe volume or longer delays between the pulses. A precise knowledge of α and insights on the particle size would allow a better estimation of the cooling time required, allowing to lower the delay between the two laser pulses and extending the domain of application of the SP-LII technique.

Gas heating by the laser-heated soot particles

Snelling et al. [240] observed anomalies in the cooling rate of laser-heated soot particles that can be explained by an increasing bath gas temperature originating from the energy liberated by the cooling of the soot particles themselves. The gas temperature was found to increase linearly with the laser fluence or the soot volume fraction as more energy is transferred to the soot phase. The excess in gas temperature was found to be $\sim$400 K for a laser fluence of 169 mJ/cm^2 at a laser fluence at 532 nm for an operating point charged with $\sim$4 ppm of soot. Other works [241, 242] have studied the same experimental point for laser fluences between 125 and 150 mJ/cm^2 at 1064 nm. Nordström et al. [241] used coherent anti-Stokes Raman spectroscopy to determine the gas temperature before and during LII. They found a $\sim$100 K increase of the bath gas temperature 2 μs after the LII pulse. Mansmann et al. [242] compared 2C pyrometry with and without the occurrence of LII pulse and found an 80 K increase in the gas temperature 7 μs after the LII pulse. Bennett et al. [243] found up to $\sim$400 K increase in gas temperature after 5μs after a laser pulse (90 mJ/cm^2 at 1064 nm) in a flame with f_v = 43 ppm (highly sooting flame). Cenker et al. [244] used a rapid camera to investigate the gas heating by LII at various laser fluences in a laminar diffusion flame. They showed that the gas heating lasts for up to several milliseconds.

These results encourage once again the usage of low fluences to limit the heating of the gas after the first pulse as much as possible to have a similar gas temperature before both LII pulses. However, as the SP-LII is incompatible with high laser fluences, this effect is expected to be negligible in most situations, except in the presence of a very high soot load, and in that case, gas heating should be addressed (for example, with the method described in [240]).

Alteration of the soot properties after the first laser pulse

Applying the SP-LII technique in a turbulent flame requires that the same soot particles be heated twice by the laser pulses. Thus, the first laser pulse must not significantly modify the soot properties. Several works [245–248] have addressed the soot alteration problem by heating soot particles with two consecutive laser pulses. The results have shown that depending on the laser fluence, the laser heating of the soot particle causes annealing that tends to enhance the soot's optical properties. Vander Wal et al. [245] found that annealing enhances the soot optical properties for fluences as low as 100 mJ/cm^2 at a laser wavelength of 1064 nm. Cenker et al. [246] found a significant increase of soot absorption for laser fluences (at 1064 nm) above 170 mJ/cm^2 (corresponding to $\sim$ 4000 K). Török et al. [247] studied three operation points of a miniCAST burner corresponding to different soot maturity states. Various combinations of first and second laser pulses were explored. They showed that pre-heating soot with a first laser pulse affects the soot properties differently depending on their maturity. By analysing the extinction coefficient of soot that was extracted from two laminar diffusion flames and irradiated by a laser source at 1064 nm, Migliorini et al. [248] found no variation of the optical properties for a fluence of 100 mJ/cm^2, while for 270 mJ/cm^2, a noticeable difference in the spectral dependence of K_{ext} was observed meaning that the laser pulse modified soot optical properties. The spread of the fluence limit observed in these works and the work [247] indicate that the modification of soot properties through laser heating depends on the soot maturity. To minimise errors from

sublimation, annealing, and other high-fluence phenomena, it is preferable to use the lowest possible laser fluences, ensuring that soot heating temperatures remain below ∼4000 K, as suggested by the findings of Cenker et al. [246]. Additionally, the first laser pulse should be set to the lowest one to limit the alteration of the soot particles' properties before the second pulse.

4.2.4 Advantages and drawbacks of the SP-LII

The advantages of the SP-LII are multiple:

- It is directly applicable in flames. Thus, it can be classified as *in-situ* and is lowly intrusive.
- It is theoretically applicable to single-shot measurements, meaning that it is applicable to turbulent flames.
- It does not require any prior estimation or assumption for the gas temperature. Thus, it relies only on LII experiments. This is especially important in turbulent flames as the gas temperature may see important variations in time for a specific spatial location, and simultaneous implementation of different setups may be complex.
- It provides an estimation of the gas temperature.
- It is easily applicable in laminar flames. Indeed, the steady behaviour of the laminar flame means that the two SP-LII laser pulses can be temporally decorrelated, simplifying the experimental setup (only one laser source is needed).
- As an LII-based technique, soot volume fraction can be estimated with traditional LII or AC-LII with no additional measurements. Additionally, if measurements are time-resolved, soot primary particle diameter can be calculated by fitting the decay of the LII signals. Thus, a single experimental setup would provide at the same time several complementary information on the soot particles: $E(m_\lambda)$, T_0, f_v, and d_p.
- Finally, it can be applied to 2D visualisation of the spatial evolution of $E(m_\lambda)$ in flames. In addition to providing complementary information on soot maturity, this would improve the spatial estimations of the soot volume fraction as spatially constant $E(m_\lambda)$ is usually considered.

It also has some drawbacks:

- It requires two laser heads when turbulent flames are to be investigated.
- It requires working at low fluences for the relation between the peak temperature and the laser fluence to be linear. Thus, the emitted LII signal is lower, inducing a lower signal-to-noise ratio.
- For single-shot measurements, the delay between the pulses, probe size and local velocity are linked. This limits the range of application of the technique when considering turbulent flames.
- Computing $E(m_\lambda)$ requires the knowledge of ρc.
- The wavelength dependence of $E(m_\lambda)$ has to be *a priori* known or can be estimated from additional measurements.

4.3 Post-processing of the data: computation of $E(m_\lambda)$ and T_0

This section presents two ways to post-process the data to compute $E(m_\lambda)$ and T_0. The first approach called the "absorption model" (AM), is based on the solving of the energy balance equation (Eq. (3.8)) when all loss terms are

neglected. The second strategy uses a look-up table (LUT) built from the solving with the LII code of the entire energy equation for multiple values of the LII code input parameters.

4.3.1 The absorption model (AM)

Derivation of the equations

With the AM, radiation, conduction, and sublimation are neglected in the energy balance equation during the laser pulse. Thus, as already demonstrated, one obtains Eq. (4.4). By considering two measurements of T_M at two different fluences $F_1 \neq F_2$, Eq. (4.4) gives the following system of two equations:

$$\begin{aligned} E(m_{\lambda_{laser}}) &= \frac{\lambda_{laser}}{6\pi}(T_{M_2} - T_{M_1})(\frac{F_2}{\rho c_2} - \frac{F_1}{\rho c_1})^{-1} \\ T_0 &= \left(\frac{F_2}{\rho c_2}T_{M_1} - \frac{F_1}{\rho c_1}T_{M_2}\right)\left(\frac{F_2}{\rho c_2} - \frac{F_1}{\rho c_1}\right)^{-1}. \end{aligned} \tag{4.6}$$

Assuming a temperature independent product ρc gives:

$$\begin{aligned} \frac{E(m_{\lambda_{laser}})}{\rho c} &= \frac{\lambda_{laser}}{6\pi}\frac{T_{M_2} - T_{M_1}}{F_2 - F_1} \\ T_0 &= \frac{F_2 T_{M_1} - F_1 T_{M_2}}{F_2 - F_1}. \end{aligned} \tag{4.7}$$

Then, $E(m_{\lambda_{laser}})$ and T_0 are directly computed from $[F_1, T_{M_1}], [F_2, T_{M_2}]$. In the following, $E(m_{\lambda_{laser}})$ is noted $E(m_\lambda)$ to simplify the notations.

Validity of the assumption neglecting the losses

With the AM data processing method, $E(m_\lambda)$ and T_0 are computed by neglecting the radiation, conduction and sublimation processes. In order to quantify the impact of this simplification, simulations have been run by deactivating each loss term in the LII code one by one and using the set $\Omega_{ref}/\{F_{2_{ref}}\}$, with F_2 varying from 0 to 250 mJ/cm^2. $E(m_\lambda)$ and T_0 are computed with the AM method from the peak temperatures that are extracted from these simulations and are compared to $E(m_\lambda)_{ref}$ and $T_{0_{ref}}$ (0.37, and 1860 K). The deviations from the reference quantities: $\frac{E(m_\lambda) - E(m_\lambda)_{ref}}{E(m_\lambda)_{ref}}$ and $\frac{T_0 - T_{0_{ref}}}{T_{0_{ref}}}$ are presented in Fig. 4.6.

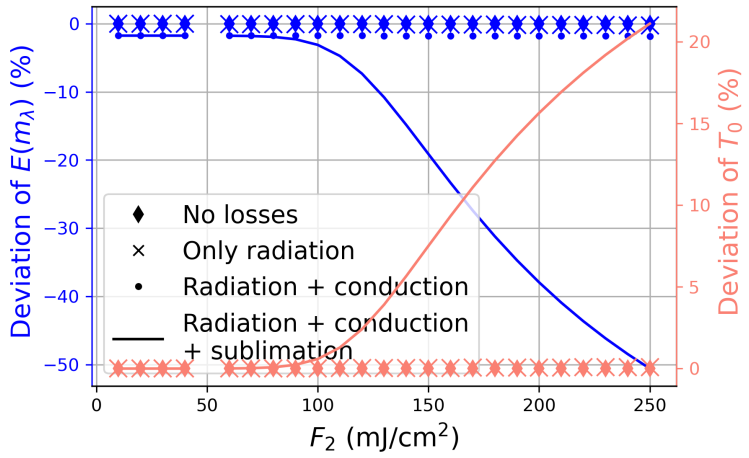

Figure 4.6: Estimations with the AM method of deviations of $E(m_\lambda)$ (left axis, in blue) and T_0 (right axis, in pink) as a function of F_2. The symbols represent the results obtained when different loss mechanisms are included in the energy balance equation: no losses (⋄), radiation losses only (×), radiation and conduction losses (•), and the combination of radiation, conduction, and sublimation losses (solid lines).

When the simulations are run without the loss terms, the values of $E(m_\lambda)_{ref}$ and $T_{0_{ref}}$ are exactly recovered, ensuring that the AM is not biased. When only radiation is considered, no significant deviation from the reference $E(m_\lambda)_{ref}$ and $T_{0_{ref}}$ is seen ($< 1\%$), confirming that radiation has a negligible impact on the results. When both radiation and conduction are considered, a small deviation from $E(m_\lambda)_{ref}$ appears ($\approx 2\%$ for this case), while there is no visible deviation for $T_{0_{ref}}$. It has been verified that a higher value of the thermal accommodation coefficient α would have increased the deviation from $E(m_\lambda)_{ref}$ but remains of the order of a few per cent. Finally, when sublimation is also considered in the LII code, no visible deviation is added for laser fluences below ~ 100 mJ/cm^2 (corresponding to the break of the curve T_M versus F with $T_{M_2} \sim$ 3500 K). However, above this value, the deviations of both $E(m_\lambda)$ and T_0 largely increase with the laser fluence. The mass accommodation coefficient β, deliberately selected high, explains why sublimation has such a strong effect even for moderate fluences.

In conclusion, these results confirm the legitimacy of neglecting the radiation term. It also points out that the neglected conduction term introduces a small underestimation of $E(m_\lambda)$ independently of the value of the laser fluence. More importantly, it illustrates that with the AM method, soot sublimation must be avoided. In the following, the simulations are run with all loss terms activated in the LII code.

4.3.2 The look-up table (LUT)

Construction and usage of the LUT

The AM method neglects losses. Therefore, its accuracy is reduced when losses become significant (small particles or sublimation activated). Therefore, a second way to determine $E(m_\lambda)$ and T_0 from two peak temperatures at two fluences is proposed here: the look-up table (LUT) method. The LUT method is based on a multi-entry table storing T_M values. This LUT has to be generated only once (using an LII code) before exploiting any experimental results. Each entry of the LUT corresponds to an input parameter of the LII code. Here, the LUT is a table of dimension 7 corresponding to $E(m_\lambda)$, T_0, F, d_p, ρ, α, and β. In practice, it is desirable to reduce the number of dimensions to reduce the time required to generate it. For instance, parameters such as α and β should be set. However, here, they are kept as parameters to study their impact on the results as these parameters are not well known. The values of the parameters used to generate the look-up table are gathered in Tab 4.2. The LUT is generated by extracting T_M from simulations obtained with the LII code for each possible combination of the input parameters.

Parameter	Unit	Minimum	Step	Maximum
$E(m_\lambda)$	–	0.1	0.05	0.5
T_0	K	1500	100	2200
F	mJ/cm^2	25	25	225
d_p	nm	1	10	41
ρ	kg/m^3	1200	100	2100
α	–	0.2	0.1	0.5
β	–	0	0.25	1

Table 4.2: Values of the input parameters of the LII code used to create the look-up table.

Once the LUT is generated, $E(m_\lambda)$ and T_0 can be retrieved with the following protocol:

1. d_p, ρ, α, and β have to be set (using experimental measurements, literature reviews or best guess).
2. Two couples of fluence and peak temperature have to be experimentally determined: $[F_1, T_{M_1}]$ and $[F_2, T_{M_2}]$.

3. The knowledge of d_p, ρ, α, β, and F_1 permits the extraction from the LUT of a sub-table of dimension two in which are stored T_M values. The dimensions of the sub-table correspond to the entries of the LUT that are not set: $E(m_\lambda)$ and T_0. A second sub-table of T_M can be extracted using F_2 instead of F_1. These two sub-tables are called Ψ_1 and Ψ_2.

4. For each element in Ψ_1 and Ψ_2, the table Ξ of dimension two is computed:

$$\Xi(E(m_\lambda), T_0) = |\Psi_1(E(m_\lambda), T_0) - T_{M_1}| + |\Psi_2(E(m_\lambda), T_0) - T_{M_2}|. \tag{4.8}$$

5. The values of $E(m_\lambda)$ and T_0 that minimise Ξ are selected as the most probable couple $[E(m_\lambda), T_0]$ for the soot particles.

It is important to note that the accuracy of the LUT can be improved without significantly increasing its generation time by artificially enhancing its discretisation through interpolation of the T_M values.

Consistency of the LUT method

The LUT method selects $E(m_\lambda)$ and T_0 as the one minimising Eq. (4.8). One can ask if the selected values are really representative of the actual values for the absorption function and the gas temperature. In order to verify the consistency of the LUT method, the reference input parameters Ω_{ref} with $T_{M_1 ref}$ and $T_{M_2 ref}$ are retained here. The expected values for the absorption function and the gas temperature are $E(m_\lambda)_{ref}$ and $T_{0_{ref}}$. It has to be noted that, for the reference case, all entries of the LUT but α_{ref} and β_{ref} are off-grid: i.e. the parameters of Ω_{ref} are not parameters used for the generation of the LUT. This has been done to test the robustness of the LUT method.

Figure 4.7 shows the computed inverse of Ξ (high values means low errors) versus $E(m_\lambda)$ and T_0. The region of lower error is narrow, and the global minimum is found for $E(m_\lambda)_{ref}$ (0.37) and $T_{0_{ref}}$ (1860 K) proving the validity of the LUT method (it has been tested in multiples other conditions).

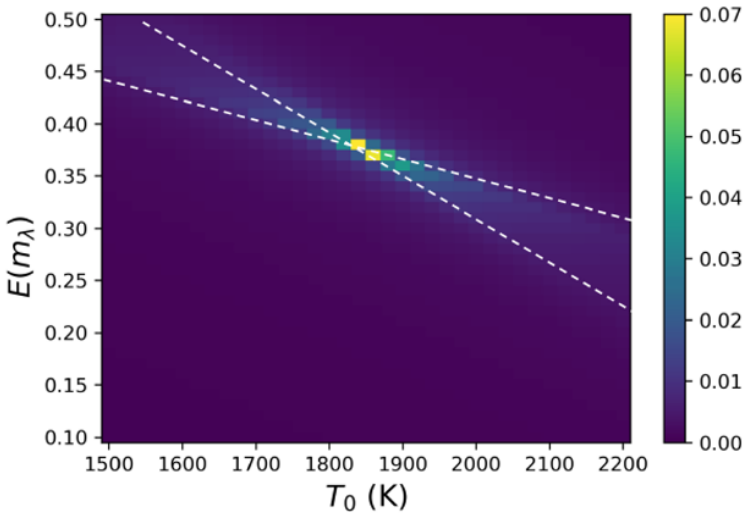

Figure 4.7: Inverse of Ξ (define by Eq.(4.8)) versus $E(m_\lambda)$ and T_0. The white dashed lines help to visualise the low error regions for the two pulses considered alone.

It can be seen that the low error region corresponds to the crossing of two diagonals represented by the white dashed lines. The diagonals correspond to the minimum error for each pulse considered alone, and their slope depends on the pulse's fluence. As a result, the region of low errors narrows when the difference in laser fluences

of the two pulses increases and widens when F_1 approaches F_2. Thus, to improve the accuracy of the LUT method pulse, from a mathematical point of view, F_1 and F_2 should be as spread as possible.

4.4 Theoretical evaluation of the SP-LII technique

4.4.1 Procedure for the theoretical evaluation of the SP-LII technique

In this section, the SP-LII is tested with numerical LII signals synthesised using the LII code. The peak temperatures T_{M_1} and T_{M_2} are extracted from simulations. Owing to this, the performance of the SP-LII can be analysed, and an uncertainty analysis of the AM and LUT methods is performed as the output of the methods should be the ones given as input of the LII code: $E(m_\lambda)_{ref}$ and $T_{0_{ref}}$. The protocol used in this section is schematically represented in Fig. 4.8. The Ω sets contain: $\Omega = \{F_1, F_2, \rho, d_p, \alpha, \beta\}$. The quantities $E(m_\lambda)_{ref}$, $T_{0_{ref}}$ and Ω^{SIM} constitute the inputs of the LII code (the superscript ^{SIM} refers to the parameters used as input of the LII code). T_{M_1} and T_{M_2} are extracted from the simulations and are considered as inputs for the AM and LUT post-processing methods along with the set Ω^{PP} to obtain $E(m_\lambda)_{post}$ and $T_{0_{post}}$. The superscript ^{PP} refers to the input parameters of the post-processing of the AM and LUT methods, and the subscript $_{post}$ is the post-processing method, either AM or LUT. Then, $E(m_\lambda)_{post}$ and $T_{0_{post}}$ are compared to the reference values: $E(m_\lambda)_{ref}$ and $T_{0_{ref}}$.

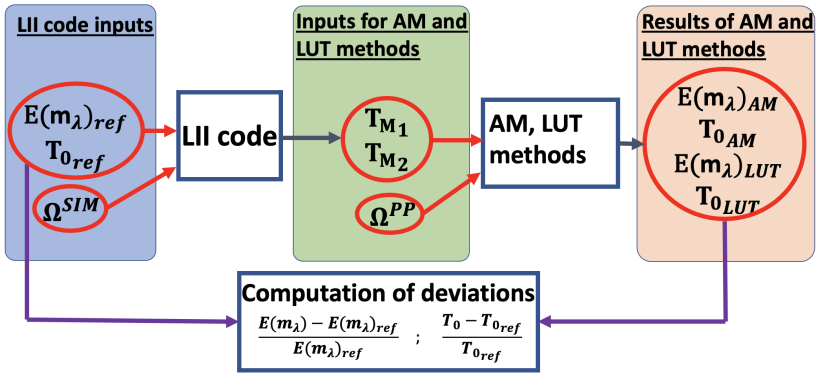

Figure 4.8: Scheme describing the SP-LII performance and uncertainty analysis procedure. The Ω sets contain: $\Omega = \{F_1, F_2, \rho, d_p, \alpha, \beta\}$.

The performance of the SP-LII technique coupled with AM or LUT post-processing methods will be first evaluated in Sec. 4.4.2 as a function of the laser fluence and of some soot properties, assuming that all parameters are well-known, i.e. $\Omega^{PP} = \Omega^{SIM}$. Then, in Sec. 4.4.3, the parameters used for the post-processing are taken to be different from those of the simulations (i.e. $\Omega^{SIM} \neq \Omega^{PP}$) in order to quantify the impact of uncertainties in these parameters on the performance of the methods.

Numerous works [236, 249–252] numerically treat the quantification of uncertainties of LII-based techniques by combining multiple sources of errors. In this work, a "one parameter at a time" procedure is used to quantify the errors on both $E(m_\lambda)$ and T_0 associated with uncertainties on multiple LII parameters and erroneous estimations of the peak soot temperature. The advantage of this approach is that it gives precise knowledge about the direct impact of each parameter: the amplitude of overestimation/underestimation of $E(m_\lambda)$ and T_0 is known for each of the parameters considered.

4.4.2 Performance of the technique

The performance of the AM and LUT methods are evaluated in this section by considering $\Omega^{SIM} = \Omega^{PP}$: the same inputs used for the generation of T_{M_1} and T_{M_2} are used as inputs for the AM and LUT post-processing. In the following, the performance of the AM and LUT methods are evaluated as a function of F_2 and d_p.

2nd pulse fluence: F_2

Simulations are run for $\Omega^{SIM}/\left\{{F_1}^{SIM},\ {F_2}^{SIM}\right\} = \Omega_{ref}/\left\{F_{1ref},\ F_{2ref}\right\}$. $F_1^{SIM} = F_1$ is set to either 50, 100 or 150 mJ/cm^2, $F_2^{SIM} = F_2$ is varied from 25 to 225 mJ/cm^2.

Figures 4.9a and 4.9b express the deviations of $E(m_\lambda)_{post}$ and T_{0post} from $E(m_\lambda)_{ref}$ and T_{0ref} for both the AM and LUT methods. The breaks in the curves correspond to the case $F_1 = F_2$ for which the SP-LII technique cannot work. As discussed in Sec. 4.3.1, the losses cause the AM method to underestimate $E(m_\lambda)$ and to overestimate T_0. Sublimation starts to have a visible impact for laser fluences higher than 100 mJ/cm^2. When the laser fluence of at least one of the pulses approaches 150 mJ/cm^2, the deviations of the AM method exceed 20% and 8% for $E(m_\lambda)$ and T_0, respectively, and continues to increase rapidly for higher fluences.

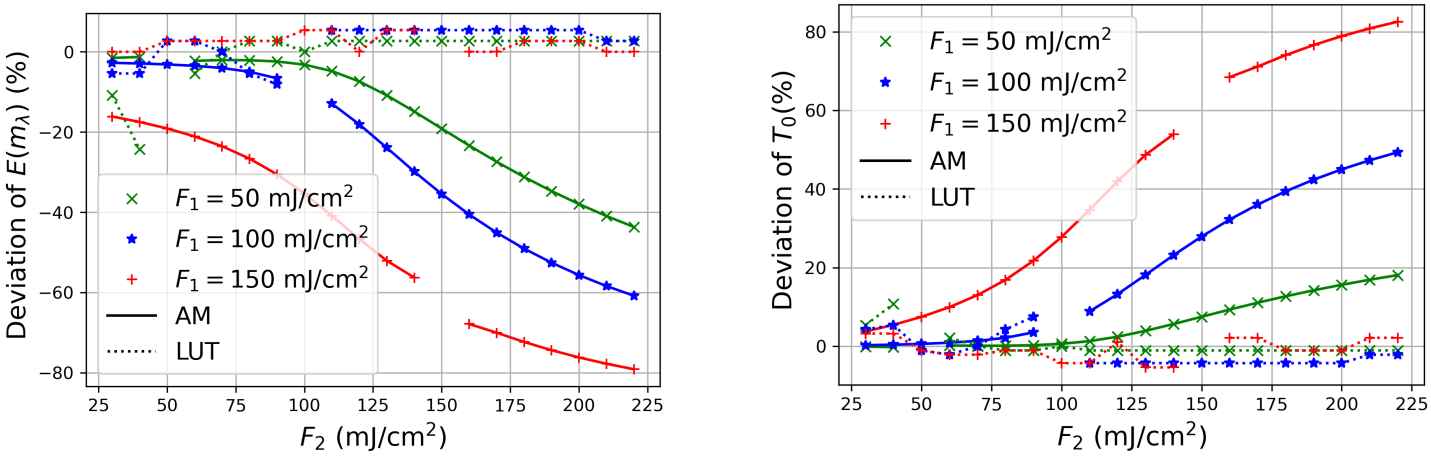

(a) (b)

Figure 4.9: Deviations in $E(m_\lambda)$ (a), and T_0 (b) obtained with the AM (solid lines) and the LUT methods (dotted line) as a function of F_2. The symbols and colours correspond to different F_1: 50 (green $\times$), 100 (blue $\star$) and 150 mJ/cm^2 (red +).

With the LUT method, the deviations stay near 5%. These low errors are primarily due to interpolation errors that may be reduced by refining the LUT database. It has to be pointed out that such good results are obtained because the same sublimation model and mass accommodation coefficient are used for both the data generation (T_{M_1} and T_{M_2}) and the LUT generation, i.e. no uncertainties on the model are considered.

Overall, sublimation significantly impacts the AM method and imposes an upper fluence (temperature) limit. In practice, this upper limit can be experimentally determined from the break of linearity in the temperature versus fluence curves (Fig. 4.2a). By contrast, the LUT method performs well for all fluences, but only because the sublimation process is assumed to be correctly represented by the model, which is certainly not the case in reality.

Soot primary particle diameter: d_p

Here, simulations are run for $\Omega^{SIM}/\left\{{d_p}^{SIM}\right\} = \Omega_{ref}/\left\{d_{p_{ref}}\right\}$ with d_p ranging from 1 to 41 nm. Figure 4.10 represents the deviation of $E(m_\lambda)$ and T_0 as a function of d_p obtained with the AM and LUT methods. Estimation with the AM method worsens when d_p is small: underestimation of d_p overcomes 10% when d_p < 5 nm. This is explained by the fact that due to stronger thermal losses, the peak temperature do depends on d_p for small d_p (as already

discussed with Fig. 4.2b). Thus, one should expect larger deviations when applying the AM method to small soot particles. Concerning the LUT, it has to be precise that the results of Fig. 4.10 for $d_p \leq 11$ nm comes from a refined table with a 1 nm step, as the initial discretisation of 10 nm (Table 4.2) was to rough for the smallest particle sizes and produced deviations exceeding 20% for $E(m_\lambda)$. This discretisation problem explains the $\sim$ 3% deviation in $E(m_\lambda)$ around d_p = 15 nm. Apart from that, above d_p = 20 nm, the deviations for both $E(m_\lambda)$ and T_0 are null. Thus, to minimise the deviations, the LUT table should be refined for small particles, while a rough discretisation is enough for larger particles (as T_M is very similar for large particles). Concerning T_0, the deviation is always under 2.5%, both for the AM and the LUT methods, indicating that the gas temperature estimation is not really sensitive to the primary particle size.

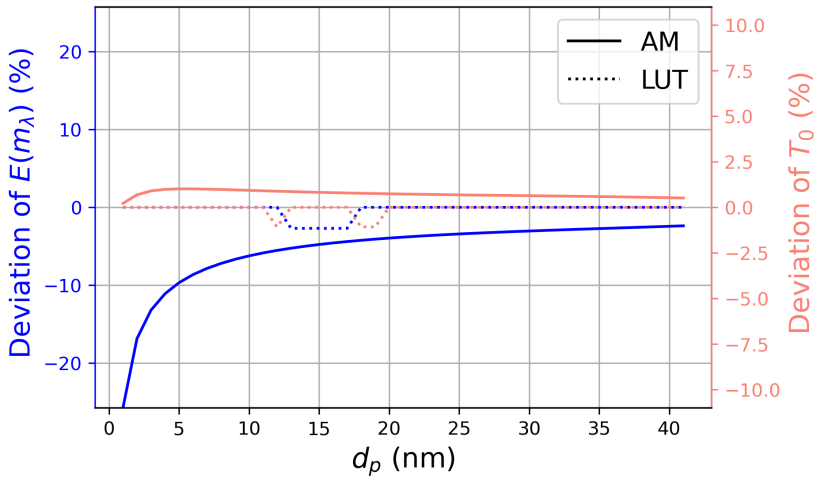

Figure 4.10: Deviations of $E(m_\lambda)$ (left axis, in blue) and T_0 (right axis, in pink) obtained with the AM (solid lines) and the LUT methods (dotted line) as a function of d_p.

4.4.3 Uncertainty analysis

The uncertainty analysis aims to investigate the sensitivity of the SP-LII technique to the parameters contained in Ω, as in practice, not all of them are known. For that, the parameters selected as input of the LII code are different from the ones used as inputs for the AM and LUT post-processing, i.e. $\Omega^{SIM} \neq \Omega^{PP}$ (Fig. 4.8). The analysis is performed for ρ for both the AM and LUT methods and for d_p, α and β solely for the LUT method as the AM method does not depend on these parameters.

Density: ρ

Here, $\Omega^{SIM} = \Omega_{ref}$, $E(m_\lambda)$ and T_0 are computed using $T_{M_1 ref}$ and $T_{M_2 ref}$ and the reference parameters without ρ_{ref}: $\Omega^{PP} / \{\rho^{PP}\} = \Omega_{ref} / \{\rho_{ref}\}$. Instead, ρ is varied from 1200 to 2100 kg/m^3, i.e. an error is intentionally introduced in the input of the post-processing. The resulting deviations from $E(m_\lambda)_{ref}$ and $T_{0_{ref}}$ are plotted in Fig. 4.11. With the AM method, the deviation of $E(m_\lambda)$ is linear with ρ while the deviation on T_0 is independent of ρ. This can be explained by the weak temperature dependence of c in the LII code. Indeed, for a temperature independent product ρc, the SP-LII technique retrieves the ratio $\frac{E(m_\lambda)}{\rho c}$ and not directly $E(m_\lambda)$, while T_0 becomes independent of ρc (Eq.(4.7)). Thus, with the AM method, an error done on ρc of X% brings the same error on $E(m_\lambda)$ without impacting T_0. The vertical black dashed line in Fig. 4.11 represents the reference density $\rho_{ref} = 1950$ kg/m^3, a value for which no deviation should be seen. The not null deviations for this value for the AM come from the neglected losses (mainly conduction). For the LUT post-processing method, the deviation of $E(m_\lambda)$ still has a linear behaviour with the same slope as for the AM but with a different offset, leading to better estimations. The oscillations seen for T_0

come from interpolation errors between the points of the look-up table.

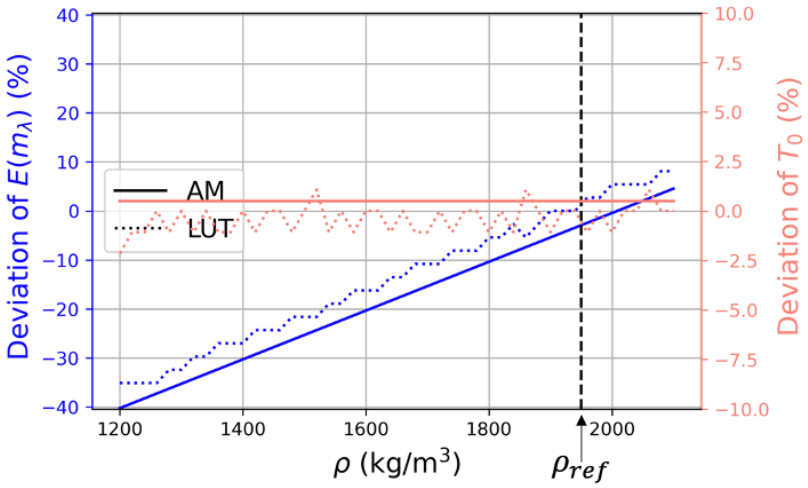

Figure 4.11: Deviations of $E(m_\lambda)$ (left axis, in blue) and T_0 (right axis, in pink) as a function of the density used for the post-processing. Results obtained with the AM and LUT methods are plotted with solid and dotted lines, respectively. The vertical black dashed lines represent the reference density.

Soot primary particle diameter: d_p

The same procedure as for the density is applied here with $\Omega^{PP}/\left\{{d_p}^{PP}\right\} = \Omega_{ref}/\left\{d_{p_{ref}}\right\}$ with d_p varying from 1 to 41 nm. Figure 4.12 represents the deviation of $E(m_\lambda)_{LUT}$ and T_{0LUT} from $E(m_\lambda)_{ref}$ and T_{0ref}.

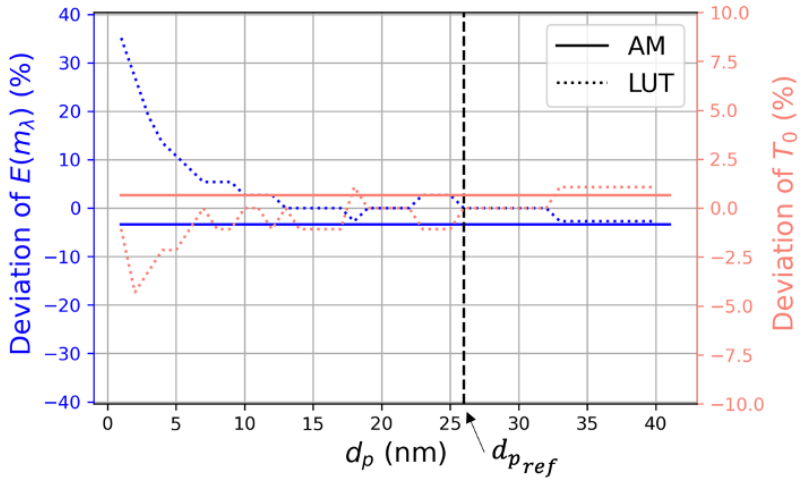

Figure 4.12: Deviations of $E(m_\lambda)$ (left axis, in blue) and T_0 (right axis, in pink) as a function of the primary particle diameter used for the post-processing. Results obtained with the AM and LUT methods are plotted with solid and dotted lines, respectively. The vertical black dashed lines represent the reference primary particle diameter.

For comparison purposes, the solid lines give the results of the AM post-processing, which is not sensitive to d_p. Similarly to what has been done for Fig. 4.10, for the LUT, the refined table (with a 1 nm step) is used for $d_p \leq 11$ nm. The deviations of the LUT method on the range $d_p = 10 - 41$ nm are below 5% for $E(m_\lambda)$ and below 2% for T_0. For lower diameters, the deviation for $E(m_\lambda)$ increases with decreasing d_p and reaches $\sim$ 35% for d_p = 1 nm. This shows that with an incorrect assumption on d_p ($d_p < 10$ nm instead of 26 nm), the estimation of $E(m_\lambda)$ with the LUT method is worse than the one of the AM method. These results indicate that the experimental determination

of d_p is not mandatory in flame regions containing mainly soot particles of relatively large d_p, as a coarse estimation would be accurate enough ($\approx 10-40$ nm). On the contrary, in flame regions where smaller soot particles may be encountered (incipient or oxidised soot particles), a wrong assumption on d_p would produce non-negligible errors (up to 35% in this example) in the estimation of $E(m_\lambda)$. The vertical black dashed line represents the reference diameter $d_{p_{ref}} = 26$ nm, a value for which no deviation should be seen. The not null deviations for this value for the AM come from the neglected losses.

Thermal accommodation coefficient: α

In LII codes, conduction losses are governed by the thermal accommodation coefficient α. In the literature, multiple values of α range from 0.23 to 0.9 [154] with values in general near 0.3 and almost always below 0.5: high uncertainties exist on the values one should select for this parameter. Thus, verifying the influence of an uncertainty of α on the SP-LII technique is important. The same procedure as for ρ and d_p is now used for α, the only difference being that the procedure is repeated for three different values of d_p as it is expected that conclusions may differ regarding the soot primary particle diameters. Here, $\Omega^{SIM}/\left\{{d_p}^{SIM}\right\} = \Omega_{ref}/\left\{d_{p_{ref}}\right\}$, ${d_p}^{SIM}$ take the values 1, 26 and 41 nm, leading each time to different T_{M_1} and T_{M_2}. $\Omega^{PP}/\left\{\alpha^{PP}\right\} = \Omega_{ref}/\left\{\alpha_{ref}\right\}$, and, α^{PP} is varied from 0.2 to 0.5. The resulting deviations of $E(m_\lambda)_{LUT}$ and $T_{0\,LUT}$ from $E(m_\lambda)_{ref}$ and $T_{0_{ref}}$ are plotted in Fig. 4.13. To limit confusion, the superscript ^{SIM} and ^{PP} are specified. The figure shows that whatever the thermal accommodation coefficient used for the post-processing, there is no notable difference in the deviations (below 4% and 2% for $E(m_\lambda)$ and T_0 respectively) for the two largest particle sizes considered here. Whereas for the smallest particles, assuming α = 0.2 or 0.5 induces a -8% and +19% difference in the deviation of $E(m_\lambda)$, respectively.

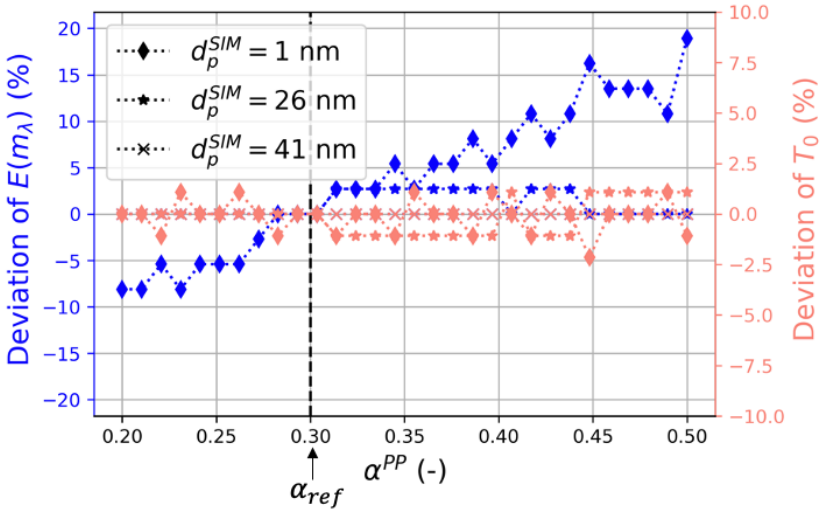

Figure 4.13: Deviations of $E(m_\lambda)$ (left axis, in blue) and T_0 (right axis, in pink). The X-axis represents α^{PP}, the thermal accommodation coefficient used for the post-processing of the LUT method. The symbols differentiate the value of the soot primary particle diameter used for the data generation: d_p^{SIM}: 1 ($\diamond$), 26 ($\star$) and 41 nm ($\times$). The vertical black dashed line represents the reference thermal accommodation coefficient $\alpha_{ref} = 0.3$.

Overall, the estimation of T_0 is not significantly affected by the uncertainty existing on α, even for the smallest soot particles. The same can be said for $E(m_\lambda)$ as long as the soot size is more than a few nanometres. Thus, in practice, it is not essential to precisely know α.

Mass accommodation coefficient: β

The values of β encountered in the literature are even more spread than for α with values ranging from 0 to 1 [113, 154]. Thus, the impact of an uncertainty on β is presented here. The high uncertainty on the value of β and its expected non-linear impact on $E(m_\lambda)_{LUT}$ and $T_{0\,LUT}$ brings the necessity to adapt the previous procedure for

the study of β. The set considered is $\Omega^{SIM}/\left\{\beta^{SIM}, F_2^{SIM}\right\} = \Omega_{ref}/\left\{\beta_{ref}, F_{2_{ref}}\right\}$, multiples values are considered for β^{SIM} between 0 and 1. $\Omega^{PP}/\left\{\beta^{PP}, {F_2}^{PP}\right\} = \Omega_{ref}/\left\{\beta_{ref}, F_{2_{ref}}\right\}$, and β^{PP} will take the values 0, 0.25, 0.5 and 1. The reference fluence $F_{2_{ref}}$ is increased to F_2 = 140 mJ/cm^2 = F_2^{SIM} = F_2^{PP} in order to have non-negligible sublimation (Fig. 4.9). The deviations are plotted in Fig. 4.14a and Fig. 4.14b as a function of β^{SIM} and for the four values of β^{PP} considered. To limit confusion, the superscript ^{SIM} and ^{PP} are specified. For comparison purposes, the solid black line represents the results obtained when using the AM method.

As expected, for $\beta^{PP} = 0$, the deviations obtained with the LUT and the AM methods are close because, in this case, they both neglect sublimation. The remaining differences are explained by the conduction losses that are accounted for by the LUT method and the interpolation errors. It appears that when the pulses have low to moderate laser fluence ($F_1 = 50$ and $F_2 = 140$ mJ/cm^2), the lack of knowledge of β can bring deviations as much as 20% for $E(m_\lambda)$ and 10% for T_0 (when $\beta^{PP} = 1$ is assumed). Thus, an unfortunate assumption about β can give a worse estimate of $E(m_\lambda)$ and T_0 than the much simpler AM method would provide. By comparing Fig. 4.14a with Fig. 4.14b, it can be seen that the deviations of T_0 are about half as large as those on $E(m_\lambda)$.

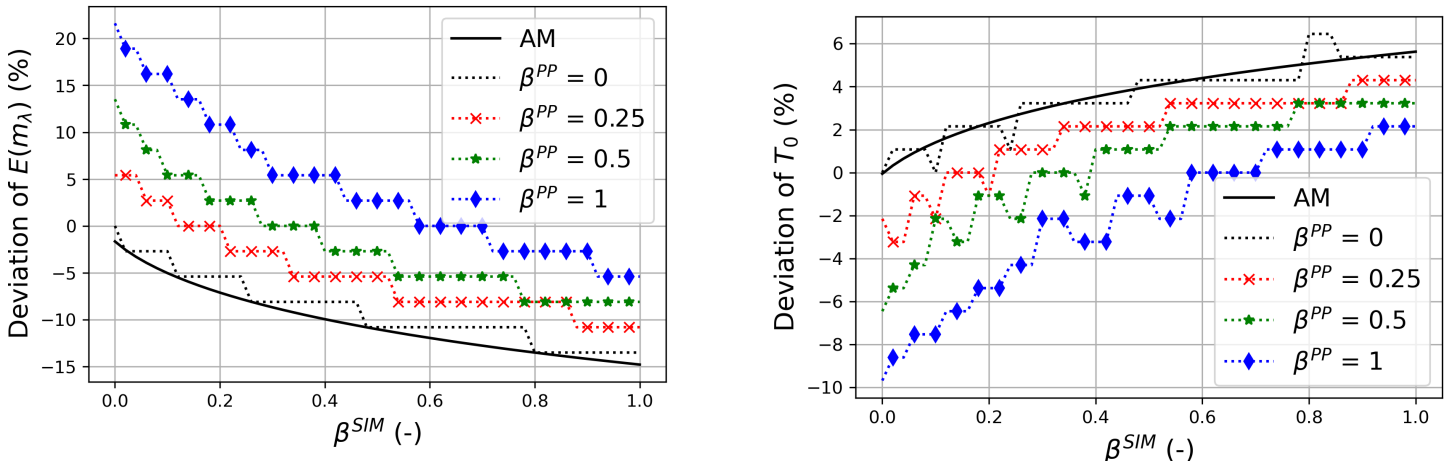

(a) (b)

Figure 4.14: Deviations of $E(m_\lambda)$ (a) and T_0 (b) as a function of β^{SIM}: the mass accommodation coefficient used for the data generation. The deviations are represented for the AM and LUT methods in solid and dotted lines, respectively. The symbols differentiate the results of the LUT method obtained with the different assumptions on the value of β^{PP}: 0 (black), 0.25 (red $\times$), 0.5 (green $\star$) and 1 (blue $\diamond$).

When working with laser fluences where little sublimation is to be expected, assuming $\beta \sim 0.2$ rather than higher values, seems to limit the maximum error done on $E(m_\lambda)$ to $\pm$ 10% and $\pm$ 5% for T_0. In practice, the potential of the LUT method is limited by the lack of knowledge of β and/or by the incorrect representation of the sublimation process and the absence of precise models for other high-temperature phenomena like annealing. This encourages working at laser fluences that do not trigger sublimation.

4.4.4 Effect of an error on the estimation of the peak soot temperature

The experimental determination of the soot temperature by 2C-LII pyrometry or by any other experimental technique is subjected to bias, causing errors in the determination of T_{M_1} and T_{M_2}. Two kinds of errors are investigated here: an overestimation of T_{M_1} of 10%, and an overestimation of both T_{M_1} and T_{M_2} by 10%. Looking at Eq. (4.7) for the AM method, and regarding what has been said in Sec. 4.3.2 about the uniqueness of solution for the LUT method, it is to be expected that the difference of fluence between the two pulses plays a role in the computed

deviations of both $E(m_\lambda)$ and T_0. Thus, the procedure retained here is the following: simulations are performed with $\Omega^{SIM}/\{F_2{}^{SIM}\} = \Omega_{ref}/\{F_{2_{ref}}\}$, where $F_2^{SIM} = F_2$ is varied from 25 to 225 mJ/cm^2. The peak temperatures T_{M_1} and T_{M_2} are extracted from the simulations, and a 10% error is added on at least one of them to obtain $\widetilde{T_{M_1}}$ and $\widetilde{T_{M_2}}$. Finally, $E(m_\lambda)_{post}$ and T_{0post} are computed with both methods with these modified peak temperature $\widetilde{T_M}$ and with parameters $\Omega^{PP} = \Omega^{SIM}$. The procedure is illustrated in Fig. 4.15.

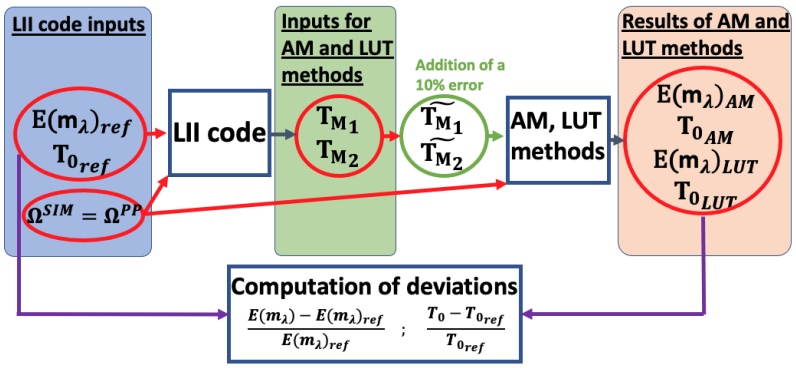

Figure 4.15: Scheme describing the procedure for the analysis of the impact of peak temperature errors on the estimation of $E(m_\lambda)$ and T_0 with the SP-LII method. The sets Ω contains: $\Omega = \{F_1, F_2, \rho, d_p, \alpha, \beta\}$.

Figure 4.16a represents the deviation of $E(m_\lambda)$ and T_0 from $E(m_\lambda)_{ref}$ and $T_{0_{ref}}$ as a function of F_2 when T_{M_1} is overestimated by 10%: $\widetilde{T_{M_1}} = 1.1 \cdot T_{M_1}$ and $\widetilde{T_{M_2}} = T_{M_2}$. The deviations of $E(m_\lambda)$ and T_0 are significantly more important than the ones for uncertainties on ρ, d_p, α and β. With the AM method, when F_2 is approaching F_1, the denominators of Eq.(4.6) shrink, so an error on T_{M_1} has a larger importance than for higher fluence differences, and the deviation from the true value skyrockets. At the highest laser fluences, significant deviations occur, primarily due to sublimation effects: $E(m_\lambda)$ is underestimated by over 30%, while T_0 is overestimated by more than 25%. For $F_1 = 50$ mJ/cm^2, the optimum laser fluence for F_2 is near 125 mJ/cm^2. Deviations with the LUT method are lower for all laser fluences than with the AM method. However, between 60 mJ/cm^2 and 190 mJ/cm^2, the 19% deviation for $T_{0\,LUT}$ from $T_{0_{ref}}$ corresponds to the upper limit of the LUT in terms of T_0 (which is 2200 K, see Tab 4.2): there is "saturation" of the look-up table. The estimation of $E(m_\lambda)$ also degrades when approaching 50 mJ/cm^2, as discussed in Sec. 4.3.2. This is due to the wider region in the error map when both laser pulses have similar fluence values, increasing the chance of selecting an incorrect couple $(E(m_\lambda)_{LUT}, T_{0\,LUT})$. It was verified, but not shown here, that if the 10% error is set on T_{M_2} instead of T_{M_1}, it leads to the same conclusion: the pulses fluences should be as spread as possible but with an upper limit given by the sublimation process.

Figure 4.16b considers the case of a systematic 10% error in the estimation of temperature, i.e. $\widetilde{T_{M_1}} = 1.1 \cdot T_{M_1}$ and $\widetilde{T_{M_2}} = 1.1 \cdot T_{M_2}$. In this case, with the AM method and at low laser fluences, the 10% error made on T_M is directly transmitted to $E(m_\lambda)$ and T_0: i.e. an X% overestimation on the peak temperature induces X% overestimation of both $E(m_\lambda)$ and T_0 (Eq.(4.7)). Concerning the LUT method, for laser fluences above 125 mJ/cm^2, the look-up table saturates (reaches its upper limit for $E(m_\lambda)$) and globally performs worse than the AM method.

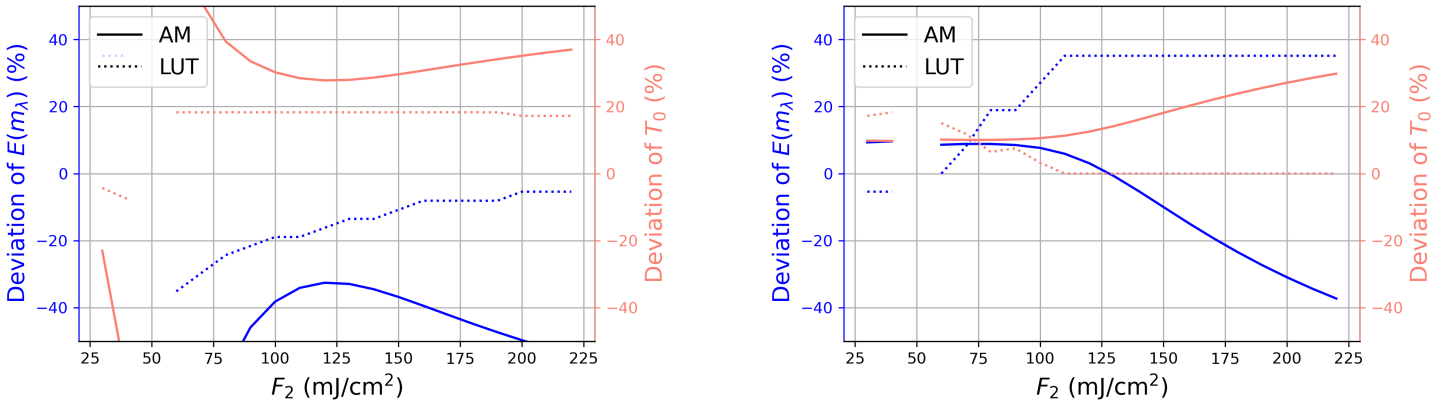

Figure 4.16: Deviations of $E(m_\lambda)$ (left axis, in blue) and T_0 (right axis, in pink) obtained using the AM method (solid lines) and the LUT method (dotted line) as a function of F_2 when (a): only T_{M_1} is overestimated by 10%, and (b): both T_{M_1} and T_{M_2} are overestimated by 10%.

Overall, both the AM and LUT methods are quite sensitive to errors in the estimation of the peak temperatures.

4.5 Conclusion

The SP-LII technique allows estimating the ratio $\frac{E(m_\lambda)}{\rho c}$. Then, the knowledge of the product ρc allows accessing $E(m_\lambda)$. The SP-LII approach consists of measuring the soot particles' peak temperature at two different laser fluences. This technique does not require prior knowledge of the local gas temperature T_0 and provides an estimation for it. The SP-LII is potentially applicable for single-shot measurements, theoretically allowing measurements in turbulent flames. In that case, the delay between the two laser pulses must be carefully selected so that it is long enough to allow the soot particles to cool down to the gas temperature but short enough to ensure that the two laser pulses heat the same group of soot particles.

Two methods to compute $E(m_\lambda)$ and T_0 have been theoretically compared using numerically synthesised LII signals obtained from an LII code. The first method called the "absorption model" (AM), neglects the loss terms in the energy equation and solves it analytically. It directly calculates $E(m_\lambda)$ and T_0 from two equations. It is a simple and efficient way to compute $E(m_\lambda)$ and T_0. However, it deviates when sublimation appears and brings an underestimation of $E(m_\lambda)$ above 10% when soot particles have a primary particle diameter below 5 nm. The second method (LUT) used to retrieve $E(m_\lambda)$ and T_0 is through a look-up table built with an LII code. It has proven to be accurate even when sublimation occurs and for all primary particle sizes, as long as the look-up table has enough data points.

An uncertainty analysis pointed out that the error made on $E(m_\lambda)$ is linear with the error made on the assumed value for the soot density, while T_0 is not impacted much. Knowledge of the soot primary particle diameter and the thermal accommodation coefficient seems to be of minor importance for T_0, but also for $E(m_\lambda)$ when particles have a diameter above $\sim$5 nm. Also, for the LUT method, in the absence of knowledge of the mass accommodation coefficient, a value below 0.2 might limit the deviation obtained using the look-up table method for low to moderate laser fluences. In addition, the peak temperatures have to be estimated as accurately as possible as this information has an important impact on the estimation of $E(m_\lambda)$ and T_0.

Globally, the LUT method performs slightly better than the AM. However, it requires more inputs that are mostly unknown, such as the soot primary particle diameter and the thermal and mass accommodation coefficients. Moreover, its accuracy relies on the validity of the models (and their parameters, such as β) describing the loss terms in

the soot energy equation considered for the generation of the table. Therefore, the LUT method has to be used with caution. Particular attention is required when using moderate to high laser fluences, as in this case, the difficult-to-model sublimation term (but also other high-temperature phenomena such as annealing) plays an important role, which can lead to larger errors. Therefore, adapted laser fluences should be selected to avoid these phenomena. Consequently, the interest in the LUT method is reduced only to account for soot particle size differences at the cost of higher complexity. In most applications, the simpler AM method should be sufficient to estimate $E(m_\lambda)$.

The recommendations for the experimental application of the separated pulse LII technique are the following:

- Avoid heating soot to temperatures inducing high-temperature phenomena that break the linear relation between peak temperature and laser fluence. An upper-temperature limit can be identified by looking at temperature versus fluence curves.
- The lower laser pulse should be set to the minimum fluence permissible, maintaining an adequate signal-to-noise ratio.
- The laser fluence of the two pulses should be selected as spread as possible to limit the impact of the error made on the estimation of the peak temperatures.
- When applied to turbulent flames:
  - The delay between the two laser pulses should be estimated considering the soot residence time in the probe volume and the soot cooling time.
  - The laser fluence of the first pulse should be lower than the second one to reduce the potential change of soot properties, which may be caused by the interaction of the high-energy laser beam with the soot particles and to reduce the bath gas heating.

This chapter introduced the SP-LII technique and evaluated its performance through numerical testing. However, it has yet to be experimentally validated under real flame conditions. In the next chapter, the SP-LII technique will be applied to a laminar diffusion flame to prove its feasibility and to investigate the spatial variation of the soot absorption function.

Part III

Experimental application: validation and limits of the SP-LII technique

Chapter 5

Pointwise measurements in a CH_4/air laminar diffusion flame

This chapter aims first to demonstrate the capability of the SP-LII to measure the soot absorption function and gas temperature in a steady flame and then to illustrate how a single experimental setup can yield four key parameters for soot characterisation: the soot absorption function $E(m_\lambda)$, gas temperature T_0, soot volume fraction f_v, and primary particle size d_p. To achieve this, a laminar diffusion CH_4/air flame is used. The steady nature of the laminar flame allows for the temporal decorrelation of the two peak soot temperature measurements required by the SP-LII, simplifying the experimental setup shown in Fig. 4.3 of the previous chapter, which was designed for instantaneous measurements. As a result, only a single laser source is needed. A 2C-LII experimental setup is implemented for the first application of the SP-LII. This chapter begins with a detailed description of the experimental setup, followed by a procedure to enhance the LII signal-to-noise ratio for low-level signals. Next, the method for applying SP-LII in a laminar flame to retrieve $E(m_\lambda)$ at the laser wavelength (1064 nm) and T_0 is carefully explained, with a particular focus on the critical step of fluence selection. The AM and LUT post-processing methods are compared at various positions along the flame centreline. The SP-LII results are evaluated against the more robust estimations of $E(m_\lambda)$ and T_0 obtained by considering more than two peak soot temperature measurements. The uncertainties in the absorption function and gas temperature obtained via SP-LII are then quantified by accounting for three factors: the soot volumetric heat capacity, primary particle size, and the wavelength dependence of the absorption function. The chapter also includes the experimental determination of soot volume fraction using AC-LII and primary particle diameter using TIRE-LII. Finally, multiple estimations of these four quantities ($E(m_\lambda)$, T_0, f_v, and d_p) are mapped into partial 2D maps to visualise their spatial variations. Some of the results presented in this chapter were published in the article: ***G. Guy et al. "Estimation of soot absorption function via the two separated pulses laser-induced incandescence technique", Applied Physics B, 129.8 (2023), p. 127*** *[134].*

Contents

5.1 Experimental setup 87
5.2 Improving the quality of low LII signals 89
5.3 First application of the SP-LII in a laminar diffusion CH_4/air flame 90
5.3.1 Selection of the laser fluence 90
5.3.2 Axial evolution of the soot absorption function $E(m_\lambda)$ and gas temperature T_0 93
LII signal and soot temperature along the flame centreline 93
AM vs LUT estimations 93
Two fluences versus multiple fluences 97

Uncertainties of the SP-LII approach 98
5.4 Cartography of $E(m_\lambda)$, T_0, f_v, and d_p **100**
5.4.1 *Soot absorption function $E(m_\lambda)$ and gas temperature T_0* 100
5.4.2 *Soot volume fraction f_v* 102
Axial profile of f_v 102
A correction for the dependence to the peak soot temperature of f_v 103
Cartography of f_v 106
5.4.3 *Soot primary particle diameter d_p* 107
Axial evolution of d_p 107
A correction for the dependence to the peak soot temperature of d_p 110
Cartography of d_p 112
5.5 Summary on the dependence to T_M of d_p and f_v **113**
5.6 Conclusion **113**

5.1 Experimental setup

The experimental setup used in this chapter is illustrated in Fig. 5.1a. It consists of three main components: a soot generation system, a laser excitation system for heating the soot, and an optical collection system for measuring the soot incandescence radiation. Compared to Fig. 4.3, only one laser source is required thanks to the steady behaviour of the laminar flame considered here. The excitation and collection systems create a conventional 2C-LII setup that will be used to extract information on $E(m_\lambda)$ and T_0 using the developed LII-based approach.

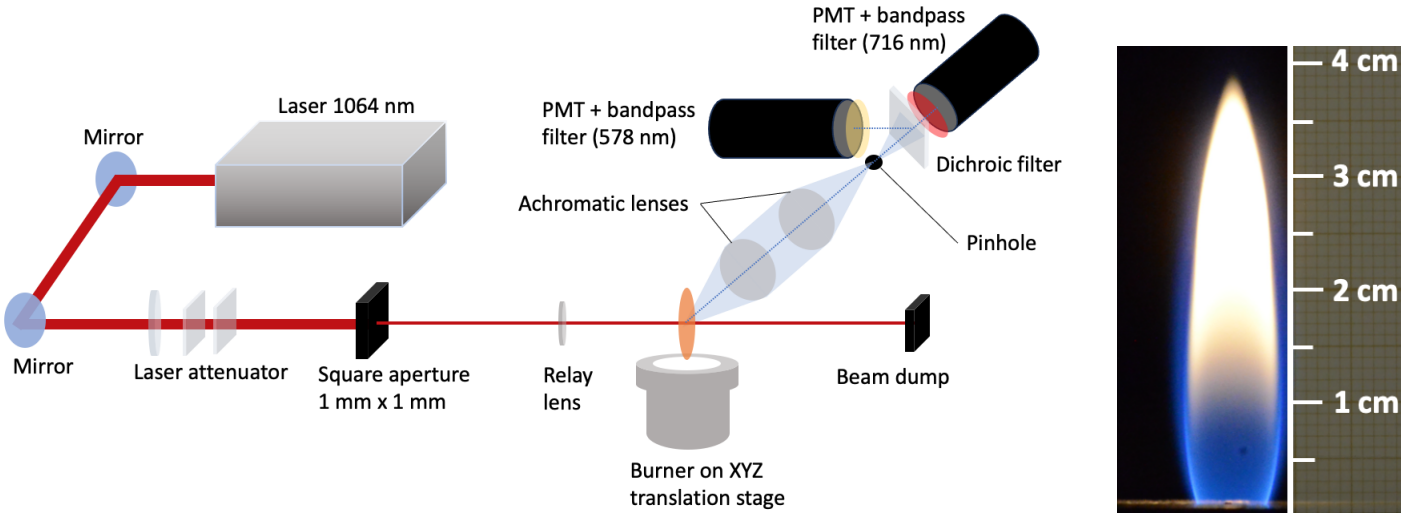

Figure 5.1: (a): Scheme of the LII experimental bench. (b): Image of the CH_4/air flame stabilised on the Yale diffusion burner.

Excitation system

The laser source is a Powerlite Continuum laser operating at 1064 nm with a full width at half maximum (FWHM) duration of ∼8 ns and with a frequency of 10 Hz. A laser attenuator composed of a half-wave plate and two polarisers allows the laser beam's fluence to be varied. The laser pulse's energy is measured with an energy measurer (Gentec-EO QE25LP-S-MB-D0). A 1 mm square aperture selects the most uniform part of the laser beam in order to heat the soot as uniformly as possible. A lens (f = 300 mm) relays the image of this aperture to form a nearly top-hat laser beam in the flame, visualised in Fig. 5.2. The uniformity of the top-hat beam is characterised by the histogram shown in Fig. 5.2, which fits a Gaussian distribution with a mean of 0.72 and a standard deviation of 0.08 (∼11% of the mean value). Analysis of the summed pixel lines and columns reveals approximately 20% maximum variation in both the horizontal and vertical profiles.

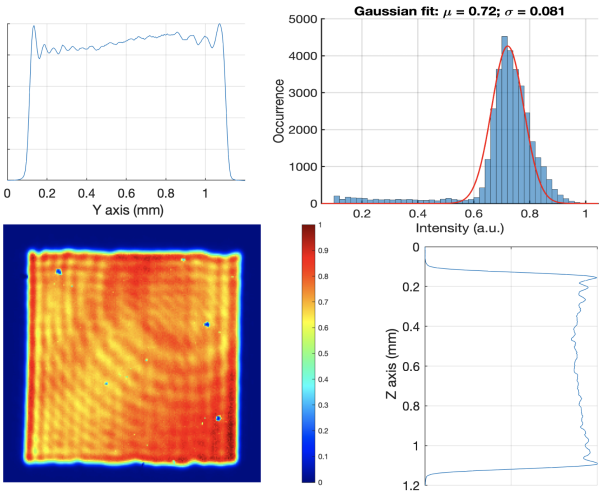

Figure 5.2: Bottom left: normalised profile of the top-hat averaged over 50 laser shots obtained with the beam profiler. Bottom right: horizontal summation of the top-hat profile. Top left: vertical summation of the top-hat profile. Top right: histogram of occurrences of the normalised intensities in the top hat.

Burner and flame condition

The soot particles are generated with a Yale diffusion co-flow burner [171]. The methane is injected through the central fuel injector of ∼3.9 mm inner diameter. The flame is stabilised with an air co-flow flowing through a porous surface of 4.8 mm inner diameter and 49.5 mm outer diameter surrounding the injector. Mass flow controllers impose methane and air mass flow rates to 0.20 and 30 ln.min^{-1} (0°C and 1 atm), respectively. The resulting flame is a stabilised ∼4 cm laminar diffusion flame (Fig. 5.1b). The yellow-orange colour of this flame indicates the presence of soot in this flame. The burner is mounted on a 3-axis translation stage. This configuration allows translating the burner to probe different positions in the flame.

Collection system

The incandescence signal is collected at 90° from the laser beam. The 2" achromatic lenses of the collection system have a focal length of f_1 = 150 mm and f_2 = 200 mm. The lens having the focal length f_1 is the closest to the flame. The signal is focused on a 500 μm diameter pinhole, resulting in a spatial resolution of 375 μm. A dichroic mirror (Semrock FF605-Di02-25x36) with a cut-off wavelength of 605 nm separates the radiations according to their wavelength. Wavelengths below 605 nm go through a bandpass filter (Edmund optics 87766) centred on λ_1 = 578 nm and with a measured FWHM $\Delta\lambda_1$ of 18 nm before being collected by one of the two HAMAMATSU R2257 photomultiplier tubes (PMT). Higher wavelengths go through the bandpass filter (Edmund optics 67053) centred on λ_2 = 716 nm, and with a measured FWHM $\Delta\lambda_2$ of 46 nm, and are collected by the second PMT. The PMT with the filter centred on λ_1 is called PM1, and the other PM2. After crossing the flame, the laser beam is collected by a photodetector (DET10A2) to monitor the laser energy stability and to trigger the signal acquisition with an 8-bit Lecroy WS434 oscilloscope (1 ns of temporal resolution). As the flame is laminar and steady, the samples are averaged over 700 single shots to ensure a good signal-to-noise ratio (SNR). The flame emission is subtracted from the LII signal.

Calibration

The system is calibrated using an OL Series 455 Integrating Sphere Calibration Standard (OL-455-2) placed at the flame's location. This calibration source includes a tungsten-halogen lamp and an integrating sphere. A more precise description of the calibration source is given in Annex C. The absolute spectral radiance of the source is known at the collection wavelengths. This allows the computation of soot temperature using 2C-LII pyrometry and the soot volume fraction using AC-LII. The calibration procedure is also presented in Annex C.

5.2 Improving the quality of low LII signals

The computation of $E(m_\lambda)$ requires the use of low fluences. Thus, especially for low-sooting regions and young soot particles, the LII signal is low, and noise sources can significantly reduce the signal quality.

Nd-YAG nanosecond lasers generally use a Q-switch to liberate the laser pulses. However, because the laser is incorrectly shielded from electromagnetic waves, it was observed that the oscilloscope catches Q-switching and generates additional noise to the photomultiplier signals. This noise was recorded without the flame and is given in Fig. 5.3. It has a maximum amplitude of approximately 1 mV for the PM1 and 0.5 mV for the PM2.

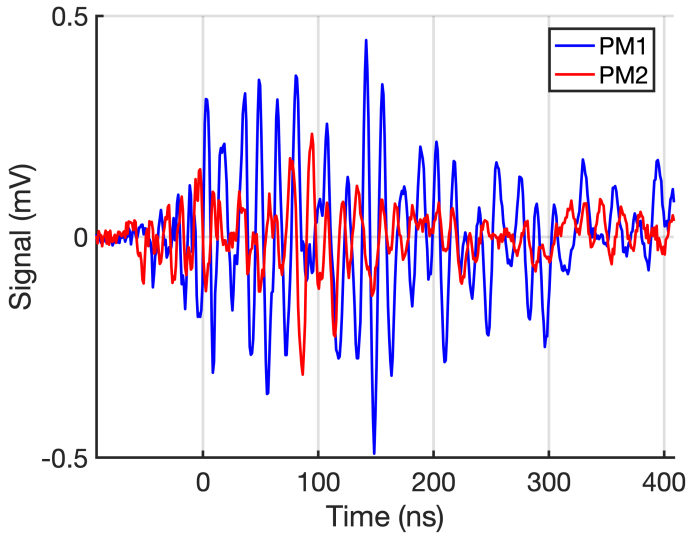

Figure 5.3: Noise from the laser recorded without the flame. The blue and red curves are the noise signals recorded on the oscilloscope channel of the PM1 and PM2, respectively.

This noise is without effect when the LII signals are strong but can significantly affect weak LII signals (roughly below 10 mV). In order to illustrate this, Fig. 5.4a gives LII signals recorded in different flame positions where the signals are weak (because of the usage of low laser fluence, a low soot volume fraction and/or young particles) with the PM2 (the one giving the weakest LII signal). It can be seen that the noise of Fig. 5.3 highly perturbs the LII signals, affecting both the peak LII signal and the temporal decay.

As the noise signal of Fig. 5.3 was found to be repeatable and independent from the laser fluence, it is possible to correct this perturbation. A direct subtraction of the noise was found to not improve the results because of small shifts (below the oscilloscope sampling period of 1 ns) between the recorded noise and the LII signals. Thus, the retained procedure consists in:

- Recording the noise without the flame.
- Recording LII signals.
- Oversample the LII signals: artificially increase the number of points of the noise and of the LII signals by interpolation. The retained timestep is 0.1 ns.
- Compute cross-correlation between the oversampled noise and LII signals, but considering only the portion of the signal before the laser pulse for which there is no LII signal (roughly before 40 ns in Fig. 5.4a). The maximum correlation gives the shift between the noise and the LII signal.
- Subtract the shifted noise to the LII signal and go back to the original sampling rate of 1 Gs/s (1 ns).

If an oscilloscope with a better sampling rate is used, oversampling the signals is not necessary.

Results after this treatment are given in figure 5.4b and clearly show the improvement in the LII signal quality, increasing the SNR. Still, it was decided to keep only the LII signals having a peak value above 1 mV.

It should be noted that the intensity of this noise is independent of the PMT supply voltage, which was set at 1600 V for PM1 and 1500 V for PM2. Increasing the supply voltage would increase SNR by amplifying the LII signal. However, raising the supply voltage to enhance the signal level was not feasible because it would cause the PMT to saturate due to the natural incandescence of the flame.

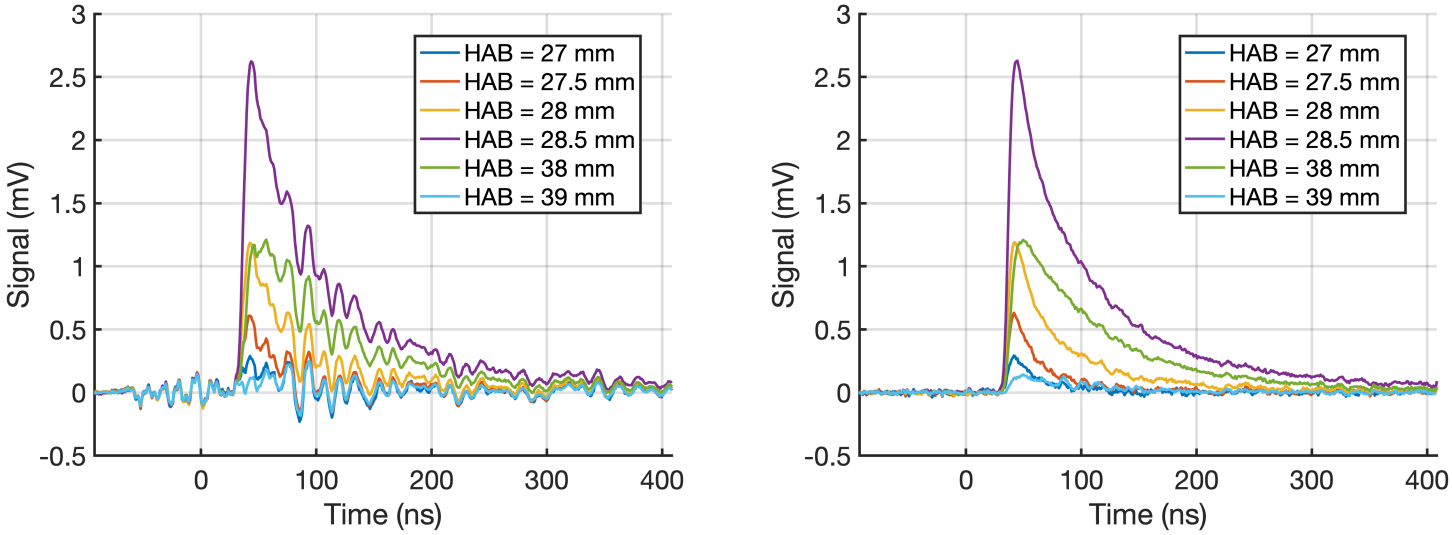

Figure 5.4: (a): LII signals recorded with the PM2 for different flame positions along the flame centreline. (b): LII signals recorded with the PM2 for different flame positions along the flame centreline after the correction procedure for the laser-generated noise. These signals were recorded in the CH_4/air flame with a laser fluence of 105 mJ/cm^2.

5.3 First application of the SP-LII in a laminar diffusion CH_4/air flame

This section presents the first application of the SP-LII in a laminar flame diffusion CH_4/air flame. The procedure utilised to obtain the axial evolution of $E(m_\lambda)$ at the laser wavelength (1064 nm) and T_0 is carefully detailed. Next, estimations with the AM and LUT post-processing methods are compared. Then, values of $E(m_\lambda)$ and T_0 obtained with the SP-LII (considering only two temperature measurements) are compared to the ones obtained considering more temperature measurements. Finally, the uncertainties resulting from the non-perfect knowledge of the soot volumetric capacity, soot size, and soot temperature are given.

5.3.1 Selection of the laser fluence

As deduced from the theoretical analysis of the previous chapter, the selection of the laser fluences is crucial for good performance of the SP-LII technique. The laser fluences should be selected:

- low enough to limit the occurrence of high-temperature phenomena like sublimation,
- high enough to produce an LII signal above the lower limit of 1 mV,
- spread enough to limit the technique's sensitivity to errors on peak temperature estimations (Fig. 4.16b).

The optimal couple of laser fluences will vary with the soot's optical properties which are themselves expected to vary spatially in the flame (Fig. 2.15b). Thus, to select the best couple of laser fluences for the study of the whole flame, LII measurements of soot particles are done for various laser fluences and at five different axial locations. These locations correspond to different soot populations with possibly different optical properties. From these LII measurements, the peak soot temperature is estimated via 2C-LII pyrometry (assuming a wavelength-independent absorption function between the two collection wavelengths). Then, the fluence couples that are best suited to the study of the flame are selected by looking at the linear regime of the temperature versus fluence curves.

The fluence curves (peak value of the LII signal versus the laser fluence) are plotted for five different axial locations in Fig. 5.5a. The signal level highly depends on the flame position, revealing a variation in soot volume fraction and/or soot emission properties.

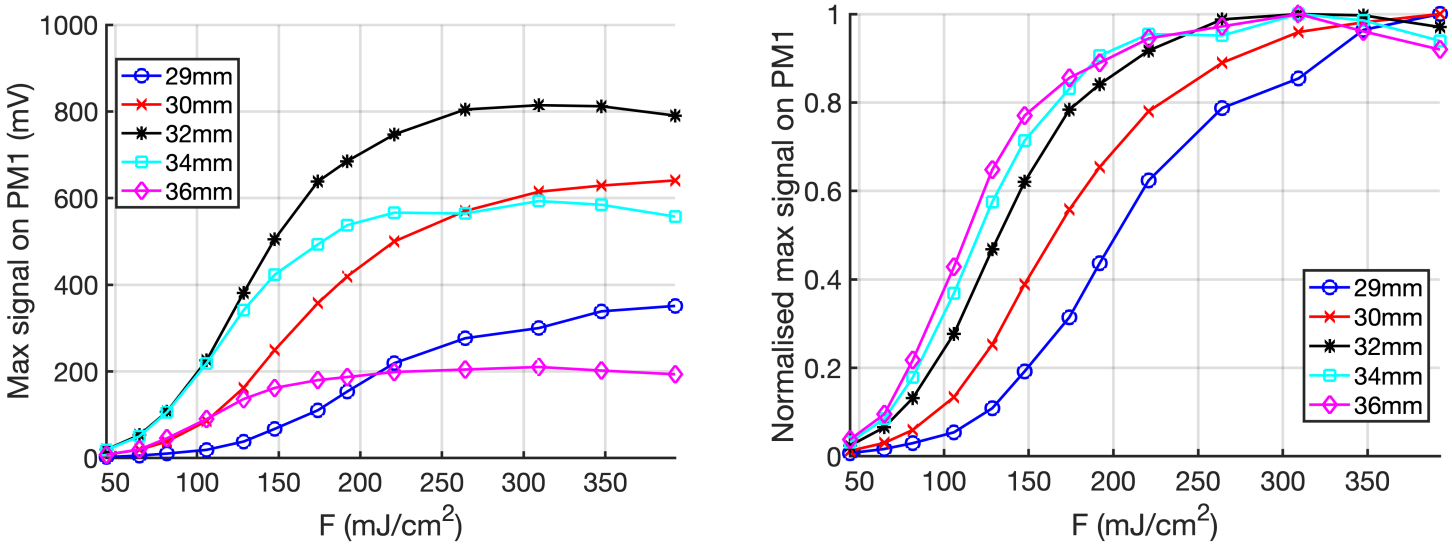

(a) (b)

Figure 5.5: (a): Maximum of the LII signal as a function of the laser fluence for five different HAB on the flame's centreline: 29 mm (blue o), 30 mm (red $\times$), 32 mm (black $*$), 34 mm (cyan $\square$) and 36 mm (magenta $\diamondsuit$). (b): Normalised version of figure (a). These curves were obtained at 578 nm, and the curves are similar for the wavelength 716 nm.

Figure 5.5b is the normalised version of Fig. 5.5a. The normalised curves reveal the responses to the laser fluence of the different soot populations at the different HABs: the higher the HAB, the more the curves are shifted to low laser fluences. However, for the HABs higher than 32 mm, the curves are close to each other, meaning similar soot populations in terms of optical properties. In comparison, the curves for HAB = 29 and 30 mm are clearly detached from each other, meaning relatively different soot populations in terms of maturity. As a result, a laser fluence of $\sim$250 mJ/cm^2 is required to reach a plateau in terms of LII signals for the soot particles at HAB $\geq$ 32 mm, while for the soot particles at HAB = 29 mm, the plateau is not clearly reached for the maximum laser fluence of the experiment: $\sim$ 400 mJ/cm^2. In other words, these curves indicate a rapid evolution of soot properties for HAB $\leq$ 32 mm, followed by a quasi-stagnation of these properties.

Figure 5.6 represents the peak soot temperature T_M estimated by 2C-LII from the LII measurements at the two collection wavelengths (578 and 716 nm). For the five HABs represented here, the temperature curves show a linear behaviour with the fluence when the temperature is below $\sim$4000 K. For higher temperatures, the linearity between T_M and F is lost due to high-temperature phenomena. These experimental results qualitatively confirm the predictions of the LII code in Fig. 4.2a: there is a region at low F, where T_M maintains a linear relationship with F. The temperature limit for this linear regime is set by looking at Fig. 5.6. By setting this limit too high, the measurements

move away from the linear regime, leading to greater error in the estimates of $E(m_\lambda)$ and T_0 (Fig. 4.9). Conversely, choosing a lower limit reduces the gap between the two laser fluences needed to estimate $E(m_\lambda)$, which also negatively impacts the results (Fig. 4.16). Based on Fig. 5.6, a temperature limit of 4000 K is retained for this flame. It is assumed that this temperature threshold can also be applied to soot particles in other regions of the flame. This selection of the temperature limit contains a degree of arbitrariness, and it has to be pointed out that it might not be valid anymore for other flames (a limit of 3500 K is set in the C_2H_4+N_2/air flame of chapter 6). A lower limit of 2600 K is introduced to ensure that the natural flame incandescence of the probe volume (which is subtracted from the LII measurements) has a low weight compared to the purely LII emission of the soot particles probed, thus reducing errors in peak temperature estimates (section 6.3.2 of the chapter 6).

The blue zone in Fig. 5.6 identifies the fluence range, allowing the computation $E(m_\lambda)$ for the five flame locations studied here. According to Fig. 5.6, the couple 65/105 mJ/cm^2 can probe all HABs from 29 to 36 mm and is best suited for the soot particles found above HAB = 30 mm as the higher peak temperature reached induces a better SNR. In addition to this couple, another couple, 106/148 mJ/cm^2, is selected for probing the younger soot particles that absorb less, which are found at HAB $\leq$ 29 mm. Here, three fluences can be selected because the flame is steady, but it would be difficult to do so for turbulent flames. It should be noted that these fluences are not necessarily the most adequate for all flames. An analysis of the peak soot temperature as a function of the laser fluence shall be systematically performed. Indeed, in chapter 6, the upper-temperature limit is set at a lower value (3500 K) as the T_M versus F curves lose linearity before the ones of Fig. 5.6.

As a side remark, it can be noticed that the fluences of Fig. 5.6 for which the temperature is linear with the fluence do correspond to the fluences for which the normalised LII signal (Fig. 5.5b) is below ~0.5: that is to say, it is possible to see the apparition of high-temperature phenomenon by looking at measurements before the inflexion point of the LII fluence curves.

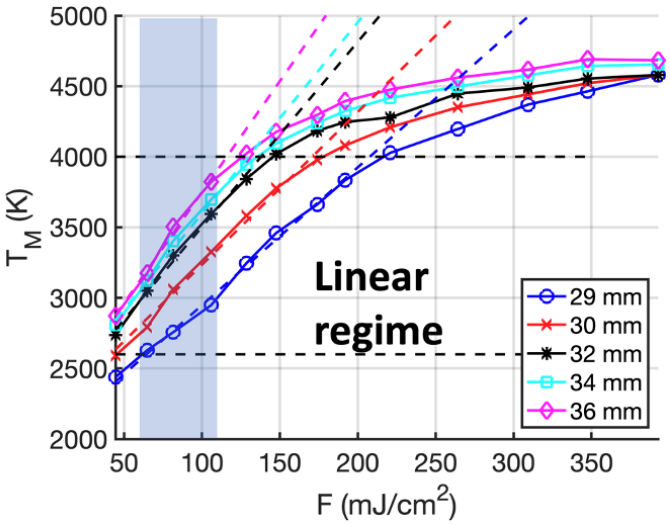

Figure 5.6: Soot peak temperature as a function of the laser fluence for five different HAB along the flame centreline: 29 mm (blue o), 30 mm (red ×), 32 mm (black ∗), 34 mm (cyan □) and 36 mm (magenta ♢). The horizontal dashed lines represent the temperature limits of 2600 K and 4000 K. The oblique dashed lines represent linear regressions of the temperature curves in the linear regime. The blue zone represents the fluences compatible with the SP-LII technique for the five HABs.

5.3.2 Axial evolution of the soot absorption function $E(m_\lambda)$ and gas temperature T_0

LII signal and soot temperature along the flame centreline

With the laser fluences selected: $\sim$ 65, 105, and 150 mJ/cm^2, LII measurements can proceed along the flame axis for these three fluence levels. Figure 5.7a represents the axial evolution of the LII signal collected with the PM1. The axial profile of the LII signal appears nearly symmetrical: it starts increasing from the lower detection limit at HAB = 27 mm to the maximum level of the signal at HAB = 32-33 mm, then it decreases until HAB = 39 mm, where the LII signal is too low to be exploited. Therefore, a maximum soot volume fraction is expected to be found near the maximum signal at HAB = 32-33 mm. It should be noted that along the flame axis, the LII signal is too weak to be detected below 27 mm with the current experimental setup. This indicates that there are too few soot particles efficiently absorbing and emitting light at heights below 27 mm on the flame axis. Consequently, the line-of-sight luminosity observed on the flame axis in Fig. 5.1b at a HAB of 27 mm probably comes from soot in the flame wings rather than from soot along the axis itself.

The corresponding axial profile of soot temperature is given in Fig. 5.7b. The temperature grows with increasing HAB, indicating that the soot particles in the highest part of the flame absorb more laser energy than the ones below, meaning that these soot particles are more mature than at lower HABs. It can be seen that the 4000 K temperature limit is not reached for any particle with the lowest laser fluence. However, the limit is crossed for HAB > 36 mm for the intermediate laser fluence, confirming that the fluence couple 65/105 mJ/cm^2 is particularly adapted for the study of this particular flame. With the highest fluence, the temperature overcomes the limit of 4000 K for HABs above 31 mm. Therefore, the usage of this fluence is limited to probing the soot particles that are difficult to heat (due to weakly absorbing properties) found in the lower HABs.

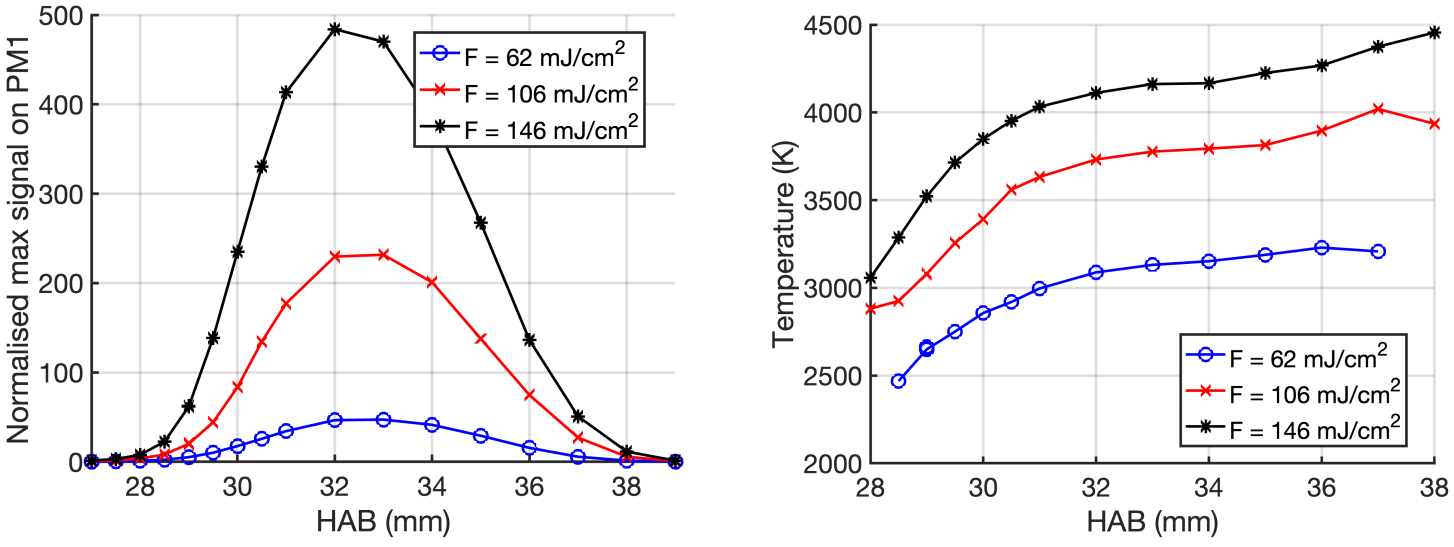

(a) (b)

Figure 5.7: Maximum of (a): the LII signal and (b): the soot temperature along the flame axis for three different laser fluences: 62 mJ/cm^2 (blue), 106 mJ/cm^2 (red), and 146 mJ/cm^2(black). Figure (a) was obtained using the PMT equipped with a bandpass filter centred on 578 nm, and the curves are similar for the wavelength of 716 nm.

AM vs LUT estimations

The absorption function and the gas temperature are estimated along the flame axis using the temperature measurements of Fig. 5.7b using both the AM and LUT post-processing methods. For each position, $E(m_\lambda)$ and T_0 are estimated considering the soot temperatures obtained with the following fluence couples:

- Couple 1: $F_1 \sim 65$ mJ/cm^2, and $F_2 \sim 105$ mJ/cm^2. This couple is adapted to probe a large part of the flame where soot are more absorbent (mature soot).
- Couple 2: $F_1 \sim 105$ mJ/cm^2, and $F_2 \sim 150$ mJ/cm^2. This couple is adapted to probe the less absorbent soot (young soot) found in the lower part of the flame.
- Couple 3: $F_1 \sim 65$ mJ/cm^2, and $F_2 \sim 150$ mJ/cm^2. This couple presents the advantage of having the highest difference between the fluence, limiting the effect of an error on the temperature estimation. In practice, its utilisation is limited due to the lower SNR of the first fluence and the highest soot temperature of the second fluence.

For the AM method, a uniform, temperature-independent product ρc equal to 4.6·10^6 J/K/m^3 is assumed [56]. Then, $E(m_\lambda)$ and T_0 are computed with:

$$E(m_\lambda) = E(m_{\lambda_{laser}}) = \rho c \frac{\lambda_{laser}}{6\pi} \frac{T_{M_2} - T_{M_1}}{F_2 - F_1}$$
$$T_0 = \frac{F_2 T_{M_1} - F_1 T_{M_2}}{F_2 - F_1}. \tag{5.1}$$

In order to test the LUT method with the experimental data of the CH_4/air flame, a look-up table adapted to this test case was generated. The parameters d_p, ρ, α and β are selected as follows:

- d_p is set to 10 nm.
- With the AM method, ρc = 4.6·10^6 J/K/m^3 was selected. However, the LII code used for the look-up table generation does not allow the change of the specific heat, which is hard-coded as a temperature-dependent function. Thus, to be consistent with the value selected with the AM method, it was decided to set the density to ρ = $\frac{4.6 \cdot 10^6}{c(T=3300K)}$ = 2067 kg/m^3.
- α is set to 0.3.
- For β, three cases was considered. The first one is β = 0. It allows the AM and the LUT methods to be confronted with the same assumptions regarding the sublimation losses (neglecting sublimation). The second case is $\beta = 0.2$. This case was considered to verify if the LUT allows for the data to be exploited where the peak soot temperature exceeds the limit of 4000 K. The value β = 0.2 was selected following the conclusion about the mass accommodation coefficient of the theoretical analysis of the SP-LII in Sec. 4.4.3 of the previous chapter. The last case is β = 0.13, the value for which the best agreement in $E(m_\lambda)$ and T_0 estimations is seen for the three couples of laser fluences.

Figures 5.8a, and 5.8b compare the estimation of $E(m_\lambda)$ and T_0 with the AM and LUT post-processing methods when sublimation is neglected ($\beta = 0$). Results were discarded when one of the two peak temperatures was outside the temperature limits of Fig. 5.6 (2600 and 4000 K for the lower and upper limits, respectively). The LUT estimations are similar to the ones of the AM, confirming the consistency of the methods. The differences between the results of the methods can be explained by the conduction losses that are accounted for with the LUT and by the rounded estimations of the LUT (discretised table).

On the flame axis, $E(m_\lambda)$ rapidly increases from 0.1 at HAB = 28 mm to 0.39 at HAB = 31 mm, followed by a stagnation up to the detection limit at 36 mm. While couple 1 allows probing HABs from 29 to 36 mm, couple 3 only adds a few points below 29 mm, but it enables catching the rapid growth of $E(m_\lambda)$ at the lower HABs. Higher laser fluences would be necessary to probe lower HABs. A direct comparison of the values of $E(m_\lambda)$ with data from the literature is not possible as this flame is not a reference flame. However, values (∼0.1-0.4) and trends ($E(m_\lambda)$ increasing with

the axial position) are consistent with what was obtained in different premixed C_2H_4/air and CH_4/air flames [54, 130, 131, 141] or for a C_2H_4/air laminar diffusion flame [51] (Fig. 2.15).

The estimated T_0 values in Fig. 5.8b range from 1900 to 2500 K with an overall tendency to increase along the flame centreline. The highest values found at HAB = 28 and 30.5 mm with the couple 3 of laser fluences are probably affected by greater uncertainties than the other points. Indeed, the estimation at HAB = 28 mm uses one of the weakest LII signals for the measurement at 105 mJ/cm^2 (not favourable SNR), while for the estimation at 30.5 mm, the temperature computed at 150 mJ/cm^2 is just below the temperature criterion set at 4000 K, meaning more significant sublimation effects than in other measurements. Since T_0 and $E(m_\lambda)$ are determined simultaneously, in positions where T_0 is affected by higher uncertainty, it is to be expected to be also true for $E(m_\lambda)$. While no direct data are available in the literature for this specific flame, the temperatures observed are consistent with the adiabatic flame temperature of a stoichiometric CH_4/air diffusion flame (2225 K), which serves as a reference for the maximum expected temperature in this flame. Almost all estimations of Fig. 5.8b are close to this adiabatic flame temperature. However, in the literature, for laminar co-flow diffusion methane flames, the temperature in the region where soot are observed is generally in the range 1500-2000 K [253–255] with the temperature increasing with the HAB on the axis, and larger temperature in the outer soot region. The increasing trend of T_0 with the HAB is globally retrieved, but the absolute values are clearly above the one found in the literature. Even if the flames of the literature are different from the present one, this might indicate a systematic overestimation of T_0 in the results presented here. The overestimation of T_0 can partly be attributed to the background subtraction from the LII signal (see Section 6.3.2 of Chapter 6), as well as the 4000 K threshold used, which should have been set lower (Fig. 5.6, where deviations from the linear regression occur before reaching 4000 K). Sublimation causes underestimation of $E(m_\lambda)$ and overestimation of T_0 (Fig. 4.9). Lowering the 4000 K threshold would require additional measurements at lower laser fluences, but the signal limit (1 mV) is quickly reached. Moreover, reducing the fluence differences significantly increases uncertainties in $E(m_\lambda)$ and T_0 (Fig. 4.16), complicating the use of lower and intermediate fluences.

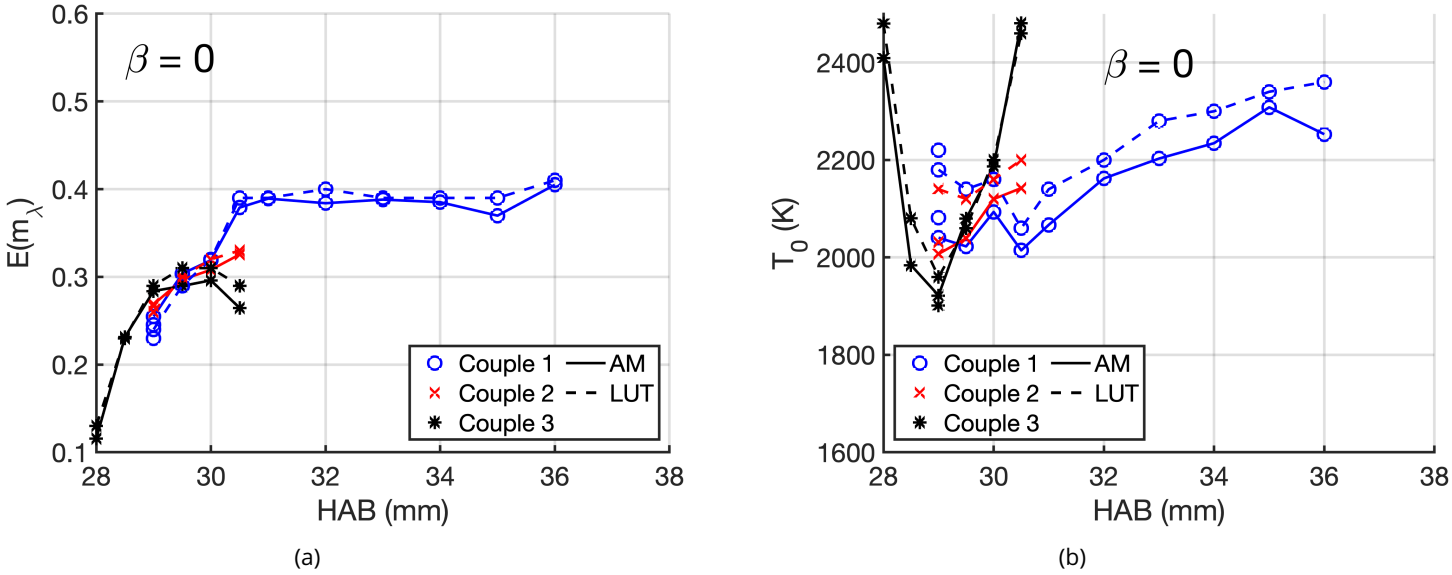

Figure 5.8: Evolution of (a): $E(m_\lambda)$ and (b): T_0 along the flame centreline for three couple of laser fluences: 64/106 mJ/cm^2 (blue ○), 64/149 mJ/cm^2 (red ×) and 106/149 mJ/cm^2 (black ∗). The solid lines represent the estimations obtained using the AM method, while the dotted lines are for the LUT method for β = 0.

Figures 5.9a, and 5.9b are identical to Figs. 5.8a, and 5.8b, but β = 0.2 was considered for the LUT, meaning that the sublimation term was activated. In this case, for the LUT, estimates of $E(m_\lambda)$ are plotted even when the maximum

temperature exceeds the limit of 4000 K because sublimation is taken into account. As the temperature constraint has been removed, the domain of application of the SP-LII is extended to HAB > 36 mm.

For couple 1, by comparing with Fig. 5.8a, estimations of $E(m_\lambda)$ and T_0 considering $\beta = 0$ or $\beta = 0.2$ are close up to HAB = 31 mm which corresponds to temperatures below 3600 K. Above HAB = 31 mm; differences increase to reach 38% for $E(m_\lambda)$ at HAB = 36 mm. At HAB = 37 mm, $E(m_\lambda)$ reaches the LUT maximum value of 0.6: the table saturates. This means that with the sublimation model considered in the LII code, and for β = 0.2, sublimation becomes to introduce error on $E(m_\lambda)$ when the temperature is above ∼3600 K. For the two other couples, estimations of $E(m_\lambda)$ and T_0 considering $\beta = 0$ or $\beta = 0.2$ are similar for HAB $\leq$ 29 mm. Then, values of $E(m_\lambda)$ strongly increase with HAB before saturating at HAB = 33 and 34 mm for the couple 3 and 2, respectively. Such high values for $E(m_\lambda)$ and such disagreements between the estimations of $E(m_\lambda)$ and T_0 for the three couples show that the sublimation process is over-predicted with $\beta = 0.2$, or that the model does not represent well the actual physical processes happening.

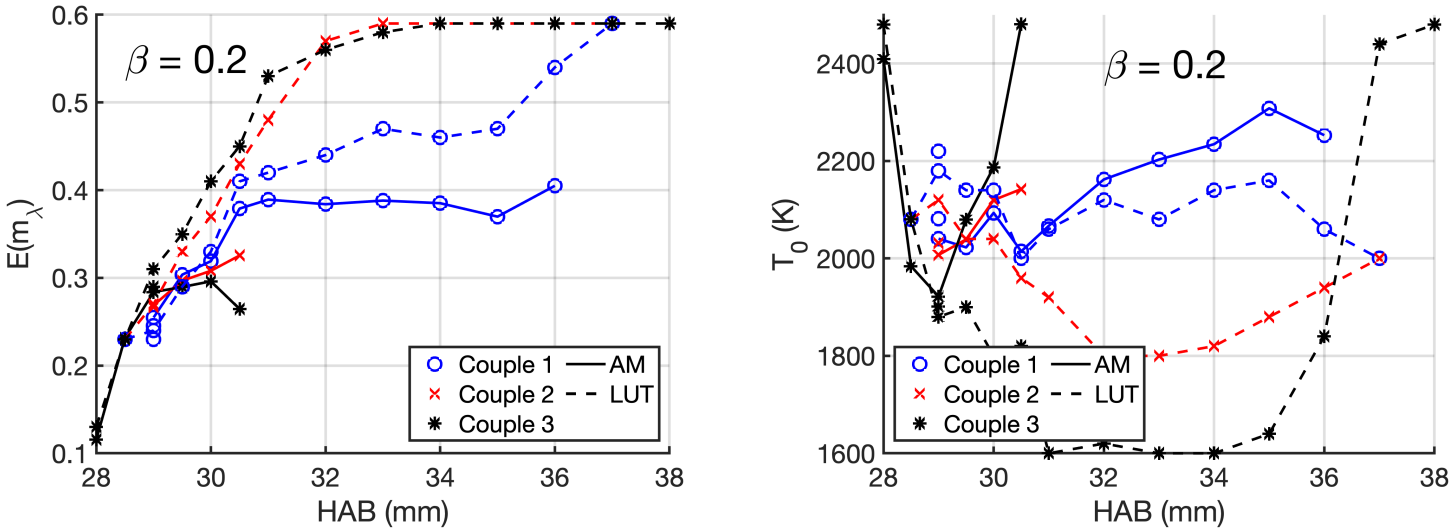

Figure 5.9: Evolution of (a): $E(m_\lambda)$ and (b): T_0 along the flame centreline for three couple of laser fluences: 64/106 mJ/cm^2 (blue ∘), 64/149 mJ/cm^2 (red ×) and 106/149 mJ/cm^2 (black ∗). The solid lines represent the estimations obtained using the AM method, while the dotted lines are for the LUT method for β = 0.2.

The best agreement for the three couples of laser fluence is found when β was set to 0.13. This case is plotted in Figs. 5.10a, and 5.10b. Estimations for the three couples are generally in excellent agreement and show at most a 25% difference at HAB = 29 mm. However, at HAB = 35 mm, a 10% difference in $E(m_\lambda)$ and a strong disagreement in T_0 are seen. This may indicate an erroneous temperature estimation for the fluence 105 mJ/cm^2.

Overall, estimations of $E(m_\lambda)$ and T_0 are close to the case where sublimation is neglected for HAB < 31 mm. Above that, differences start increasing: at first, slowly in the plateau section (∼31<HAB<∼35 mm), where $E(m_\lambda)$ reaches ∼0.5 at HAB = 36 mm, before sharply increasing at the flame's extremity. Yon et al. [51] have also observed a steep increase of $E(m_\lambda)$ at the tip of another C_2H_4/air laminar diffusion flame. The results presented here also point in that direction. However, the present results at HAB > 36 mm are at the limit of detection and thus have a low SNR. In addition, estimated temperatures are above 4000 K, indicating a non-negligible impact of the high-temperature phenomenon such as sublimation, so the results in terms of $E(m_\lambda)$ and T_0 for the LUT depend on the accuracy of the sublimation model. Thus, results must be interpreted with caution.

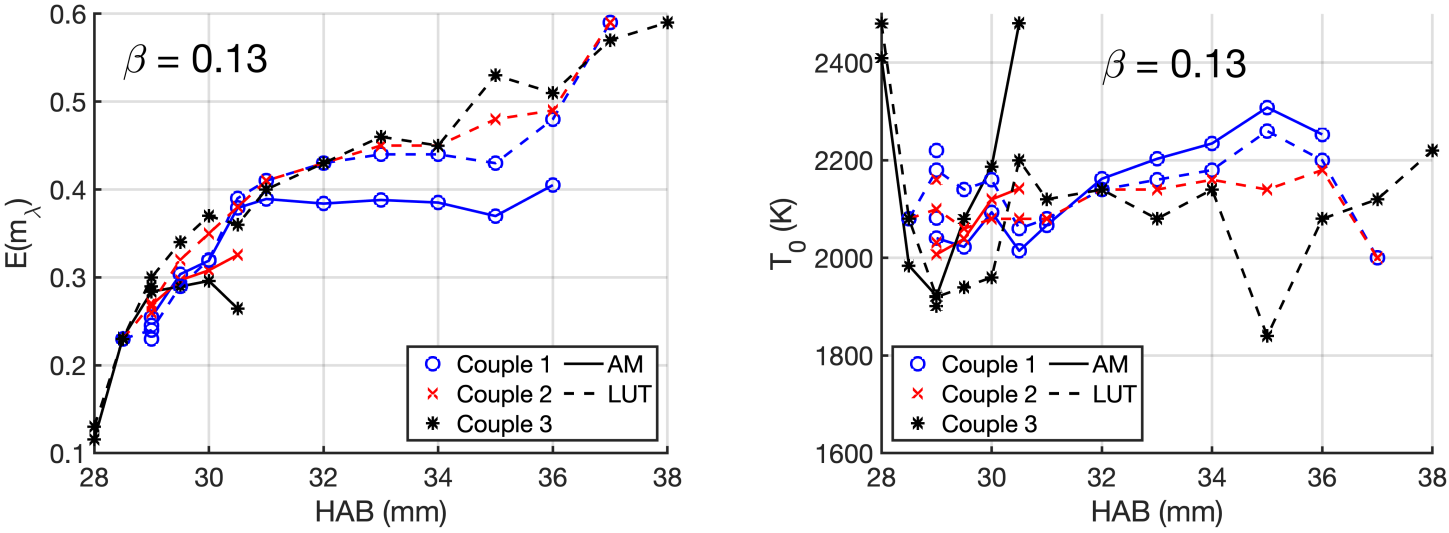

Figure 5.10: Evolution of (a): $E(m_\lambda)$ and (b): T_0 along the flame centreline for three couple of laser fluences: 64/106 mJ/cm^2 (blue $\circ$), 64/149 mJ/cm^2 (red $\times$) and 106/149 mJ/cm^2 (black $*$). The solid lines represent the estimations obtained using the AM method, while the dotted lines are for the LUT method for β = 0.13.

These results also show that neglecting sublimation underestimates $E(m_\lambda)$ and overestimates T_0, confirming the theoretical results of the precedent chapter. It has to be noticed that the HABs for which the estimations of the LUT (considering either $\beta = 0.13$ or 0.2) are close to the case where no sublimation is considered do correspond to the ones for which the peak temperatures are the lowest: <$\sim$3500-3600 K. Therefore, if the sublimation model solved by the LII model is accurate, this may indicate that in order not to be affected by sublimation, the temperature limit of 4000 K should be lowered to 3500-3600 K. That is to say, sublimation (or other high-temperature phenomenon) starts playing a role as soon as $\sim$3500 K in the present flame. These results should be interpreted with care and do not legitimise the usage of high fluences for the SP-LII when using the LUT post-processing method with β = 0.13. Indeed, sublimation and other high-temperature processes are known to be difficult to model, and the fact that the estimation of $E(m_\lambda)$ and T_0 overlay for β = 0.13 should not be enough to legitimate this specific value for the accommodation coefficient as the best one, especially if other flame conditions are considered, nor to prove the correctness of the sublimation model. On the contrary, the strong variations in $E(m_\lambda)$ and T_0 with the hypothesis made on β confirm the necessity to avoid high laser fluences even when using the LUT method. The accuracy of the LUT method is strongly affected by the uncertainties in the model's parameters, such as β and on the models themselves. Thus, in the following, only the simplest approach is considered, i.e. the AM method.

Two fluences versus multiple fluences

Looking at Fig. 5.6, it is evident that using more than two different laser fluences would increase the precision of the estimation of $E(m_\lambda)$ and T_0. The SP-LII relies on temperature measurements at only two laser fluences because it has been designed for application to turbulent flames, and using more than two laser pulses would be extremely difficult. However, in laminar flames, the possible temporal decorrelation of the measurements allows taking as many measurements at different fluences as possible. Then, $E(m_\lambda)$ and T_0 can be computed similarly to [33]: using a linear regression of the temperature versus fluence curves (dotted lines in Fig. 5.6). Still, this implies more intensive measurement campaigns, in which the time dedicated to the multiplication of the fluence considered cannot be devoted to other flame conditions and is restricted to steady flames. In the following, values of $E(m_\lambda)$ and T_0 obtained with two laser fluences (SP-LII) are compared to the ones obtained using more than two fluences to evaluate

the loss of accuracy when using the SP-LII.

The relation between the temperature and the fluence is:

$$T_M = \frac{6\pi}{\rho c \lambda_{laser}} E(m_\lambda) F + T_0 = \Gamma F + T_0, \tag{5.2}$$

Then, $E(m_\lambda)$ is given by:

$$E(m) = \Gamma \frac{\rho c \lambda_{laser}}{6\pi}. \tag{5.3}$$

The $E(m_\lambda)$ and T_0 values obtained through linear regression of the temperature versus fluence curves in Fig. 5.6 for five HABs (29, 30, 32, 34, and 36 mm) are compared in Figs. 5.11a, and 5.11b to those derived using the AM method considering only temperatures between 2600 and 4000 K in both cases.

For $E(m_\lambda)$, both methods show similar trends, with differences remaining within approximately 15%. The T_0 results are also very close, with a maximum difference of about 75 K. This indicates that considering only two fluences does not significantly degrade the results and confirms that the SP-LII could potentially be applied in turbulent flames. However, using more fluences is more robust as it relies on multiple measurements, thereby reducing the impact of any erroneous temperature estimation from the SP-LII. In the following of this chapter, only results with the SP-LII are presented.

It is worth mentioning that because sublimation tends to make the SP-LII underestimate $E(m_\lambda)$ and overestimate T_0 (as seen in Fig. 4.9), one might have expected higher $E(m_\lambda)$, and lower T_0 values from the linear regression method compared to the AM method. This expectation arises because the higher number of measurements at low peak temperature (between 5 and 8 depending on the HAB) with the linear regression method would attenuate the impact of sublimation (that affects only high-temperature estimations).

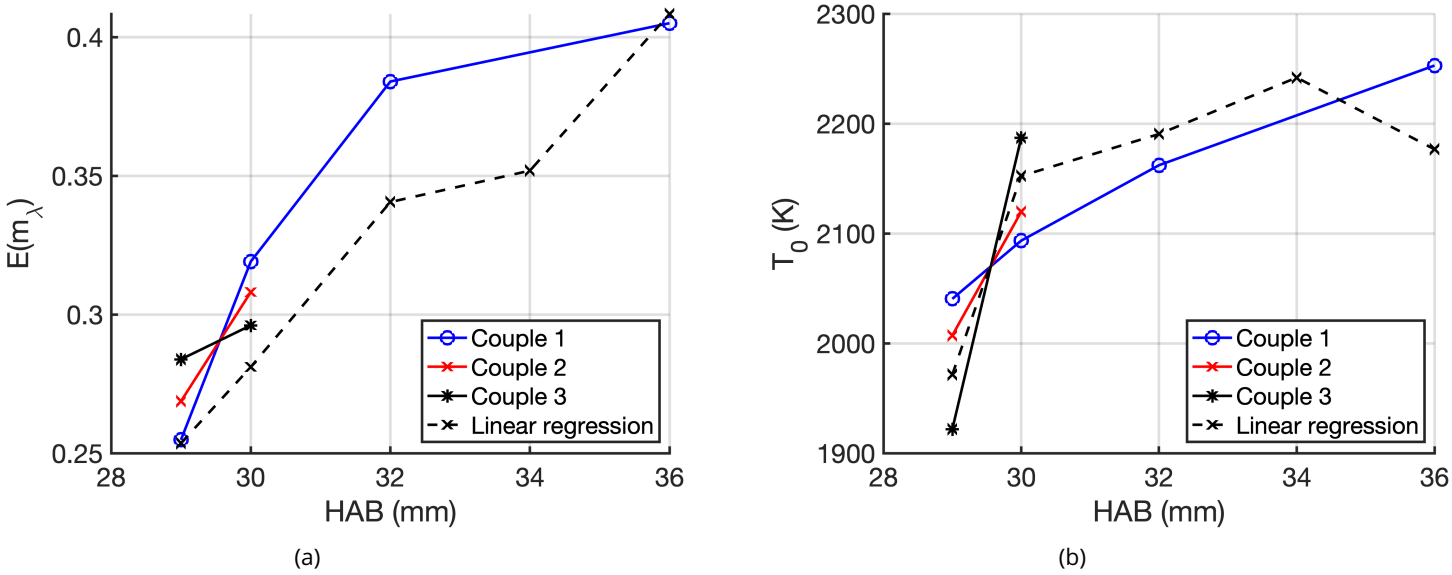

Figure 5.11: (a): $E(m_\lambda)$, and (b): T_0 along the flame centreline estimated with the AM method for three couple of laser fluences: couple 1 (blue ○), couple 2 (red ×) and couple 3 (black ∗). Estimated with the linear regression method are given by the black dashed line.

Uncertainties of the SP-LII approach

The assumptions of the SP-LII approach induce uncertainties on the computed values for both $E(m_\lambda)$ and T_0. Here, the uncertainties are quantified along the flame's axis for the AM method.

First, as the SP-LII technique allows access to $\frac{E(m_\lambda)}{\rho c}$, the estimated value of $E(m_\lambda)$ depends on the product ρc. As previously discussed in Section 4.4.3 of Chapter 4, an error of X% on ρc brings the same error on $E(m_\lambda)$. Unfortunately, very little data about this product is available in the literature (see literature review of Section 2.6.3). Thus, it is difficult to quantify the existing uncertainty on ρc realistically. Consequently, uncertainties coming from a potential error on ρc are not provided here. Secondly, with the AM method, the conduction losses are neglected. This brings an error depending on the particle size. Figure 4.10 shows that using the AM method brings an underestimation of $E(m_\lambda)$ that can go as high as 15% for soot particle of 2.5 nm (roughly the minimum soot size detectable by LII [113]). A 15% underestimation of the absorption function is then retained. Concerning T_0, the same results showed only a $\sim$ 1% overestimation. The corresponding uncertainty region for $E(m_\lambda)$ and T_0 along the flame's axis are plotted in Fig. 5.12a, and Fig. 5.12b.

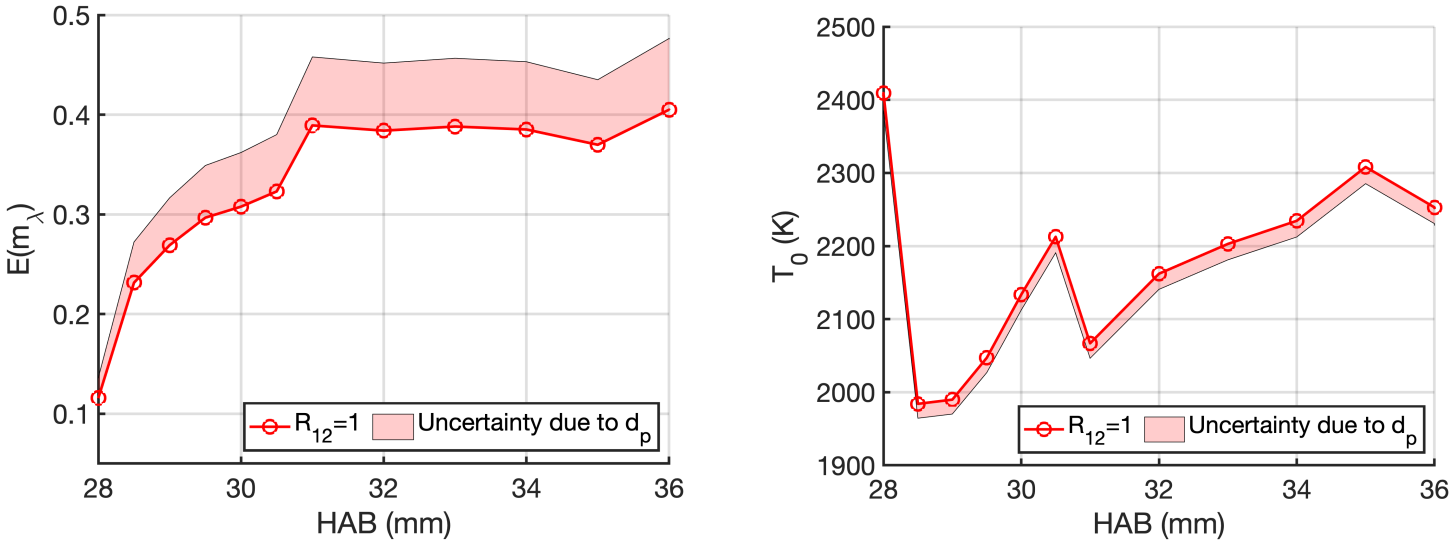

Figure 5.12: $E(m_\lambda)$ (a), and T_0 (b) along the flame centreline (red ○). The red-shaded region represents the +15% and -1% uncertainties on $E(m_\lambda)$ and T_0, respectively, due to the effect of d_p on the conduction losses.

Finally, the uncertainty attributed to the assumption of unity $R_{12} = \frac{E(m_{\lambda_1=578\text{ nm}})}{E(m_{\lambda_2=716\text{ nm}})}$, i.e. a wavelength independent absorption function when calculating T_M by 2C-LII, must be quantified. For that, the peak soot temperatures are recomputed by considering the extreme values for R_{12} that can be found in the literature. In [50], Bescond et al. studied the wavelength dependence of the absorption function of soot from diverse sources. The highest value for the ratio R_{12} is 1.3. It corresponds to soot particles with a high organic content generated by a miniCAST soot generator. Inversely, using the formula in [30], which links the absorption function and the wavelength, one finds $R_{12} = 0.94$.

Figures 5.13a and 5.13b show the evolution of $E(m_\lambda)$ and T_0 along the flame's axis for the three considered values of R_{12}: 0.94, 1 and 1.3. The uncertainty zone due to the assumption of unity R_{12} corresponds to the blue area in between the estimations of $E(m_\lambda)$ considering R_{12} = 0.94 and R_{12} = 1.3. The assumptions R_{12} = 0.94 results in a 5 to 11% increase of the absolute value of $E(m_\lambda)$ depending on the HAB, while assuming R_{12} = 1.3 results in a 27 to 31% decrease of $E(m_\lambda)$. It seems unlikely that R_{12} significantly deviates from 1, especially in the regions with HAB > 31 mm, where $E(m_\lambda)$ (with R_{12} = 1) corresponds to the values for mature soot commonly encountered in the literature [31]. Figure 5.13a shows that assuming a higher value for R_{12} leads to lower estimates of $E(m_\lambda)$. This is a significant observation, as it implies that for young soot particles, where R_{12} may exceed 1 (refer to section 2.6.2), assuming R_{12} = 1 would cause the SP-LII technique to overestimate the actual value of $E(m_\lambda)$. In other words, a

low value of $E(m_\lambda)$ cannot originate from the uncertainty on R_{12} but does result from the presence of young (lowly absorbing) particles. Concerning T_0, the uncertainty on R_{12} results in a ∼-10% and ∼+2% for R_{12} = 1.3 and R_{12} = 0.94, respectively.

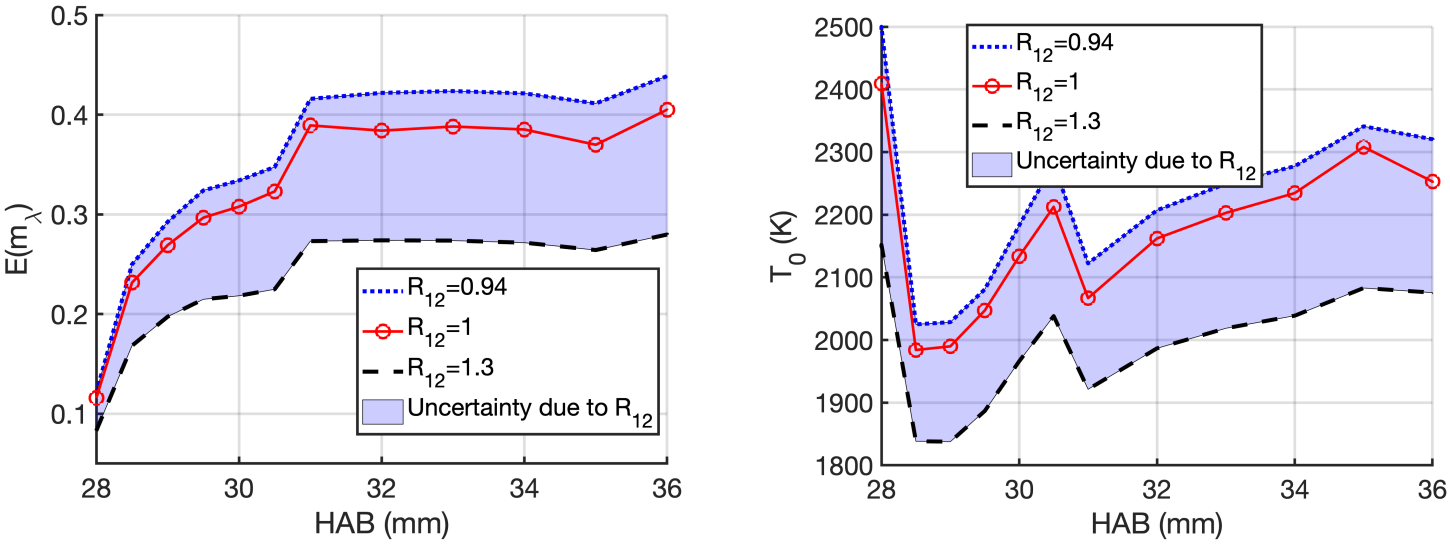

(a) (b)

Figure 5.13: (a): $E(m_\lambda)$ and (b): T_0 along the flame centreline considering three different values of R_{12}: 0.94 (blue dotted line), 1 (red ∘) and 1.3 (black dashed line). The blue-shaded region between the dotted and dashed lines represents the uncertainty regions due to the uncertainty on R_{12}.

Overall, the assumptions of neglected conduction losses and R_{12} = 1 induce approximately a ± 30% uncertainty on the absorption function and a -11% to +2% uncertainty for T_0. However, one must remember that this does not include the hardly quantifiable error done on ρc, which is directly transferred to $E(m_\lambda)$. In addition, other sources of errors not inherent to the SP-LII technique, like measurements and calibration errors, are not included.

5.4 Cartography of $E(m_\lambda)$, T_0, f_v, and d_p

The previous section indicated that $E(m_\lambda)$ and T_0 can be experimentally determined with the SP-LII. In this section, the axial measurements of the previous section are completed by radial ones for five different HABs (23, 25, 28, 31 and 35 mm). The measurements are done with the same three laser fluences: 65, 105, and 150 mJ/cm^2. This will provide a realistic idea of the 2D spatial distribution of $E(m_\lambda)$, and T_0 in the flame. In addition, soot volume fraction f_v and soot primary particle diameter d_p, are computed from the same measurements.

5.4.1 Soot absorption function $E(m_\lambda)$ and gas temperature T_0

$E(m_\lambda)$ and T_0 are computed with the AM post-processing method and are gathered in partial 2D maps in Fig. 5.14. When multiples estimations of $E(m_\lambda)$ are available for one flame position (for instance, for 29 ≤ HAB ≤ 30.5 mm in Fig. 5.11a), the averaged value is retained.

The axial behaviour of $E(m_\lambda)$ and T_0 were already described. Radially, $E(m_\lambda)$ increases rapidly with the radial position for the three lowest HABs (23, 25 and 28 mm) while it is spatially constant and equal to ∼ 0.4 for HAB = 31 and 35 mm. A smaller probe volume and more measurement points would be necessary to properly catch the rapid radial evolution of $E(m_\lambda)$ at low HABs. Globally, the inner and lower part of the flame contains soot particles with

low values of $E(m_\lambda)$ corresponding to young soot. The higher and outer part of the flame contains more mature soot characterised by higher values for $E(m_\lambda)$. Yon et al. [51] presented a 2D map of $E(m_{\lambda=810\text{nm}})$ (Fig. 2.15b) for an C_2H_4/air laminar diffusion flame stabilised on a Gülder burner. Similarly to the present work, they found $E(m_\lambda)$ values ranging from 0.1 to 0.4, with the highest values for $E(m_\lambda)$ at the outer part of the flame and the smallest values in the lower inner part of the flame. However, the trends are not identical as they found low values for $E(m_\lambda)$ above the flame wing and a sharp increase of $E(m_\lambda)$ at the flame tip. However, as the flame conditions are different, it is not strictly consistent to compare the two flames directly.

Figure 5.14b gives the gas temperature estimated by the SP-LII. The lowest values are generally found in the flame core, while the largest values are found on the external part of the flame, which seems to indicate the zone of oxidation. This is reinforced by the fact that the high-temperature zones do correspond to zones where f_v decreases (see Fig. 5.19a hereafter). T_0 ranges from 1980 to 2410 K, with an average value of 2160 K. As previously discussed, these values are above the literature in laminar diffusion methane/air flames (1500-2000 K) [253–255]. Given these differences, the present estimations of T_0 are likely overestimated. It is to be remembered that the SP-LII retrieves the soot temperature before the laser pulse and not directly the gas temperature. There may be a temperature difference between the gas phase and the particles, possibly due to the exothermic reaction of soot oxidation. Also, Fig. 5.10b, and Fig. 5.14b also show high fluctuations in estimations of T_0 in neighbouring points. Thus, the present estimations of the SP-LII furnish only a rough estimation of T_0.

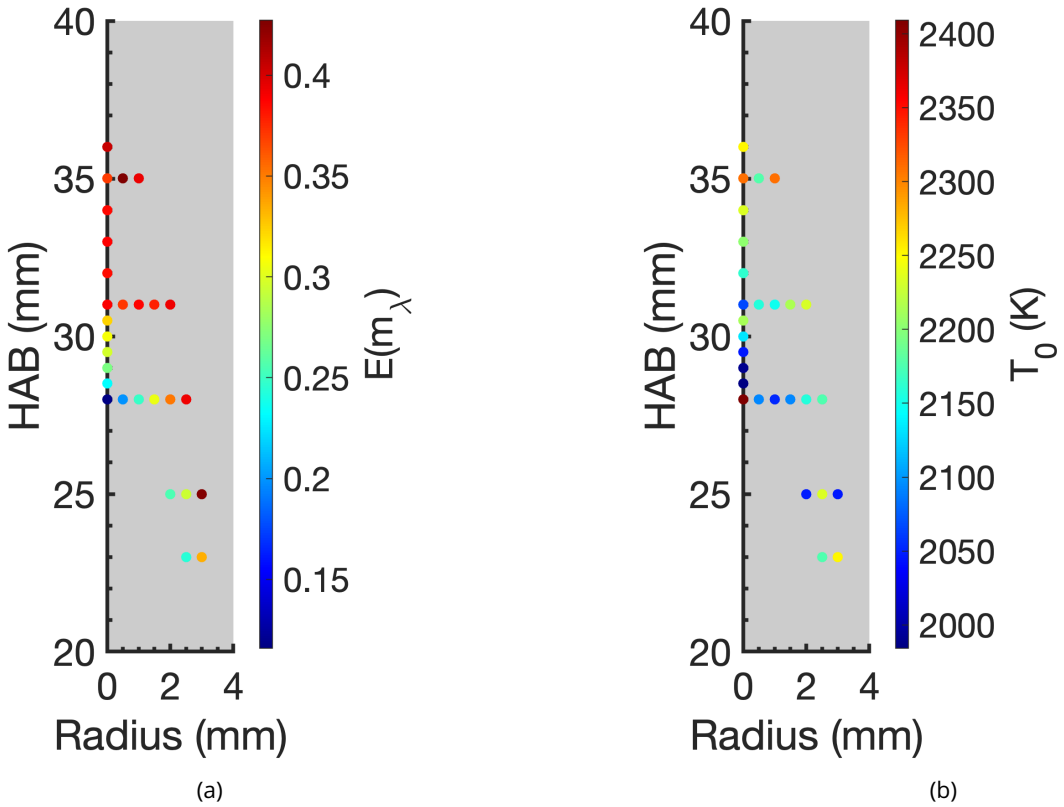

Figure 5.14: Cartography of (a): $E(m_\lambda)$ at λ = 1064 nm and (b): T_0. The size of the coloured disks is representative of the collection surface of 375 μm diameter of the collection system.

5.4.2 Soot volume fraction f_v

The soot volume fraction is computed at prompt ($T = T_M$) by AC-LII using a laser fluence of 105 mJ/cm^2 with:

$$f_v = \frac{1}{12\pi hc^2 \cdot E(m_\lambda) \cdot L_{laser} \cdot C_{\lambda,\text{calib}}} \frac{S_\lambda^{LII}}{\frac{\Delta\lambda}{\lambda^6} e^{-\frac{hc}{\lambda k_B T}}} \tag{5.4}$$

where λ can be λ_1 = 578 nm, or λ_2 = 716 nm.

Generally, in the literature, a spatially uniform $E(m_\lambda)$ (independent from soot maturity) is set when computing f_v. The value selected is often that of mature soot ($\sim$0.3-0.45) [40, 46, 159, 174, 233, 256–260]. Here, f_v is calculated in two ways: firstly, by assuming a uniform value of 0.39 for the absorption function as it is the value that corresponds to the mature soot of this flame. Then, the spatial distribution of $E(m_\lambda)$ of Fig. 5.14a obtained with the SP-LII is considered. It has to be pointed out that the SP-LII furnishes $E(m_\lambda)$ at the laser wavelength (1064 nm). Thus, it is assumed here that $E(m_{\lambda=1064nm}) = E(m_{\lambda=578nm}) = E(m_{\lambda=716nm})$.

Axial profile of f_v

Figure 5.15 shows the axial evolution of f_v obtained with both PMTs assuming a uniform or varying $E(m_\lambda)$. Curves for both PMTs are almost perfectly superimposed: there is no difference if one uses the signal of the PM1 or PM2 to compute f_v. Thus, in the following, the LII signal collected with the PM1 is used to estimate f_v. The local minimum of f_v found for HAB = 31 mm when using the $E(m_\lambda)$ distribution obtained with the SP-LII is due to the sharp increase of $E(m_\lambda)$ at that location (Fig. 5.13), which is probably overestimated. The f_v profile obtained for $E(m_\lambda)$ = 0.39 shows lower estimations for HAB < 31 mm. Thus, not accounting for the spatial inhomogeneities of $E(m_\lambda)$ while assuming a value for it that is the one for more mature soot (0.39 here) underestimates the concentration of young soot particles. This was to be expected, given the linear relation between the LII signal and the product $f_v E(m_\lambda)$ (Eq. (5.4)).

Since this flame is not a reference case, direct comparison with literature data is not possible. However, the present results will be compared to the reference M80 flame studied by Bartos et al. [261]. The M80 flame is produced using the same burner as in this work, with a fuel mixture of 80% CH_4 (0.211 slpm) and 20% N_2 (0.053 slpm). The mass flow rates were adjusted to achieve a cold bulk velocity of 35 cm/s for both the fuel mixture and the air co-flow, resulting in a 37 mm-high flame. In [261], f_v was determined using classical LII at 1064 nm with a fluence of 600 mJ/cm^2, and calibration was based on the work of [194]. Along the flame centreline, f_v increased from HAB = 29 mm to HAB = 32 mm, reaching approximately 45 ppm before decreasing to the detection limit at HAB = 37 mm. The similarity between the present results and the M80 reference flame, both in trend and absolute values, reinforces confidence in the accuracy of the f_v estimations in this work.

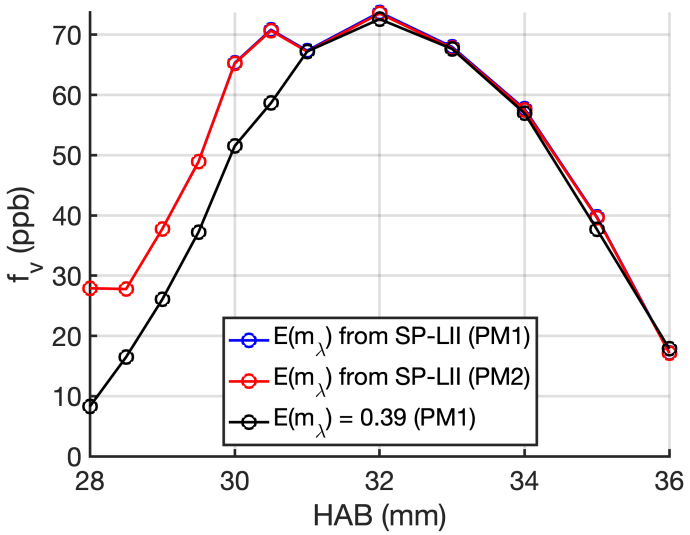

Figure 5.15: Evolution of f_v along the flame axis. The blue and red curves represent the estimations based on the LII signal at 578 and 716 nm, respectively. Both use the $E(m_\lambda)$ estimation given by the SP-LII. The black curve is obtained using the LII signal at 578 nm and assuming a uniform $E(m_\lambda)$ of 0.39. Results are obtained for a fluence of 106 mJ/cm^2.

A correction for the dependence to the peak soot temperature of f_v

The soot volume fraction calculated using AC-LII is known to vary with laser fluence [196, 210, 226, 262]: f_v increases with increasing laser fluences up to a peak value, after which it decreases as the fluence continues to increase. This phenomenon is known as the f_v anomaly. If the dependence is significant, this may be problematic when comparing f_v in different locations obtained for a given laser fluence for which the peak soot temperature is not homogeneous.

Figure 5.16a represents the values of f_v estimated by AC-LII versus the laser fluence for five different flame positions. f_v clearly varies with the laser fluence: at low fluence, f_v increases with F; then it decreases for higher fluences. While the decrease seen at high fluence is expected to be -at least partially- due to high-temperature phenomena like sublimation, it is not the case for the initial increase with fluence. This initial increase is currently not fully understood. This problem is further investigated in chapter 6, and no try for explanations are given here. Instead, a way to correct for this peak soot temperature dependence is proposed to enable more consistent comparisons of f_v across different flame locations, where varying heating temperatures can occur.

The fluences for which the maximum f_v occurs appear to depend on the HAB: the lowest HAB, the highest is the fluence. As it was found in Section 5.3.2 that the particles at low HAB absorb less and so do not have the same temperature as the more absorbing ones, f_v was replotted in Fig. 5.16b versus T_M instead of F. The f_v curves are normalised to show that all curves are superimposed indicating that the f_v anomaly depends on the maximum temperature of the soot T_M, and not on the laser fluence F. The maximum f_v is found for T_M ~4000 K. For lower T_M values, f_v rapidly decrease: a 30% smaller f_v is found for T_M ~3000 K. For larger temperatures, f_v decays even faster. It is remarkable that the peak value is obtained at 4000 K, a value retained as the high-temperature limit for the SP-LII in this flame.

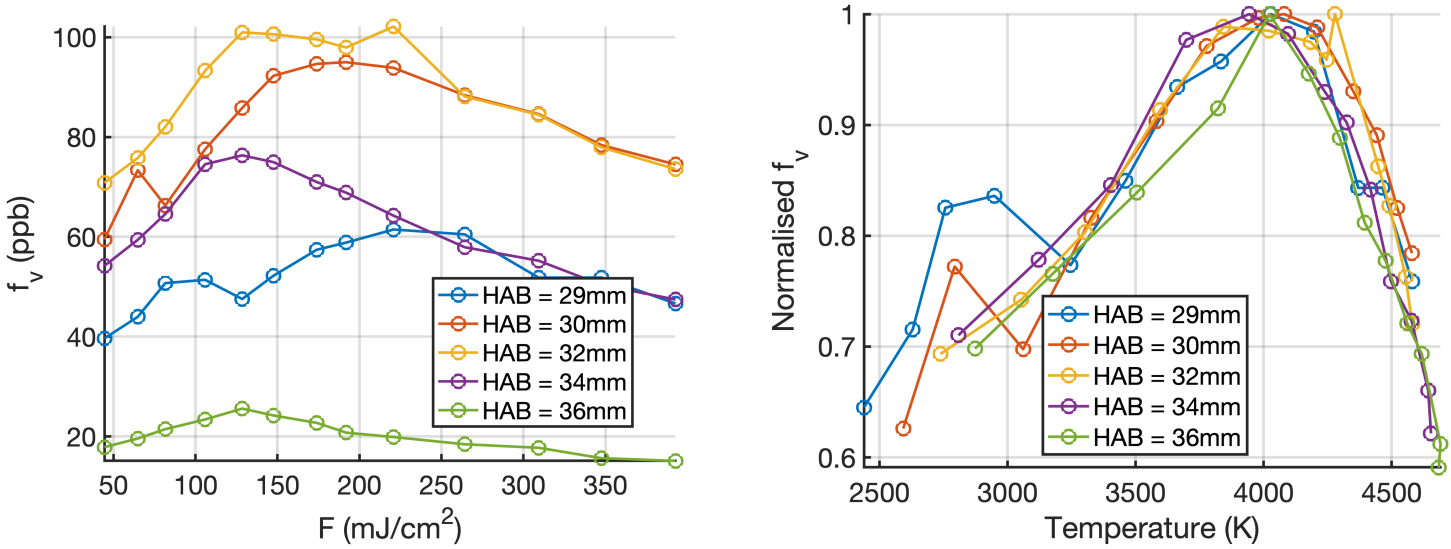

Figure 5.16: Evolution of f_v for five HABs along the flame axis, versus (a): the laser fluence, and (b): the peak soot temperature.

Uniformly heating soot particles with varying $E(m_\lambda)$ to the same temperature without triggering sublimation (which would decrease f_v) is not feasible. This poses a challenge when comparing f_v values from different locations based on a single laser fluence, as the non-uniform soot temperatures across locations can lead to misinterpretations of f_v trends.

Looking at Fig. 5.16a, selecting laser fluences between 100 and 150 mJ/cm^2 can help mitigate the temperature dependence of f_v. At these moderate fluence levels, most of the soot reaches temperatures around 4000 K, bringing f_v estimations close to their maximum values, which allows for a more reliable comparison. Alternatively, as the soot particles in the five studied locations appear to respond identically to the peak soot temperature, extrapolating this observation to the whole flame, it is possible to use Fig. 5.16a to correct the f_v estimation according to T_M by applying a correction factor (depending on T_M) to f_v. A correction function is constructed considering the curve of Fig. 5.16b for HAB = 32 mm. The correction function is plotted along with the normalised curve for HAB = 32 mm in Fig. 5.17a.

The corrected and normalised profiles of f_v are given in Fig. 5.17b. It is clear that the correction makes the f_v estimation less dependent on T_M.

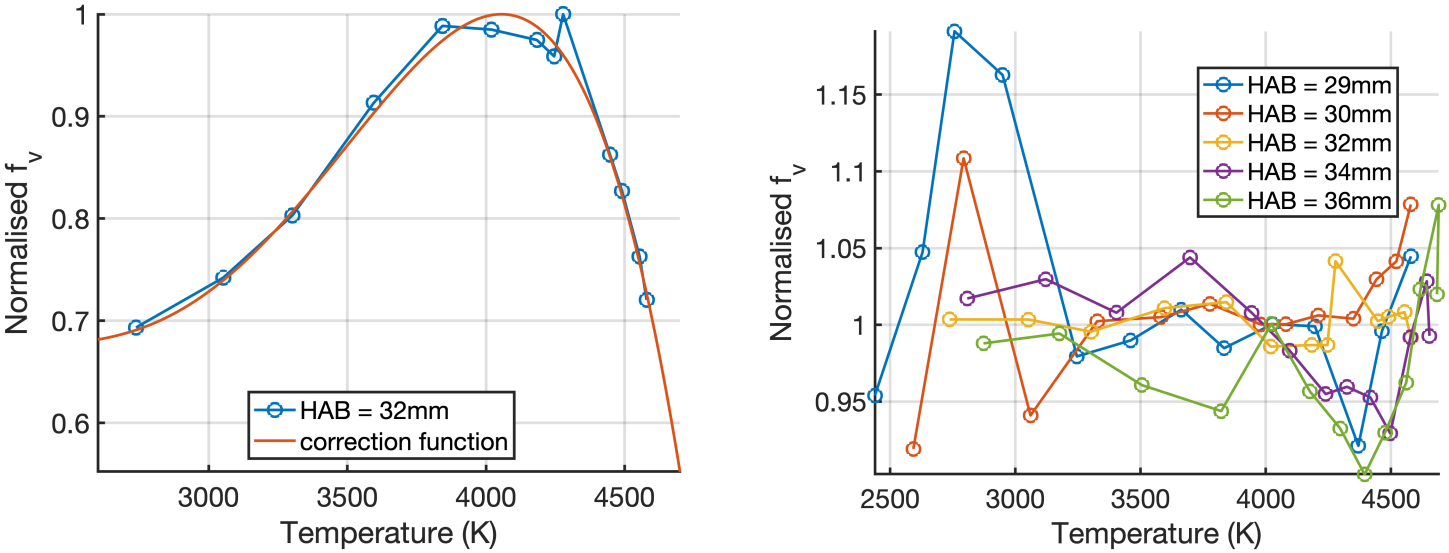

(a) (b)

Figure 5.17: (a): Normalised estimation of f_v at HAB = 32 mm (in blue) used to create the function to correct the temperature dependence of f_v (red). (b): Estimations of normalised f_v versus peak soot temperature after correction for temperature dependence for five HABs along the flame axis.

This correction is tested along the flame axis in Fig. 5.18 for the three laser fluences ($\sim$ 65, 105, and 150 mJ/cm^2), considering the distribution of $E(m_\lambda)$ computed with the SP-LII. After the correction, the three axial profiles of f_v are very close, with a maximum difference below 10 ppb, while it was above 25 ppb without correction. Thus, the application of such a correction for the T_M dependence allows for the measurement of f_v to be almost independent of T_M. The profile for F_3, the largest fluence, is almost identical whether it is corrected for T_M or not. This is because most of the temperatures are very close to 4000 K (Fig. 5.7b), the temperature for which the correction is small. The maximum correction is $\sim$ 25% for the lowest HAB as T_M is 3000 K here. This shows that when no correction is applied, in order to minimise the dependence of T_M, it is preferable to use relatively high laser fluences for f_v measurements, which confirms current practice in the literature.

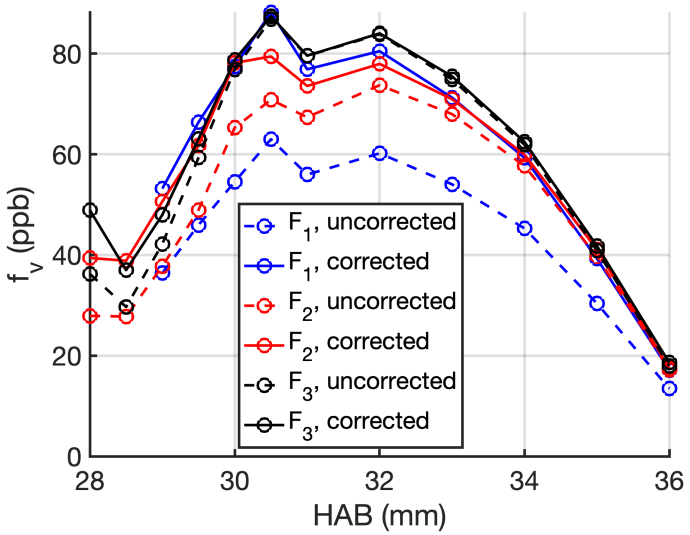

Figure 5.18: Evolution of f_v along the flame axis for the three selected laser fluences: F_1 = $\sim$65 mJ/cm^2 (blue), F_2 = $\sim$105 mJ/cm^2 (red), and F_3 = $\sim$150 mJ/cm^2 (black). Solid and dashed lines correspond to data corrected and uncorrected for T_M, respectively. The absorption function used to compute f_v is the distribution obtained with the SP-LII.

Cartography of f_v

The soot volume fraction obtained assuming the distribution of $E(m_\lambda)$ from SP-LII measurements is plotted in Fig.5.19a, and f_v obtained with $E(m_\lambda)$ = 0.39 is given in Fig. 5.19b. Figure 5.19b is extended compared to 5.19a as $E(m_\lambda)$ is not available in every position (due to the requirements on the maximum allowable temperature and SNR). Both profiles are computed at prompt, for a laser fluence of 105 mJ/cm^2. They are corrected for temperature dependence with the correction function of Fig. 5.17a. The correction reduces the temperature dependence by bringing the estimation of f_v to its maximum value. However, the choice to bring f_v to the maximum value is arbitrary, and nothing indicates that this maximum value is the true value of f_v. Still, this allows for a more legitimate comparison of its spatial variations between flame portions where soot particles have different T_M for a given laser fluence. Thus, the absolute values must not be entirely trusted, but at least the trends in spatial variations should be correct. This diffusion flame does not produce many soot particles as the maximum soot volume fraction is below 100 ppb. Soot are mostly found on the flame axis and not on the wings. The wings are sparsely populated in terms of f_v compared to the flame centreline. On the axis, f_v increases between HAB = 28 and 31 mm before decreasing when approaching the flame's outer edges, probably due to oxidation.

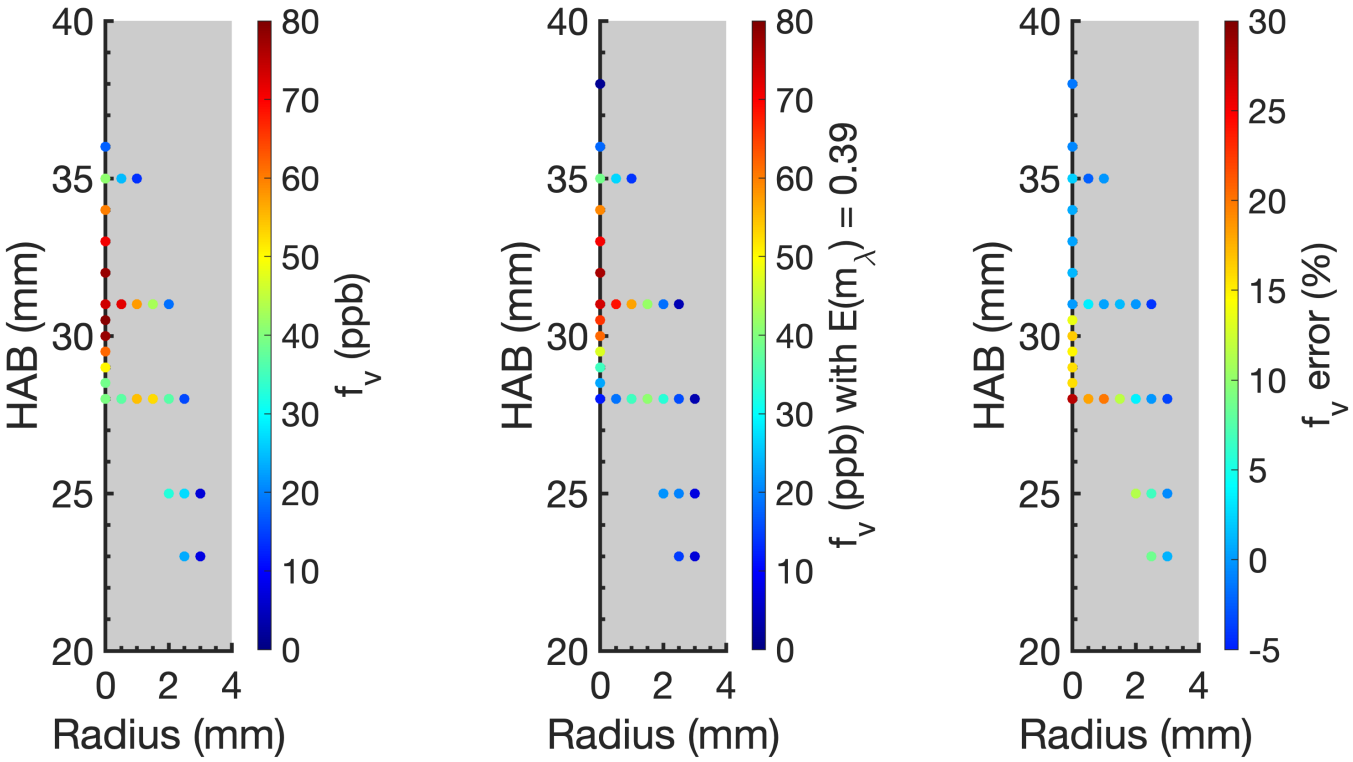

Figure 5.19: Cartography of f_v computed assuming (a): the varying distribution of $E(m_\lambda)$ of Fig. 5.14a, and (b): a uniform $E(m_\lambda)$ = 0.39. Figure (c) corresponds to the relative difference between (b) and (a): $\frac{f_v(E(m_\lambda)=0.39)-f_v}{f_v}$. f_v is computed from the LII signal collected at 578 nm. The data are obtained for a fluence of 106 mJ/cm^2 and are corrected for the peak temperature dependence.

Figure 5.19c represents the relative difference between Fig. 5.19b, and 5.19a. Important differences are found where soot particles are young, i.e. in the lower inner part of the flame, because the value selected for $E(m_\lambda)$ for the uniform case corresponds to mature soot. However, the global agreement is good as the maturation process is fast in this flame, and most particles are mature. This shows that neglecting the spatial variations of $E(m_\lambda)$ and assuming a value for $E(m_\lambda)$ that corresponds to mature soot (as generally done in the literature) induces an underestimation

of the soot volume fraction for the younger soot particles, but globally bring low error if the maturation process is rapid in the flame. It also brings a shift in the location of maximum f_v to higher HABs on the flame axis and a different soot formation dynamic: in the inner part of the flame, f_v increases more rapidly in Fig. 5.19b than in Fig. 5.19a, giving the impression of a higher rate of soot formation (nucleation and/or growth). Then, if soot formation processes are of interest, it is important to account for the non-uniformity in $E(m_\lambda)$ when comparing experimental results to numerical ones in flame zones with important variations of soot maturity.

5.4.3 Soot primary particle diameter d_p

The soot primary particle diameter, d_p, is determined by fitting the decay of the LII signals, following the methodology described in Section 3.4.4. In this thesis, when using PMTs, this approach was preferred to fitting temperature decays, as it proved more effective for two key reasons. First, slight impedance mismatches in the experimental setup caused small bumps in the LII signal. These bumps, while minor in the LII signal, became amplified when calculating temperatures using the ratio of the LII signals at two different wavelengths. Second, the signal-to-noise ratio of the PMT with the longer wavelength filter (716 nm) was lower than that of the shorter wavelength, and it deteriorated rapidly during soot cooling. This led to increased noise in the temperature estimates for non-prompt measurements. As a result, determining d_p based on LII signal decay, rather than temperature decay, was preferred. This method only requires the temporal decay of the LII signal at a single wavelength, with better accuracy achieved using the shorter wavelength (578 nm).

Calculating d_p requires setting several key parameters: T_0, T, α, λ, ρc, M_{gas}, and γ_{gas}. Here, λ is either 578 or 716 nm, T_M is determined by 2C-LII, and T_0 is obtained by SP-LII. Other parameters are assumed to be uniform across the flame, specifically: α = 0.3, ρc = 4.6·10^6 J/K/m^3, M_{gas} = 28 g/mol, and γ_{gas} = 1.29. A sensitivity analysis, as shown in Fig. 3.8b of Chapter 3, revealed that γ_{gas}, and T_0 significantly influence d_p determination. Concerning T_0, a 10% overestimation leads to a $\sim$20% underestimation of d_p. Given that T_0 estimated by SP-LII was found to be relatively high, d_p is calculated not only using the SP-LII-derived T_0 but also assuming uniform values of 1600, 1800, and 2000 K for comparison.

Axial evolution of d_p

Figure 5.20a represents the temporal evolution of normalised LII signals recorded at 578 nm for a laser fluence of 105 mJ/cm^2 at various axial locations. The small bump visible at 140 ns on the LII signal decay curves is an artefact due to a non-perfect match of the impedance between the experimental apparatus. The figure shows that the decay of the signal increases with the HAB, up to HAB = 32 mm, then continuously decreases up to the limit of SNR. On the basis of this figure, since the decay time is influenced by the average size of the primary particles, an axial increase in the average size of the primary soot particles is to be expected, followed by a decrease.

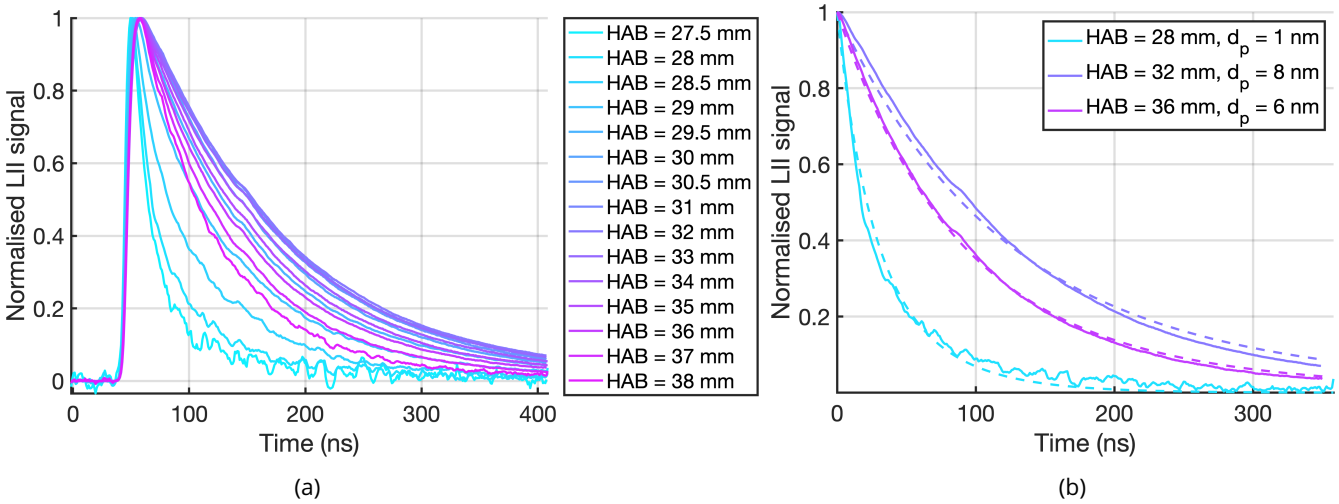

Figure 5.20: (a): Normalised LII signal decay at various HAB along the flame axis. (b): Normalised LII signal decay at HAB = 28, 32, and 36 mm, with corresponding fits using Eq. (3.29), and assuming T_0 as determined by SP-LII. The laser fluence is 105 mJ/cm^2, and the detection wavelength is 578 nm.

Figure 5.20b shows three LII signals with their fit, and the corresponding values for d_p are given in the legend. The fits are visually of good quality for the three positions represented here. As discussed below, the relatively low values of d_p obtained, especially the one for HAB = 28 mm (d_p = 1 nm), are partly due to the high value of T_0 found with the SP-LII.

Figure 5.21 represents the evolution of d_p along the flame centreline obtained from the LII signals at 105 mJ/cm^2. Blue and red curves are obtained considering the T_0 obtained with the SP-LII, and the gray curves are obtained for a uniform temperature of 1600, 1800, and 2000 K with the shade darkening as the temperature increases. The figure shows that the d_p estimations are quasi-identical, whether considering the LII signals at 578 (PM1) or 716 nm (PM2). The difference is of about 3% except for the lowest estimation (1 nm) where it increases to 10%. Therefore, in the following, d_p values will be reported using the signal at 578 nm, as it offers higher SNR.

As anticipated, d_p increases up to a HAB of 31-32 mm, after which the particle size begins to decrease. This trend suggests that the processes contributing to the growth of primary particles (surface growth, coalescence) are dominant initially, while above approximately 32 mm, soot oxidation becomes the predominant factor. It has to be noted that the qualitative behaviour of d_p and f_v are identical on the centreline.

Estimations of d_p with lower T_0 (1600, 1800, or 2000 K) yields higher values for d_p. This illustrates that the estimation of d_p is significantly affected by the inaccurate evaluation of the gas temperature obtained from experiments or assumptions. For instance, if the gas temperature would be of 1600 K, the d_p obtained at 31 mm would be 60% larger, and, at HAB = 28 mm, where the SP-LII derived T_0 yields d_p = 1 nm, using 1600 K leads to an increase by a factor of 3. However, while the absolute values of d_p are probably underestimated due to the likely overestimation of T_0, the trend should be relatively unaffected.

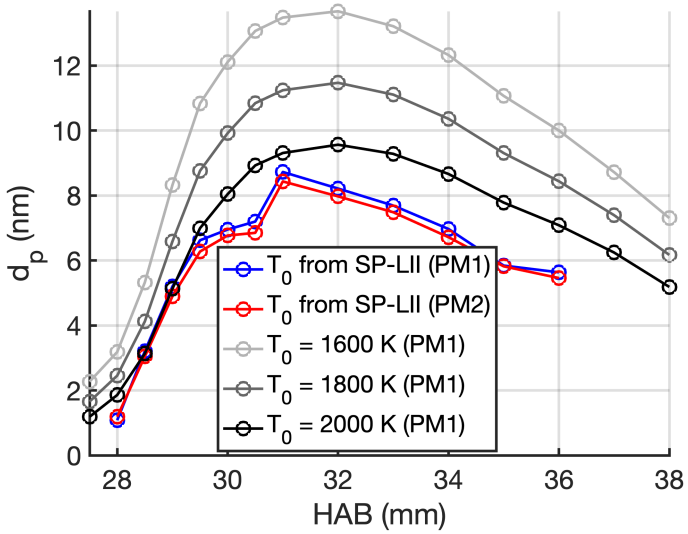

Figure 5.21: Evolution of d_p along the flame axis. The blue and red curves represent the estimations based on the LII signal at 578 and 716 nm, respectively. Both use the T_0 estimation given by the SP-LII. The varying grey curves represent the LII decay at 578 nm, assuming uniform T_0 values of 1600 K, 1800 K, and 2000 K, with the shade darkening as the temperature increases. Results are obtained for a fluence of 106 mJ/cm^2.

The d_p values obtained in this study are lower than those typically reported for CH_4 laminar diffusion flames, which generally fall within the range of 10-25 nm, as observed in studies utilising TIRE-LII or TEM techniques [29, 254, 263, 264]. However, the flames in these studies differ from the present one, particularly in terms of the maximum soot volume fraction, which is significantly higher in those works. Additionally, when time-resolved LII signals are provided [29, 264], the decay rate is slower compared to the ones of Fig. 5.20a, especially at the lowest HABs, suggesting that the soot particles in this study may indeed have small d_p values. Other works considering either premixed laminar hydrocarbon flames [113, 265], or acetylene pyrolysis behind a shock wave [139] found sub 5 nm particles with TIRE-LII from LII signal having comparable decay rate to the ones at the lowest HABs in Fig. 5.20a.

Notably, Bladh et al. [265] reported d_p values ranging from 2.5 to 12 nm at a detection wavelength of 575 nm (similar to the 578 nm used here). The time required for the LII signal to decay to 20% of its peak value varied between ∼45 and ∼130 ns, with a gas temperature decreasing from around 1700 K at HAB = 8 mm to 1500 K at HAB = 16 mm. They employed the temperature-dependent expressions for ρ and c from [205], for which the product ρc at high temperatures (2000-4000 K) is weakly dependent on temperature and approximates the constant value used in this study (4.6·10^6 J/K/m^3). However, their thermal accommodation coefficient was 0.37, compared to 0.3 in this study. In the present work, the time to decay to 20% of the maximum LII signal ranges from ∼50 ns at HAB = 28 mm to ∼200 ns at HAB = 32 mm, corresponding to d_p values between 1 to 9 nm when using the SP-LII derived T_0, or 3 to 14 nm when assuming T_0 = 1600 K. Since d_p is directly proportional to α, using a value of 0.37 would have resulted in d_p estimates approximately 23% higher. Given that, it is likely that d_p is indeed below 10 nm, at least for HABs below 30 mm. However, values such as 1 nm seem to be too low and might indicate an overestimation of T_0, or γ_{gas}.

It has to be reminded that the shielding effect, which is not accounted for in this analysis, tends to overestimate d_p for soot aggregates [131, 207]. Unfortunately, due to the lack of information on aggregate size in this study, it is not possible to assess the extent of its impact on the present results. Also, it has to be pointed out that, similarly to f_v, d_p also suffers from a dependence on the peak soot temperature of its estimation.

A correction for the dependence to the peak soot temperature of d_p

Just like for f_v, d_p also suffers from T_M effects. Figure 5.22a represents the estimated values for d_p versus the laser fluence for five different flame positions. d_p increases with F up to a peak value and decreases for higher fluences. If plotted versus T_M (Fig. 5.22b), the curves of d_p also are superimposed for the five positions studied here. The decrease of d_p at high temperatures was expected due to sublimation and/or laser fragmentation, which is known to decrease the particle size. However, the peak d_p is obtained at $\sim$ 3500 K to be compared to the 4000 K for f_v. This might be due to the fact that with sublimation activated, the LII signal decays faster shortly after the laser pulse due to the additional thermal losses of sublimation. As sublimation is neglected here, this will lead to an additional underestimation of d_p. If this is indeed verified, the fact that the peak value is found at 3500 K might indicate that sublimation starts as soon as 3500 K for the soot produced in this flame.

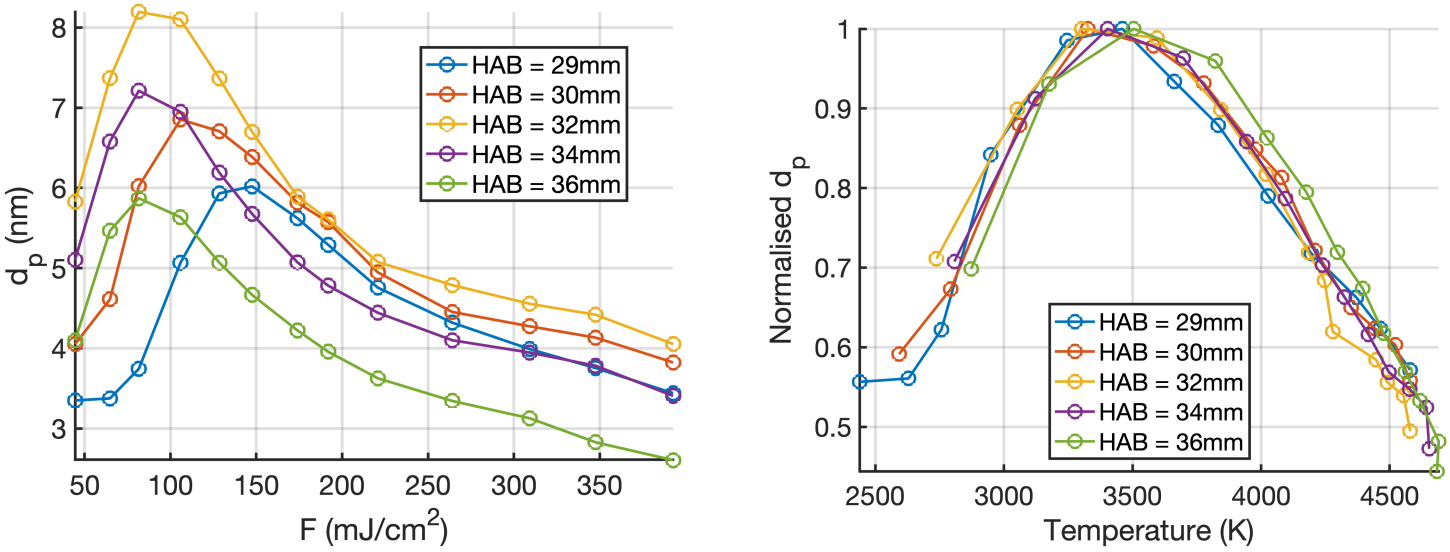

(a) (b)

Figure 5.22: Evolution of d_p, for five HABs along the flame axis, versus (a): the laser fluence, and (b): the peak soot temperature.

Similarly to what has been done for f_v, a correction function can be utilised to correct the dependence of d_p on the peak temperature. The correction function is constructed considering the curve at HAB = 30 mm and is given in Fig. 5.23a. The corrected and normalised profiles of d_p are given in Fig. 5.23b. It is clear that the correction makes the d_p estimation less dependent on the peak soot temperature: Omitting very low and very high temperatures, d_p now shows a ± 5% variation with the temperature.

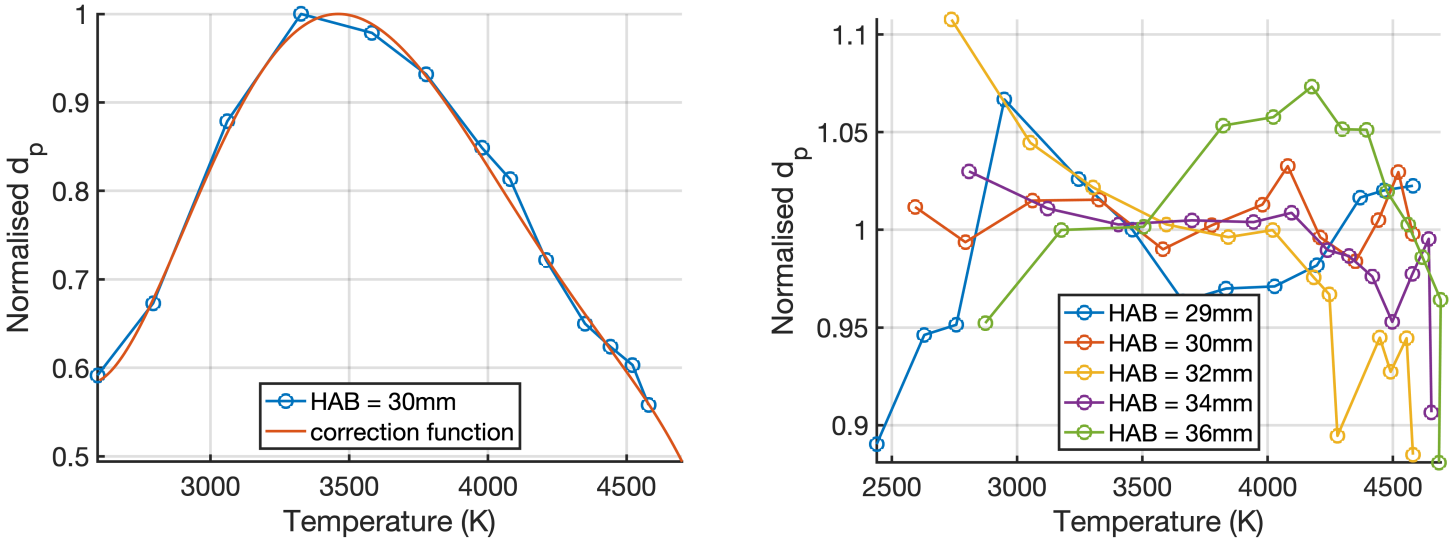

Figure 5.23: (a): Normalised estimation of d_p at HAB = 30 mm (in blue) used to create the function to correct the temperature dependence of d_p (red). (b): Normalised d_p versus peak temperature after correction for temperature dependence for five HABs along the flame axis.

Figure 5.24 represents the axial evolution of d_p without and with the temperature dependence correction for the three laser fluences ($\sim$ 65, 105, and 150 mJ/cm^2), and considering a uniform T_0 = 1800 K. The correction greatly improves the agreement between the estimations done at the three laser fluences: after the correction, the maximum difference in d_p for the three curves is below 1 nm compared to more than 2 nm before the correction. Unlike for f_v, the agreement of the corrected and uncorrected curve for F_3 is not so good. This is explained by the fact that the correction function for d_p peaks for 3500 K instead of 4000 K. However, for F_2, the corrected and uncorrected data are very similar (change by $\sim$1 nm) because the temperatures of most of the soot are around 3500 K for this fluence. This illustrates that when not considering sublimation and using only one laser fluence, it is not possible to have at the same time T_M independent measurements of f_v and d_p if no correction for T_M is considered.

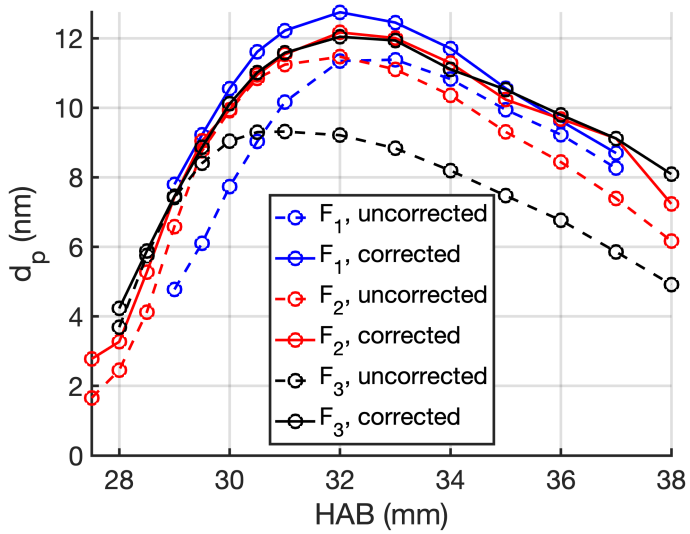

Figure 5.24: Evolution of d_p along the flame axis for the three selected laser fluences: F_1 = $\sim$65 mJ/cm^2 (blue), F_2 = $\sim$105 mJ/cm^2 (red), and F_3 = $\sim$150 mJ/cm^2 (black). Solid and dashed lines correspond to data corrected and uncorrected for T_M, respectively. A uniform value of T_0 = 1800 K was assumed to compute d_p.

Cartography of d_p

Figures 5.25a, and 5.25b represent partial 2D maps of d_p computed assuming the varying distribution of T_0 of Fig.5.14b, and a uniform value of 1800 K respectively. Figure 5.25b is extended compared to 5.25a as T_0 (estimated with the SP-LII) is not available in every position. The laser fluence is 105 mJ/cm^2, and the d_p are corrected for the peak soot temperature dependence with the correction function of Fig. 5.23a. Similarly to f_v, the correction reduces the temperature dependence of d_p, allowing for a more legitimate comparison of its spatial variations, but is made on an arbitrary choice, so the absolute values of d_p must not be entirely trusted; only the trends in its spatial variations should be correct.

Figures 5.25a, and 5.25b are qualitatively identical, only the absolute values of d_p change. In the whole flame, d_p stays below 12 nm. Low d_p values are observed in the lower inner region of the flame, where younger particles are present, and at the flame tip, where soot are expected to undergo oxidation. Therefore, a low d_p value may correspond either to a young particle or to a mature particle that has been oxidised. Differentiating between these scenarios is possible only through the information provided by $E(m_\lambda)$. This distinction would be particularly valuable in turbulent flames, where turbulent mixing could transport mature, oxidised particles to lower HAB locations.

It can be noticed that while f_v and d_p are comparable along the flame centreline, the wings show a different trend: d_p values are relatively high, while f_v is relatively low. Additionally, it is important to note that the estimated values of d_p -although probably underestimated- are low, mainly below 10 nm; regarding what has been said in the theoretical study of the SP-LII, this implies that $E(m_\lambda)$ is probably underestimated by at most 15%.

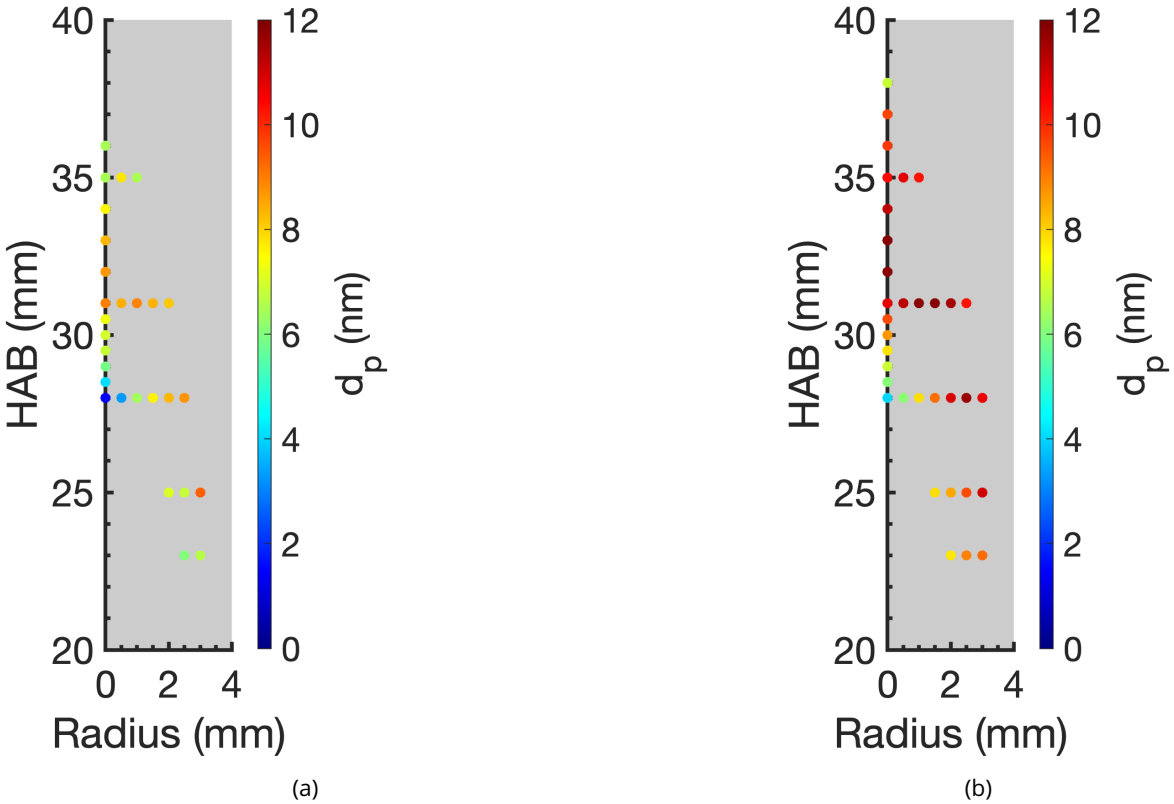

Figure 5.25: Cartography of d_p computed assuming (a): the varying distribution of T_0 of Fig. 5.14b obtained with the SP-LII, and (b): a uniform T_0 = 1800 K. d_p is computed from the LII signal decay obtained at 578 nm. The data are obtained for a fluence of 106 mJ/cm^2 and are corrected for the peak temperature dependence.

5.5 Summary on the dependence to T_M of d_p and f_v

The estimations of f_v and d_p depend on T_M. They both first increase with increasing F, then decrease for higher F values. A maximum value of these quantities is found when T_M equals ∼4000 and ∼ 3500 K for f_v and d_p, respectively. For high values of T_M, the soot particles are subjected to the high-temperature phenomenon (including sublimation and laser fragmentation) that can partly explain the decreasing trend of both f_v and d_p with T_M. However, for low values of T_M, no such temperature dependence should be found. Concerning f_v, this problem is known in the literature. It is referred to as the "f_v anomaly" and is addressed in Chapter 6 in which some possible explanations are given and might also explain what is seen for d_p.

This dependence is highly undesirable as it creates errors in the estimation of d_p and f_v that are dependent upon the T_M, the latter of which is not homogeneous in the flame mainly due to particles having different absorption functions, but also because of variation in initial soot temperature (gas temperature).

This effect can be mitigated upstream by carefully selecting laser fluences that bring the majority of the soot population near the maximum values of d_p and f_v. However, achieving T_M -independent measurements of both f_v and d_p simultaneously with a single laser fluence is not feasible, as the peak values for f_v and d_p occur at different peak temperatures.

Alternatively, based on the fact that all soot populations respond identically to T_M, a correction can be applied. The correction function reduces the temperature dependence by bringing the estimation of f_v and d_p to their maximum value. However, the choice to bring them to the maximum value is arbitrary, and nothing indicates that this maximum value is the actual value of f_v or d_p, but this allows for a more legitimate comparison of the spatial variation of these quantities in flame portions where soot particles have different T_M for a given laser fluence. Thus, the absolute values must not be entirely trusted, but at least the trends in spatial variations should be correct.

As a final remark, the correction requires multiple measurements at different fluences and locations and requires that all soot populations respond identically to T_M, which might not always be the case. Also, this correction is "artificial"; it corrects *a posteriori* and does not identify nor correct the source of the problem (unlike the procedure given in chapter 6).

5.6 Conclusion

A 2C-LII experimental setup was implemented to apply the SP-LII technique in a laminar diffusion CH_4/air flame. $E(m_\lambda)$, T_0, f_v, and d_p are computed exclusively from LII measurements, excluding the need for additional experimental techniques that would increase the complexity of the experimental setup.

A way to improve the signal quality was implemented to exploit the LII signals recorded with low laser fluences. Then, the crucial step of the SP-LII, which is the laser fluences selection, is made from the curves of peak soot temperature T_M as a function of laser fluences obtained at different HABs on the flame's axis. The challenge lies in balancing conflicting requirements: lower temperatures minimise soot alteration but result in a reduced signal-to-noise ratio while selecting widely spaced laser fluences is necessary to limit errors in peak soot temperature estimation. Additionally, soot particles have varying $E(m_\lambda)$ values, leading to different peak temperatures when heated at the same laser fluence. Therefore, compromises must be made when selecting laser fluences. In this study, three fluences were chosen to probe a wide range of soot populations effectively.

Two post-processing methods are considered: the absorption model (AM) and the look-up table (LUT). They show similar results for both $E(m_\lambda)$ and T_0. With the LUT post-processing method, the mass accommodation coefficient

giving the best agreement in our case was found to be $\beta = 0.13$. If the sublimation model correctly describes the physical process happening, the LUT method (with β = 0.13) may allow the application of the SP-LII even when some sublimation occurs, but this was not proven, so high T_M should be avoided. Estimations of $E(m_\lambda)$ and T_0 considering two or multiple laser fluences were compared. The difference was below 20%, showing that considering two fluences gives fair estimations. However, this underlines that, when possible, multiplying the number of laser fluences should be preferred. In order to assess the uncertainty inherent to the SP-LII, three sources of errors are considered: the volumetric heat capacity, the wavelength dependence of the absorption function, and the conduction losses. Regarding the first one, as the SP-LII retrieve $\frac{E(m_\lambda)}{\rho c}$, the uncertainty on ρc directly impacts $E(m_\lambda)$, but not T_0. Unfortunately, too little literature information is available on ρc to properly quantify the impact of the assumption made on its value. Regarding the other two, their cumulated impact was assessed to be $\pm$30% on $E(m_\lambda)$, and -10% to +2% on T_0.

Estimations of $E(m_\lambda)$, and T_0 are given for multiple axial and radial positions. Overall, the absorption function evolved from $\sim$0.1 in the lower and inner part of the flame up to a maximum of 0.4 at the flame edges. The flame studied is not a reference flame, so a direct comparison with the literature is not possible. However, trends and absolute values of $E(m_\lambda)$ retrieved with the SP-LII were found to be coherent with the literature available for other flames. The retrieved T_0 values are consistent with the adiabatic flame temperature but are likely overestimated. In similar studies of other CH_4/air laminar diffusion flames, temperatures in the soot region are typically reported in the range of 1500-2000 K, whereas this study finds values between 1900-2400 K. Moreover, considering the significant spatial fluctuations observed in neighbour flame positions, it can be inferred that these results provide only a rough estimation of T_0.

Soot volume fraction and soot primary particle diameter were estimated, both of which exhibit sensitivity to T_M. To ensure valid spatial comparisons, a correction was applied to make these estimates independent of T_M, though the correction involved an arbitrary decision regarding the absolute value. High soot volume fractions are found on the flame centreline and not in the flame wings, while high d_p are found in the wings and on the centreline, indicating a lower number of soot primary particles in the wings compared to the centreline.

f_v was estimated considering both the spatial variation of $E(m_\lambda)$ and a uniform $E(m_\lambda)$ = 0.39. Not accounting for spatial variations of $E(m_\lambda)$ brings an underestimation of f_v for the younger soot and slightly shifts the position of maximum f_v to higher HAB on the flame axis.

Estimation showed that d_p is below 10 nm for most of the flame. However, the overestimation of T_0 and the uncertainties in parameters such as ρc, α, γ_{gas} hinder precise estimation of d_p.

In this chapter, it has been demonstrated that a single 2C-LII experimental setup can effectively retrieve local information about $E(m_\lambda)$, T_0, f_v, and d_p in a laminar flame using PMTs. This setup offers a comprehensive optical diagnostic tool for soot analysis. However, obtaining spatial variations of these quantities is inconvenient with the current configuration, as it requires performing LII measurements for each spatial position. Thus, the next chapter explores replacing the PMTs with cameras, allowing for improved spatial resolution and more efficient data acquisition.

Chapter 6

2D measurements in a C_2H_4+N_2/air reference flame

The previous chapter demonstrated that four key soot-related parameters: absorption function $E(m_\lambda)$, gas temperature T_0, soot volume fraction f_v, and primary particle diameter d_p can be determined using LII measurements exclusively. However, the spatial resolution of these measurements was limited due to the use of photomultiplier tubes, which are 0D sensors. To overcome this limitation, the current chapter focuses on extending the LII setup for spatially resolved measurements of these parameters. This is achieved by replacing the photomultiplier tubes with cameras. The 2D measurements are performed in a reference 60%C_2H_4+40%N_2/air laminar diffusion flame which has been extensively studied in the literature, providing data for comparison and validation of the results presented in this thesis. Guidelines for the data processing are first established, identifying a temperature threshold for the computation of $E(m_\lambda)$ and T_0. The impact of background subtraction on the four key quantities is also evaluated, and a correction procedure is proposed. This correction partly solved the issue of the f_v anomaly -the abnormal dependence of f_v to the soot heating temperature- observed in the previous chapter. Finally, the results obtained by following the guidelines highlighted in this work are compared with existing literature data. This chapter is the focus of an article currently under submission: ***G. Guy et al. "Accessing $E(m_\lambda)$, T_0, f_v, and d_p with a single LII experimental setup: guidelines, difficulties, and comparison with the literature", in submission.***

Contents

6.1 Experimental setup **117**
6.1.1 Setup 117
6.1.2 Data acquisition 118
6.2 From pointwise measurements (0D) to 2D spatially resolved measurements **119**
6.2.1 Image pre-processing 119
Flatfield correction 120
Procedure for aligning the images obtained at 578 and 716 nm 121
6.2.2 Temporal resolution: selection of the gate delay 122
6.2.3 Comparison with photomultiplier tubes 124
6.3 Guidelines and data correction methodology **126**
6.3.1 Selection of the laser fluence 126
Effect of laser fluence selection 128

6.3.2 Background subtraction: impact, correction procedure and application . . . 135
Theoretical illustration . . . 135
Correction procedure . . . 138
Application to experimental data . . . 139
6.4 Benchmark with the literature data . . . **144**
6.4.1 Soot absorption function $E(m_\lambda)$ . . . 145
6.4.2 Gas temperature T_0 . . . 147
6.4.3 Soot primary particle diameter d_p . . . 149
6.4.4 Soot fraction volume f_v . . . 151
6.5 Conclusion . . . **154**

6.1 Experimental setup

6.1.1 Setup

The experimental setup is represented in Fig. 6.1b. It is similar to the setup described in section 5.1 of Chapter 5, with an identical excitation system but different flame and collection systems.

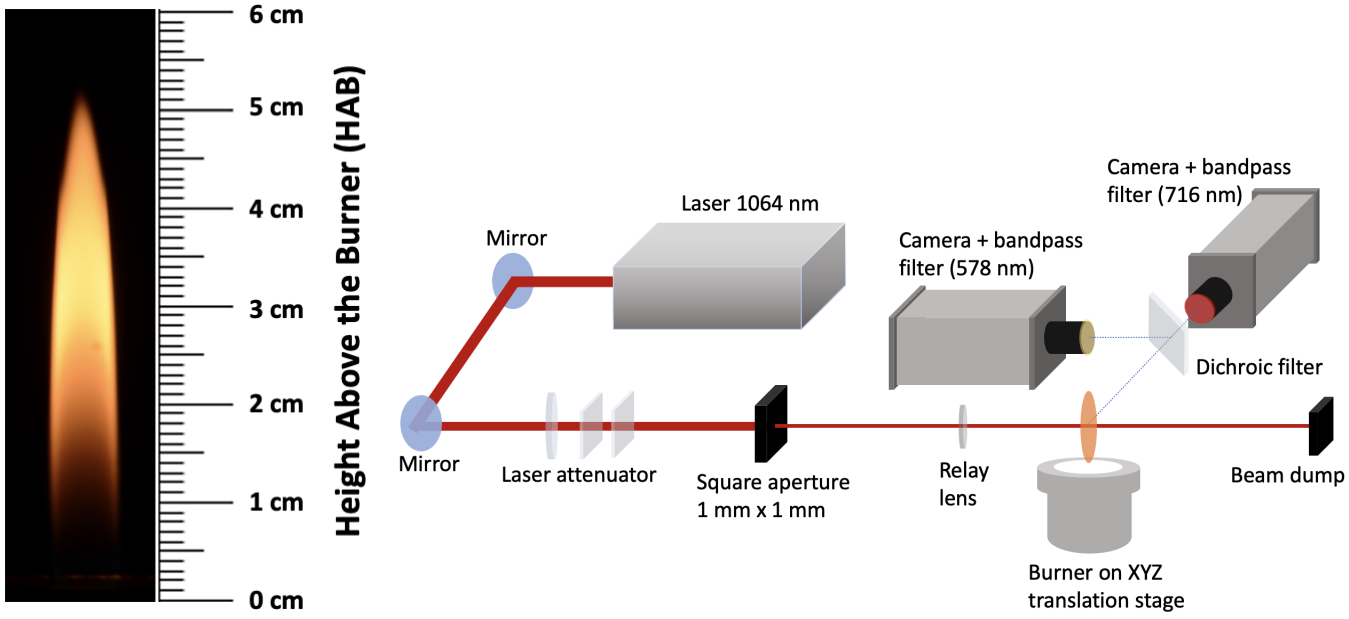

(a) (b)

Figure 6.1: (a): Image of the C_2H_4+N_2/air flame stabilised on the Yale diffusion burner. (b): Scheme of the 2C-LII experimental bench.

Burner and flame condition

The burner is the same as for the CH_4/air flame of the previous chapter. However, the flame condition is changed to the reference 60% C_2H_4+40% N_2/air Yale flame of [266]. A mixture of 0.140 ln.min^{-1} (0°C and 1 atmosphere) of C_2H_4 and 0.093 ln.min^{-1} of N_2 is flowing through the central injector. The flame is stabilised by a 38 ln.min^{-1} air co-flow exiting the porous surface. The volumetric flow rates were selected to match the standard condition of an exiting velocity of 35 cm.s^{-1} (20°C and 1 atmosphere). The flame is a $\sim$5 cm laminar diffusion flame pictured in Fig. 6.1a. The flame presents yellow/orange colour characteristics of the soot incandescence and appears visually more luminous than the CH_4/air flame previously investigated, indicating a potentially higher concentration of soot particles.

Collection system

The LII signal is collected at 90° from the laser beam and is split according to the wavelength by a dichroic mirror with a cut-off wavelength of 605 nm (Thorlabs DMLP605nm). The two cameras (EMICCD PIMAX 4) collecting the signal are equipped with identical camera lenses (105 mm of focal length, $f/2.8$) and equipped with different bandpass filters centred on λ_1 = 578 nm (Edmund optics 87766, FWHM of 18 nm), and λ_2 = 716 nm (Edmund optics 67053, FWHM of 46 nm). These bandpass filters are the same models as the ones used for the PMTs. The spatial resolution is such that 1 pixel represents $\sim$45.4 μm in the flame. The gate width of the cameras is set to 8 ns. The cameras and the laser are synchronised using a pulse generator (BNC 575 series). The LII measurements are done with a gain of 180 and 43 for the camera 1 (578 nm) and 2 (716 nm), respectively.

Calibration procedure

The same calibration source as for the CH_4/air flame is used: an integrating sphere OL-455-2 (Annex C). The calibration source is used for absolute calibration of the LII measurements but also to perform a flatfield correction of the cameras (section 6.2.1).

6.1.2 Data acquisition

The laser beam is shaped into a 1 mm square top-hat, so measurements over the whole flame cannot be made at once. To obtain indications about the distribution of the soot properties across the flame, multiple measurements are done at HABs ranging from 20 to 48 mm with a step of 2 mm and are gathered in a single image. That way, good indications about the flame distribution of the soot properties is obtained. Figures 6.2a and 6.2b shows the purely LII signal for all the HAB considered and for a laser fluence of 55 mJ/cm^2, recorded with the camera 1 (578 nm) and 2 (716 nm), respectively. The positions indicated in Fig. 6.2 are reference pixels selected to illustrate the spatial variations in soot properties. Their coordinates are given in Table 6.1.

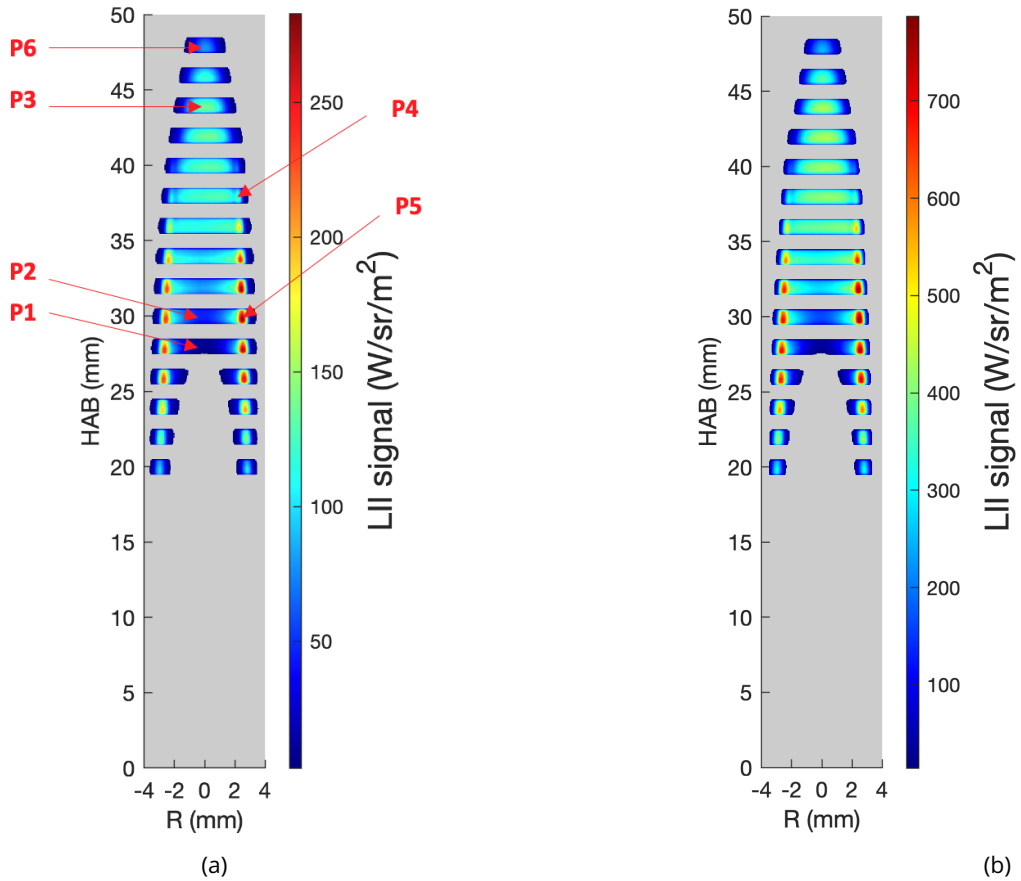

Figure 6.2: LII signal recorded at (a): 578 nm and at (b): 716 nm for a laser fluence of ~55 mJ/cm^2. The background was subtracted from the LII signal. Red arrays in figure (a) show the reference positions selected in this chapter.

Position	HAB (mm)	R (mm)
P1	28	-0.2
P2	30	-0.2
P3	44	-0.2
P4	38	2.2
P5	30	2.4
P6	48	-0.2

Table 6.1: Coordinates of the reference positions of Fig. 6.2a.

To accurately compute $E(m_\lambda)$ and T_0, LII measurements were conducted at ten different laser fluences: 25, 35, 45, 55, 65, 80, 100, 120, 140, and 160 mJ/cm^2 for each position. Precise alignment of the LII signal images recorded at 578 nm and 716 nm is crucial for determining the soot peak temperature using 2C-LII, especially due to the sharp signal gradients in the flame wings. The alignment process is detailed in the following section.

When it comes to d_p, while PMTs provide high temporal resolution of the LII signal, cameras typically lack this capability. However, for laminar steady flames, the temporal evolution of the LII signal can still be accessed by shifting the camera's exposure in time. By capturing multiple recordings of the LII signal at different moments after the laser pulse, the temporal decay of the signal can be reconstructed [163, 168]. Here, a laser fluence of 100 mJ/cm^2 is used, with measurements taken at varying instants by adjusting the camera gate delay (GD) between 0 and 850 ns after the laser pulse. To capture the soot cooling process, 12 GDs values are considered: 0, 10, 30, 60, 100, 150, 240, 350, 450, 550, 700, and 850 ns.

Images of the flame emission (without LII) are recorded and subtracted from the LII images. The signal-to-noise ratio (SNR) is improved by averaging 1000 images for each experimental condition. Due to the high number of measurements realised, the data acquisition was semi-automatised: a MATLAB script changed the HAB and the camera's GD and launched the camera acquisition automatically.

6.2 From pointwise measurements (0D) to 2D spatially resolved measurements

This section, divided into three subsections, presents the preliminary work undertaken to transition from pointwise (0D) measurements with photomultiplier tubes (PMTs) to 2D spatially resolved measurements using cameras. The first subsection focuses on image pre-processing. Since cameras lack temporal resolution, the second subsection addresses the selection of the instant corresponding to GD = 0 ns, defining the precise timing relative to the laser pulses when signal collection begins. Finally, temperature, absorption function, and gas temperature measurements obtained with PMTs are compared to those from the camera to ensure consistency between the two sensors.

6.2.1 Image pre-processing

Before any computations, the raw images require pre-processing for flatfield correction and alignment of the images taken with the two cameras. Flatfield correction is necessary to have a reliable image of the flame, and image alignment of each camera is necessary for correct temperature calculations.

Flatfield correction

In a CCD cell, each pixel responds differently to a given incident flux. As a result, even if the incident flux is uniform across the CCD cell, the resulting image will exhibit spatial inhomogeneities. Flatfield correction solves this issue.

To perform flatfield correction, an image must be recorded where the incident flux is uniform across all pixels (i.e., all pixels are equally illuminated). In this thesis, the uniform flux was obtained by positioning the exit of the calibration lamp's integrating sphere at the flame's location. The homogeneous light output from the integrating sphere ensures a uniform flux distribution. The images recorded by the two cameras are shown in Fig. 6.3. If the CCD cells had a uniform response, the resulting images would have been uniform. However, the fields show a 10-20% inhomogeneity, which is especially problematic when calculating temperatures, as this requires pixel-by-pixel image division.

Flatfield correction is applied by dividing the LII measurement images by the reference flatfield image shown in Fig. 6.3 on a pixel-by-pixel basis. It has to be noted that since the lamp's spectral radiance is known, Fig. 6.3 is presented in units of W/sr/m^2. Therefore, by performing the flatfield correction, both the flatfield and the absolute calibration of the LII image are obtained.

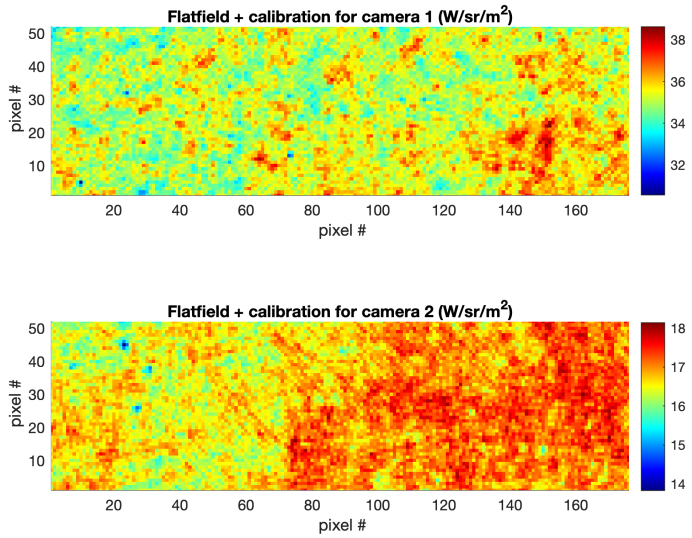

Figure 6.3: Calibration images for both cameras. The top image is for the camera 1 (578 nm), and the bottom one is for the camera 2 (716 nm). The intensity is given in W/sr/m^2.

Figure 6.4a gives a comparison before/after the flatfield correction of the LII signal obtained with the camera 1 for a laser fluence of F = 100 mJ/cm^2 at HAB = 30 mm. The high gradient of the signal in the figure makes it difficult to see the improvement in the quality of the flatfield correction. That is why Fig. 6.4b shows the radial evolution of the raw and flatfield corrected LII signal (normalised) for a single row of pixels. The corrected profile is clearly smoother. The non-symmetrical profile is explained by the laser attenuation through the flame as the laser beam arrives from the right of the flame. This treatment will be systematically applied to the measurements.

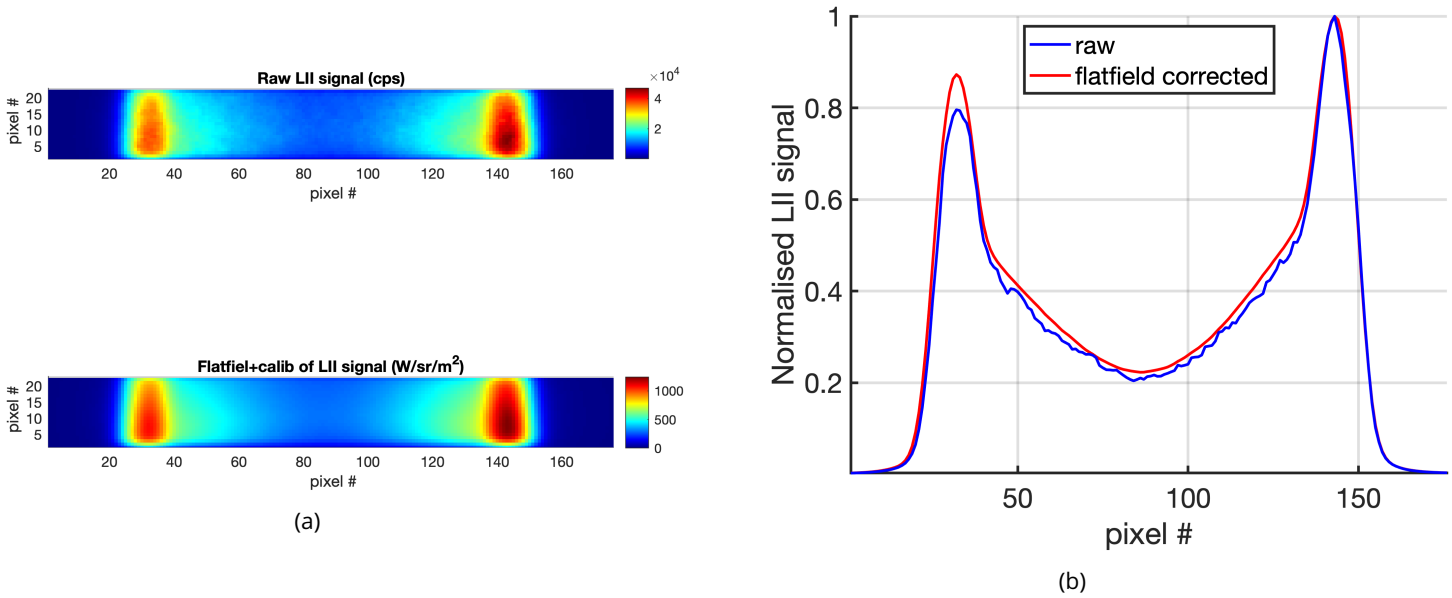

Figure 6.4: (a): LII signal recorded with at 578 nm, for a laser fluence of ∼100 mJ/cm^2 at HAB = 30 mm. The top image represents the raw signal (background subtracted), while the bottom image is after the flatfield correction. (b): Radial evolution of the raw and flatfield corrected LII signals (normalised) for a single row of pixels of image (a).

Procedure for aligning the images obtained at 578 and 716 nm

When computing the ratio of images obtained with different cameras (therefore having a different points of view), the perfect alignment of the images is crucial. As the temperature field is computed from the ratio of LII signals, efforts were made to have the same magnification, angle, and viewpoint with both cameras. For that, before any measurement, it was verified, using a target, that both cameras did look at the same spatial region. This provides pixel alignment. However, it was found that a sub-pixel misalignment can create anomalies when computing the ratio (very high or very low values, meaning very low/high temperature and significant asymmetry). To address this issue, background images were recorded just seconds before each LII measurement to minimise potential misalignment effects when subtracting the background from the LII signal. This step helped reduce errors due to sub-pixel misalignments. Also, to achieve sub-pixel alignment, the following alignment procedure was adopted before computing the ratio of LII images:

- Increase the size of the background subtracted LII signals images (obtained with the two cameras) by a factor of 10 using bilinear interpolation.
- Calculate the cross-correlation between the two LII signal images.
- Shift one of the images according to the indices giving the maximum correlation.
- Bin the images to return to their original size.

An illustration of the effect of this procedure is given in Fig. 6.5. The top image (before alignment) shows anomalously high values of the ratio on the bottom of the image. These are partly corrected after the procedure is applied, as shown in the bottom image. This illustrates a vertical misalignment, but horizontal misalignment can also appear and is particularly problematic due to the higher horizontal gradient of signal in the wings.

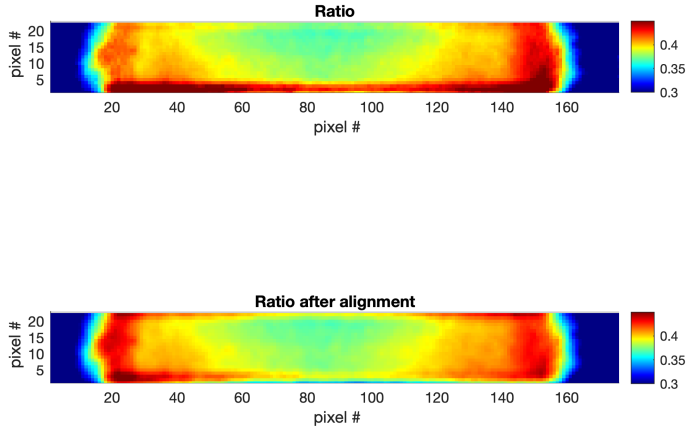

Figure 6.5: Ratio of LII signals at wavelengths 578 and 716 nm before (top image) and after the application of the alignment procedure (bottom image), for a laser fluence of $\sim$100 mJ/cm^2 at HAB = 30 mm.

6.2.2 Temporal resolution: selection of the gate delay

Cameras do not give the temporal resolution that is accessible with photomultiplier tubes. Therefore, using cameras, the instant at which the signal starts to be recorded -the gate delay- has to be carefully selected to catch the peaks of the LII signals, allowing the peak temperature to be computed. However, the instant at which the peak temperature is reached depends on the thermal losses of the particle (dominated by the conduction losses for the fluences of interest in this thesis). These thermal losses mainly depend on the particle geometry and on the temperature difference between the gas and the particle. The larger the losses (high fluence, high absorption function or high surface-to-volume ratio), the sooner the peak temperature appears. Thus, depending on the laser fluence, the absorption function and the geometry of the soot, the peak temperature may be reached at different instants. This would imply that the selected gate delay would be optimal only for one population of soot at one fluence.

This subsection aims to demonstrate the dependence of the peak LII signal on the gate delay, considering different soot populations and laser fluences. Based on this analysis, an optimal gate delay is selected to ensure the most accurate capture of peak LII signals and temperatures for all relevant soot populations and laser fluences. The chosen gate delay will be applied to the measurements presented in this chapter and in Chapter 7.

For that, measurements of the LII signal are made for three laser fluences: 40 (low), 100 (medium), and 150 (high) mJ/cm^2, and for gate delay varying from 0 to 20 ns with a 2 ns step (the choice of the instant corresponding to 0 ns is arbitrarily set to an instant before the end of the laser pulse, and it does not impact the results). These measurements are done at HAB = 28 mm, where there are variations in the soot absorption function and soot primary particle size with the radial position.

Three zones corresponding to different soot populations are considered (delimited by white squares in Fig. 6.6a): position 1 corresponds to the flame wings where soot are mature and have a large primary particle diameter, position 3 is closer to the flame axis, and correspond to younger soot (small d_p and low $E(m_\lambda)$, while position 2 is an intermediate one. The difference in the absorption function can be seen by the different temperatures they reach in the bottom image of Fig. 6.6a.

Figure 6.6b represents the temporal evolution of the LII signal over 20 ns for these three positions and obtained with both cameras for a laser fluence of 100 mJ/cm^2. The LII signal does not show a smooth evolution, but the temporal dependence is identical for the two cameras. The figure shows that the peak LII signal arrives between $\sim$4 and 12 ns for the three populations.

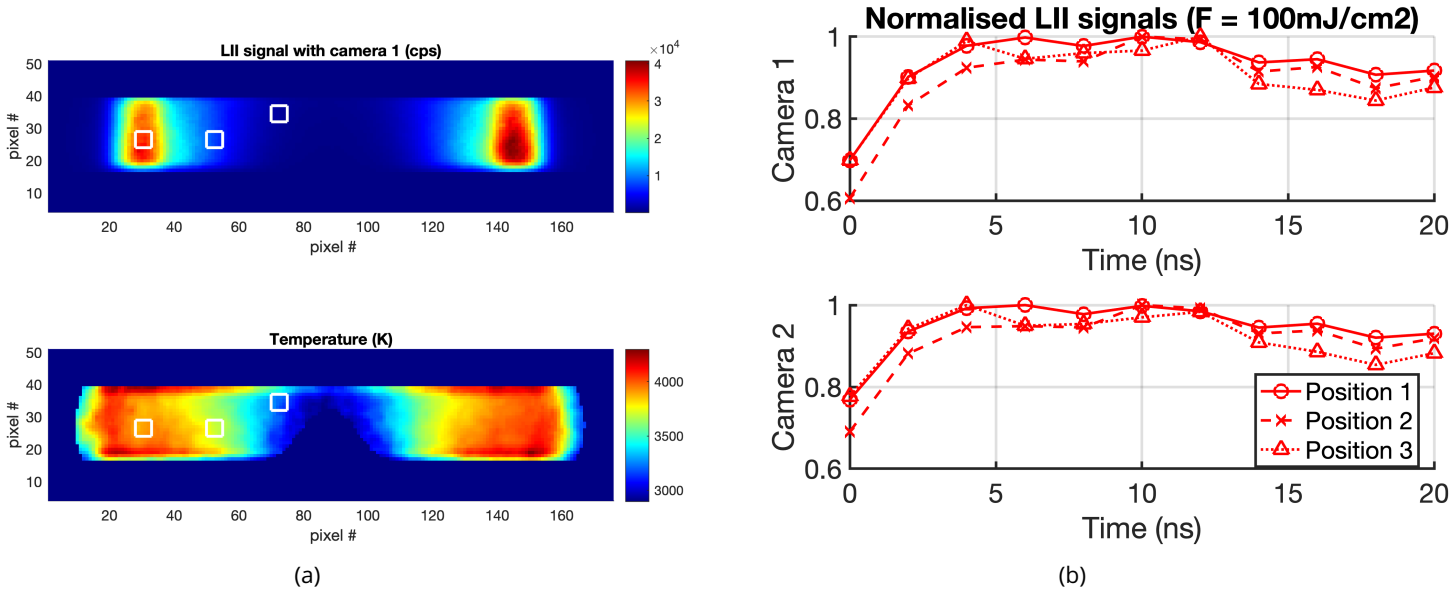

Figure 6.6: (a): Raw image of the LII signal recorded at 578 nm at a HAB of 28 mm (top image), and corresponding temperature (bottom image). The white squares represent the three positions considered for the gate delay study. Positions 1, 2, and 3 are defined from the left to the right of the image. (b): Normalised LII signals versus time for both camera and for the three positions of figure (a): Position 1 (solid line and ○), 2 (dashed line with ×) and 3 (dotted line with △).

The soot temperature versus the gate delay is given by Fig. 6.7b. For position 1 with the highest fluence, measurements below 14 ns are not exploited as they were above the imposed camera saturation limit. In contrast, for position 3 and for the lowest fluence, no temperature estimation is made due to a too-low LII signal. The temperature profiles show a flatter behaviour compared to the LII signals. Fluctuations in LII signals and temperature are greater in situations of low SNR (position 3 and/or low fluence). It is easier to see the instant of the peak temperature in Fig. 6.7b, which shows the normalised temperature profiles. From this figure, the peak temperature is reached between 6 and 12 ns for the three soot populations and for the three laser fluences.

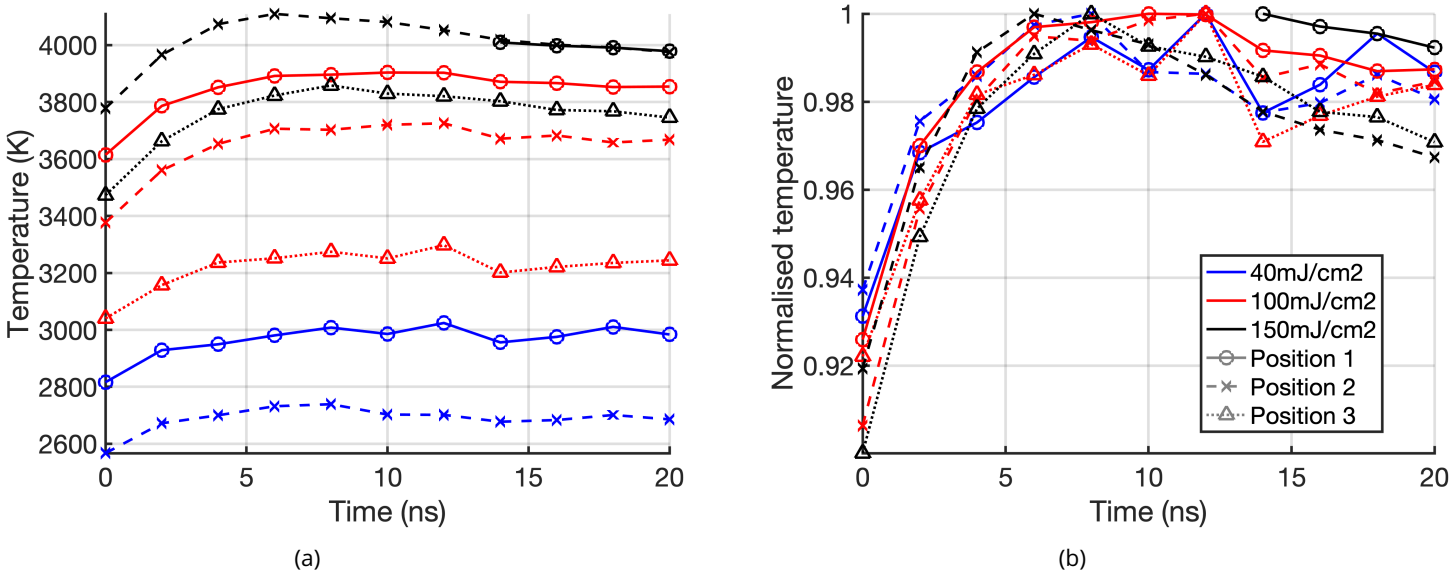

Figure 6.7: (a): Soot temperature versus gate delay. Temperatures are given for three laser fluences: 40 mJ/cm^2 (blue), 100 mJ/cm^2 (red), 150 mJ/cm^2 (black), and for the three positions of Fig. 6.6a: Position 1 (solid line and ○), 2 (dashed line with ×) and 3 (dotted line with △). (b): Normalised version of (a). The choice of the instant corresponding to GD = 0 is arbitrary and does not impact the results.

Regarding these relatively low variations in the instant of maximum LII signal and temperature for the various cases presented here, it was decided to set the value of the gate delay to the instant corresponding to 7 ns in these figures. Therefore, in this thesis, when it comes to 2D camera measurements (Chapter 6 and 7), all measurements are performed with a gate delay of 7 ns. According to Fig. 6.7b, and Fig. 6.6b, a realistic estimation of the impact of this choice is an underestimation of the peak temperature below 2% and an underestimation of the LII signal by 5% at most.

6.2.3 Comparison with photomultiplier tubes

In order to check the correctness of the camera measurements, some measurements with the PMTs and the cameras were recorded in parallel. Measurements are done for six different fluences (35, 45, 55, 65, 80, and 100 mJ/cm^2) at HAB = 30 mm. For the PMTs, multiple radial positions are probed from 0 to 3 mm.

The soot temperatures computed from the PMTs and the cameras are given in Fig. 6.8 for multiple radial positions and for the six laser fluences. For low laser fluences, the temperatures obtained with the PMTs are $\sim$100 K lower than that of the cameras, and this difference reduces when the fluence increases. This trend of lower temperatures at low fluences for the PMTs compared to the cameras is difficult to explain. However, one possible element of response would be the fact that the optical sensors used here are not particularly well suited to measurements in the upper part of the visible range: their quantum efficiency decreases over the width of the second collection wavelength, from 696 to 736 nm, and this is particularly true for the camera. As a result, the sensitivity in the vicinity of 696 nm is much higher than at 736 nm, which can affect measurements when moving away from the calibration point (done using a tungsten lamp with a brightness temperature of 3000 K): as the lower the heating temperatures, the larger will be the emission at 736 nm compared to 696 nm. This means that at lower temperatures, the LII signal collected at the second wavelength would be more underestimated than at higher temperatures, leading to an overestimation of the maximum soot temperature by 2C-LII pyrometry. In summary, the non-uniform quantum efficiency in the second collection window may introduce distortions in the temperature estimates.

At higher radial positions, specifically in the flame wings (R = 2.5–3 mm), the estimates show poor agreement. This last discrepancy can partly be attributed to the region's high variability in soot properties, including particle size and absorption function. As a result, even minor misalignments between the cameras and PMTs cause them to capture different soot populations, leading to significant differences in the measured temperatures. In the wings region, PMT estimations are higher than those from the camera, particularly at high fluence/temperature. This trend is the opposite of what is observed at lower radial positions, suggesting that an additional factor is influencing the results. Since the wings are characterised by very high LII signals, it is possible that the sensor response begins to deviate from linearity as the soot heating temperature increases (that is to say, when the LII signal approaches the saturation limit of the camera).

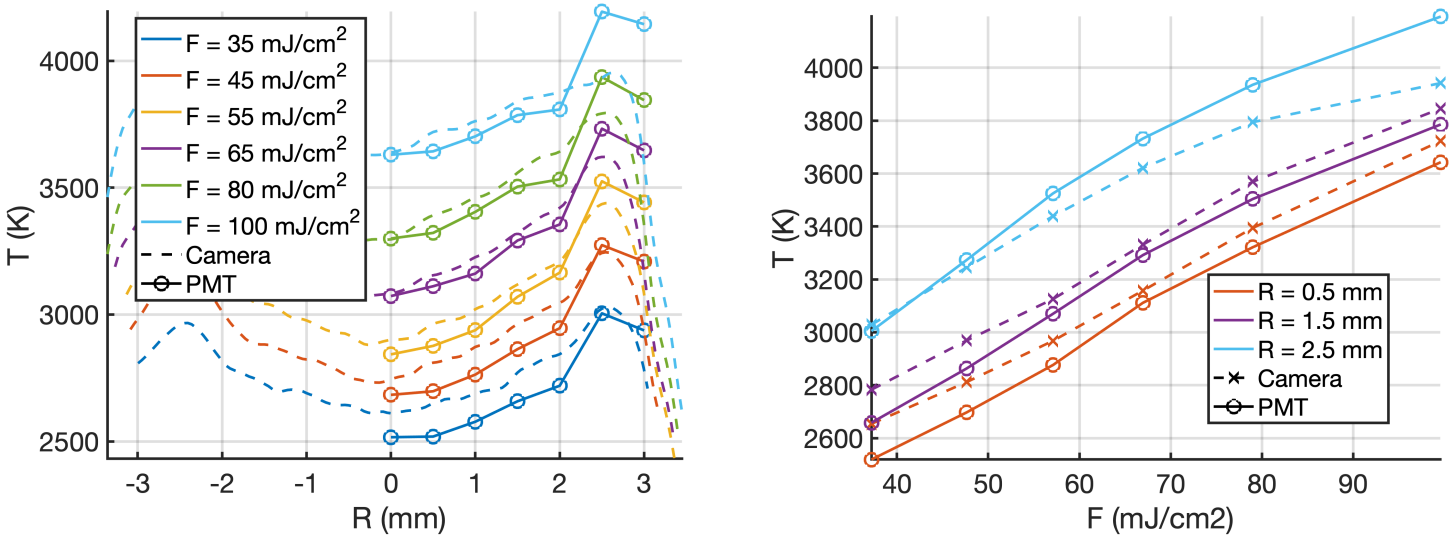

Figure 6.8: (a): Soot temperature versus radial position for multiple laser fluences. Temperatures computed using PMTs and cameras are given by the solid lines with ∘ symbols and by the dashed lines, respectively. (b): Soot temperature versus laser fluence for multiple radial positions. Temperatures computed using PMTs and cameras are given by the solid lines with ∘ symbols and by the dashed lines with × symbols, respectively. As the collection surface for the PMT is 225 μm, almost 5 times the size of a camera pixel, the estimations of temperature using the data from the cameras have been averaged over 5x5 pixels.

The computation of $E(m_\lambda)$ and T_0 from the temperatures below 3500 K of the previous figure are given in Fig. 6.9. As the temperature estimations are lower than that of the camera for low fluences, $E(m_\lambda)$ retrieved with the PMTs are ∼12% higher than when cameras are used, while T_0 is up to ∼ 200 K lower. In the wings, R > 2 mm, the differences are higher. Overall, absolute values of $E(m_\lambda)$ and T_0 show a ∼10% difference, with larger differences in the wings, possibly due to PMTs/cameras misalignment. Still, the results qualitatively agree as they both show an increase in $E(m_\lambda)$ and T_0 with the radial position. These results were achieved despite differences in sensors, calibration, sensor response characteristics, the lack of temporal resolution in the camera, and the absence of spatial resolution in the PMTs. Therefore, this global agreement between the sensors is comforting and allows the usage of the cameras for LII measurements.

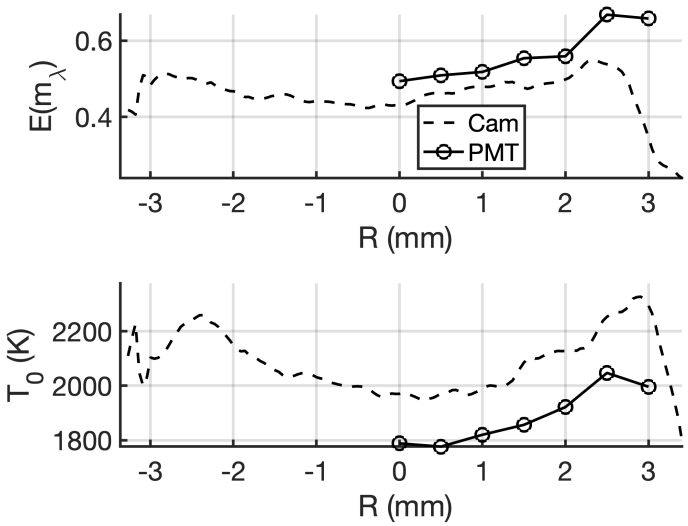

Figure 6.9: Radial distribution of absorption function (top) and gas temperature (bottom) computed using PMTs (solid line with ∘ symbols) and cameras (dashed line). Measurements are done at HAB = 30 mm.

6.3 Guidelines and data correction methodology

This chapter shows the possibility of obtaining 2-D spatial evolution of four complementary soot information: $E(m_\lambda)$, T_0, f_v, and d_p with a single two-color laser-induced incandescence (2C-LII) setup and limiting experimental settings. This represents the only work presenting simultaneously these four information with a 2D resolution using only one LII setup dealing with the main LII challenges. Based on the literature and on the results of the previous chapter, one of the main challenges is selecting the appropriate laser fluence:

- The non-intrusive behaviour of the LII technique may be questionable when high soot temperatures are reached due to the high-temperature phenomenon that may alter the optical properties, morphology, and quantity [245, 246, 248, 262, 267–273] of the pristine soot particles.
- The Auto-Compensated LII (AC-LII) displays an anomalous f_v dependence with the laser fluence as pointed out by Smallwood [226] and observed by others researchers [196, 262]. This anomaly is referred to as the f_v anomaly. In specific, the measured f_v increases with the laser fluence before reaching a peak value and subsequently decreasing due to sublimation [196]. Estimates of f_v were found to vary by up to a factor of 8 [196, 226] with laser fluence. The origin of this anomaly is partly attributed by Liu et al. [196] to the laser fluence uniformity in the laser top-hat beam. Then, the usage of detection wavelengths in the upper end of the visible spectrum helps to reduce the impact of a non-uniform top-hat laser beam [210]. In addition, to overcome the laser fluence dependence of f_v that is more pronounced at low laser fluences, it was recommended [226, 262] to perform measurements with AC-LII at laser fluences for which the dependence is reduced, that is to say, to work at a temperature above the sublimation threshold. Unfortunately, this is the opposite of the original recommendation of Snelling et al. [267] to use low laser fluence.
- In addition to the purely LII signal, the measured signal contains an incandescence signal -which is part of the background- coming from all the soot particles at the flame temperature that are on the optical path of the detector [240]. This non-LII part of the total incandescent signal of the probe volume is generally small compared to the LII signal, so, generally, no additional correction is made when subtracting the background. Still, Sipkens et al. [250] showed by means of numerical simulations that background subtraction is responsible for an apparent decrease in f_v as the soot particles cool after being heated by the laser pulse. Therefore, background subtraction may introduce errors in the quantitative interpretation of the LII signal, particularly when measurements are conducted at low laser fluences or with a delay after the LII peak. The impact on the results is likely to vary depending on the laser fluence.

This section provides guidelines for the proper acquisition and processing of LII measurements to accurately estimate key soot quantities ($E(m_\lambda)$, T_0, d_p, f_v) within a reasonable experimental timeframe. It is divided into two subsections. The first subsection addresses the selection of the laser fluences, focusing on how to effectively estimate soot properties using a reduced number of measurements. The second subsection tackles the issue of background subtraction, presents a correction procedure for it, and evaluates the errors introduced by background subtraction.

6.3.1 Selection of the laser fluence

The objective here is to identify the experimental settings allowing to determine $E(m_\lambda)$, T_0, f_v, and d_p while minimising the number of acquisitions. In Chapter 5, $E(m_\lambda)$, T_0 are computed with the SP-LII from two measurements of T_M at different laser fluences. Three laser fluences were retained to have a good idea of the spatial evolution of $E(m_\lambda)$, T_0. Here, LII measurements were done for ten different laser fluences to have reliable measurements of $E(m_\lambda)$, T_0, which will be compared to the ones obtained considering fewer laser fluences. Thus, the first step

requires selecting the right laser fluences, allowing the accurate determination of $E(m_\lambda)$ and T_0 for different soot populations by considering T_M from ten different laser fluences from 25 to 160 mJ/cm^2.

The temperature computed by 2C-LII for four laser fluences: 25, 55, 100 and 160 mJ/cm^2 are given in 2D maps in Fig. 6.10 to illustrate the increasing of T_M with F and the spatial inhomogeneities of T_M. Temperatures are higher on the flame wings and lower in the bottom inner part of the flame. As T_M depends on multiples parameters, including $E(m_\lambda)$ and T_0, it is not directly possible to infer that the soot particles present in the region with larger T_M have large values of $E(m_\lambda)$ as T_0 is unknown and is surely not uniform. Thus, high temperatures found in the wings region may be due to strongly absorbing soot particles and/or to a high local gas temperature.

At a fluence of 160 mJ/cm^2, temperature data are not provided in the wings and at certain positions in the middle of the flame due to camera saturation. Saturation occurred because the same camera settings were kept unchanged for all laser fluences to ensure consistent comparisons between measurements.

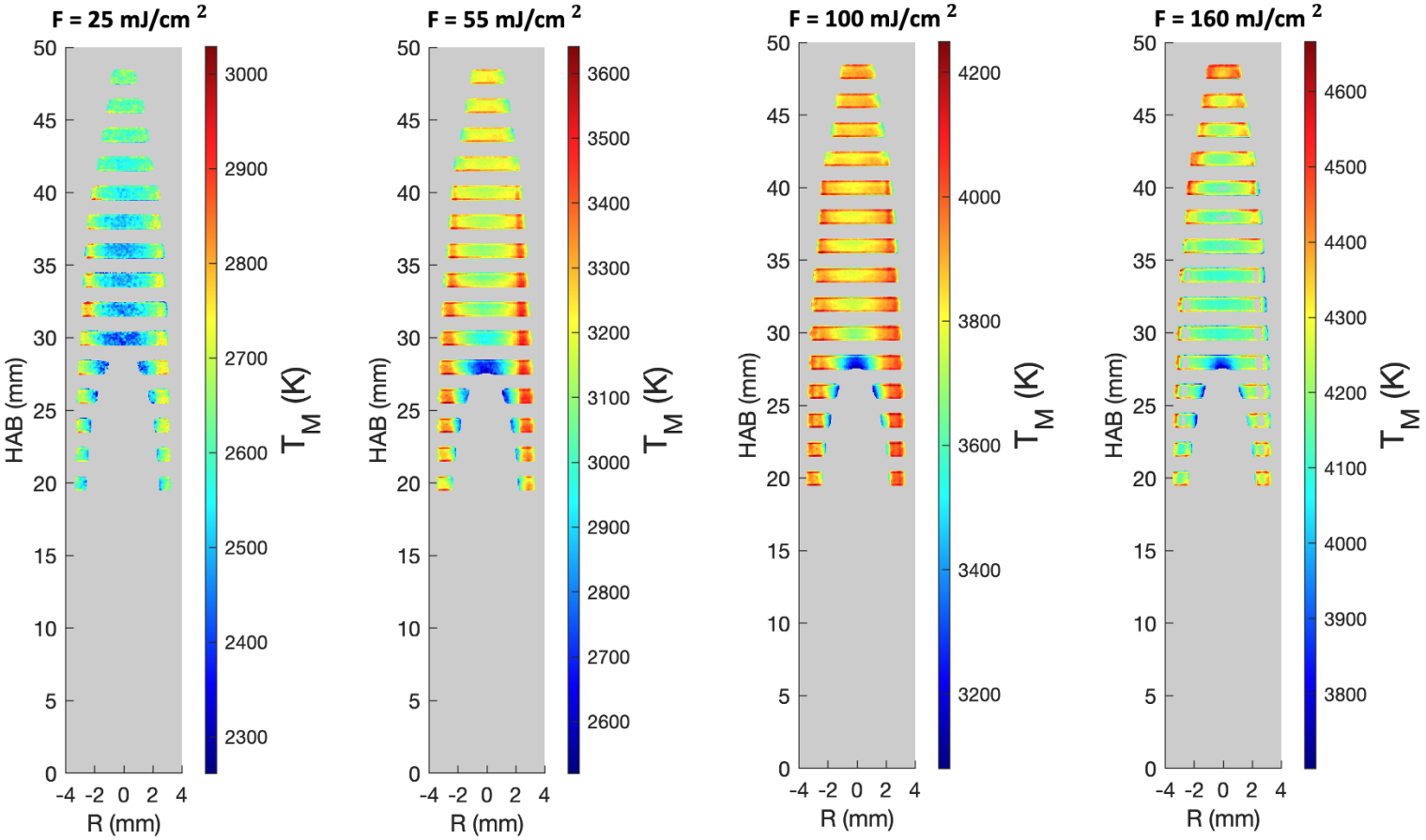

Figure 6.10: Temperatures for different laser fluences: (a): 25, (b): 55, (c): 100, and (d): 160 mJ/cm^2. For 160 mJ/cm^2, temperatures are not reported in the wings and in some positions in the middle of the flame due to camera saturation: the cameras were set and calibrated for low fluence measurements.

$E(m_\lambda)$ and T_0 can be computed from the curves of peak temperature versus laser fluences [33, 134]. Figure 6.11a shows examples of such curves for soot particles found in the reference positions represented in Fig. 6.2a. A break in the linearity of the curves appears depending on their position, i.e. particle maturity. A simple criterion can be defined by stating that the linearity is generally lost when the temperature exceeds a limit of ~3500 K, even if for the

particles in position 1 and 2, this limit seems to be pushed to higher values as observed in [270]. Since the linearity of the soot peak temperature is needed to rely on Eq. (4.5), to extract information on $E(m_\lambda)$ and T_0, only the points for which the temperature is below 3500 K will be considered in the following. This limit is more restrictive than the one imposed in the previous chapter (4000 K), potentially indicating that the soot particles have different properties in the two flames.

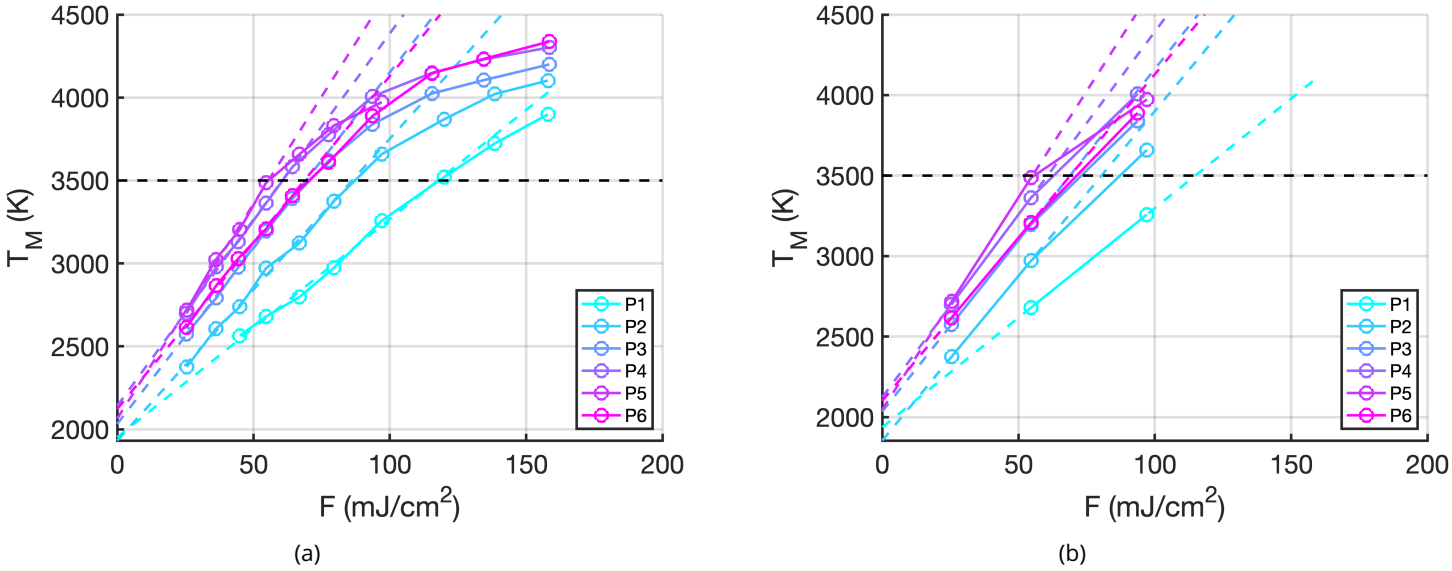

Figure 6.11: (a): Soot peak temperature versus laser fluence for different pixel locations (solid line with ○). Each colour corresponds to a different pixel location (Fig. 6.2). The dashed lines represent the linear regression obtained considering the temperatures below 3500 K. The horizontal black dashed line represents the temperature limit of 3500 K. Figure (b) is identical to figure (a), but only the three laser fluences 25, 55, and 100 mJ/cm^2 are considered.

Effect of laser fluence selection

Soot absorption function and gas temperature

Using as most laser fluences as possible is better for fitting T_M to F via Eq. 4.5 to provide more robust values for both $E(m_\lambda)$ and T_0 while allowing to probe soot populations with different absorption function (see Chapter 5). However, here, the values of $E(m_\lambda)$ and T_0 computed considering all measurements for which T_M < 3500 K (linear regime) are compared to the values computed using only three laser fluences. This approach is considered to demonstrate that spatially resolved 2D measurements of $E(m_\lambda)$ and T_0 in a laminar flame can be achieved with a limited set of measurements at different laser fluences, maintaining acceptable accuracy in the estimation of $E(m_\lambda)$ and T_0. Reducing the number of laser fluences lowers experimental costs but is also advantageous for future applications in turbulent flames, where implementing multiple simultaneous laser fluences is particularly challenging.

The choice of the laser fluences is based on Fig. 6.11a. The selected fluences should bring the temperature of the different soot populations below the identified limit of 3500 K while being sufficiently spaced apart for good accuracy of the estimations of $E(m_\lambda)$ and T_0 in the presence of bias in the soot peak temperature estimation (Fig. 4.16).

Laser fluences of 25 and 55 mJ/cm^2 allow probing the soot populations represented by positions 2 to 6, but 25 mJ/cm^2 is not adequate for the soot representative of position 1 (SNR too low). Thus, a third laser fluence of 100 mJ/cm^2 is selected. In this way, soot that is more difficult to heat can be probed, considering the measurements obtained at 55 and 100 mJ/cm^2. The T_M-F curves considering only these three laser fluences (25, 55, and 100 mJ/cm^2) are given in Fig. 6.11b. Because of the temperature criteria, for a given position, the calculation of $E(m_\lambda)$ and T_0 is performed using only two of the three laser fluences and corresponds to the absorption model of the SP-LII (Eq. (4.7)). It has

to be noted that the laser fluences selected here are lower than the ones selected for the CH_4/air flame of Chapter 5, as the temperatures reached are higher for a given fluence, indicating more absorbing particles in the present flame.

The computed values for the flame positions identified in Fig. 6.2 are given in Table 6.2. Figures 6.12 and 6.13 compare the spatial distribution of $E(m_\lambda)$ and T_0 obtained with three laser fluences ($E(m_\lambda)_{SP-LII}$), all fluences ($E(m_\lambda)_{fit}$), along with their relative difference. The estimation with only three laser fluences slightly deteriorates compared to the one with all fluences. The maps are less homogeneous, and some locations on the lower part of the flame are missing. This happens because 25 mJ/cm^2 is not enough to induce enough LII signal for the less absorbing particles, while 100 mJ/cm^2 brings the temperature above 3500 K for the most absorbing particles. The distribution of relative deviation of $E(m_\lambda)$ and T_0 are fit to Gaussian functions to quantify the differences between the "three fluences" and "all fluences" maps. Concerning $E(m_\lambda)$, the mean is +0.3% (+0.002) with a standard deviation of 4% (0.024). For T_0, the mean is -0.5% (-10 K) with a standard deviation of 2.1% (45 K). Therefore, the difference between considering a limited number of laser fluence or more fluences is very low (negligible overestimation of $E(m_\lambda)$, and low underestimation of T_0).

	$\boldsymbol{E(m_\lambda)}$, $\boldsymbol{T_0}$ (K)		$\boldsymbol{d_p}$ (nm)	
Position	3 laser fluences	All laser fluences	T < 3500 K	All T
P1	0.35, 1937	0.34, 1952	12	12
P2	0.53, 1854	0.47, 1932	18	18
P3	0.55, 2034	0.55, 2033	19	20
P4	0.59, 2123	0.58, 2142	30	29
P5	0.68, 2047	0.67, 2065	48	47
P6	0.53, 2100	0.52, 2122	15	15

Table 6.2: $E(m_\lambda)$ and T_0, obtained considering three laser fluences and all fluences. The d_p values obtained by considering only temperatures below 3500 K, as well as those calculated using all temperature values, are reported. Results are given for the six positions represented in Fig. 6.2.

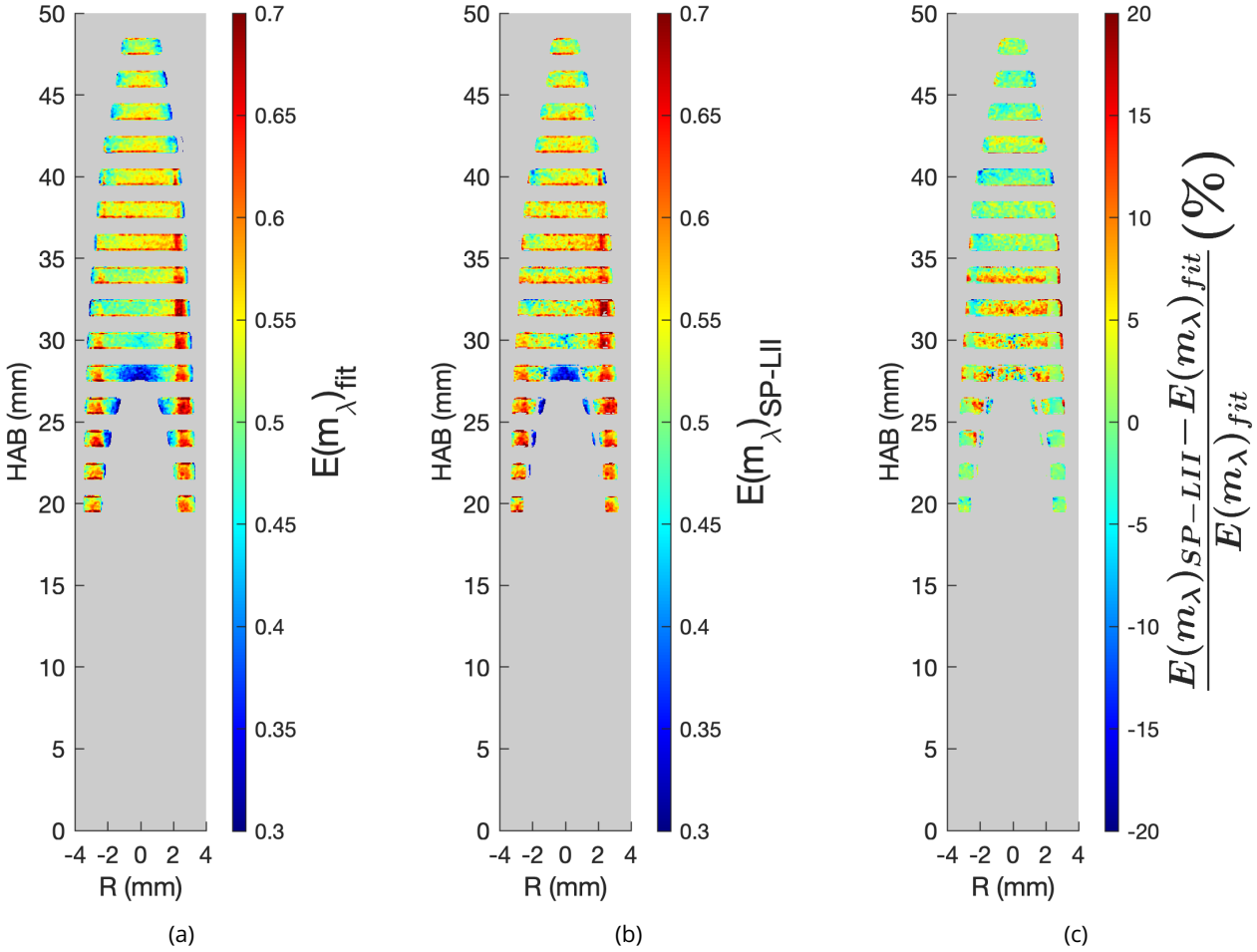

Figure 6.12: Soot absorption function determined with: (a): all measurements, and (b): measurements at 25, 55, and 100 mJ/cm^2. In both cases, only measurements with a temperature below 3500 K are considered. (c): Relative difference between the two maps (b) and (a). Subscripts "SP-LII" and "fit" refer to the data obtained considering three laser fluences and all the fluences, respectively.

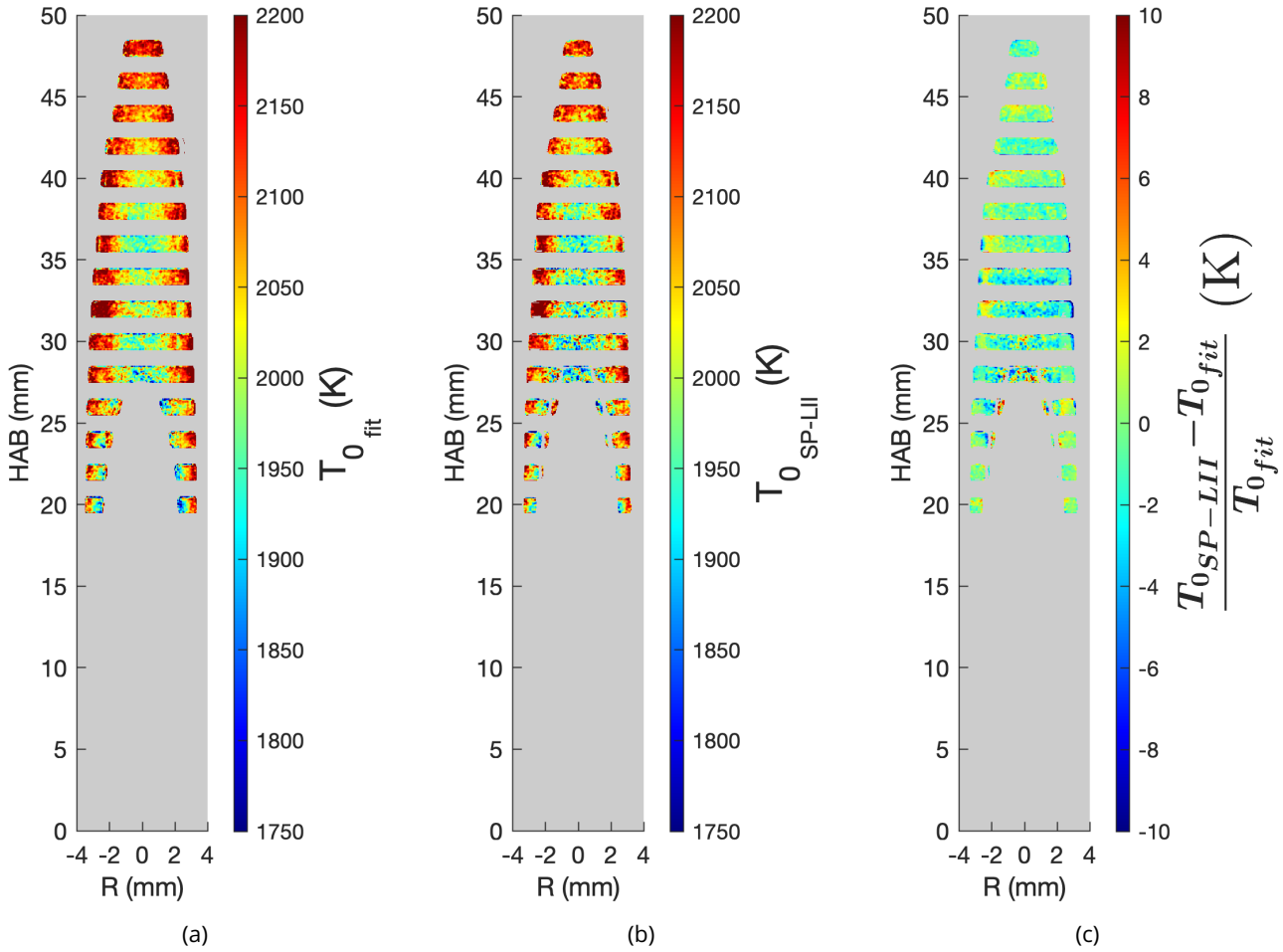

Figure 6.13: Gas temperature determined with: (a): all measurements having a temperature below 3500 K, and (b): measurements at 25, 55, and 100 mJ/cm^2 having a temperature below 3500 K. (c): Relative deviation between the two maps (b) and (a). Subscripts "SP-LII" and "fit" refers to the data obtained considering three laser fluences, and all the fluences, respectively.

Soot primary particle diameter

d_p is computed by fitting the temperature decays (Sec. 3.4.4). Attempts to calculate d_p from the LII signal fit yielded inconsistent results, possibly due to insufficient temporal resolution (i.e., too few measurement points). Since temperature fitting provided consistent results and required fewer measurements, no effort was made to improve the temporal discretisation of the LII signal when using camera measurements.

For the calculation of d_p, a laser fluence of 100 mJ/cm^2 is considered. Such laser fluence value was selected to heat enough the particles with low absorption function values. However, this fluences makes the highly absorbing particles to reach peak temperatures above the set limit of 3500 K. To control the validity of the criterion on temperature (T < 3500 K) for the d_p determination, values of d_p obtained considering all measurements and the ones only below 3500 K are compared. Figure 6.14 represents the reduced soot temperature $ln\left(\frac{T(t)-T_0}{T_M-T_0}\right)$ versus time for the six reference flame locations. The gas temperature used is the one obtained considering only three laser fluences. The computed values of d_p for these positions are given in Table 6.2.

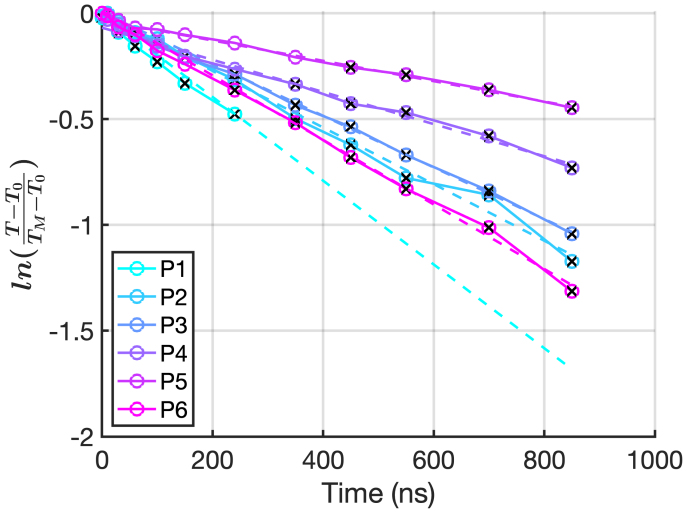

Figure 6.14: $ln\left(\frac{T-T_0}{T_M-T_0}\right)$ versus time after the laser pulse (solid line with ○). Each colour corresponds to a different pixel location (Fig. 6.2). The dashed lines represent the linear regression obtained considering the temperatures below 3500 K. The x symbols represents measurements below 3500 K.

Two-dimensional fields of d_p obtained considering all temperatures is compared to the one obtained considering only the temperatures below 3500 K in Fig. 6.15. When all temperatures are considered, d_p is always smaller than when considering only results with T < 3500 K, probably due to the accelerated cooling at early instant caused by stronger thermal losses. Globally, there is little differences in d_p: the fit to a Gaussian of the distributions of difference and relative deviation gives no deviation (same average) but a standard deviation of 1 nm, and 5% respectively. The difference is more pronounced in the wing region, where it can locally overcome 10 nm. The overall small differences found can be attributed to the important number of measurements realised (12 different instants) for which the temperature is below 3500 K, allowing to greatly recover the signal decay.

It has to be pointed out that because of the high peak temperature reached by the more absorbent soot particles, it is possible that these particles have undergo a partial loss of matter leading to a reduction of their size. In that case, d_p may be underestimated for the ones reaching temperature above 3500 K.

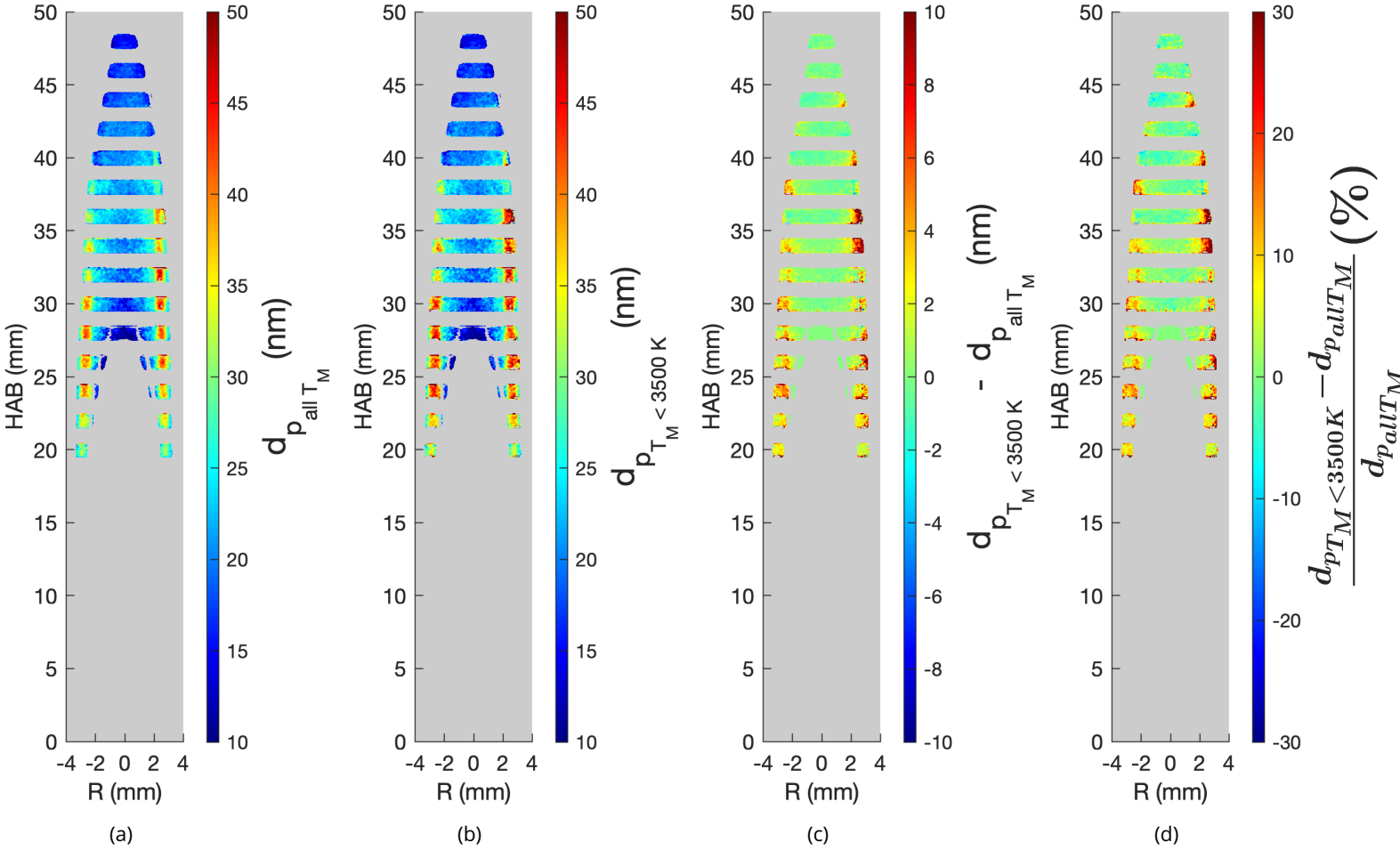

Figure 6.15: Soot primary particle diameter determined from: (a): all temperature measurements, and (b): measurements having a temperature below 3500 K. (c) and (d): Difference, and relative deviation between the two maps (b) and (a), respectively. Subscripts "T_M < 3500 K" and "all T_M" refers to the d_p obtained considering only T_M below 3500 K, and considering all T_M, respectively.

Soot volume fraction

Once $E(m_\lambda)$ is known, f_v is computed at prompt ($T = T_M$) by AC-LII using Eq. (3.23). Figure 6.16 gives f_v computed for four laser fluences: 25, 55, 100, and 160 mJ/cm^2. f_v should be independent of the laser fluence, with maybe a decrease for the highest fluences due to mass loss by phase change. The results show that f_v increases with the laser fluence, illustrating the so-called f_v anomaly [196, 210, 226, 262]. Figure 6.17 better illustrates the fluence dependence of f_v: for the six reference positions, f_v increases with the laser fluence up to a factor of ~2.8.

Elements of explanation for the f_v anomaly are discussed in this thesis. The following subsection addresses the effect of background subtraction on the f_v anomaly and proposes a correction for it. Additionally, Annex G shows that the f_v anomaly may be caused by a polydispersion of temperature in the probe volume.

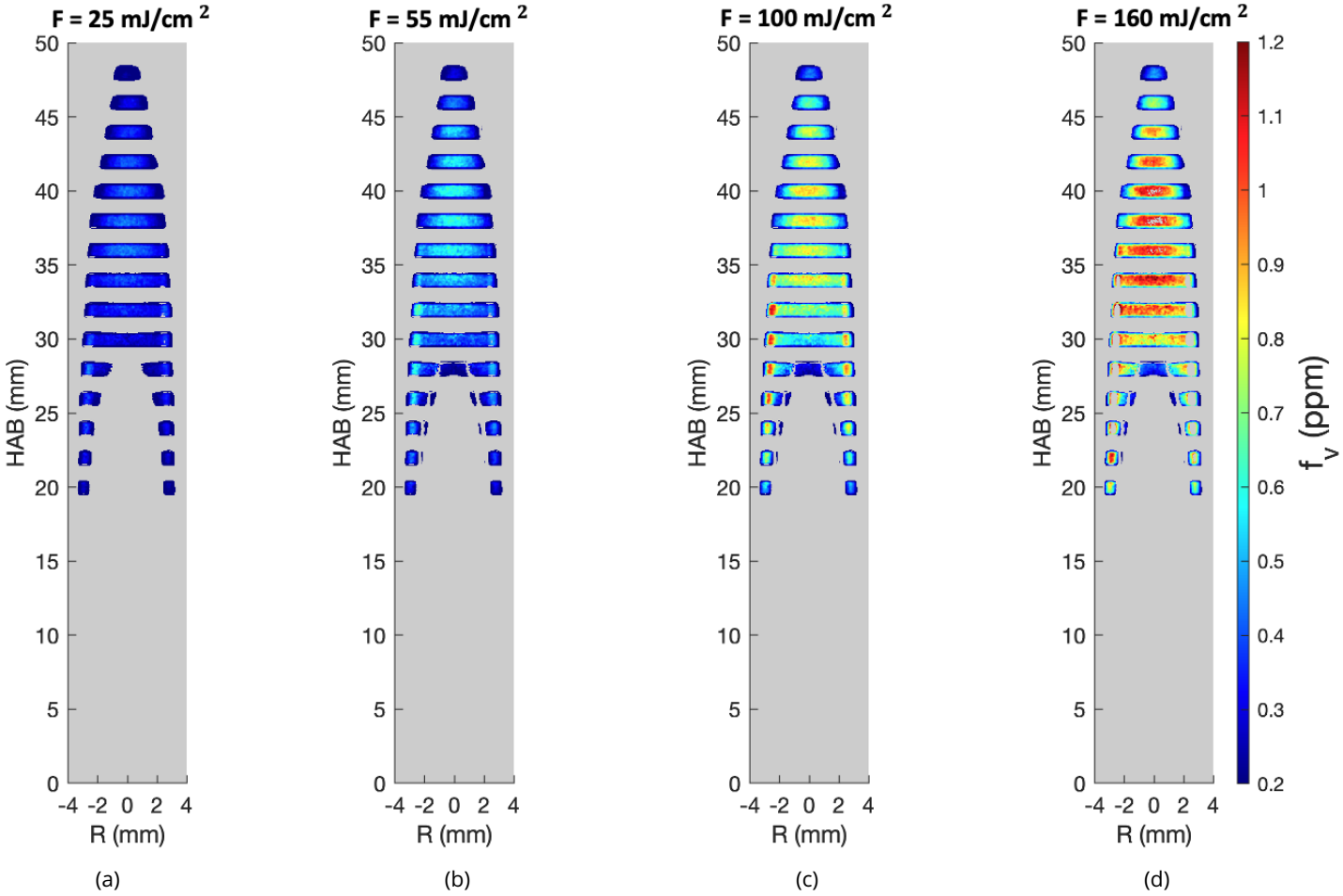

Figure 6.16: Soot volume fraction for different laser fluences: (a): 25, (b): 55, (c): 100, and (d): 160 mJ/cm^2. The spatial variation of $E(m_\lambda)$ is accounted for, and is the one computed considering three laser fluence (Fig. 6.12b). In figure (d), estimations are not available on the flame wings due to camera saturation.

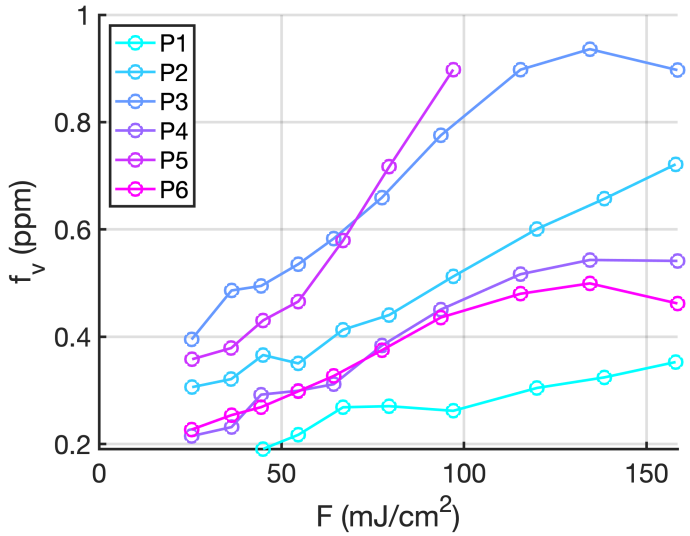

Figure 6.17: Soot volume fraction versus the laser fluence. Each colour corresponds to a different pixel location (Fig. 6.2).

6.3.2 Background subtraction: impact, correction procedure and application

This subsection examines the impact of background subtraction on the LII signal and its effect on LII-derived quantities, with a particular focus on f_v to determine whether it can explain the experimentally observed f_v anomaly. To address this, a theoretical investigation is first conducted. Then, a post-processing procedure is introduced to correct for the background subtraction. Finally, this correction method is applied to experimental data, and its effects on $E(m_\lambda)$, T_0, f_v, and d_p are discussed.

Theoretical illustration

The background signal, measured when the laser is not applied, is generally subtracted from the LII signal measured after the laser irradiation to discriminate the part of the signal due to the laser irradiation. This allows the removal of parasite signals originating from regions other than the probe volume, but it also removes the non-laser-induced incandescence signal of the probe volume. This issue is described in the following, along with a discussion of its consequences. Figure 6.18 schematically reproduces the different contributions to the measured signal with and without laser irradiation.

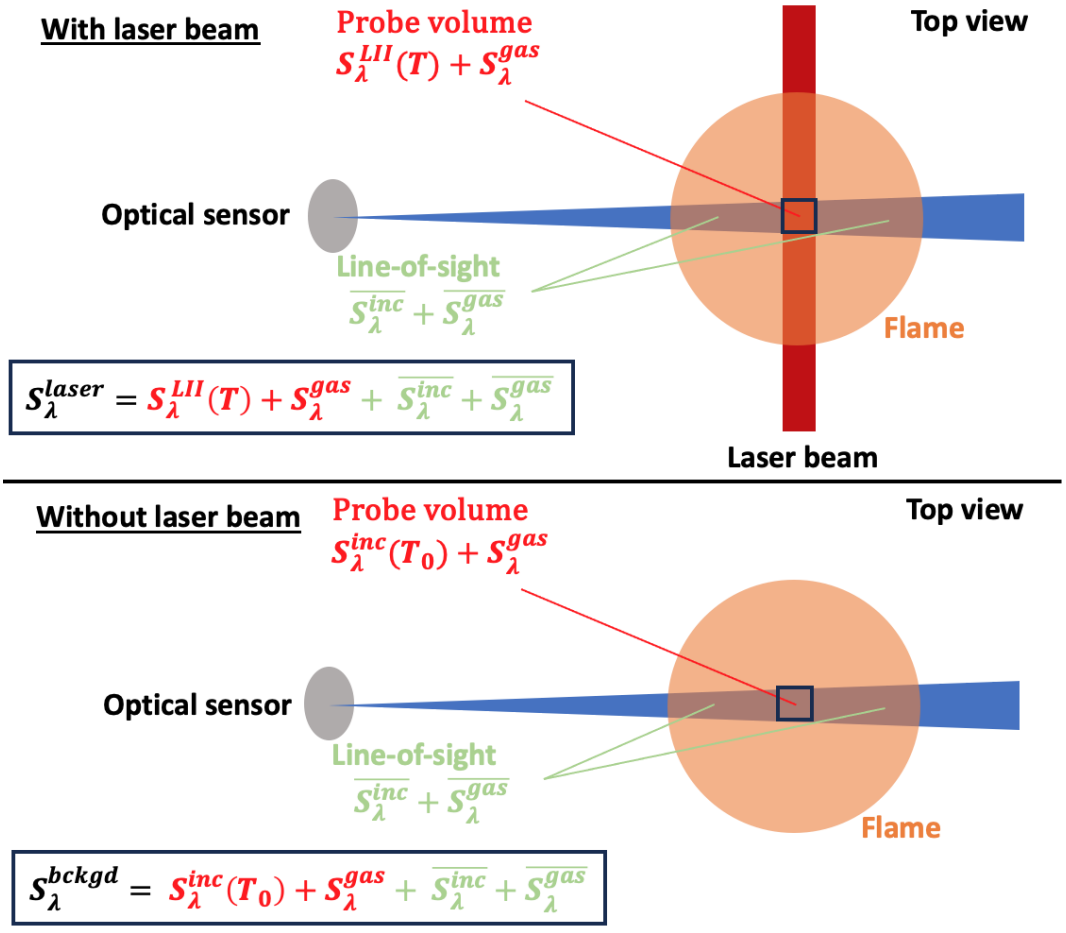

Figure 6.18: Schemes illustrating the origin of the signal measured in a flame with an optical sensor in the presence of a laser beam (top scheme) and without a laser beam (bottom scheme).

In the presence of a laser beam, the signal S_λ^{laser} measured for a wavelength λ, is:

$$S_\lambda^{laser} = S_\lambda^{LII}(T) + \overline{S_\lambda^{inc}} + S_\lambda^{gas} + \overline{S_\lambda^{gas}}, \tag{6.1}$$

The notations of this subsection are the following:

- $S_\lambda^{inc}(T_0)$ is the incandescence signal of the soot in the probe volume heated at the gas temperature T_0,
- $S_\lambda^{LII}(T)$ denotes the total soot incandescence in the probe volume in the presence of laser irradiation. It has to be noted that $S_\lambda^{LII}(T)$ = $S_\lambda^{inc}(T)$. The superscript ^{LII} is used to underline that a laser pulse is used.
- $\overline{S_\lambda^{inc}}$ is the incandescence signal of the soot integrated over the line-of-sight of the optical sensor (excluding the probe volume), i.e. in front of and behind the probe volume.
- S_λ^{gas} and $\overline{S_\lambda^{gas}}$ are the non-incandescence part of the signal in the probe volume and over the line-of-sight of the optical sensor (excluding the probe volume), respectively. These non-incandescence signals originate from the gaseous species that are in the line of sight of the optical sensor. S_λ^{gas} is assumed to be identical with and without the presence of a laser beam: no fluorescence or any other processes affect the gaseous species. This is ensured by the choice of the laser wavelength high enough (1064 nm) to not excite the gaseous species, by the selection of laser fluences low enough not to induce a strong C_2 and C_3 fluorescence emission, and by the selection of the spectral collection windows excluding the C_2, and C_3 emission bands.

The undesirable part of the incandescence signal, which does not originate from the incandescence of the soot in the probe volume (blue region in the scheme of Fig. 6.18), and the non-incandescence signal is removed by subtracting the measured signal without the laser beamS_λ^{bckgd}:

$$S_\lambda^{bckgd} = S_\lambda^{inc}(T_0) + \overline{S_\lambda^{inc}} + S_\lambda^{gas} + \overline{S_\lambda^{gas}} \tag{6.2}$$

Subtracting Eq. (6.1) and Eq. (6.2) gives:

$$\begin{aligned} S_\lambda^{LII^*} &= S_\lambda^{laser} - S_\lambda^{bckgd} \\ &= S_\lambda^{LII}(T) - S_\lambda^{inc}(T_0) \end{aligned} \tag{6.3}$$

By doing so, the part of the incandescence signal originating from the probe volume at flame temperature $S_\lambda^{inc}(T_0)$ is also removed, and the resulting signal $S_\lambda^{LII^*}$ is different from the total incandescence signal $S_\lambda^{LII}(T)$ in the probe volume. The omission of $S_\lambda^{inc}(T_0)$ is problematic when the heated soot reaches a temperature close to the initial temperature of the soot T_0, in other words, when it becomes problematic when the purely laser-induced incandescence signal has the same order of magnitude as the incandescence emission at T_0 [240, 250].

To illustrate the effect of background subtraction (considering $S_\lambda^{LII^*}$ instead of S_λ^{LII}) on the LII signal, as well as on the temperature and the soot volume fraction, the theoretical expression of the LII signal (Eq. 3.19) is considered. In addition, For simplicity in notation, it is assumed that $12\pi hc_{light}^2 f_v L_{laser} C_{calib,\lambda} E(m_\lambda)\Delta\lambda = 1$:

$$S_\lambda^{LII}(T) = \frac{1}{\lambda^6} e^{-\frac{hc_{light}}{k_B \lambda T}}, \tag{6.4}$$

Using this expression, $S_\lambda^{LII}(T)$ is computed at 578 and 716 nm and for soot temperatures from 2300 to 4500 K. Then, $S_\lambda^{LII^*} = S_\lambda^{LII}(T) - S_\lambda(T_0)$ is computed for different gas temperatures: 1800, 2000, and 2200 K.

The soot temperature T^* is recomputed by 2C-LII from $S_\lambda^{LII^*}(T)$ at 578 and 716 nm:

$$T^* = \frac{hc_{light}}{k_B}\left(\frac{1}{\lambda_2}-\frac{1}{\lambda_1}\right)\frac{1}{\ln\left(\frac{S_{\lambda_1}^{LII^*}}{S_{\lambda_2}^{LII^*}}\left(\frac{\lambda_1}{\lambda_2}\right)^6\right)}. \tag{6.5}$$

Finally, the estimated soot volume fraction ${f_v}^*$ obtained from $S_\lambda^{LII^*}$ and T^* is computed with Eq.(3.23). T^* and ${f_v}^*$ represents what would be experimentally obtained by considering the background subtracted signals $S_\lambda^{LII^*}(T)$ instead of $S_\lambda^{LII}(T)$.

The normalised signals $\frac{S_\lambda^{LII^*}(T)}{S_\lambda^{LII}(T)}$ (the pure LII signal over total incandescence signal) are given in Fig. 6.19 versus the soot temperature and for the three gas temperature. The temperature difference $T^* - T$ is plotted in Fig. 6.20a, and ${f_v}^*$ is normalised by dividing it with the arbitrary set soot volume fraction and is presented in Fig. 6.20b.

As expected, the error of the LII signal increases with T_0 and decreases with T. The error is below 5% for all the gas temperatures investigated once T is above 3500 K. However, it rapidly increases for lower soot temperatures. The error on the signal also depends on the wavelength, with a higher signal underestimation for the higher wavelengths as the background is larger at 716 nm than at 578 nm at flame temperatures. This behaviour explains the temperature overestimation of Fig. 6.20a. This overestimation decreases with increasing T. It approaches 9% for the worst case studied here (T_0 = 2200 K and T = 2300 K).

Background subtraction always overestimates the soot temperatures and underestimates the incandescence signal. According to Eq.(3.23), both effects induce an underestimation of the estimated soot volume fraction. It results in a large error on ${f_v}^*$ than on T^* or $S_\lambda^{LII^*}$. In the worst case, f_v is underestimated by more than 80%, and is still $\sim$ 10% for T = 3500 K and T_0 = 2200 K.

It has to be reminded that this simple analysis does not account for the high-temperature effects, such as sublimation, which is known to decrease f_v once activated ($\sim$ 3500 K according to Fig. 6.11) high soot temperature are reached. Therefore, if no other effects are considered, it appears that the true soot volume fraction might be underestimated regardless of the soot temperature.

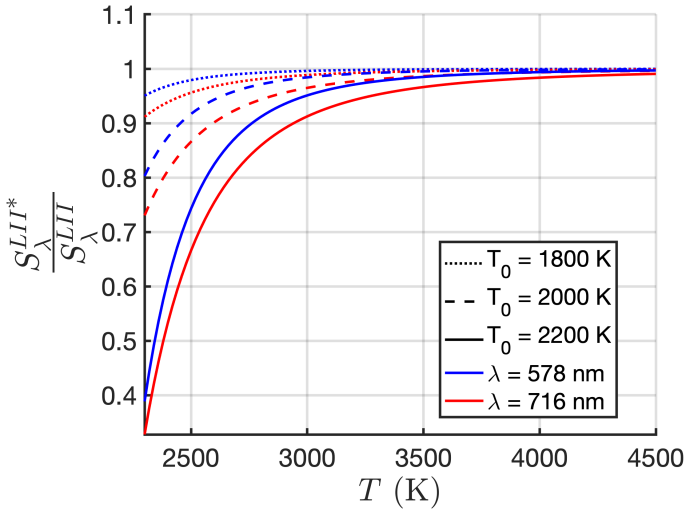

Figure 6.19: Ratio of the background subtracted (purely LII) signal $S_\lambda^{LII^*}$ to the total incandescence signal S_λ^{LII} as a function of laser-heated soot temperature. Results are given for two wavelengths, 578 nm (blue) and 716 nm (red), and for three local gas temperatures: 1800 K (dotted lines), 2000 K (dashed lines), and 2200 K (solid lines).

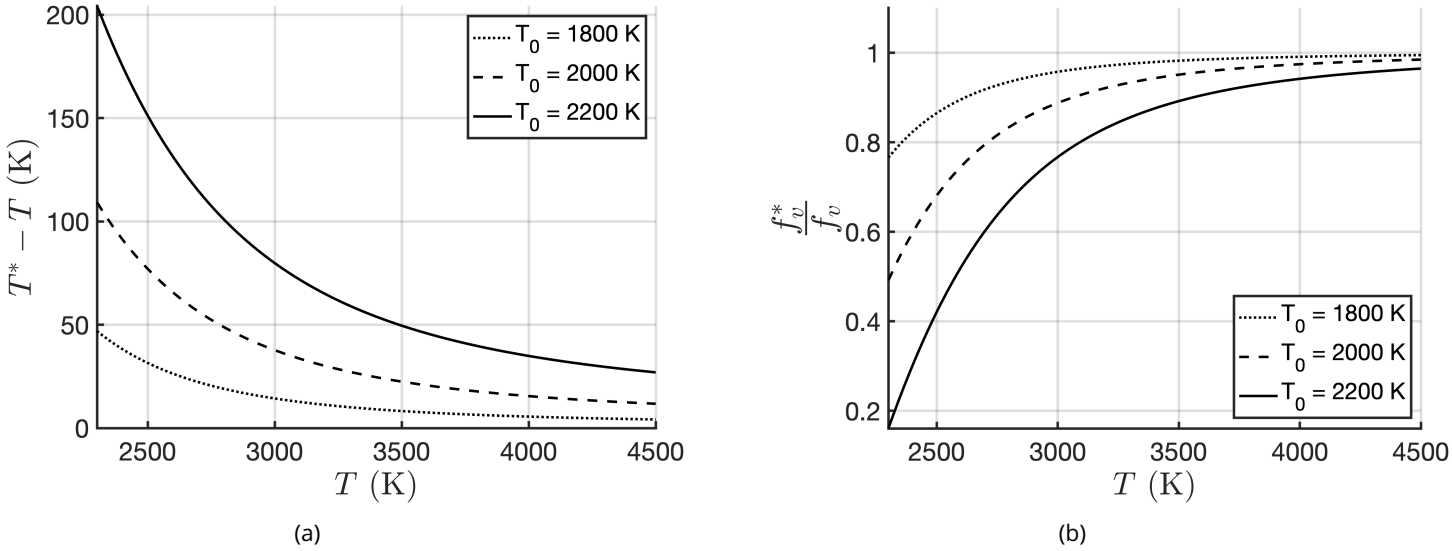

Figure 6.20: (a): Difference between soot temperature T^* estimated by 2C-LII from the background-subtracted signals and true laser-heated soot temperature T. (b): Ratio of the soot volume fraction $f_v{}^*$ estimated considering T^* and the background subtracted signals $S_\lambda^{LII^*}$ to the true soot volume fraction f_v. Results are given versus the true soot temperature and for three local gas temperatures: 1800 K (dotted lines), 2000 K (dashed lines), and 2200 K (solid lines).

These theoretical results show that the background subtraction has a moderate effect on the estimation of T and S_λ^{LII} but an important effect on f_v. The importance of the errors induced depends on both the soot and gas temperature, which have higher impacts when both temperatures are close. This indicates that when performing measurements where the difference between T_0 and T is only a few hundred kelvins, it is highly preferable to account for the background subtraction. As in this thesis, low laser fluences (low peak temperatures) are considered, it was decided to correct for the background subtraction. Therefore, in the following, a correction procedure is proposed and applied to experimental data to exhibit the effect background subtraction has on f_v, but also on $E(m_\lambda)$, T_0, and d_p.

Correction procedure

A correction procedure to retrieve $S_\lambda^{LII}(T)$ from the experimentally obtained background-subtracted signal $S_\lambda^{LII^*}(T)$ is proposed in the following. From the expression of the LII signal (Eq. (3.19)), $S_\lambda^{LII^*}(T)$ can be expressed as:

$$S_\lambda^{LII^*}(T) = S_\lambda^{LII}(T) - S_\lambda^{inc}(T_0) = \alpha_\lambda(e^{-\frac{hc}{k_B\lambda T}} - e^{-\frac{hc}{k_B\lambda T_0}}). \tag{6.6}$$

where $\alpha_\lambda = 12\pi hc^2 f_v L_{laser} C_{\lambda,calib} \frac{E(m_\lambda)}{\lambda^6}\Delta\lambda$.
As $S_\lambda^{LII}(T) = \alpha_\lambda e^{-\frac{hc}{k_B\lambda T}}$, $S_\lambda^{inc}(T_0) = \alpha_\lambda e^{-\frac{hc}{k_B\lambda T_0}}$ can be expressed as:

$$S_\lambda^{inc}(T_0) = S_\lambda^{LII}(T)\frac{e^{-\frac{hc}{k_B\lambda T_0}}}{e^{-\frac{hc}{k_B\lambda T}}} = S_\lambda^{LII}(T)e^{-\frac{hc}{k_B\lambda}\left(\frac{1}{T_0}-\frac{1}{T}\right)}. \tag{6.7}$$

Combining Eq. (6.6) and Eq. (6.7) gives:

$$S_\lambda^{LII}(T) = \frac{S_\lambda^{LII^*}(T)}{1 - e^{-\frac{hc}{k_B\lambda}\left(\frac{1}{T_0}-\frac{1}{T}\right)}}. \tag{6.8}$$

$S_\lambda^{LII}(T)$ is computed with Eq. 6.8 which requires the experimentally determined background subtracted LII signal $S_\lambda^{LII^*}(T)$, but also the soot temperature after laser heating (for a prompt detection, $T = T_M$) and the gas temperature which are both *a priori* unknown. Therefore, an iterative procedure is necessary.

The iterative procedure adopted is described in Fig. 6.21. The procedure contains two nested "while" loops, one for T_M that is estimated by 2C-LII, and one for T_0 that is calculated by fitting T_M to F (so requires T_M at different laser fluences). As pointed out by Snelling et al. [240], the loop for $T = T_M$ converges in a few iterations while the one for T_0 added in this work fails for some pixel positions. It has to be noticed that the correction procedure is more complex than in [240], but it does not require to know or assume the gas temperature value.

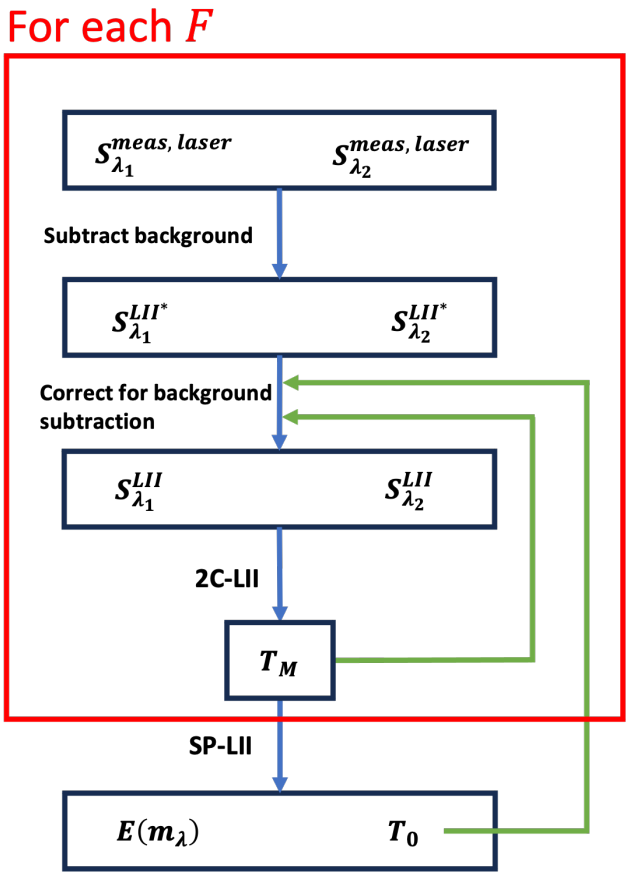

Figure 6.21: Scheme of the correction procedure adopted to account for the background subtraction.

Application to experimental data

The previous correction procedure for the background subtraction is applied to experimental data collected on the Yale 60% reference flame. Results in terms of LII signal, T_M, $E(m_\lambda)$, T_0, f_v and d_p are presented with and without the correction. For the computation of $E(m_\lambda)$ and T_0, only three laser fluences are considered: 25, 55, and 100 mJ/cm^2, and only the measurements with T_M < 3500 K are considered.

LII signal and soot peak temperature

Figure 6.22a shows the uncorrected and corrected LII signals at 578 nm as a function of flame radius at HAB = 28 mm for the ten laser fluences considered. As expected, at higher fluences, the correction has little effect, as non-LII incandescence is negligible compared to the pure LII signal. However, at lower fluences, the correction adds up to ∼10% of the LII signal at 578 nm and up to ∼20% at 716 nm (not shown). The stronger correction at 716 nm indicates

an impact on T_M, which is plotted in Figure 6.22b for all fluences. For the lowest fluence, the corrected temperatures are about 100 K lower, affecting the estimates of $E(m_\lambda)$ and T_0, and consequently f_v and d_p.

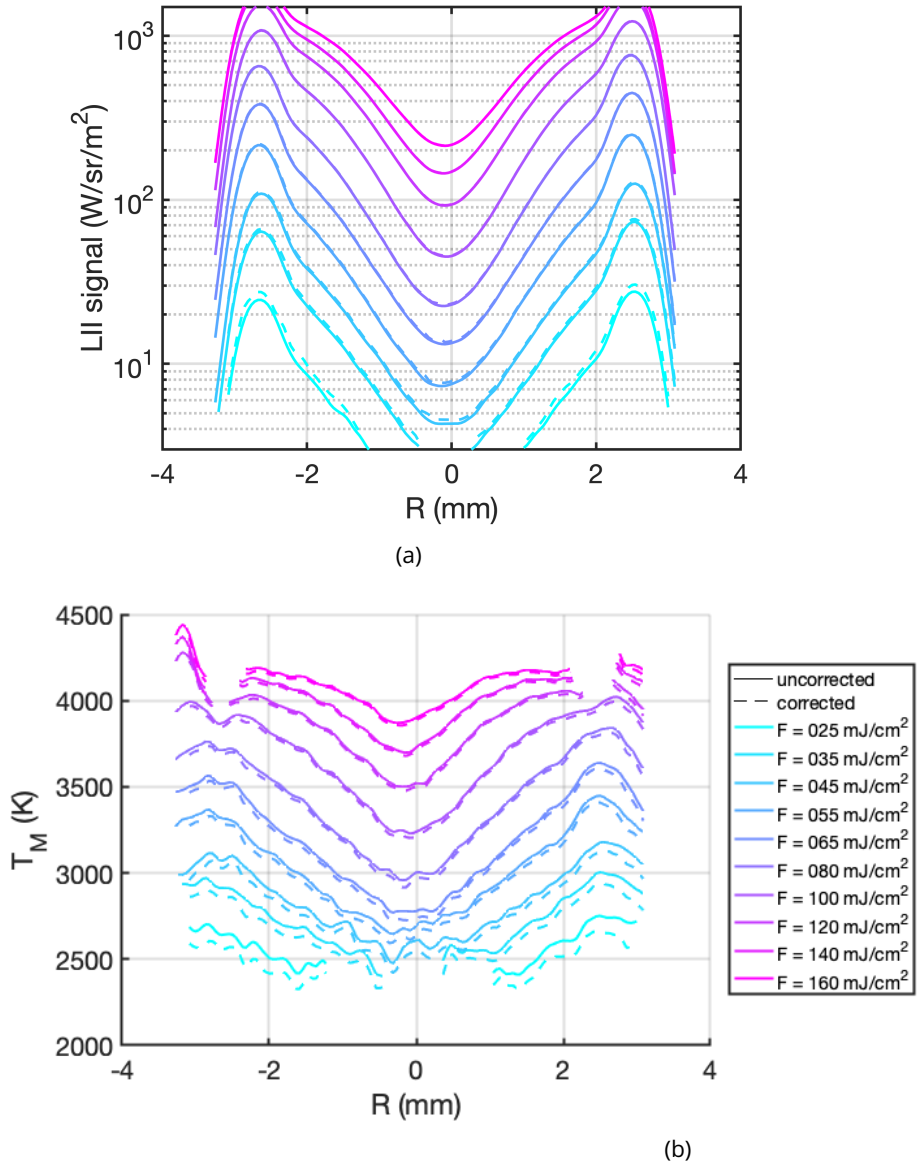

Figure 6.22: (a): LII signal recorded at 578 nm versus flame radius at HAB = 28 mm. (b): Soot peak temperature computed by 2C-LII versus flame radius at HAB = 28 mm. Colours from cyan to magenta represent the different laser fluences from 25 to 160 mJ/cm^2. The continuous line represents uncorrected data, while the dashed line indicates data that has been corrected for background subtraction. To smooth the visualisation, the pixels have been averaged in super-pixels of 3x3.

Soot absorption function and gas temperature

The relative difference between the corrected and uncorrected $E(m_\lambda)$ and T_0 are given in Fig. 6.23. The radial cross sections are presented in Fig. 6.24 for different HABs (20, 28, 42, and 48 mm). Globally, the correction induces a $\sim$6% increase in $E(m_\lambda)$ and a $\sim$5% ($\sim$100 K) decrease in T_0. This is explained by the fact that at low laser fluences, the corrected T_M are lower than uncorrected ones, inducing a stronger slope of T_M versus F (stronger $E(m_\lambda)$) and a lower ordinate at origin (lower T_0).

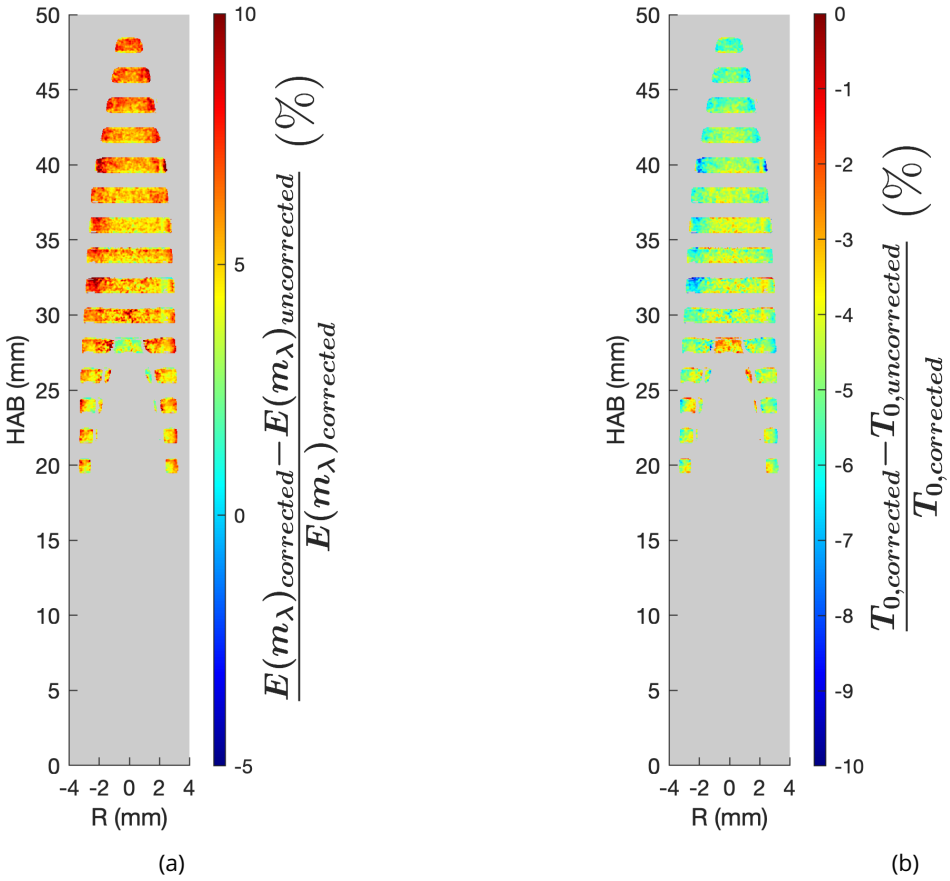

(a) (b)

Figure 6.23: Relative difference between corrected and uncorrected (a): absorption function, (b): gas temperature.

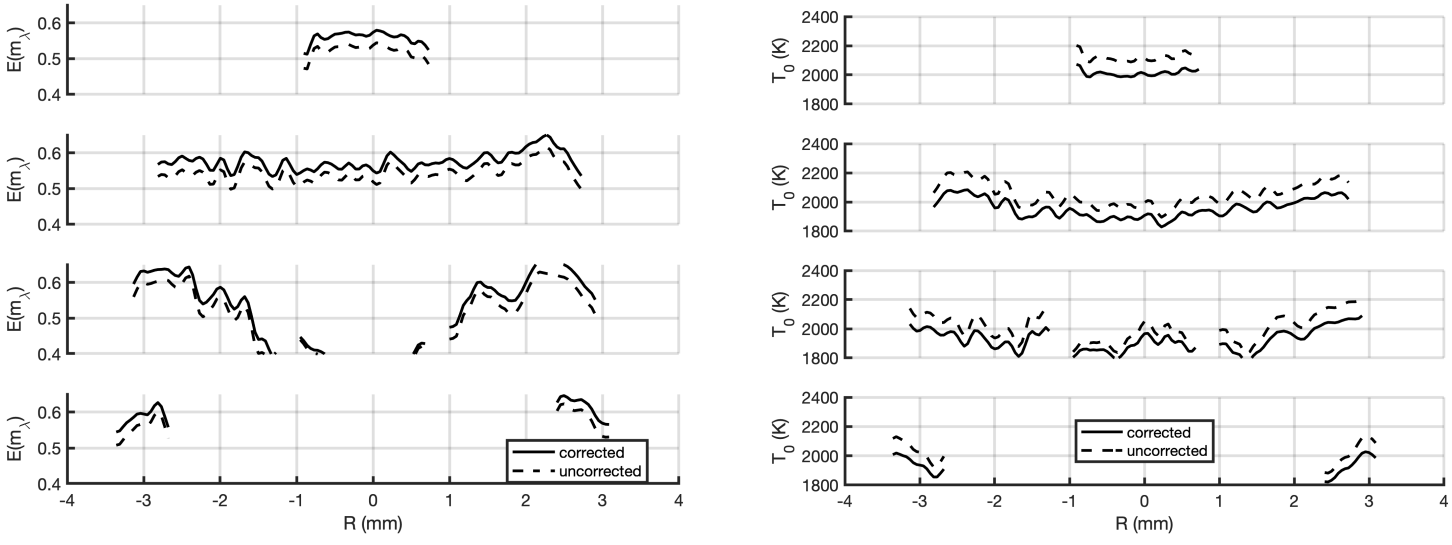

(a) (b)

Figure 6.24: Radial evolution of (a): absorption function, and (b): gas temperature for four HAB, from bottom to top: 20, 28, 42, and 48 mm. The continuous and dashed lines are for corrected and uncorrected data, respectively.

Soot primary particle size

The soot primary particle diameter d_p may also be affected by the background subtraction as its determination

requires soot temperature at different delays after the laser pulse and the gas temperature. Figure 6.25a gives the 2D map of the relative difference between the corrected and uncorrected data, and Fig. 6.25b represents the radial cross evolution of d_p (corrected and uncorrected) for four HABs.

The effect of background subtraction is to underestimate d_p. In the present conditions, the effect of the background correction on d_p is relatively weak and rarely overcomes 10%, and it results in, on average, a 4% increase after correction. This can be explained by:

- The measurements were conducted at a laser fluence of $\sim$100 mJ/cm^2. Consequently, the soot temperatures at prompt or immediately following the laser pulse are significantly higher than the gas temperature, meaning that the effects of background subtraction are negligible.
- The background subtraction leads to an overestimation of both the soot temperature and the gas temperature. While an overestimation of the soot temperature induces an underestimation of d_p, an overestimation of T_0 tends to overestimate d_p. Thus, these overestimations partially compensate for each other.

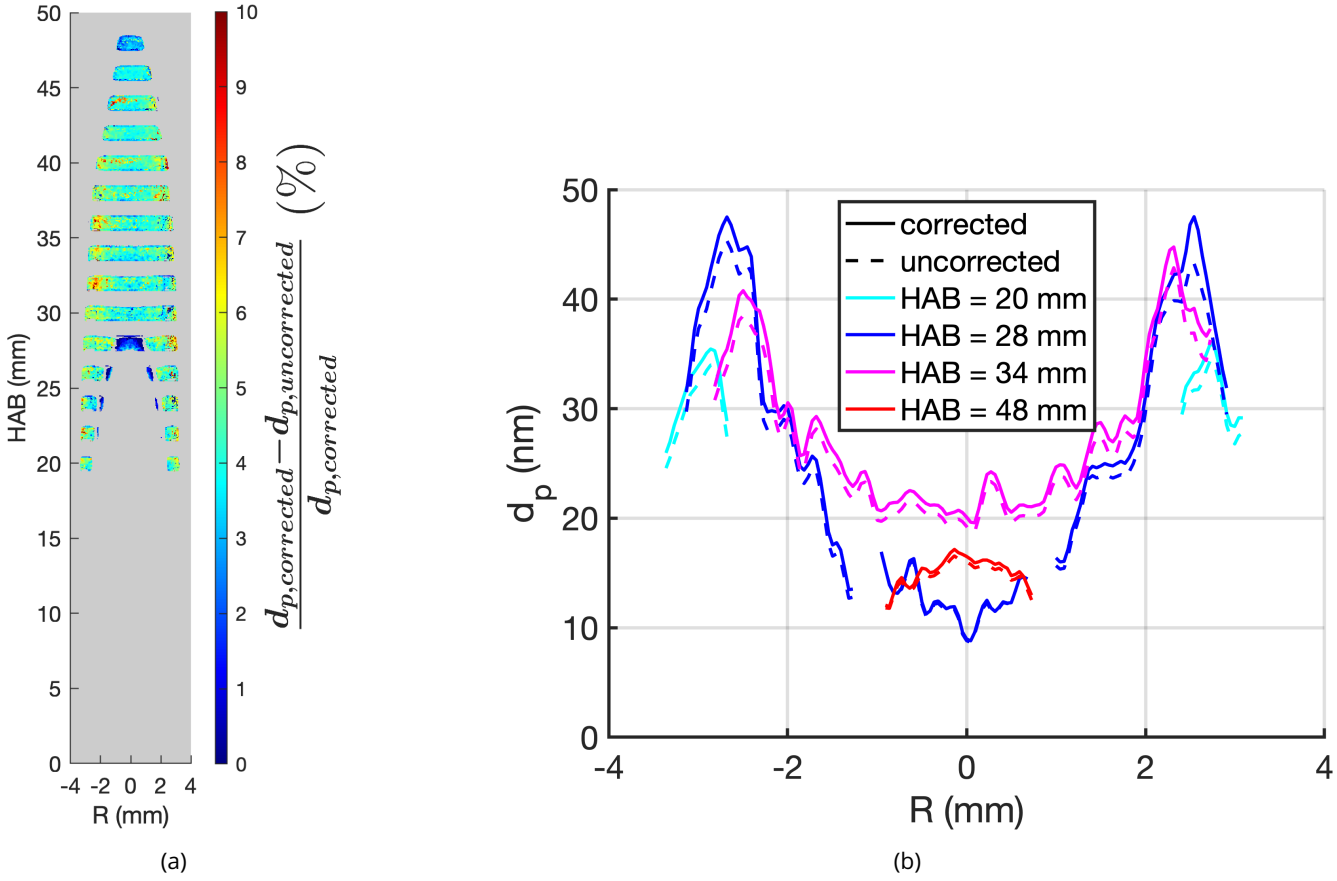

Figure 6.25: (a): Relative difference between corrected and uncorrected soot primary particle diameter. (b): Radial evolution of the soot primary particle diameter for four HABs: 20 mm (cyan), 28 mm (blue), 42 mm (magenta), and 48 mm (red). The continuous and dashed lines are for corrected and uncorrected data, respectively.

Soot volume fraction

Figure 6.26a gives the corrected and uncorrected f_v versus the laser fluence. After correction, f_v still increases with the laser fluence, but by a reduced amount. The correction has two main effects. The first is that as the soot absorption function after correction is higher, f_v computed from Eq. (3.23) becomes lower than for uncorrected values. Secondly, at low laser fluences, the corrected f_v is higher (due to the increase in LII signal and decrease in

temperature estimations with the correction). This combination of effects results in a reduced fluence dependency at low laser fluences and a lower soot volume fraction for the laser fluences for which the background is negligible. The soot volume fraction computed from the corrected data for laser fluences of 25, 55, 100, and 160 mJ/cm^2 is presented as 2D maps in Fig. 6.27. This visualisation provides a comprehensive view of the correction's effects. The soot volume fraction obtained at 25 mJ/cm^2 now aligns more closely with that at 55 mJ/cm^2 compared to Fig. 6.16, while no significant differences are observed at higher laser fluences. This reduced fluence dependence at low laser fluence underlines the involvement of the background subtraction in the f_v anomaly. However, a strong laser fluence dependence remains between the estimation at low and high laser fluence, meaning that other phenomena are at stake.

Figure 6.26b gives the corrected f_v versus the corrected T_M and is normalised by the value of f_v estimated for T_M ~3100 K. Similarly to what has been seen in the previous chapter, it shows that the f_v anomaly is driven by the peak temperature rather than the laser fluence: after correction, f_v is contained in a $\pm$20% interval when T_M is below 3500 K, and steeply increases above this value. This is true for all the locations presented here, which are representative of different soot populations (different $E(m_\lambda)$ and d_p). This indicates that the phenomenon causing this abnormal increase in f_v could be linked to the soot peak temperature and that the activation threshold is ~3500 K.

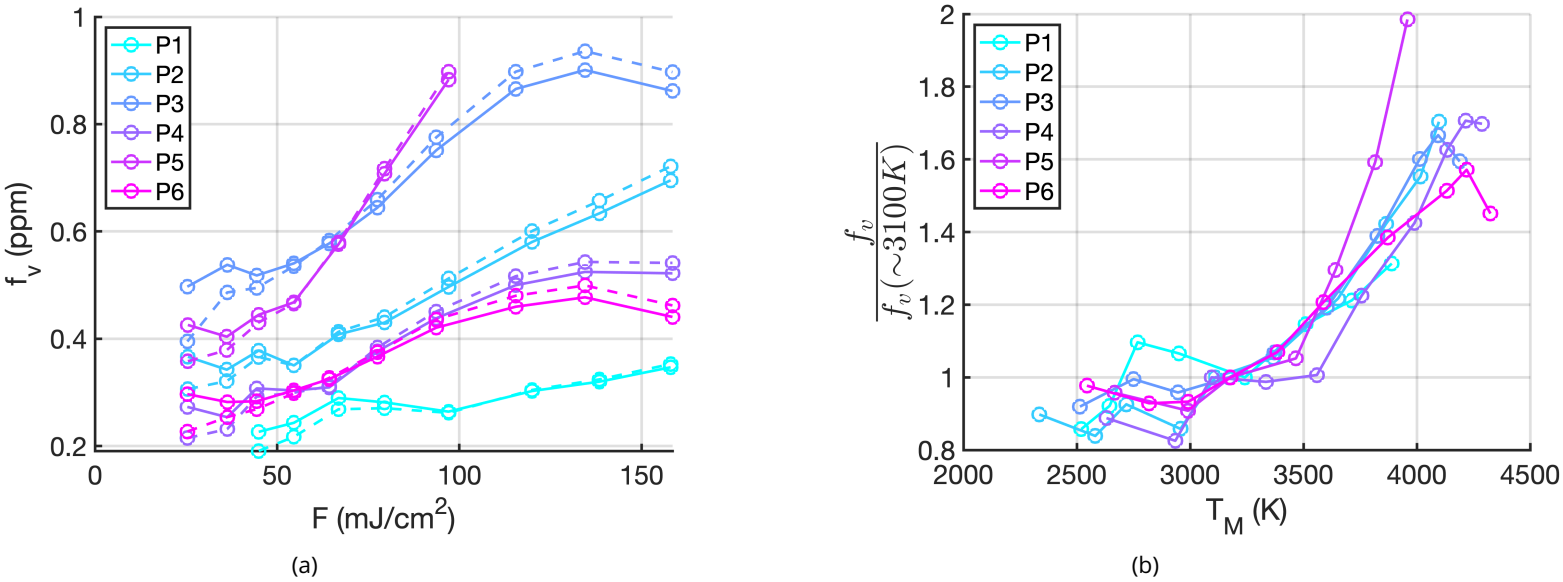

Figure 6.26: (a): Soot volume fraction versus laser fluence for the reference pixel locations. Data corrected for the background subtraction are given in solid lines, while uncorrected ones are in dashed lines. (b): $\frac{f_v}{f_v(\sim 3100K)}$. Each colour corresponds to a different pixel location (Fig. 6.2).

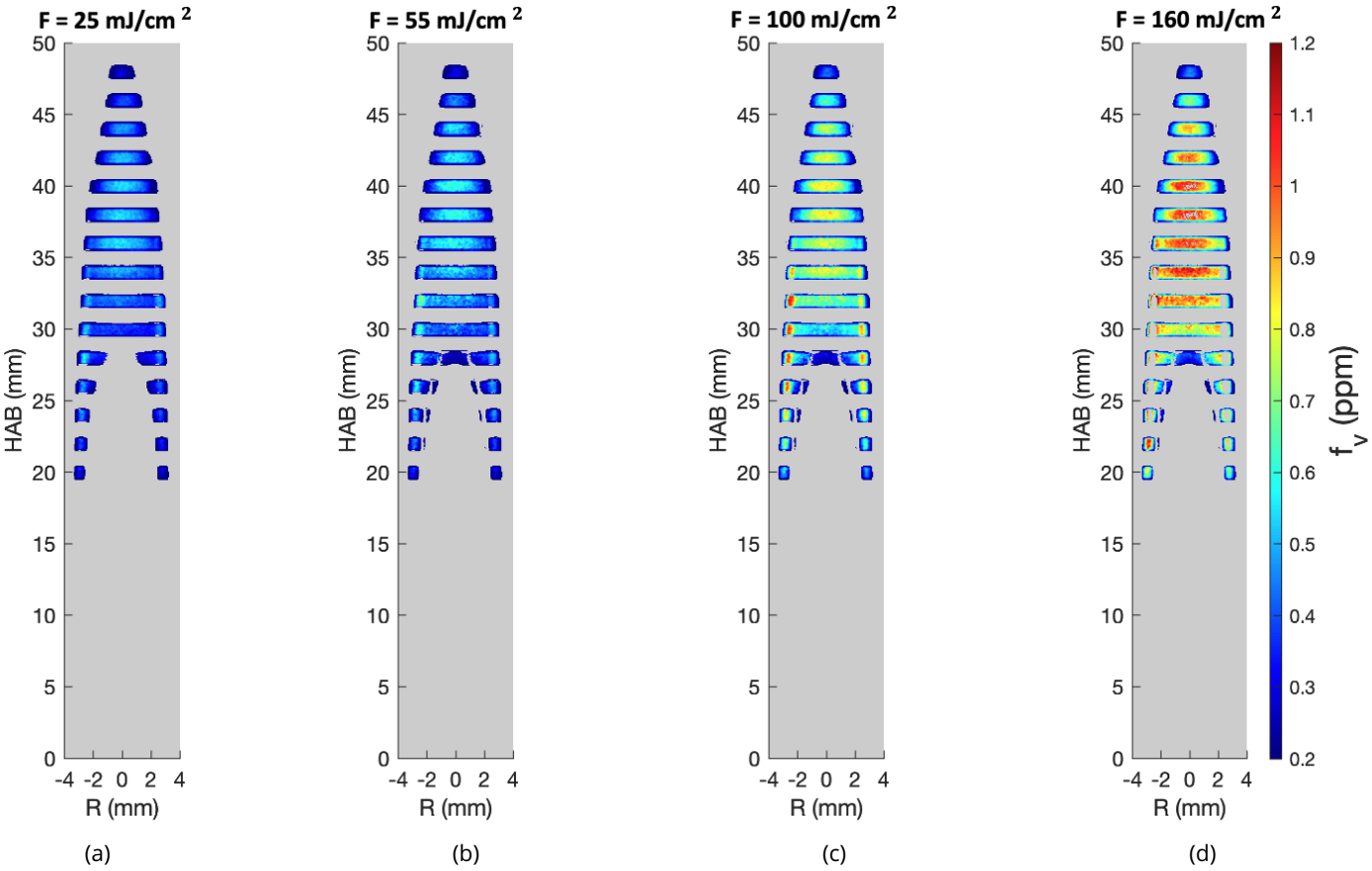

Figure 6.27: Soot volume fraction estimated by AC-LII for different laser fluences: (a): 25, (b): 55, (c): 100, and (d): 160 mJ/cm^2. The actual $E(m_\lambda)$ spatial distribution was considered. In figure (d), estimations are not available on the flame wings due to camera saturation. Data are corrected for background subtraction.

The question of which laser fluence should be selected for f_v measurements is not easily answered. On the one hand, low laser fluences should be preferred as alteration of soot properties and mass loss due to partial phase change of soot material is limited, and the background corrected data shows a relatively weak temperature-dependent behaviour. However, there is a non-uniform heating of the particles in the probe volume casing biased estimation of soot temperature toward hot soot and underestimation of f_v (Annex G). On the other hand, for moderate laser fluences (bringing soot temperature above 3500 K and just below the soot sublimation temperature), f_v shows a strong dependence on temperature and fluences. For the highest laser fluences, the temperature is more uniform as all soot particles reach the sublimation temperature, but there is an alteration of soot particles with a potential change in their properties and a reduction of their mass [247, 248, 262, 269, 270].

6.4 Benchmark with the literature data

In the previous sections, some guidelines have been provided to obtain $E(m_\lambda)$, T_0, f_v, and d_p. It was suggested to consider only the measurements for T_M < 3500 K and to apply an iterative procedure to account for the background effect on the T_M estimation, and, consequently all other desired quantities. This section compares the values of $E(m_\lambda)$, T_0, f_v, and d_p obtained in this work for the 60% Yale flame with those reported in the literature [146, 194, 216, 274–276] to estimate how the proposed strategy works compared to the state-of-the-art..

6.4.1 Soot absorption function $E(m_\lambda)$

The evolution of $E(m_\lambda)$ along the flame centreline is given Fig. 6.28 and the 2D map is provided in Fig. 6.29a. The axial evolution of $E(m_\lambda)$ in Fig. 6.28 shows a rapid increase in $E(m_\lambda)$ followed by a quasi plateau. The 2D map of Fig. 6.29a similarly shows a steep gradient in the lower part of the flame. This indicates that the maturation process is rapid. The lowest values are found in the flame inner part (similar to the results in the methane flame of Chapter 5). The maximum values are found in the flame wings with a maximum value of $E(m_\lambda)$ ~0.7. Overall, $E(m_\lambda)$ is mostly uniform in the flame to a value around 0.55-0.6. This quasi spatial homogeneity in $E(m_\lambda)$ indicates that the traditional practice of assuming a uniform value for $E(m_\lambda)$ to compute f_v does not introduce much error except for the wings and lower inner flame regions.

On the flame axis, (Fig. 6.28) $E(m_\lambda)$ shows an almost "plateau" behaviour approaching the flame tip. On the contrary, Yon et al. [51] (Fig. 2.16b) observed a different trend for $E(m_\lambda)$, whose value strongly increases when approaching the flame edges in a different laminar C_2H_4/air flame. However, the flame edge is characterised by a smaller signal-to-noise ratio (as f_v is lower), and small flame fluctuations can have a higher impact through averaging. Thus, caution should be considered when interpreting these results.

It has to be noted that Fig. 6.29a is not symmetrical: values at the right of the flame are higher than the ones at the left. This can be explained by the laser extinction through the flame width. The actual laser fluence on the left side of the flame is lower than on the right side (where the laser arrives). As the laser fluence without attenuation is used to compute $E(m_\lambda)$, lower estimations for $E(m_\lambda)$ can be expected where laser attenuation is important, i.e. where the path integrated soot volume fraction is important.

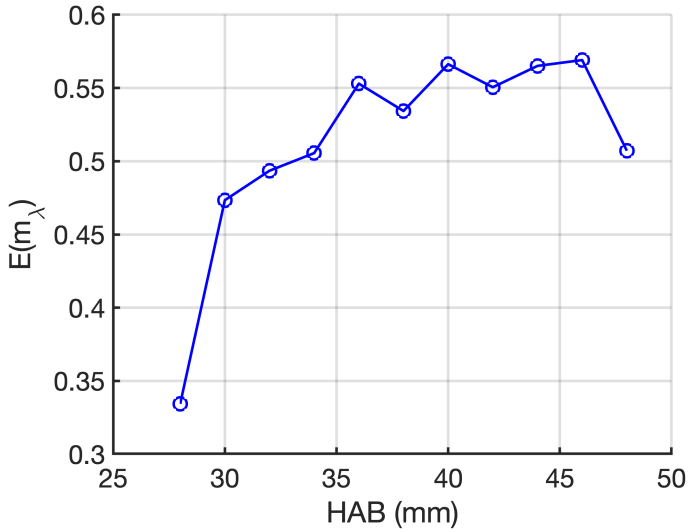

Figure 6.28: Axial evolution of the soot absorption function at 1064 nm.

.

For the considered flame, no $E(m_\lambda)$ results are found in the literature. However, Kempema et al. [146] obtained the spatial evolution of the soot dispersion exponent α_{disp} for the flame conditions studied here (Fig. 6.29b). The dispersion exponent gives the wavelength dependence of $E(m_\lambda)$ according to: $E(m_\lambda) \propto \lambda^{-(\alpha_{disp}-1)}$. Therefore, a dispersion exponent of 1 corresponds to an absorption function independent from the wavelength, which is representative of mature soot, while values above one correspond to an absorption function increasing when the wavelength decreases, which is characteristic of younger particles (2.6.2). Most of the flame shows a value of α_{disp} near 1.2, while the maximum values are found in the lower part of the flame. A qualitative comparison of these maps

can be done as less mature soot particles (with low $E(m_\lambda)$) are expected to show higher dispersion exponent than more mature ones. The core of the flames, which shows approximately uniform values for $E(m_\lambda)$, also has a uniform α_{disp}. Also, regions of lower $E(m_\lambda)$ values in Fig. 6.29a match the region where α_{disp} is the highest in [146], i.e. mainly the lower and inner part of the flame. This reinforces confidence in the qualitative estimation of $E(m_\lambda)$ evolution in the flame. However, higher values of $E(m_\lambda)$ found in the wings do not correspond to lower α_{disp} while they indeed found a lower α_{disp} in the wings of the 80%C_2H_4+20%N_2 reference flame.

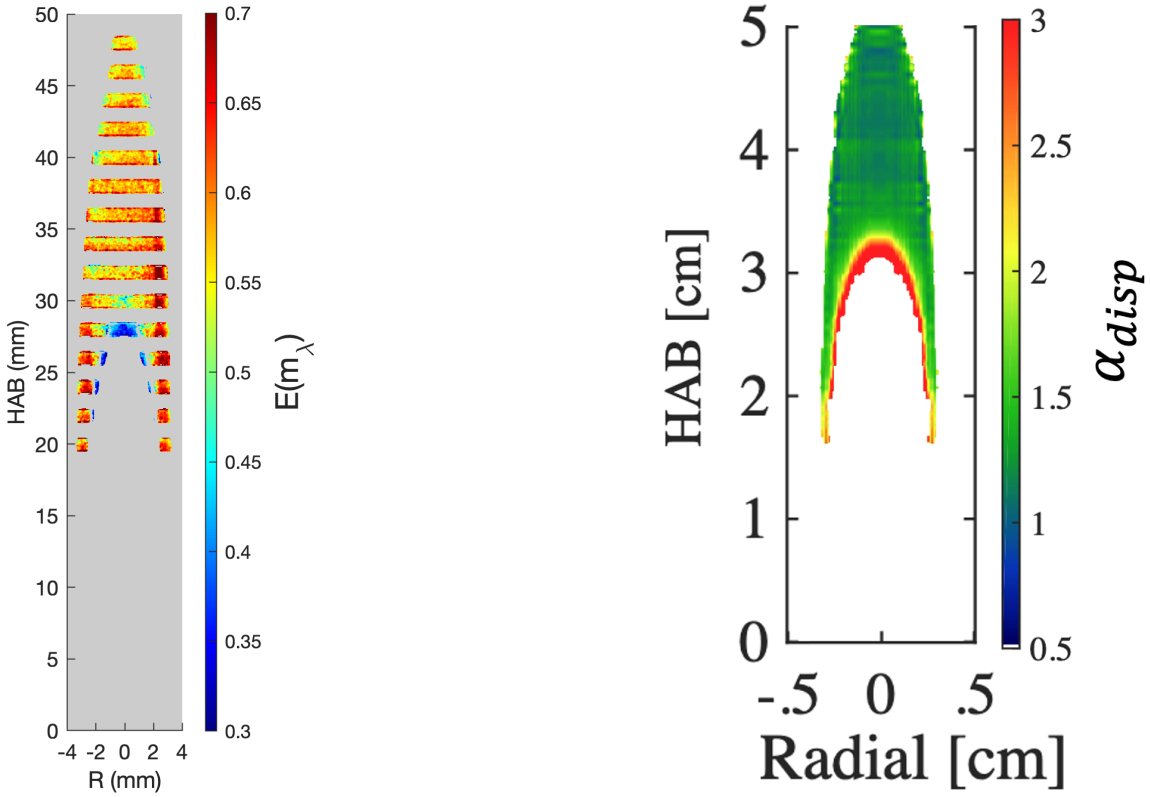

Figure 6.29: (a): Soot absorption function at 1064 nm. (b): Dispersion exponent α_{disp}. Adapted from [146].

Still, the values of $E(m_\lambda)$ appear to be higher than those typically reported in the literature, which are generally below 0.45. An exception is the work by Beyer and Greenhalgh [277], where estimates from LII measurements were between 0.4 and 0.6 for carbon black samples under high vacuum conditions. In particular, in the reference 80% C_2H_4+20%N_2/air flame, which is similar to the present flame, Kempema et al. [146] found absorption function ranging from 0.35 and 0.44 by combining thermophoretic sampling and spectral light extinction. Retaining a value of $E(m_\lambda)$ = 0.55 for mature soot for this work gives values around 25-60% higher than those in the literature. These high estimations of $E(m_\lambda)$ can originate from:

- It was shown that considering only three laser fluences globally overestimated $E(m_\lambda)$, but is, on average, negligible (< 1%) (Fig. 6.12).
- The work available in Annex G.1 shows that in the presence of laser fluence non-uniformity or polydispersion of $E(m_\lambda)$ in the probe volume, the computed $E(m_\lambda)$ is always overestimated. For the retained conditions, an overestimation of the average $E(m_\lambda)$ of 15% and 20% was found for laser fluence uniformity and absorption function polydispersion, respectively. However, other LII-based estimations of $E(m_\lambda)$ (in [30, 54, 131] for example) also suffer from these flaws and should also contain such overestimations. Thus, this cannot entirely

explain the difference encountered here.

- The ratio $\frac{E(m_\lambda=578nm)}{E(m_\lambda=716nm)}$ was assumed to be 1. However, the analysis in Fig. 5.13 of Chapter 5 demonstrated that changing this ratio to 1.3 instead of 1 resulted in decreases of 30% and 10% for $E(m_\lambda)$ and T_0, respectively. Considering the results of Kempema et al. of Fig. 6.29b, $\alpha_{disp} \approx 1.2$ in most of the flame, corresponding to $\frac{E(m_\lambda=578nm)}{E(m_\lambda=716nm)}$ = 1.044. Therefore, if the α_{disp} values in Fig. 6.29b are accurate, the assumption of a unity ratio cannot fully explain the 25-60% higher values for $E(m_\lambda)$ found in this work. However, the value of α_{disp} found on the lower inner part of the flame of $\sim$ 3, would correspond to $\frac{E(m_\lambda=578nm)}{E(m_\lambda=716nm)}$ = 1.535, meaning that $E(m_\lambda)$ and T_0 for the youngest particles are largely overestimated. However, as noted by Kempema et al. [146], areas with high values for α_{disp} might be affected by spectrally dependent absorption from soot precursors, which could affect the measurement by overestimating the values of α_{disp}.
- The strategy employed estimates the ratio $\frac{E(m_\lambda)}{\rho c}$ from the slope of the T_M-F curve, meaning the value of $E(m_\lambda)$ is directly dependent on the assumed value of ρc. While several studies have investigated soot density [278–280], information on specific heat is limited. Consequently, the product ρc is not well-documented in the literature. In this work, a value of 4.6· 10^6 J/K/kg [56] was selected, which is 13% higher than the value used in other studies [30, 141] where ρc was taken as 3.99· 10^6 J/K/kg. Had the lower value been used, the calculated $E(m_\lambda)$ would have been 13% lower as well: for instance, $E(m_\lambda)$ = 0.5 would have resulted in $E(m_\lambda)$ = 0.43.

The combination of these factors partially explains the high estimations of $E(m_\lambda)$ in the present work, but other sources of uncertainties cannot be excluded.

The higher values of $E(m_\lambda)$ found in the wings compared to the flame core were not widely reported in the literature. However, Yon et al. [51] similarly observed elevated $E(m_\lambda)$ values in the wings of another C_2H_4/air flame. This suggests that the soot particles in the wings may differ from those in the flame core. Since the measurement actually determines $\frac{E(m_\lambda)}{\rho c}$, the variation could arise from either a higher volumetric heat capacity $V_c = \rho c$ in the wings or a higher $E(m_\lambda)$. However, the method of Yon et al. should be independent of V_c, excluding this possibility. Alternatively, the high $E(m_\lambda)$ values in the wings might result from an underestimation of the ratio $R_{12} = \frac{E(m_\lambda=578nm)}{E(m_\lambda=716nm)}$ (Fig. 5.13 in Chapter 5). Yet, this is unlikely as Kempema et al. [146] showed that the dispersion exponent in the flame wings is similar to, or even slightly lower than, that in the flame core. Therefore, it seems plausible that $E(m_\lambda)$ is indeed higher in the wings. Nevertheless, it is important to keep in mind that the wings of the flames are regions where the LII signal exhibits a significant radial-gradient (Fig. 6.2). As temperature calculations using 2C-LII require precise alignment of images recorded at two different wavelengths, this high signal gradient, combined with slight misalignment between images, can lead to errors in temperature calculations, which in turn can affect the determination of the absorption function.

6.4.2 Gas temperature T_0

The axial and radial evolutions of T_0 are given in Fig. 6.30. They are compared to the one obtained by Kuhn et al. [216] and by Franzelli et al. [233] by pyrometry. 2D maps are also given in Fig. 6.31a.

The three 2D maps show qualitative agreement: gas temperature is higher on the flame's external surface than on its inside. The present estimation of T_0 is always above the other two, typically by 100-150 K compared to the values reported in [216, 275]. This difference can partly be explained by the different hypotheses on the wavelength dependence of the soot particles; Kuhn et al. [216, 275] assumed the dispersion exponent to be α_{disp} = 1.38 and showed that assuming α_{disp} = 1 (as in this work) leads to an increase of T_0 of 50 K. In this work, the gas temperature was also measured via pyrometry and compared with Kuhn et al.'s results in Annex E, using the same assumption for α_{disp}, showing good agreement. Overall, the fair agreement with the literature data shows the potential of the

proposed strategy to recover a consistent gas temperature without the use of additional diagnostics.

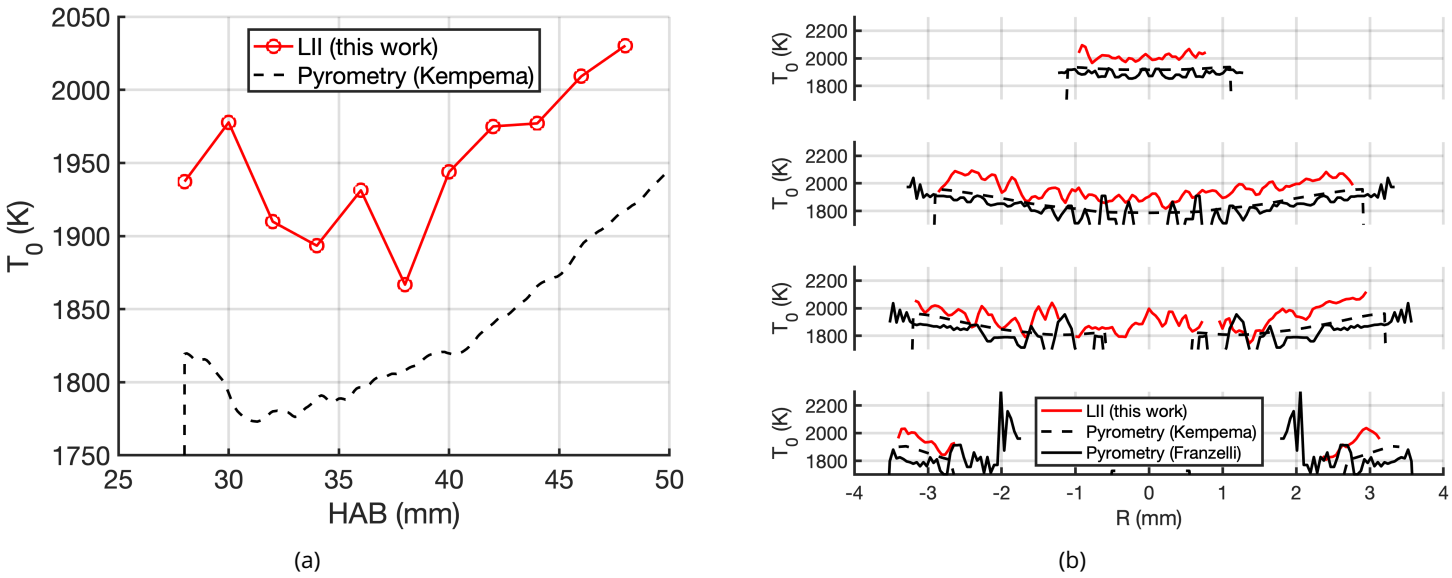

Figure 6.30: (a): Axial, and (b): radial evolution of the gas temperature in the 60% reference Yale flame, obtained from LII with the method of [33, 134] in this work (red), and by ratio pyrometry [216] (dashed black lines), and [233] (solid black lines). The radial profiles in figure (b) correspond to HAB = 20, 28, 34, and 48 mm from bottom to top. The axial profile for the data of [233] is not plotted as it is too noisy on the axis.

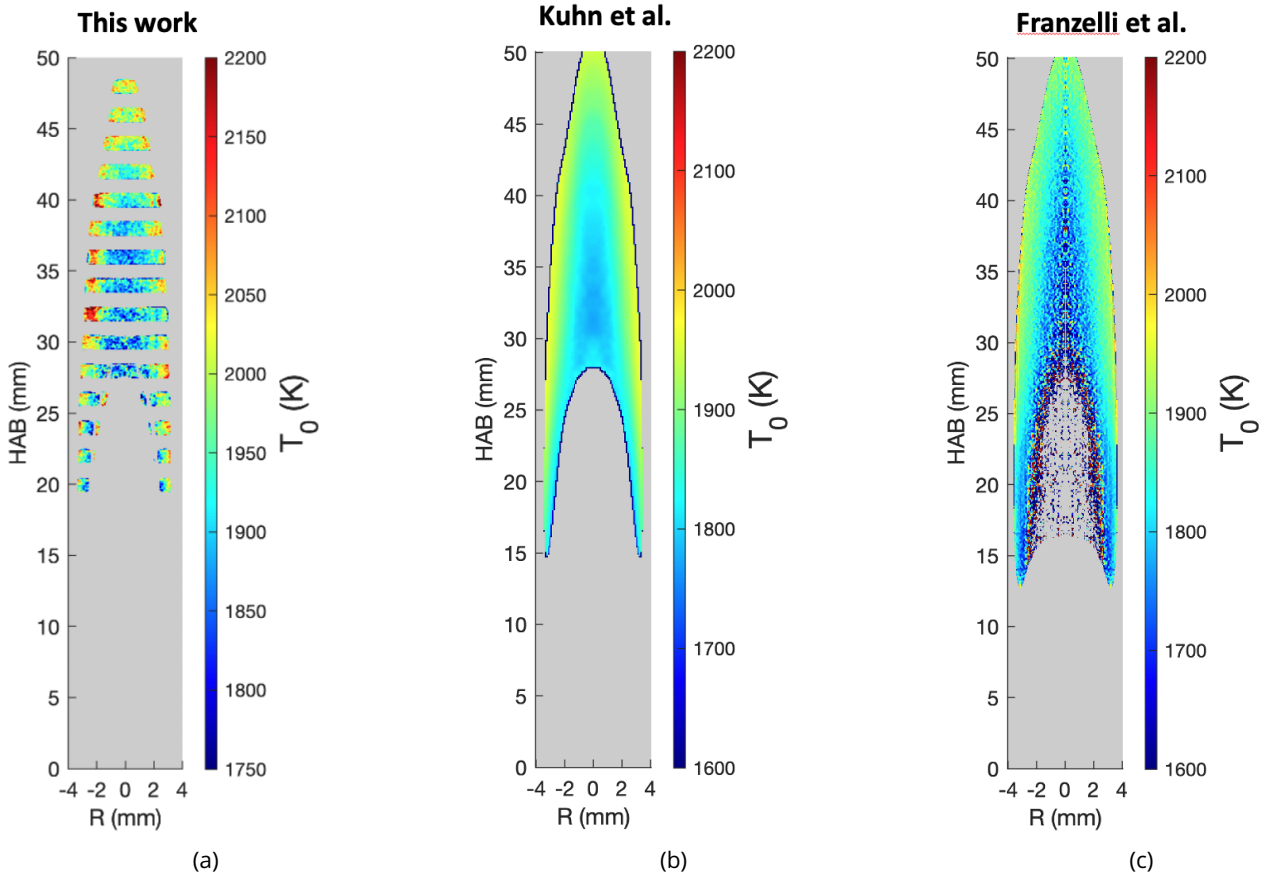

Figure 6.31: Gas temperature in the 60% reference Yale flame, obtained (a) with the method of [33, 134] (this work), (b): by ratio pyrometry (from [216]), and (c): by ratio pyrometry (from [233]).

6.4.3 Soot primary particle diameter d_p

A sequence of LII signals at 0, 60, and 240 ns for a laser fluence of 100 mJ/cm^2 is given in Fig. 6.32 to visualise that the cooling process does not occur at the same speed at all flame positions. The incandescence signal is consistently stronger in the wings. After 240 ns, the signal in the wings decreases to approximately half its initial value, while in the rest of the flame, the signal has decayed by more than a factor of two. This slower decay rate in the wings may suggest a larger primary particle diameter of soot in those regions of the flame.

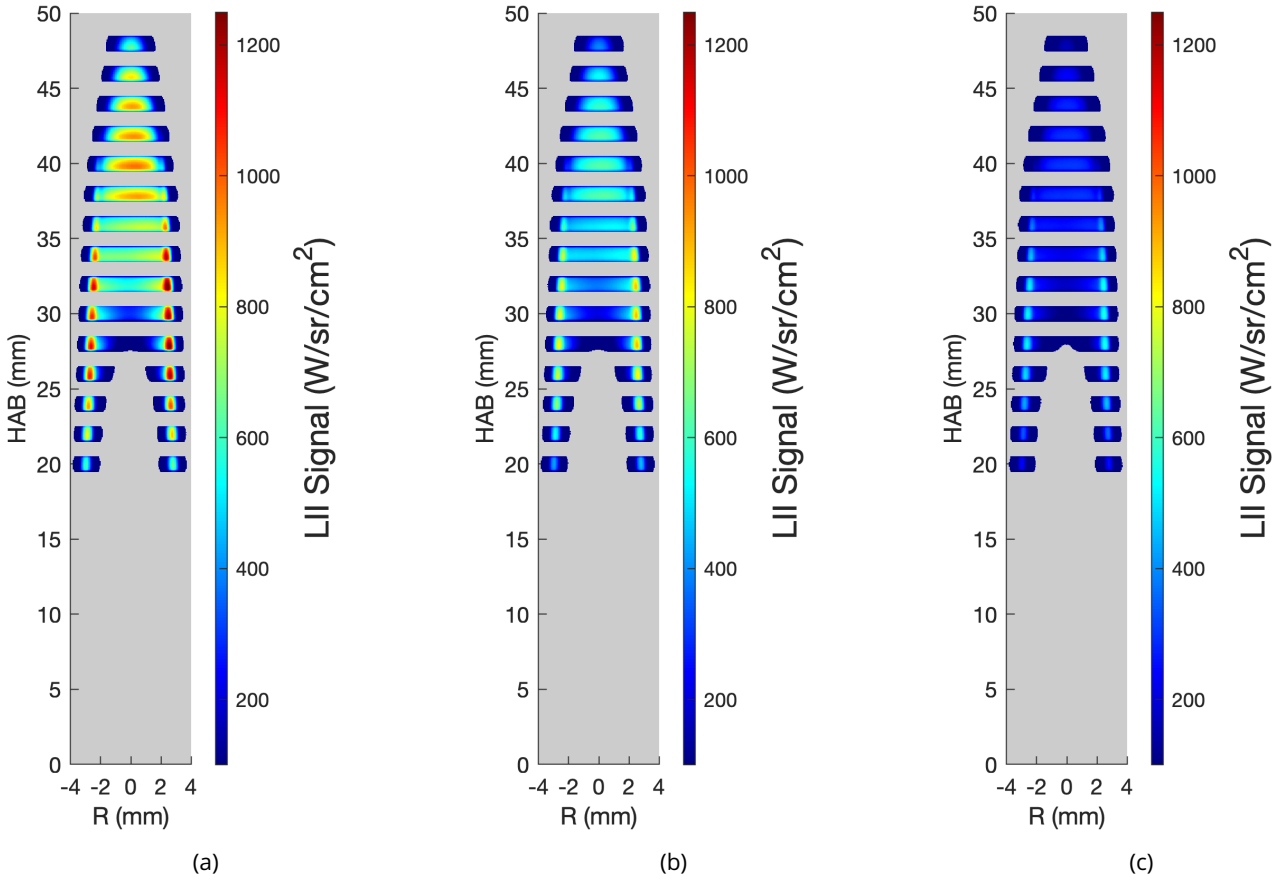

Figure 6.32: LII Signal at 578 nm for a laser fluence of ∼100 mJ/cm^2 in the reference 60% Yale flame, obtained at (a): 0 ns, (b): 60 ns, and (c): 240 ns after the laser pulse.

The 2D map of d_p presented in Fig. 6.33a is obtained by TIRE-LII from the temporal decay of the soot temperature (Eq. (3.26) and Eq. (3.27)). The gas temperature considered is the one of Fig. 6.31a. The largest values for d_p (40 to 50 nm) are found in the flame wings. Smaller particles are found in two zones: the inner part of the flame and the flame tip. The former may correspond to relatively young particles that have not yet undergone strong surface growth, while the latter is likely to be due to partial soot oxidation.

Franzelli et al. [233] also used TIRE-LII to retrieve d_p from LII measurements. They computed d_p assuming a uniform gas temperature of 1700 K and considered both monodispersed and polydispersed soot populations. Their results are shown in Figs 6.33b and Fig. 6.33c, for the monodispersed and polydispersed case, respectively. For comparison purposes, radial cuts are given in Fig. 6.34a. The qualitative behaviour of d_p is similar to that of this work. However, d_p is, on average, 20 and 15 nm above the ones of this work for the monodispersed and polydispersed cases, respectively.

Botero et al. [228] performed TEM measurements of d_p for this reference flame. These TEM measurements are compared in Fig. 6.34b to the LII-derived ones of this work. As the TEM measurements at one HAB possibly contain the soot at various radial regions at the same HAB, the LII measurements are plotted both only on the flame axis and averaged over the radial position. TEM measurements indicate an increase from 12 nm at HAB = 10 mm to 28 nm at HAB = 25 mm, followed by a decrease to 12 nm at HAB = 49 mm. Radially averaged LII measurements globally match the TEM data and show a decrease from 35 nm at HAB = 22 to 15 nm at HAB = 48 mm. On the contrary, the profile along the centreline shows a rapid increase at low HAB: d_p goes from 10 nm at HAB = 28 mm to 20 nm at HAB = 36 (surface growth), stays roughly constant up to HAB = 46 mm before decreasing to 17 nm at HAB = 48 mm (oxidation). Botero et al. [228] indicated that for HAB $\leq$ 25 mm, they removed the larger aggregates in order to limit the contribution from the wings in their measurements. This may explain the $\sim$30% difference at HAB = 20 mm.

Therefore, the present estimations of d_p qualitatively agree with the literature and show consistent values compared to TEM measurements.

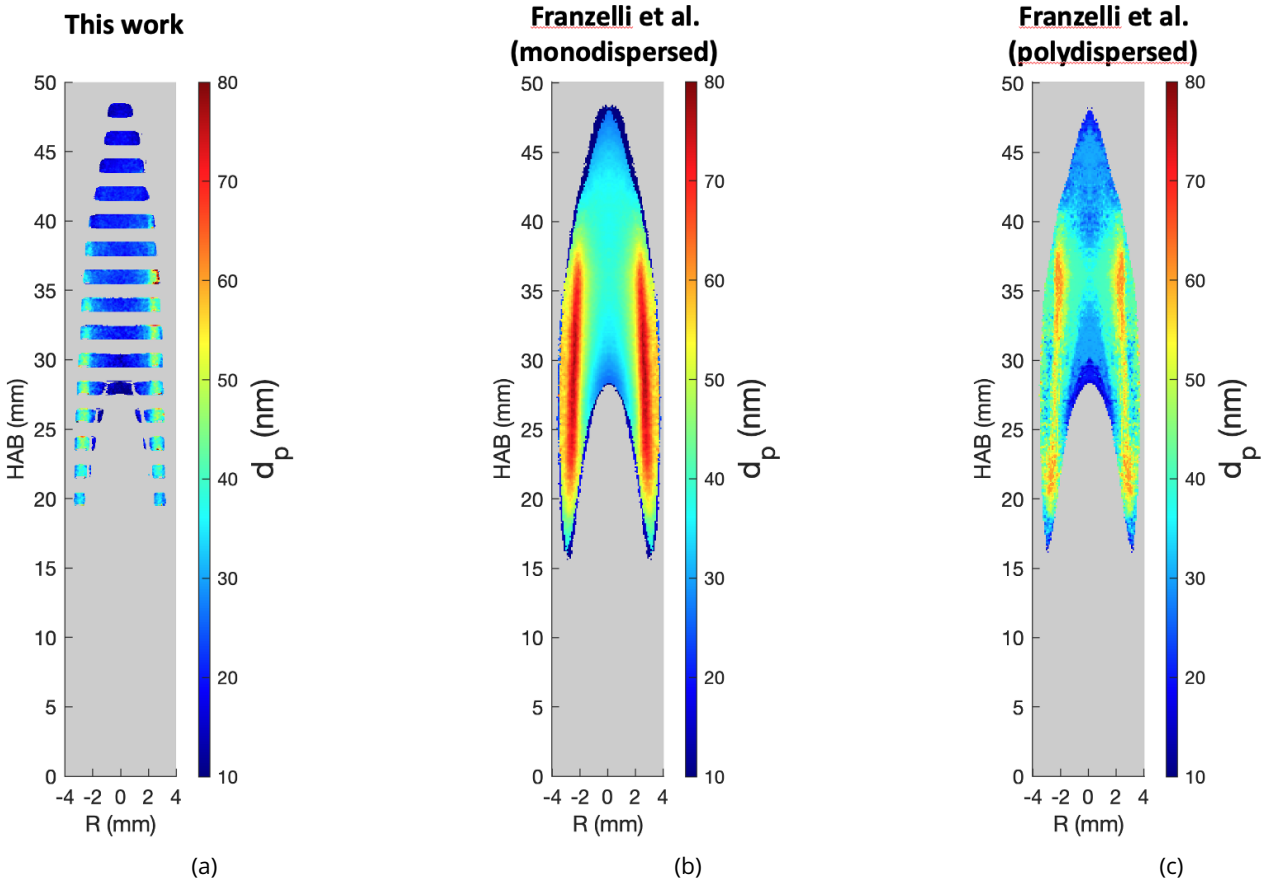

Figure 6.33: Soot primary particle size obtained by TIRE-LII. Figures (a), this work (considering only temperatures below 3500 K), and (b) [233] are obtained assuming a monodispersed soot population, while for the figure (c) [233], a polydisperse soot population was assumed.

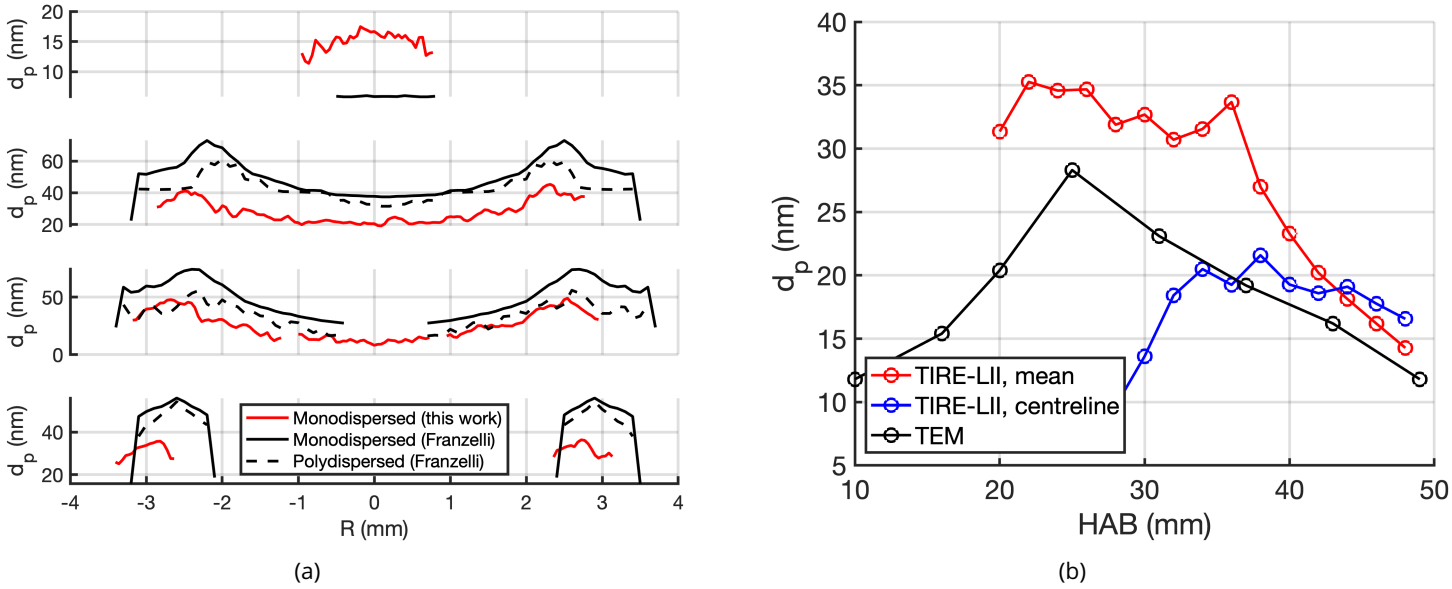

Figure 6.34: Soot primary particle size versus HAB obtained with TIRE-LII in red and blue (this work) and with TEM in black (from [228]). LII measurements of d_p are given along the flame axis in blue and averaged over the flame radius in red.

6.4.4 Soot fraction volume f_v

The profiles of f_v obtained in this work by AC-LII were already presented in Fig. 6.27 for multiple laser fluences. Results from the literature for the same flame condition are provided in Fig. 6.35d. Kuhn et al. [216] obtained f_v by pyrometry using consumer digital camera (RGB channels) and large band filters. They assumed a dispersion exponent of 1.38 ($E(m_\lambda)$ vary as $\lambda^{-0.38}$), and assumed a value of 8.6 for the extinction coefficient: $K_{ext} = 6\pi E(m_\lambda)$. Smooke et al. [194] used "traditional" LII [27, 28] (as opposed to AC-LII) with a laser fluence of 300 mJ/cm^2 at 532 nm and collected the signal at 405 nm. The calibration was made by extinction at 532 nm at a laser fluence less than 10 mJ/cm^2, and they considered an extinction coefficient of 10. Franzelli et al. [233] used LII with a laser fluence of 450 mJ/cm^2 at 1064 nm and collected the signal at 425 nm. The calibration was done with modulated absorption/emission technique, the data were corrected for soot self-absorption, and they took the spectral dependence of m_λ from Chang and Charalampopulos [281].

When comparing literature results in Fig. 6.35d, it is observeeed that data from Smooke et al. [194] (Fig. 6.35b) is shifted down by $\sim$ 4 mm compared to the others, possibly due to slightly different flame conditions. The profile from Franzelli et al. [233] (Fig. 6.35c) shows pronounced wings (compared to the flame core) and almost twice the soot volume fraction compared to the two other results. However, these three profiles show similar trends.

Axial and radials comparison with the literature of the f_v profiles obtained with a laser fluence of 25, 55, 100 and 160 mJ/cm^2 are given in Figs. 6.36a, and 6.36b, respectively. Thanks to the background correction, f_v obtained by AC-LII at 25 and 55 mJ/cm^2 are very similar (although the former is more noisy due to a lower signal). However, due to the f_v anomaly, a significant difference exists with the results obtained for higher laser fluences. The profiles obtained for 25, 55, 100 mJ/cm^2 are quite below the ones of the literature, with a soot volume fraction that is clearly lower (up to 3 times lower). f_v obtained at 160 mJ/cm^2, for which the temperature criterion is exceeded in the while flame (Fig. 6.10), was also reported to explain this difference. It is observed that the profile obtained with the highest laser fluence agrees better with the pyrometry estimations of [216] and the LII estimation of [194]. Figure 6.35d gives a 2D map of the relative difference between these two profiles. The AC-LII at 160 mJ/cm^2 estimations are generally 20% below the pyrometry, possibly due to the relatively high values found for $E(m_\lambda)$ in this work and to the difference in

the soot absorption function dependence with wavelength between these works. As in this work, the cameras were set and calibrated to be used in a low laser fluence regime; estimation of f_v is not available in the wings where the highest soot load is found.

It should be noted that in the present estimations of f_v at low to moderate fluences, the differences in f_v between the wings and the flame core are less pronounced than in the data from the literature [194, 216, 233]. This is because the distribution of T_M and $E(m_\lambda)$ are taken into account here. The profile of $E(m_\lambda)$ of Fig. 6.29a shows 20-40% higher values in the wings compared to the flame core. Thus, f_v in the wings is reduced by the same percentage compared to using a uniform $E(m_\lambda)$, as done in the three referenced works. Therefore, if the current qualitative estimations of $E(m_\lambda)$ are accurate (higher $E(m_\lambda)$ in the wings than in the core), it suggests that f_v is usually overestimated in the wings of the flame when constant $E(m_\lambda)$ is considered.

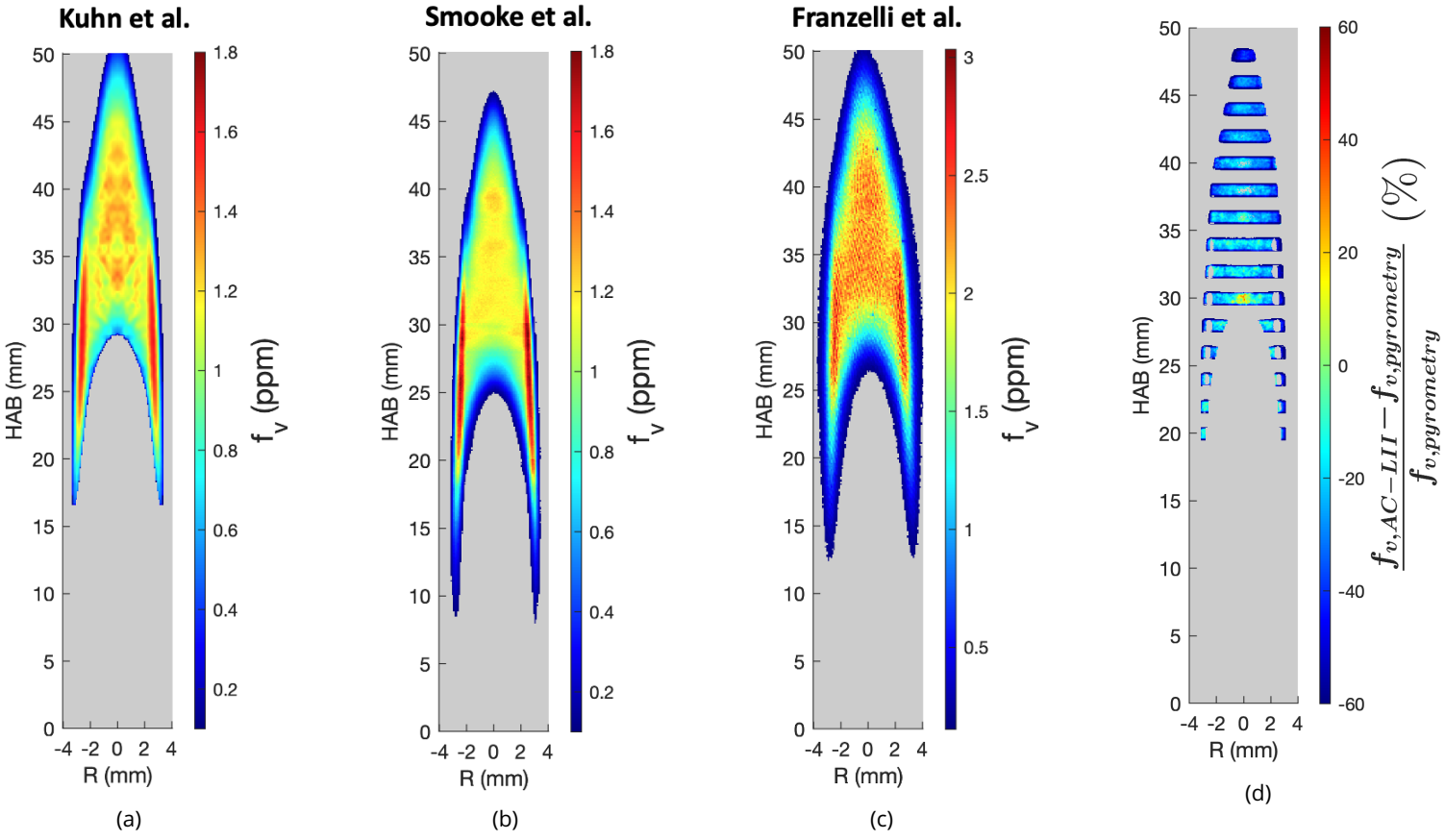

Figure 6.35: Soot volume fraction for the reference 60% Yale flame obtained with (a): pyrometry [216], and (b): LII at λ_{laser} = 532 nm with a laser fluence of 300 mJ/cm^2 [194]. (c): LII at λ_{laser} = 1064 nm with a laser fluence of 450 mJ/cm^2 [233]. (d): relative difference of f_v between the AC-LII profile obtained at F = 160 mJ/cm^2 and the pyrometry profile of (a).

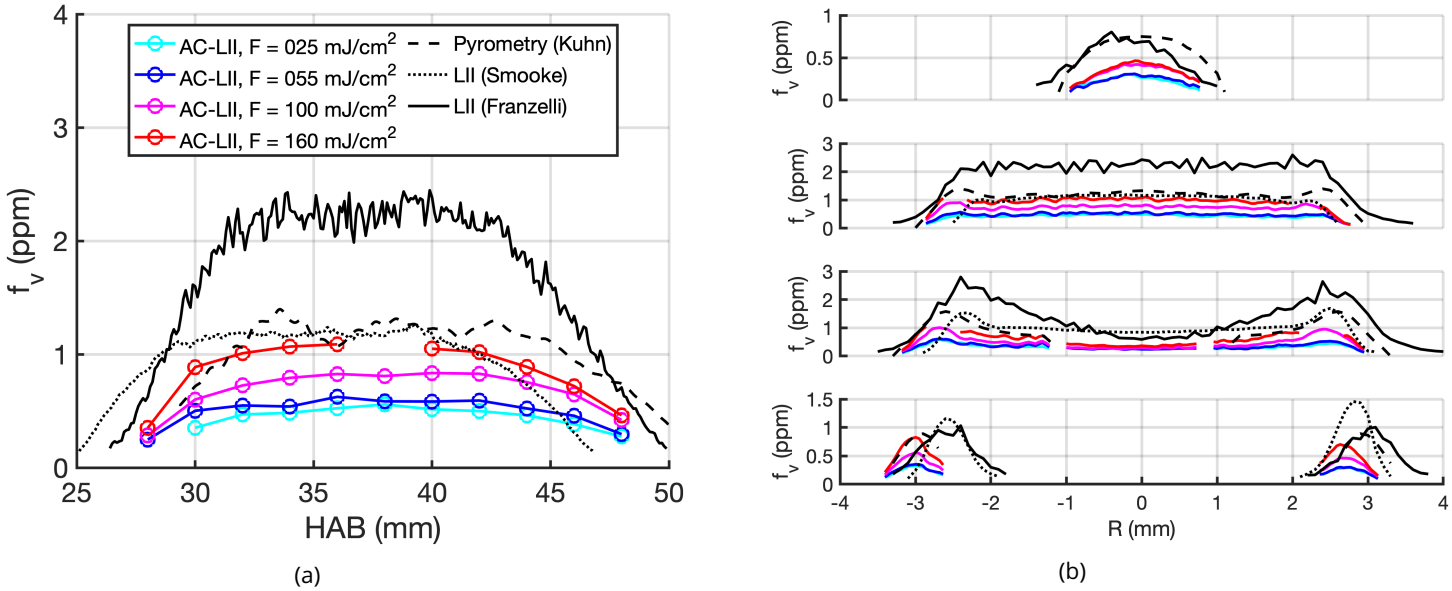

Figure 6.36: (a): Axial, and (b): radial evolution of the soot volume fraction in the 60% reference Yale flame obtained by AC-LII for four laser fluences: 25, 55, 100, and 160 mJ/cm^2 in cyan, blue, magenta, and red, respectively. The radial profiles in figure (b) correspond to HAB = 20, 28, 34, and 48 mm from bottom to top. Results obtained by pyrometry presented in [216] are given by the black dashed lines, LII results obtained at λ_{laser} = 532 nm with a laser fluence of 300 mJ/cm^2 [194] are given by the black dotted lines, and LII at λ_{laser} = 1064 nm with a laser fluence of 450 mJ/cm^2 [233]

Compared to other methods, pyrometry measurements offer the advantage of not requiring laser heating. Thus, it does not suffer from the f_v anomaly. However, pyrometry requires deconvolution post-processing and, like AC-LII, depends on assumptions regarding the spectral behaviour and absolute value of the soot absorption function, $E(m_\lambda)$ (although if absorption measurements are available, assumptions about the spectral behaviour of $E(m_\lambda)$ are not necessary [51]). The previous results indicated that estimations at the highest fluence (160 mJ/cm^2) correspond better to the literature data, including the one derived from pyrometry. However, f_v was computed from different assumptions. To ensure a consistent comparison between the pyrometry results from Kuhn et al. [216] and the present ones, AC-LII estimations were recalculated with the assumption $R_{12} = \frac{E(m_{\lambda=578nm})}{E(m_{\lambda=716nm})}$ = 1.085, based on $E(m_\lambda)$ varying as $\lambda^{-0.38}$. This higher value for R_{12} reduces the estimated T_M and $E(m_\lambda)$, leading to an increase in f_v as indicated by Eq. (3.23). However, since the values of $E(m_\lambda)$ differ between this study and that of Kuhn et al., results were plotted in Fig. 6.37 in terms of $f_v E(m_\lambda)$ rather than f_v to eliminate the dependence on the assumption retained for the absolute value of $E(m_\lambda)$. This time, measurements taken at moderate laser fluences (between 55 and 100 mJ/cm^2) show the closest agreement with the pyrometry results, while those at 160 mJ/cm^2 significantly exceed the pyrometry values. This discrepancy underscores that $f_v E(m_\lambda)$ (and f_v) is highly sensitive to assumptions about the wavelength dependence and absolute value of $E(m_\lambda)$. Given the substantial uncertainties surrounding both the absolute values and spectral dependence of $E(m_\lambda)$ and considering potential variations across the flame, it is suggested that comparisons between different works should be made in terms of $f_v E(m_\lambda)$ rather than f_v, to rely on consistent assumptions for $E(m_\lambda)$ and avoid misinterpretation. These findings support once again conducting AC-LII measurements at low to moderate rather than high laser fluences.

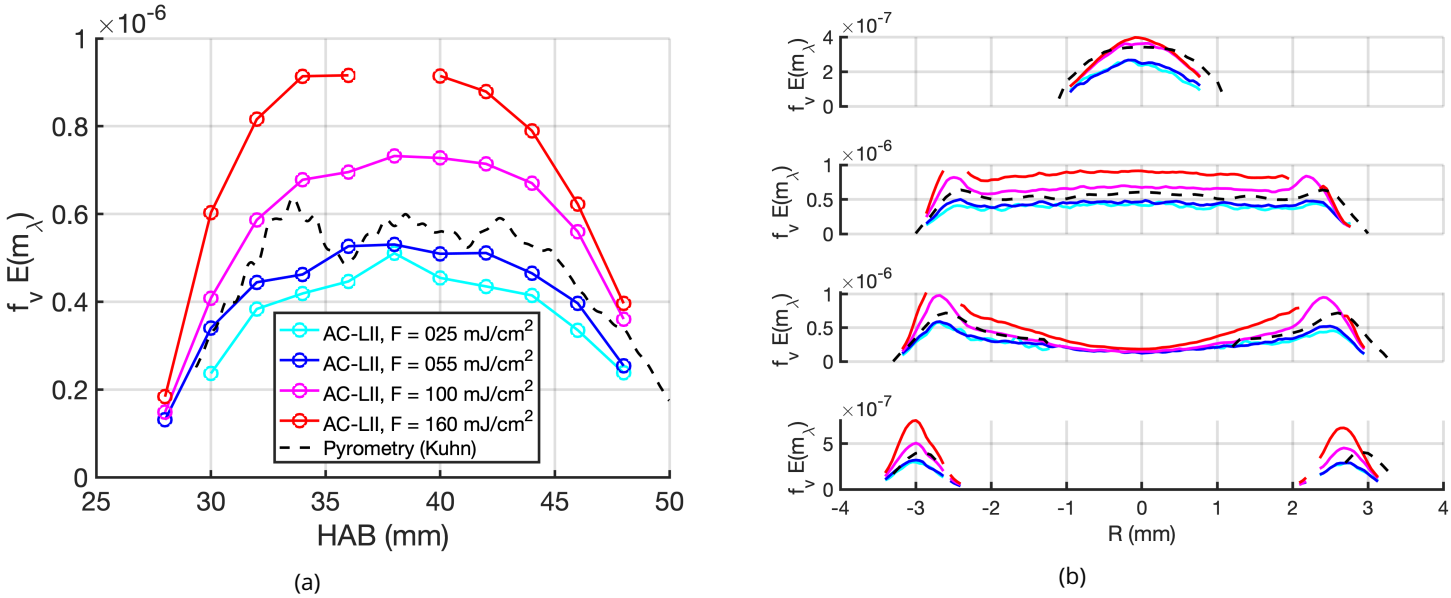

Figure 6.37: (a): Axial, and (b): radial evolution of $f_v E(m_\lambda)$ in the 60% reference Yale flame obtained by AC-LII for four laser fluences: 25, 65, 100, and 160 mJ/cm^2 in cyan, blue, magenta, and red, respectively. The ratio of absorption function was taken equal to 1.085 and corresponds to the assumption that $E(m_\lambda)$ vary as $\lambda^{-0.38}$. The radial profiles in figure (b) correspond to HAB = 20, 28, 34, and 48 mm from bottom to top. Results obtained by pyrometry presented in [216] are given by the black dashed lines.

6.5 Conclusion

The experimental setup of Chapter 5 was modified to estimate the 2D spatial variations of the four following quantities: absorption function $E(m_\lambda)$, gas temperature T_0, soot volume fraction f_v, and primary particle diameter d_p. These LII measurements have been performed in the 60%C_2H_4+40%N_2/air reference Yale laminar diffusion flame to offer comparison possibility with the literature. The first stage of this work involved identifying guidelines for data processing and presenting a correction procedure for background subtraction, followed by a second phase where the obtained results were compared with the literature.

The guidelines were identified based on the following evidences:

- The curves of soot peak temperature T_M versus laser fluence F deviate from linearity around 3500 K, signalling the onset of non-linear high-temperature processes such as soot sublimation. By using a conservative approach, the determination of $E(m_\lambda)$ and T_0 was done considering a limit of 3500 K. While greater precision and a broader range of $E(m_\lambda)$ values can be achieved from a greater number of laser fluences, using just three (25, 55, and 100 mJ/cm^2) still provided a consistent spatial distribution of $E(m_\lambda)$ and T_0, successfully capturing nearly all soot populations with significantly reduced experimental time and costs.
- The soot particle diameter d_p derived from temperature decay below 3500 K closely matched the values obtained without this temperature constraint, suggesting that the 3500 K limit may be relaxed.
- f_v shows a strong dependence to the laser fluence -known as the f_v anomaly- over the whole fluence range investigated in this work (25 to 160 mJ/cm^2). f_v is increasing with the soot peak temperature up to approximately 4100 K, and decays for higher temperatures. Theoretical results show that the background subtraction leads to an overestimate the soot temperature, and underestimate S_λ^{LII} both of which contribute to an underestimation of f_v. The effect strongly depends on the difference between the soot and gas temperatures. Therefore, when the temperature difference is only a few hundred kelvins, i.e. at low laser fluences, or long

after the laser pulse, it is highly preferable to account for the background subtraction. Consequently, a correction procedure was proposed and applied to experimental data. Background subtraction induces a $\sim$6% underestimation of the absorption function, a $\sim$5% overestimation of T_0, and a $\sim$4% underestimation of d_p. The correction greatly reduced the fluence dependency of f_v below $\sim$ 3500 K, but it has no effect at higher temperatures.

From these results, it was concluded that LII measurements should be conducted at low laser fluences leading to temperatures below 3500 K, and should be corrected for background correction. Using these criteria, the present 2D fields of $E(m_\lambda)$, T_0, f_v, and d_p were compared with literature data. $E(m_\lambda)$ was found to be largely uniform throughout the flame, supporting the common practice in the LII community of assuming a constant value for calculating f_v. Nevertheless, lower values are found in the lower and inner parts of the flame, while the largest values are found in the wing. Therefore, given that the present spatial distribution of $E(m_\lambda)$ are accurate, assuming a uniform $E(m_\lambda)$ tends to underestimate f_v in the lower inner part of the flame, and overestimates it in the wings. Absolute values of $E(m_\lambda)$ are found to be higher than the most encountered values of the literature for other flames, including our previous work on a CH_4/air flame. However, no direct comparison is possible since no $E(m_\lambda)$ data exists in the literature for the considered flame. The relatively high values of this work may be attributed, among other things, to a temperature inhomogeneities in the collection volume, to the assumption on the wavelength dependency of $E(m_\lambda)$ and to the fact that what is actually determined is $\frac{E(m_\lambda)}{\rho c}$ while there is a lack precise data for ρc. The gas temperature was found to be $\sim$100 K higher than the pyrometry measurements of the literature. This difference is partly due to different assumptions on the soot absorption function's wavelength dependency, but can be considered in line with state-of-the art diagnostics. Soot primary particle diameter estimation qualitatively agree to other TIRE-LII data, and is also in good agreement with TEM measurements. Values of $f_v E(m_\lambda)$ were compared with those obtained from pyrometry (unaffected by the f_v anomaly) under the same assumptions. The comparison supported measurements taken at low to moderate fluences.

This work demonstrates the feasibility to obtain spatially resolved $E(m_\lambda)$, T_0, f_v, and d_p fields in laminar flames using a single LII setup. It could benefit from replacing the top-hat laser beam with a laser sheet to image the whole flame at once, significantly reducing experimental duration and simplifying post-processing.

Part IV

Insight on soot formation in $C_2H_4 - H_2$ flames

Chapter 7

Effect on soot production of blending H_2 to C_2H_4

In this chapter, the LII setup from Chapter 6 is applied to explore how blending hydrogen with ethylene influences soot production in laminar diffusion flames. The C_2H_4+N_2 flame previously examined is taken as a reference and is compared to a C_2H_4+H_2 flame with identical thermal power and volumetric flow rates in order to ensure similar flame dynamics. $E(m_\lambda)$, T_0, f_v, and d_p are measured in the H_2-blended flame following the methodology outlined in the previous chapter. By comparing the results between the two flames, this chapter aims to analyse how hydrogen blending affects temperature distribution, soot formation, maturation, and oxidation processes. Then, numerical simulations of the flames are compared with the experimental results to assess the accuracy of the numerical model, particularly in predicting soot volume fraction. Additionally, a comparison between the numerically computed carbon-to-hydrogen ratio of soot particles and the experimentally measured $E(m_\lambda)$ is made to investigate the relationship between these quantities and to validate the numerical model's capability in capturing information about the soot maturation process.

Contents

7.1 Dilution of carbonaceous fuels . . . 159
- 7.1.1 Why hydrogen blending? . . . 159
- 7.1.2 Effects of blending hydrocarbons fuels . . . 159
- 7.1.3 Hydrogen blends in literature . . . 160
- 7.1.4 Objectives of the present work . . . 161

7.2 Experimental and numerical setup . . . 162
- 7.2.1 Flame conditions . . . 162
- 7.2.2 Experimental setup . . . 162
- 7.2.3 Numerical setup . . . 162

7.3 Experimental comparison of the reference and H_2-blended flames . . . 163
- 7.3.1 Flame natural emission . . . 164
- 7.3.2 LII signal . . . 165
- 7.3.3 Soot absorption function $E(m_\lambda)$ . . . 166
- 7.3.4 Gas temperature T_0 . . . 168
- 7.3.5 Soot volume fraction f_v . . . 170
- 7.3.6 Soot primary particle diameter d_p . . . 172

7.4 Comparison of the numerical results with the experimental profiles of f_v, T_0, and $E(m_\lambda)$ **174**
7.4.1 Comparison of the gas temperature T_0 175
7.4.2 Comparison of f_v 176
7.4.3 Comparison of $E(m_\lambda)$ 178
7.5 Conclusion **180**

7.1 Dilution of carbonaceous fuels

7.1.1 Why hydrogen blending?

Hydrogen blending consists of adding hydrogen to a given fuel. This reduces the part of the original fuel in the resulting blend. This approach has several advantages:

1. It reduces direct CO_2 emissions if hydrogen replaces a carbonaceous fuel.
2. Up to a certain hydrogen percentage in the fuel blend, existing combustion and distribution systems require minimal modifications, making this solution both cost-effective and rapidly deployable. For instance, regarding the French gas distribution, most networks can receive up to 6% hydrogen (by volume) without major modifications and up to 20% with limited investments [282]. Another example of hydrogen blending would be with diesel (for instance: [283, 284]) for use in engines with only minor structural changes to the powertrain.
3. When hydrogen is produced from non-carbonaceous sources, hydrogen blending can help reduce reliance on imported hydrocarbons, thereby decreasing energy dependence on exporting countries. Still, in 2020, the hydrogen was quasi-totally produced from fossil fuels (natural gas, oil, and coal), with a negligible part generated through water electrolysis ($\sim$0.03% according to the IEA [285]).

However, even if the direct emissions of CO_2 are reduced by hydrogen blending (due to a reduction of the carbon mass flow rate at constant flame thermal power), a reduction of the soot production and emission is not guaranteed. Several studies have showed that hydrogen blending can either inhibit [182, 183, 286–293] or enhance [44, 292–294] the soot production depending on the flame conditions. Thus, it would be beneficial to understand the effect of hydrogen blending to carbonaceous fuels on soot production to target specific conditions that would limit the soot emission.

7.1.2 Effects of blending hydrocarbons fuels

The effects of the dilution of hydrocarbons with either inert or active diluent species on soot production have been largely studied in the literature. These effects can be separated into four categories (thermal, chemical, dilution, and diffusion effects):

- **Thermal effect:** Modifying the fuel mixture alters the adiabatic flame temperature. Lowering the flame temperatures inhibits soot formation [77, 78]. Glassman [81] indicated that the temperature effects cause a logarithmic variation in the soot volume fraction.
- **Chemical effect:** Active diluents such as H_2 do participate in chemical reactions and can favour or inhibit the formation of gaseous species participating in the soot chemistry.
- **Dilution effect:** The dilution of hydrocarbons lowers the carbon flow rate injected. Increasing the dilution by inert species of the fuel jet mixture was found to induce a proportional reduction of the soot volume fraction [81].
- **Diffusion effect:** The modification of thermal and mass diffusion in fuel blends can impact soot production. Glassman [81] noted that diluents with low thermal diffusivity are more effective at reducing soot levels. However, Axelbaum et al. [295] conducted experiments by adding helium, neon, argon, and krypton to C_3H_8 or C_2H_4 in counterflow diffusion flames. Their results revealed an increasing trend in soot volume fraction with the molar mass of the diluent: krypton produced the highest soot level, while helium generated the lowest (up to a factor of 2). Since all the diluents are monoatomic, they share the same molar specific heat. This explains

the small measured temperature difference of just 34 K between cases, which is too small to account for the observed variations in soot volume fraction. The study of Axelbaum et al. [295] underscores the importance of preferential diffusion in soot formation. The differences in soot volume fraction were attributed to changes in the local concentrations of fuel and soot precursors, driven by the differing mass diffusion rates of the inert additives.

7.1.3 Hydrogen blends in literature

The first studies on the impact of hydrocarbon-hydrogen fuel blends on soot production emerged in the 1960s. Interest in this area has accelerated over the past decade due to growing concerns about global CO_2 emission reduction. Consequently, numerous configurations have been investigated both numerically and experimentally.

Typically, H_2 is blended into a reference flame, and the results are compared to those of the reference flame to highlight H_2's effect on soot production. Some studies have attempted to isolate the various effects induced by blending (thermal, chemical, dilution, and diffusion) by considering fuel blending with other inert diluents (often He or N_2). Different strategies are adopted for the dilution. In one approach, the diluent is added to the reactant flow, increasing the volumetric flow rate, a process referred to as "addition." Alternatively, part of the reactant flow is replaced by the diluent, either maintaining or changing the volumetric flow rate. This is referred to here as "substitution." To compare similar flames, the authors maintain certain quantities constant between the reference and diluted flames. One or more of the following parameters are typically held constant: carbon flow rate, mass flow rate, volumetric flow rate, equivalence ratio ϕ, or carbon-to-oxygen ratio C/O.

Tables 7.1, and 7.2 summarise the conditions of various laminar diffusion and laminar premixed flames studied in the literature, along with the observed effects of H_2 on soot production. For cases with multiple diluents, a ranking is provided, and the most effective diluent for soot suppression is listed on the far right of the table.

Reference	Type	Reactants	Strategy	fixed quantities	Effect on soot production
[288]	Exp	C_2H_2/air	S: H_2	ϕ	inhibit
[288]	Exp	C_2H_2/air	A: H_2	CFR	inhibit
[294]	Num+Exp	$C_2H_2 + N_2$/air	S: H_2	CFR & VFR	inhibit
[296]	Exp	$C_2H_4 + N_2$/air	A: H_2	CFR	inhibit, $H_2 > N_2$
[296]	Exp	$C_2H_4 + N_2$/air	S: H_2	VFR	inhibit, $H_2 > N_2$
[286]	Exp	C_2H_4/air	A: H_2, He	CFR	inhibit, $He > H_2$
[286]	Exp	C_3H_8 or C_4H_{10}/air	A: H_2, He	CFR	inhibit, $H_2 \sim He$
[297]	Num	C_2H_4/air	A: H_2, He	CFR	inhibit, $He > H_2$
[291]	Exp	C_2H_4/air	A:H_2, He	CFR	inhibit, $He > H_2$
[291]	Exp	C_2H_4/air	S: H_2	VFR	inhibit
[298]	Num	CH_4 or C_2H_4/air	A: H_2, He	CFR	inhibit, $H_2 > He$
[44]	Exp	$C_2H_4 + N_2$/air	S: H_2, He, Ar, NH_3	CFR & VFR	$H_2 \sim He > N_2 \sim Ar > NH_3$
[44]	Exp	$C_2H_4 + N_2$/air	A: H_2, He, Ar, NH_3	CFR	$N_2 > H_2 \sim He > Ar > NH_3$
[44]	Exp	$CH_4 + N_2$/air	S: H_2, He, Ar, NH_3	CFR & VFR	$H_2 >> Ar > N_2 \sim He > NH_3$
[44]	Exp	$CH_4 + N_2$/air	A: H_2, He, Ar, NH_3	CFR	$H_2 >> N_2 > Ar \sim He > NH_3$
[143]	Exp+Num	$C_2H_4 + N_2/O_2 + N_2$	S: H_2	power	inhibit

Table 7.1: Summary of several studies in the literature that have investigated the mixing of H_2 in laminar diffusion flames. "Exp" and "Num" refer to experimental and numerical studies, respectively. "CFR", "MFR", and "VFR" represent carbon, mass, and volumetric flow rate, respectively. "A" and "S" indicate addition and substitution of the diluent, respectively, and are followed by the species considered for the dilution.

Reference	Type	Reactants	Strategy	fixed quantities	Effect on soot production
[182, 183, 290]	Num+Exp	C_2H_4+air	S: H_2, He	VFR & C/O	inhibit, $He > H_2$
[299]	Num	C_2H_2+air	S: H_2	MFR and ϕ	inhibit
[289]	Num	C_2H_2+air	S: H_2	VFR & ϕ	inhibit
[292, 300]	Exp	$CH_4 + O_2 + N_2$	S: H_2	CFR & VFR & C/O	inhibit
[292, 300]	Exp	$CH_4 + O_2 + N_2$	A: H_2	CFR & C/O	promote
[301]	Exp	C_2H_4+air	A: H_2	C/O	equivalent

Table 7.2: Summary of several studies in the literature that have investigated the mixing of H_2 in laminar premixed flames. "Exp" and "Num" refer to experimental and numerical studies, respectively. "CFR", "MFR", and "VFR" represent carbon, mass, and volumetric flow rate, respectively. "A" and "S" indicate addition and substitution of the diluent, respectively, and are followed by the species considered for the dilution.

In most cases, blending H_2 with pure hydrocarbons inhibits soot production, but this is not always the case. In addition, the effectiveness of H_2 as a soot suppressant can vary: it may be less effective [44, 296, 298], more effective [182, 183, 286, 290, 291, 297], or equally effective [44, 286] compared to other diluents such as He or N_2. This variability is particularly notable when comparing H_2 with He dilution in equal proportions. Both gases have similar diffusivities and yield similar adiabatic flame temperatures, suggesting that differences in soot suppression are likely due to the chemical effects of H_2, which appear to be dependent on specific flame conditions.

In their review of the effects of H_2 on soot formation in hydrocarbon flames, Wang et al. [293] conclude that the chemical effect of H_2 appears to primarily act on the soot nucleation process, followed by soot surface growth, then on soot oxidation. This chemical effect is strongly influenced by factors such as fuel type, oxygen concentration, and ambient pressure. The studies reviewed propose various reaction pathways for the chemical effects of H_2, sometimes yielding conflicting results. Notably, the H-abstraction mechanism is often suggested to be influenced by H_2 blending. Blending H_2 alters the concentrations of molecular and atomic hydrogen in the flame, thereby affecting the rate of the H-abstraction process. This, in turn, impacts the formation and growth of aromatic species through:

$$A_i + H \Leftrightarrow {A_i}^* + H_2 \tag{7.1}$$

A low $\frac{H}{H_2}$ ratio tends to enhance the backward reaction rate of Eq. (7.1), promoting the recombination of radical species into stable molecules. This inhibits the growth of aromatic species, reducing the formation of PAHs and, consequently, lowering soot nucleation and growth. This mechanism is believed to explain the variations in PAH concentrations when hydrogen is blended into the fuel.

7.1.4 Objectives of the present work

In the studies gathered in Tables 7.2, and 7.1, the H_2-blended flames exhibit higher thermal power than the reference flames. However, in real-world scenarios in which hydrocarbons would be partially replaced by H_2, thermal power would be maintained to minimise modifications of the operating conditions. Therefore, the flames investigated in this chapter -the reference and the H_2-blended flames- both have the same thermal power. While this results in a lower carbon flow rate in the H_2-blended flame, it does not necessarily ensure reduced soot production. This work aims to examine the effect of H_2 blending on soot formation when flame power is held constant in flames having similar flow dynamics (same volumetric flow rate). To achieve this, f_v and d_p are measured in 2D with high spatial resolution in both reference and H_2-blended flames, enabling a detailed assessment of the impact of H_2 on these parameters. The absorption function $E(m_\lambda)$ is also analysed to determine whether H_2 blending influences soot maturation and absorption properties, while T_0 is also monitored. Furthermore, the experimental results are used to validate a state-of-the-art soot formation model developed by the CRECK modelling team [302–305].

7.2 Experimental and numerical setup

7.2.1 Flame conditions

The 60%C_2H_4 + 40%N_2/air flame is chosen as the reference flame, as it has been thoroughly investigated in the previous chapter. For the H_2-blended flame, the N_2 of the reference flame is replaced with H_2, and a portion of the C_2H_4 is also substituted by H_2 to maintain the same thermal power of 140 W. The flame conditions are summarised in Table 7.3. The volumetric flow rates are adjusted to ensure that the total fuel flow rate remains identical (as well as the fuel injection velocity: 35 cm/s), preserving a similar flame structure and dynamic between the reference and H_2-blended flames. The C_2H_4 and H_2 volumetric flow rate in the H_2-blended flame is 0.120 and 0.114 nl/min (0°C, 1atm), respectively. The air flow rate is unchanged (38 nl/min). The C_2H_4 flow rate is reduced by 14% compared to the reference flame, inducing the same reduction of the carbon mass flow rate. This implies that the hydrogen contributes to 14% of the flame thermal power. It has to be pointed out that, at the injection, the ethylene dilution is increased from 40% in the reference flame to 49% for the hydrogen flame. The adiabatic flame temperature at stoichiometry is computed with the NASA software "Chemical Equilibrium with Applications" available online [306]. It is 2323 K and 2366 K for the reference and H_2-blended flames, respectively.

Flame conditions		
	Reference flame	**Hydrogen flame**
Injection velocity (20°C)	**35 cm/s**	
Thermal power	**140 W**	
Fuel composition (%vol)	$\mathbf{60\%C_2H_4 + 40\%N_2}$	$\mathbf{51\%C_2H_4 + 49\%H_2}$
Carbon flow rate	**2.52 mg/s**	**2.16 mg/s**
Adiabatic flame temperature at stoichiometry	**2323 K**	**2366 K**

Table 7.3: Flame conditions for the reference flame and the H_2-blended flame.

For the sake of brevity, in what follows, the H_2-blended flame is referred to as the H_2 flame.

7.2.2 Experimental setup

The experimental setup is the same as described in Sec. 6.1, with no changes to the camera settings. The same measurement methodology is followed.

7.2.3 Numerical setup

CFD simulations have been run by B. Franzelli to complement the experimental estimations with information about the gas phase composition and the soot carbon-to-hydrogen ratio $\frac{C}{H}$. Simulations are run both for the reference and for the H_2 flames. The numerical setup is briefly described below.

The solver is the 1-D laminar flame solver of the OpenSmoke++ framework [302]. The gas phase is solved using the high-temperature CRECK mechanism of [303]. 244 gaseous species are considered with $\sim$6000 reactions. The model used for soot particles is the CRECK soot model described in [304, 305]. Within this model, heavy PAH and soot particles are arranged in 25 sections of lumped pseudo species called BINs. Lumped pseudo-species with a number of carbon atoms between 20 and 320 are classified as heavy PAH and are arranged in BINs 1 to 4, while larger ones (up to hundreds of millions of C atoms) are classified as soot particles in BINs 5 to 25. BINs 5 to 12 are spheres

from 2.02 to 10.11 nm. BIN12 represents the primary particles that are the building block of the soot aggregates represented by the BINs 13 to 25. Density is varying from 1.1 kg/m^3 for BIN5 to 1.85 kg/m^3 for BIN25. Each BIN is subdivided into three sub-BINs (A, B, and C) according to the carbon-to-hydrogen ratio of the lumped pseudo-species. $\frac{C}{H}$ and the equivalent sphere diameter of each BIN are available in [307]. Kinetic reactions for the BINs are classified into six classes: HACA mechanism, soot inception, surface growth, dehydrogenation, coalescence/aggregation, and oxidation. In total, the CRECK soot model contains 84 lumped-pseudo species (BIN) with ∼10000 reactions.

Due to the steady behaviour of the laminar flame and the axisymmetric geometry of the flame, the numerical domain selected is axisymmetrical. The numerical domain extends from -2.5 mm to +120 mm (0 mm corresponds to the injector exit) in the direction of the burner axis (vertical dimension) and from 0 to 38 mm in the radial dimension. The mesh is composed of roughly 15000 cells and is refined in the flame region, as well as near the burner surface. Figure 7.1 shows the numerical domain with the meshing, along with a picture of the H_2 flame.

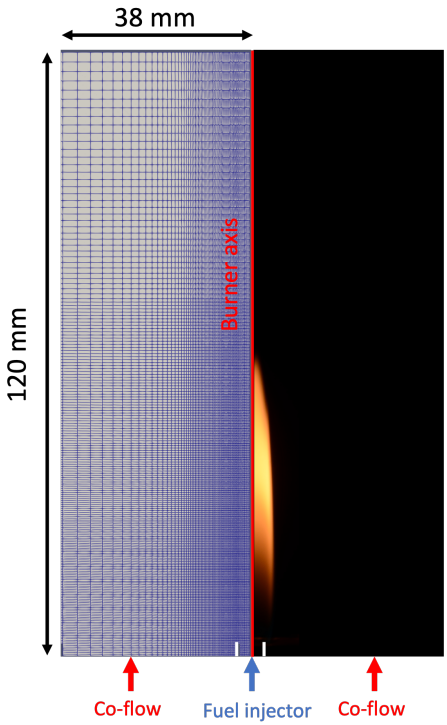

Figure 7.1: Mesh of the numerical domain and image of the C_2H_4+N_2/air flame.

Numerical calculation output notably contains the gas temperature, the soot volume fraction, and the mass fraction Y_i of the gaseous species and of the BINs species. The carbon-to-hydrogen ratio of the soot particles is computed from the outputs of the code as explained in Annex H.

7.3 Experimental comparison of the reference and H_2-blended flames

The impact of substituting N_2 with H_2 on f_v remains uncertain. In the present flames, blending H_2 increases the dilution of C_2H_4 (49% compared to 40% in the reference flame) and reduces the carbon flow rate by 14%, factors that would typically inhibit soot formation. However, unlike N_2, H_2 is chemically reactive and can influence soot production. Additionally, H_2 and N_2 differ in their diffusion properties, which further complicates their effects on

soot. Finally, the literature suggests that H_2 is generally less effective than N_2 in suppressing soot formation (Table 7.1). Therefore, experimental investigation is essential to clarify these effects.

This section compares the two flames based on experimentally measured quantities: radiated signal, absorption function, temperature, soot volume fraction, and mean soot primary particle diameter. The goal is to determine whether the substitution of H_2 alters the absorption function or the mean primary particle diameter of the soot, as well as to assess its impact on the soot volume fraction and its spatial distribution.

7.3.1 Flame natural emission

The natural emission from both flames was captured using a commercial camera without any filters. The images obtained are shown in figure 7.2, for which identical exposure times were used for both images.

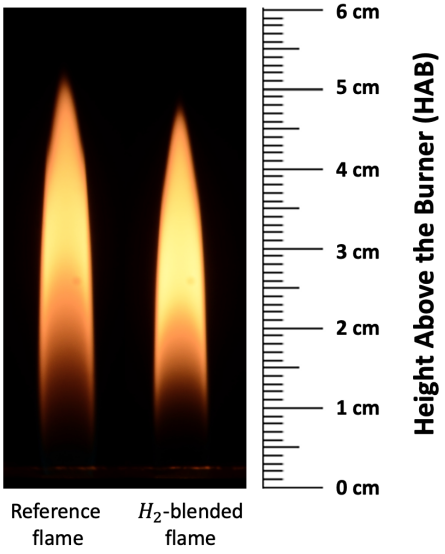

Figure 7.2: Pictures of the reference flame (left) and of the H_2 flame (right). Pictures were obtained using a commercial camera without a filter.

The orange/yellow colour indicates the presence of soot in both flames. Both are closed flames, meaning that most of the soot particles are oxidised before leaving the flame. The H_2 diluted flame appears $\sim$4 mm shorter than the reference flame, while it has a comparable radius. The H_2 flame appears more luminous than the reference flame. However, since these images show line-of-sight integrated signals, it is not possible to know whether the increased radiation in the H_2 flame originates from the core, the wings, or both. Based on the theoretical expression of the soot incandescence signal: $S_\lambda^{inc}(T) = 12\pi hc_{light}^2 f_v V_{col} \frac{E(m_\lambda)}{\lambda^6} \frac{1}{e^{\frac{hc_{light}}{\lambda k_B T}} - 1}$, an increase in luminosity indicates that at least one of the following quantities is higher across the flame width in the H_2 flame:

- soot volume fraction,
- flame temperature,
- soot absorption function.

It is tempting to attribute the more intense radiation of the flame to a larger f_v as the adiabatic flame temperatures of the flames are very close and because the soot absorption function is usually taken constant. However, the adiabatic flame temperature only indicates the maximum temperature that is likely to be encountered and does not inform the temperature spatial distribution. The soot absorption function may also be different for these flames and non-spatially uniform in the flame, as already seen for the reference and CH_4 flames of chapters 5, and 6. Therefore,

from this figure, it is not possible to state that the soot concentration is higher in the H_2 flame. Information extracted from LII signals will be used in the following to answer this question.

7.3.2 LII signal

Figure 7.3 shows the LII signal (background-corrected) at 578 nm for both flames, obtained for a laser fluence of 55 mJ/cm^2. Unlike the natural emission in Fig. 7.2, this LII signal is not integrated over the sensor's line of sight but corresponds directly to the soot incandescence within a specific slice of the flame.

The LII signal profile reveals substantial structural differences between the H_2-blended flame and the reference flame. In the wings, the reference flame shows a maximum LII signal intensity of 290 W/m^2/sr, while the H_2-blended flame reaches only about 220 W/m^2/sr, i.e., a reduction of roughly 25%. However, in the core of the flame, the LII signal for the H_2 flame is almost twice as intense as that of the reference flame. The spatial extent of the wings also differs, with the H_2 flame wings disappearing around a HAB of 28-30 mm, compared to 36-38 mm in the reference flame. Along the centreline, the LII signal appears earlier in the H_2 flame, starting at a HAB of 22 mm compared to 28 mm for the reference, and it disappears at a HAB of 48 mm. These changes suggest, assuming similar flow velocities for both flames, that in the centreline of the H_2 flame, soot particles -which are the origin of the LII signal- appear (are formed) and disappear (are oxidised) earlier, indicating an acceleration in the chemistry at the origin of the soot formation and destruction.

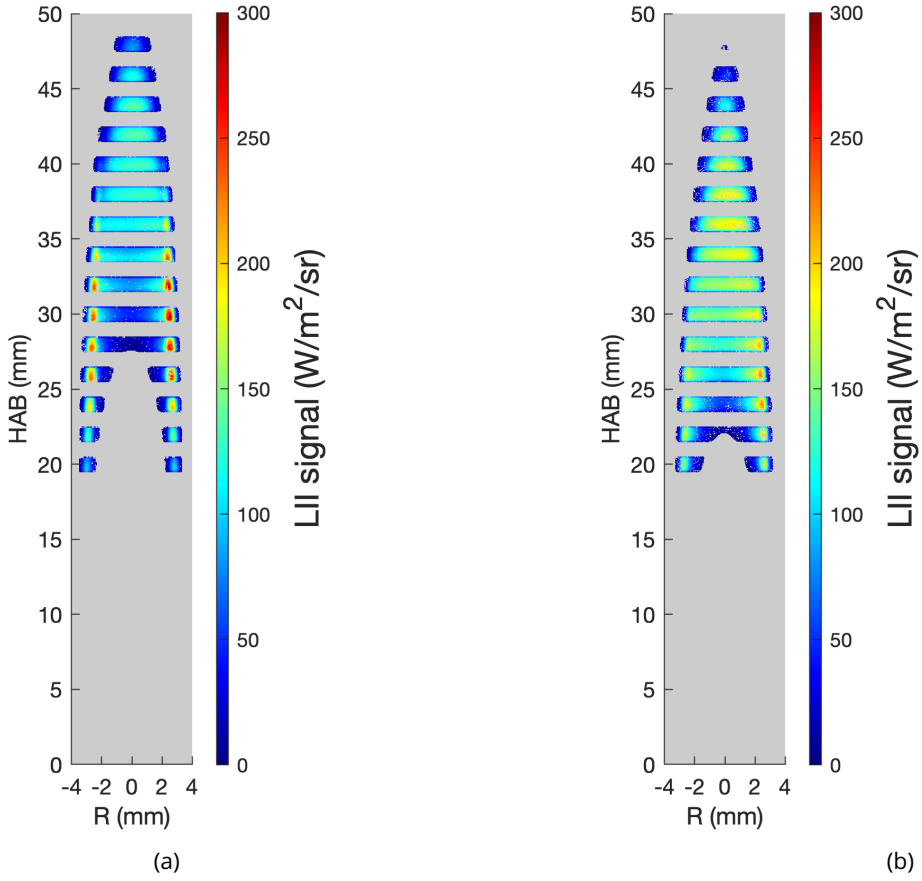

Figure 7.3: LII signal at 578 nm for a laser fluence of 55 mJ/cm^2 in (a): the reference flame, and (b): the H_2 flame.

7.3.3 Soot absorption function $E(m_\lambda)$

The absorption function is calculated following the same procedure as in the previous chapter by fitting the linear portion of the T_M vs F curves using the equation:

$$T_M = \frac{6\pi}{\rho c \lambda_{laser}} E(m_{\lambda_{laser}}) F + T_0, \tag{7.2}$$

The absorption function in both flames is represented as 2D maps in Fig. 7.4. Axial and radial profiles (at HAB = 20, 22, 28, and 40 mm) are given in Fig. 7.5. In both flames, lower $E(m_\lambda)$ are mostly found in the inner and lower part of the flames and correspond to recently formed particles. The value of $E(m_\lambda)$ on the core of the flame is not significantly different (∼10%), with ∼0.55 and 0.5 for the reference and H_2 flame, respectively. However, for the H_2 flame, $E(m_\lambda)$ in the wings is only slightly higher than on the centreline, while the difference is clearly more pronounced for the reference flame.

The axial profiles of $E(m_\lambda)$ display nearly identical trends, characterised by an initial increase at low HABs followed by a plateau at higher HABs. However, the profiles for the H_2 flame are shifted 5-6 mm upstream compared to the reference flame. In the H_2 flame, $E(m_\lambda)$ stabilises at a plateau value of 0.5, whereas the reference flame reaches a slightly higher value (0.55). These findings align with recent results from Garcia et al. [143], which reported no significant differences in the maximum values of $E(m_\lambda)$ when blending C_2H_4 with H_2, while maturation (the increase in $E(m_\lambda)$) takes place at lower HABs when H_2 is added.

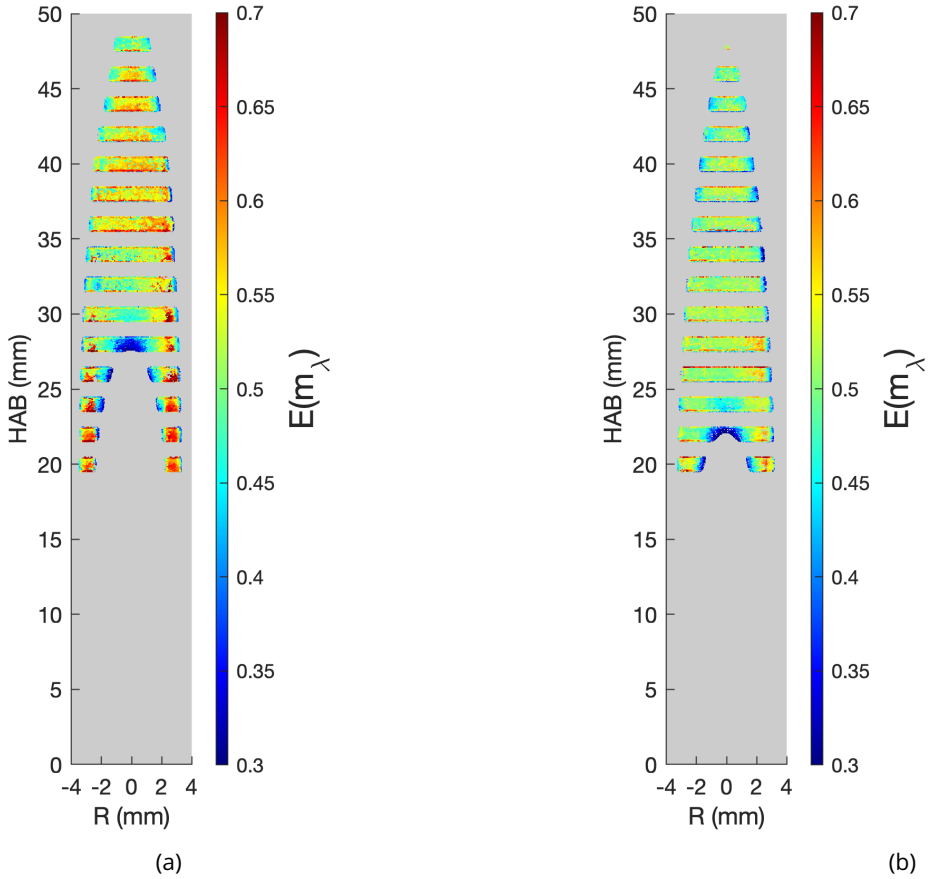

Figure 7.4: Soot absorption function for (a): the reference flame, and (b): the H_2 flame.

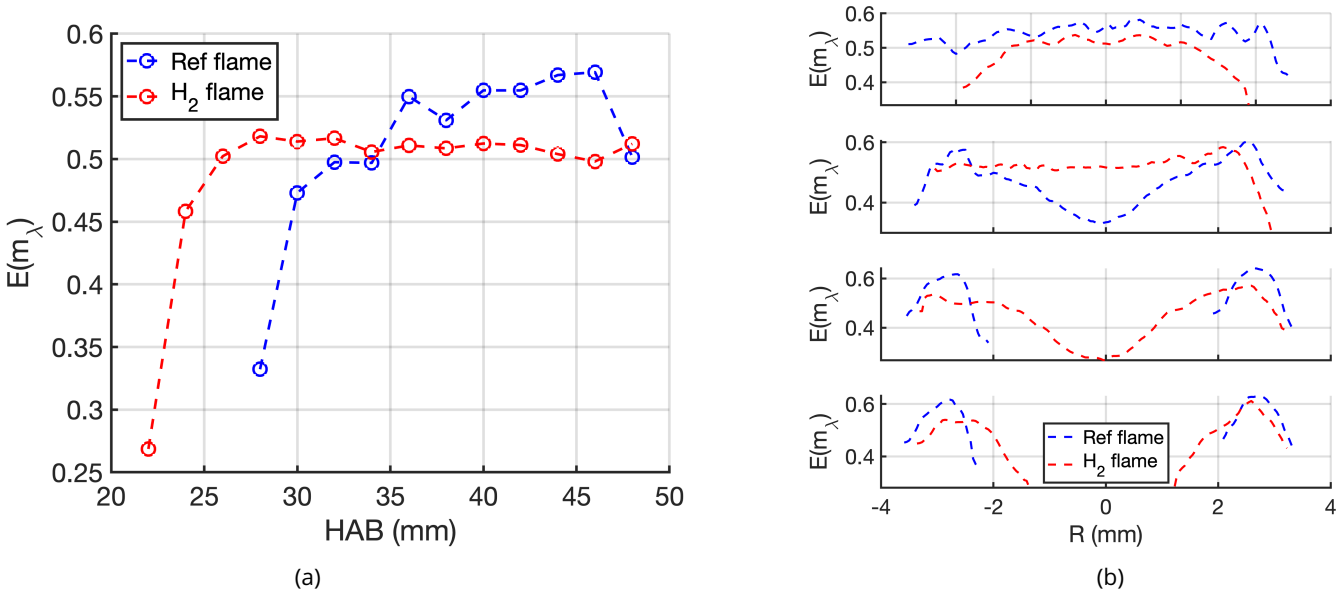

Figure 7.5: (a): Soot absorption function versus the HAB for the reference flame (blue) and the H_2 flame (red). (b): Soot absorption function versus the radius at different HABs (from bottom to top: 20, 22, 28, 40 mm) for the reference flame (blue) and the H_2 flame (red).

Histograms of occurrences of $E(m_\lambda)$ available in Fig. 7.6 show a narrower distribution for the H_2 flame, centred around 0.5, confirming the mostly uniform behaviour of $E(m_\lambda)$ that can be seen looking at Fig. 7.4b. High values above 0.6 are not found in the H_2 flame, contrary to the reference flame. As a result, $E(m_\lambda)$ is, in general, slightly lower in the H_2 flame than for the reference flame. H_2 blending did change the $E(m_\lambda)$ distribution, but not the value for mature soot in the flame centreline that is 0.5-0.55.

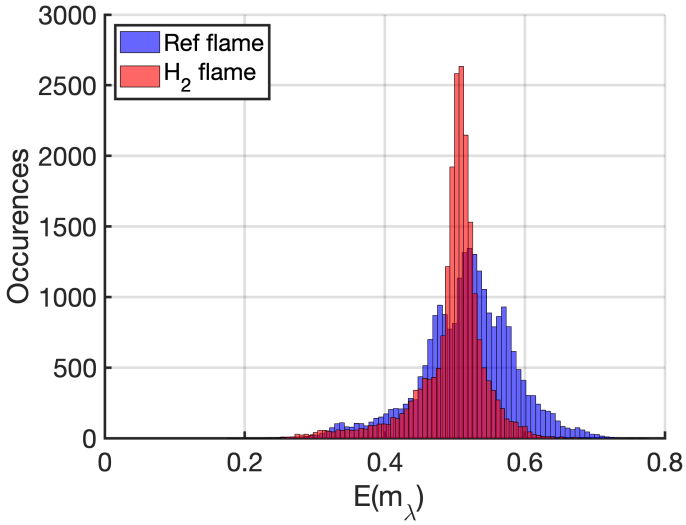

Figure 7.6: Histogram of the soot absorption function for the reference flame (blue) and the H_2 flame (red).

From these results, H_2 blending shifts the $E(m_\lambda)$ distribution to lower HABs: mature soot are found at lower HABs compared to the reference flame. H_2 blending does not appear to significantly affect the value of $E(m_\lambda)$ for mature soot. However, the very high values found in the wings of the reference flame (above 0.6) were not observed in the H_2 flame, which raises questions about the mechanisms behind these high values.

7.3.4 Gas temperature T_0

The gas temperature is determined from the linear fit of the T_M versus F curves (similar to what has been done in the previous chapter) and by 2C pyrometry (see Annex E). To differentiate between the two, the first method is labelled as "LII," while the second is referred to as "Pyro." Pyrometry was included as it provides a secondary comparison of T_0 and offers smoother T_0 profiles (except on the flame centreline due to the data inversion algorithm), facilitating the interpretation of the results. It is important to note that for both methods, the same assumption is made regarding the wavelength dependence of $E(m_\lambda)$: it is assumed to be wavelength-independent.

Figure 7.7 displays 2D maps of gas temperature obtained by LII and pyrometry. In addition, to highlight the differences between the two flames, axial and radial profiles of T_0 at HAB = 20, 22, 28, and 40 mm are included in Fig. 7.8. The two methods give quite similar results. The 2D profiles show that the region of higher temperatures (above $\sim$2000 K) is the exterior edge of the profiles -where the LII and incandescence signals disappear- indicating that the soot disappears in these regions, probably due to their oxidation. The interior of the flame is cooler and stays below 2000 K, with lower values found on the centreline at the lowest HABs.

According to the pyrometry estimations, the maximum temperature -found at the exterior edges of the 2D profiles- is about 50 K higher in the H_2 flame compared to the reference flame. The average temperature is similar for both flames: approximately 2030 K for both flames based on LII measurements, while the pyrometric results show slightly lower values: 1970 K for the reference flame and 1990 K for the H_2 flame.

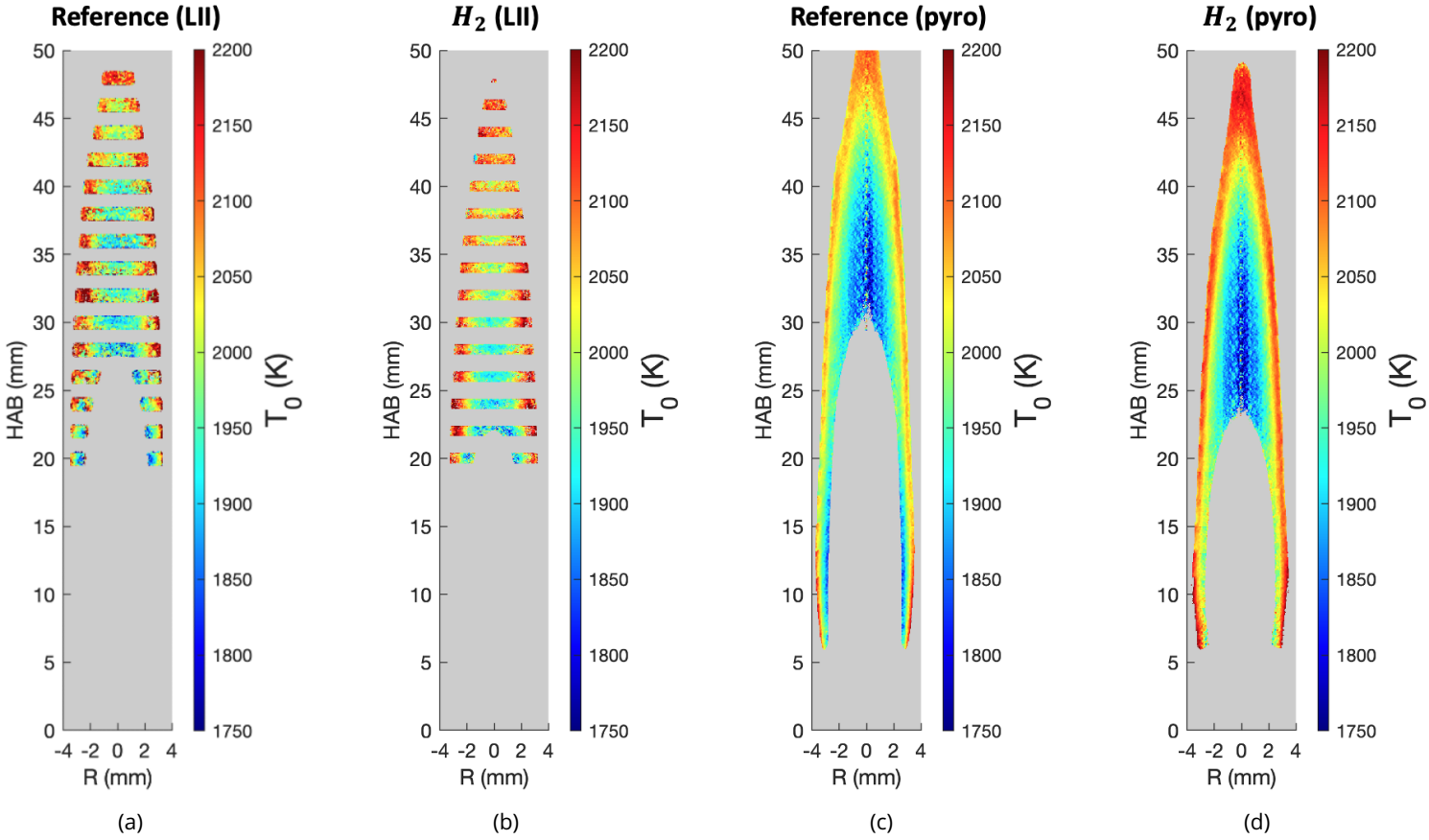

Figure 7.7: (a) and (b): Gas temperature obtained from LII measurements (linear fit method) for the reference flame and the H_2 flame, respectively. (c) and (d): Gas temperature obtained by pyrometry for the reference flame and the H_2 flame, respectively.

The LII signal on the flame centreline appears near HAB = 28 mm for the reference flame and 22 mm for the H_2

flame. In contrast, the natural incandescence signal appears slightly later, at HAB = 30 mm for the reference flame and 23 mm for the H_2 flame. This indicates the presence of soot at lower HAB in the H_2 flame. This also highlights that (with the present settings) LII can detect soot particles having lower absorption and emission properties (found at lower HABs in the flame core) compared to pyrometry. On the flame centreline, the temperature profiles obtained by pyrometry are shifted upstream for the H_2 flame by 4 mm. The amplitude of the fluctuations in the LII profiles does not allow the same conclusions to be drawn. Still on the centreline, the temperature is roughly identical below $\sim$35 mm, while it becomes higher for the H_2 flame between 35 and 48 mm, with temperature differences reaching 100 K.

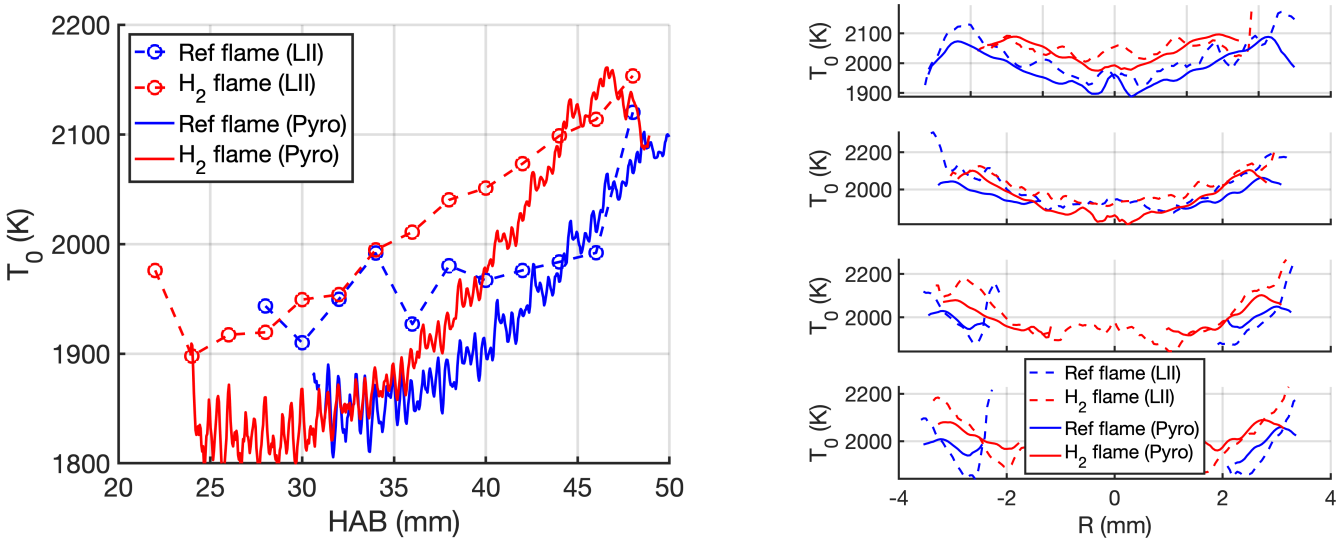

Figure 7.8: (a): Gas temperature versus the HAB for the reference flame (blue) and the H_2 flame (red). Estimations by LII are in dashed lines with circles, while estimations from pyrometry are in solid lines. For the pyrometry data, as the data on the centreline are of poor quality, it is the data for R = -150μm is plotted instead of R = 0 mm. (b): Gas temperature versus the radius at different HABs (from bottom to top: 20, 22, 28, 40 mm), for the reference flame (blue) and for the H_2 flame (red). In order to reduce fluctuation, the axial plot is smothered with a rectangular window of 5 pixels.

The present results indicate that H_2 blending does not significantly affect the temperature fields other than shifting it upstream, providing a similar thermal environment to the soot particle of both flames. The upstream shift of the temperature field might be attributed to the increased reactivity of the fuel mixture: the high reactivity of H_2 accelerates the exothermic reactions involved in fuel decomposition, leading to earlier heat release, and ultimately increased temperature at lower HABs and residence times, but this would need additional measurements to be confirmed.

As a side note, the temperature difference between the flames, typically less than 100 K, cannot explain the observed disparity in LII signals shown in Fig. 7.3. Given that the incandescence signal varies exponentially with temperature, a difference of 100 K would lead to a substantial change in the emitted signal. For example, at 716 nm, the emission at 2000 K is approximately 40% higher than at 1900 K. However, in Fig. 7.3, the H_2 flame produces 2-3 times more signal along the centreline near HAB = 30-35 mm. Therefore, the differences in T_0 alone cannot account for the increased luminosity of the H_2 flame. Since both $E(m_\lambda)$ and T_0 are similar between the two flames, the most likely explanation is that the soot volume fraction, f_v, is higher in the H_2 flame, explaining the stronger incandescence signal.

7.3.5 Soot volume fraction f_v

The soot volume fraction obtained from AC-LII measurements with a laser fluence of 55 mJ/cm^2 is presented in 2D maps for both flames in Fig. 7.9. Axial and radial cuts are also given in Fig. 7.10.

The f_v distribution varies significantly between the two flames. In the reference flame, f_v values in the wings are similar to those at the core, while in the H_2 flame, the maximum f_v occurs along the centreline for heights above 24 mm, with the wings being much less pronounced. The axial profiles reveal that soot particles are detected 6 mm earlier in the H_2 flame, with the peak f_v occurring roughly 4 mm earlier as well. Between HAB = 30-36 mm, soot concentration in the H_2 flame is 1.6 to 2 times higher than in the reference flame. Above 44 mm, the soot concentration in the H_2 flame drops below that of the reference flame. This higher soot concentration in the H_2 flame can explain the higher luminosity of this flame. The peak f_v level aligns with the findings of Steinmetz et al. [44], who reported a ~60% increase in the maximum f_v when substituting N_2 with H_2 in the same reference flame while maintaining a constant carbon flow rate (resulting differently from our case, in an increase of the flame thermal power).

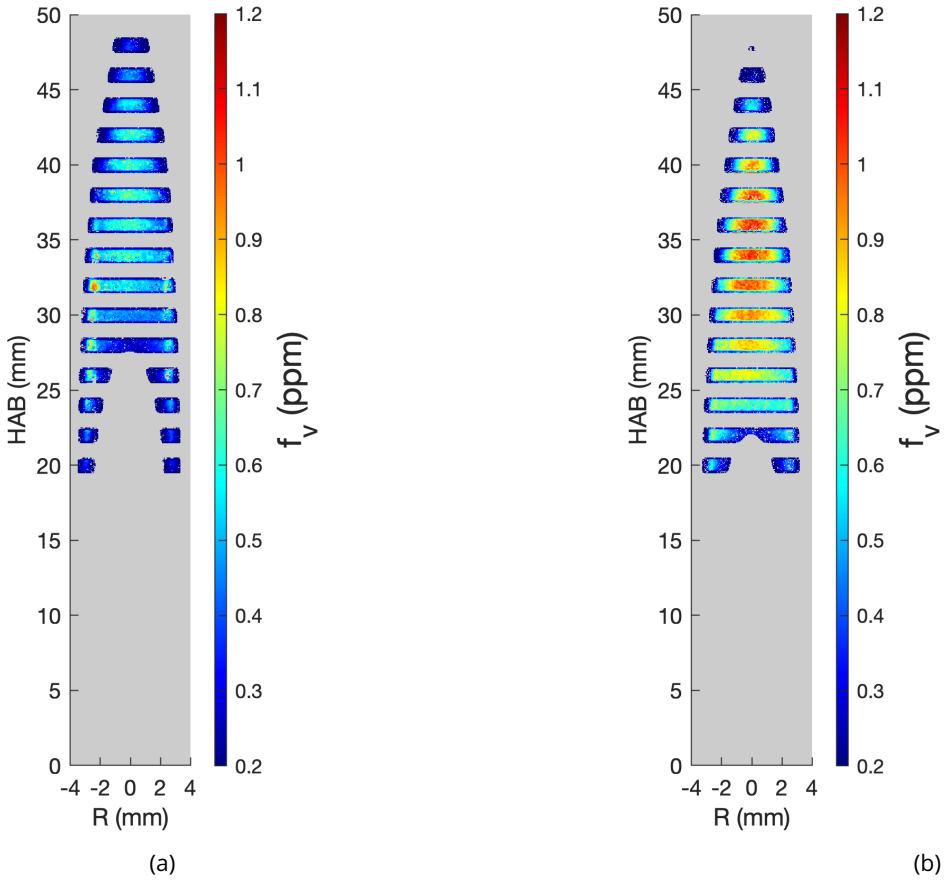

Figure 7.9: Experimental soot volume fraction for (a): the reference flame, and (b): the H_2 flame. The laser fluence is 55 mJ/cm^2.

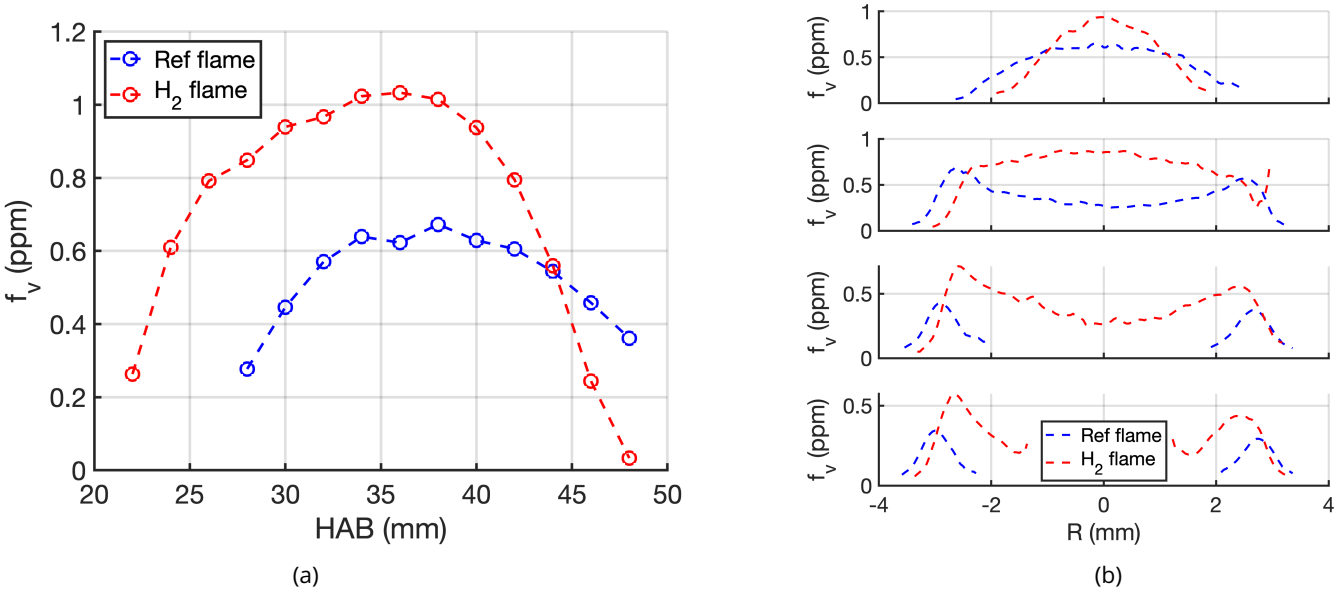

Figure 7.10: (a): Soot volume fraction versus the HAB for the reference flame (blue) and the H_2 flame (red). (b): Soot volume fraction versus the radius at different HABs (from bottom to top: 20, 22, 28, 40 mm), for the reference flame (blue) and for the H_2 flame (red).

Radially integrated soot volume fraction: β_{soot}

The f_v profile shown in Fig. 7.9 provides information on the soot volume fraction within a slice of the flame but is not adapted to follow the axial evolution of the soot load. Indeed, as these laminar diffusion flames are axisymmetric, the soot located in the wings of the flames contribute more to the overall soot volume than the same f_v found on the centreline, as it covers a larger circumferential area when integrated around the flame (contribution in soot volume scale with the radial position). To assess the evolution of the soot load along the HAB, the f_v distribution can be radially integrated for each HABs. The radially integrated soot volume fraction β_{soot} (in ppm.m^2) is [308]:

$$\beta_{soot} = \int_0^{R_{flame}} \int_0^{2\pi} f_v(r) r dr d\theta \approx \pi \sum_{i=-\frac{N_{pixel}}{2}}^{\frac{N_{pixel}}{2}} f_v(i) R \Delta R, \tag{7.3}$$

where R_{flame} is the flame radius, N_{pixel} is the number of pixels in the radial direction, ΔR is the pixel size (45.4 μm), R_i and $f_v(i)$ are the radial position and the value of the soot volume fraction for the pixel number i, respectively.

The axial evolution of β_{soot} given in Fig. 7.11 provides a more complete picture of how the soot load evolves along the HAB. It is remarkable that the maximum value of β_{soot} is almost identical in the two flames although not reached for the same HAB, with the H_2 flame reaching it at HAB = 24-26 mm, against HAB = 32 mm for the reference flame. An increase in soot volume fraction with the HAB indicates that soot nucleation and/or surface growth is dominant at a given height, while a decrease suggests that oxidation becomes the prevailing process. Therefore, assuming similar evolution of the velocity fields in both flames, the observed trend for β_{soot} suggests that soot formation and oxidation occur at lower HABs in the H_2 flame.

The integration of β_{soot} over the HAB range (from 20 to 48 mm) reveals that the total soot volume in the H_2 flame is 7% greater than in the reference flame.

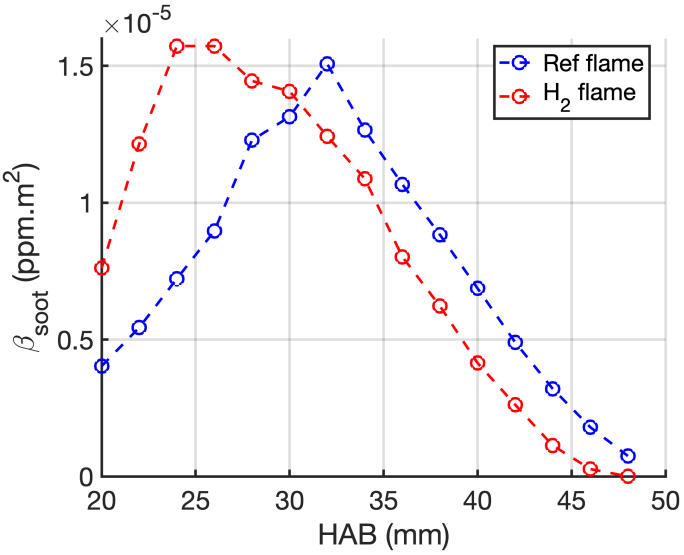

Figure 7.11: Radially integrated soot volume fraction versus the HAB. Blue and red curves correspond to the reference and H_2 flames, respectively.

In summary, H_2 substitution changes the soot concentration and spatial repartition: it boosts f_v on the centreline, while soot particles are less present in the wings. However, the axial evolution of f_v and β_{soot} are similar in both flames but shifted upstream in the H_2 flame. The integrated soot volume (between 20 and 48 mm) is slightly increased, even if the H_2 flame is less spatially extended. The higher peak volume of f_v and soot volume is surprising for the H_2 flame as the carbon flow rate was reduced by 14 %, and indicates that H_2 is likely to promote soot compared to N_2, potentially due to its chemical effects.

7.3.6 Soot primary particle diameter d_p

The mean soot primary particle diameter is determined using TIRE-LII by fitting the temporal decay of the soot particle temperature (refer to Section 3.4.4). For this calculation, the gas temperature is required, and the values obtained from LII are used. Results for both flames are presented as 2D maps in Fig. 7.12 and are completed by axial and radial profiles (at HAB = 20, 22, 28, and 40 mm) in Fig. 7.13a, and 7.13b, respectively.

In both flames, smaller soot particles are observed in the lower inner regions (where the particles are weakly absorbing, indicating younger particles) and at the tip of the flame (where the particles undergo strong oxidation), while larger particles are observed in the wings. The wings of the reference flame contain larger particles, with diameters ranging from 40 to 50 nm, compared to approximately 35 nm in the H_2 flame. The axial profiles for both flames are similar, though the profile for the H_2 flame is shifted upstream by 4-6 mm. Initially, both profiles exhibit an increase in d_p, indicating surface growth and/or particle coalescence, followed by a decrease as oxidation occurs. For both flames, the peak particle diameter along the centreline is just over 20 nm.

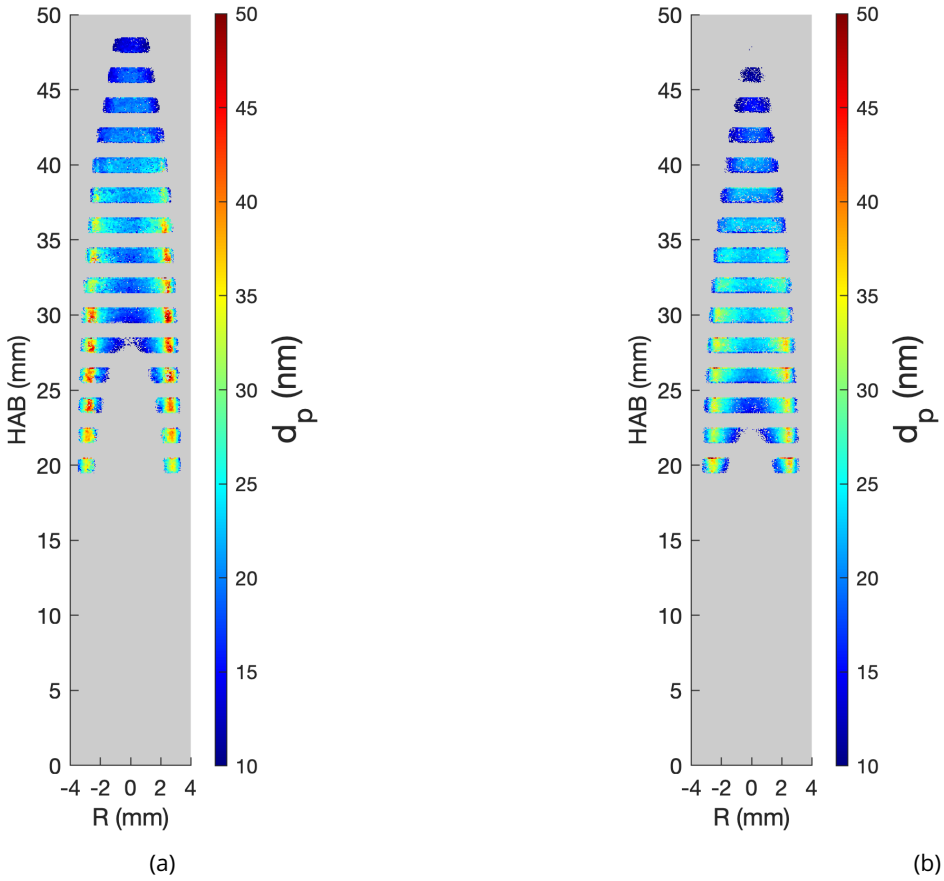

Figure 7.12: Experimental soot primary particle diameter for (a): the reference flame, and (b): the H_2 flame.

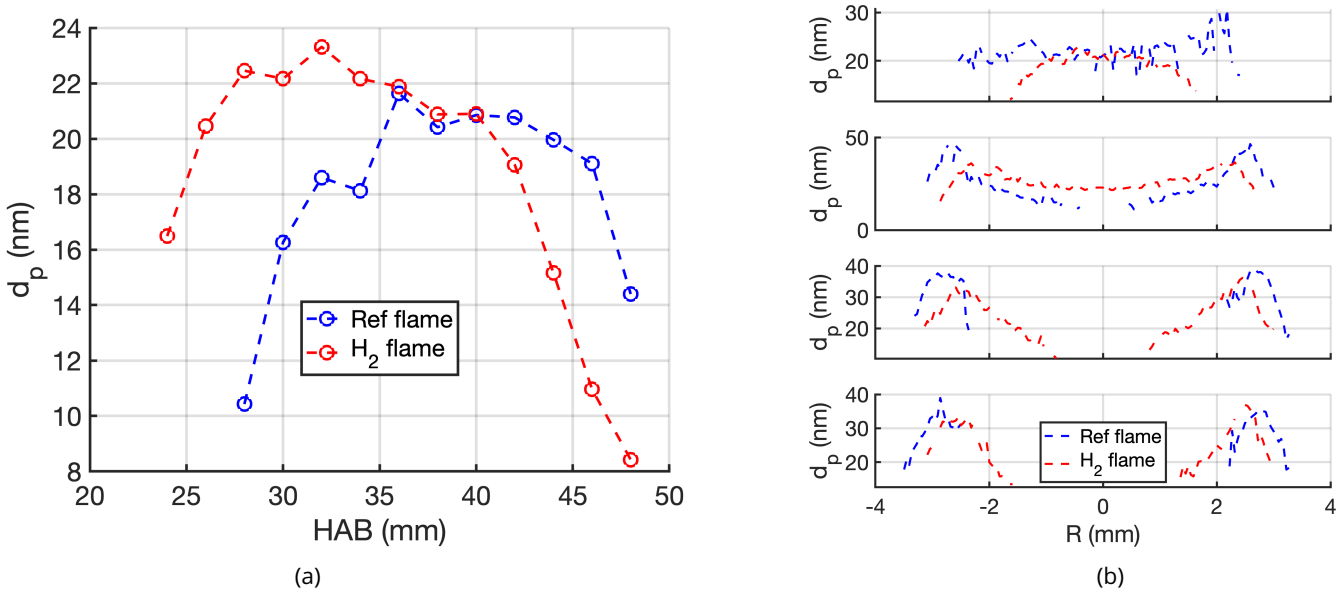

Figure 7.13: (a): Soot primary particle size versus the HAB for the reference flame (blue) and the H_2 flame (red). (b): Soot primary particle diameter versus the radius at different HABs (from bottom to top: 20, 22, 28, 40 mm), for the reference flame (blue) and for the H_2 flame (red).

The average d_p for the probed regions of the flames is 23 nm in both flames. However, the repartition of d_p is slightly different (Fig. 7.14). The distribution of d_p in the H_2 flame is symmetrical around its mean value (23 nm).

In comparison, the reference flame has more big particles with d_p above 30 nm (particles in the wings) but also presents more small particles with a maximum of occurrence for 20 nm, resulting in a median slightly below those of the H_2 flame with 22 nm.

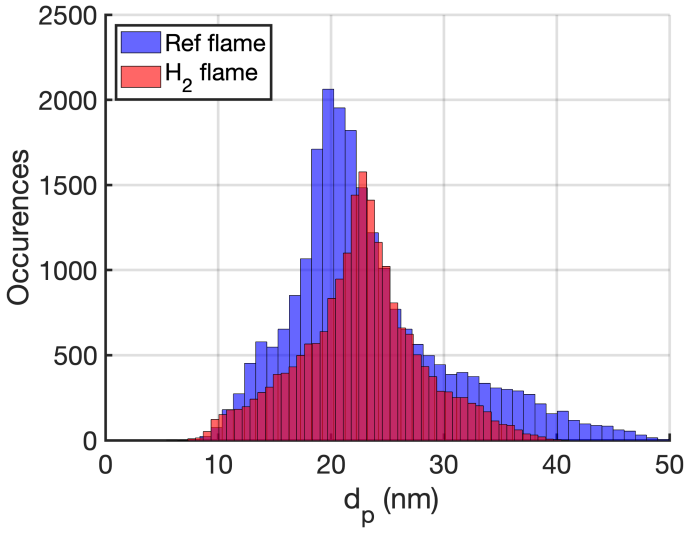

Figure 7.14: Histogram of soot primary particle size for the reference flame (blue) and the H_2 flame (red).

Therefore, in this work, H_2 blending does not impact much the mean primary particle size, nor its value on the centreline (although it shifts the profile upstream), but reduces the maximum d_p found in the wings. Zhao et al. [291] found no effect on d_p when adding H_2 to another C_2H_4/air laminar diffusion flame. This is in contrast with the results of other works on hydrogen blending [183, 296], which found a reduction of d_p when H_2 was blended to the fuel in other flame conditions (premixed and diffusion). The variety of results of the literature and the different behaviour in the centreline and wings in the present work shows that the effect of H_2 on d_p is challenging to predict *a priori* in specific conditions and that experimental studies are still required to eventually identify general behaviour on the effects of H_2 on the soot production. It is important to note that the d_p estimations derived from LII measurements at each pixel location represent mean primary particle sizes and do not provide information about the actual size distribution within each pixel. Additionally, this method offers no information about the size of particles exiting the flame. It would be valuable to obtain precise soot particle size distributions at various flame positions to examine the effect of H_2 on the actual particle size. This is especially important at the flame tip to assess the size of any particles exiting the flame, which is crucial for evaluating potential health risks.

7.4 Comparison of the numerical results with the experimental profiles of f_v, T_0, and $E(m_\lambda)$

The experimental measurements revealed significant differences between the two flames. To fully understand the origin of these differences, additional data on the gas-phase composition (specifically the concentration and nature of soot precursors and oxidative species) would be necessary. Unfortunately, the current LII experimental setup does not allow for the measurement of such information. However, CFD simulations can provide insight into the local concentrations of these gaseous species, as well as soot distribution across the entire flame. Before relying on these simulations, they must first be validated against experimental data. Therefore, this section focuses on comparing numerical predictions of f_v and T_0 with the experimental results presented in the previous section. Additionally,

since both the soot absorption function $E(m_\lambda)$ and the ratio $\frac{C}{H}$ are linked to soot maturity (as discussed in Section 2.6), experimentally determined $E(m_\lambda)$ values and numerically computed $\frac{C}{H}$ are confronted to assess their degree of correlation.

7.4.1 Comparison of the gas temperature T_0

Numerically obtained gas temperature is plotted in Fig. 7.15, with the right and left halves corresponding to the H_2 and reference flames, respectively. Similarly to the experimental results of Fig. 7.7 (pyro + LII), the higher temperature values are in the upper part of the flame and on the external border of the flame, where soot oxidation is expected. The 2D maps and the radial cuts (at HAB = 20, 22, 28, and 40 mm) of Fig. 7.16b show that numerical temperatures are, for most of the flame at least 100 K below experimental estimations.

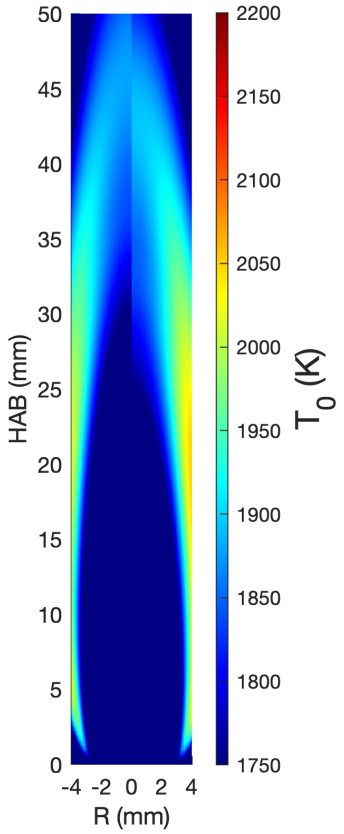

Figure 7.15: Numerical estimation of the gas temperature for the reference flame (left part), and the H_2 flame (right part).

On the flame centreline (Fig. 7.16a), the numerical profiles of the two flames are almost identical (same trend, with maximum values differing by only 5 K), but one of the H_2 flames is shifted 3.3 mm upstream. On the flame centreline, the gas temperatures obtained from numerical simulations are 100-200 K below the experimental temperatures obtained by LII but are much closer to the ones obtained by pyrometry. Higher differences are found at low HABs and at the tip of the flames, where differences can overcome 300 K.

The numerical results successfully capture the upstream shift in the temperature distribution and, overall, show good qualitative agreement with the experimental data. While the simulations predict lower temperatures than those measured experimentally, the numerical values are still consistent with the experimental data, considering the inherent uncertainties. These uncertainties primarily stem from assumptions about the wavelength depen-

dence of the soot absorption function. As discussed in Section 5.3.2 of Chapter 5 and in Annex E, deviations from this assumption can significantly impact temperature estimates (up to +200 K). This effect is particularly pronounced for younger soot particles, which may exhibit a stronger wavelength dependence in their absorption function (see Section 2.6.2). Additionally, thermal equilibrium between the soot and the gas phase is assumed. However, this may not always hold, especially during soot oxidation, where exothermic reactions could locally increase the soot temperature. Therefore, it can be concluded that the numerical simulations are able to fairly predict the gas temperature in these flames.

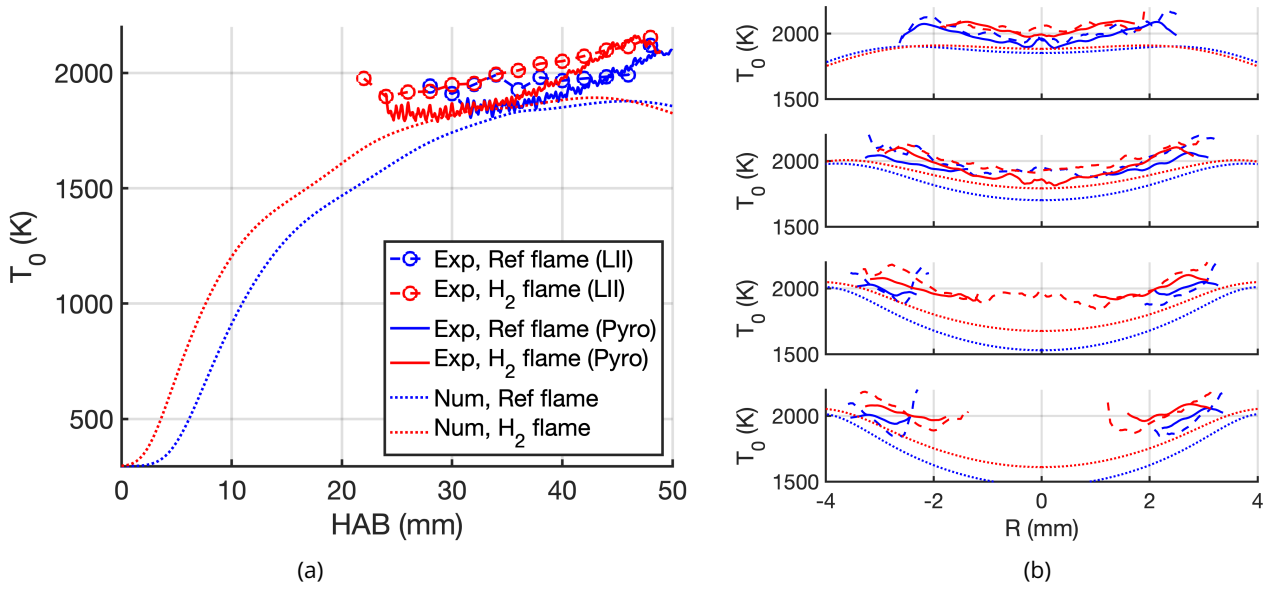

Figure 7.16: (a): Gas temperature versus the HAB for the reference flame (blue) and the H_2 flame (red). (b): Gas temperature versus the radius at different HABs (from bottom to top: 20, 22, 28, 40 mm), for the reference flame (blue) and for the H_2 flame (red). Estimations from the experimental results are in dashed lines (LII) and solid lines (pyrometry), and the dotted lines correspond to the numerical results. For the pyrometry data, as the data on the centreline are of poor quality, it is the data for R = -150μm is plotted instead of R = 0 mm. In order to reduce fluctuation, the axial plot is smothered with a rectangular window of 5 pixels.

7.4.2 Comparison of f_v

The numerically obtained f_v is shown in 2D in Fig.7.17a, with the right and left halves corresponding to the H_2 and reference flames, respectively. Normalised radial cuts for heights above the burner (HAB = 20, 22, 28, and 40 mm) are provided in Fig. 7.17b to allow for a qualitative comparison with the experimental data.

The numerical predictions tend to overestimate the soot concentration compared to experimental measurements, with peak values around 1.8 ppm in the simulations versus $\sim$1.1 ppm experimentally, resulting in a 64% difference. For the reference flame, the numerical results predict that f_v peaks in the wings up to HAB = 35 mm, which aligns with experimental observations. However, the predicted peak f_v in the wings is about 80% higher than on the flame centreline, which contrasts with experimental data, where f_v is nearly equal in both regions. In the case of the H_2 flame, the wings are predicted to extend up to HAB = 28 mm, significantly higher than the experimental observation of wing disappearance at around HAB = 24-26 mm. Similar to the reference flame, f_v values in the wings compared to the values on the centreline are overestimated in the numerical results, showing 1.8 ppm compared to less than 0.8 ppm in the experimental data at the same positions.

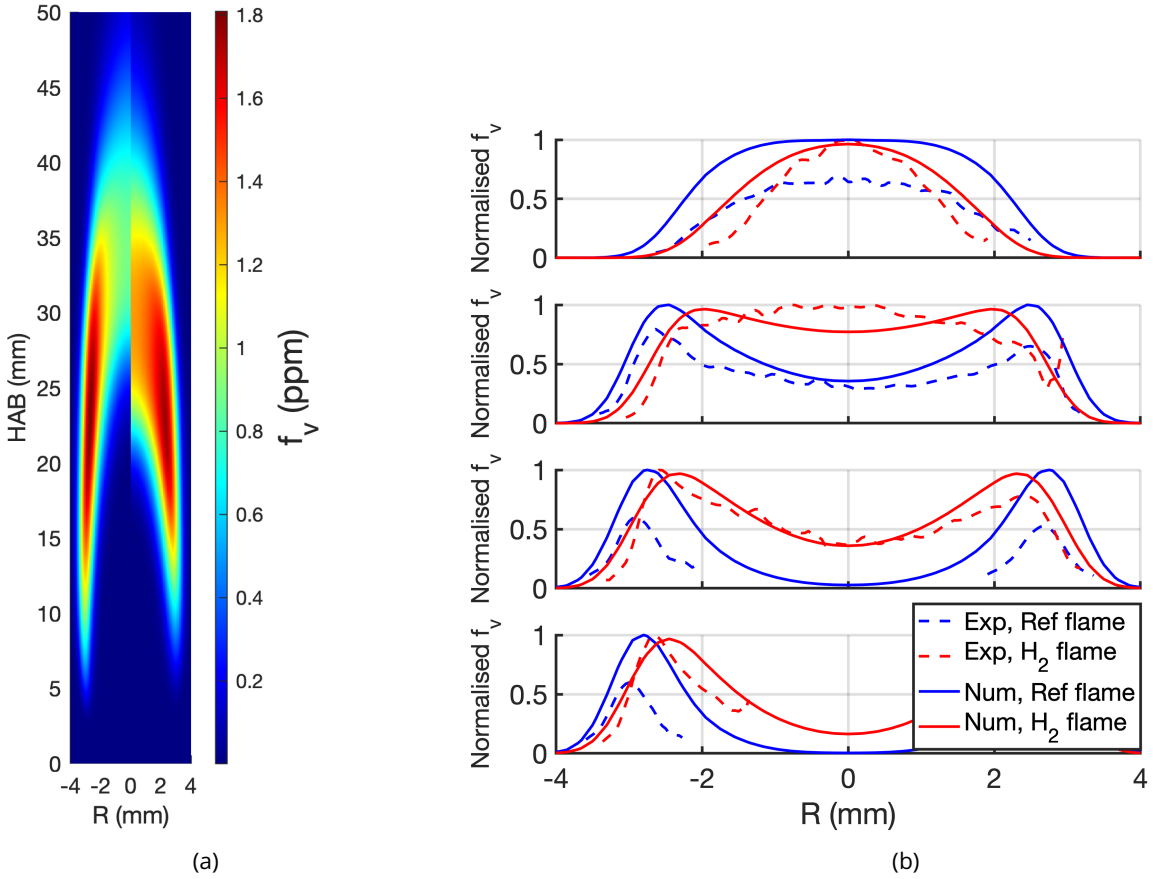

Figure 7.17: (a): Numerical soot volume fraction for the reference flame (left) and the H_2 flame (right). (b): Soot volume fraction versus the radius at different HABs (from bottom to top: 20, 22, 28, 40 mm) for the reference flame (blue) and for the H_2 flame (red). Estimations from the experimental results are in dashed lines, and the solid lines correspond to the numerical results.

The axial profiles of f_v in Fig. 7.18a demonstrate that the numerical model successfully captures the increase in f_v at the flame centreline with H_2 blending. The numerical results show a 46% rise in peak f_v, compared to a 54% increase in the experimental data, though the numerical values are ~30% higher than the experimental ones. The upstream shift of the f_v profile with the H_2 flame is also well reproduced by the model, but the numerical profiles are ahead of the experimental ones by 2-6 mm.

Radially integrated soot volume fraction: β_{soot}

The radially integrated soot volume fraction, β_{soot}, shows a maximum value 2.8 times larger in the numerical results compared to the experimental data. To account for this discrepancy, β_{soot} is normalised in Fig. 7.18a.

As the f_v distributions are shifted upstream for the numerical results, profiles of β_{soot} also follow this trend. Below 24 mm, normalised β_{soot} is numerically overestimated. This overestimation is primarily due to the numerical model's overprediction of soot in the flame wings. However, it is to be expected that experimental results under predict β_{soot} at low HAB, as in this region, the young particle characterised by lowly absorbing and emitting properties are not all detected with the present experimental settings, leading to an apparent absence of soot particles near the flame centreline at low HAB, lowering the value of β_{soot}. Numerically, the total soot load (between HAB = 20 and 48 mm) is predicted to be 12% lower for the H_2 flame (11% lower over the entire flame), whereas the experimental results show a higher soot load in the H_2 flame. This shows that the numerical model does not capture the overall increase in soot load with H_2 blending.

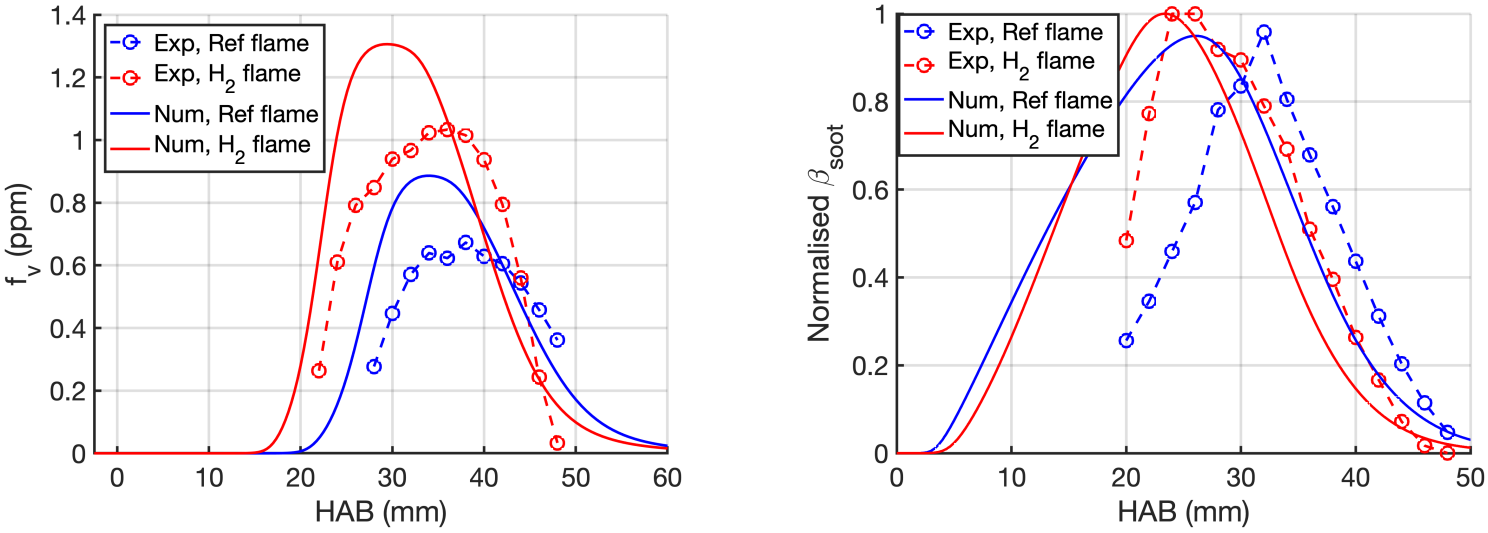

Figure 7.18: (a): Axial evolution of the soot volume fraction for the reference flame (blue) and the H_2 flame (red). (b): Radially integrated soot volume fraction versus the HAB. Blue and red curves correspond to the reference and H_2 flames, respectively. Experimental results are in dashed lines and were obtained with a laser fluence of 55 mJ/cm^2, while experimental ones are in solid lines.

Quantitatively, there are notable differences between the numerical and experimental estimations of f_v, with the numerical results clearly overpredicting soot volume fraction. This discrepancy likely comes from both inaccuracies in the numerical model and experimental uncertainties due to the f_v anomaly. However, qualitatively, the numerical model captures several key trends. It successfully reproduces the increase in f_v at the flame centreline with H_2 blending and accurately predicts the magnitude of this increase. The upstream shift of the f_v profile due to H_2 blending is also well captured. For the reference flame, the model correctly predicts the spatial extent of the soot wings, though it does not with the H_2 flame. While the numerical model does capture the reduction of f_v in the wings in the H_2 flame, the attenuation is much weaker than observed experimentally. In addition, for both flames, the model overestimates f_v in the flame wings, suggesting higher values relative to the centreline than were measured experimentally. Though there is no perfect quantitative agreement between simulation and experiment, the qualitative trends globally align, with the primary divergence being an overprediction of soot in the wings, particularly in the H_2 flame.

7.4.3 Comparison of $E(m_\lambda)$

In this thesis, $E(m_\lambda)$ is of prior interest because it is required to compute f_v by AC-LII, but also because it allows tracking of the soot maturity. Unfortunately, $E(m_\lambda)$ cannot be obtained numerically using the CRECK model. However, $\frac{C}{H}$ can be numerically computed, and both $E(m_\lambda)$ and $\frac{C}{H}$ are known to increase with the maturation process [51, 70]. Specifically, experimentally obtained $\frac{C}{H}$, and the mass absorption coefficient $MAC = \frac{6\pi E(m_\lambda)}{\rho}$ were found to be somehow correlated in [127, 309], the MAC was found to be low and weakly increasing with the increase of $\frac{C}{H}$ up to a limit value of about 10. Above this value, the MAC steeply increases. Recently, Garcia et al. [143] compared $E(m_\lambda)$ computed from the soot maturity coefficient ($\alpha_{soot} - 1$) experimentally determined with the method of Yon et al. [51], to the numerically derived soot maturity coefficient computed from the soot carbon-to-hydrogen ratio, and found a qualitative agreement between these quantities. Therefore, here, the experimentally obtained $E(m_\lambda)$ is confronted with the numerical $\frac{C}{H}$ to verify if a certain degree of correlation exists between them. If so, the CRECK model could follow the soot maturation process by monitoring the spatial evolution of $\frac{C}{H}$.

$\frac{C}{H}$ is computed in post-processing as described in Annex H. Its spatial evolution for the reference and H_2 flame is given in Fig. 7.19a, it is to be compared to the experimental $E(m_\lambda)$ profiles of Fig. 7.4a and Fig. 7.4b. $\frac{C}{H}$ is given only in zones where the numerical soot volume fraction is above 1 ppb.

The minimum and maximum values of $\frac{C}{H}$ are 2.3 and ∼19.7 for both flames. $\frac{C}{H}$ increases both with the HAB and with the radial distance. $\frac{C}{H}$ growths almost identically radially in both flames, while on the centreline, an upstream shift of 6 mm is observed for the H_2 flame. Radial cross sections are given in Fig. 7.19b. Globally, low values of $E(m_\lambda)$ do corresponds to low $\frac{C}{H}$, and *vice-versa*. However, the high values of $E(m_\lambda)$ found in the wings of the reference flame do not correspond to values of $\frac{C}{H}$ higher than in the upper part of the flame. Therefore, if the present higher estimations of $E(m_\lambda)$ in the wings reflect reality, this indicates that the CRECK model cannot catch this behaviour.

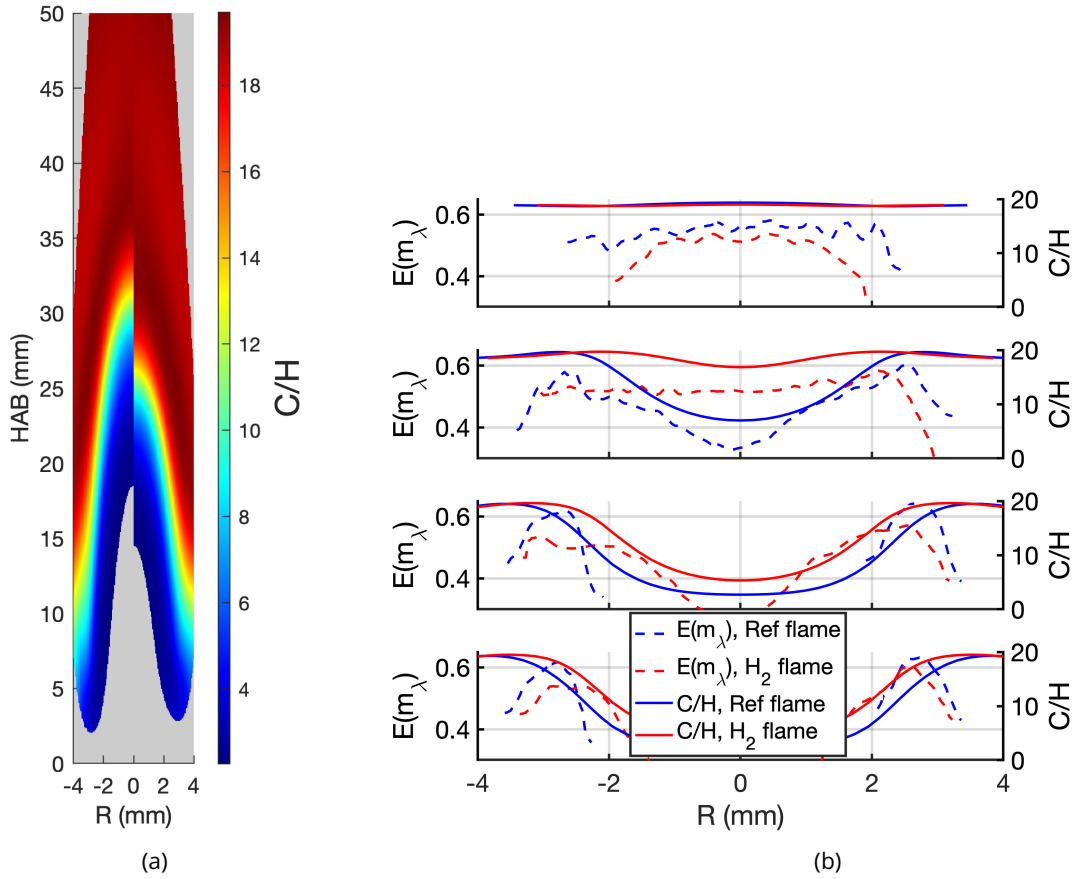

Figure 7.19: (a): Numerical estimation of the carbon-to-hydrogen ratio for the reference flame (left part) and the H_2 flame (right part). $\frac{C}{H}$ is given only in zones where f_v > 1 ppb. (b): Soot absorption function versus the radius at different HABs (from bottom to top: 20, 22, 28, 40 mm) for the reference flame (blue) and for the H_2 flame (red). Experimental estimations are in dashed lines, and the solid lines correspond to the numerical estimation of $\frac{C}{H}$.

The comparison of the ratio $\frac{C}{H}$ and $E(m_\lambda)$ along the flame's centerline is shown in Fig. 7.20a. The region where $E(m_\lambda)$ exhibits a steep increase corresponds to a sharp rise in the $\frac{C}{H}$ ratio. The numerical estimation of $\frac{C}{H}$ is able to capture the upstream shift in the maturation process caused by H_2 blending. However, while $E(m_\lambda)$ stops increasing at a HAB of 32-36 mm for the reference flame and 28 mm for the H_2 flame, the ratio $\frac{C}{H}$ continues increasing from 15 to 19. If the numerical $\frac{C}{H}$ are accurately retrieved, this would mean that the soot graphitisation continues while not affecting the soot absorption properties.

When plotting $E(m_\lambda)$ against $\frac{C}{H}$ for each flame position (Fig. 7.20b), three distinct zones can be identified based on

the $\frac{C}{H}$ values. For $\frac{C}{H}$ below ~10, an increase in $\frac{C}{H}$ correlates with a rise in $E(m_\lambda)$. In the range of $\frac{C}{H}$ between 10 and 18.7, $E(m_\lambda)$ stabilises around 0.5-0.55, becoming largely independent of $\frac{C}{H}$. Above $\frac{C}{H}$ = 18.7, up to the maximum value of 19.7, $E(m_\lambda)$ varies widely between 0.3 and 0.7. The higher values correspond to the wings of the reference flame, while the lower values are found at the flame's outer edge, where $E(m_\lambda)$ is lower than at the core. This behaviour is better seen with the H_2 flame, as for the reference flame, the results are more scattered.

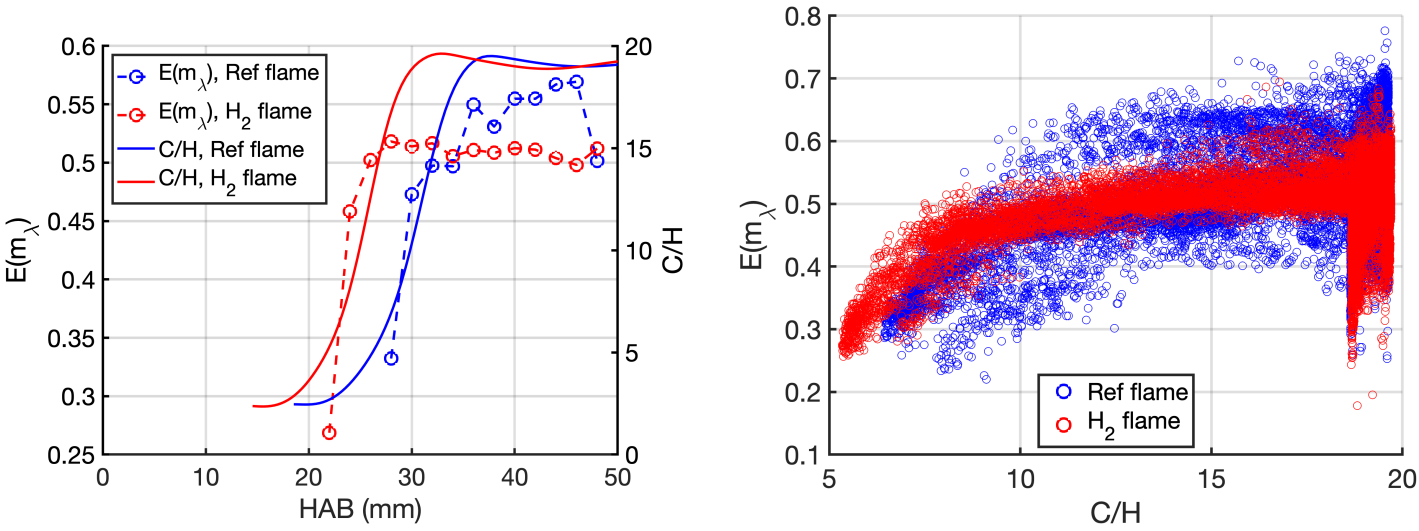

(a) (b)

Figure 7.20: (a): Soot absorption function obtained from the LII measurements versus the HAB for the reference flame (blue dashed) and the H_2 flame (red dashed), and carbon-to-hydrogen ratio obtained from the numerical simulations for the reference flame (blue solid) and the H_2 flame (red solid). (b): Soot absorption function (experimental) versus carbon-to-hydrogen ratio (numerical) for the reference flame (blue) and for the H_2 flame (red).

Overall, $E(m_\lambda)$ and $\frac{C}{H}$ are partially correlated in these flames: values of $\frac{C}{H}$ below 10 indicate the presence of not fully maturated soot particles. Higher values correspond to mature soot. This contrasts with the results of [127, 309] in which the MAC was found to increase for $\frac{C}{H}$ above 10. This might indicate that the numerical profile of $\frac{C}{H}$ should be shifted upstream so that the experimentally observed gradient of $E(m_\lambda)$ corresponds to the growth of $\frac{C}{H}$ from 10 to 19.7. Putting that last remark apart, considering the correlation between the low value of $\frac{C}{H}$ and of $E(m_\lambda)$, the present results indicate that monitoring the low values of $\frac{C}{H}$ allows using $\frac{C}{H}$ as a maturity tracer in the context of the use of the CRECK soot model.

7.5 Conclusion

This chapter investigated the impact of hydrogen blending on soot production in hydrocarbon flames by comparing a reference C_2H_4+N_2 flame with a C_2H_4+H_2 flame. Both flames have the same volumetric flow rate to keep a similar flame dynamic and have the same thermal power. The flames were experimentally analysed using LII to measure $E(m_\lambda)$, T_0, f_v, and d_p.

The results revealed that H_2-blending alters the flame characteristics and soot production dynamics:

- The H_2 flame is shorter, has approximatively the same width than the reference flame and presents a more intense luminosity.
- The flame wings are less pronounced: the LII signal is weaker and disappears at lower HAB, while the flame core radiates more.

- The axial profiles of f_v, d_p, $E(m_\lambda)$, and T_0 are shifted upstream (by 4-6 mm): soot appear, maturate, and oxidise at smaller HABs.
- While $E(m_\lambda)$ values are generally consistent between the two flames. Low values are found in the lower inner part of both flames. However, the high values observed in the wings of the reference flame were mostly absent in the H_2 flame. Overall, H_2 seems not to significantly affect $E(m_\lambda)$.
- The temperature profile is also shifted upstream in the H_2 flame, with only slight increases in maximum (+50 K) and average (+20 K) temperatures, indicating that both flames present a similar thermal environment for the soot development.
- f_v increases in the flame core but decreases in the wings. The total soot volume in the H_2 flame is slightly higher than in the reference flame.
- d_p is larger in the wings than at the centreline for both flames. In the wings, the particles are smaller by 5-10 nm in the H_2 flame compared to the reference flame. However, on the centreline, d_p values are similar to the reference flame, though shifted upstream. The smallest primary particles are found in the inner lower part of the profiles (young soot) and at the flame tip (oxidised soot) for both flames, while the mean d_p is identical in both flames with 23 nm.

Overall, hydrogen blending causes soot formation, maturation, and oxidation to occur at lower HABs. H_2 was found to enhance the soot production compared to N_2. However, the reasons behind this behaviour remain unclear and require further investigation into gas-phase species concentrations and soot nucleation/growth/oxidation rates, which could be obtained from numerical simulations.

Experimental results were compared to numerical simulations in order to validate the numerical model. Concerning the temperature profiles, the numerical predictions for temperature were generally lower by at least 100 K, but the experimental trends are reproduced. The soot volume fraction was also reasonably predicted, with the simulations correctly capturing the increased soot concentration in the core and the reduced wings in the H_2 flame. However, the model overestimated soot formation, especially in the wings, and was not able to catch the increase in soot volume with H_2 blending.

Experimentally determined $E(m_\lambda)$ and numerically computed $\frac{C}{H}$ are found to be partially correlated. Values of $\frac{C}{H}$ below 10 indicate the presence of not fully maturated soot particles, while higher values generally correspond to mature soot. Thus, tracking $\frac{C}{H}$ informs about maturity and soot absorption function variations.

In conclusion, the numerical model adequately captures the qualitative behaviour of soot formation in these flames, making it a valuable tool for exploring the mechanisms behind the differences in soot production with H_2 blending. However, the exploitation of the numerical simulations to explain the differences observed in soot concentration profiles was not performed in this thesis and is left for future work.

Chapter 8

Conclusions and perspectives

8.1 Conclusions

Soot particles are a harmful atmospheric pollutant with significant impacts on human health. Due to their adverse effects, emissions regulations are becoming increasingly strict. To effectively reduce soot emissions, fundamental research is essential to understand the soot formation processes better and improve knowledge of their properties. Experimental studies play a critical role not only in providing data to validate numerical models but also in deepening our understanding of soot particle characteristics and their formation mechanisms. Among the available experimental methods, the Laser-Induced Incandescence (LII) technique is a powerful tool for investigating soot quantities, including soot volume fraction f_v, primary particle size d_p, and the absorption function $E(m_\lambda)$, while providing instantaneous, spatially resolved 2D measurements.

In this thesis, the LII technique was employed to characterise soot particles in laboratory flames. Recognising that flames mainly operate in turbulent regimes, this diagnostic was chosen for its potential use in the study of soot production in turbulent flames. For that, an LII-based experimental method was developed by considering the constraints due to turbulent flame conditions. The separated-pulses LII (SP-LII) technique was proposed to measure the soot absorption function and the gas temperature T_0 in turbulent flames. A numerical analysis of this technique was conducted to evaluate its performance and uncertainties. The experimental setup required for SP-LII was presented in detail, along with some requirements for the proper application of the technique.

As a first step, the feasibility of the SP-LII technique has been proven by considering laminar diffusion flames and pointwise measurements. To achieve this, an experimental LII test bench was designed and implemented. Quantitative measurements of $E(m_\lambda)$ and T_0 were carried out, complemented by soot volume fraction measurements via auto-compensated LII, and primary particle diameter measurements using time-resolved LII. All four quantities were derived only from LII measurements, minimising the need for additional tools and reducing the complexity and cost of the experimental setup.

In a second phase, the experimental system was improved to perform 2D measurements, providing spatially resolved data for $E(m_\lambda)$, T_0, f_v, and d_p. Measurements in a reference laminar diffusion flame were compared with existing literature data, generally showing good agreement. Effort was made to obtain high-quality measurements and improve the accuracy of the estimation of the four quantities of interest. Specifically, efforts were made to address the f_v anomaly, which corresponds to an anomalous dependence of the soot volume fraction to the laser fluence or, more accurately, to the temperature of the soot particles after a laser pulse. This led to the development

of a background correction procedure that reduced the impact of the f_v anomaly.

Finally, the effect of H_2-blending on the soot formation was investigated. This is done since a potential approach to reduce CO_2 emissions without drastically redesigning combustion systems is blending hydrogen with conventional hydrocarbon fuels. While this reduces CO_2 emissions, the impact of hydrogen on soot formation remains uncertain. To investigate this, a reference flame and a hydrogen-blended flame, both having the same thermal power and volumetric flow rates, were experimentally considered. In the hydrogen-blended flame, soot particles appear, mature, and oxidise at lower HABs than in the reference flame. The hydrogen-blended also showed a change in the soot repartition with an increase in the soot volume fraction in the flame core and an attenuation of it in the wings. These findings suggest that various chemical mechanisms may be at play in different regions of the flame. While flame temperature increased slightly, the soot absorption function and the soot primary particle size were relatively unaffected, except in the flame wings, where d_p decreased by $\sim$25%. The experimental data were compared with numerical simulations, showing overall qualitative agreement, thus validating the soot model. It was observed that the carbon-to-hydrogen ratio (derived from simulations) increased with $E(m_\lambda)$ (determined experimentally), suggesting that the soot maturation process can be tracked using the current numerical model.

In summary, the key contributions of this PhD work are:

- A novel experimental technique (SP-LII) was proposed for measuring instantaneous spatially resolved $E(m_\lambda)$ and T_0 fields.
- An LII experimental setup was implemented at the EM2C laboratory, enabling direct access to $E(m_\lambda)$, T_0, f_v, and d_p within flames using only LII.
- Spatially resolved maps of $E(m_\lambda)$ were obtained in three laminar diffusion flames. This work presents the first spatially resolved 2D maps of $E(m_\lambda)$ obtained using LII. This confirmed that the traditional assumption of a uniform $E(m_\lambda)$ for the computation of f_v introduces acceptable errors for the considered flames, as soot maturation occurs rapidly, leading to fairly uniform values within the flame.
- Hydrogen was found to promote soot formation compared to nitrogen in such a way that even by reducing the carbon flow rate by 14%, an increase of 7% in the soot load was observed within the flames investigated here.

8.2 Perspectives

This thesis presents several potential avenues for extending the current work, including the following:

- **Improvement of the experimental bench for 2D measurements:** A significant improvement would be to upgrade the 2D experimental setup used in Chapters 6 and 7. The current setup, relying on a top-hat laser beam, only allows in-flame measurements of a narrow region (1 mm in height). Replacing the top-hat laser beam with a laser sheet could enable imaging of a larger flame portion simultaneously, significantly reducing experimental time and simplifying data post-processing. This change would facilitate the exploration of more flame conditions, thereby enriching experimental databases.

  Transitioning to a laser sheet may introduce new challenges. Notably, the laser sheet's typically narrower width (hundreds of microns) compared to the 1 mm-wide top-hat beam would decrease the signal-to-noise ratio of the LII measurements, complicating LII measurements at low laser fluences. In addition, having a laser sheet of several centimetres in height makes it difficult to have the same degree of fluence homogeneity as a top hat. These fluence variations along the sheet height would need correction due to the high sensitivity of $E(m_\lambda)$

and T_0 to laser fluence. Finally, the laser sheet should be designed to minimise contraction and expansion, ensuring uniformity across the flame width. This will maintain a constant laser fluence throughout the flame, which is crucial for accurate measurements.

- **Application of the SP-LII in turbulent flames:** Due to time constraints, the SP-LII technique, which was designed to retrieve $E(m_\lambda)$ and T_0 from instantaneous measurements in turbulent flames, was not tested in turbulent flames. Accessing $E(m_\lambda)$ in a turbulent flame would allow for the differentiation between young soot (low $E(m_\lambda)$) and mature soot (high $E(m_\lambda)$), which, due to mixing, may not follow the typical trend observed in laminar flames, where young soot is found in the lower regions and mature soot higher up in the flame. Additionally, the temperature information provided by T_0 would help determine whether the soot is located in burned gas pockets or has been transported into regions of fresh gas.

  Before applying SP-LII to instantaneous measurements, it should first be validated on a laminar flame. This involves verifying that $E(m_\lambda)$ and T_0 measured with two consecutive laser pulses of different fluence (separated by $\sim$10 μs) are consistent with those derived using the same fluences but with a longer interpulse delay, ensuring that each pulse probes different soot particles. This step would confirm that the first pulse does not significantly affect the soot particles. Following this, still using a laminar flame, instantaneous measurements of $E(m_\lambda)$ and T_0 should be compared to time-averaged results to ensure that SP-LII can reliably capture these values.

  A significant trouble that may arise with single-shot measurement is the lower LII signal quality. The limiting factor for improving the LII signal level in this thesis was the luminosity of the flame, which saturates the photomultiplier tubes (PMTs). This noise source might be lowered by equipping the PMTs with shutters opening slightly before the measure.

- **Combining experimental instrument for soot sizing:** The LII-based measurements of mean soot primary particle diameter could be completed by measurements with Transmission Electron Microscopy (TEM) and Scanning Mobility Particle Sizer (SMPS). These techniques would allow a more complete characterisation of soot morphology, including fractal dimension, radius of gyration, and electrical mobility diameter, and TEM would provide more robust estimates of d_p. Additionally, SMPS can capture soot particle size distributions, which is particularly interesting at the flame tip, offering valuable insights into the size and numbers of soot particles exiting the flame. This is especially relevant for health concerns, as smaller soot particles tend to pose higher toxicity risks.

- **Exploitation of the numerical data:** Although the soot model was validated in Chapter 7, the information furnished by the numerical simulation (gas-phase concentrations, soot nucleation, growth, and oxidation rates) was not exploited to explain the observed differences in soot production between the reference and H_2 flames.

  Future work could focus on tracking the influence of H_2 blending on the species involved in soot inception and growth, such as C_2H_2, C_3H_3, aromatics, and PAHs, to identify those responsible for the enhanced soot formation on the flame centreline and the weaker soot production in the wings of the H_2 flame. This analysis would help clarify the chemical effects of H_2 on soot production.

Appendix A

Prerequisites for radiative heat transfer

Some bases of radiative transfer are given here to show the origin of the equations that are exploited throughout this thesis. The excellent book on thermal transfer of reference [310] was used for this annexe.

A.1 Monochromatic directional flux

Considering the geometry of Fig. A.1, the monochromatic directional flux $d^5\Phi'_\lambda$ exchanged by the two elements of surfaces dS_1 and dS_2 can be expressed as:

$$d^5\Phi'_\lambda = L'_\lambda\left(O_1, u_1\right) dS_1 \cos\left(\theta_1\right) d\Omega_1 d\lambda \quad [W], \tag{A.1}$$

where the solid angle $\Omega_1 = \frac{dS_2 cos(\theta_2)}{O_1O_2^2}$ is the view of dS_2 from O_1, $L'_\lambda\left(O_1, u_1\right)$ is the monochromatic directional luminance, and θ_1 is the angle between n_1 the normal of dS_1 and the vector O_1O_2.

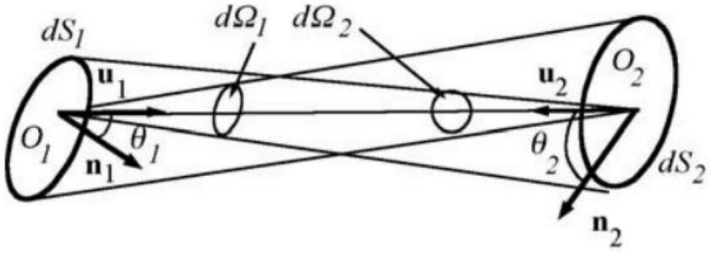

Figure A.1: Scheme of two surfaces exchanging by radiation. Image taken from [310].

In the following, the following assumptions are made:

- The monochromatic directional luminance is isotrop: $L'_\lambda\left(O_1, u_1\right) = L_\lambda\left(O_1\right)$.
- The monochromatic directional luminance is uniform over the surface of the object: $L_\lambda\left(O_1\right) = L_\lambda$.

A.2 Monochromatic surface flux

Monochromatic surface flux through a solid angle delimited by a cone

The monochromatic surface flux $\frac{d^3\Phi_\lambda}{dS_1}$ emitted by an element of surface dS_1 in a solid angle Ω delimited by a cone of angle θ (Fig. A.2) is:

$$\begin{aligned}\frac{d^3\Phi_\lambda}{dS_1} &= \int_\Omega L_\lambda \cos(\theta_1)\, d\Omega_1 d\lambda \\ &= \int_{\theta_1=0}^{\theta_1=\theta}\int_{\phi=0}^{\phi=2\pi} \cos(\theta_1)\sin(\theta_1)\, d\theta_1 d\phi_1 \cdot L_\lambda d\lambda \\ &= \pi sin^2(\theta)\cdot L_\lambda d\lambda \quad [W.m^{-2}],\end{aligned} \tag{A.2}$$

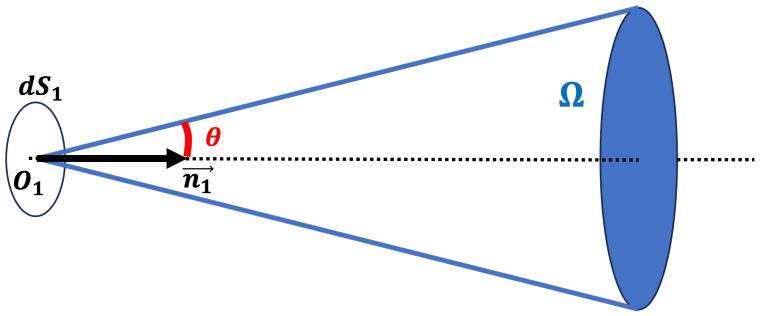

Figure A.2: Element of surface emitting in a solid angle delimited by a cone centred on O_1, and of normal n_1.

Hemispherical monochromatic flux

The hemispherical monochromatic emitted flux corresponds to the flux emitted in all directions in the half-space facing dS_1. It is obtain with Eq. (A.2) for $\theta = \frac{\pi}{2}$:

$$\left(\frac{d^3\Phi_\lambda}{dS_1}\right)_{hemi} = \int_{2\pi sr} L_\lambda d\lambda d\Omega_1 = \pi\cdot L_\lambda d\lambda \quad [W.m^{-2}], \tag{A.3}$$

A.3 Radiative fluxes of simple surfaces

Here, the emitted flux by radiation of a flat surface and of a sphere between λ_{inf} and λ_{sup} over a solid angle Ω delimited by a cone of angle θ is computed assuming that θ is small.

Radiative flux of a flat surface

The flat surface is a disk of surface S. The normal of S at the centre of the disk makes a null angle with the normal of the cone's basis. It is assumed that each element of the surface of the disk has a negligible angle compared to the normal of the cone. This allows the decoupling of the surface integral and solid angle integral:

$$\begin{aligned}\Phi_{\lambda_{inf},\lambda_{sup}} &= \int_S\int_\Omega\int_{\lambda_{inf}}^{\lambda_{sup}} L_\lambda\lambda\cos(\theta_1)\sin(\theta_1)\, d\Omega_1 dS_1 \\ &= \int_S dS_1\cdot\int_{\theta_1=0}^{\theta_1=\theta}\int_{\phi=0}^{\phi=2\pi}\cos(\theta_1)\sin(\theta_1)\, d\theta_1 d\phi\cdot\int_{\lambda_{inf}}^{\lambda_{sup}} L_\lambda d\lambda \\ &= S\cdot\pi sin^2(\theta)\cdot\int_{\lambda_{inf}}^{\lambda_{sup}} L_\lambda d\lambda \\ &\approx S\cdot\Omega\cdot\int_{\lambda_{inf}}^{\lambda_{sup}} L_\lambda d\lambda \quad [W],\end{aligned} \tag{A.4}$$

Radiative flux of a sphere

The diameter of the sphere is d_p. Thanks to the spherical symmetry of a sphere, the emission in a solid angle Ω of a sphere is simply the total emission of the sphere over 4π steradians times $\frac{\Omega}{4\pi}$:

$$\begin{aligned}\Phi_{\lambda_{inf},\lambda_{sup}} &= \frac{\Omega}{4\pi}\int_S\int_{2\pi sr}\int_{\lambda_{inf}}^{\lambda_{sup}} L_\lambda d\lambda\cos(\theta_1)\,d\Omega_1 dS_1 \\ &= \frac{\Omega}{4\pi}\int_S dS_1\cdot\int_{\lambda_{inf}}^{\lambda_{sup}}\left(\frac{d^3\Phi_\lambda}{dS_1}\right)_{hemi} \\ &= \frac{\Omega}{4\pi}\pi d_p^2\cdot\pi\cdot\int_{\lambda_{inf}}^{\lambda_{sup}} L_\lambda d\lambda \quad [W],\end{aligned} \tag{A.5}$$

Appendix B

Expression of the collected incandescence signal

The theoretical expression of the power emitted emitted (over 4π steradians) by a concentration of soot particles f_v in a volume V_{col} at a temperature T, and for a wavelength λ is given by Eq. (3.7) that is reminded here:

$$I_{soot}(\lambda, T) = 48\pi^2 h c_{light}^2 f_v V_{col} \frac{E(m_\lambda)}{\lambda^6} \frac{1}{e^{\frac{hc_{light}}{\lambda k_B T}} - 1} \quad [W.nm^{-1}]. \tag{B.1}$$

The corresponding signal captured by an optical system between the wavelengths λ_{inf} and λ_{sup} (centred on λ), over the solid angle Ω, during a time τ is:

$$S_\lambda^{LII}(T) = \int_0^\tau \int_{\lambda_{inf}}^{\lambda_{sup}} 48\pi^2 h c_{light}^2 f_v V_{coll} \frac{\Omega}{4\pi} \Sigma_{\lambda'} \frac{E(m_{\lambda'})}{\lambda'^6} \frac{1}{e^{\frac{hc_{light}}{\lambda' k_B T}} - 1} d\lambda' dt. \tag{B.2}$$

The optical system is composed of several optical elements (lenses, filters) and an optical sensor (photomultiplier tube or camera). These optical elements have a wavelength-dependent transmitivity, and the sensor has a wavelength-dependent quantum efficiency. The apparatus function Σ_λ accounts for the optics' transmitivities and sensor's quantum efficiency.

In LII, V_{col} corresponds to the volume corresponding to the crossing of the laser beam and the vision of the detection system. In this thesis, the laser beam is at 90° of the detection line-of-sight, and the laser beam has a square cross-section of side L_{laser}. The collection volume is assumed to be $V_{col} = L_{laser} S_{col}$ where S_{col} surface of collection of the collection system (Fig. B.1 for illustration).

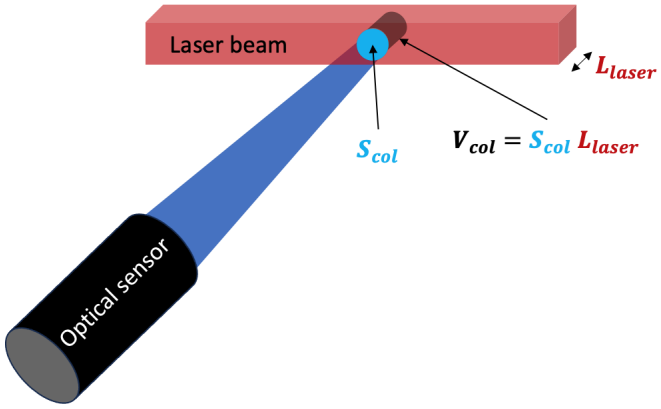

Figure B.1: Scheme representing the probe volume corresponding to the crossing of the laser beam and the sensor's line of sight.

Assuming that the emission of the soot remains constant during the optical sensor's exposure time, the term inside the integral is constant with respect to τ, and the temporal integral simplifies to $\int_0^\tau dt = \tau$. Additionally, it is assumed that the wavelength-dependent terms do not vary significantly across the filter's bandpass [λ_{inf}, λ_{sup}], allowing using their value at the centre wavelength of the filter. In these conditions, and using Wien's approximation ($e^{\frac{hc}{\lambda k_B T}} >> 1$), Eq. (B.2) reduces to:

$$S_\lambda^{LII}(T) = \tau \cdot S_{col} \cdot \Omega \cdot \Sigma_\lambda \cdot 12\pi hc^2 f_v L_{laser} E(m_\lambda) \frac{\Delta\lambda}{\lambda^6} e^{-\frac{hc}{\lambda k_B T}}, \tag{B.3}$$

where $\Delta\lambda = \lambda_{sup} - \lambda_{inf}$.

Among the optical system parameters, τ is known, and S_{col} can be estimated (from the sensor/pinhole size, the focal length of the lenses). However, Ω and Σ_λ are unknown. With 2C-LII (Eq. 3.20), the temperature is computed from the ratio of $S_{LII,\,\lambda}$ at two different wavelengths λ_1, and λ_2. Thus, $\tau \cdot S_{col} \cdot \Omega$ disappear if the collection systems (recording LII signals at λ_1, and λ_2) have the same collection angle and surface. However, it requires the knowledge of $\frac{\Sigma_{\lambda_1}}{\Sigma_{\lambda_2}}$. In addition, with AC-LII (Eq. 3.23), f_v is computed by inverting Eq. (B.3). Thus, it requires the knowledge of the absolute value of $\tau \cdot S_{col} \cdot \Omega \cdot \Sigma_\lambda$ (at λ_1 or λ_2). Thus, a calibration of the optical system is required to obtain the calibration constant $C_{calib,\lambda} = \tau \cdot S_{col} \cdot \Omega \cdot \Sigma_\lambda$, at λ_1 and λ_2. The procedure to obtain $C_{calib,\lambda}$ is presented in Annex C.

Appendix C

Calibration of the optical system

The calibration of the optical system is required for the measurements of the absolute soot incandescence signal to obtain the soot temperature by 2C-LII (Eq. (3.20)), and the soot volume fraction by AC-LII (Eq. (3.23)). For that, measurements are performed using a calibration source.

C.1 Calibration source

The calibration source used in this thesis is composed of a tungsten lamp coupled with an integrating sphere, as illustrated in Fig.C.1a. The integrating sphere ensures that the radiation exiting it is uniformly distributed. The exit port of the sphere has a diameter of 25 mm. The luminance of the light emitted from the sphere can be adjusted using a shutter that partially obstructs the sphere's entry port. This shutter is operated by a micrometre screw, allowing precise control of the luminance. A dedicated sensor inside the sphere continuously measures this luminance.

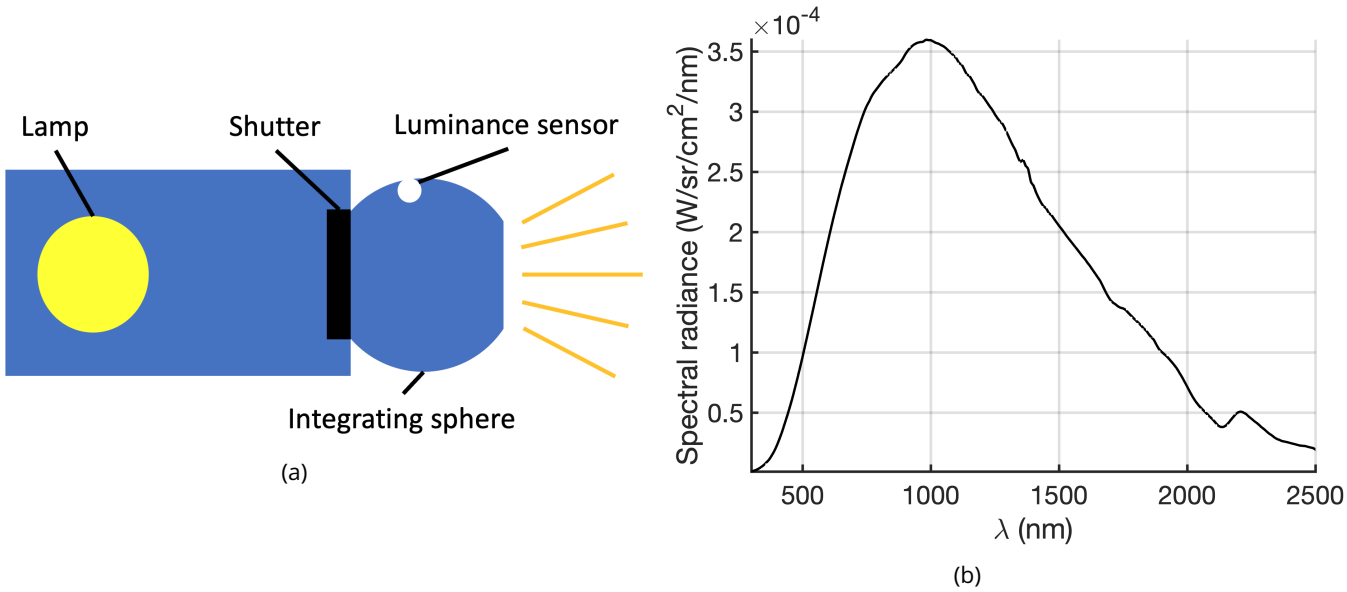

Figure C.1: (a): Scheme of the calibration source. (b): Spectral radiance of the calibration source furnished by the lamp manufacturer at a brightness temperature 3000 K and for the reference luminance: Γ_{ref} = 32877 fL.

The spectral radiance of the calibration source $L_{\lambda}^{calib}(T,\Gamma)$ is known from the calibration of the manufacturer at a brightness temperature of T_{ref} = 3000 K and for a luminance of Γ_{ref} = 32877 fL (which almost correspond to the maximum output luminance of the calibration source). The distribution of the spectral radiance in these reference conditions is given in Fig. C.1b.

C.2 Calibration procedure

For the calibration of the collection system (which includes the optics used to gather the LII signal and the optical sensor), the exit port of the calibration source is precisely positioned where the flame would be during LII measurements, ensuring the collection angle remains identical. The collection system's components and settings are kept identical for both calibration and LII measurements. The goal of these calibration measurements is to achieve absolute calibration of the system, meaning that the signal recorded with PMTs or cameras can be converted into radiance (W/sr/m^2). This is accomplished by determining the calibration constants $C_{calib,\lambda} = \tau \cdot S_{col} \cdot \Omega \cdot \Sigma_{\lambda}$, using the known spectral radiance of the calibration source. The procedure is detailed in the following.

C.2.1 Expression of the signal collected during calibration

From the expression of the radiative flux of a flat surface given in Annex A, the signal of the calibration source (at a brightness temperature T, and luminance L), collected between the wavelengths λ_{inf}, and λ_{sup}, over the solid angle Ω, and during a time τ by the optical system is:

$$S_{\lambda}^{calib}(T,\Gamma) = \int_0^{\tau} \int_{\lambda_{inf}}^{\lambda_{sup}} S_{coll} \cdot \Omega \cdot \Sigma_{\lambda'} L_{\lambda'}^{calib}(T,\Gamma) d\lambda' dt, \tag{C.1}$$

Under the hypothesis of time-independent emission, and assuming that Σ_{λ} is constant over [$\lambda_{inf}, \lambda_{sup}$], Eq. (C.1) reduces to:

$$S_{\lambda}^{calib}(T,\Gamma) = \tau \cdot S_{coll} \cdot \Omega \cdot \Sigma_{\lambda} \int_{\lambda_{inf}}^{\lambda_{sup}} L_{\lambda'}^{calib}(T,\Gamma) d\lambda', \tag{C.2}$$

The calibration constant $C_{calib,\lambda} = \tau \cdot S_{coll} \cdot \Omega \cdot \Sigma_{\lambda}$ can be expressed as:

$$C_{calib,\lambda} = \frac{S_{\lambda}^{calib}(T,\Gamma)}{\int_{\lambda_{inf}}^{\lambda_{sup}} L_{\lambda'}^{calib}(T,\Gamma) d\lambda'} \tag{C.3}$$

C.2.2 Computation of the calibration constant $C_{calib,\lambda}$

Rewriting Eq. (C.3) at T_{ref}, and Γ_{ref}:

$$C_{calib,\lambda} = \frac{S_{\lambda}^{calib}(T_{ref},\Gamma_{ref})}{\int_{\lambda_{inf}}^{\lambda_{sup}} L_{\lambda'}^{calib}(T_{ref},\Gamma_{ref}) d\lambda'} \tag{C.4}$$

The spectral radiance of the calibration source $L_{\lambda}^{calib}(T,\Gamma)$ is known at (T_{ref}, Γ_{ref}) and is plotted in Fig. C.1b. Therefore, from this figure, the quantity $\int_{\lambda_{inf}}^{\lambda_{sup}} L_{\lambda}^{calib}(T_{ref},\Gamma_{ref}) d\lambda$ can be calculated.

In this thesis, the collection systems are equipped with bandpass filters centred on $\lambda_1 = 578$ and $\lambda_2 = 716$ nm, whose transmission spectrum is given in Fig. C.2. The limit of 50% transmission of the filters is [569,587] and [693,739] nm.

Therefore, the quantity $\int_{\lambda_{inf}}^{\lambda_{sup}} L_{\lambda}^{calib}(T_{ref}, \Gamma_{ref})d\lambda$ is computed assuming rectangular windows [569,587] and [693,739], using the data of Fig. C.1b. Values of 0.0031 W/sr/cm^2, and 0.0131 W/sr/cm^2, are obtained for λ_1 and λ_2, respectively.

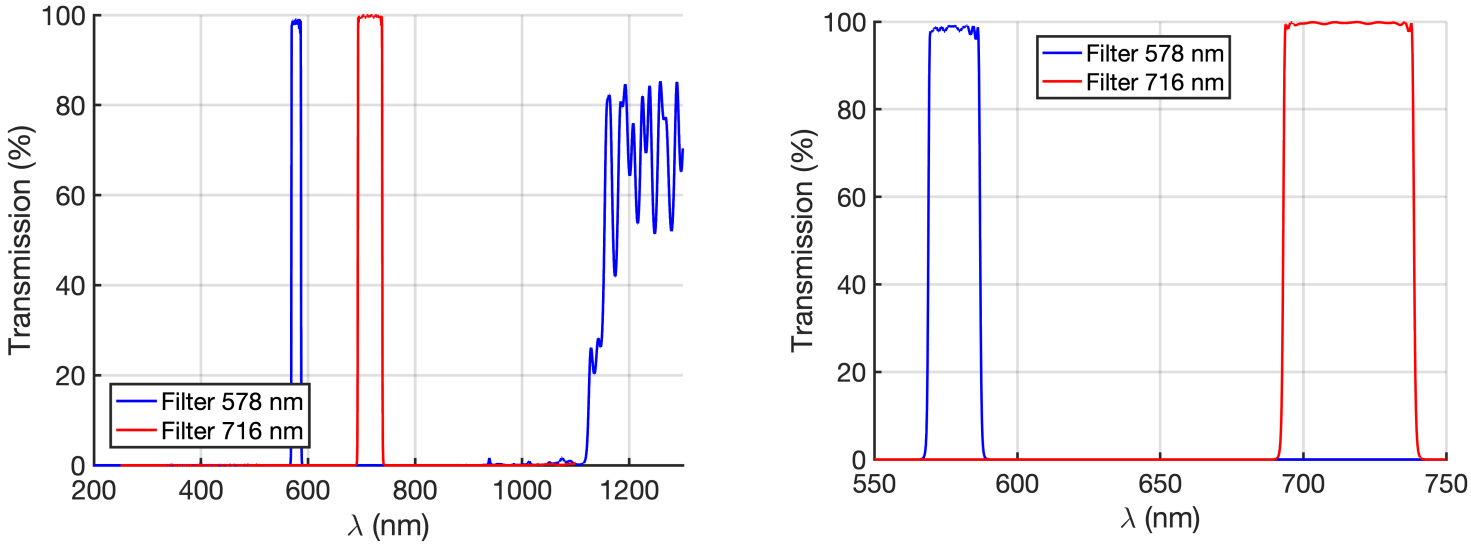

Figure C.2: (a) and (b): Transmission of the bandpass filters centred on 578 nm (Edmund Optics 87766) in blue and on 716 nm (Edmund Optics 67053) in red. Figure (b) is identical to figure (a) on a reduced wavelength range. The data are those of the manufacturer.

Once $\int_{\lambda_{inf}}^{\lambda_{sup}} L_{\lambda}^{calib}(T_{ref}, \Gamma_{ref})d\lambda$ is known, the calibration constant, $C_{calib,\lambda}$, can be determined from the measurement of $S_{\lambda}^{calib}(T_{ref}, \Gamma_{ref})$. However, at T_{ref}, the optical sensor may reach saturation for a luminance Γ_{ref}, requiring the calibration to be performed at a lower luminance Γ by partially closing the shutter of the calibration source. In such cases, $S_{\lambda}^{calib}(T_{ref}, \Gamma)$ is measured instead of $S_{\lambda}^{calib}(T_{ref}, \Gamma_{ref})$.

Assuming the sensor responds linearly to the incoming flux, the collected signal is expected to scale linearly with luminance. Thus, $S_{\lambda}^{calib}(T_{ref}, \Gamma_{ref})$ can be extrapolated from the lower luminance measurement using the linear relationship:

$$S_{\lambda}^{calib}(T_{ref}, \Gamma_{ref}) = S_{\lambda}^{calib}(T_{ref}, \Gamma)\frac{\Gamma_{ref}}{\Gamma} \tag{C.5}$$

Finally as Γ is known from the luminance sensor of the sphere, $C_{calib,\lambda}$ is obtained with:

$$C_{calib,\lambda} = \frac{\Gamma_{ref}}{\Gamma}\frac{S_{\lambda}^{calib}(T_{ref}, \Gamma)}{\int_{\lambda_{inf}}^{\lambda_{sup}} L_{\lambda'}^{calib}(T_{ref}, \Gamma_{ref})d\lambda} \tag{C.6}$$

Once $C_{calib,\lambda}$ is known at λ_1 and λ_2 -the central wavelength of the collection windows- the soot temperature and the soot volume fraction can be computed by 2C-LII (Eq. (3.20)), and AC-LII (Eq. (3.23)), respectively.

Appendix D

Spectroscopic measurements

D.1 Experimental setup

Figure D.1 represents the setup used for spectroscopic measurements. Only the collection system is different from the setup presented in Chapter 6. The light is collected using the same lenses as for the PMT measurements and is focused into a 365 μm optical fibre. Then, the light enters the spectroscope Teledyne Princeton Instrument HRS-500, equipped with a grating of 150 grooves/mm. An intensified camera PIMAX 2 records the signal between 440 and 720 nm (it was not possible to go above 720 nm with the present setup because of second-order signals). The camera gate width is 8 ns, and the camera gain was set to its maximum value. Signals are averaged over 1000 acquisitions.

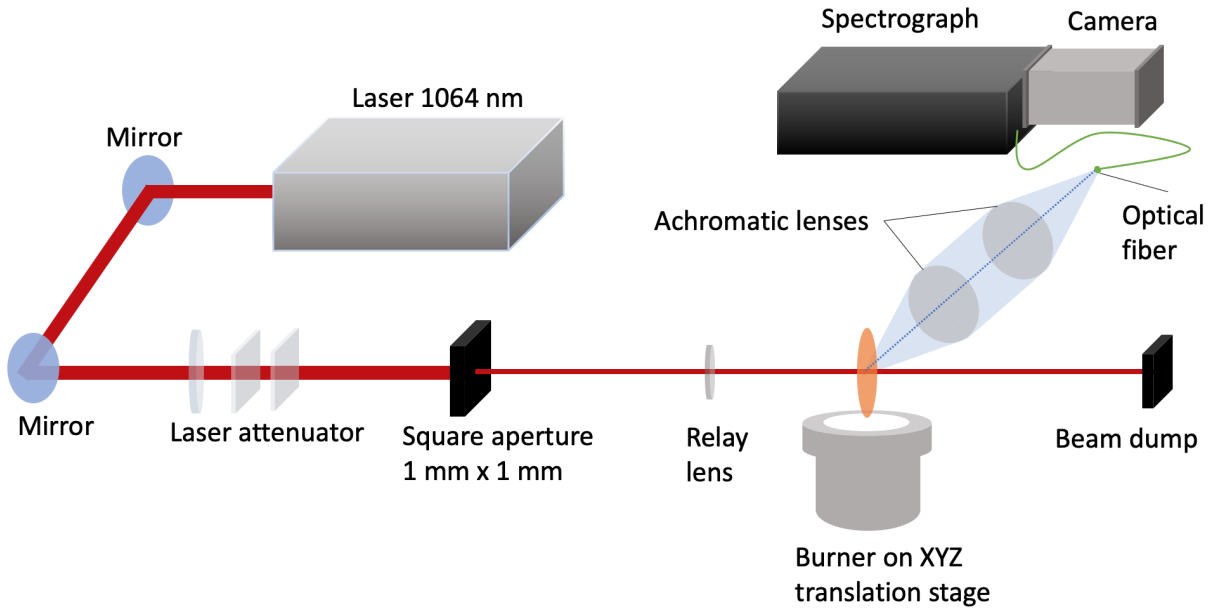

Figure D.1: Scheme of the experimental bench for spectroscopic measurements.

D.2 Apparition of Swan bands

Spectroscopic measurements of soot particles at different radial positions at HAB = 28 mm and at different laser fluence (0, 35, 75, 150, and 300 mJ/cm^2) are given in Fig. D.2. HAB = 28 mm was chosen because it corresponds to the axial position for which the most different soot populations (in terms of maturity) are present in the reference $C_2H_4 + N_2$/air flame. It has to be pointed out that even with the camera gain at its maximum, the maximum signal is 20000 cps over 65000. Therefore, measurements at low laser fluences produced very few signals; as a consequence, results are very noisy.

The shape of the normalised spectra in Fig. D.2 depends both on the laser fluence and on the in-flame position. In the absence of laser heating (F = 0 mJ/cm^2), the spectra at all positions have similar shapes reflecting a similar temperature. At higher laser fluences, differences in the spectra appear: higher radial positions show more blue-shifted spectra, indicating (from Wien's law) that the soot temperature is higher for higher radial positions. C_2 Swan fluorescence bands near 515 nm start to be visible at 150 mJ/cm^2 and are more visible for the soot particles that are at higher radial positions. For F = 300 mJ/cm^2, the Swan bands are clearly visible for all radial positions, and three bands can be distinguished: 457-474, 501-520, and 530-565 nm. The results indicate that Swan bands appear at laser fluences higher than 75 mJ/cm^2 but lower than 150 mJ/cm^2. Considering the temperatures estimated from these spectra (presented in the next section), the appearance of the Swan bands corresponds to soot temperatures reaching approximately 4000 K, exceeding the temperature limits established in Chapters 6, and 7, and aligning with the limits outlined in Chapter 5.

Therefore, the combination of the low laser fluences employed in this study and the selected collection windows for recording the LII signal (569-587 and 693-739 nm) ensures that the fluorescence of C_2 and C_3 does not interfere with the LII measurements.

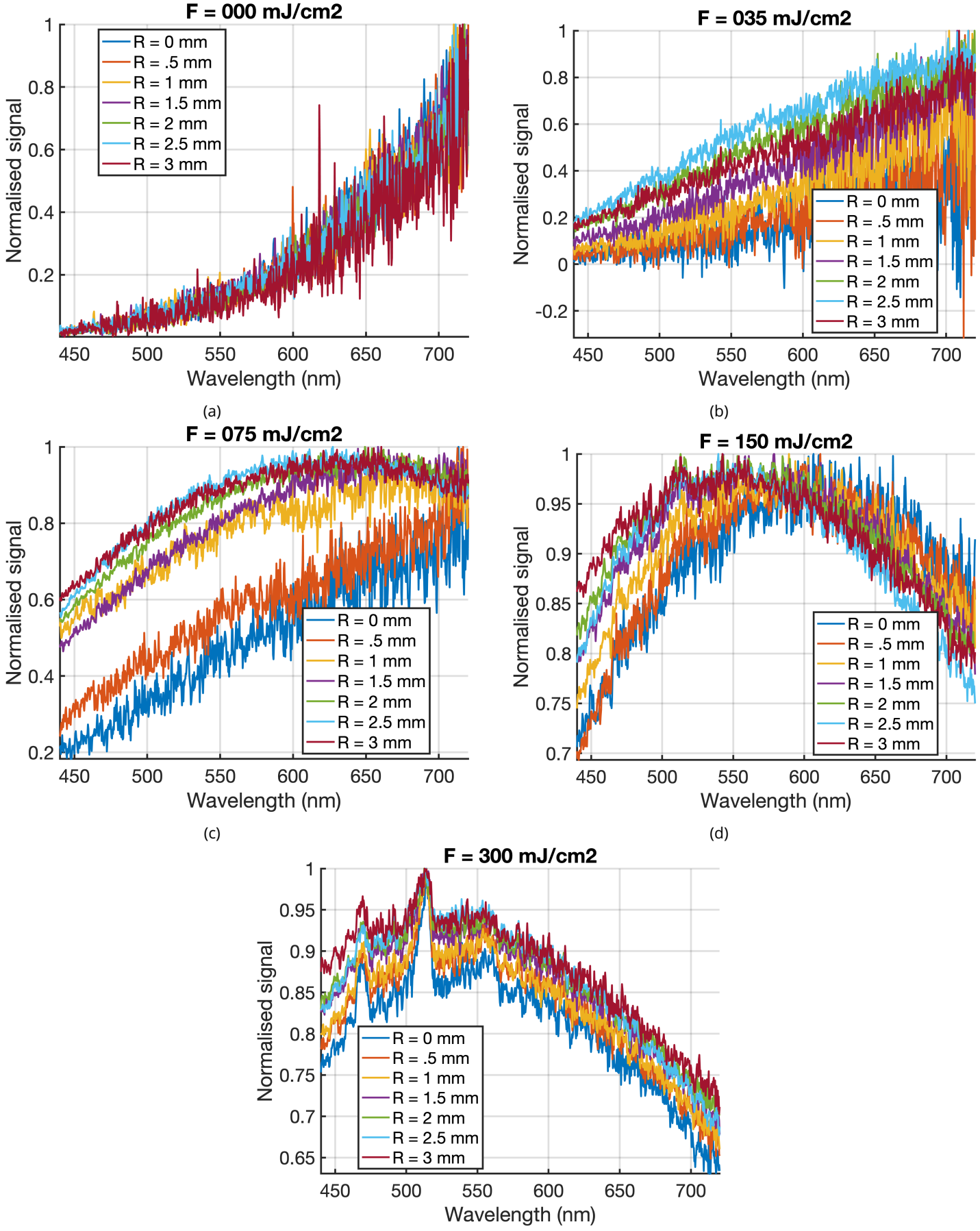

Figure D.2: Incandescence spectra for radial positions varying from 0 to 3 mm at HAB = 28 mm in the C_2H_4+N_2/air flame diffusion flame Measurements are given in Figs. (a) to (e) for multiple laser fluence: 0, 35, 75, 150, and 300 mJ/cm^2, respectively.

D.3 Temperature measurements from spectral fit

One can obtain the soot temperature by fitting the spectra of Fig. D.2 with the theoretical spectra (see section 3.4.2). For that, $E(m_\lambda)$ will be supposed to be wavelength independent. For the fluences above 150 mJ/cm^2, the fits are done, ignoring the spectral bands where Swan fluorescence can be found (457-474, 501-520, and 530-565 nm).

The spectra for all laser fluences, and for R = 2 mm, along with the temperature deduced from the function fitted to the spectra, are given in Fig. D.3 both in log and normal scale. This figure shows that the fit procedure is working well. The temperatures retrieved seem to be coherent as well: as expected, the temperature increases with the laser fluence.

The temperatures obtained from the spectral fit are compared to the one computed by 2C-LII in Fig D.4 on the flame centreline and at different radial positions at HAB = 28 mm. Results are coherent between the two methods. Axial profiles are globally very close with a difference below 100 K except for high fluences (150 mJ/cm^2) where the temperature obtained by spectral fit can be up to $\sim$200 K higher than the 2C-LII ones. The radial profiles are also in agreement, although with slightly higher differences.

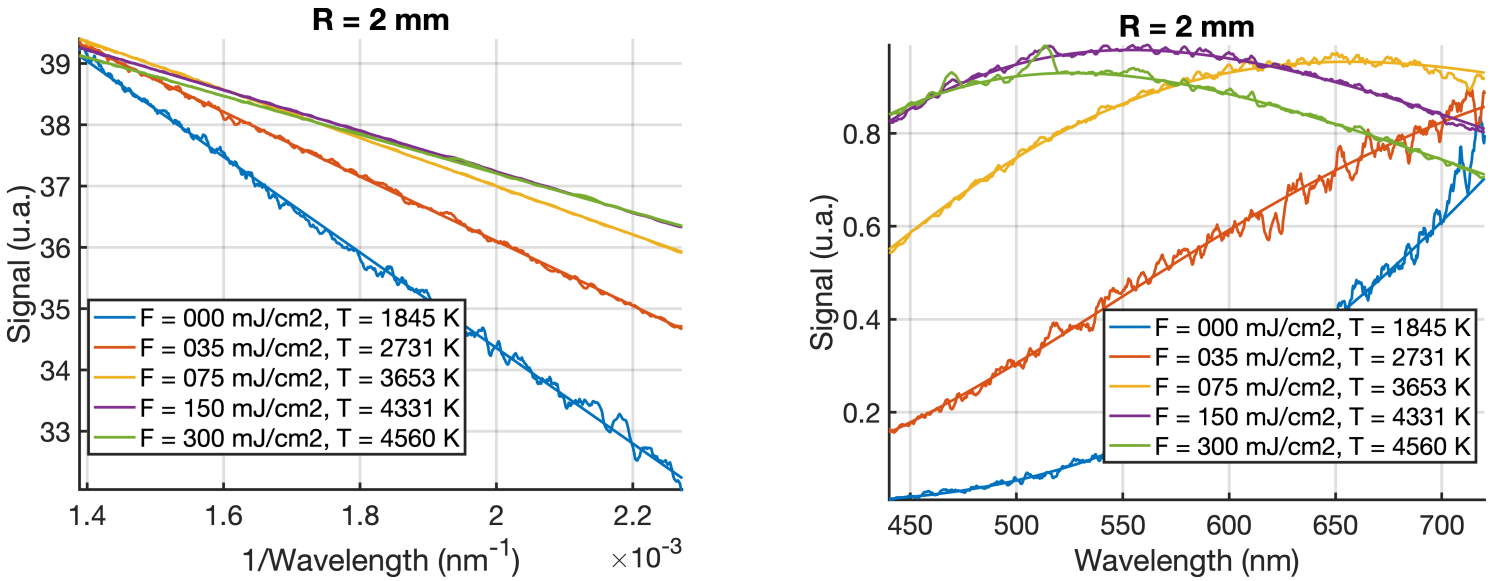

(a) (b)

Figure D.3: Incandescence spectra and their corresponding fit for a radial position of 2 mm at HAB = 28 mm in the C_2H_4+N_2/air flame diffusion flame. Temperatures obtained are given in the legend. Figure (a) gives $ln\left(\frac{S_\lambda^{LII}}{S_{\lambda_{ref}}^{LII}}\left(\frac{\lambda}{\lambda_{ref}}\right)^6\frac{E(m_{\lambda_{ref}})}{E(m_\lambda)}\right)$ while figure (b) gives the normalised incandescence spectra. For a better visualisation, signals are averaged using a rectangular window of 10 points.

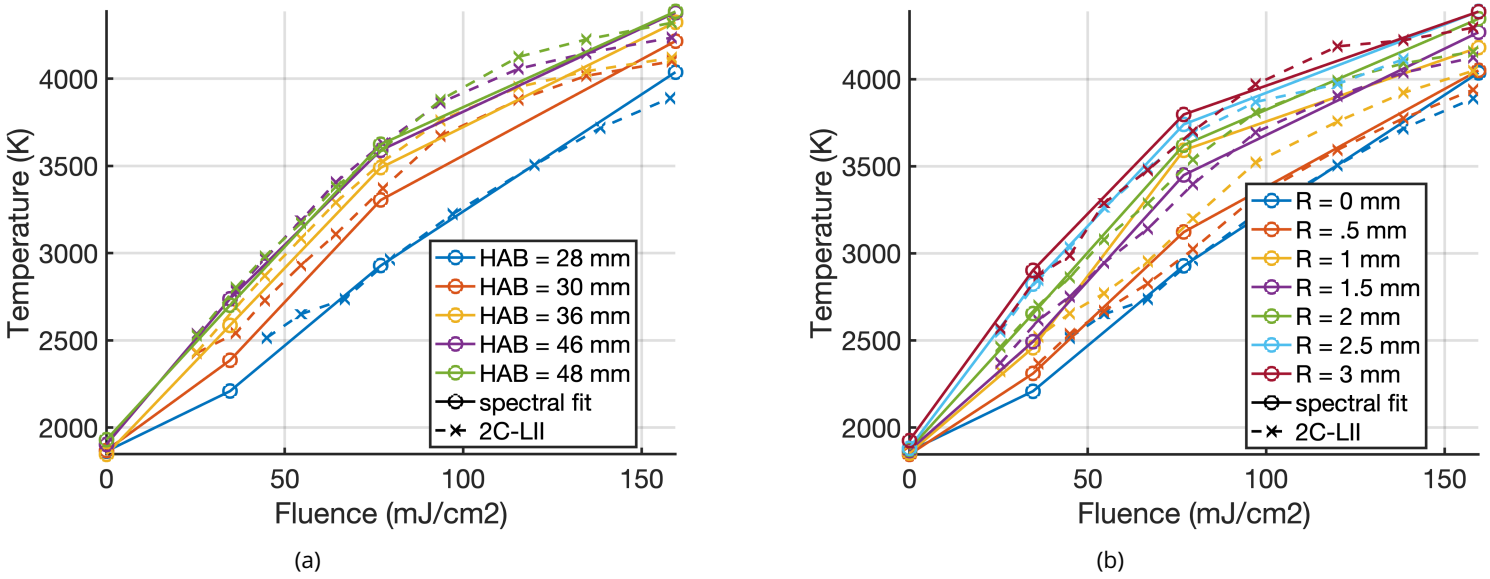

Figure D.4: Comparison of the soot peak temperature obtained by 2C-LII (dashed line with x symbols) and by spectral fit (solid line with o symbols), versus the laser fluence, and for (a): different positions along the flame centreline, and (b): different radial positions at HAB = 28 mm.

Appendix E

Gas temperature by emission pyrometry

In the absence of laser heating, the soot particles, at the flame temperature, emit an incandescence signal that can be collected and processed to approximate the gas temperature. In this annex, the gas temperature is computed by 2C emission pyrometry. Compared to 2C-LII, emission pyrometry offers the advantage of being less intrusive for the soot particles as they are not heated by a laser beam, thereby minimising potential alterations of their properties. However, the collected signal is integrated over the line-of-sight of the optical sensor, capturing emissions from all the soot particles along the width of the flame. In the case of an axisymmetric flame, the usage of an Abel inversion algorithm is required to obtain the emission corresponding to a slice of the flame. The soot temperature is then derived from the soot incandescence signal, S_{λ}^{inc}, measured at two wavelengths, using the same equation as in 2C-LII pyrometry:

$$T = \frac{hc_{light}}{k_B}\left(\frac{1}{\lambda_2}-\frac{1}{\lambda_1}\right)\frac{1}{\ln\left(\frac{S_{\lambda_1}^{inc}}{S_{\lambda_2}^{inc}}\frac{E(m_{\lambda_2})}{E(m_{\lambda_1})}\left(\frac{\lambda_1}{\lambda_2}\right)^6\frac{\Delta\lambda_2}{\Delta\lambda_1}\frac{C_{calib,\lambda_2}}{C_{calib,\lambda_1}}\right)}. \tag{E.1}$$

Soot temperature measurements were conducted for both the C_2H_4+N_2/air and C_2H_4+H_2/air flames, investigated in Chapters 6, and 7, respectively. For these measurements, the camera gate width was increased from 8 ns to 10 μs, while the camera gain was reduced. Due to these new settings, a new calibration of the optical system was necessary to access the new calibration constants $C_{calib,\lambda}$ at both collection wavelengths.

Figure E.1a shows the natural incandescence of the $C_2H_4 + N_2$/air flame, recorded at 578 nm using the collection system depicted in Fig. 6.1b. Unlike the LII signal, this recorded signal represents a line-of-sight integrated measurement. As a result, it is not possible to determine whether the signal at a given position originates from soot particles in the wings or the core of the flame. The corresponding Abel-inverted signal, shown in Fig. E.1b, represents the emission from soot particles within the vertical slice of the flame containing the flame centerline. It shows a maximum signal in the flame wings, suggesting higher soot concentration, and/or higher emission properties, and/or higher temperatures in that region.

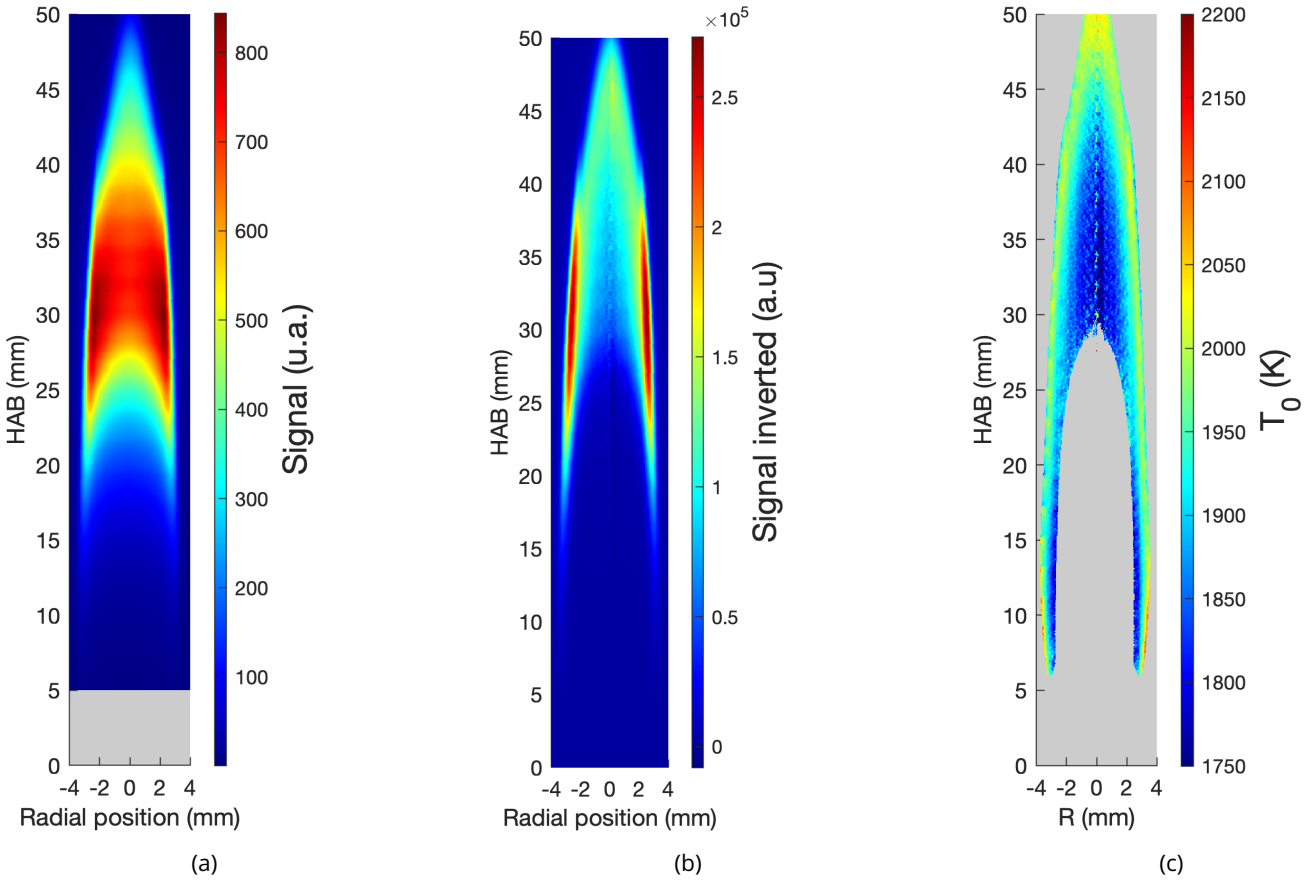

Figure E.1: (a): Signal recorded at 578 nm in the $C_2H_4 + N_2$/air flame. (b): Signal recorded with camera 1 after Abel inversion. (c): Soot temperature without laser heating obtained by emission pyrometry in the reference $C_2H_4 + N_2$/air flame, assuming a dispersion exponent of 1.38.

The soot temperature calculated from the Abel-inverted signals at 578 nm and 716 nm using Eq. (E.1) is compared to the results obtained by Kuhn et al. [216], who also used pyrometry in the same flame. To ensure consistency in the comparison, the same assumption regarding the wavelength dependence of the soot absorption function is adopted. Specifically, a dispersion exponent α_{disp} of 1.38 is used ($E(m_\lambda) \propto \frac{1}{\lambda^{\alpha_{disp}-1}}$), resulting in a ratio $R_{12} = \frac{E(m_{\lambda=578nm})}{E(m_{\lambda=716nm})}$ = 1.085. The resulting temperature map is shown in Fig.E.1c, while the soot temperature from Kuhn et al. [216] is shown in Fig. 6.31b. Their data, available on the website [311], allows a direct comparison of the two results, with the temperature difference between these two maps being plotted in Fig. E.2a.

The temperature ranges from 1800-2000 K for most of the flame, with higher values on the outer edges of the flame. The two temperature maps show good agreement in the core of the flame, but the present results are higher than those of Kuhn et al. on the flame's outer edges. The difference can overcome 100 K, and, on average, the present measurements are 41 K higher, with a standard deviation of 42 K. These differences may be due to slight misalignments between the temperature maps, minor variations in flame conditions, or the distinct collection systems and calibration procedures used in the two studies. Indeed, their collection system differs from the one used here (Section 6.1). Kuhn et al. utilised the three channels (red-green-blue) of a commercial Nikon D90 camera without bandpass filters, which resulted in differences in calibration and data processing compared to the present ones. Nevertheless, the concordance between the two maps supports the temperatures obtained here.

The soot temperature was also computed under the assumption of a wavelength-independent absorption function and is compared to the assumption of a dispersion exponent α_{disp} of 1.38 (Fig. E.1c) in Fig. E.2b. The results show

that assuming α_{disp} = 1 results in higher temperature values, with the difference increasing at higher temperatures. On average, the temperature difference is 60 K, with a standard deviation of 13 K.

The temperature obtained from SP-LII (Fig. 6.31a) is compared to that from emission pyrometry in Fig. E.2c. Both are obtained using a wavelength-independent absorption function. The results from the two methods are generally consistent, with an average temperature difference of 16 K. However, due to the dispersion of the results of the SP-LII measurements in neighbouring points, a standard deviation of 83 K is observed between the SP-LII and emission pyrometry results.

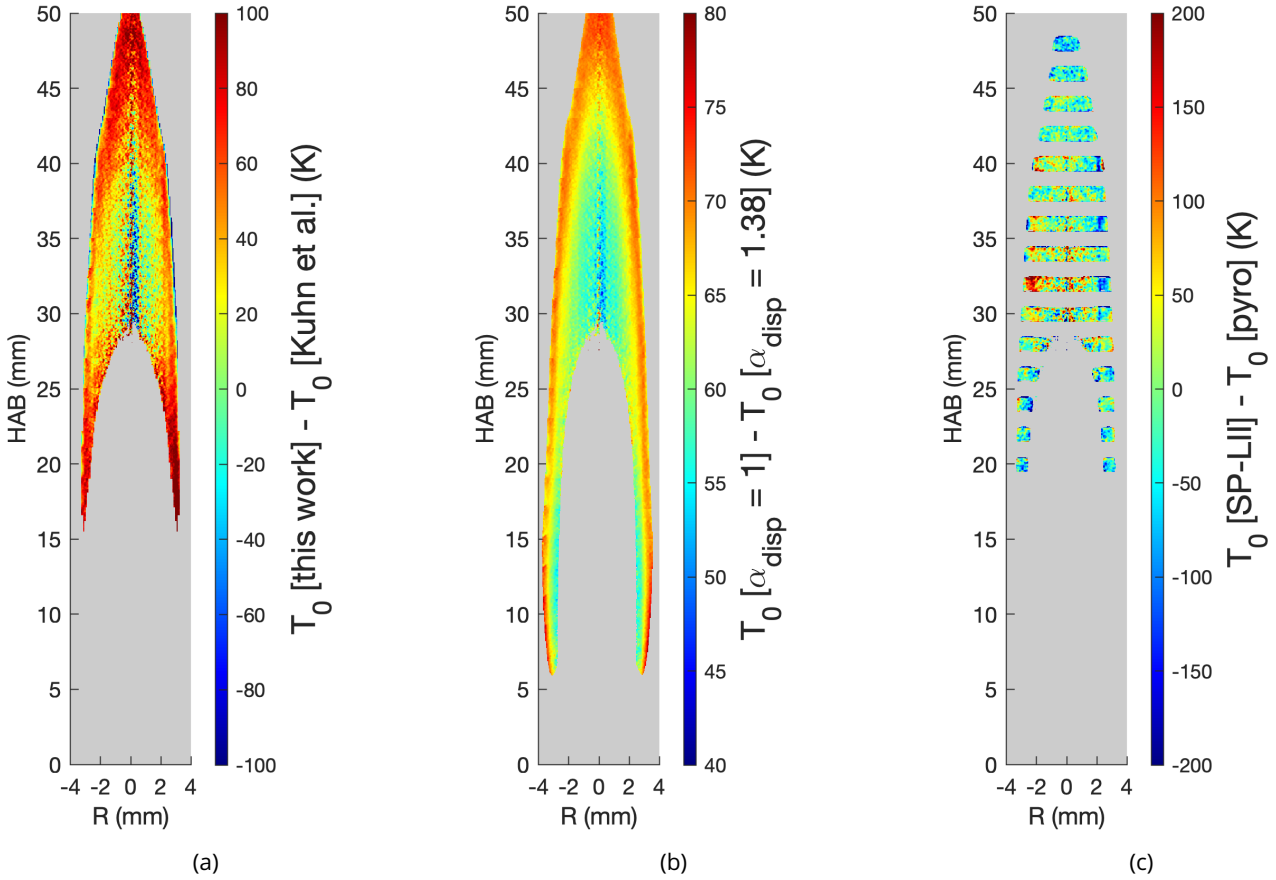

Figure E.2: (a): Difference between the soot temperature obtained in this work and obtained by Kuhn et al. [216]. Both are obtained assuming a dispersion exponent of 1.38. (b): Difference between the soot temperature obtained assuming a dispersion exponent of 1 (wavelength independent) and 1.38, respectively. (c): Difference between the soot temperature obtained with the SP-LII and by emission pyrometry. A dispersion exponent of 1 (wavelength independent) is assumed in both cases.

Appendix F

RANSAC algorithm for the automatic computation of $E(m_\lambda)$, and T_0

Due to the non-linear evolution of the temperature with the laser fluence at temperature, $E(m_\lambda)$ and T_0 have to be computed using measurements under a specific temperature limit. This temperature limit may vary between flames or even spatially in the flame due to a spatial variation of the soot particles' properties. Indeed, for the CH_4/air flame, the temperature limit was set to 4000 K (Fig. 5.6), while for the $C_2H_4 + N_2$/air flame, the limit was set to 3500 K (Fig. 6.11a). Although the limit of 4000 K for the CH_4/air flame was overestimated, the linearity is clearly broken for higher temperatures in this flame compared to the $C_2H_4 + N_2$/air flame. Moreover, in the latter flame, the limit of 3500 K appears over-restrictive for the younger soot particles (Fig. 6.11).

To circumvent the need to give a maximum temperature criterion, which might be over-restrictive for some flame positions, preventing the computation of $E(m_\lambda)$ and T_0 (for youngest particles), a Random sample consensus (RANSAC) algorithm can be utilised. RANSAC is an iterative technique used to estimate the parameters of a mathematical model from data sets that include both inliers and outliers. In this context, inliers are measurements of T_M that show a linear relationship with F, while outliers are those that deviate from this linear trend. Given enough iteration, RANSAC isolates the measurements that align with the linear model and disregards those that do not. Once the inliers are identified, the parameters $E(m_\lambda)$ and T_0 are calculated using a linear regression based solely on these data points.

The application of the RANSAC algorithm is illustrated in Fig. F.1: the data points aligned (in blue) are used for the linear regression while the others (red) are rejected.

A RANSAC algorithm was used to compute $E(m_\lambda)$ and T_0 with linear regression in the case of the $C_2H_4+N_2$/air flame. The algorithm is very convenient as the number of spatial locations probed (pixels) is very high (several thousand). It still requires setting a constraint on the maximum distance allowable to the fit to distinguish inliers and outliers. Also, even if the temperate limit is relaxed, a limit still has to be given (but higher than if not using RANSAC); otherwise, the RANSAC algorithm can find inliers to be the data point having a temperature near the sublimation temperature as they are nearly aligned in the temperature plateau region.

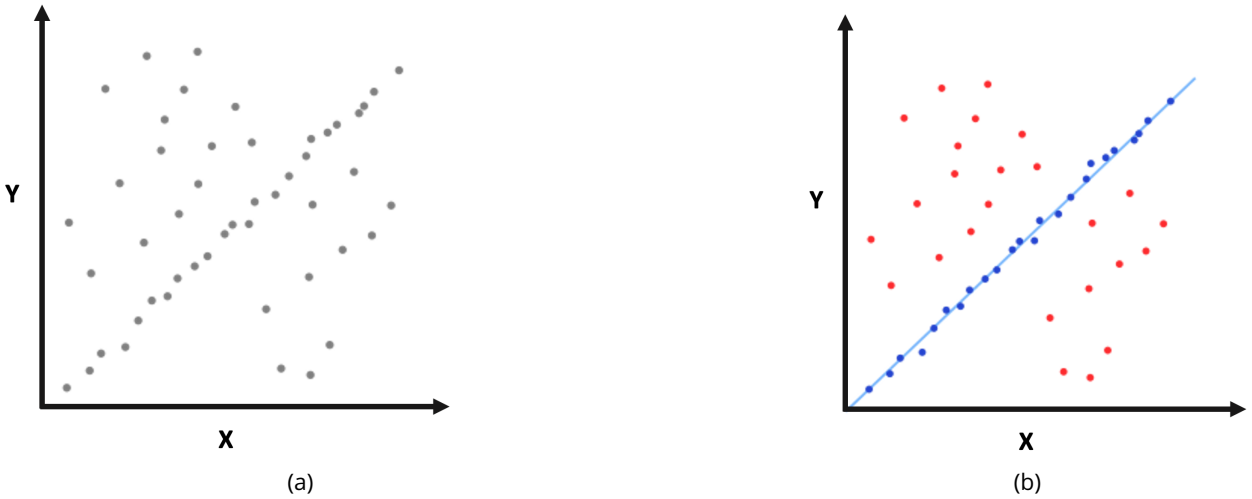

Figure F.1: (a): Dataset with many outliers for which a line has to be fitted. (b): Inliers found by the RANSAC algorithm are in blue, while outliers are in red. Figures from [312].

Figure F.2 represents the temperature versus fluence curves for the reference positions defined in Fig. 6.2a. The T_M points retained for the linear regression obtained with the automatic script are marked by a black cross. While the temperature limit was increased from 3500 to 3900 K, it is clear that the algorithm is able to reject the outlier points while keeping all inlier points in the linear regime even for temperatures above 3500 K.

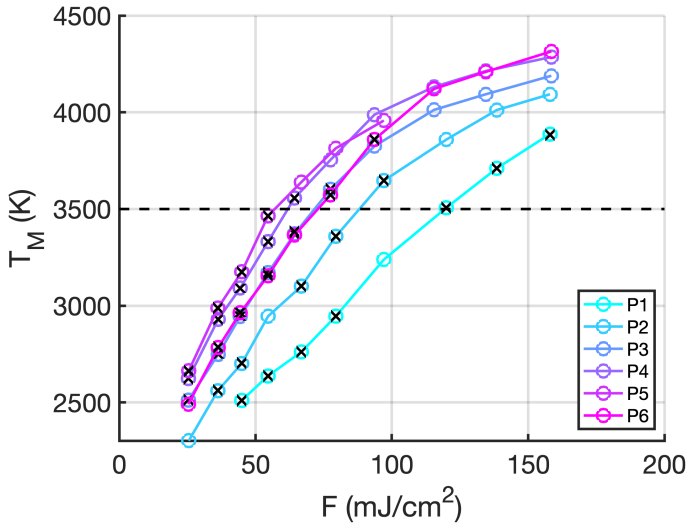

Figure F.2: Peak soot temperature versus laser fluence for different pixel locations. The black cross represents the data points retained by the RANSAC algorithm for computing $E(m_\lambda)$ and T_0 with a linear regression. Each colour corresponds to a different pixel location. The dashed black horizontal line represents the 3500 K limit imposed in Chapter 6 for the data processing.

The usage of a RANSAC algorithm presents multiple advantages. In the case of aberrant temperature estimations at low fluence, these estimations are automatically disregarded. In addition, as no strong temperature limit is given, the estimations of T_M above 3500 K that still follow the inliers trend are kept, making the estimation more robust and extending the range of $E(m_\lambda)$, T_0, that can be probed. However, measurements of T_M at multiple F are required to make a trend appear.

Appendix G

Polydispersion of the temperature of laser-heated soot in the probe volume

The LII experiments can be subjected to many errors that may not be avoided easily, such as the one due to inhomogeneities of the properties of the soot population ($E(m_\lambda)$, d_p, ...) in the probe volume or of the local laser fluence distribution. Liu et al. [196, 210] experimental and numerically investigated the effect of laser non-uniformity for a range of laser fluence between 40 and 400 mJ/cm^2. It was shown that laser fluence non-uniformities induce temperature inhomogeneities in the probe volume: some soot are hotter than others. This leads to estimations of soot temperatures biased towards the hottest soot, which in turn leads to an underestimation of the soot volume fraction. This f_v underestimation is stronger for lower laser fluences. In addition, the stronger the fluence uniformity, or the lower the detection wavelength, the more important these errors are. By comparing their numerical and experimental results, they concluded by saying that this uniformity is partly responsible but does not entirely explain the experimentally observed f_v anomaly.
In this section, a similar analysis is conducted by considering the effect of F and $E(m_\lambda)$ on the experimental results: f_v, $E(m_\lambda)$, T_0, and d_p.

G.1 Numerical setup

The LII code presented in Section 3.3 is used for the numerical investigation of the polydispersion in laser fluence and soot absorption function in the collection volume.

Inputs of the LII code
The selected reference values for the inputs of the LII code are gathered in Table G.1. Reference values of $E(m_\lambda)$, T_0, ρ, d_p are chosen to be representative of LII experiments. Concerning α, and β, the commonly used values 0.3 and 1 [154] are retained, respectively. No reference value is given for the laser fluence as it will be varied from 0 to 500 mJ/cm^2. The LII signals are computed at the same wavelengths as the experiment: 578 and 716 nm.

LII code inputs		
Parameter	**Unit**	**Value**
$E(m_\lambda)_{ref}$	–	0.4
$T_{0_{ref}}$	K	1860
$d_{p_{ref}}$	nm	26
ρ_{ref}	kg/m^3	1950
α_{ref}	–	0.3
β_{ref}	–	1

Table G.1: Reference input parameters for the LII code.

G.2 Polydispersion of laser fluence: top-hat non-uniformity

Similarly to the work of Liu et al. [196], a non-uniformity in laser fluence in the top-hat is numerically studied here to understand its impacts on $E(m_\lambda)$, T_0, f_v, and d_p. The laser fluence distribution is a double Dirac configuration: the second Dirac pulse has twice the laser fluence of the first one $F_2 = 2F_1$. The mean laser fluence $F_{mean} = \frac{F_1+F_2}{2}$ is varied from 0 to 360 mJ/cm^2. The LII code is used to generate LII signals at 578 and 716 nm for two identical soot particles heated at different fluences: a first soot (referred to as "cold" soot) is heated at F_1, and a second one (referred to as "hot" soot) at $F_2 = 2F_1$. The total LII signal (summation of the LII signal coming from both particles) is processed to compute the peak effective temperature by 2C-LII. Absorption function and gas temperature are retrieved from a linear regression of the effective soot temperature versus F_{mean}. The soot volume fraction is obtained from the theoretical expression of the LII signal (Eq. (3.23)), and the soot primary particle size is obtained from the temperature temporal decay.

Figure G.1a shows the evolution with the laser fluence of the normalised peak of the LII signal for each particle and the total signal. The temperature of the hot and the cold soot, as well as the effective peak temperature computed from the peak total LII signal by 2C-LII, are given in Fig. G.1a. As expected, the cold soot curves are shifted to higher laser fluences compared to the one of the hot soot. For laser fluences below 100 mJ/cm^2, the normalised total LII signal is closer to the one of the hot soot and starts moving away from it at higher laser fluences. As a result, the computed effective temperature is well above the mass averaged temperature: it is clearly biased towards the hot soot temperature. This comes from the dominant contribution of the hot soot in the LII signal due to the exponential dependence on the temperature of Planck's law. However, because of the sublimation process, for higher average laser fluences, the temperature of both soot is getting closer. Thus, the effective temperature becomes representative of the true temperature of the soot.

The linear regression of the effective temperature gives $E(m_\lambda)$ = 0.46 and T_0 = 1858 K. That is to say that T_0 is almost perfectly retrieved (the reference value is 1860 K) while $E(m_\lambda)$ is overestimated by 15% due to the laser beam's non-uniformity.

Figure G.1c shows f_v computed from the peak total LII signal, the peak effective temperature, and with $E(m_\lambda)$ = 0.46 (computed value) or 0.4 (true value) versus the laser fluence. The real soot volume fraction at the LII signal peak is also given and includes sublimation due to the laser heating. All profiles are normalised by the initial soot volume fraction. The computed f_v profiles can be separated in two: above $\sim$200 mJ/cm^2 where the computed and real value of f_v are similar, and below where there is a significant difference between them which depends on the average laser fluence. Above 200 mJ/cm^2, the soot particles heated at F_1 and F_2 have approximately the same temperature due to sublimation. Thus, the computed effective temperature is representative of the actual soot temperatures, and as a result, f_v computed from this effective temperature is close to the true f_v. However, below $\sim$200 mJ/cm^2, the

behaviour of f_v follows the one of the ratio of the LII signal of the cold to the one of the hot soot (green curve of Fig. G.1a): f_v is further underestimated when the coldest soot participation to the total LII signal is low. The qualitative dependence of f_v with the laser fluence is similar to the one of Liu et al. [196]. Similarly, f_v is always underestimated by at least 10% (with the exception of extremely low laser fluences that are experimentally not viable). However, in this work, the dependence of f_v with the fluence is much weaker: considering the true $E(m_\lambda)$, the maximum underestimation of f_v is only 25 % (and fluence dependence of f_v is $\sim$15% if very low laser fluences are ignored) while Liu et al. [196] found almost 70% of underestimation. Such a difference cannot be explained by the different parameters of the LII codes (detection wavelengths, absorption function...) nor the different laser fluence distributions, as here, the fluence distribution is more spread, and the effect on f_v is reduced. Neither the differences in sublimation models and parameters can explain it, as the largest differences between the results are found at low laser fluences.

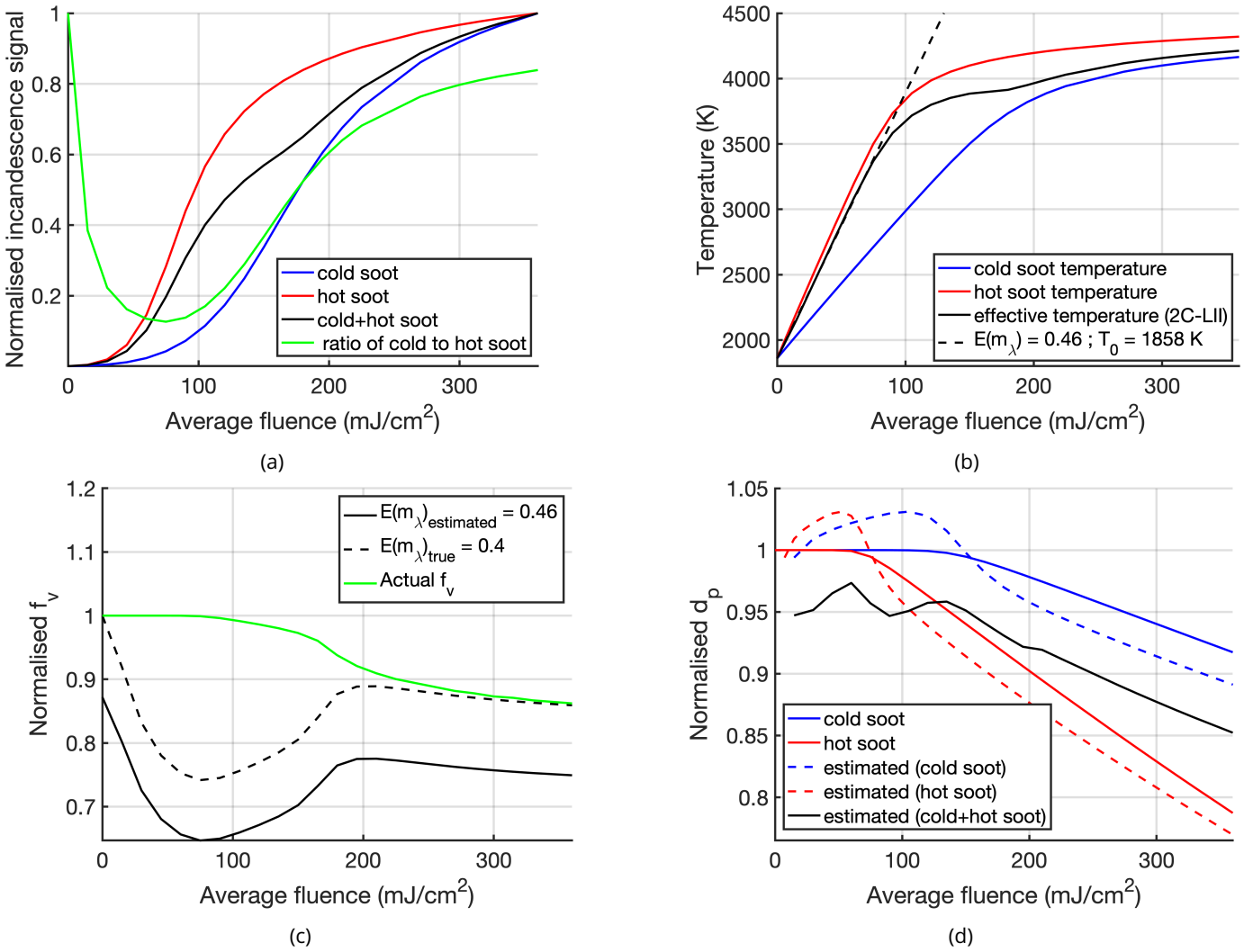

Figure G.1: (a): Normalised maximum of the LII signal at 578 nm versus the average laser fluence for the cold soot heated at F_1 (blue) and the hot soot heated at F_2 (red). The total incandescence signal resulting from the two soot particles is given in black. The signals are normalised by their maximum. The green line represents the ratio of the blue and red curves.
(b): Peak soot temperatures versus the average laser fluence for the soot heated at F_1 (blue), the soot heated at F_2 (red), and the effective soot temperature (black) computed from the total incandescence signal. The black dashed line is the linear regression of the effective temperature curve. This linear regression, corresponds to $E(m_\lambda)$ = 0.46, and T_0 = 1858 K.
(c): Normalised soot volume fraction versus the average laser fluence. The soot volume fraction is computed by AC-LII assuming: $E(m_\lambda)$ = 0.4 (dashed black), and $E(m_\lambda)$ = 0.46, (solid black). The actual soot volume fraction, including soot sublimation, is given in green. The profiles are normalised by the initial value of the soot volume fraction.
(d): Normalised soot primary particle diameter versus the average laser fluence. The actual values of d_p for the cold and hot soot are given by the solid blue and red lines, respectively. The estimated values of d_p with the methodology presented in Sec. 3.4.4 are given for the cold and hot soot by the dashed blue and red lines. The values of d_p estimated from the effective soot temperature are given in black.
The average laser fluence is the mean between F_1 and F_2.

The conclusion of both the present work and [196] are similar: the experimentally observed fluence dependence of f_v is much greater than the numerical one: the polydispersion in laser fluence cannot totally explain the f_v anomaly. The profile with $E(m_\lambda)$ = 0.46 is identical to the one for 0.4 but with an additional (fluence independent) 13% underestimation of f_v: the laser beam non-uniformity brings an indirect underestimation of f_v through the erroneous estimation of $E(m_\lambda)$. The primary particle diameter for the cold and hot soot are given in Fig. G.1d, d_p decreases with laser fluence due to sublimation. The estimations of d_p with the method described in Sec. 3.4.4 from the temperature curves are also plotted. This shows that d_p is well retrieved. At low laser fluences, d_p is overestimated by at most 3%. For higher laser fluences for which sublimation occurs, d_p is underestimated by 2%. The estimation obtained

from the effective temperature curve is ∼5% below the reference d_p for low laser fluences when no sublimation occurs, and as sublimation gets stronger, it gets closer to the average between the cold and hot soot diameters. Thus, the non-uniformity of the laser fluence does not impact the estimated value for d_p much and has a negligible dependence on the laser fluence.

G.3 Polydispersion of the soot absorption function in the probe volume

A polydispersion in $E(m_\lambda)$ in the probe volume can be encountered, similarly to a laser fluence polydispersion. This will introduce non-uniformity of soot temperature in the probe volume. The more absorbent particles will mainly participate in the total incandescence signal as their temperature will be higher (due to stronger absorption), but also due to their stronger emission.

A procedure similar to the laser fluence polydispersion is considered here. The probe volume is assumed to contain two soot particles with different absorption functions: one with $E(m_\lambda)$ = 0.2 (referred to as the "cold" soot), and one with $E(m_\lambda)$ = 0,4 (referred as "hot" soot). Computations are done for laser fluences ranging from 0 to 500 mJ/cm^2. It has to be noted that the absorption function values have been selected such that the product $E(m_\lambda)F$ for both soot particles are equal to the ones for the fluence polydispersion case.

Results in terms of peak normalised incandescence signal, temperatures, soot volume fraction estimation, and primary particle diameter are given in Fig. G.2a, G.2b, G.2c, and G.2d respectively. Qualitatively, the observation made for the laser fluence non-uniformity case holds. However, due to its higher emissivity, the total incandescence signal is even more due to the hot soot. As a result, the effective temperature is almost identical to the hot soot one. This induces a larger bias of the estimation of $E(m_\lambda)$: a value of 0.36 is obtained, i.e. a value 20% higher than the mean absorption function of 0.3. Then, computing f_v with this value of $E(m_\lambda)$ instead of 0.3 results in an additional laser fluence-independent underestimate of f_v of 17%. The computed f_v still follows the trend of the ratio of LII signals until sublimation becomes significant. Due to the different absorption functions, the ratio of the LII signal of the soot with $E(m_\lambda)$ = 0.2 to the one with $E(m_\lambda)$ = 0.4 varies between 0.5 and 0.06 compared to a variation between 1 and 0.13 for the laser fluence non-uniformity case. This weaker fluence dependence brings a weaker fluence dependence of the estimation of f_v. As a result, omitting low laser fluences, the polydispersion of $E(m_\lambda)$ is responsible for only a $\sim$ 5% variation of f_v with the laser fluence. For laser fluences above 300 mJ/cm^2, even if the mean absorption function $E(m_\lambda)$ = 0.3 is used, a difference subsist with the real f_v. This comes from the fact that a larger portion of the hot soot is sublimated, so the mass averaged $E(m_\lambda)$ becomes lower than 0.3.

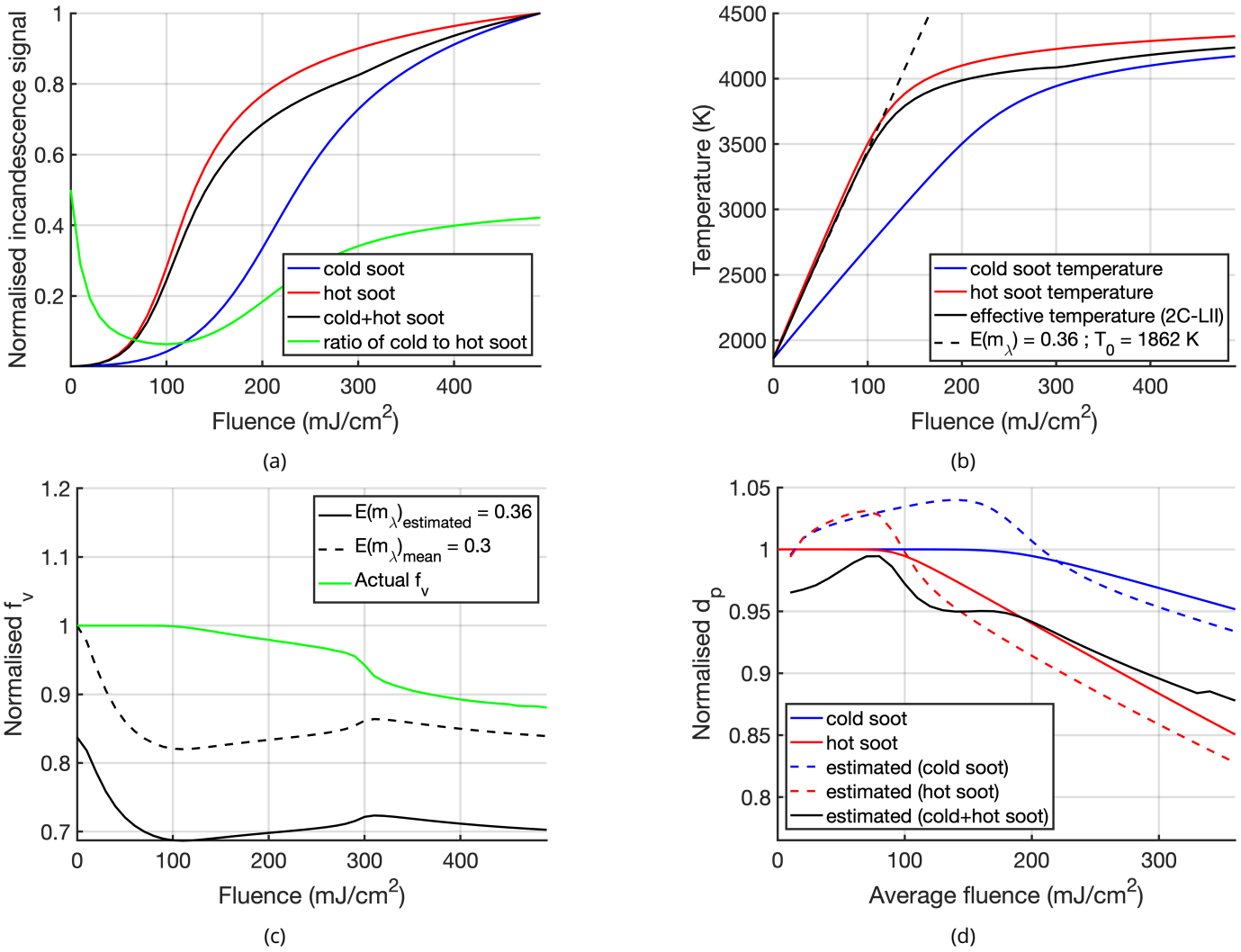

Figure G.2: (a): Normalised maximum of the LII signal at 578 nm versus the laser fluence for the cold soot having $E(m_\lambda)$ = 0.2 (blue), and the hot soot having $E(m_\lambda)$ = 0.4 (red). The total incandescence signal resulting from the two soot particles is given in black. The signals are normalised by their maximum. The green line represents the ratio of the blue and red curves.
(b): Peak soot temperatures versus the average laser fluence for the cold soot (blue), the hot soot (red), and the effective soot temperature (black) computed from the total incandescence signal. The black dashed line is the linear regression of the effective temperature curve. This linear regression, corresponds to $E(m_\lambda)$ = 0.36, and T_0 = 1862 K.
(c): Normalised soot volume fraction versus the laser fluence. The soot volume fraction is computed by AC-LII assuming: $E(m_\lambda)$ = 0.3 (dashed black), and $E(m_\lambda)$ = 0.36, (solid black). The actual soot volume fraction, including soot sublimation, is given in green. The profiles are normalised by the initial value of the soot volume fraction.
(d): Normalised soot primary particle diameter versus the average laser fluence. The actual values of d_p for the cold and hot soot are given by the solid blue and red lines, respectively. The estimated values of d_p with the methodology presented in Sec. 3.4.4 are given for the cold and hot soot by the dashed blue and red lines. The values of d_p estimated from the effective soot temperature are given in black.

G.4 Discussion on the possibility of attributing the f_v anomaly to temperature inhomogeneities

A polydispersion in either F or $E(m_\lambda)$ induces temperature inhomogeneities in the probe volume. Effective temperatures are biased towards the hottest soot. Then, the absorption function recovered is always greater than its average value in the probe volume. T_0 and d_p are only slightly affected. However, f_v is consistently underestimated (by a maximum of 34% in this study) and is fluence dependent. As the numerical trends match the experimental ones, it is tempting to attribute the f_v anomaly to polydispersion (of laser fluence and absorption function). How-

ever, given the high inhomogeneities in F and $E(m_\lambda)$ selected for the numerical study and the moderate fluence dependency, it seems unlikely that the f_v anomaly is solely due to polydispersion effects. Polydispersion of soot size was not considered here. However, other works [250, 313] showed that for prompt detection of the incandescence signal, it does not introduce errors in f_v estimations.

Thus, other phenomena may be at stake. Sipkens et al.[250] showed that the detector response might provoke smoothing and temporal shift of the incandescence signal that will affect temperature estimations, and so every other quantity computed from the temperatures. As another option, an alteration of the soot may happen above $\sim$3500 K. In that case, soot properties such as absorption properties may be responsible for the f_v anomaly as pointed out by Migliorini et al. [262]. The former case may signify that f_v retrieved for heating temperature above 3500 K may not represent the true value.

Appendix H

Computation of the carbon-to-hydrogen ratio

For each flame position, the global carbon-to-hydrogen ratio $\frac{C}{H}$ is computed from the mass fraction of the BIN representing the soot particles and from the carbon-to-hydrogen ratio of each of these BIN species (available in [314]). $\frac{C}{H}$ represents, for each flame position, the total number of carbon atoms composing all classes of soot divided by the total number of hydrogen atoms composing all classes of soot:

$$\frac{C}{H} = \frac{\sum_{i=5}^{25} \left(\sum_{j=\{A,B,C\}} N_{Ci,j} \right)}{\sum_{i=5}^{25} \left(\sum_{j=\{A,B,C\}} N_{Hi,j} \right)} \tag{H.1}$$

where $N_{Ci,j}$, and $N_{Hi,j}$ are the number of carbon and hydrogen atoms in the BIN number i having the level of maturity j, respectively. It is reminded that the soot particles are represented by the BIN classes from i = 5 to 25. Each class number has three maturity levels A, B, and C, having each a different hydrogen-to-carbon ratio $\left(\frac{H}{C}\right)_{i,j}$.

The number of carbon and hydrogen atoms is obtained starting from the mass fraction of the BINi, of maturity class j, $Y_{i,j}$:

$$\begin{aligned} Y_{i,j} &= \frac{m_{i,j}}{m_{tot}} \\ &= \frac{m_{C,i,j} + m_{H,i}}{m_{tot}} \\ &= \frac{n_{C,i,j} M_C + n_{H,i,j} M_H}{m_{tot}} \\ &= n_{C,i,j} \frac{M_C + \left(\frac{H}{C}\right)_{i,j} M_H}{m_{tot}} \end{aligned} \tag{H.2}$$

where $m_{i,j}$ is the total mass of the BIN species $\{i,j\}$ at the considered flame location. $m_{C,i,j}$ and $m_{H,i}$ are the mass of carbon and hydrogen atoms in the BIN species $\{i,j\}$, respectively. $n_{C,i,j}$ and $n_{H,i}$ are the number of mole of carbon and hydrogen atoms from the BIN species $\{i,j\}$ at the considered flame location, respectively. m_{tot} is the total mass, including all BIN and gaseous species. M_C = 12 g/mol, and M_H = 1g/mol are the carbon and hydrogen

molar mass, respectively.

Inverting Eq. (H.2) gives the total number of moles of carbon atoms due to the species BIN$_{i,j}$:

$$n_{C,i,j} = \frac{Y_{i,j} m_{tot}}{M_C + \left(\frac{H}{C}\right)_{i,j} M_H} \tag{H.3}$$

The number of carbon atoms due to the species BIN$_{i,j}$, is obtained by multiplying $n_{C,i,j}$ by the Avogadro number: $N_{Ci,j} = n_{C,i,j} N_{avogadro}$. Then, as $\left(\frac{H}{C}\right)_{i,j} = \frac{N_{H,i,j}}{N_{C,i,j}}$, the number of hydrogen atoms of the species BIN$_{i,j}$ is:

$$N_{H,i,j} = N_{C,i,j} \left(\frac{H}{C}\right)_{i,j} \tag{H.4}$$

Then, the carbon-to-hydrogen ratio is rewritten as:

$$\frac{C}{H} = \frac{\sum_{i=5}^{25} \left(\sum_{j=\{A,B,C\}} \frac{Y_{i,j}}{M_C + \left(\frac{H}{C}\right)_{i,j} M_H} \right)}{\sum_{i=5}^{25} \left(\sum_{j=\{A,B,C\}} \frac{Y_{i,j}}{M_C + \left(\frac{H}{C}\right)_{i,j} M_H} \left(\frac{H}{C}\right)_{i,j} \right)} \tag{H.5}$$

The values of the ratio $\left(\frac{H}{C}\right)_{i,j}$ are available in [314] for all BIN species and are gathered in Tab. H.1.

	$\frac{H}{C}$		
	A	**B**	**C**
Heavy PAHs			
BIN1	0.8	0.5	0.2
BIN2	0.775	0.4	0.2
BIN3	0.75	0.3	0.1
BIN4	0.725	0.2	0.05
Soot particles			
BIN5	0.7	0.2	0.05
BIN6	0.675	0.2	0.05
BIN7	0.65	0.2	0.05
BIN8	0.625	0.2	0.05
BIN9	0.6	0.2	0.05
BIN10	0.575	0.2	0.05
BIN11	0.55	0.2	0.05
BIN12	0.525	0.2	0.05
Soot aggregates			
BIN13	0.5	0.2	0.05
BIN14	0.475	0.2	0.05
BIN15	0.45	0.2	0.05
BIN16	0.425	0.2	0.05
BIN17	0.4	0.2	0.05
BIN18	0.375	0.2	0.05
BIN19	0.35	0.2	0.05
BIN20	0.325	0.2	0.05
BIN21	0.3	0.2	0.05
BIN22	0.3	0.2	0.05
BIN23	0.3	0.2	0.05
BIN24	0.3	0.2	0.05
BIN25	0.3	0.2	0.05

Table H.1: Hydrogen-to-carbon ratio for each class of BIN representing either heavy PAHs (BIN1 to 4) or soot particles (BIN5 to 25). Values from [314].

Bibliography

[1] International Energy Agency. *Energy Statistics Data Browser*. 2023. url: https://www.iea.org/data-and-statistics/data-tools/energy-statistics-data-browser?country=WORLD&fuel=Energy%20supply&indicator=TESbySource.

[2] International Energy Agency. *World Energy Outlook*. 2023. url: https://www.iea.org/reports/world-energy-outlook-2023.

[3] T. R. Barfknecht. "Toxicology of soot". In: *Progress in Energy and Combustion Science* 9.3 (1983), pp. 199–237.

[4] M. P. Sierra-Vargas and L. M. Teran. "Air pollution: Impact and prevention". In: *Respirology* 17.7 (2012), pp. 1031–1038.

[5] R. Prasad and V. R. Bella. "A Review on Diesel Soot Emission, its Effect and Control". In: *Bulletin of Chemical Reaction Engineering & Catalysis* 5.2 (2010), pp. 69–86.

[6] M. Shiraiwa, K. Selzle, and U. Pöschl. "Hazardous components and health effects of atmospheric aerosol particles: reactive oxygen species, soot, polycyclic aromatic compounds and allergenic proteins". In: *Free Radical Research* (2012).

[7] A. D'Anna. *Combustion Generated Fine Carbonaceous Particles*. KIT Scientific Publishing, 2014.

[8] K. Jadhav, Raghuraj, E. Ray, K. Vaghasiya, and R. K. Verma. "Chapter 3 - Neurodegenerative disorders due to inhalation of various small particles". In: *Nanomedical Drug Delivery for Neurodegenerative Diseases*. Ed. by Awesh K. Yadav, Rahul Shukla, and S. J. S. Flora. Academic Press, 2022, pp. 41–54.

[9] D. Loomis, Y. Grosse, B. Lauby-Secretan, F. E. Ghissassi, V. Bouvard, L. Benbrahim-Tallaa, N. Guha, R. Baan, H. Mattock, and K. Straif. "The carcinogenicity of outdoor air pollution". In: *The Lancet Oncology* 14.13 (2013), pp. 1262–1263.

[10] B. Kumfer and I. Kennedy. "The role of soot in the health effects of inhaled airborne particles". In: *Combustion generated fine carbonaceous particles, in: Proceedings of an International Workshop held in Villa Orlandi, Karlsruhe University Press, Anacapri*. 2009, pp. 1–15.

[11] *Air quality in Europe 2022 — European Environment Agency*.

[12] J. Hansen and L. Nazarenko. "Soot climate forcing via snow and ice albedos". In: *Proceedings of the National Academy of Sciences* 101.2 (2004), pp. 423–428.

[13] T. C. Bond et al. "Bounding the role of black carbon in the climate system: A scientific assessment". In: *Journal of Geophysical Research: Atmospheres* 118.11 (2013), pp. 5380–5552.

[14] N. Bellouin et al. "Bounding Global Aerosol Radiative Forcing of Climate Change". In: *Reviews of Geophysics* 58.1 (2020).

[15] R. Teoh, U. Schumann, E. Gryspeerdt, M. Shapiro, J. Molloy, G. Koudis, C. Voigt, and M. E. J. Stettler. "Aviation contrail climate effects in the North Atlantic from 2016 to 2021". In: *Atmospheric Chemistry and Physics* 22.16 (2022), pp. 10919–10935.

[16] M. Z. Jacobson. "Strong radiative heating due to the mixing state of black carbon in atmospheric aerosols". In: *Nature* 409.6821 (2001), pp. 695–697.

[17] J. E. Penner, S. Y. Zhang, and C. C. Chuang. “Soot and smoke aerosol may not warm climate”. In: *Journal of Geophysical Research: Atmospheres* 108.D21 (2003).

[18] G. Myhre et al. “Anthropogenic and Natural Radiative Forcing.” In: *Climate Change 2013: The Physical Science Basis. Contribution of Working Group I to the Fifth Assessment Report of the Intergovernmental Panel on Climate Change* (2013).

[19] H. GG. Wagner. “Soot formation in combustion”. In: *Symposium (International) on Combustion*. Seventeenth Symposium (International) on Combustion 17.1 (1979), pp. 3–19.

[20] B. S. Haynes and H. Gg. Wagner. “Soot formation”. In: *Progress in Energy and Combustion Science* 7.4 (1981), pp. 229–273.

[21] F. E. Lockwood, Z. G. Zhang, S. U. S. Choi, and W. Yu. *Effect of Soot Loading on the Thermal Characteristics of Diesel Engine Oils*. SAE Technical Paper 2001-01-1714. Warrendale, PA: SAE International, 2001.

[22] F. Liu, J-L. Consalvi, and F. Nmira. “The importance of accurately modelling soot and radiation coupling in laminar and laboratory-scale turbulent diffusion flames”. In: *Combustion and Flame*. Special issue and Perspective on the Chemistry and Physics of Carbonaceious Particle Formation 258 (2023), p. 112573.

[23] H. Chu, J. Qi, S. Feng, W. Dong, R. Hong, B. Qiu, and W. Han. “Soot formation in high-pressure combustion: Status and challenges”. In: *Fuel* 345 (2023), p. 128236.

[24] G. Borman and K. Nishiwaki. “Internal-combustion engine heat transfer”. In: *Progress in Energy and Combustion Science* 13.1 (1987), pp. 1–46.

[25] M. P. Mengüc, R. Viskanta, and C. R. Ferguson. “Multidimensional Modeling of Radiative Heat Transfer in Diesel Engines”. In: *SAE Transactions* 94 (1985), pp. 728–745.

[26] A. C. Eckbreth. “Effects of laser-modulated particulate incandescence on Raman scattering diagnostics”. In: *Journal of Applied Physics* 48.11 (1977), pp. 4473–4479.

[27] L. A. Melton. “Soot diagnostics based on laser heating”. In: *Applied Optics* 23.13 (1984), pp. 2201–2208.

[28] R. L. Vander Wal and K. J. Weiland. “Laser-induced incandescence: Development and characterization towards a measurement of soot-volume fraction”. In: *Applied Physics B* 59.4 (1994), pp. 445–452.

[29] R. L. Vander Wal, T. M. Ticich, and A. Brock Stephens. “Can soot primary particle size be determined using laser-induced incandescence?” In: *Combustion and Flame* 116.1 (1999), pp. 291–296.

[30] D. R. Snelling, F. Liu, G. J. Smallwood, and Ö. L. Gülder. “Determination of the soot absorption function and thermal accommodation coefficient using low-fluence LII in a laminar coflow ethylene diffusion flame”. In: *Combustion and Flame* 136.1 (2004), pp. 180–190.

[31] F. Liu, J. Yon, A. Fuentes, P. Lobo, G. J. Smallwood, and J. C. Corbin. “Review of recent literature on the light absorption properties of black carbon: Refractive index, mass absorption cross section, and absorption function”. In: *Aerosol Science and Technology* 54.1 (2020), pp. 33–51.

[32] H. A. Michelsen, M. B. Colket, P.-E. Bengtsson, A. D’Anna, P. Desgroux, B. S. Haynes, J. H. Miller, G. J. Nathan, H. Pitsch, and H. Wang. “A Review of Terminology Used to Describe Soot Formation and Evolution under Combustion and Pyrolytic Conditions”. In: *ACS Nano* 14.10 (2020), pp. 12470–12490.

[33] S. De Iuliis, F. Migliorini, F. Cignoli, and G. Zizak. “Peak soot temperature in laser-induced incandescence measurements”. In: *Applied Physics B* 83.3 (2006), p. 397.

[34] S. Qi, Z. Sun, Z. Wang, Y. Liu, Y. He, S. Liu, K. Wan, G. J. Nathan, and M. Costa. “Effects of gas preheat temperature on soot formation in co-flow methane and ethylene diffusion flames”. In: *Proceedings of the Combustion Institute* 38.1 (2021), pp. 1225–1232.

[35] Y. He, S. Qi, S. Liu, S. Xin, Y. Zhu, and Z. Wang. “Effects of the Gas Preheat Temperature and Nitrogen Dilution on Soot Formation in Co-flow Methane, Ethane, and Propane Diffusion Flames”. In: *Energy & Fuels* 35.9 (2021), pp. 7169–7178.

[36] Z. Zhang, L. Zhou, X. He, L. Chen, and H. Wei. “Effect of preheating air temperature on sooting tendency in laminar co-flow diffusion flame of n-heptane”. In: *Combustion and Flame* 251 (2023), p. 112719.

[37] B. F. Kock, T. Eckhardt, and P. Roth. “In-cylinder sizing of diesel particles by time-resolved laser-induced incandescence (TR-LII)”. In: *Proceedings of the Combustion Institute* 29.2 (2002), pp. 2775–2782.

[38] M. Hofmann, W. G. Bessler, C. Schulz, and H. Jander. “Laser-induced incandescence for soot diagnostics at high pressures”. In: *Applied Optics* 42.12 (2003), pp. 2052–2062.

[39] L. L. McCrain and W. L. Roberts. “Measurements of the soot volume field in laminar diffusion flames at elevated pressures”. In: *Combustion and Flame* 140.1 (2005), pp. 60–69.

[40] M. Hofmann, B.F. Kock, T. Dreier, H. Jander, and C. Schulz. “Laser-induced incandescence for soot-particle sizing at elevated pressure”. In: *Applied Physics B* 90.3 (2008), pp. 629–639.

[41] B. G. Sarnacki and H. K. Chelliah. “Sooting limits of non-premixed counterflow ethylene/oxygen/inert flames using LII: Effects of flow strain rate and pressure (up to 30 atm)”. In: *Combustion and Flame*. Special Commemorative Issue: Professor Chung King (Ed) Law 70th Birthday 195 (2018), pp. 267–281.

[42] M. Mannazhi, S. Török, J. Gao, and P.-E. Bengtsson. “Soot maturity studies in methane-air diffusion flames at elevated pressures using laser-induced incandescence”. In: *Proceedings of the Combustion Institute* 38.1 (2021), pp. 1217–1224.

[43] C. R. Shaddix and K. C. Smyth. “Laser-induced incandescence measurements of soot production in steady and flickering methane, propane, and ethylene diffusion flames”. In: *Combustion and Flame* 107.4 (1996), pp. 418–452.

[44] S. A. Steinmetz, H. A. Ahmed, W. R. Boyette, M. J. Dunn, W. L. Roberts, and A. R. Masri. “Effects of ammonia and hydrogen on the sooting characteristics of laminar coflow flames of ethylene and methane”. In: *Fuel* 307 (2022), p. 121914.

[45] M. Kuribayashi, Y. Mizutani, Y. Ishizuka, N. Taki, and T. Aizawa. “Effects of Ambient Oxygen Concentration on Soot Processes in Diesel Spray Flame - A Qualitative Comparison between TEM Analysis and LII/Scattering Laser Measurements”. In: *SAE International Journal of Fuels and Lubricants* 7.3 (2014), pp. 693–703.

[46] Y. Zhang, F. Liu, D. Clavel, G. J. Smallwood, and C. Lou. “Measurement of soot volume fraction and primary particle diameter in oxygen enriched ethylene diffusion flames using the laser-induced incandescence technique”. In: *Energy* 177 (2019), pp. 421–432.

[47] K. C. Oh and H. D. Shin. “The effect of oxygen and carbon dioxide concentration on soot formation in non-premixed flames”. In: *Fuel* 85.5 (2006), pp. 615–624.

[48] F. Marcuccilli, P. Gilot, B. Stanmore, and G. Prado. “Experimental and theoretical study of diesel soot reactivity”. In: *Symposium (International) on Combustion*. Twenty-Fifth Symposium (International) on Combustion 25.1 (1994), pp. 619–626.

[49] A. D. H Clague, J. B Donnet, T. K Wang, and J. C. M Peng. “A comparison of diesel engine soot with carbon black1”. In: *Carbon* 37.10 (1999), pp. 1553–1565.

[50] A. Bescond, J. Yon, F. X. Ouf, C. Rozé, A. Coppalle, P. Parent, D. Ferry, and C. Laffon. “Soot optical properties determined by analyzing extinction spectra in the visible near-UV: Toward an optical speciation according to constituents and structure”. In: *Journal of Aerosol Science* 101 (2016), pp. 118–132.

[51] J. Yon, J. J. Cruz, F. Escudero, J. Morán, F. Liu, and A. Fuentes. “Revealing soot maturity based on multi-wavelength absorption/emission measurements in laminar axisymmetric coflow ethylene diffusion flames”. In: *Combustion and Flame* 227 (2021), pp. 147–161.

[52] H. A. Michelsen. “Probing soot formation, chemical and physical evolution, and oxidation: A review of in situ diagnostic techniques and needs”. In: *Proceedings of the Combustion Institute* 36.1 (2017), pp. 717–735.

[53] A. Baldelli, U. Trivanovic, T. A. Sipkens, and S. N. Rogak. “On determining soot maturity: A review of the role of microscopy- and spectroscopy-based techniques”. In: *Chemosphere* 252 (2020), p. 126532.

[54] A. V. Eremin, E. V. Gurentsov, and R. N. Kolotushkin. “The change of soot refractive index function along the height of premixed ethylene/air flame and its correlation with soot structure”. In: *Applied Physics B* 126.8 (2020), p. 125.

[55] J. Morán, C. Henry, A. Poux, and J. Yon. “Impact of the maturation process on soot particle aggregation kinetics and morphology”. In: *Carbon* 182 (2021), pp. 837–846.

[56] H. A. Michelsen. “Effects of maturity and temperature on soot density and specific heat”. In: *Proceedings of the Combustion Institute* 38.1 (2021), pp. 1197–1205.

[57] L. Möller, G. Holland, and M. Laue. “Diagnostic Electron Microscopy of Viruses With Low-voltage Electron Microscopes”. In: *Journal of Histochemistry & Cytochemistry* 68.6 (2020), pp. 389–402.

[58] M. Commodo, K. Kaiser, G. De Falco, P. Minutolo, F. Schulz, A. D’Anna, and L. Gross. “On the early stages of soot formation: Molecular structure elucidation by high-resolution atomic force microscopy”. In: *Combustion and Flame* 205 (2019), pp. 154–164.

[59] N. Shibata, Y. Kohno, A. Nakamura, S. Morishita, T. Seki, A. Kumamoto, H. Sawada, T. Matsumoto, S. D. Findlay, and Y. Ikuhara. “Atomic resolution electron microscopy in a magnetic field free environment”. In: *Nature Communications* 10.1 (2019), p. 2308.

[60] M. Pawlyta and H. Hercman. “Transmission electron microscopy (TEM) as a tool for identification of combustion products: Application to black layers in speleothems”. In: *Annales Societatis Geologorum Poloniae* 86 (2016).

[61] F.-X. Ouf et al. “First in-flight synchrotron X-ray absorption and photoemission study of carbon soot nanoparticles”. In: *Scientific Reports* 6.1 (2016), p. 36495.

[62] W. Kim, C. M. Sorensen, D. Fry, and A. Chakrabarti. “Soot aggregates, superaggregates and gel-like networks in laminar diffusion flames”. In: *Journal of Aerosol Science* 37.3 (2006), pp. 386–401.

[63] C. M. Sorensen and G. C. Roberts. “The Prefactor of Fractal Aggregates”. In: *Journal of Colloid and Interface Science* 186.2 (1997), pp. 447–452.

[64] C. M. Sorensen. “Light Scattering by Fractal Aggregates: A Review”. In: *Aerosol Science and Technology* 35.2 (2001), pp. 648–687.

[65] T. T. Charalampopoulos and H. Chang. “Agglomerate parameters and fractal dimension of soot using light scattering—effects on surface growth”. In: *Combustion and Flame* 87.1 (1991), pp. 89–99.

[66] R. P. Bambha, M. A. Dansson, P. E. Schrader, and H. A. Michelsen. “Effects of volatile coatings on the laser-induced incandescence of soot”. In: *Applied Physics B* 112.3 (2013), pp. 343–358.

[67] R. P. Bambha and H. A. Michelsen. “Effects of aggregate morphology and size on laser-induced incandescence and scattering from black carbon (mature soot)”. In: *Journal of Aerosol Science* 88 (2015), pp. 159–181.

[68] R. L. Vander Wal and A. J. Tomasek. “Soot nanostructure: dependence upon synthesis conditions”. In: *Combustion and Flame* 136.1 (2004), pp. 129–140.

[69] T. Ishiguro, Y. Takatori, and K. Akihama. “Microstructure of diesel soot particles probed by electron microscopy: First observation of inner core and outer shell”. In: *Combustion and Flame* 108.1 (1997), pp. 231–234.

[70] M. Alfè, B. Apicella, R. Barbella, J. N. Rouzaud, A. Tregrossi, and A. Ciajolo. “Structure–property relationship in nanostructures of young and mature soot in premixed flames”. In: *Proceedings of the Combustion Institute* 32.1 (2009), pp. 697–704.

[71] M. Z. Jacobson. “Short-term effects of controlling fossil-fuel soot, biofuel soot and gases, and methane on climate, Arctic ice, and air pollution health”. In: *Journal of Geophysical Research: Atmospheres* 115.D14 (2010).

[72] A. Gomez, M. G. Littman, and I. Glassman. “Comparative study of soot formation on the centerline of axisymmetric laminar diffusion flames: Fuel and temperature effects”. In: *Combustion and Flame* 70.2 (1987), pp. 225–241.

[73] I. Glassman. “Soot formation in combustion processes”. In: *Symposium (International) on Combustion* 22.1 (1989), pp. 295–311.

[74] H. Böhm, D. Hesse, H. Jander, B. Lüers, J. Pietscher, H. G. G. Wagner, and M. Weiss. “The influence of pressure and temperature on soot formation in premixed flames”. In: *Symposium (International) on Combustion* 22.1 (1989), pp. 403–411.

[75] I. Glassman, O. Nishida, and G. Sidebotham. “Critical Temperatures of Soot Formation”. In: *Soot Formation in Combustion: Mechanisms and Models*. Ed. by Henning Bockhorn. Berlin, Heidelberg: Springer, 1994, pp. 316–324.

[76] Ö. L. Gülder and D. R. Snelling. “Formation and temperature of soot particles in laminar diffusion flames with elevated temperatures”. In: *Symposium (International) on Combustion*. Twenty-Third Symposium (International) on Combustion 23.1 (1991), pp. 1509–1515.

[77] Ö. L. Gülder. “Soot formation in laminar diffusion flames at elevated temperatures”. In: *Combustion and Flame* 88.1 (1992), pp. 75–82.

[78] Ö. L. Gülder and David R. Snelling. “Influence of nitrogen dilution and flame temperature on soot formation in diffusion flames”. In: *Combustion and Flame* 92.1 (1993), pp. 115–124.

[79] Ö. L. Gülder. “Effects of oxygen on soot formation in methane, propane, and n-Butane diffusion flames”. In: *Combustion and Flame* 101.3 (1995), pp. 302–310.

[80] C. Chu, A. Naseri, T. Mitra, M. Dadsetan, A. Sediako, and M. J. Thomson. “The effect of elevated reactant temperatures on soot nanostructures in a coflow diffusion ethylene flame”. In: *Proceedings of the Combustion Institute* 38.2 (2021), pp. 2525–2532.

[81] I. Glassman. “Sooting laminar diffusion flames: Effect of dilution, additives, pressure, and microgravity”. In: *Symposium (International) on Combustion*. Twenty-Seventh Sysposium (International) on Combustion Volume One 27.1 (1998), pp. 1589–1596.

[82] S. Garnayak, S. Mohapatra, S. K. Dash, B. J. Lee, and V. M. Reddy. “Effect of the Preheated Oxidizer Temperature on Soot Formation and Flame Structure in Turbulent Methane-Air Diffusion Flames at 1 and 3 atm: A CFD Investigation”. In: *Energies* 14.12 (2021), p. 3671.

[83] J. S. Mcarragher and K. J. Tan. “Soot Formation at High Pressures: A Literature Review”. In: *Combustion Science and Technology* (1972).

[84] D. B. Olson, J. C. Pickens, and R. J. Gill. “The effects of molecular structure on soot formation II. Diffusion flames”. In: *Combustion and Flame* 62.1 (1985), pp. 43–60.

[85] G. W. Sidebotham and I. Glassman. “Flame temperature, fuel structure, and fuel concentration effects on soot formation in inverse diffusion flames”. In: *Combustion and Flame* 90.3 (1992), pp. 269–283.

[86] D. D. Das, P. C. St. John, C. S. McEnally, S. Kim, and L. D. Pfefferle. “Measuring and predicting sooting tendencies of oxygenates, alkanes, alkenes, cycloalkanes, and aromatics on a unified scale”. In: *Combustion and Flame* 190 (2018), pp. 349–364.

[87] J. W. Martin, M. Salamanca, and M. Kraft. “Soot inception: Carbonaceous nanoparticle formation in flames”. In: *Progress in Energy and Combustion Science* 88 (2022), p. 100956.

[88] H. Jin, W. Yuan, W. Li, J. Yang, Z. Zhou, L. Zhao, Y. Li, and F. Qi. “Combustion chemistry of aromatic hydrocarbons”. In: *Progress in Energy and Combustion Science* 96 (2023), p. 101076.

[89] P. Pepiot-Desjardins, H. Pitsch, R. Malhotra, S. R. Kirby, and A. L. Boehman. “Structural group analysis for soot reduction tendency of oxygenated fuels”. In: *Combustion and Flame* 154.1 (2008), pp. 191–205.

[90] M. Lapuerta, O. Armas, J. J. Hernández, and A. Tsolakis. “Potential for reducing emissions in a diesel engine by fuelling with conventional biodiesel and Fischer–Tropsch diesel”. In: *Fuel* 89.10 (2010), pp. 3106–3113.

[91] J. Manin, S. Skeen, L. Pickett, E. Kurtz, and J. E. Anderson. “Effects of Oxygenated Fuels on Combustion and Soot Formation/Oxidation Processes”. In: *SAE International Journal of Fuels and Lubricants* 7.3 (2014), pp. 704–717.

[92] A. Gómez, J. A. Soriano, and O. Armas. “Evaluation of sooting tendency of different oxygenated and paraffinic fuels blended with diesel fuel”. In: *Fuel* 184 (2016), pp. 536–543.

[93] L. Liu, H. Xu, Q. Zhu, H. Ren, and X. Li. “Soot formation of *n*-decane pyrolysis: A mechanistic view from ReaxFF molecular dynamics simulation”. In: *Chemical Physics Letters* 760 (2020), p. 137983.

[94] X. Mercier, O. Carrivain, C. Irimiea, A. Faccinetto, and E. Therssen. “Dimers of polycyclic aromatic hydrocarbons: the missing pieces in the soot formation process”. In: *Physical Chemistry Chemical Physics* 21.16 (2019), pp. 8282–8294.

[95] M. Frenklach. “Reaction mechanism of soot formation in flames”. In: *Physical Chemistry Chemical Physics* 4.11 (2002), pp. 2028–2037.

[96] H. Richter and J. B. Howard. “Formation of polycyclic aromatic hydrocarbons and their growth to soot—a review of chemical reaction pathways”. In: *Progress in Energy and Combustion Science* 26.4 (2000), pp. 565–608.

[97] C. S. McEnally, L. D. Pfefferle, B. Atakan, and K. Kohse-Höinghaus. “Studies of aromatic hydrocarbon formation mechanisms in flames: Progress towards closing the fuel gap”. In: *Progress in Energy and Combustion Science* 32.3 (2006), pp. 247–294.

[98] E. Jiaqiang, W. Xu, Y. Ma, D. Tan, Q. Peng, Y. Tan, and L. Chen. “Soot formation mechanism of modern automobile engines and methods of reducing soot emissions: A review”. In: *Fuel Processing Technology* 235 (2022), p. 107373.

[99] M. Frenklach and H. Wang. “Detailed modeling of soot particle nucleation and growth”. In: *Symposium (International) on Combustion*. Twenty-Third Symposium (International) on Combustion 23.1 (1991), pp. 1559–1566.

[100] M. Frenklach, D. W. Clary, W. C. Gardiner, and S. E. Stein. “Effect of fuel structure on pathways to soot”. In: *Symposium (International) on Combustion*. Twenty-First Symposuim (International on Combustion) 21.1 (1988), pp. 1067–1076.

[101] M. Frenklach. “On the driving force of PAH production”. In: *Symposium (International) on Combustion* 22.1 (1989), pp. 1075–1082.

[102] H. F. Calcote. “Mechanisms of soot nucleation in flames—A critical review”. In: *Combustion and Flame* 42 (1981), pp. 215–242.

[103] M. Frenklach, D. W. Clary, W. C. Gardiner, and S. E. Stein. “Detailed kinetic modeling of soot formation in shock-tube pyrolysis of acetylene”. In: *Symposium (International) on Combustion*. Twentieth Symposium (International) on Combustion 20.1 (1985), pp. 887–901.

[104] M. Sakai, H. Iguma, K. Kondo, and T. Aizawa. *Nanostructure Analysis of Primary Soot Particles Directly Sampled in Diesel Spray Flame via HRTEM*. SAE Technical Paper 2012-01-1722. Warrendale, PA: SAE International, 2012.

[105] K. O. Johansson, F. El Gabaly, P. E. Schrader, M. F. Campbell, and H. A. Michelsen. “Evolution of maturity levels of the particle surface and bulk during soot growth and oxidation in a flame”. In: *Aerosol Science and Technology* 51.12 (2017), pp. 1333–1344.

[106] T. Ishiguro, N. Suzuki, Y. Fujitani, and H. Morimoto. “Microstructural changes of diesel soot during oxidation”. In: *Combustion and Flame* 85.1 (1991), pp. 1–6.

[107] J. Song, M. Alam, A. L. Boehman, and U. Kim. “Examination of the oxidation behavior of biodiesel soot”. In: *Combustion and Flame* 146.4 (2006), pp. 589–604.

[108] C. Gu, H. Lin, J. Camacho, B. Lin, C. Shao, R. Li, H. Gu, B. Guan, Z. Huang, and H. Wang. "Particle size distribution of nascent soot in lightly and heavily sooting premixed ethylene flames". In: *Combustion and Flame* 165 (2016), pp. 177–187.

[109] B. K. Mandal, A. Sarkar, and A. Datta. "Numerical Prediction of the Soot and NO Formation in a Confined Laminar Diffusion Flame without and with Air Preheat". In: *Proceedings of the Institution of Mechanical Engineers, Part A: Journal of Power and Energy* 220.5 (2006), pp. 473–486.

[110] C. Chu, Y. Amidpour, N. A. Eaves, and M. J. Thomson. "An experimental and numerical study of the effects of reactant temperatures on soot formation in a coflow diffusion ethylene flame". In: *Combustion and Flame* 233 (2021), p. 111574.

[111] T. R. Melton, F. Inal, and S. M. Senkan. "The effects of equivalence ratio on the formation of polycyclic aromatic hydrocarbons and soot in premixed ethane flames". In: *Combustion and Flame* 121.4 (2000), pp. 671–678.

[112] F. Inal and S. M. Senkan. "Effects of equivalence ratio on species and soot concentrations in premixed n-heptane flames". In: *Combustion and Flame* 131.1 (2002), pp. 16–28.

[113] C. Betrancourt et al. "Investigation of the size of the incandescent incipient soot particles in premixed sooting and nucleation flames of n-butane using LII, HIM, and 1 nm-SMPS". In: *Aerosol Science and Technology* 51.8 (2017), pp. 916–935.

[114] C. Betrancourt, X. Mercier, F. Liu, and P. Desgroux. "Quantitative measurement of volume fraction profiles of soot of different maturities in premixed flames by extinction-calibrated laser-induced incandescence". In: *Applied Physics B* 125.1 (2019), p. 16.

[115] P. Clothier, B. Aguda, A. Moise, and H. Pritchard. "How Do Diesel-Fuel Ignition Improvers Work?" In: *Chemical Society Reviews - CHEM SOC REV* 22 (1993).

[116] D. Stratiev. "Effect of gasoline hydrocarbon composition on the properties of the blend gasoline/bioethanol". In: *Oxidation Communications* 34.1 (2011), pp. 183–192.

[117] M. Botero, S. Mosbach, and M. Kraft. "Sooting tendency and particle size distributions of n-heptane/toluene mixtures burned in a wick-fed diffusion flame". In: *Fuel* 169 (2015).

[118] A. P. P. Pires, Y. Han, J. Kramlich, and M. Garcia-Pérez. "Chemical Composition and Fuel Properties of Alternative Jet Fuels". In: BioRes_13_2_2632 (2018). Ed. by United States. Federal Aviation Administration. Center of Excellence for Alternative Jet Fuels and Environment and Washington State University.

[119] B. T. Brem et al. "Effects of Fuel Aromatic Content on Nonvolatile Particulate Emissions of an In-Production Aircraft Gas Turbine". In: *Environmental Science & Technology* 49.22 (2015), pp. 13149–13157.

[120] *The focus on aromatics in automotive fuels specifications*. url: `https://www.concawe.eu/wp-content/uploads/cr112-aromatics-2003-01897-01-e.pdf`.

[121] S. J. Harris and A. M. Weiner. "Chemical Kinetics of Soot Particle Growth". In: *Annual Review of Physical Chemistry* 36.1 (1985), pp. 31–52.

[122] M. Alfè, B. Apicella, J. N. Rouzaud, A. Tregrossi, and A. Ciajolo. "The effect of temperature on soot properties in premixed methane flames". In: *Combustion and Flame* 157.10 (2010), pp. 1959–1965.

[123] K. A. Jensen, J. M. Suo-anttila, and L. G. Blevins. "Measurement of Soot Morphology, Chemistry, and Optical Properties in the Visible and Near-Infrared Spectrum in the Flame Zone and Overfire Region of Large Jp-8 Pool Fires". In: *Combustion Science and Technology* 179.12 (2007), pp. 2453–2487.

[124] K. H. Homann and H. Gg. Wagner. "Some new aspects of the mechanism of carbon formation in premixed flames". In: *Symposium (International) on Combustion* 11.1 (1967), pp. 371–379.

[125] A. D'Alessio, A. Di Lorenzo, A. F. Sarofim, F. Beretta, S. Masi, and C. Venitozzi. "Soot formation in methane-oxygen flames". In: *Symposium (International) on Combustion*. Fifteenth Symposium (International) on Combustion 15.1 (1975), pp. 1427–1438.

[126] B. Zhao, K. Uchikawa, and H. Wang. “A comparative study of nanoparticles in premixed flames by scanning mobility particle sizer, small angle neutron scattering, and transmission electron microscopy”. In: *Proceedings of the Combustion Institute* 31.1 (2007), pp. 851–860.

[127] C. Russo, M. Alfè, J.-N. Rouzaud, F. Stanzione, A. Tregrossi, and A. Ciajolo. “Probing structures of soot formed in premixed flames of methane, ethylene and benzene”. In: *Proceedings of the Combustion Institute* 34.1 (2013), pp. 1885–1892.

[128] B. Apicella, P. Pré, J. N. Rouzaud, J. Abrahamson, R. L. V. Wal, A. Ciajolo, A. Tregrossi, and C. Russo. “Laser-induced structural modifications of differently aged soot investigated by HRTEM”. In: *Combustion and Flame* 204 (2019), pp. 13–22.

[129] M. R. Kholghy, A. Veshkini, and M. J. Thomson. “The core–shell internal nanostructure of soot – A criterion to model soot maturity”. In: *Carbon* 100 (2016), pp. 508–536.

[130] S. Maffi, S. De Iuliis, F. Cignoli, and G. Zizak. “Investigation on thermal accommodation coefficient and soot absorption function with two-color Tire-LII technique in rich premixed flames”. In: *Applied Physics B* 104.2 (2011), pp. 357–366.

[131] H. Bladh, J. Johnsson, N. E. Olofsson, A. Bohlin, and P. E. Bengtsson. “Optical soot characterization using two-color laser-induced incandescence (2C-LII) in the soot growth region of a premixed flat flame”. In: *Proceedings of the Combustion Institute* 33.1 (2011), pp. 641–648.

[132] G. Cléon, T. Amodeo, A. Faccinetto, and P. Desgroux. “Laser induced incandescence determination of the ratio of the soot absorption functions at 532 nm and 1064 nm in the nucleation zone of a low pressure premixed sooting flame”. In: *Applied Physics B* 104.2 (2011), pp. 297–305.

[133] F. Migliorini, K. A. Thomson, and G. J. Smallwood. “Investigation of optical properties of aging soot”. In: *Applied Physics B* 104.2 (2011), pp. 273–283.

[134] G. Guy, C. Betrancourt, and B. Franzelli. “Estimation of soot absorption function via the two separated pulses laser-induced incandescence technique”. In: *Applied Physics B* 129.8 (2023), p. 127.

[135] J. Yon, R. Lemaire, E. Therssen, P. Desgroux, A. Coppalle, and K. F. Ren. “Examination of wavelength dependent soot optical properties of diesel and diesel/rapeseed methyl ester mixture by extinction spectra analysis and LII measurements”. In: *Applied Physics B* 104.2 (2011), pp. 253–271.

[136] E. V. Gurentsov. “A review on determining the refractive index function, thermal accommodation coefficient and evaporation temperature of light-absorbing nanoparticles suspended in the gas phase using the laser-induced incandescence”. In: *Nanotechnology Reviews* 7.6 (2018), pp. 583–604.

[137] J. Yi, C. Betrancourt, N. Darabiha, and B. Franzelli. “Estimation of spectral absorption function range via LII measurements of flame-synthesized TiO2 nanoparticles”. In: *Applied Physics B* 129.11 (2023), p. 179.

[138] C. Barrera, V. Castro, F. Escudero, J. J. Cruz, I. Verdugo, J. Yon, and A. Fuentes. “Maturity characterization of soot in laminar coflow diffusion flames of methane/anisole under different oxygen indices”. In: *Experimental Thermal and Fluid Science* 151 (2024), p. 111101.

[139] A. Eremin, E. Gurentsov, E. Popova, and K. Priemchenko. “Size dependence of complex refractive index function of growing nanoparticles”. In: *Applied Physics B* 104.2 (2011), pp. 285–295.

[140] C. Schulz, B.F. Kock, M. Hofmann, H. Michelsen, S. Will, B. Bougie, R. Suntz, and G. Smallwood. “Laser-induced incandescence: recent trends and current questions”. In: *Applied Physics B* 83.3 (2006), pp. 333–354.

[141] S. Bejaoui, S. Batut, E. Therssen, N. Lamoureux, P. Desgroux, and F. Liu. “Measurements and modeling of laser-induced incandescence of soot at different heights in a flat premixed flame”. In: *Applied Physics B* 118.3 (2015), pp. 449–469.

[142] F. Escudero, J. J. Cruz, I. Verdugo, N. Gutierrez, F. Liu, J. Yon, and A. Fuentes. “Effect of maturity on soot volume fraction measurements using the AC-LII technique in a laminar coflow ethylene diffusion flame”. In: *Proceedings of the Combustion Institute* (2022).

[143] A. García, I. Verdugo, J. J. Cruz, F. Escudero, V. Yap, J. Gallardo, R. Demarco, J. Yon, and A. Fuentes. “Effect of hydrogen addition on soot maturity and volume fraction of ethylene non-premixed flames under different oxygen indices”. In: *Proceedings of the Combustion Institute* 40.1 (2024), p. 105539.

[144] D. R. Snelling, K. A. Thomson, G. J. Smallwood, O. L. Guider, E. J. Weckman, and R. A. Fraser. “Spectrally Resolved Measurement of Flame Radiation to Determine Soot Temperature and Concentration”. In: *AIAA Journal* 40.9 (2002), pp. 1789–1795.

[145] E. Therssen, Y. Bouvier, C. Schoemaecker-Moreau, X. Mercier, P. Desgroux, M. Ziskind, and C. Focsa. “Determination of the ratio of soot refractive index function E(m) at the two wavelengths 532 and 1064 nm by laser induced incandescence”. In: *Applied Physics B* 89.2-3 (2007), pp. 417–427.

[146] N. J. Kempema, B. Ma, and M. B. Long. “Investigation of in-flame soot optical properties in laminar coflow diffusion flames using thermophoretic particle sampling and spectral light extinction”. In: *Applied Physics B* 122.9 (2016), p. 232.

[147] F. P. Hagen, R. Suntz, H. Bockhorn, and D. Trimis. “Dual-pulse laser-induced incandescence to quantify carbon nanostructure and related soot particle properties in transient flows – Concept and exploratory study”. In: *Combustion and Flame* 243 (2022), p. 112020.

[148] S. Bejaoui, R. Lemaire, P. Desgroux, and E. Therssen. “Experimental study of the E(m, λ)/E(m, 1064) ratio as a function of wavelength, fuel type, height above the burner and temperature”. In: *Applied Physics B* 116.2 (2014), pp. 313–323.

[149] X. López-Yglesias, P. E. Schrader, and H. A. Michelsen. “Soot maturity and absorption cross sections”. In: *Journal of Aerosol Science* 75 (2014), pp. 43–64.

[150] J. Simonsson, N.-E. Olofsson, S. Török, P.-E. Bengtsson, and H. Bladh. “Wavelength dependence of extinction in sooting flat premixed flames in the visible and near-infrared regimes”. In: *Applied Physics B: Lasers and Optics* 119.4 (2015), pp. 657–667.

[151] T. S. Totton, D. Chakrabarti, A. J. Misquitta, M. Sander, D. J. Wales, and M. Kraft. “Modelling the internal structure of nascent soot particles”. In: *Combustion and Flame* 157.5 (2010), pp. 909–914.

[152] F. X. Ouf, S. Bourrous, S. Fauvel, A. Kort, L. Lintis, J. Nuvoli, and J. Yon. “True density of combustion emitted particles: A comparison of results highlighting the influence of the organic contents”. In: *Journal of Aerosol Science* 134 (2019), pp. 1–13.

[153] R. A. Dobbins, G. W. Mulholland, and N. P. Bryner. “Comparison of a fractal smoke optics model with light extinction measurements”. In: *Atmospheric Environment*. Conference on visibility and fine particles 28.5 (1994), pp. 889–897.

[154] H.A. Michelsen et al. “Modeling laser-induced incandescence of soot: a summary and comparison of LII models”. In: *Applied Physics B* 87.3 (2007), pp. 503–521.

[155] B. F. Kock, B. Tribalet, C. Schulz, and P. Roth. “Two-color time-resolved LII applied to soot particle sizing in the cylinder of a Diesel engine”. In: *Combustion and Flame* 147.1 (2006), pp. 79–92.

[156] R. L. V. Wal and T. M. Ticich. “Cavity ringdown and laser-induced incandescence measurements of soot”. In: *Applied Optics* 38.9 (1999), pp. 1444–1451.

[157] R. L. Vander Wal, Z. Zhou, and M. Y. Choi. “Laser-induced incandescence calibration via gravimetric sampling”. In: *Combustion and Flame* 105.4 (1996), pp. 462–470.

[158] N. P. Tait and D. A. Greenhalgh. “PLIF Imaging of Fuel Fraction in Practical Devices and LII Imaging of Soot”. In: *Berichte der Bunsengesellschaft für physikalische Chemie* 97.12 (1993), pp. 1619–1624.

[159] S. De Iuliis, F. Migliorini, F. Cignoli, and G. Zizak. “2D soot volume fraction imaging in an ethylene diffusion flame by two-color laser-induced incandescence (2C-LII) technique and comparison with results from other optical diagnostics”. In: *Proceedings of the Combustion Institute* 31.1 (2007), pp. 869–876.

[160] D. R. Snelling, G. J. Smallwood, F. Liu, Ö. L. Gülder, and W. D. Bachalo. “A calibration-independent laser-induced incandescence technique for soot measurement by detecting absolute light intensity”. In: *Applied Optics* 44.31 (2005), p. 6773.

[161] R. Hadef, K. P. Geigle, W. Meier, and M. Aigner. “Soot characterization with laser-induced incandescence applied to a laminar premixed ethylene–air flame”. In: *International Journal of Thermal Sciences* 49.8 (2010), pp. 1457–1467.

[162] P. Desgroux, N. Lamoureux, and A. Faccinetto. “Combining performances of E(m)-corrected LII and absorption for in situ measurements of the volume fraction of 2-4 nm soot particles.” In: *Journal of Aerosol Science* (2024), p. 106385.

[163] S. Will, S. Schraml, and A. Leipertz. “Two-dimensional soot-particle sizing by time-resolved laser-induced incandescence”. In: *Optics Letters* 20.22 (1995).

[164] S. Will, S. Schraml, and A. Leipert. “Comprehensive two-dimensional soot diagnostics based on laser-induced incandescence (LII)”. In: *Symposium (International) on Combustion* 26.2 (1996), pp. 2277–2284.

[165] S. Will, S. Schraml, K. Bader, and A. Leipertz. “Performance characteristics of soot primary particle size measurements by time-resolved laser-induced incandescence”. In: *Applied Optics* 37.24 (1998), pp. 5647–5658.

[166] C. Allouis, A. D’Alessio, C. Noviello, and F. Beretta. “Time Resolved Laser Induced Incandescence for Soot and Cenospheres Measurements in Oil Flames”. In: *Combustion Science and Technology* 153.1 (2000), pp. 51–63.

[167] B. Axelsson, R. Collin, and P.-E. Bengtsson. “Laser-induced incandescence for soot particle size measurements in premixed flat flames”. In: *Applied Optics* 39.21 (2000), pp. 3683–3690.

[168] R. Hadef, K. P. Geigle, J. Zerbs, R. A. Sawchuk, and D. R. Snelling. “The concept of 2D gated imaging for particle sizing in a laminar diffusion flame”. In: *Applied Physics B* 112.3 (2013), pp. 395–408.

[169] H. Bockhorn, H. Geitlinger, B. Jungfleisch, Th Lehre, A. Schön, Th Streibel, and R. Suntz. “Progress in characterization of soot formation by optical methods”. In: *Physical Chemistry Chemical Physics* 4.15 (2002), pp. 3780–3793.

[170] S. Török, M. Mannazhi, and P.-E. Bengtsson. “Laser-induced incandescence (2 and 2C) for estimating absorption efficiency of differently matured soot”. In: *Applied Physics B* 127.7 (2021), p. 96.

[171] C. S. McEnally, A. M. Schaffer, M. B. Long, L. D. Pfefferle, M. D. Smooke, M. B. Colket, and R. J. Hall. “Computational and experimental study of soot formation in a coflow, laminar ethylene diffusion flame”. In: *Symposium (International) on Combustion* 27.1 (1998), pp. 1497–1505.

[172] S. Prucker, W. Meier, and W. Stricker. “A flat flame burner as calibration source for combustion research: Temperatures and species concentrations of premixed H2/air flames”. In: *Review of Scientific Instruments* 65.9 (1994), pp. 2908–2911.

[173] B. Quay, T. W. Lee, T. Ni, and R. J. Santoro. “Spatially resolved measurements of soot volume fraction using laser-induced incandescence”. In: *Combustion and Flame* 97.3 (1994), pp. 384–392.

[174] J. Delhay, P. Desgroux, E. Therssen, H. Bladh, P.-E. Bengtsson, H. Hönen, J. D. Black, and I. Vallet. “Soot volume fraction measurements in aero-engine exhausts using extinction-calibrated backward laser-induced incandescence”. In: *Applied Physics B* 95.4 (2009), pp. 825–838.

[175] F. Schneider, S. Suleiman, J. Menser, E. Borukhovich, I. Wlokas, A. Kempf, H. Wiggers, and C. Schulz. “SpraySyn—A standardized burner configuration for nanoparticle synthesis in spray flames”. In: *Review of Scientific Instruments* 90.8 (2019), p. 085108.

[176] *Mini Cast 5201C et 5203C*. url: `https://www.addair.fr/generateurs/jing-generateurs/mini-cast-5201c-et-5203c/`.

[177] Palas GmbH. *DNP digital 3000*. url: `https://www.palas.de/en/product/dnpdigital3000`.

[178] D. R. Snelling, G. J. Smallwood, R. A. Sawchuk, W. S. Neill, D. Gareau, W. L. Chippior, F. Liu, Ö. L. Gülder, and W. D. Bachalo. *Particulate Matter Measurements in a Diesel Engine Exhaust by Laser-Induced Incandescence and*

the Standard Gravimetric Procedure. SAE Technical Paper 1999-01-3653. Warrendale, PA: SAE International, 1999.

[179] A. R. Coderre, K. A. Thomson, D. R. Snelling, and M. R. Johnson. "Spectrally resolved light absorption properties of cooled soot from a methane flame". In: *Applied Physics B* 104.1 (2011), pp. 175–188.

[180] T. Mouton, X. Mercier, M. Wartel, N. Lamoureux, and P. Desgroux. "Laser-induced incandescence technique to identify soot nucleation and very small particles in low-pressure methane flames". In: *Applied Physics B* 112.3 (2013), pp. 369–379.

[181] C. R. Shaddix, J. E. Harrington, and K. C. Smyth. "Quantitative measurements of enhanced soot production in a flickering methane/air diffusion flame". In: *Combustion and Flame*. 25th Symposium (International) on Combustion Papers 99.3 (1994), pp. 723–732.

[182] F. Migliorini, S. Mancarella, S. Bianchi, S. De Iuliis, F. Cignoli, and G. Zizak. "Preliminary Investigation on the Influence of Hydrogen Addition in Air/C2H4 Premixed Flames". In: *Meeting of Italian Section of the Combustion Institute, Ischia, June 20-23* (2007).

[183] S. De Iuliis, S. Maffi, F. Migliorini, F. Cignoli, and G. Zizak. "Effect of hydrogen addition on soot formation in an ethylene/air premixed flame". In: *Applied Physics B* 106.3 (2012), pp. 707–715.

[184] R. Lemaire. "Etude de l'impact de la combustion de différents types de carburants sur les caractéristiques physico-chimiques des particules de suie par couplage de l'Incandescence et de la Fluorescence Induite par Laser". In: (2008), p. 274.

[185] D. W. Senser, J. S. Morse, and V. A. Cundy. "Construction and novel application of a flat flame burner facility to study hazardous waste combustion". In: *Review of Scientific Instruments* 56.6 (1985), pp. 1279–1284.

[186] M. Leschowski, T. Dreier, and C. Schulz. "A Standard Burner for High Pressure Laminar Premixed Flames: Detailed Soot Diagnostics". In: *Zeitschrift für Physikalische Chemie* 229.5 (2015), pp. 781–805.

[187] J. P. Schwarz et al. "The Detection Efficiency of the Single Particle Soot Photometer". In: *Aerosol Science and Technology* 44.8 (2010), pp. 612–628.

[188] S. Bejaoui, X. Mercier, P. Desgroux, and E. Therssen. "Laser induced fluorescence spectroscopy of aromatic species produced in atmospheric sooting flames using UV and visible excitation wavelengths". In: *Combustion and Flame* 161.10 (2014), pp. 2479–2491.

[189] J. Zerbs, K. P. Geigle, O. Lammel, J. Hader, R. Stirn, R. Hadef, and W. Meier. "The influence of wavelength in extinction measurements and beam steering in laser-induced incandescence measurements in sooting flames". In: *Applied Physics B* 96.4 (2009), pp. 683–694.

[190] H. A. Michelsen, C. Schulz, G. J. Smallwood, and S. Will. "Laser-induced incandescence: Particulate diagnostics for combustion, atmospheric, and industrial applications". In: *Progress in Energy and Combustion Science* 51 (2015), pp. 2–48.

[191] T. Ni, J. A. Pinson, S. Gupta, and R. J. Santoro. "Two-dimensional imaging of soot volume fraction by the use of laser-induced incandescence". In: *Applied Optics* 34.30 (1995), pp. 7083–7091.

[192] P. O. Witze, S. Hochgreb, D. Kayes, H. A. Michelsen, and C. R. Shaddix. "Time-resolved laser-induced incandescence and laser elastic-scattering measurements in a propane diffusion flame". In: *Applied Optics* 40.15 (2001), pp. 2443–2452.

[193] H A. Michelsen, P. O. Witze, D. Kayes, and S. Hochgreb. "Time-resolved laser-induced incandescence of soot: the influence of experimental factors and microphysical mechanisms". In: *Applied Optics* 42.27 (2003), pp. 5577–5590.

[194] M. Smooke, M. Long, B. Connelly, M. Colket, and R. Hall. "Soot formation in laminar diffusion flames". In: *Combustion and Flame* 143.4 (2005), pp. 613–628.

[195] A Bejaoui. "Étude spectroscopique des suies et de leurs précurseurs par Incandescence et Fluorescence Induite par laser". In: (2012), p. 239.

[196] F. Liu, S. Rogak, D. R. Snelling, M. Saffaripour, K. A. Thomson, and G. J. Smallwood. “Effects of laser fluence non-uniformity on ambient-temperature soot measurements using the auto-compensating laser-induced incandescence technique”. In: *Applied Physics B* 122.11 (2016), p. 286.

[197] B. Menkiel, A. Donkerbroek, R. Uitz, R. Cracknell, and L. Ganippa. “Measurement of in-cylinder soot particles and their distribution in an optical HSDI diesel engine using time resolved laser induced incandescence (TR-LII)”. In: *Combustion and Flame* 159.9 (2012), pp. 2985–2998.

[198] C. R. Shaddix and T. C. Williams. “Analysis of laser focusing effect on quantification of LII images”. In: *Proceedings of the Combustion Institute* 38.1 (2021), pp. 1729–1736.

[199] C. Bohren and Huffman D. *Absorption and scattering of light by small particles*. Wiley, 1983.

[200] Ü. Ö. Köylü and G. M. Faeth. “Optical Properties of Soot in Buoyant Laminar Diffusion Flames”. In: *Journal of Heat Transfer* 116.4 (1994), pp. 971–979.

[201] T. L. Farias, Ü. Ö. Köylü, and M. G. Carvalho. “Range of validity of the Rayleigh–Debye–Gans theory for optics of fractal aggregates”. In: *Applied Optics* 35.33 (1996), p. 6560.

[202] J. Yon, A. Bescond, and F. Liu. “On the radiative properties of soot aggregates part 1: Necking and overlapping”. In: *Journal of Quantitative Spectroscopy and Radiative Transfer* 162 (2015), pp. 197–206.

[203] C. M. Sorensen, J. Yon, F. Liu, J. Maughan, W. R. Heinson, and M. J. Berg. “Light scattering and absorption by fractal aggregates including soot”. In: *Journal of Quantitative Spectroscopy and Radiative Transfer* 217 (2018), pp. 459–473.

[204] F. Liu, K. J. Daun, D. R. Snelling, and G. J. Smallwood. “Heat conduction from a spherical nano-particle: status of modeling heat conduction in laser-induced incandescence”. In: *Applied Physics B* 83.3 (2006), pp. 355–382.

[205] H. A. Michelsen. “Understanding and predicting the temporal response of laser-induced incandescence from carbonaceous particles”. In: *The Journal of Chemical Physics* 118.15 (2003), pp. 7012–7045.

[206] F. O. Goodman. *Dynamics of Gas-Surface Scattering*. Elsevier, 2012.

[207] F. Liu, M. Yang, F. A. Hill, D. R. Snelling, and G. J. Smallwood. “Influence of polydisperse distributions of both primary particle and aggregate size on soot temperature in low-fluence LII”. In: *Applied Physics B* 83.3 (2006), pp. 383–395.

[208] A. L. Bodor. *Numerical modelling of soot formation and evolution in laminar flames with detailed kinetics*.

[209] A. L. Bodor, A. Cuoci, T. Faravelli, and B. Franzelli. “A forward approach for the validation of soot sizing models using laser-induced incandescence (LII)”. In: *Applied Physics B* 126.3 (2020), p. 49.

[210] F. Liu and G. J. Smallwood. “Effects of Detection Wavelengths on Soot Volume Fraction Measurements Using the Auto-Compensating LII Technique”. In: *Combustion Science and Technology* 194.1 (2022), pp. 144–158.

[211] F. Liu, D. R. Snelling, K. A. Thomson, and G. J. Smallwood. “Sensitivity and relative error analyses of soot temperature and volume fraction determined by two-color LII”. In: *Applied Physics B* 96.4 (2009), pp. 623–636.

[212] F. Goulay, L. Nemes, P. E. Schrader, and H. A. Michelsen. “Spontaneous emission from C2(d $3\Pi g$) and C3(A $1\Pi u$) during laser irradiation of soot particles”. In: *Molecular Physics* 108.7-9 (2010), pp. 1013–1025.

[213] S. S. Harilal, Riju C. Issac, C. V. Bindhu, V. P. N. Nampoori, and C. P. G. Vallabhan. “Optical emission studies of species in laser-produced plasma from carbon”. In: *Journal of Physics D: Applied Physics* 30.12 (1997), p. 1703.

[214] S. di Stasio and P. Massoli. “Influence of the soot property uncertainties in temperature and volume-fraction measurements by two-colour pyrometry”. In: *Measurement Science and Technology* 5.12 (1994), p. 1453.

[215] C. Beatrice, C. Bertoli, N. C. Cirillo, N. D. Giacomo, and S. Di Stasio. “Two-Colour Pyrometry Measurements of Soot Loading in a Diesel Engine Burning Model Fuels of Varying Quality”. In: *Combustion Science and Technology* 110-111.1 (1995), pp. 321–339.

[216] P. B. Kuhn, B. Ma, B. C. Connelly, M. D. Smooke, and M. B. Long. “Soot and thin-filament pyrometry using a color digital camera”. In: *Proceedings of the Combustion Institute* 33.1 (2011), pp. 743–750.

[217] Ü. Ö. Köylü, C. S. McEnally, D. E. Rosner, and L. D. Pfefferle. “Simultaneous measurements of soot volume fraction and particle size / microstructure in flames using a thermophoretic sampling technique”. In: *Combustion and Flame* 110.4 (1997), pp. 494–507.

[218] Z.-Q. Zhou, T. U. Ahmed, and M. Y. Choi. “Measurement of dimensionless soot extinction constant using a gravimetric sampling technique”. In: *Experimental Thermal and Fluid Science* 18.1 (1998), pp. 27–32.

[219] M. Y. Choi, G. W. Mulholland, A. Hamins, and T. Kashiwagi. “Comparisons of the soot volume fraction using gravimetric and light extinction techniques”. In: *Combustion and Flame* 102.1 (1995), pp. 161–169.

[220] C. S. McEnally, Ü. Ö. Köylü, L. D. Pfefferle, and D. E. Rosner. “Soot volume fraction and temperature measurements in laminar nonpremixed flames using thermocouples”. In: *Combustion and Flame* 109.4 (1997), pp. 701–720.

[221] A. Sankaranarayanan, S. Lal, R. Sasidharakurup, I. Namboothiri, A. Chowdhury, and N. Kumbhakarna. “Droplet combustion studies on novel cage hydrocarbons using color-ratio pyrometry”. In: *Fuel* 282 (2020), p. 118816.

[222] T.P Jenkins and R.K Hanson. “Soot pyrometry using modulated absorption/emission”. In: *Combustion and Flame* 126.3 (2001), pp. 1669–1679.

[223] G. Legros, Q. Wang, J. Bonnety, M. Kashif, C. Morin, J.-L. Consalvi, and F. Liu. “Simultaneous soot temperature and volume fraction measurements in axis-symmetric flames by a two-dimensional modulated absorption/emission technique”. In: *Combustion and Flame* 162.6 (2015), pp. 2705–2719.

[224] P. S. Greenberg and J. C. Ku. “Soot volume fraction imaging”. In: *Applied Optics* 36.22 (1997), pp. 5514–5522.

[225] D. R. Snelling, R. A. Sawchuk, G. J. Smallwood, and K. Thomson. “Measurement of soot concentration and bulk fluid temperature and velocity using modulated laser-induced incandescence”. In: *Applied Physics B* 119.4 (2015), pp. 697–707.

[226] G. J. Smallwood. *A Critique of Laser-Induced Incandescence for the Measurement of Soot*.

[227] R. K. Chakrabarty, N. D. Beres, H. Moosmüller, S. China, C. Mazzoleni, M. K. Dubey, L. Liu, and M. I. Mishchenko. “Soot superaggregates from flaming wildfires and their direct radiative forcing”. In: *Scientific Reports* 4.1 (2014), p. 5508.

[228] M. L. Botero, N. Eaves, J. A. H. Dreyer, Y. Sheng, J. Akroyd, W. Yang, and M. Kraft. “Experimental and numerical study of the evolution of soot primary particles in a diffusion flame”. In: *Proceedings of the Combustion Institute* 37.2 (2019), pp. 2047–2055.

[229] A. I. Medalia and F. A. Heckman. “Morphology of aggregates—II. Size and shape factors of carbon black aggregates from electron microscopy”. In: *Carbon* 7.5 (1969), pp. 567–582.

[230] J. P. Hessler, S. Seifert, and R. E. Winans. “Spatially resolved small-angle x-ray scattering studies of soot inception and growth”. In: *Proceedings of the Combustion Institute* 29.2 (2002), pp. 2743–2748.

[231] J. Yon et al. “Investigation of soot oxidation by coupling LII, SAXS and scattering measurements”. In: *Combustion and Flame* 190 (2018), pp. 441–453.

[232] S. Schraml, S. Dankers, K. Bader, S. Will, and A. Leipertz. “Soot temperature measurements and implications for time-resolved laser-induced incandescence (TIRE-LII)”. In: *Combustion and Flame* 120.4 (2000), pp. 439–450.

[233] B. Franzelli, M. Roussillo, P. Scouflaire, J. Bonnety, R. Jalain, T. Dormieux, S. Candel, and G. Legros. “Multi-diagnostic soot measurements in a laminar diffusion flame to assess the ISF database consistency”. In: *Proceedings of the Combustion Institute* 37.2 (2019), pp. 1355–1363.

[234] M. Singh, J. P. Abrahamson, and R. L. Vander Wal. “Informing TiRe-LII assumptions for soot nanostructure and optical properties for estimation of soot primary particle diameter”. In: *Applied Physics B* 124.7 (2018), p. 130.

[235] K.J. Daun, B.J. Stagg, F. Liu, G.J. Smallwood, and D.R. Snelling. “Determining aerosol particle size distributions using time-resolved laser-induced incandescence”. In: *Applied Physics B* 87.2 (2007), pp. 363–372.

[236] F. J. Bauer, K. J. Daun, F. J. T. Huber, and S. Will. “Can soot primary particle size distributions be determined using laser-induced incandescence?” In: *Applied Physics B* 125.6 (2019), p. 109.

[237] P. Roth and A. V. Filippov. “In situ ultrafine particle sizing by a combination of pulsed laser heatup and particle thermal emission”. In: *Journal of Aerosol Science* 27.1 (1996), pp. 95–104.

[238] C. E. Batten. “Spectral optical constants of soots from polarized angular reflectance measurements”. In: *Applied Optics* 24.8 (1985), pp. 1193–1199.

[239] J. Mullins and A. Williams. “The optical properties of soot: a comparison between experimental and theoretical values”. In: *Fuel* 66.2 (1987), pp. 277–280.

[240] D. R. Snelling, K. A. Thomson, F. Liu, and G. J. Smallwood. “Comparison of LII derived soot temperature measurements with LII model predictions for soot in a laminar diffusion flame”. In: *Applied Physics B* 96.4 (2009), pp. 657–669.

[241] E. Nordström, N.-E. Olofsson, J. Simonsson, J. Johnsson, H. Bladh, and P.-E. Bengtsson. “Local gas heating in sooting flames by heat transfer from laser-heated particles investigated using rotational CARS and LII”. In: *Proceedings of the Combustion Institute* 35.3 (2015), pp. 3707–3713.

[242] R. Mansmann, K. Thomson, G. Smallwood, T. Dreier, and C. Schulz. “Sequential signal detection for high dynamic range time-resolved laser-induced incandescence”. In: *Optics Express* 25.3 (2017), p. 2413.

[243] A. M. Bennett, E. Cenker, and W. L. Roberts. “Effects of soot volume fraction on local gas heating and particle sizing using laser induced incandescence”. In: *Journal of Aerosol Science* 149 (2020), p. 105598.

[244] E. Cenker, A. Bennett, and W. L. Roberts. “Investigations of the long-term effects of LII on soot and bath gas”. In: *Aerosol Science and Technology* 51.12 (2017), pp. 1354–1367.

[245] R. L. Vander Wal, T. M. Ticich, and A. B. Stephens. “Optical and microscopy investigations of soot structure alterations by laser-induced incandescence”. In: *Applied Physics B* 67.1 (1998), pp. 115–123.

[246] E. Cenker and W. L. Roberts. “Quantitative effects of rapid heating on soot-particle sizing through analysis of two-pulse LII”. In: *Applied Physics B* 123.3 (2017), p. 74.

[247] S. Török, M. Mannazhi, S. Bergqvist, K. C. Le, and P.-E. Bengtsson. “Influence of rapid laser heating on differently matured soot with double-pulse laser-induced incandescence”. In: *Aerosol Science and Technology* 56.6 (2022), pp. 488–501.

[248] F. Migliorini, S. De Iuliis, R. Dondè, M. Commodo, P. Minutolo, and A. D’Anna. “Nanosecond laser irradiation of soot particles: Insights on structure and optical properties”. In: *Experimental Thermal and Fluid Science* 114 (2020), p. 110064.

[249] B. M. Crosland, M. R. Johnson, and K. A. Thomson. “Analysis of uncertainties in instantaneous soot volume fraction measurements using two-dimensional, auto-compensating, laser-induced incandescence (2D-AC-LII)”. In: *Applied Physics B* 102.1 (2011), pp. 173–183.

[250] T. A. Sipkens, J. Menser, R. Mansmann, C. Schulz, and K. J. Daun. “Investigating temporal variation in the apparent volume fraction measured by time-resolved laser-induced incandescence”. In: *Applied Physics B* 125.8 (2019), p. 140.

[251] T. A. Sipkens, N. R. Singh, and K. J. Daun. “Time-resolved laser-induced incandescence characterization of metal nanoparticles”. In: *Applied Physics B* 123.1 (2016), p. 14.

[252] P. J. Hadwin, T. A. Sipkens, K. A. Thomson, F. Liu, and K. J. Daun. “Quantifying uncertainty in soot volume fraction estimates using Bayesian inference of auto-correlated laser-induced incandescence measurements”. In: *Applied Physics B* 122.1 (2016), p. 1.

[253] M. D. Smooke, C. S. McEnally, L. D. Pfefferle, R. J. Hall, and M. B. Colket. “Computational and experimental study of soot formation in a coflow, laminar diffusion flame”. In: *Combustion and Flame* 117.1 (1999), pp. 117–139.

[254] A. M. Vargas and Ö. L. Gülder. “Pressure dependence of primary soot particle size determined using thermophoretic sampling in laminar methane-air diffusion flames”. In: *Proceedings of the Combustion Institute* 36.1 (2017), pp. 975–984.

[255] L. Basta, A. Pignatelli, F. Sasso, F. Picca, M. Commodo, P. Minutolo, J. W. Martin, and A. D’Anna. “The effect of ozone on soot formation in partially premixed laminar methane/air flames”. In: *Fuel* 373 (2024), p. 132342.

[256] H. Bladh, P.-E. Bengtsson, J. Delhay, Y. Bouvier, E. Therssen, and P. Desgroux. “Experimental and theoretical comparison of spatially resolved laser-induced incandescence (LII) signals of soot in backward and right-angle configuration”. In: *Applied Physics B* 83.3 (2006), p. 423.

[257] A. Boiarciuc, F. Foucher, and C. Mounaïm-Rousselle. “Soot volume fractions and primary particle size estimate by means of the simultaneous two-color-time-resolved and 2D laser-induced incandescence”. In: *Applied Physics B* 83.3 (2006), p. 413.

[258] M. Bouvier, G. Cabot, J. Yon, and F. Grisch. “On the use of PIV, LII, PAH-PLIF and OH-PLIF for the study of soot formation and flame structure in a swirl stratified premixed ethylene/air flame”. In: *Proceedings of the Combustion Institute* 38.1 (2021), pp. 1851–1858.

[259] A. Guibaud, J.M. Citerne, J.M. Orlac’h, O. Fujita, J.-L. Consalvi, J.L. Torero, and G. Legros. “Broadband modulated absorption/emission technique to probe sooting flames: Implementation, validation, and limitations”. In: *Proceedings of the Combustion Institute* 37.3 (2019), pp. 3959–3966.

[260] M. Roussillo, P. Scouflaire, S. Candel, and B. Franzelli. “Experimental investigation of soot production in a confined swirled flame operating under perfectly premixed rich conditions”. In: *Proceedings of the Combustion Institute* 37.1 (2019), pp. 893–901.

[261] D. Bartos, M. Sirignano, M. J. Dunn, A. D’Anna, and A. R. Masri. “Soot inception in laminar coflow diffusion flames”. In: *Combustion and Flame* 205 (2019), pp. 180–192.

[262] F. Migliorini, S. De Iuliis, S. Maffi, and G. Zizak. “Saturation curves of two-color laser-induced incandescence measurements for the investigation of soot optical properties”. In: *Applied Physics B* 120.3 (2015), pp. 417–427.

[263] H. Chu, W. Han, W. Cao, M. Gu, and G. Xu. “Effect of methane addition to ethylene on the morphology and size distribution of soot in a laminar co-flow diffusion flame”. In: *Energy* 166 (2019), pp. 392–400.

[264] F. Patiño, J. J. Cruz, I. Verdugo, J. Morán, J. L. Consalvi, F. Liu, X. Du, and A. Fuentes. “Soot primary particle sizing in a n-heptane doped methane/air laminar coflow diffusion flame by planar two-color TiRe-LII and TEM image analysis”. In: *Fuel* 266 (2020), p. 117030.

[265] H. Bladh, N.-E. Olofsson, T. Mouton, J. Simonsson, X. Mercier, A. Faccinetto, P.-E. Bengtsson, and P. Desgroux. “Probing the smallest soot particles in low-sooting premixed flames using laser-induced incandescence”. In: *Proceedings of the Combustion Institute* 35.2 (2015), pp. 1843–1850.

[266] M. D. Smooke, R. J. Hall, M. B. Colket, J. Fielding, M. B. Long, C. S. McEnally, and L. D. Pfefferle. “Investigation of the transition from lightly sooting towards heavily sooting co-flow ethylene diffusion flames”. In: *Combustion Theory and Modelling* 8.3 (2004), pp. 593–606.

[267] D. R. Snelling, G. J. Smallwood, F. Liu, Ö. L. Gülder, and W. D. Bachalo. “A calibration-independent laser-induced incandescence technique for soot measurement by detecting absolute light intensity”. In: *Applied Optics* 44.31 (2005), p. 6773.

[268] F. Liu, B. J. Stagg, D. R. Snelling, and G. J. Smallwood. “Effects of primary soot particle size distribution on the temperature of soot particles heated by a nanosecond pulsed laser in an atmospheric laminar diffusion flame”. In: *International Journal of Heat and Mass Transfer* 49.3 (2006), pp. 777–788.

[269] N.-E. Olofsson, J. Johnsson, H. Bladh, and P.-E. Bengtsson. “Soot sublimation studies in a premixed flat flame using laser-induced incandescence (LII) and elastic light scattering (ELS)”. In: *Applied Physics B* 112.3 (2013), pp. 333–342.

[270] N.-E. Olofsson, J. Simonsson, S. Török, H. Bladh, and P.-E. Bengtsson. “Evolution of properties for aging soot in premixed flat flames studied by laser-induced incandescence and elastic light scattering”. In: *Applied Physics B* 119.4 (2015), pp. 669–683.

[271] R. L Vander Wal and M. Y. Choi. “Pulsed laser heating of soot: morphological changes”. In: *Carbon* 37.2 (1999), pp. 231–239.

[272] S. De Iuliis, F. Cignoli, S. Maffi, and G. Zizak. “Influence of the cumulative effects of multiple laser pulses on laser-induced incandescence signals from soot”. In: *Applied Physics B* 104.2 (2011), pp. 321–330.

[273] H. A. Michelsen, A. V. Tivanski, M. K. Gilles, L. H. V. Poppel, M. A. Dansson, and P. R. Buseck. “Particle formation from pulsed laser irradiation of soot aggregates studied with a scanning mobility particle sizer, a transmission electron microscope, and a scanning transmission x-ray microscope”. In: *Applied Optics* 46.6 (2007), pp. 959–977.

[274] B. C. Connelly. *Quantitative characterization of steady and time-varying, sooting, laminar diffusion flames using optical techniques*. 2009.

[275] N. J. Kempema. *Quantitative Characterization of Sooting Ethylene Coflow Laminar Diffusion Flames with Optical Diagnostics and Thermophoretic Sampling*. 2016.

[276] N. J. Kempema and M. B. Long. “Combined optical and TEM investigations for a detailed characterization of soot aggregate properties in a laminar coflow diffusion flame”. In: *Combustion and Flame* 164 (2016), pp. 373–385.

[277] V. Beyer and D. A. Greenhalgh. “Laser induced incandescence under high vacuum conditions”. In: *Applied Physics B* 83.3 (2006), pp. 455–467.

[278] M. M. Maricq and N. Xu. “The effective density and fractal dimension of soot particles from premixed flames and motor vehicle exhaust”. In: *Journal of Aerosol Science* 35.10 (2004), pp. 1251–1274.

[279] G. Lefevre. *Caractérisation des propriétés radiatives des nanoparticules de suie en présence de composés organiques*. 2018.

[280] J. Olfert and S. Rogak. “Universal relations between soot effective density and primary particle size for common combustion sources”. In: *Aerosol Science and Technology* 53.5 (2019), pp. 485–492.

[281] H.-C. Chang and T. T. Charalampopoulos. “Determination of the wavelength dependence of refractive indices of flame soot”. In: *Proceedings of the Royal Society of London. Series A: Mathematical and Physical Sciences* 430.1880 (1997), pp. 577–591.

[282] carbone4. *Low-carbon hydrogen: what are the relevant medium-term uses in a decarbonized world?* 2022. url: `https://www.carbone4.com/files/Carbone_4_low_carbon_hydrogen.pdf`.

[283] M. Wright and A. Lewis. “Decarbonisation of heavy-duty diesel engines using hydrogen fuel: a review of the potential impact on NO x emissions”. In: *Environmental Science: Atmospheres* 2 (2022).

[284] H. A. Alrazen, A. R. Abu Talib, R. Adnan, and K. A. Ahmad. “A review of the effect of hydrogen addition on the performance and emissions of the compression – Ignition engine”. In: *Renewable and Sustainable Energy Reviews* 54 (2016), pp. 785–796.

[285] International Energy Agency. *Global Hydrogen Review 2021*. 2021. url: `https://www.iea.org/reports/global-hydrogen-review-2021`.

[286] Ö. L. Gülder, D. R. Snelling, and R. A. Sawchuk. “Influence of hydrogen addition to fuel on temperature field and soot formation in diffusion flames”. In: *Symposium (International) on Combustion* 26.2 (1996), pp. 2351–2358.

[287] D. X. Du, R. L. Axelbaum, and C. K. Law. “Soot formation in strained diffusion flames with gaseous additives”. In: *Combustion and Flame* 102.1 (1995), pp. 11–20.

[288] P. Pandey, B. P. Pundir, and P. K. Panigrahi. “Hydrogen addition to acetylene–air laminar diffusion flames: Studies on soot formation under different flow arrangements”. In: *Combustion and Flame* 148.4 (2007), pp. 249–262.

[289] S.-H. Park, K.-M. Lee, and C.-H. Hwang. “Effects of hydrogen addition on soot formation and oxidation in laminar premixed C2H2/air flames”. In: *International Journal of Hydrogen Energy* 36.15 (2011), pp. 9304–9311.

[290] F. Migliorini, S. De Iuliis, F. Cignoli, G. Zizak, and M. Sirignano. “Effect of Hydrogen Addition on Soot volume Fraction in Rich Premixed Ethylene/Air Flames”. In: *Meeting of Italian Section of the Combustion Institute, Torino, June 17-20* (2008).

[291] H. Zhao, R. Stone, and B. Williams. “Investigation of the Soot Formation in Ethylene Laminar Diffusion Flames When Diluted with Helium or Supplemented by Hydrogen | Energy & Fuels”. In: *Energy & Fuels* 28.3 (2014), pp. 2144–2151.

[292] H.-Q. Do, A. Faccinetto, L.-S. Tran, P. Desgroux, L. Gasnot, A. El Bakali, and X. Mercier. “Hydrogen as a fuel additive in laminar premixed methane flames: Impact on the nucleation and growth of soot particles”. In: *Fuel* 315 (2022), p. 123125.

[293] Y. Wang, M. Gu, Y. Zhu, L. Cao, B. Zhu, J. Wu, Y. Lin, and X. Huang. “A review of the effects of hydrogen, carbon dioxide, and water vapor addition on soot formation in hydrocarbon flames”. In: *International Journal of Hydrogen Energy* 46.61 (2021), pp. 31400–31427.

[294] M. Wang, X. Qian, Y. Suo, Y. Ye, G. Li, and Z. Zhang. “Effect of Hydrogen Addition on Soot Formation and Emission in Acetylene Laminar Diffusion Flame”. In: *ACS Omega* 8.28 (2023), pp. 24893–24900.

[295] R. L. Axelbaum, C. K. Law, and W. L. Flower. “Preferential diffusion and concentration modification in sooting counterflow diffusion flames”. In: *Symposium (International) on Combustion* 22.1 (1989), pp. 379–386.

[296] Z. Sun, B. Dally, G. Nathan, and Z. Alwahabi. “Effects of hydrogen and nitrogen on soot volume fraction, primary particle diameter and temperature in laminar ethylene/air diffusion flames”. In: *Combustion and Flame*. Special Issue in Honor of Norbert Peters 175 (2017), pp. 270–282.

[297] H. Guo, F. Liu, G. J. Smallwood, and Ö. L. Gülder. “Numerical study on the influence of hydrogen addition on soot formation in a laminar ethylene–air diffusion flame”. In: *Combustion and Flame* 145.1 (2006), pp. 324–338.

[298] F. Liu, Y. Ai, and W. Kong. “Effect of hydrogen and helium addition to fuel on soot formation in an axisymmetric coflow laminar methane/air diffusion flame”. In: *International Journal of Hydrogen Energy* 39.8 (2014), pp. 3936–3946.

[299] M. Wei, J. Liu, G. Guo, and S. Li. “The effects of hydrogen addition on soot particle size distribution functions in laminar premixed flame”. In: *International Journal of Hydrogen Energy* 41.14 (2016), pp. 6162–6169.

[300] H.-Q. Do, L.-S. Tran, L. Gasnot, X. Mercier, and A. El Bakali. “Experimental study of the influence of hydrogen as a fuel additive on the formation of soot precursors and particles in atmospheric laminar premixed flames of methane”. In: *Fuel* 287 (2021), p. 119517.

[301] B. S. Haynes, H. Jander, H. Mätzing, and H. Gg. Wagner. “The influence of gaseous additives on the formation of soot in premixed flames”. In: *Symposium (International) on Combustion*. Nineteenth Symposium (International) on Combustion 19.1 (1982), pp. 1379–1385.

[302] A. Cuoci, A. Frassoldati, T. Faravelli, and E. Ranzi. “OpenSMOKE++: An object-oriented framework for the numerical modeling of reactive systems with detailed kinetic mechanisms”. In: *Computer Physics Communications* 192 (2015), pp. 237–264.

[303] W. Pejpichestakul, E. Ranzi, M. Pelucchi, A. Frassoldati, A. Cuoci, A. Parente, and T. Faravelli. “Examination of a soot model in premixed laminar flames at fuel-rich conditions”. In: *Proceedings of the Combustion Institute* 37.1 (2019), pp. 1013–1021.

[304] A. Nobili, A. Cuoci, W. Pejpichestakul, M. Pelucchi, C. Cavallotti, and T. Faravelli. “Modeling soot particles as stable radicals: a chemical kinetic study on formation and oxidation. Part I. Soot formation in ethylene laminar premixed and counterflow diffusion flames”. In: *Combustion and Flame* 243 (2022), p. 112073.

[305] A. Nobili, W. Pejpichestakul, M. Pelucchi, A. Cuoci, C. Cavallotti, and T. Faravelli. “Modeling soot particles as stable radicals: a chemical kinetic study on formation and oxidation. Part II. Soot oxidation in flow reactors and laminar flames”. In: *Combustion and Flame* 243 (2022), p. 112072.

[306] NASA. *Chemical Equilibrium with Applications*. url: `https://cearun.grc.nasa.gov/`.

[307] A. Nobili, L. Pratali Maffei, A. Baggioli, M. Pelucchi, A. Cuoci, C. Cavallotti, and T. Faravelli. “On the radical behavior of large polycyclic aromatic hydrocarbons in soot formation and oxidation”. In: *Combustion and Flame* 235 (2022), p. 111692.

[308] K. Muñoz-Feucht, A. Fuentes, and J. L. Consalvi. “Soot volume fraction measurements in a forest fuel layer”. In: *Experimental Thermal and Fluid Science*. Eighth Mediterranean Combustion Symposium 56 (2014), pp. 61–68.

[309] C. Russo, F. Stanzione, A. Tregrossi, and A. Ciajolo. “Light Absorption Coefficient and Hydrogen Content as Key Properties for Inferring Structural Features of Soot”. In: *Combustion Science and Technology* 186.4-5 (2014), pp. 634–643.

[310] J. Taine, F. Enguehard, and E. Iacona. *Transferts thermiques - 5E edition*. OCLC: 1236132565. S.l.: DUNOD, 2014.

[311] *Sooting Yale Coflow Diffusion Flames*. url: `http://guilford.eng.yale.edu/yalecoflowflames/sooting.html`.

[312] Wikipedia. *Random sample consensus*. url: `https://en.wikipedia.org/wiki/Random_sample_consensus`.

[313] F. Liu and G. J. Smallwood. “Relationship between soot volume fraction and LII signal in AC-LII: effect of primary soot particle diameter polydispersity”. In: *Applied Physics B* 112.3 (2013), pp. 307–319.

[314] W. Pejpichestakul, A. Frassoldati, A. Parente, and T. Faravelli. “Kinetic modeling of soot formation in premixed burner-stabilized stagnation ethylene flames at heavily sooting condition”. In: *Fuel* 234 (2018), pp. 199–206.

Resumé

Les particules de suie sont des particules carbonées formées par la combustion incomplète de combustibles contenant du carbone (hydrocarbures, biomasse). Elles sont une agrégation de particules plus petites - les particules primaires de suie - d'une taille typique de 3 à 50 nm. Les particules de suie sont des polluants atmosphériques nocifs qui ont un impact significatif sur la santé humaine ainsi que sur l'environnement. En raison de leurs effets néfastes, les réglementations en matière d'émissions deviennent de plus en plus strictes. Pour réduire efficacement les émissions de suie, la recherche fondamentale est essentielle pour mieux comprendre les processus de formation de la suie et améliorer notre connaissance de leurs propriétés.

Les travaux expérimentaux jouent un rôle essentiel dans l'amélioration de notre compréhension des processus de formation de la suie et dans la validation des modèles de formation des suies dans les flammes. La technique d'incandescence induite par laser (LII), qui est au cœur de cette thèse, est un diagnostic optique permettant de mesurer *in situ* les particules de suie dans les flammes. Durant la LII, un pulse laser à haute énergie chauffe les particules de suie à de très hautes températures (2500-4500 K), ce qui amène ces suies à rayonner fortement par incandescence. En collectant le signal LII émit, il est possible d'obtenir des informations sur les suies chauffées par le laser. La LII permet de mesurer la température des suies, la fraction volumique de suie f_v, le diamètre des particules primaires de suie d_p, et la fonction d'absorption des suies $E(m_\lambda)$, qui caractérise l'émission/absorption de la lumière par les particules. Au cours de leur développement, les particules de suie voient leurs propriétés physiques, optiques et chimiques évoluer avec leur niveau de maturité (allant de particules naissantes à totalement mature). La connaissance de $E(m_\lambda)$ permet de caractériser la maturité des suies.

Reconnaissant que les flammes brûlent principalement dans le régime turbulent, une technique basée sur la LII a d'abord été théoriquement développée pour mesurer $E(m_\lambda)$ et la température du gaz T_0 dans des conditions de flammes turbulentes : la technique de la LII à pulses séparés (SP-LII). Cette technique repose sur la mesure des températures atteintes par les suies après chauffage par deux pulses lasers consécutifs. Deux méthodes de traitement des données sont présentées, la plus simple nommée "absorption model" (AM) repose sur des simplifications du bilan énergétique appliqué à une suie, et l'autre plus complète nommée "look-up table" (LUT) nécessite l'utilisation d'un code LII (un code numérique simulant le processus LII). Une analyse numérique de la technique SP-LII a été réalisée pour évaluer ses performances et ses incertitudes. Cette analyse a notamment montré qu'il est important de minimiser l'erreur sur la mesure de température des suies. Mais aussi qu'il est crucial de choisir avec attention la fluence des pulses laser pour limiter la chauffe des suies à une température inférieure à leur température de sublimation. La méthode AM à prouvé être efficace dans la plupart des cas, mais perd en précision lorsque les particules de suie sont chauffée à des températures amenant une sublimation partielle. Globalement, la méthode LUT est légèrement plus performante que la méthode AM. Cependant, elle nécessite plus d'entrées qui sont pour la plupart inconnues. La méthode AM sera donc préférée dans ce travail.

Dans un premier temps, la faisabilité de la technique SP-LII a été démontrée en considérant une flamme de diffusion

laminaire CH_4/air et des mesures ponctuelles. Pour ce faire, un banc d'essai expérimental a été conçu et mis en œuvre. Des mesures quantitatives de $E(m_\lambda)$ et T_0 ont été effectuées par SP-LII, complétées par des mesures de f_v et d_p via la LII auto-compensée (AC-LII) et la LII résolue en temps (Tire-LII), respectivement. Ces quatre quantités ont été dérivées uniquement à partir des mesures LII, ce qui a permis de minimiser le besoin de diagnostics supplémentaires et de réduire la complexité et le coût de la campagne expérimentale. L'étape cruciale de choix des fluences laser est basé sur la limite de linéarité des courbes de température de chauffe des suies T_M en fonction de la fluence laser. La flamme étudiée n'étant pas une flamme de référence, les résultats obtenus sont comparés à ceux de la littérature pour des flammes comparables, et ont montré un bon accord, démontrant ainsi la viabilité de l'approche retenue.

Dans un second temps, le banc expérimental a été modifié pour effectuer des mesures 2D de $E(m_\lambda)$, T_0, f_v, et d_p. Ces mesures ont été effectuées dans une flamme de diffusion laminaire (C_2H_4+N_2/air) de référence afin de valider la stratégie proposée par rapport aux données de la littérature existante. Un effort particulier a été fait pour améliorer la précision de la caractérisation des suies, notamment en s'adressant à la "f_v anomaly" : une dépendance anormale de la fraction volumique des suies à la fluence du pulse laser chauffant les suies. Une correction est proposée pour réduire cette dépendance illégitime de f_v à la fluence laser, et il est montré que pour cette flamme, les mesures doivent être effectué en considérant des fluences laser amenant à des températures de suies en dessous de 3500 K. La comparaison des résultats à la littérature montre globalement un bon accord malgré une surestimation de $E(m_\lambda)$ pour les suies matures.

Enfin, ce travail a exploré les effets de l'hydrogène sur la formation de suie en comparant une flamme d'éthylène de référence à une flamme d'hydrogène-éthylène, en se concentrant sur les différences de f_v, d_p, T_0, et $E(m_\lambda)$. Les mesures expérimentales ont révélé que le mélange avec H_2 modifie la structure de flamme (flamme plus courte, décalage en amont de l'apparition, la maturation et l'oxydation des suies le long de l'axe de la flamme). De plus, f_v est presque doublé dans le cœur de la flamme tandis qu'il est réduit dans les ailes. Le volume total de suies dans la flamme est également augmenté alors que la quantité de carbone injecté est réduite. Cependant, $E(m_\lambda)$, T_0, et d_p ne sont pas impactés de manière significative. Les résultats expérimentaux ont été comparés à des simulations numériques afin de valider un modèle de suie détaillé. En ce qui concerne les profils de température, les prévisions numériques sont généralement inférieures d'au moins 100 K, mais les tendances expérimentales sont reproduites. La fraction volumique de suie a également été raisonnablement prédite, les simulations capturant correctement l'augmentation de la concentration de suie dans le cœur et la réduction des ailes dans la flamme H_2. Cependant, le modèle a surestimé la formation de suie, en particulier dans les ailes, et n'a pas été en mesure de saisir l'augmentation du volume de suie avec le mélange de H_2. Une corrélation a pu être établie entre $E(m_\lambda)$ déterminé expérimentalement et $\frac{C}{H}$ calculé numériquement. Ainsi, le suivi de $\frac{C}{H}$ renseigne sur la maturité et les variations de la fonction d'absorption de la suie. En conclusion, le modèle numérique capture de manière adéquate le comportement qualitatif de la formation de suie dans ces flammes, ce qui en fait un outil précieux pour explorer les mécanismes à l'origine des différences dans la production de suie avec le mélange H_2. Cependant, l'exploitation des simulations numériques pour expliquer les différences observées dans les profils de concentration de suie n'a pas été réalisée dans cette thèse et est laissée pour un travail futur.

Cette thèse démontre que quatre quantités clé pour l'étude des suies peuvent être mesurées dans des flammes laminaires à l'aide d'un seul dispositif expérimental, qui pourrait être étendu à des applications dans des conditions de flammes turbulentes.